

**INMATEH -**

**AGRICULTURAL  
ENGINEERING**

**SEPTEMBER - DECEMBER**

*No liability is assumed by the editorial staff for the content of scientific papers and opinions published in this volume. They represent the author's point of view*

## *Editorial*

*The National Institute of Research-Development for Machines and Installations designed to Agriculture and Food Industry - INMA Bucharest has the oldest and most prestigious research activity in the field of agricultural machinery and mechanizing technologies in Romania.*

### *Short History*

- ✓ *In 1927, the first research Center for Agricultural Machinery in Agricultural Research Institute of Romania - ICAR (Establishing Law was published in O.D. no. 97/05.05.1927) was established;*
- ✓ *In 1930, was founded The Testing Department of Agricultural Machinery and Tools by transforming Agricultural Research Centre of ICAR- that founded the science of methodologies and experimental techniques in the field (Decision no. 2000/1930 of ICAR Manager - GHEORGHE IONESCU ȘIȘEȘTI);*
- ✓ *In 1952, was established the Research Institute for Mechanization and Electrification of Agriculture - ICMA Băneasa, by transforming the Department of Agricultural Machines and Tools Testing;*
- ✓ *In 1979, the Research Institute of Scientific and Technological Engineering for Agricultural Machinery and Tools - ICSITMUA was founded - subordinated to Ministry of Machine Building Industry - MICM, by unifying ICMA subordinated to MAA with ICPMA subordinated to MICM;*
- ✓ *In 1996 the National Institute of Research-Development for Machines and Installations designed to Agriculture and Food Industry - INMA was founded - according to G.D. no. 1308/25.11.1996, by reorganizing ICSITMUA, G.D no. 1308/1996 coordinated by the Ministry of Education and Research G.D. no. 823/2004;*
- ✓ *In 2008 INMA has been accredited to carry out research and developing activities financed from public funds under G.D. no. 551/2007, Decision of the National Authority for Scientific Research - ANCSno. 9634/2008.*

*As a result of widening the spectrum of communication, dissemination and implementation of scientific research results, in 2000 was founded the institute magazine, issued under the name of SCIENTIFIC PAPERS (INMATEH), ISSN 1583 – 1019.*

*Starting with volume 30, no. 1/2010, the magazine changed its name to INMATEH - *Agricultural Engineering*, appearing both in print format (ISSN 2068 - 4215), and online (ISSN online: 2068 - 2239). The magazine is bilingual, abstract being published in native language and English, with a rhythm of three issues / year: January-April, May-August, September-December and is recognized by CNCSIS – with B<sup>+</sup> category. Published articles are from the field of AGRICULTURAL ENGINEERING: technologies and technical equipment for agriculture and food industry, renewable energy, machinery testing, environment, transport in agriculture etc. and are evaluated by specialists inside the country and abroad, in mentioned domains.*

*Technical level and performance processes, technology and machinery for agriculture and food industry increasing, according to national requirements and European and international regulations, as well as exploitation of renewable resources in terms of efficiency, life, health and environment protection represent referential elements for the magazine „INMATEH - *Agricultural Engineering*”.*

*We are thankful to all readers, publishers and assessors.*

*Editor in chief,*

*Ph. D. Eng. Vladut Nicolae-Valentin*

**Managing Editorial Board - INMA Bucharest****Editor in Chief****Nicolae-Valentin VLADUȚ**

Ph.D.Eng, SR I

**Executive Editor****Lucreția POPA**

Ph.D.Eng, SR I

**Assistant Editor****Mihai-Gabriel MATACHE**

Ph.D.Eng, SR I

**Logistic support, database****Virgil MURARU**

Ph.D.Eng, SR I

**Scientific Secretary****Cârdei Petre, math.****Official translator****RADU Daniela-Cristina, English****Editorial Board**

- Prof.Ph.D.Eng. QUENDLER Elisabeth – Austria, Univ. of Natural Resources & Applied Life Sciences;
- Ir. HUYGHEBAERT Bruno – Belgia, Walloon Agricultural Research Center CRA-W;
- Prof.Ph.D.Eng. FABBRO Dal Inacio Maria - Brazil, Campinas State University;
- Prof.Ph.D.Eng. ATANASOV Atanas – Bulgaria, "Angel Kanchev" University of Rousse
- Prof.Ph.D.Eng. BILANDZIJA Nikola – Croatia, Zagreb University, Faculty of Agriculture;
- Prof.Ph.D.Eng. KOSUTIC Silvio – Croatia, Zagreb University, Faculty of Agriculture;
- Prof.Ph.D.Eng. GONZALEZ Omar - Cuba, Central University "Marta Abreu" de las Villas;
- Prof.Ph.D.Eng. KATHIJOTES Nicholas – Cyprus, University of Nicosia;
- Prof.Ph.D.Eng. HERAK David - Czech Republic, Czech University of Agriculture Prague;
- Prof.Ph.D.Eng. COZ Alberto – Spain, University of Cantabria, School of Nautical Studies;
- Prof.Ph.D.Eng. FENYVESI László – Hungary, Hungarian Institute of Agricultural Engineering Godolo;
- Ph.D.Eng. ALIZADEH Mohammad Reza– Iran, Rice Research Institute of Iran (RRII);
- Prof.Ph.D.Eng. DE WRACHIEN Daniele - Italy, State University of Milan;
- Ph.D.Eng. BIOCCA Marcello - Italy, Agricultural Research Council;
- Prof.Ph.D.Eng. SARAUSKIS Egidijus – Lithuania, Vytautas Magnus University, Faculty of Agricultural Engineering;
- Prof.Ph.D.Eng. EKIELSKI Adam - Poland, Warsaw University of Life Sciences;
- Prof.Ph.D.Eng. SAVIN Lazar– Serbia, Univ.of Novi Sad,
- Prof.Ph.D.Eng. SIMKIC Mirko– Serbia, Univ.of Novi Sad;
- Prof.Ph.D.Eng. ERTEKIN Can - Turkey, Akdeniz University Antalya;
- Prof.Ph.D.Eng. KABAŞ Önder –Turkey, Akdeniz University;
- Prof.Ph.D.Eng. SELVİ Kemal Çağatay - Turkey, Ondokuz Mayıs University;
- Prof.Ph.D.Eng. BULGAKOV Volodymyr – Ukraine, National University of Life and Environmental Sciences of Ukraine
- Prof.Ph.D.Eng. HEVKO Roman Bohdanovich - Ternopil National Economic University, Faculty of Agricultural Economics and Management
- Prof. Ph.D. Eng. PARASCHIV Gigel - Romania, Politehnica University of Bucharest;
- Prof. Ph.D. Eng. VOICU Gheorghe - Romania, P.U. Bucharest;
- Prof. Ph.D.Eng. BIRIȘ Sorin - Romania, P.U. Bucharest;
- Prof.Ph.D.Eng. MAICAN Edmond - Romania, Politehnica University of Bucharest;
- Prof. Ph.D.Eng. TEODORESCU Răzvan-Ionuț - Romania, USAMV Bucharest;
- Prof.Ph.D. Eng. VLASE Sorin - Romania, "Transilvania" University of Brașov;
- Prof.Ph.D.Eng. FILIP Nicolae - Romania, Technical University Cluj Napoca;
- Prof.Ph.D. Eng. COZAR Onuc-Romania, „Babes-Bolyai” University of Cluj-Napoca;
- Prof. Ph.D. Eng. ȚENU Ioan - Romania, USAMV Iași;
- Prof.Ph.D. Eng. HERIȘANU Nicolae - Romania, Politehnica University of Timisoara
- Prof.Ph.D.Eng. GERGEN Iosif - Romania, USAMVB Timișoara;
- Prof.Ph.D.Eng. BORDEAN Despina-Maria - Romania, USAMVB Timișoara;
- Prof.Ph.D.Eng. BUNGESCU Sorin - Romania, USAMVB Timișoara;
- Ph.D.Eng. VOICEA Iulian - Romania, INMA Bucharest
- Ph.D.Eng. DEAK Gyorgy - Romania, INCDPM;
- Prof. Ph.D.Eng. BELC Nastasia - Romania, IBA Bucharest;
- Ph.D. Eng. BUȚU Alina - Romania, INCDSB Bucharest

**INMATEH - Agricultural Engineering journal is indexed in the next international databases:**

ELSEVIER /SciVerse SCOPUS, CLARIVATE ANALYTICS - WEB of SCIENCE- Emerging Sources Citation Index (ESCI),  
 ULRICHS Web: Global Serials Directory, CABI, SCIPRO, Index COPERNICUS International, EBSCO Publishing,  
 Elektronische Zeitschriftenbibliothek

**INMATEH - Agricultural Engineering****vol. 62, no.3 / 2020**

e-ISSN: 2068 – 2239; p: ISSN: 2068 – 4215

<https://inmateh.eu/>E-mail: [inmatehjournal@gmail.com](mailto:inmatehjournal@gmail.com)Edited by: **INMA Bucharest****Copyright: INMA Bucharest / Romania**

National Institute for Research-Development of Machines and Installations  
 Designed for Agriculture and Food Industry - INMA Bucharest  
 6, Ion Ionescu de la Brad Bvd., sector 1, Bucharest, ROMANIA

## CONTENT

		Page(s)
1.	<p><b>PARAMETER OPTIMIZATION AND EXPERIMENT OF ORCHARD DOUBLE ROW DITCHING-FERTILIZING MACHINE / 果园双行开沟施肥机的参数优化与试验</b></p> <p>HongJian Zhang<sup>1)</sup>, ChunBao Xu<sup>1)</sup>, ShuangXi Liu<sup>1,2)</sup>, Hao Jiang<sup>1)</sup>, Xuemei Liu<sup>1)</sup>, JinXing Wang<sup>*1,3)</sup></p> <p><sup>1)</sup> College of Mechanical and Electronic Engineering, Shandong Agricultural University, Taian / China;  <sup>2)</sup> Shandong Provincial Key Laboratory of Horticultural Machinery and Equipment, Taian 271018, China;  <sup>3)</sup> Shandong Provincial Engineering Laboratory of Agricultural Equipment Intelligence, Taian 271018, China</p>	09
2.	<p><b>STUDY ON THE BEHAVIOR OF A BATTERY MOUNTED ON AN ELECTRIC TRACTOR PROTOTYPE / STUDIUL PRIVIND COMPORTAMENTUL UNEI BATERII DE ACUMULATORI MONTATĂ PE UN PROTOTIP DE TRACTOR ELECTRIC</b></p> <p>Cristea M.<sup>1)</sup>, Matache M.<sup>1)</sup>, Sorică C.<sup>1)</sup>, Biriș S.Șt.<sup>*2)</sup>, Ungureanu N.<sup>2)</sup>, Cristea R.D.<sup>2)</sup></p> <p><sup>1)</sup> INMA Bucharest;  <sup>2)</sup> Universities Polytechnic Bucharest, Faculty of Biotechnical Systems Engineering / Romania</p>	19
3.	<p><b>EXPERIMENTAL RESEARCH ON COMPREHENSIVE PERFORMANCE OF COUPLED MUFFLER BASED ON SPLIT-STREAM RUSHING PRINCIPLE / 基于分流气体对冲原理的耦合消声器综合性能的试验研究</b></p> <p>Jing Xue, Pei Wu<sup>*)</sup>, He Su, Yongan Zhang, Haijun Zhang</p> <p>College of Mechanical and Electrical Engineering, Inner Mongolia Agricultural University, Hohhot 010018, China</p>	29
4.	<p><b>DESIGN OF TEMPERATURE AND HUMIDITY CONTROLLER OF AGRICULTURAL INTELLIGENT TOBACCO HOUSE BASED ON STM32 / 基于 STM32 的农业智能烤烟房温湿度控制仪的设计</b></p> <p>He Hong</p> <p>College of Electronic Engineering, Xi'an Aeronautical University, Shaanxi, 710077 / China</p>	39
5.	<p><b>INNOVATIVE MAINTENANCE AND FEEDING OF WEANING PIGLETS BASED ON NEW TECHNICAL MEANS / ИННОВАЦИОННОЕ СОДЕРЖАНИЕ И КОРМЛЕНИЕ ПОРОСЯТ-ОТЪЕМЫШЕЙ НА ОСНОВЕ НОВЫХ ТЕХНИЧЕСКИХ СРЕДСТВ</b></p> <p>Nikolai Mikhailovich Morozov, Leonid Maksimovich Tsoy, Aleksander Nikolaevich Rasskazov</p> <p>Institute of livestock mechanization–filial of Federal state budget scientific institution "Federal research centre of agricultural engineering VIM" (IMJ –filial of FNAC VIM)</p>	49
6.	<p><b>RELATIONSHIP BETWEEN SOIL MOVEMENT AND POWER CONSUMPTION IN A FURROW-OPENING ROTARY BLADE / 圆盘式开沟刀土壤移动规律与功耗关系研究</b></p> <p>Kuan Qin, Xiaolong Liang, Chengmao Cao<sup>*)</sup>, Liangfei Fang</p> <p>College of Engineering, Anhui Agricultural University, Anhui Province, Hefei 230036, China</p>	55
7.	<p><b>SIMULATION ANALYSIS ON THE PERFORMANCE OF SPLITTING AND PICKING DEVICES OF CORN HARVESTER / 玉米收获机分禾与摘穗装置性能仿真分析</b></p> <p>Tai Jianjian, Li Haitao<sup>*)</sup>, Du Yuefeng, Mao Enrong, Guan Yunyi, Long Xinjian</p> <p><sup>1)</sup>China Agricultural University, College of Engineering, Beijing/China</p>	69
8.	<p><b>MOVEMENT OF THE PARTICLE ON THE INTERNAL SURFACE OF THE SPHERICAL SEGMENT ROTATING ABOUT A VERTICAL AXIS / РУХ ЧАСТИНКИ ПО ВНУТРІШНІЙ ПОВЕРХНІ СФЕРИЧНОГО СЕГМЕНТА, ЯКИЙ ОБЕРТАЄТЬСЯ НАВКОЛО ВЕРТИКАЛЬНОЇ ОСІ</b></p> <p>Sergiy Pylypaka<sup>1)</sup>, Victor Nesvidomin<sup>1)</sup>, Tatiana Volina<sup>*2)</sup>, Larysa Sirykh<sup>3)</sup>, Liudmyla Ivashyna<sup>3)</sup></p> <p><sup>1)</sup> National University of Life and Environmental sciences of Ukraine, Faculty of Design and Engineering, Kiev / Ukraine;  <sup>2)</sup> Sumy National Agrarian University, Faculty of Engineering and Technology, Sumy / Ukraine;  <sup>3)</sup> Sumy Regional Institute of Postgraduate Pedagogical Education, Faculty of Advanced Training and Retraining, Sumy / Ukraine</p>	79
9.	<p><b>DESIGN, ANALYSIS AND TEST OF SMALL ROTARY LAWN MOWER OF SINGLE-DISC TYPE / 小型单元盘割草机设计、分析与试验</b></p> <p>ShouYong Xie, Hang Zhao, ShangHong Yang, QiuJu Xie, MingJin Yang<sup>*)</sup></p> <p>Southwest University, College of Engineering and Technology, Chongqing Key Laboratory of Agricultural Equipment for Hilly and Mountainous Regions / P. R. China</p>	89
10.	<p><b>MOVEMENT STABILITY OF A SECTION OF THE MACHINE FOR BLACK FALLOW CULTIVATION IN A LONGITUDINAL-VERTICAL PLANE / СТИЙКІСТЬ РУХУ СЕКЦІЇ МАШИНИ ДЛЯ ОБРОБКИ ПАРІВ В ПОЗДОВЖНЬО-ВЕРТИКАЛЬНІЙ ПЛОЩИНІ</b></p> <p>V. Bulgakov<sup>1)</sup>, S. Ivanovs<sup>2)</sup>, V. Nadykto<sup>3)</sup>, V. Kaminskiy<sup>4)</sup>, L. Shymko<sup>1)</sup>, H. Kaletnik<sup>5)</sup></p> <p><sup>1)</sup>National University of Life and Environmental Sciences of Ukraine; <sup>2)</sup>Latvia University of Life Sciences and Technologies, Latvia; <sup>3)</sup>Dmytro Motornyi Tavria State Agrotechnological University Ukraine;  <sup>4)</sup> National Science Centre "Institute of Agriculture of NAAS", Ukraine;  <sup>5)</sup> Vinnytsia National Agrarian University, Ukraine</p>	99

		Page(s)
11.	<p><b>EXPERIMENTAL CHECKING OF MATHEMATICAL MODELS DESCRIBING THE FUNCTIONING ADEQUACY OF BRIDGE SYSTEMS IN AGRICULTURAL TRACK SYSTEM /</b>  <b>TILTU VEIDU UZBŪVES MATEMĀTISKĀ MODEĻA ATBILSTĪBAS EKSPERIMENTĀLA PĀRBAUDE</b>  <b>PRAKTISKAI IZMANTOŠANAI LAUKSAIMNIECĪBAS TRANSPORTA SISTĒMĀ</b>            Ivanovs S.<sup>1)</sup>, Bulgakov V.<sup>2)</sup>, Kuvachov V.<sup>3)</sup>, Kaletnik H.<sup>4)</sup>, Shymko L.<sup>2)</sup>, Ilnatiev Y.<sup>3)</sup>  <sup>1)</sup> Latvia University of Life Sciences and Technologies, Latvia; <sup>2)</sup> National University of Life and Environmental Sciences of Ukraine; <sup>3)</sup> Dmytro Motornyi Tavria State Agrotechnological University, Ukraine,  <sup>4)</sup> Vinnytsia National Agrarian University, Ukraine</p>	107
12.	<p><b>RESEARCH ON MAXIMUM POWER POINT TRACKING'S ALGORITHM</b>  <b>OF PHOTO-VOLTAIC CELL ARRAY FOR GREENHOUSE /</b>  <i>用于农业大棚的光伏阵列最大功率点跟踪算法研究</i>            Liming Wei<sup>1)</sup>, Yangyun Wu<sup>1)</sup>, Nan Ji<sup>1)</sup>, Boheng Li<sup>2)</sup>, Xiujuan Guo<sup>1)</sup>, Bin Li*<sup>1, 3)</sup>  <sup>1)</sup> Institute of Electrical &amp; Computer, Jilin Jianzhu University, Changchun / China;  <sup>2)</sup> School of Electrical Engineering and Telecommunications, University of New South Wales, Sydney / Australia;  <sup>3)</sup> College of Computer Science and Technology, Jilin University, Changchun / China</p>	115
13.	<p><b>EXPERIMENTAL STUDY OF LIQUID SLOSHING FORCE CHARACTERISTICS IN RECTANGULAR</b>  <b>TANK OF SPRAYER UNDER HARMONIC EXCITATION /</b>  <i>简谐激励下喷雾机矩形药箱内液体晃动力特性实验研究</i>            Jizhou Zheng<sup>1,2)</sup>, Xiang Han<sup>1)</sup>, Haoran Guo<sup>1)</sup>, Jialin Hou<sup>1,2)</sup>, Xinyu Xue<sup>3)</sup>  <sup>1)</sup> Shandong Agricultural University, College of Mechanical and Electronic Engineering / China  <sup>2)</sup> Shandong Provincial Key Laboratory of Horticultural Machineries and Equipment / China  <sup>3)</sup> Nanjing Research Institute for Agricultural Mechanization of Ministry of Agriculture and Rural Affairs / China</p>	125
14.	<p><b>FOOD LOSSES IN PRIMARY CEREAL PRODUCTION. A REVIEW /</b>  <b>RISIPA ALIMENTARA LA NIVELUL PRODUCTIEI AGRICOLE PRIMARE. REVIEW</b>            Oana-Mihaela Dumitru<sup>1)</sup>, Sorin Iorga<sup>1)</sup>, Valentin Vlăduț<sup>2)</sup>, Carmen Brăcăcescu<sup>2)</sup>  <sup>1)</sup> National Research and Development Institute for Food Bioresources -IBA Bucharest / Romania;  <sup>2)</sup> National Institute for Research-Development of Machines and Installations Designed for Agriculture and Food Industry - INMA Bucharest / Romania</p>	133
15.	<p><b>TESTING, ANALYSIS AND COMPARISON FOR CHARACTERISTICS OF AGRICULTURAL FIELD AND</b>  <b>ASPHALT ROAD ROUGHNESS / 农田地面与沥青路面不平整度特征的测试、分析与比较</b>            Lijuan Wang, Jianguo Yan*, Shengshi Xie, Chunguang Wang            Inner Mongolia Agricultural University, College of Mechanical and Electrical Engineering, Hohhot, China</p>	147
16.	<p><b>USING CFD SIMULATION TO INVESTIGATE THE IMPACT OF FRESH AIR VALVES ON POULTRY</b>  <b>HOUSE AERODYNAMICS IN CASE OF A SIDE VENTILATION SYSTEM /</b>  <b>ВИКОРИСТАННЯ CFD МОДЕЛЮВАННЯ ДЛЯ ОЦІНКИ ВПЛИВУ ПРИПЛИВНОГО КЛАПАНА НА</b>  <b>АЕРОДИНАМІКУ ПТАШНИКА ПРИ БОКОВІЙ СИСТЕМІ ВЕНТИЛЯЦІЇ</b>            Trokhaniak V.I.<sup>1)</sup>, Rogovskii I.L.<sup>1)</sup>, Titova L.L.<sup>1)</sup>, Dziubata Z.I.<sup>2)</sup>, Luzan P.H.<sup>3)</sup>, Popyk P.S.<sup>1)</sup>  <sup>1)</sup> National University of Life and Environmental Sciences of Ukraine / Ukraine;  <sup>2)</sup> Separated Subdivision of National University of Life and Environmental Sciences of Ukraine Berezhan Agrotechnical Institute / Ukraine; <sup>3)</sup> Central Ukrainian National Technical University / Ukraine</p>	155
17.	<p><b>INVESTIGATION OF OPERATIONAL PARAMETERS OF COATINGS FOR REBUILDING WORN-OUT</b>  <b>CAST-IRON PARTS OF SELF-PROPELLED AGRICULTURAL MACHINES /</b>  <b>ИЗСЛЕДВАНЕ НА ЕКСПЛОАТАЦИОННИ ПАРАМЕТРИ НА ПОКРИТИЯ ЗА ВЪЗСТАНОВЯВАНЕ НА</b>  <b>ИЗНОСЕНИ ЧУГУНЕНИ ДЕТАЙЛИ ОТ САМОХОДНИ ЗЕМЕДЕЛСКИ МАШИНИ</b>            Bekana D. L.<sup>1)</sup>, Kolev Z. D.<sup>1)</sup>, Kadirova S. Y.<sup>2)</sup>, Nenov T. R.<sup>2)</sup>, Kadikyanov G. P.<sup>3)</sup>  <sup>1)</sup> Ruse University "Angel Kanchev", Agrarian – Industrial Faculty / Bulgaria  <sup>2)</sup> Ruse University "Angel Kanchev", Faculty of Electrical Engineering, Electronics and Automation / Bulgaria  <sup>3)</sup> Ruse University "Angel Kanchev", Faculty of Transport / Bulgaria</p>	165
18.	<p><b>RESEARCH ON SEED SEPARATION PROCESS ON A GRAVITY-CASCADE SEPARATOR /</b>  <b>ДОСЛІДЖЕННЯ ПРОЦЕСУ СЕПАРУВАННЯ НАСІННЯ НА СЕПАРАТОРІ ГРАВІТАЦІЙНО-</b>  <b>КАСКАДНОГО ТИПУ</b>            Igor Dudarev<sup>1)</sup>, Lyudmyla Zabrodotska, Vasyl Satsiuk, Iryna Taraymovich, Vasyl Olkhovskiy            Lutsk National Technical University / Ukraine</p>	173
19.	<p><b>INTELLIGENT CONTROL TECHNOLOGY OF AGRICULTURAL GREENHOUSE OPERATION ROBOT</b>  <b>BASED ON FUZZY PID PATH TRACKING ALGORITHM /</b>  <i>基于模糊 PID 路径跟踪算法的农业温室作业机器人智能控制技术</i>            Ren Qun            Bozhou University, Department of Electronic and Information Engineering, Bozhou, Anhui / China</p>	181
20.	<p><b>RECOGNITION TECHNOLOGY OF AGRICULTURAL PICKING ROBOT BASED ON IMAGE DETECTION</b>  <b>TECHNOLOGY / 基于图像检测技术的农业采摘机器人识别技术</b>            Yujie Jin            School of Information Science and Engineering, Changsha Normal University, Hunan / China</p>	191

		Page(s)
21.	<p><b>EFFECTS OF DIFFERENT PLASTIC FILMS MULCHING ON SOIL TEMPERATURE AND MOISTURE AND FILM MECHANICAL PROPERTY /</b>  <i>不同地膜覆盖对土壤温湿度及地膜力学特性的影响</i></p> <p>Wang Long<sup>1, 2, 3</sup>, Wang Xufeng<sup>2, 3</sup>, Hu Can<sup>1, 2, 3</sup>, He Xiaowei<sup>1, 2, 3</sup>, Guo Wensong<sup>2, 3</sup>, Hou Shulin<sup>1*</sup></p> <p><sup>1</sup>) College of Engineering, China Agricultural University, Beijing / China; <sup>2</sup>) College of Mechanical and Electronic Engineering, Tarim University, Alar Xinjiang / China; <sup>3</sup>) Key Laboratory of Colleges &amp; Universities under the Department of Education of Xinjiang Uygur Autonomous Region, Alar Xinjiang / China</p>	201
22.	<p><b>EFFECT OF FAN'S PARAMETERSON ADHESION MECHANISM OF THRESHED RAPE MIXTURETO CLEANING SIEVE /</b>  <i>风机参数对油菜脱出物与清选筛的粘附性影响</i></p> <p>Zhang Tao<sup>1,2</sup>, Li Yaoming<sup>1,2</sup>, Xu Lizhang<sup>1,2</sup>, Qing Yiren<sup>1,2</sup></p> <p><sup>1</sup>) Key Laboratory of Modern Agricultural Equipment and Technology, Jiangsu University, Zhenjiang / China  <sup>2</sup>) School of agricultural equipment engineering, Jiangsu University, Zhenjiang / China</p>	211
23.	<p><b>ANALYSIS OF VISUAL NAVIGATION EXTRACTION ALGORITHM OF FARM ROBOT BASED ON DARK PRIMARY COLOUR /</b>  <i>基于暗原色的农田机器人视觉导航提取算法分析</i></p> <p>Zhongkun Hou</p> <p>Department of Mechatronics and Information Engineering, Sichuan College of Architectural Technology, Deyang City, Sichuan Province / China</p>	219
24.	<p><b>A MONITORING SYSTEM OF AGRICULTURAL EQUIPMENT FIELD POSITION BASED ON GPS AND GIS / 一种基于 GPS 和 GIS 农业装备田间位置的监控系统</b></p> <p>Zhenyu Yang<sup>*1</sup>, Zeqiu Chen<sup>2</sup>, Ken Chen<sup>3</sup></p> <p><sup>1</sup>)School of Earth and Space Sciences, Peking University, Beijing / China  <sup>2</sup>)School of Information Engineering, China University of Geosciences (Beijing), Beijing / China  <sup>3</sup>)School of Computer and Information Engineering, Heilongjiang University of Science and Technology, Harbin / China</p>	229
25.	<p><b>STUDY ON TEMPERATURE FIELD OF ASYMMETRIC LARGE-SPAN ARCH SHEDS UNDER LOW-TEMPERATURE ENVIRONMENT /</b>  <i>非对称大跨度拱棚低温环境下的温度场研究</i></p> <p>Kai Zhou<sup>1</sup>, Zhiwei Meng<sup>1</sup>, Min Wei<sup>2</sup>, Jialin Hou<sup>1</sup>, Tianguo Jin<sup>3</sup>, Tianhua Li<sup>*1</sup></p> <p><sup>1</sup>) College of Mechanical and Electronic Engineering, Shandong Agricultural University, Taian / China;  <sup>2</sup>) College of Horticulture Science and Engineering, Shandong Agricultural University, Taian / China;  <sup>3</sup>) School of Mechatronics Engineering, Harbin Institute of Technology, Harbin / China</p>	239
26.	<p><b>INCREASING THE PERFORMANCE OF CYLINDRICAL SEPARATORS FOR CEREAL CLEANING, BY USING AN INNER HELICAL COIL / CREȘTEREA PERFORMANȚELOR SITELOR CILINDRICE PENTRU CURĂȚIREA CEREALELOR, PRIN UTILIZAREA UNEI SPIRE INTERIOARĂ ELICOIDALĂ</b></p> <p>Costin Mircea <sup>1</sup>, Florin Nenciu <sup>*1</sup>, Valentin Vlăduț <sup>1</sup>, Gheorghe Voicu <sup>2</sup>, Dan Cujbescu <sup>1</sup>, Iuliana Gageanu <sup>1</sup>, Iulian Voicea <sup>1</sup></p> <p><sup>1</sup>)INMA Bucharest / Romania; <sup>2</sup>) University Politehnica of Bucharest / Romania</p>	249
27.	<p><b>THE DESIGN OF GROUND AIR DUAL PURPOSE AGRICULTURAL INFORMATION ACQUISITION ROBOT / 地空两用农业信息采集机器人的设计</b></p> <p>Qinlan Li</p> <p>Tianshui Normal University, Tianshui, Gansu / China</p>	259
28.	<p><b>EXPERIMENTAL RESEARCHES ON DETERMINING THE WEAR OF CHISEL KNIFEMADE OF THREE TYPES OF MATERIALS / CERCETĂRI EXPERIMENTALE PRIVIND DETERMINAREA UZURII CUTITELOR TIP DALTA REALIZATE DIN TREI TIPURI DE MATERIALE DIFERITE</b></p> <p>Vladutoiu L. <sup>1</sup>, Fehete T. L. <sup>2</sup>, Grigorel A. <sup>1</sup>, Sorică E. <sup>1</sup>, Petre A. A. <sup>1</sup>, Cristea O.D. <sup>1</sup></p> <p><sup>1</sup>) INMA Bucharest; <sup>2</sup>) UT Cluj</p>	269
29.	<p><b>THE DEVELOPMENT OF PORTABLE DETECTOR FOR APPLES SOLUBLE SOLIDS CONTENT BASED ON VISIBLE AND NEAR INFRARED SPECTRUM /</b>  <i>基于可见光和近红外光谱的便携式苹果可溶性固形物含量检测仪的研制</i></p> <p>Fa Peng<sup>1</sup>, ShuangXi Liu<sup>*2</sup>, Hao Jiang<sup>2</sup>, XueMei Liu<sup>2</sup>, JunLin Mu<sup>2</sup>, JinXing Wang<sup>2</sup></p> <p><sup>1</sup>) Beijing Agricultural Equipment Research Centre, Beijing / China;  <sup>2</sup>) College of Mechanical and Engineering, Shandong Agricultural University, Taian / China</p>	277
30.	<p><b>ANALYSIS AND OPTIMIZATION ON THE PROCESS OF ADJUSTABLE DOUBLE DRUM CASTOR SHELLING BASED ON DISCRETE ELEMENT METHOD /</b>  <i>基于离散元的可调式双滚筒蓖麻脱壳过程分析及优化</i></p> <p>Hou Junming, Zhu Hongjie, Jinpeng Li, Enchao Yao, Hu Weixue</p> <p>Shenyang Agricultural University, College of Engineering / China</p>	289

		Page(s)
31.	<p><b>NUMERICAL SIMULATION AND EXPERIMENTAL STUDY ON PELLETTING MOTION LAW OF AGROPYRON SEEDS UNDER VIBRATION FORCE FIELD / 振动力场作用下冰草种子丸化运动规律数值模拟与试验研究</b></p> <p>Hou Zhanfeng<sup>1)</sup>; Yi Qiu<sup>2)</sup>; Zhi Chen<sup>1*)</sup>; Lijie Chen<sup>1)</sup>; Shao Zhiwei<sup>1)</sup></p> <p><sup>1)</sup>Inner Mongolia Agricultural University, College of Mechanical and Electrical Engineering, Inner Mongolia, China; <sup>2)</sup>Yangzhou Polytechnic Institute, College of Transportation Engineering, Jiangsu / China</p>	299
32.	<p><b>ASSESSMENT OF APPLE DAMAGE CAUSED BY A FLEXIBLE END-EFFECTOR / 柔性末端执行器抓握过程苹果损伤评估</b></p> <p>LingXin Bu<sup>1)</sup>, ChengKun Chen<sup>1,2)</sup>, GuangRui Hu<sup>1)</sup>, JianGuo Zhou<sup>1)</sup>, Adilet Sugirbay<sup>1,3)</sup>, Jun Chen<sup>*1)</sup></p> <p><sup>1)</sup> College of Mechanical and Electronic Engineering, Northwest A&amp;F University, Yangling / China; <sup>2)</sup> Guizhou University of Traditional Chinese Medicine, Guiyang / China; <sup>3)</sup> Technical faculty, S. Seifullin Kazakh Agro Technical University, Astana / Kazakhstan</p>	309
33.	<p><b>INFLUENCE OF THE SWEEP ANGLE OF THE CROSS KNIFE OPENER ON SOIL DISTURBANCE / 十字槽开沟器横刀后掠角对土壤扰动的影响</b></p> <p>Chengcheng Guo<sup>1)</sup>, Guohua Li<sup>1)</sup>, Junchang Zhang<sup>*1)</sup>, Xiunan Jin<sup>1)</sup>, Jingfeng Xue<sup>1)</sup>, Chenxi He<sup>1)</sup>, Liqun Lu<sup>1)</sup></p> <p><sup>1)</sup> College of Mechanical and Electronic Engineering, Northwest A&amp;F University, Yang ling / China</p>	317
34.	<p><b>NUMERICAL 3D ANALYSIS OF A MINI WIND TURBINE WITH HORIZONTAL AXIS, FOR IMPLEMENTATION IN AGRICULTURAL FARMS / ANALIZA NUMERICA 3D A UNEI TURBINE EOLIENE DE PUTERE MICA CU AX ORIZONTAL IN VEDEREA IMPLEMENTARII IN FERMELE AGRICOLE</b></p> <p>George Ipate<sup>1)</sup>, Gabriel Alexandru Constantin<sup>1)</sup>, Sorin Ștefan Biris<sup>1)</sup>, Gheorghe Voicu<sup>1)</sup>, Carmen Otilia Rusanescu<sup>1)</sup>, Vasilica Ștefan<sup>2)</sup></p> <p><sup>1)</sup> POLITEHNICA University of Bucharest / Romania; <sup>2)</sup> INMA Bucharest / Romania</p>	325
35.	<p><b>OPTIMAL ANALYSIS OF FARM AGRICULTURAL MACHINERY EQUIPMENT BASED ON MATHEMATICAL MODELING / 基于数学模型的农业机械优化分析</b></p> <p>Zefeng Zhang</p> <p>School of Mathematics and Computer Science, Xinyang Vocational and Technical College, Xinyang / China</p>	333
36.	<p><b>PARAMETER OPTIMIZATION AND EXPERIMENTAL RESEARCH ON THE HAMMER MILL / 锤片式粉碎机参数优化与试验研究</b></p> <p>Di Wang, Changbin He, Haiqing Tian<sup>*</sup>, Fei Liu, Tao Zhang, Hongqi Zhang</p> <p>Inner Mongolia Agricultural University, College of Mechanical and Electrical Engineering, Hohhot/China</p>	341
37.	<p><b>DESIGN AND APPLICATION OF MULTIFUNCTIONAL PERFORMANCE TEST PLATFORM FOR SOIL-ENGAGING TILLAGE COMPONENTS / 多功能触土耕作部件性能检测平台设计与应用</b></p> <p>Zhiqian Sun<sup>1)</sup>, Zhou Yang<sup>2,3)</sup>, Jieli Duan<sup>2)</sup>, Jun Li<sup>2)</sup></p> <p><sup>1)</sup> Experimental Basis and Practical Training Centre, South China Agricultural University, Guangzhou / China; <sup>2)</sup> College of Engineering, South China Agricultural University, Guangzhou / China; <sup>3)</sup> Guangdong Provincial Key Laboratory of Conservation and Precision Utilization of Characteristic Agricultural Resources in Mountainous Areas, Meizhou / China</p>	351
38.	<p><b>OPTIMIZATION ON EFFICIENT COMBUSTION PROCESS OF SMALL-SIZED FUEL ROLLS MADE OF OLEAGINOUS FLAX RESIDUES / ОПТИМІЗАЦІЯ ЕФЕКТИВНОГО ПРОЦЕСУ ГОРІННЯ МАЛОГАБАРИТНИХ ПАЛИВНИХ РУЛОНІВ ІЗ ЗАЛИШКІВ ПІСЛЯ ЗБИРАННЯ ЛЬОНУ ОЛІЙНОГО</b></p> <p>Svitlana Yaheliuk<sup>1)</sup>, Volodymyr Didukh<sup>2)</sup>, Vitaly Busnyuk<sup>2)</sup>, Galina Boyko<sup>3)</sup> Oleksandr Shubalyi<sup>4)</sup></p> <p><sup>1)</sup>Lutsk National Technical University Department of Commodity Research and Expertise Customs, Lutsk/ Ukraine; <sup>2)</sup> Lutsk National Technical University, Department of agricultural engineering, Lutsk, Ukraine; <sup>3)</sup>Kherson National Technical University, Department of Commodity Studies, Standardization and Certification / Kherson, Ukraine; <sup>4)</sup> Lutsk National Technical University, Department of Economics, Lutsk, Ukraine</p>	361
39.	<p><b>DEVELOPMENT OF THE AERODYNAMIC DRYING METHOD FOR THE CRUSHED VEGETAL MASS / ELABORAREA METODEI DE USCARE AERODINAMICĂ A MASEI VEGETALE TOCĂȚĂ</b></p> <p>Hăbășescu I.<sup>1)</sup>, Cerempei V.<sup>2)</sup>, Molotcov Iu.<sup>1)</sup>, Popa L.<sup>3)</sup></p> <p><sup>1)</sup>ITA Mecagro Chișinău / Moldova; <sup>2)</sup>UASM Chisinau / Republic of Moldova <sup>3)</sup>National Institute for Research-Development of Machines and Installations Designed for Agriculture and Food Industry - INMA Bucharest / Romania</p>	369
40.	<p><b>DYNAMICS OF PROPORTIONAL SPEED CONTROL VERSUS SERVO SPEED CONTROL OF A HOSE / CABLE SPOOLING DEVICE FOR DRUM / DINAMICA REGLĂRII PROPORȚIONALE A VITEZEI VERSUS SERVOREGLAREA VITEZEI DEPĂNĂTORULUI DE FURTUN / CABLU AL TAMBURULUI</b></p> <p>Alexandru-Polifron Chiriță<sup>*1)</sup>, Marian Blejan<sup>1)</sup>, Teodor-Costinel Popescu<sup>1)</sup>, Ana-Maria Popescu<sup>1)</sup></p> <p><sup>1)</sup> INOE 2000 - Subsidiary Hydraulics and Pneumatics Research Institute / Romania</p>	379

# PARAMETER OPTIMIZATION AND EXPERIMENT OF ORCHARD DOUBLE ROW DITCHING-FERTILIZING MACHINE

/

## 果园双行开沟施肥机的参数优化与试验

HongJian Zhang<sup>1)</sup>, ChunBao Xu<sup>1)</sup>, ShuangXi Liu<sup>1,2)</sup>, Hao Jiang<sup>1)</sup>, Xuemei Liu<sup>1)</sup>, JinXing Wang<sup>\*1,3)</sup> <sup>1</sup>

<sup>1)</sup> College of Mechanical and Electronic Engineering, Shandong Agricultural University, Taian 271018, China;

<sup>2)</sup> Shandong Provincial Key Laboratory of Horticultural Machinery and Equipment, Taian 271018, China;

<sup>3)</sup> Shandong Provincial Engineering Laboratory of Agricultural Equipment Intelligence, Taian 271018, China;

Tel: +86 05388246826; E-mail: jinxingw@163.com

DOI: <https://doi.org/10.35633/inmateh-62-01>

**Keywords:** orchard, ditching-fertilizing machine, central composite test, response surface, parameter optimization

### ABSTRACT

In order to improve the fertilization uniformity and stability of the orchard double row ditching-fertilizing machine, the design was optimized. Firstly, the factors affecting the movement of the fertilizer particles were analysed in combination with the kinetic model of the fertilizer particles during the falling process. Secondly, the influence of each factor on the fertilization uniformity was analysed by single factor variance. Finally, the Box-Behnken central composite method was used to establish a mathematical model of fertilization uniformity of the orchard double row ditching-fertilizing machine, and regression statistical variance, response surface, and contour lines were used to analyse the influence of each mechanism parameter on the fertilization uniformity. The test results show that: when the test parameters of the conveyer belt speed is within 165~235  $r \cdot \min^{-1}$ , the advancing velocity is within 0.8~1.2  $m \cdot s^{-1}$ , and the guide plate angle is changed within the range of 15~45°, the degree of influence of each factor on the fertilization uniformity from high to low is the conveyer belt speed, advancing velocity, the angle of the guide plate, and the conveyer belt speed; when the conveyer belt speed is 214  $r \cdot \min^{-1}$ , advancing velocity is 1  $m \cdot s^{-1}$ , and the angle of the guide plate is 37°, the fertilizer coverage reaches 100%, and the fertilization uniformity is increased from 86.31% to 90.73%, and the fertilization stability is improved. The research results provide a theoretical basis for the design and optimization of orchard ditching-fertilizing machine.

### 摘要

为提高果园双行开沟施肥机的施肥均匀度和稳定性,对果园双行开沟机进行优化设计。首先结合肥料颗粒下落过程中的动力学模型,分析影响肥料颗粒运动的各因素。其次通过单因素方差分析各因素对施肥均匀度的影响。最后采用 Box-Behnken 中心组合试验设计方法,建立果园双行开沟施肥机施肥均匀度的数学模型,通过回归统计方差、响应曲面和等高线分析各机构参数对施肥均匀度的影响规律。试验结果表明:在前进速度 0.8~1.2  $m \cdot s^{-1}$ , 传送带转速 165~235  $r \cdot \min^{-1}$ , 导板角度 15°~45°的试验参数范围内,各因素对施肥均匀度的影响程度从高到低依次为传送带转速、前进速度、导板角度;当传送带转速为 214  $r \cdot \min^{-1}$ 、前进速度为 1.0  $m \cdot s^{-1}$ 、导板角度为 37°的参数条件下,肥料覆盖率达 100%,施肥均匀度由原来的 86.31%提高到 90.73%,施肥稳定性提高。研究结果为果园开沟施肥机的设计和优化提供了理论依据。

### INTRODUCTION

China has superior natural conditions suitable for the growth of fruit trees. It is a large country for fruit growing. After more than 40 years of development, China has become the main supply base and processing base for fruit in the world. Its fruit output and output value are among the highest in the world. Fruit production has become one of the pillar industries of China's agriculture (Huairui Shu et al, 2018; Jingyan Wang et al, 2019). Fertilization of fruit trees is a key operation in the growing of fruit trees. The quality of fertilization directly affects the absorption of nutrients in fruit trees. Reasonable fertilization is an important measure to ensure high yield, stable yield and increased yield of fruit trees (Dayong Han et al, 2010; Congju Shen et al, 2019; Xiaochun Zheng et al, 2011).

<sup>1</sup> HongJian Zhang, Ph.D. Stud. Eng.; ChunBao Xu, M.S. Stud. Eng.; ShuangXi Liu, As. Ph.D. Eng.; Hao Jiang, M.S. Stud. Eng.; Xuemei Liu, M.S. Stud. Eng.; JinXing Wang, Prof. Ph.D. Eng.

At present, orchards in the full fruit season mostly use ditching-fertilizing machines for stripe fertilization (Chen Ma et al, 2017). Fertilization uniformity is a key factor that affects the effect of fertilization operations, and is an important index for evaluating the performance and effect of working tools (Junliang Fan et al, 2016; Jing Ma et al, 2016; Rui Wang et al, 2017; Zhou Zhou et al, 2009). Overseas, Hofstee et al (1990, 1992, 1994, 1995) made in-depth research on fertilization uniformity, including the effect of fertilizer size, friction coefficient and recovery coefficient on the distribution of fertilizer movement. In China, Yang Qinglu et al. (2019) carried out numerical analysis of particle motion based on the coupled method of discrete element and hydrodynamics, studied the flow characteristics of fertilizer particles in a pneumatic concentration and distribution type fertilizer separator, and obtained the optimal value of fluidity and uniformity of airflow and fertilizer in the fertilizer separating device. Qi Xingyuan et al. (2018) based on the pneumatic variable fertilizer applicator, theoretically analysed the fertilizer movement in its sprayer and simulated the air flow field, and obtained the optimal speed and baffle structure of the fertilizer removal wheel, which has a significant effect on the fertilization uniformity in the fertilization range of a single sprayer. Wang Jinfeng et al. (2018) carried out design analysis on key components of the deep-field fertilizing device on the paddy field side, and used a quadrature orthogonal rotation combination design test to obtain the mathematical model of the relationship among the speed of the fertilizer wheel, the advance speed of the rice transplanter, the wind speed of the fan and the uniformity of fertilization.

After comprehensive analysis of research status at home and abroad, it is found that the uniformity of fertilization affects the effect of fertilization. With the advancement of orchard mechanization, the promotion scope of orchard ditching-fertilizing machine has increased, but there are problems such as low fertilization uniformity and poor stability. For this reason, based on the existing orchard ditching-fertilizing machine, the single factor and Box-Behnken central composite experiment was adopted to establish mathematical model of fertilization uniformity, and to analyse the correlation between different structural parameters and fertilization uniformity through regression statistical variance, response surface, and contour lines to provide theoretical basis for the design and optimization of orchard ditching-fertilizing machine.

## MATERIALS AND METHODS

### Overall structure

At present, the new orchards in Bohai Bay, Northwest Loess Plateau and other main apple producing areas mostly adopt the planting mode of short anvil close planting, the row spacing of orchards is between 3.5~4.0m, and the plant spacing is between 1.5~1.8m. In order to improve the operation efficiency and combine the apple planting mode, the orchard double row ditching-fertilizing machine is designed. The structure of the whole machine is shown in Figure 1, which is mainly composed of traction frame, frame, organic fertilizer box, compound fertilizer box, ditching device, fertilizer discharge device, etc. The main technical parameters of the whole machine are shown in Table 1.

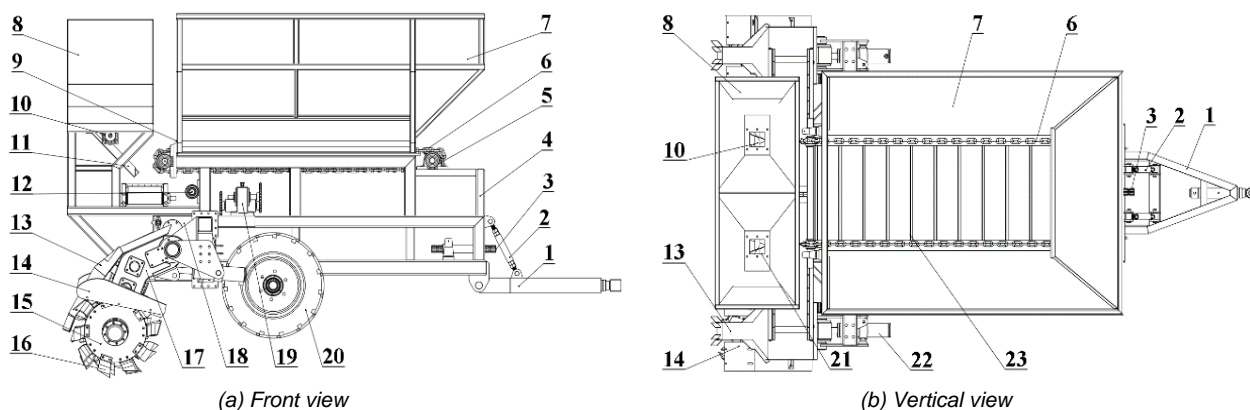


**Fig. 1 - Orchard double row ditching-fertilizing machine**

- 1) traction frame; 2) adjusting pulling pipe; 3) transmission shaft; 4) frame; 5) fertilizer discharge chain wheel; 6) O-chain; 7) organic fertilizer box; 8) compound fertilizer box; 9) organic fertilizer discharge port; 10) fertilizer discharge auger; 11) fertilizer transport plate; 12) fertilizer discharge transmission box; 13) fertilizer guide plate; 14) soil cover; 15) ditching cutterhead; 16) ditching cutter; 17) ditching transmission box; 18) main transmission box; 19) fertilizer transport transmission box; 20) wheels; 21) fertilizer discharge port; 22) hydraulic cylinder; 23) fertilizer discharge scraper

Table 1

Main technical parameters		
Parameter	Value	Units
Structure form	traction type	-
Tractor power	≥58.8	kW
Operation speed	0.8~1.2	m·s <sup>-1</sup>
Overall dimension (length × width × height)	4030×2470×2150	mm
Depth of ditching	0~400	mm
Width of ditching	350	mm
Compound fertilizer application amount	0~9.0	kg·m <sup>-1</sup>
Fertilizer application amount	0~2.2	kg·m <sup>-1</sup>
Compound fertilizer box volume	2450	L
Fertilizer box volume	650	L

### Working principle

When working, the orchard double row ditching-fertilizing machine advances under the tractor's traction, the ditching cutter cuts into the soil and throws up the soil. The compound fertilizer and the chemical fertilizer are discharged by the fertilizer discharge scraper and the fertilizer discharge auger respectively, and fall into the opened trench through the fertilizer conveyer belt and the fertilizer guide plate. Meanwhile, the ditching soil cover blocks the soil thrown up by the ditching cutter and makes it fall back into the opened trench, realizing the integration of ditching, fertilization and covering soil. Part of the tractor's power is transmitted to the fertilizer transport transmission box to drive the fertilizer conveyer belt to rotate to realize the fertilizer conveying operation, and other power is transmitted to the main transmission box. Part of the power of the main transmission box is transferred from the first and second output shafts to the ditching transmission box to drive the ditching cutter to rotate and realize ditching operation; other power of the main transmission box is transferred from the third output shaft to the fertilizer discharge transmission box to drive the fertilizer discharge scraper and fertilizer discharge auger to rotate and realize fertilizer discharge operation. The power transmission route is shown in Figure 2.

Through the analysis of the movement of fertilizer particles, we know that there are three factors that affect the fertilizer discharge effect of the orchard double row ditching-fertilizing machine: one is the mechanical structure parameters of the machine; the other is the characteristics of the fertilizer itself; the third is the environmental factors. Under the influence of irresistible environmental factors and the characteristics of fertilizer itself, this study mainly studies the influence of the structural parameters of the machine on the law of fertilizer discharge to solve the problems in practical work.

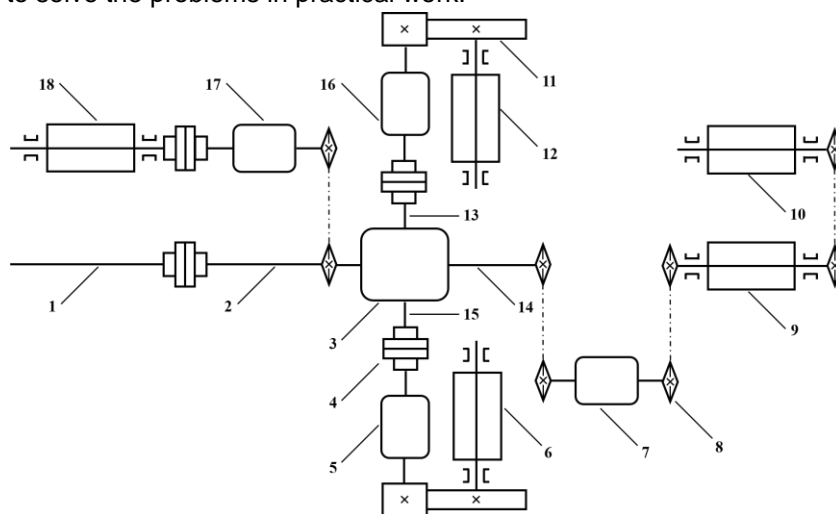


Fig. 2 - Power transmission route

- 1) tractor rear power output shaft; 2) main transmission box input shaft; 3) main transmission box; 4) coupling; 5) right ditching transmission box; 6) right ditching cutterhead; 7) fertilizer discharge transmission box; 8) chain drive; 9) fertilizer discharge scraper; 10) fertilizer discharge auger; 11) gear drive; 12) left ditching cutterhead; 13) main transmission box first output shaft; 14) main transmission box third output shaft; 15) main transmission box second output shaft; 16) left ditching transmission box; 17) fertilizer transport transmission box; 18) fertilizer conveyer belt

### Test conditions

The test was carried out in the test base of Gaomi Yifeng Machinery Co., Ltd. in December 2019. The weather is sunny, the temperature is  $-4\sim-3^{\circ}\text{C}$ , the southwest wind, the wind speed is less than 2 km/h, the air relative humidity is 64%, and the test ground is relatively flat, with an area of about 650 m<sup>2</sup>. The fertilizer used in the experiment is spherical compound fertilizer produced by Stanley Agricultural Group Co., Ltd. the N: P<sub>2</sub>O<sub>5</sub> : K<sub>2</sub>O is 15:15:15, the total nutrient is more than 45%, the water content is 1.12%, and the average diameter of particles is 4.19 mm. The test method and index refer to GB/T5262—2008 general provisions for the determination of test conditions for agricultural machinery and NY/T1003—2006 standard test method for operation quality evaluation of fertilizing machinery. Figure 3 is the test diagram of orchard double row ditching-fertilizing machine.



Fig. 3 - Test of orchard double row ditching-fertilizer machine

### Evaluation of fertilization uniformity

The fertilization operation schedule of the orchard double row ditching-fertilizer machine was tested, and the operation length of a single row is 50m for each double-row operation, of which the length of the measuring area is 30 m and the length of the reserve area at both ends is 10 m. Each row along the travel direction was divided into 30 sections as the measuring area according to the continuous length of 10cm, and a total of 60 sections were tested. During the test, the ditching device will be raised in the preparation area, and the calibration machine will enter the working state. After that, the measuring area will be passed at the normal working speed. The fertilizer dropped in each section was collected separately and weighed by an electronic balance. Under a single operation stroke, the fertilization uniformity was calculated according to formula (1), (2), (3), (4) after the completion of all measurement areas.

$$\bar{x} = \frac{\sum_{i=1}^n x_i}{n} \quad (1)$$

$$\sigma = \sqrt{\frac{\sum_{i=1}^n (x_i - \bar{x})^2}{n-1}} \quad (2)$$

$$CV = \frac{\sigma}{\bar{x}} \times 100\% \quad (3)$$

$$CU = 1 - CV \quad (4)$$

Where,  $\bar{x}$  is the mean value of fertilizer mass, g;  $x_i$  is the fertilizer mass of the  $i^{\text{th}}$  measurement area, g;  $n$  is the number of measurement areas selected in the operation area;  $\sigma$  the standard deviation of fertilizer mass, g;  $CV$  is the coefficient of variation of fertilizer distribution, %;  $CU$  is the stability coefficient of fertilizer distribution, %.

### Test design

Granular organic fertilizers fall into the fertilizer guiding mechanism by means of fertilizer discharge mechanism, with a certain initial velocity  $V_p$ . After the granular organic fertilizer enters the fertilizer guiding mechanism, it is subjected to gravity  $G_p$ , buoyancy  $F_{fp}$ , and air resistance  $F_{zp}$ . After the interaction, it finally falls into the ditch of the orchard ditching-fertilizer machine.

$$\text{Gravity:} \quad G_p = \rho_p V_p g \quad (5)$$

$$\text{Buoyancy:} \quad F_{fp} = \rho_a V_p g \quad (6)$$

$$\text{Air resistance: } F_{zp} = \frac{1}{2} K \rho_p S_p V_p^2 \tag{7}$$

$$\text{Air resistance coefficient: } K = \frac{3}{8} C_D \rho_a \frac{1}{\rho_p r_p} \tag{8}$$

There is a correlation between drag coefficient  $C_D$  and Reynolds number  $R_e$ :

$$R_e = 2 \frac{r_p V_p \rho_p}{\eta_a} \tag{9}$$

In equations (5), (6), (7), (8), (9):

- $\rho_p$ -granular organic fertilizer density;  $V_p$ -volume of granular organic fertilizer;  $\rho_a$ -air density;
- $\eta_a$ -aerodynamic viscosity;  $v_p$ -granular organic fertilizer velocity;
- $S_p$ -granular organic fertilizer frontal area;  $r_p$ -granular organic fertilizer radius;  $g$ -gravity acceleration;

Assuming that the positive direction of the Z axis is opposite to the direction of gravity of the granular organic fertilizer, the equation of motion of the granular organic fertilizer in the X, Y, and Z directions is:

$$\text{X direction: } \frac{d^2x}{dt^2} = -K V_{Px} \sqrt{V_{Px}^2 + V_{Py}^2 + V_{Pz}^2} \tag{10}$$

$$\text{Y direction: } \frac{d^2y}{dt^2} = -K V_{Py} \sqrt{V_{Px}^2 + V_{Py}^2 + V_{Pz}^2} \tag{11}$$

$$\text{Z direction: } \frac{d^2z}{dt^2} = -K V_{Pz} \sqrt{V_{Px}^2 + V_{Py}^2 + V_{Pz}^2} \tag{12}$$

In equations (10), (11), (12):

- $v_{Px}$ -the velocity component in the X direction;
- $v_{Py}$ -the velocity component in the Y direction;
- $v_{Pz}$ -the velocity component in the Z direction;

Through the analysis of the movement state of fertilizer particles after they leave the fertilizer device, it is found that the conveyer belt speed, advancing velocity and guide plate angle affect the amount of fertilizer applied and the movement state of fertilizer particles. With the fertilization uniformity as the experimental index, the single factor test was conducted with the conveyer belt speed, advancing velocity and guide plate angle as the factors, and the results are shown in Table 2. It can be seen from Table 2 that the speed of conveyer belt has a very significant effect on the fertilization uniformity ( $P < 0.01$ ), and the guide plate angle and advancing velocity have a significant effect on the fertilization uniformity ( $P < 0.05$ ).

Table 2

Single-factor test results			
Project	Conveyer belt speed [r·min <sup>-1</sup> ]	Advancing velocity [m·s <sup>-1</sup> ]	Guide plate angle [°]
P Value	0.00015	0.0138	0.0273

According to the results of single factor analysis, the conveyer belt speed  $x_1$ , advancing velocity  $x_2$  and guide plate angle  $x_3$  were selected as the test factors, and the fertilization uniformity was used as the evaluation index. The Box-Behnken composite test design method was adopted. The value range of each factor and the factors and levels in the test are shown in Table 3. The experimental scheme and results of Box-Behnken are shown in Table 4.

Table 3

Factors and levels			
Level	Conveyer belt speed X1 [r·min <sup>-1</sup> ]	Advancing velocity X2 [m·s <sup>-1</sup> ]	Guide plate angle X3 [°]
-1	165	0.8	15
0	200	1.0	30
1	235	1.2	45

Table 4

Box-Behnken design scheme and response values of fertilization uniformity

Test serial number	Conveyer belt speed $x_1$ [r·min <sup>-1</sup> ]	Advancing velocity $x_2$ [m·s <sup>-1</sup> ]	Guide plate angle $x_3$ [°]	Fertilization uniformity [%]
1	200	1.0	30	90.10
2	165	1.0	45	85.00
3	200	0.8	15	85.65
4	165	0.8	30	82.65
5	165	1.2	30	84.35
6	200	1.2	15	86.20
7	235	0.8	30	90.40
8	200	1.0	30	91.10
9	200	1.0	30	89.80
10	235	1.2	30	83.30
11	200	0.8	45	85.30
12	165	1.0	15	87.65
13	200	1.0	30	90.40
14	235	1.0	45	88.95
15	235	1.0	15	84.65
16	200	1.2	45	89.15
17	200	1.0	30	90.30

## RESULTS AND ANALYSIS

### Test analysis results

The Design Expert statistical analysis software was used to perform a polynomial regression analysis on the experimental data in Table 4, the regression equation of the fertilization uniformity of the orchard ditching-fertilizing machine was obtained:

$$Y=90.34+0.96x_1-0.12x_2+0.53x_3-2.20x_1x_2+1.74x_1x_3+0.83x_2x_3-2.59x_1^2-2.58x_2^2-1.19x_3^2 \quad (13)$$

Significance test and variance analysis of mathematical model were carried out, and the results are shown in Table 5. According to the data results, the regression model was significant ( $P<0.05$ ), indicating that the model established was meaningful. The modified determination coefficient of the model is 0.70, and the regression determination coefficient  $R^2$  is 0.87, indicating that the gap between the actual measurement value and the mathematical model is small, that is, the model has a high degree of fit to the data, the regression model is significant, the test error is small, and can better describe the experimental results, so the establishment of this regression equation is correct (Yuanyu Qian et al, 2018; Zhihong Yu et al, 2018).

Table 5

Regression statistical variance analysis results

Project	Freedom	Sum of squares	Mean square	F Value	P Value
$x_1$	1	7.32	7.32	2.98	0.1279
$x_2$	1	0.12	0.12	0.05	0.8279
$x_3$	1	2.26	2.26	0.92	0.3695
$x_1^2$	1	19.36	19.36	7.89	0.0262
$x_1x_2$	1	12.08	12.08	4.92	0.0621
$x_1x_3$	1	2.72	2.72	1.11	0.3273
$x_2^2$	1	28.22	28.22	11.50	0.0116
$x_2x_3$	1	27.95	27.95	11.38	0.0119
$x_3^2$	1	5.95	5.95	2.42	0.1634
Model	9	112.36	12.48	5.09	0.0217
Residual	7	17.18	2.45		
Total	16	129.54			

It can be seen from the results of the regression statistical analysis of variance in Table 5, that  $x_1$  (the conveyer belt speed),  $x_2$  (the advancing velocity) and  $x_3$  (the guide plate angle) have no significant effect on the uniformity of fertilization in the linear term of the model;  $x_1^2$  and  $x_2^2$  have significant effects on the fertilization uniformity, and  $x_3^2$  has no significant effect in the quadratic term of the model. Considering the interaction effects,  $x_1x_2$  and  $x_2x_3$  have significant effects on the fertilization uniformity, and  $x_1x_3$  has no significant effect. According to the analysis of the significance of the impact, it can be known that within the range of the selected factors, the order of influence on the uniformity of fertilization from high to low is as follows: the conveyer belt speed > the advancing velocity > the guide plate angle.

### Response Surface Analysis of Fertilization Uniformity

Design-Expert was used to plot the response surface of fertilization uniformity, the effect of various factors on fertilization uniformity can be seen, and the relationship between various variables can be determined and tested (Jin Yuan et al, 2018). One of the conveyer belt speed, advancing velocity and the guide plate angle is fixed at the middle level, and analyse the effect of the other two factors and their interaction on fertilization uniformity. The interaction results are shown in Fig. 4 ~ 6.

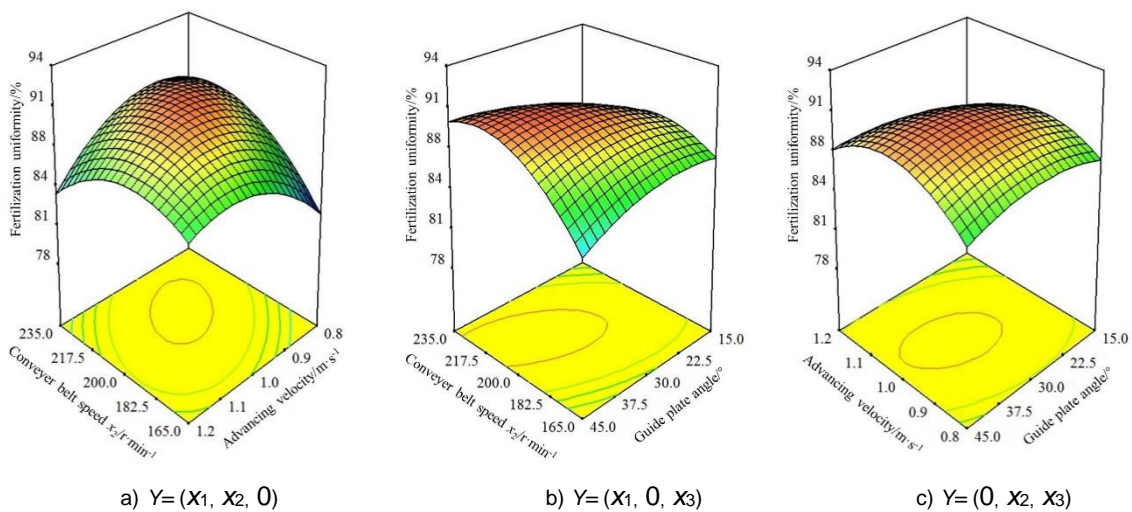


Fig. 4 - Interactive effects of different experimental factors on fertilization uniformity

In Figure 4a, the fertilization uniformity response surface opens downward, showing the interactive influence of the advancing velocity and the conveyer belt speed on the fertilization uniformity when the guide plate angle is  $30^\circ$ . When the conveyer belt speed is  $217.5 \text{ r}\cdot\text{min}^{-1}$  and the advancing velocity is  $1 \text{ m}\cdot\text{s}^{-1}$ , the fertilization uniformity is the highest. It can be seen from the contour map that the effect of the conveyer belt speed on the fertilization uniformity is more significant than that of the advancing velocity. When the angle of the guide plate is  $30^\circ$ , the conveyer belt speed is at any level, and the uniformity of fertilizer application increases first and then decreases with the increase of the advancing velocity. When the conveyer belt speed is low, the effect of the advancing velocity on the fertilization uniformity is obvious, as shown in the figure, the fertilization uniformity curve in the figure is steep. This shows that when the conveyer belt speed is in the range of  $165\text{--}182.5 \text{ r}\cdot\text{min}^{-1}$ , properly increasing the advancing velocity can significantly improve the fertilization uniformity. When the angle of the guide plate is  $30^\circ$ , the advancing velocity is at a low level, and the uniformity of fertilization shows an increasing trend with the increase of the conveyer belt speed, and the influence of the conveyer belt speed on the uniformity of the fertilization is obvious, as shown in the steep curve in the figure. This shows that when the advancing velocity is within the range of  $0.8\text{--}0.9 \text{ m}\cdot\text{s}^{-1}$ , increasing the conveyer belt speed can significantly improve the uniformity of fertilization; when the advancing velocity is at a medium and high level, the uniformity of fertilization increases first as the conveyer belt speed and then decreases, it shows that when the advancing velocity is in the range of  $0.9\text{--}1.2 \text{ m}\cdot\text{s}^{-1}$ , maintaining the conveyer belt speed at  $200 \text{ r}\cdot\text{min}^{-1}$  can improve the fertilization uniformity. When the conveyer belt speed (the advancing velocity) is low, the amount of fertilization is small, and part of the trench is not covered by fertilizer, which reduces the uniformity of fertilization. Increasing the conveyer belt speed (the advancing velocity) appropriately can speed up the fertilizer movement rate and increase fertilization amount, reducing the area in the trench that is not evenly covered by fertilizer, and improving the uniformity of fertilization.

In Figure 4b, the fertilization uniformity response surface opens downward, showing the interactive effect of the conveyer belt speed and the guide plate angle on the fertilization uniformity when the advancing velocity is  $1.0 \text{ m}\cdot\text{s}^{-1}$ , and when the conveyer belt speed is  $217.5 \text{ r}\cdot\text{min}^{-1}$ , and the angle of the guide plate is  $45^\circ$ , the fertilization uniformity is the highest. It can be seen from the contour map that the effect of the conveyer belt speed on the fertilization uniformity is more significant than that of the guide plate angle. When the advancing velocity is  $1.0 \text{ m}\cdot\text{s}^{-1}$ , the conveyer belt speed is low, and the amount of fertilizer applied is small. As the angle of the guide plate increases, the movement time of the fertilizer on the guide plate becomes longer, and the amount of fertilizer per unit time becomes smaller. Part of the area is not evenly covered by fertilizer, which leads to a decrease in the uniformity of fertilizer application with the increase of the angle of the guide plate; when the conveyer belt speed is at medium and high levels, the amount of fertilization is large. There are more areas covered by the fertilizer repeatedly in the trench. As the angle of the guide plate increases, the movement time of the fertilizer on the guide plate becomes longer, and the amount of fertilizer per unit time becomes smaller. The area covered by fertilizers repeatedly decreases, leading to an increase in the uniformity of fertilization as the angle of the guide plate increases. When the advancing velocity is  $1.0 \text{ m}\cdot\text{s}^{-1}$ , the angle of the guide plate is at any level, and the fertilization uniformity increases first and then decreases with the increase of the conveyer belt speed, and the angle of the plate is at a high level, the effect of the conveyer belt speed on uniformity is more significant. The curve shown in the figure is steeper. With the increase of the conveyer belt speed, the amount of fertilizer applied per unit time becomes larger, and the area not covered by the fertilizer uniformly in the trench decreases. This means that when the angle of the guide plate in the range of  $37.5\sim 45^\circ$ , increasing the conveyer belt speed can significantly improve the fertilization uniformity.

In Fig.4c, the response surface of the fertilization uniformity opens downward, showing the interactive effect of the advancing velocity and the guide plate angle on the fertilization uniformity when the conveyer belt speed is  $200 \text{ r}\cdot\text{min}^{-1}$ , and when the advancing velocity is  $1.0 \text{ m}\cdot\text{s}^{-1}$  and the angle of the guide plate is  $30^\circ$ , the fertilization uniformity is the highest. It can be seen from the contour map that the influence of the advancing velocity on the fertilization uniformity is more significant than that of the guide plate angle. When the conveyer belt speed is  $200 \text{ r}\cdot\text{min}^{-1}$ , the advancing velocity is at any level, and the fertilization uniformity increases first and then decreases with the increase of the angle of the guide plate. When the advancing velocity is at a high level, the influence of the guide plate angle on fertilization uniformity is obvious, as shown in the figure, the fertilization uniformity curve is steeper, indicating that when the advancing velocity is in the range of  $1.1\sim 1.2 \text{ m}\cdot\text{s}^{-1}$ , appropriately increasing the angle of the guide plate can significantly improve the fertilization uniformity; when the advancing velocity is at a medium and low levels that in the range of  $0.8\sim 1.1 \text{ m}\cdot\text{s}^{-1}$ , maintaining the guide plate angle at a medium level can improve the fertilization uniformity. When the conveyer belt speed is  $200 \text{ r}\cdot\text{min}^{-1}$ , and the angle of the guide plate is at any level, the uniformity of fertilization increases first and then decreases with the increase of the advancing velocity. When the advancing velocity is low (the angle of the guide plate is high), the amount of fertilization is small, and some areas in the trench are not covered by fertilizer, which reduces the uniformity of fertilization. Increasing the angle of the guide plate or the advancing velocity appropriately can speed up the fertilizer movement rate and increase fertilization amount, reducing the area in the trench that is not evenly covered by fertilizer, and improving the uniformity of fertilization.

#### **Optimization of fertilization uniformity response surface**

According to the analysis of the measured data, it can be known that the conveyer belt speed, the advancing velocity and the guide plate angle have a certain effect on the uniformity of fertilization. The best condition for fertilization uniformity is obtained by overlapping three response surface graphs. The conveyer belt speed is within  $165\sim 235 \text{ r}\cdot\text{min}^{-1}$ , the advancing velocity is within  $0.8\sim 1.2 \text{ m}\cdot\text{s}^{-1}$ , and the guide plate angle is changed within the range of  $15\sim 45^\circ$ . When the conveyer belt speed is  $214 \text{ r}\cdot\text{min}^{-1}$ , the advancing velocity is  $1.0 \text{ m}\cdot\text{s}^{-1}$ , and the angle of the guide plate is  $37^\circ$ , the fertilization uniformity is the best, reaching 90.66%.

#### **Field test**

In December 2019, an apple gardening test was conducted at Yishui Henghe Farm. The test garden is standardized for planting with a row spacing of 4m and a plant spacing of 1.5 m. The terrain is flat, the soil quality is loam, and the soil pH is 6.7.

Before optimization, the conveyer belt speed is  $180 \text{ r}\cdot\text{min}^{-1}$ , the advancing velocity is  $0.8 \text{ m}\cdot\text{s}^{-1}$ , the angle of the guide plate is  $20^\circ$ . After optimization, the conveyer belt speed is  $214 \text{ r}\cdot\text{min}^{-1}$ , the advancing velocity is  $1.0 \text{ m}\cdot\text{s}^{-1}$ , the angle of the guide plate is  $37^\circ$ , and the verification test was repeated three times. The results are shown in Table 6.

The test results show that the uniformity of fertilizer release after optimization is 90.73%, which indicates that the test results after optimizing the parameters of the equipment are consistent with the actual values of

the response surface analysis. At the same time, the suitability of the established mathematical model is verified. After optimization, the machine fertilization depth reaches 35 cm, the fertilization uniformity is 90.73%, and the average depth of ditching is 40 cm, which meets the technical requirements for ditching and fertilizing in orchards.

Table 6

Field test results.					
Project	Tractor power [kW]	Amount of work	Depth of ditching [mm]	Depth of Fertilization [mm]	Fertilization uniformity [%]
Before optimization	44.13	2	400	350	86.31
After optimization	44.13	2	400	350	90.73

## CONCLUSIONS

(1) Establish a fertilization uniformity model. A single-factor and Box-Behnken central composite test is used to establish a mathematical model of fertilization uniformity. It is found through experiments that the mathematical model of fertilization uniformity is accurate and reliable, which provides a theoretical basis for the design and improvement of the orchard ditching-fertilizing machine.

(2) There are optimal values for the technical parameters of the orchard ditching-fertilizing machine. The structural parameters of the fertilizer device have a significant effect on the uniformity of fertilization. Under the conditions when the conveyor belt speed is 214.

$r \cdot \text{min}^{-1}$ , the advancing velocity is  $34r \cdot \text{min}^{-1}$ , and the angle of the guide plate is  $37^\circ$ , the uniformity of fertilization is optimal, increasing from 86.31% to 90.73%, and the fertilization stability was improved.

(3) Although the effects of structural parameters on fertilization uniformity have been completed, the effects of shapes of fertilizers on fertilization uniformity have not been studied. The effects of different shapes of fertilizers on fertilization uniformity will be the next research object.

## ACKNOWLEDGEMENT

This work was supported by the National Key Research and Development Programme of China and National Apple Industry Technology System Project (Grant numbers 2016YFD0201104, CARS-27).

## REFERENCES

- [1] Fan J., Zhang F., Wu L., Yan S., Xiang Y., (2016), Field evaluation of fertigation uniformity in drip irrigation system with pressure differential tank. *Transactions of the Chinese Society of Agricultural Engineering*, vol.32, issue 12, pp.96-101.
- [2] Han D., Lv Z., Cui F., Shen X., (2010), Design of the fertilizing machine for fruit trees. *Journal of Agricultural Mechanization Research*, vol.32, issue 12, pp.65-68.
- [3] Hofstee J. W., Huisman W., (1990), Handling and spreading of fertilizers part 1: Physical properties of fertilizer in relation to particle motion. *Journal of Agricultural Engineering Research*, vol.47, pp.213-234.
- [4] Hofstee J. W., (1992), Handling and spreading of fertilizers: Part 2, Physical properties of fertilizer, measuring methods and data. *Journal of Agricultural Engineering Research*, vol.53, pp.141-162.
- [5] Hofstee J. W., (1994), Handling and Spreading of Fertilizers: Part 3, Measurement of Particle Velocities and Directions with Ultrasonic Transducers, Theory; Measurement System, and Experimental Arrangements. *Journal of Agricultural Engineering Research*, vol.58, issue 1, pp.1-16.
- [6] Hofstee J. W., (1995), Handling and Spreading of Fertilizers: Part 4 The Reciprocating Spout Type Fertilizer Spreader. *Journal of Agricultural Engineering Research*, vol.62, issue 2, pp.9-24.
- [7] Hofstee J. W., (1995), Handling and Spreading of Fertilizers: Part 5, The Spinning Disc Type Fertilizer Spreader. *Journal of Agricultural Engineering Research*, vol.62, issue 3, pp.143-162.
- [8] Li M., Zhang T., Dong X., Wang C., Niu Z., Ge C., Wei L., (2016), Parameter optimization on scraper fertilizer feed unit of 3ZSP-2 type sugarcane intertillage fertilizer applicator-cum-hiller. *Transactions of the Chinese Society of Agricultural Engineering*, vol.32, issue 23, pp.36-42.
- [9] Liu S., Zhang H., Wang J., Zhang C., Sun L., Qi W., (2017), Optimization design of fertilizer-guiding mechanism for orchard ditching and fertilizing machine. *Journal of Chinese Agricultural Mechanization*, vol.38, issue 07, pp.45-53.

- [10] Ma C., Meng H., Kan Z., Qi J., (2017), The research current situation and development countermeasure of the orchard organic fertilizer deep application of disc ditching machine. *Journal of Agricultural Mechanization Research*, vol.39, issue 10, pp.12-17,28.
- [11] Ma J., Yan H., Wang C., (2016), Effect of end gun on/off on variable rate fertigation uniformity and its improvement for centre pivot irrigation system. *Journal of Hydraulic Engineering*, vol.47, issue 12, pp.1577-1584.
- [12] Qi X., Zhou Z., Lin S., Xu L., (2018), Design of Fertilizer Spraying Device of Pneumatic Variable-rate Fertilizer Applicator for Rice Production. *Transactions of the Chinese Society for Agricultural Machinery*, vol.79, issue S1, pp.164-170,180.
- [13] Qian Y., Liu K., (2018), Optimization of soil Cd extraction process using the response surface methodology. *Chinese Journal of Environmental Engineering*, vol.12, issue 12, pp.3448-3455.
- [14] Shen C., Jia S., Zhang L., Zhou Y., Li F., Dai Y., Zhang J., Ma W., (2019), Development of caterpillar self-propelled orchard gas explosion subsoiling and fertilizer machine. *Transactions of the Chinese Society of Agricultural Engineering (Transactions of the CSAE)*, vol.35, issue 17, pp.1-11.
- [15] Shu H., Chen X., (2018), The current task of the development of fruits industry in China. *China Fruits*, vol.2018, issue 02, pp.1-3.
- [16] Shi Y., Chen M., Wang X., Morice O.O., Li C., Ding W., (2018), Design and Experiment of Variable-rate Fertilizer Spreader with Centrifugal Distribution Cover for Rice Paddy Surface Fertilization. *Transactions of the Chinese Society for Agricultural Machinery*, vol.49, issue 03, pp.86-93,113.
- [17] Wang J., Gao G., Wang W., Wang J., Yan D., Chen B., (2018), Design and Experiment of Key Components of Side Deep Fertilization Device for Paddy Field. *Transactions of the Chinese Society for Agricultural Machinery*, vol.49, issue 06, pp.92-104.
- [18] Wang J., Li Z., Li M., Zhao D., Li E., Cheng C., Li Y., (2019), Based on Chinese situation, built a powerful country with Chinese characteristics in apple production. *China Fruits*, vol.05, pp.1-6.
- [19] Wang R., Wang W., Hu X., Yang X., Li H., (2017), Impact of fertilizer proportion and fertilizer-water ratio on clogging of filter by fertilizer pump in microirrigation. *Transactions of the Chinese Society of Agricultural Engineering*, vol.33, issue 23, pp.117-122.
- [20] Wang X., Yue B., Gao X., Zheng Z., Zhu R., Huang Y., (2018), Design and Experiment of Variable-rate Fertilizer Spreader with Centrifugal Distribution Cover for Rice Paddy Surface Fertilization. *Transactions of the Chinese Society for Agricultural Machinery*, vol.49, issue 10, pp.124-136.
- [21] Yang Q., Li Z., Li H., He J., Wang Q., Lu C., (2019), Numerical Analysis of Particle Motion in Pneumatic Centralized Fertilizer Distribution Device Based on CFD-DEM. *Transactions of the Chinese Society for Agricultural Machinery*, vol.50, issue 08, pp.81-89.
- [22] Yuan J., Liu Q., Liu X., Zhang T., Zhang X., (2014), Simulation of Multi-fertilizers Blending Process and Optimization of Blending Cavity Structure in Nutrient Proportion of Variable Rate Fertilization. *Transactions of the Chinese Society for Agricultural Machinery*, vol.45, issue 06, pp.125-132.
- [23] Yuan J., Mao M., Li M., Liu S., Wu F., Hu Z., Qin C., (2018), Optimization of CMP Processing Parameters for YG8 Cemented Carbide Inserts Based on RSM. *China Mechanical Engineering*, vol.29, issue 19, pp.2290-2297.
- [24] Yu Z., Huai S., Wang W., (2018), Leakage rate and optimization of working parameters for cylinder pickup collector based on spring-finger trajectory. *Transactions of the Chinese Society of Agricultural Engineering*, vol.34, issue 4, pp.37-43.
- [25] Zheng X., Lu H., Che J., Zhai B., Zhao Z., Wang Y., (2011), Investigation of present yield and fertilization on Fuji apple in Baishui county. *Journal of Northwest A & F University (Natural Science Edition)*, vol.39, issue 09, pp.145-151,158.
- [26] Zhou Z., Fu Z., Wang X., Qi L., (2009), Experiment of fertigation uniformity of drip fertigation machine. *Transactions of the Chinese Society of Agricultural Engineering*, vol.25, issue 05, pp.7-13.

## STUDY ON THE BEHAVIOR OF A BATTERY MOUNTED ON AN ELECTRIC TRACTOR PROTOTYPE

/

### STUDIU PRIVIND COMPORTAMENTUL UNEI BATERII DE ACUMULATORI MONTATĂ PE UN PROTOTIP DE TRACTOR ELECTRIC

Cristea M.<sup>1)</sup>, Matache M.<sup>1)</sup>, Sorică C.<sup>1)</sup>, Biriș S.Șt.<sup>\*2)</sup>, Ungureanu N.<sup>2)</sup>, Cristea R.D.<sup>2)</sup> <sup>1</sup>

<sup>1)</sup> National Institute for Research-Development of Machines and Installations Designed for Agriculture and Food Industry – INMA Bucharest / Romania;

<sup>2)</sup> University POLITEHNICA of Bucharest, Faculty of Biotechnical Systems Engineering / Romania

<sup>\*)</sup> Corresponding author, E-mail address: biris.sorinstefan@gmail.com

First author E-mail: mario.cristea@gmail.com

DOI: <https://doi.org/10.35633/inmateh-62-02>

**Keywords:** battery management, electric tractor, pollution

#### ABSTRACT

*In this article it is studied the behaviour of a rechargeable battery, which outputs a maximum power capacity of 17 kWh that's being used as the main source of the prototype electric tractor developed at INMA Bucharest. This tractor is equipped with 16 kW electric motor, 4 speed gearbox and 4x4 traction. The charging mode of the battery when it is supplied with different powers from the current source was studied, but also the power delivery mode when the tractor is in operation and different loads occur. The energy consumption of the battery has also been studied, from the moment when the tractor is put into operation, driving on flat asphalt or agricultural land, with or without load and also in extreme traction conditions, for ploughing or towing heavy loads.*

#### REZUMAT

*În acest articol este studiat modul de comportare a unei baterii de acumulatori, care poate debita o energie maximă de 17kWh, ce este folosită ca sursă principală de energie la prototipul tractorului electric dezvoltat în cadrul INMA Bucuresti. Tractorul este echipat cu un motor electric cu putere 16kW, cutie de viteze cu 4 trepte și tracțiune 4x4. A fost studiat modul de încărcare al bateriei atunci când este alimentată cu puteri diferite de la sursa de curent dar și modul de livrare a energiei atunci când tractorul este supus diferitelor regimuri de lucru în funcționare. De asemenea a fost studiat consumul de energie din baterie de la momentul când tractorul este pus în funcțiune, rularea pe teren plan, asfaltat sau teren agricol, cu sau fără sarcină dar și în condiții extreme de tracțiune, la lucrări de arat sau tractarea unor sarcini mari.*

#### INTRODUCTION

Romania's agricultural area is about 14 million ha, ranking 7th place in Europe, 9.7 million ha of which are arable land.

The processing in the modern agrotechnical conditions targeting at this surface, implies a complex technical-material base, in which the agricultural tractors have the main role. (*Ministry of Agriculture and Rural Development*).

According to the population density of Romania, each inhabitant has about 0.41 ha of arable land, a value superior to many countries in the European Union and almost double the EU average, which is 0.212 ha/inhabitant.

On a farm in Romania, a tractor is used for about 10,000 hours after which it is taken out of use, while in other U.E. member countries, the use of a tractor on a farm does not exceed 4,000 hours ([www.madr.ro](http://www.madr.ro)). According to statistics (figure 1), until 2016, over 200,000 tractors were officially registered in Romania. Analysing this data, it can be seen that from 1990 to 2016 the number of tractors increased by about 50,000 units. We can consider that of the 150,000 tractors registered before 1990, a large part was in operation in 2016 as well. These units certainly do not meet the new environmental protection requirements and the pollution of the environment by them is significant.

<sup>1</sup> Cristea M., Ph.D. Stud. Eng.; Matache M., Ph.D. Eng.; Sorică C., Ph.D. Eng.; Biriș S.Șt., Ph.D. Eng.; Ungureanu N., Ph.D. Eng.; Cristea R.D., Stud.

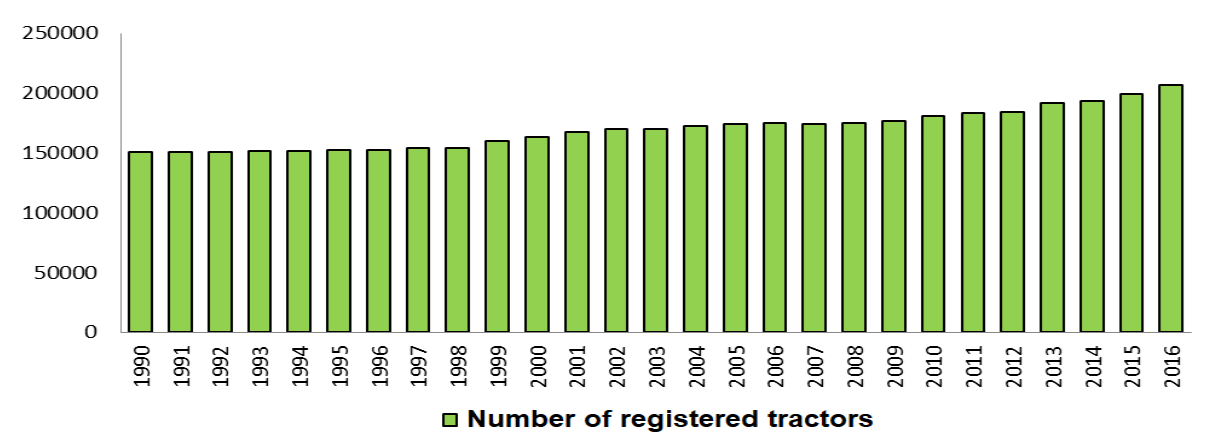


Fig. 1 - Evolution of the number of tractors in Romania

It has been shown that noxious substances lead to acid rain, ozone depletion and soil degradation. Monoxide and nitrogen dioxide (NO<sub>x</sub>) are gases generated as a result of combustion, when the engine is hot, and material particles (PM) which are composed mainly of carbon particles and other substances harmful to the environment and life, occur as a result of incomplete combustion of fuel during the operation of heat engines, especially when the engine is colder.

Specific regulations have been created to reduce the emissions generated by heat engines and the new conditions imposed by Tier 4 on reducing pollution have led to changes in the construction of tractor engines and combine harvesters. The regulations imposed by Tier 4A came into force on January 1, 2011, setting the levels of particles and pollutants allowed for heat engines over 174 hp (130 kW), and the emergence of Tier 4B regulations led to the need to meet more drastic conditions, with applicability from 2014, for all heat engines that fall under the scope of these regulations (<https://www.agrimedia.ro/articole/scr-devine-o-certitudine-la-tractoare-si-combine>).

These regulations are studied and amended so that pollution is reduced as much as possible, thus creating new documents in the field, such as: Directive 2009/29/EC of the European Parliament and of the Council of 23 April 2009 amending Directive 2003/87/EC to improve and extend the Community scheme for greenhouse gas emission allowance trading (EU emission allowances, "EU ETS") and Decision 406/2009 / EC of the European Parliament and of the Council of 23 April 2009 on the efforts of Member States to reduce greenhouse gas emissions so as to comply with the Community's commitments to reduce greenhouse gas emissions by 2020 (Decision on the sharing of efforts, "ESD"). There are studies conducted worldwide that show very clearly that the use of renewable energy reduces oil consumption and as a result, emissions are reduced. In support of these studies, vehicles have been designed and built that are powered by renewable energy and that are clean from the point of view of pollution. Well-known manufacturers in the field such as John Deere, Soletrac, Fendt and others already have in their portfolio prototypes of electric tractors. *Huisong Gao* presents the main concerns that exist even at the level of small manufacturers for the development of electric tractors (*Gao H. et al, 2020*). There are concerns about lowering the price of electric tractors by replacing expensive electronic control components with other equipment that performs the same tasks but is much cheaper and can be programmed using existing programs in research laboratories. *Yanni Chen* and colleagues demonstrate how to replace the controller of an electric tractor, an expensive component of the propulsion system, with a programmable logic circuit that is much cheaper (*Yanni Chen, et al, 2016*). Energy savings are highlighted in the study conducted by *Oscar Lagnelöv* which compares the charging systems used in electric tractors (*Lagnelöv O. et al, 2020*).

In densely populated countries, such as India, the problems posed by pollution and fuel economy are widely studied and the introduction of new technologies in agriculture occupies an important place in research (*Ashish M., et al, 2020*).

Some of the advantages of clean energy sources (green energy) compared to conventional energy sources (fossil energy sources or energy sources that are depleted and there is no possibility to regenerate), could be the following:

1. extremely low pollution and environmental impact;
2. they can ensure energy independence;

3. they can provide energy to activities carried out in territories where there is no possibility of connection to the electricity grid;
4. new branches of industry can be developed;
5. they are sources of income;
6. they are easily renewable.

Often, the use of renewable energy sources requires a higher financial effort, incurring additional costs with the distribution and recovery of this type of energy. As a result, such projects involve financial solutions to reduce payback periods and increase economic performance.

In this context, this article analyses the behaviour of a rechargeable battery, used as the main energy source for the prototype of the electric tractor developed within INMA Bucharest.

## MATERIALS AND METHODS

For the tests, a prototype general purpose electric tractor was used fitted with a 4-speed gearbox for going forward and a shifter to be able to use the 4 gears for reversing (with 4X4 traction), an asynchronous three-phase model AME200 electric motor of 16kW which is controlled by a Curtis controller and a 144V, 120 A rechargeable battery controlled by a management system (battery management system BMS) model Orion 2 (<https://www.orionbms.com/products/orion-bms-standard/>) used to charge the battery using a 6.6 kW (6.6KW HK-J) charger.

The figure below shows the electric tractor used in the tests.



**Fig. 2 - The prototype electric tractor used in the tests**

The prototype general purpose electric tractor has been designed to be used with electric motors with powers from 6kW to 50kW, has 4X4 traction, hydraulic system for both power steering and agricultural equipment that can be connected to the tractor and a PTO with 2 speeds (540 and 1000 rpm). Given that this tractor is designed to use only the electrical power generated by a battery, all electronic subsystems are designed for low power consumption. The main technical characteristics of the electric tractor are:

- Maximum length: 3330 mm;
- Maximum width: 1530 mm (with mirrors 1730 mm);
- Maximum height (cabin): 2530 mm;
- Wheelbase: 2020 mm;
- Gauge: 1280 mm front; 1250 mm rear;
- Ground clearance: 260 mm (front);
- Total weight: 1970 kg;
- Maximum speed from GPS: 28 km/h.

The battery used is built from 10 3.6V cells mounted in series; there are 4 such packages that are all connected in series. At the cell level there is a temperature sensor used by the BMS to accurately monitor the "health" status of each cell. Also, with the help of specialized sensors, the BMS has information on the state of charge of each cell.

The figure below shows the construction of the battery.



Fig. 3 - 144V battery

When charging the battery, a 6.6 kW charger is used which, with the help of a control network (Controller Area Network, CAN Bus), communicates with the BMS and the motor controller to determine the charging mode according to the existing power of the mains. Battery parameters are saved and archived on an SD card, and can be viewed with a computer using specialized software

The connection block diagram is shown below (figure 4) ([cdn.shopify.com/s/files/1/1820/0269/files/orionbms\\_2\\_wiring\\_and\\_installation\\_manual.pdf?1289632542684048831](https://cdn.shopify.com/s/files/1/1820/0269/files/orionbms_2_wiring_and_installation_manual.pdf?1289632542684048831)).

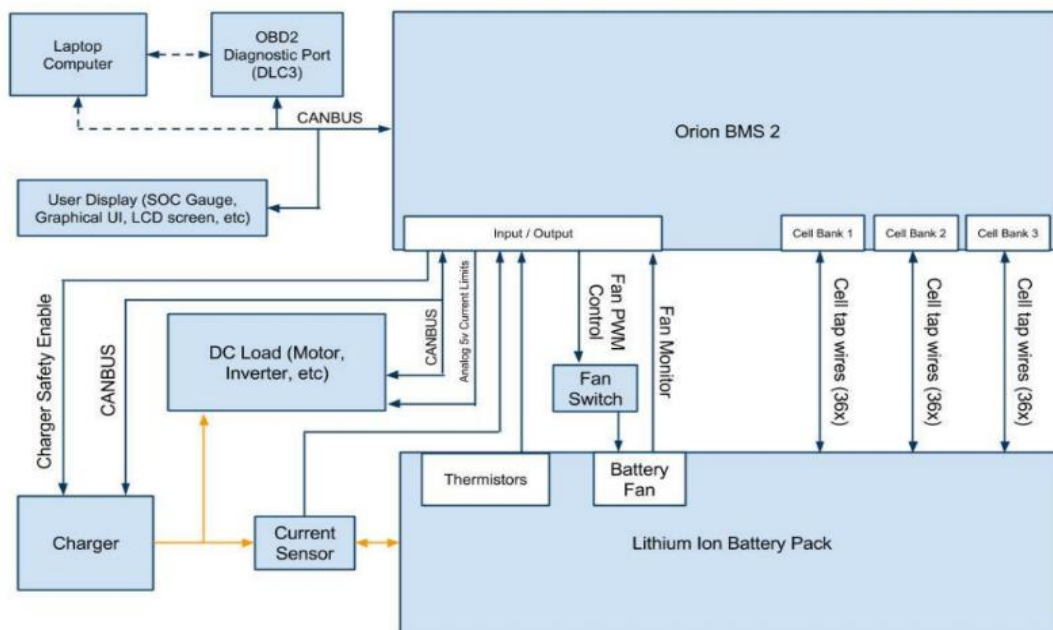


Fig.4 - System connections

During the experiments the following parameters were observed:

1. The time required to charge the battery;
2. Operating time of the battery on the tractor without load, on level ground;
3. Operating time of the battery on the tractor, having different loads and on rough terrain;
4. Maximum traction force on asphalt, until loss of traction;
5. Maximum traction force in the field, until loss of traction.

Prior to the start of the test, the battery was subjected to a series of three charge-discharge cycles on the test bench for the batteries, in this way the cells that make up the battery are brought into a normal mode of operation, thus avoiding the possibility of occurrence during the tests of errors that could alter the final results. The charger used has a maximum power of 6.6 kW, is designed to charge LiFePO<sub>4</sub>/lithium cell-based batteries and is thus designed to communicate with the battery management system. It is a charger that has a high efficiency, high stability, small size and high degree of protection (IP67). It also has an energy efficiency of up to 95% and only 93% at maximum power, operating over a wide range of input voltages AC90V ~ AC400V 45 ~ 65 Hz, with high tolerance to fluctuations in electrical networks. It has intelligent functions including the possibility of temperature compensation in the charging process, preventing battery damage caused by excessive charging, considerably extending battery life.

The tractor's electric motor controller receives signals from the battery management system, including the battery state of charge (SOC), discharge values, terminal voltage and temperature. According to the information received through the CAN, the monitoring and protection functions are activated for the system, as a whole, to operate safely.

The control system monitors the current, voltage and temperature of the motor and other electrical equipment, which simultaneously send signals to the electronic controller to check the safety of the electrical circuit of the equipment (Yanni C., 2016).

**Table 1**

The main technical characteristics of the charger	
Technical data	Value
AC input voltage	AC90 V~AC400 V
AC frequency input	45~65 Hz
AC power factor	≥0.98
Maximum load efficiency	≥93%
IP protection rating	IP67
Operating temperature	-40°C....+55°C
Storage temperature	-40°C...+100°C
Mechanical dimensions (mm)	353(L)*230(W)*160(H)
Net weight	17 kg

Battery parameter visualization software is provided by Ewert Energy Systems, Inc. at <https://www.orionbms.com>. This software will continue to be used to study the battery.

**RESULTS**

During the charging tests from a 220 V and 32 A source, an average of 125 minutes required to charge the battery from 10% to 90% of maximum capacity was measured.

The power consumed from the energy source is:

$$P=UI, (W) \tag{1}$$

$$P_C=PK, (W) \tag{2}$$

where

*P*- power consumed from the power supply; *U*- power supply voltage, 220V

*I*- power supply current, maximum 32A; *P<sub>C</sub>*- power charged by the charger

*K*- loader efficiency coefficient, 0.93%

The graph below shows the voltage of the battery during a 90-minute charge. (figure 5).

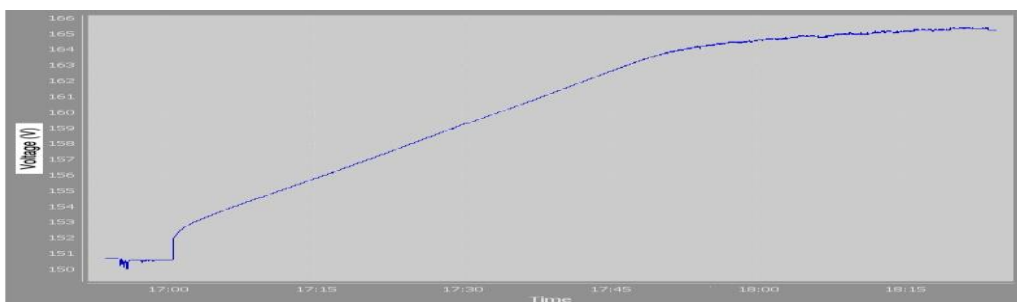


**Fig. 5 - Battery charging voltage**

Battery charging limits are set by software according to the characteristics of each battery and all these parameters are stored in the internal memory of the BMS. The entire BMS controls the current and voltage values that the charger delivers to the battery.

An example of charging current control is shown in figure 6, for which in settings the maximum charging current was set to 100 A.

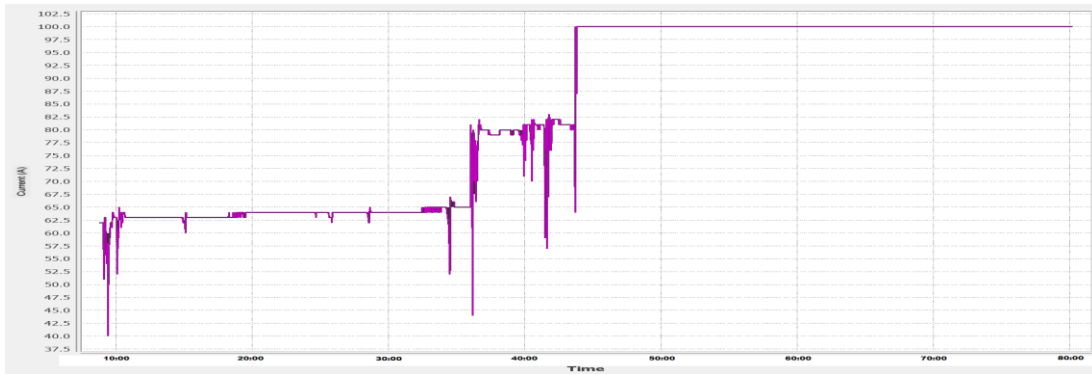


Fig. 6 - Charging current limitation

After charging the battery to 90%, the tractor has been moved on level ground, on asphalt and arable land to establish the autonomy of the battery when the tractor has no other load than that required for self-driving. The maximum speed achieved by the electric tractor prototype was 24 Km/h, the speed indicated by GPS. The tractor operated in these conditions for 260 minutes until the battery reached 10% state of charge. The figures below show the voltage variations that occur at different tractor loads and the voltage drop over time. It can be observed that at the cell level, in percentages, the same voltage variations occur.

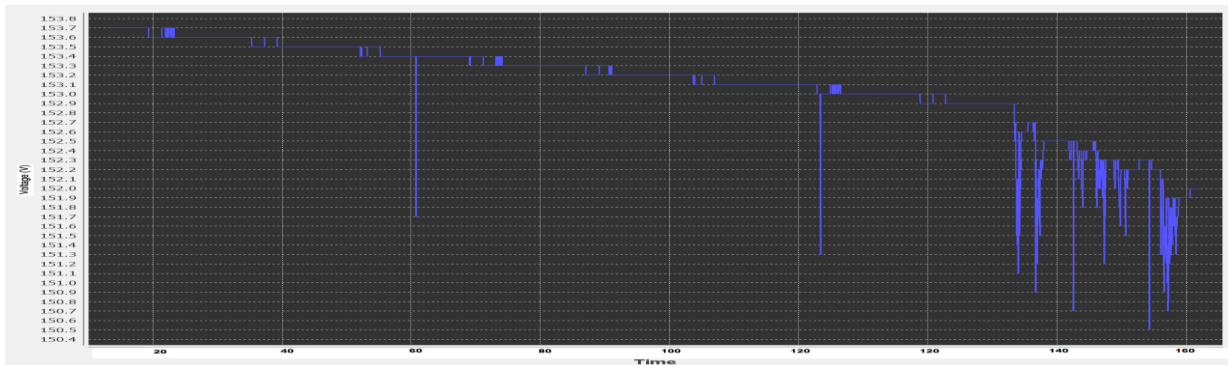


Fig. 7 - Voltage variation during operation for 160 minutes, tractor prototype

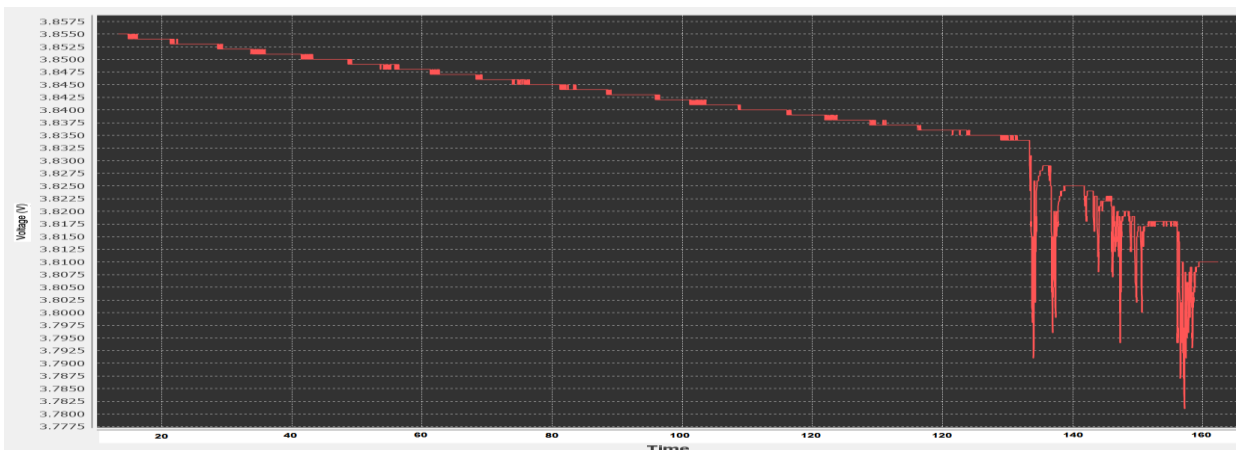


Fig. 8 - Variation of voltage at cell level during operation for 160 minutes

During the next charge of the battery, up to 90% of capacity, a power source of 220V and 16A was used, resulting in a charging time of 254 minutes.

The load test was performed with an empty trailer, weighing 1800 kg, to which were added standard weights totalling 2000 kg. The route was made on flat land (asphalt and agricultural land), rough terrain and arable land. The tractor operated in these conditions for 217 minutes.

In figure 9 a decrease in voltage can be seen, when the tractor has a load for 60 minutes, it goes from 164.8V to 161.2V with peak voltage drops of up to 159.8V.

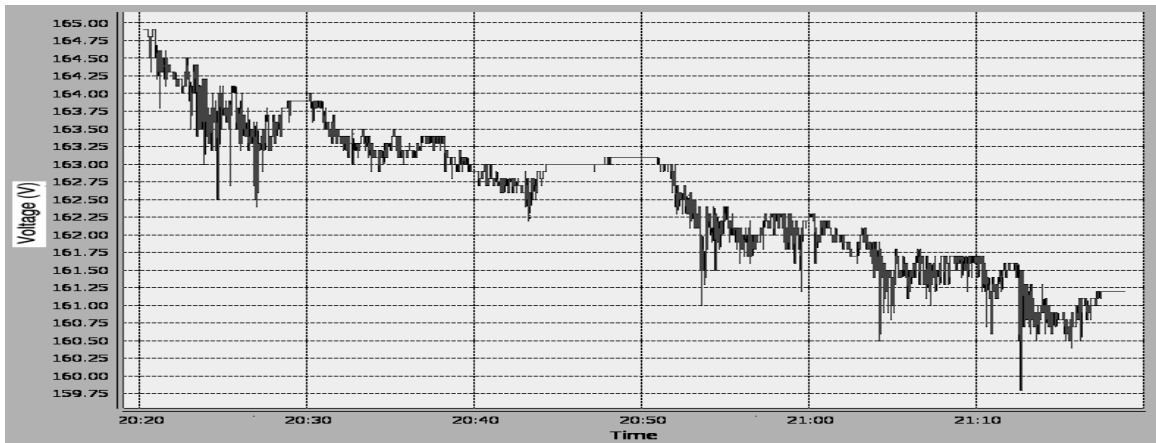


Fig. 9 - Voltage variation in one hour of operation with load

Current consumption under the same conditions can reach peaks of up to 61A, this is highlighted in figure 10.

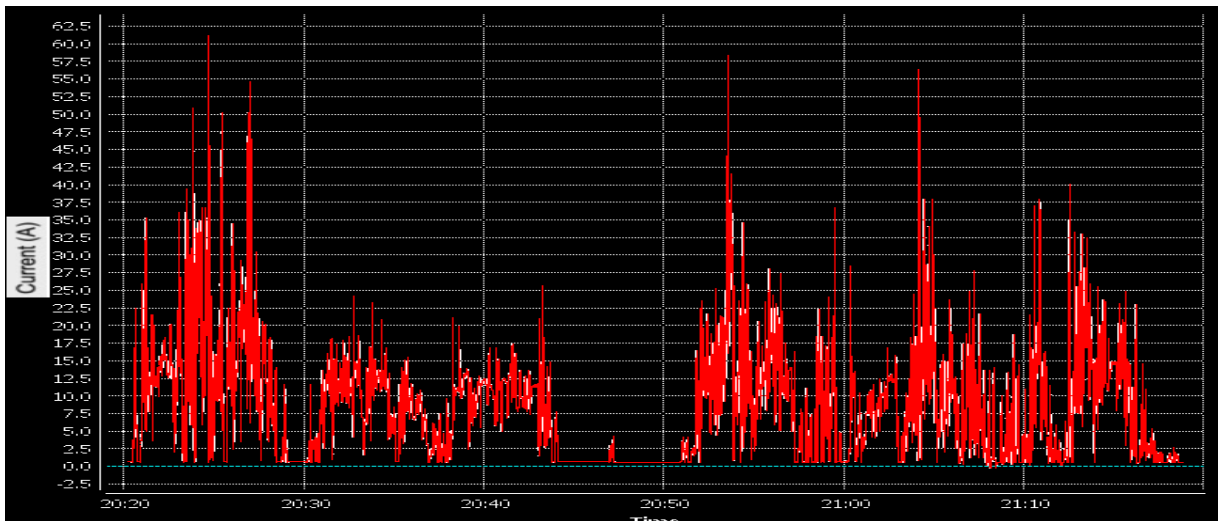


Fig. 10 - Current variation in one hour of operation with load

Another charging test was performed using a 6Ah power outlet. Using this power source, the battery had to be charged for 11 hours to reach 90% state of charge. The graph below shows 5 hours of charging.

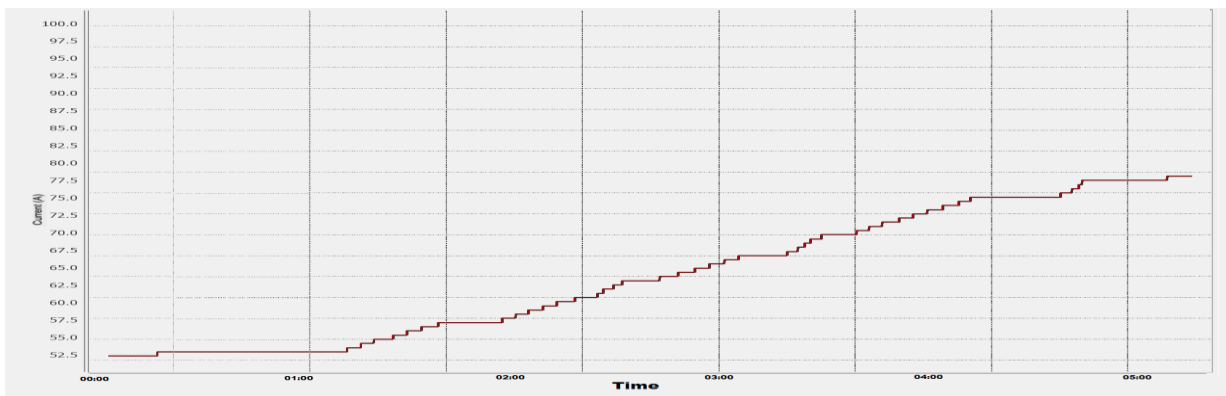
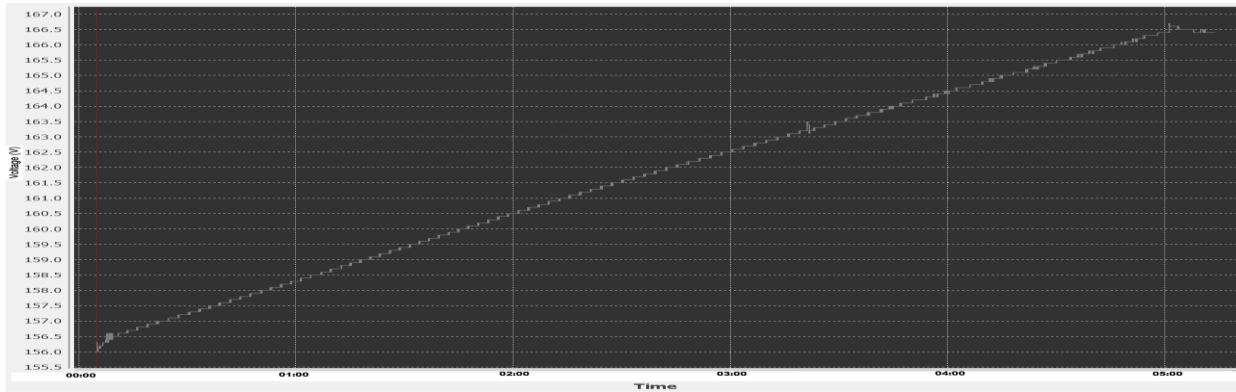


Fig.11 - Amperage graph during 5 hours of charging

The figure below shows the voltage increase graph when charging from a 6Ah source:



**Fig. 12 - Voltage graph during 5 hours of charging.**

After the battery was charged to 90% capacity, the tractor was used for one of the heaviest tasks that can be assigned to a tractor, namely the basic tillage (ploughing), for about an hour. The surface shown was 2000 sqm, the working depth of the reversible plough with two furrows being 20 cm.

During this task, the battery power consumption was monitored. The current consumption is shown in figure 13; the current peaks that occur at high loads, reaching over 400A, can be clearly seen.

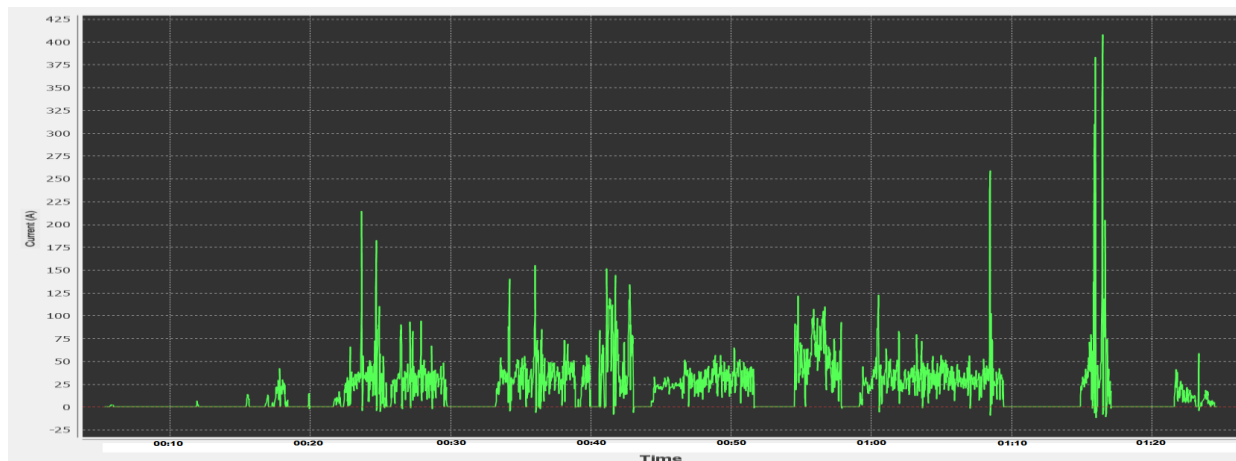


**Fig. 13 - Ploughing current consumption**

In addition to the current, we also have the voltage variation that occurs for the load conditions to which the tractor is subjected, figure 14 showing the voltage drop while the tractor was ploughing. Under these conditions, the voltage drop in 80 minutes is 8.6V, from 157.8 to 149.2V with a peak drop of up to 138.2V.

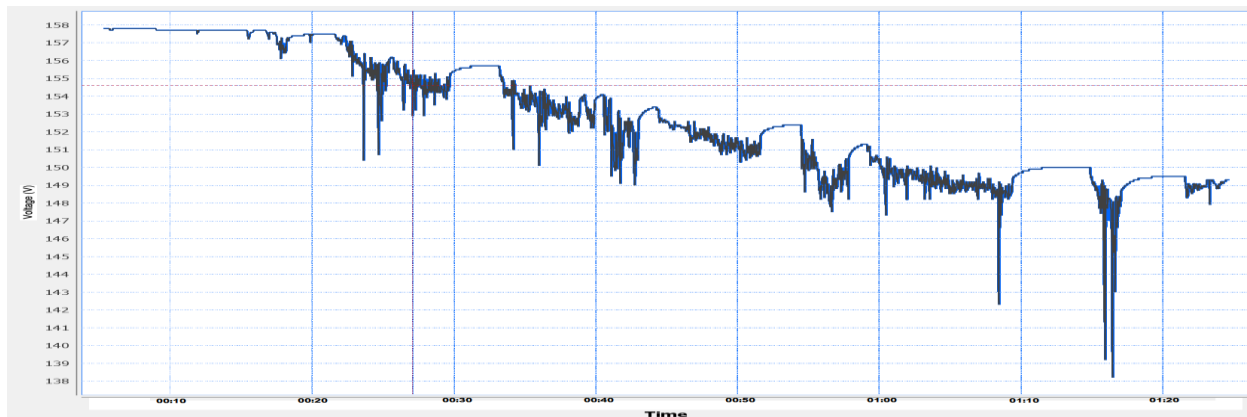


**Fig. 14 - Voltage drop during ploughing**

Globally, research in the field of tractor construction is aimed at optimizing fuel consumption, reducing maintenance costs, increasing the interval between overhauls and thus increasing the number of operating hours of tractors. Research into the construction of tractors aims not only to increase economic efficiency but also to drastically reduce the pollution generated by the production of a tractor but also the pollution produced by a tractor over the entire period from the sale of the tractor to decommissioning.

Thus, in order to assess the actual power of a tractor, tests are carried out by means of the drawbar under controllable and well-established conditions. Force measurement may also be performed with dynamometric vehicles (DV) which are vehicles specially instrumented and designed to measure the horizontal force on the traction of agricultural tractors. The CREA laboratory in Treviglio, Italy, has designed a new torque tester for tractors with up to 200 kW (245 kW at the wheel) and a maximum traction force of 118 kN (12032.65 kgf) (Cutini M. and Bisaglia C., 2016).

The traction test was performed on asphalt, the traction tires used were size 11.2-24 on the rear axle and 6.00-16 on the front axle. As the front axle load is low for this type of tractor, the use of wheels with a diameter equal to that of the rear wheel is not justified (Duțu M.F., et al, 2019). The traction test was performed on agricultural land in the same atmospheric conditions, the temperature in the atmosphere being 23.1 degrees Celsius and air humidity 45%. The dynamometer used had a measuring range of 50 kN with a division of 0.5 kN.

The tests were carried out by loading the tractor with a fixed load mounted on the ground and coupled to its drawbar. The forces were noted when the slip phenomenon appeared on the drive wheels. The object of the study being the behaviour of the battery, the experimental determinations did not take into account the necessary conditions for the exact determination of all the forces that appear in the tractor-load system.

The following forces resulted from the traction test:

1. Asphalt traction 15 kN (1529 kgf) with 4X2 and 16.5 kN (1682 kgf) with 4X4;
2. Traction on agricultural land 18kN (1835 kgf) with 4X2 and 21.5kN (2192 kgf) with 4X4.

Instantaneous energy consumption when the tractor is subjected to extreme loads, on asphalt with 4X2 traction and maximum slip, is shown in the graph below.

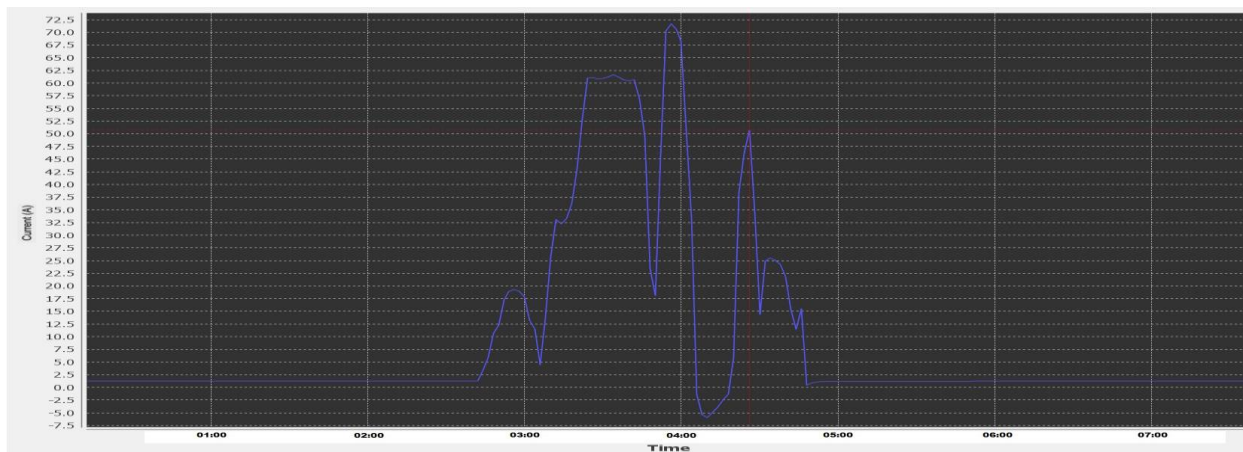


Fig. 15 - Current consumption of the electric tractor prototype at maximum load

The maximum battery current was 71.7 A, the average voltage was 151.5 V resulting in an instantaneous consumption of 10.9 kW. This consumption was recorded at the time of the 4X2 traction test on paved terrain.

## CONCLUSIONS

After all the tests performed, it can be considered that a general-purpose tractor chassis can be electrically operated from batteries.

According to the charging / discharging graphs as well as the behaviour in real conditions, it can be said that the battery behaves within normal limits, compared to the results obtained by other electric tractor developers. Charging up to 90% of total capacity took 3 hours, which is the average charging time obtained by other equipment of the same type. The average operating time on duty was approximately 4 hours, being an autonomy that falls within the average reported values in other scientific papers.

The advantages of using the electric tractor, especially indoors, are clearly superior to a traditional tractor. In closed spaces, such as greenhouses or solariums, charging stations with power supplied by the national network or renewable sources can be placed to use the time when the machine is not in use results in an increase of efficiency. If the tractor is used in the open field, there is even the possibility of bringing mobile charging stations that can be located as close as possible to the place where these machines are used, to use solar or wind energy in order to produce the energy needed to charge the batteries.

The best advantage of electrically powered tractors is the lack of emissions into the atmosphere. Another positive aspect is the low impact on the ground because when the machine is powered by a battery there is no risk of fossil fuels leaking that may reach the work surface by mistake or as a result of an accident. The tested battery managed to complete the proposed tasks in conditions very close to normal. Battery manufacturing technologies being in full development will surely end up with a much shorter charging time, extended operating time and a much longer operating time. These things combined with the declining price of batteries will make them a very good replacement for fossil fuels. Also, the replacement of fossil fuels with batteries is already a necessary thing if we look at it from the point of view of pollution. At the moment, the production, integration and use of electricity as fuel may seem financially expensive and inefficient, but the long-term calculation shows that, on the contrary, this technology will bring great financial benefits and especially in terms of environmental impact.

## ACKNOWLEDGEMENT

This work was supported by a grant of the Romanian Research and Innovation Ministry, through Sector Plan, contract no. 1PS/2019 and a grant of the Romanian Ministry of Research and Innovation CCDI - UEFISCDI, Project number PN-III-P1-1.2-PCCDI-2017-0254, Contract no. 27 PCCDI / 2018, within PNCDI III.

## REFERENCES

- [1] Ashish Malik, Shivam Kohli, (2020), Electric tractors: Survey of challenges and opportunities in India. *Materials today: Proceedings*, Volume 28, Part 4, pp. 2318-2324. [10.1016/j.matpr.2020.04.585](https://doi.org/10.1016/j.matpr.2020.04.585)
- [2] Chen Yanni, Xie Bin, Mao Enrong, (2016), Electric Tractor Motor Drive Control Based on FPGA. *IFAC-Papers On Line*, Volume 49, Issue 16, pp. 271-276. <https://doi.org/10.1016/j.ifacol.2016.10.050>
- [3] Cutini M., Bisaglia C., (2016), Development of a dynamometric vehicle to assess the drawbar performance of high-powered agricultural tractors. *Journal of Terramechanics*, Volume 65, pp. 73-84.
- [4] Duțu M.F., Biriș S.Șt., Duțu I.C., Iordache S.D., (2019), The study of the dynamics of the tractor aggregate on wheels, formula 4x4, towed machine. *Research people and actual tasks on multidisciplinary sciences*, pp.179-183, Lozenec / Bulgaria.
- [5] Gao Huisong, Xue Jinlin, (2020), Modelling and economic assessment of electric transformation of agricultural tractors fuelled with diesel. *Sustainable Energy Technologies and Assessments*, Volume 39. <https://doi.org/10.1016/j.seta.2020.100697>
- [6] Lagnelöv O., Larsson G., Nilsson D., Larssolle A., Hansson P.A., (2020), Performance comparison of charging systems for autonomous electric field tractors using dynamic simulation. *Biosystems Engineering* Volume 194, pp. 121-137. [10.1016/j.biosystemseng.2020.03.017](https://doi.org/10.1016/j.biosystemseng.2020.03.017)
- [7] \*\*\* Directive 2009/29 / EC of the European Parliament and of the Council of 23 April 2009 amending Directive 2003/87 / EC to improve and extend the Community system for the trading of greenhouse gas emission allowances.  
<https://eur-lex.europa.eu/legal-content/RO/TXT/PDF/?uri=CELEX:32009L0029&from=EN>
- [8] \*\*\* Ministry of Agriculture and Rural Development, *Strategy for the development of the agri-food sector in the medium and long term 2020 2030*. [www.madr.ro](http://www.madr.ro)
- [9] \*\*\*[cdn.shopify.com/s/files/1/1820/0269/files/orionbms2\\_wiring\\_and\\_installation\\_manual.pdf?1289632542684048831](https://cdn.shopify.com/s/files/1/1820/0269/files/orionbms2_wiring_and_installation_manual.pdf?1289632542684048831)
- [10] \*\*\*[evolveelectrics.com/products/1239-e](https://evolveelectrics.com/products/1239-e)
- [11] \*\*\*[www.agrimedia.ro/articole/scr-devine-o-certitudine-la-tractoare-si-combine](http://www.agrimedia.ro/articole/scr-devine-o-certitudine-la-tractoare-si-combine)
- [12] \*\*\*[www.arq.ro/tractorul-utilajul-agricol-care-a-schimbata-in-totalitate-eficienta-activitatilor-agricole/25071](http://www.arq.ro/tractorul-utilajul-agricol-care-a-schimbata-in-totalitate-eficienta-activitatilor-agricole/25071)
- [13] \*\*\*[www.orionbms.com/products/orion-bms-standard/](http://www.orionbms.com/products/orion-bms-standard/)

# EXPERIMENTAL RESEARCH ON COMPREHENSIVE PERFORMANCE OF COUPLED MUFFLER BASED ON SPLIT-STREAM RUSHING PRINCIPLE

## 基于分流气体对冲原理的耦合消声器综合性能的试验研究

Jing Xue, Pei Wu\*, He Su, Yongan Zhang, Haijun Zhang<sup>1</sup>

College of Mechanical and Electrical Engineering, Inner Mongolia Agricultural University, Hohhot 010018, China

Tel: +86 13500697822; E-mail: jdwupei@163.com

DOI: <https://doi.org/10.35633/inmateh-61-03>

**Keywords:** coupled muffler, split-stream rushing principle, acoustic performance, exhaust resistance performance

### ABSTRACT

Based on the split-stream rushing principle and multi-unit coupling theory, a new type of coupled muffler for diesel engine was designed, and the experimental study on the acoustic performance and exhaust resistance performance was completed. The results show that the growth rate of insertion loss of the coupled muffler within 200 Hz is 34.01% compared to the original muffler. The average fuel consumption reduction rate of the diesel engine with the coupled muffler is 19.16% lower than that of the original muffler. Therefore, the coupled muffler can achieve the comprehensive goal of good acoustic performance and low exhaust resistance.

### 摘要

依据分流气体对冲原理和分级耦合理论设计了一种柴油机新型耦合消声器，完成了声学性能和排气阻力性能的试验研究。结果显示，新型消声器在 200Hz 内插入损失相对于原机消声器的增长率为 34.01%。柴油机安装耦合消声器后相比原机消声器的平均油耗降低率为 19.16%。耦合消声器通过降低消声器内气流速度可以实现声学性能好且排气阻力低的综合目标。

### INTRODUCTION

Diesel engines are still widely used in current transportation vehicles and agricultural machinery, but the noise of diesel engine is loud, and the main source of the noise is exhaust noise (He Su *et al.*, 2020).

Generally, reactive mufflers are installed to control the exhaust noise of diesel engines, but the traditional reactive mufflers existing have their own defects, and a single structure cannot meet the requirements of good acoustic performance in wide frequency range (Yongan Zhang *et al.*, 2017).

At present, passive mufflers are still widely used. Its noise elimination mechanism is to eliminate noise through the destructive interference of pressure waves and prevent sound energy from continuing to be transmitted downstream. In recent years, a large number of researches on passive mufflers have been carried out, but there is no major change in the principle of passive muffler. The main work is focused on optimizing the internal structure of the muffler to further improve its performance. For example, an expansion chamber structure with two inlets and one outlet was designed to optimize the insertion loss of muffler (Hua X. *et al.*, 2014), a type of multi-chamber perforated resonator (MCPR) was used to attenuate broadband noise (Rong Guo *et al.*, 2016), a multi-chamber micro-perforated muffler with adjustable transmission loss was studied (Longyang Xiang *et al.*, 2017), a simple expansion chamber muffler with U-shaped corrugated pipes was applied and its experiments of the comprehensive performance were carried out (Fei Xue *et al.*, 2018), the acoustic attenuation characteristics of three-pass mufflers with perforated inlet and outlet tubes were analysed (Yiliang Fan *et al.*, 2019).

In recent years, noise control idea of dual-mode mufflers or semi-active mufflers has been proposed to improve noise control of low frequency. A cross-flow semi-active impedance compound muffler was proposed and its internal structural parameters could be changed to adjust the noise sound pressure level and frequency characteristics at the outlet (Xiaotian Bai, 2016), and a semi-active muffler based on HQ tube to control low-frequency noise in the exhaust pipe was proposed, but the results showed that the acoustic

<sup>1</sup> Jing Xue, As. Ph.D. Stud. Eng.; Pei Wu, Prof. Ph.D. Eng.; He Su, Lect. Ph.D. Eng.; Yongan Zhang, Prof. Ph.D. Eng.; Haijun Zhang, Lect. M.S. Eng.

performance of the semi-active muffler above 350 Hz was poor compared with the passive muffler (Yawei Zhu *et al.*, 2017).

The sound elimination principle of the active muffler is to generate a sound wave with the same magnitude and opposite phase as the original sound pressure through the active system to cancel out the original sound field in a certain area. However, the active muffler has not been well applied and promoted, which includes the accuracy of the addition of secondary sound field, signal detection of the original noise field and the controller design. At the same time, the exhaust system of diesel engine is under severe condition of high temperature, high pressure, high speed, strong chemical corrosion, large smoke and dust, which causes many difficulties in the realization of active mufflers (Zhu Congyun *et al.*, 2017; Sang-Myeong Kim., 2018).

It can be seen that the existing passive, semi-active and active mufflers have their own advantages and disadvantages. The noise reduction performance still needs to be improved and the stability of the low-frequency noise reduction effect for diesel engines should be improved.

Moreover, it is found that if the noise attenuation performance of a wide frequency band is guaranteed, the pressure loss of the muffler is often too large (He Su *et al.*, 2018). The most critical factor affecting the overall performance of the exhaust muffler is the airflow velocity in the muffler (Pei Wu *et al.*, 2010). In view of this, our research group has proposed a new type of split-stream-rushing exhaust muffler unit, which can effectively reduce the flow velocity of the internal muffler (Yongan Zhang *et al.*, 2018).

As we all know, a complete diesel exhaust muffler is composed of several muffler units, and a separate split-stream-rushing muffler unit also needs to be coupled with a traditional reactive muffler unit to form a complete muffler. Based on this, a structure of a new type of coupled muffler for diesel engine is proposed in this paper, and the multi-unit coupling problem of the split-stream-rushing muffler unit and the traditional reactive muffler units to achieve better acoustic performance in wider frequency band and lower exhaust resistance at the same time. The airflow velocity in the muffler will be reduced through split-stream-rushing muffler unit in front to avoid excessive airflow regeneration noise and exhaust back pressure, and then acoustic performance of the low frequency will be further improved through a small amount of traditional reactive muffler units so as to achieve comprehensive improvement of acoustic performance and exhaust resistance performance.

## MATERIALS AND METHODS

### MODEL DESIGN OF COUPLED MUFFLER

In order to reduce the middle and low frequency noise and some high-frequency noises of diesel engines, the new coupled muffler structure of diesel engines proposed by the author was to couple the outlet of the split-stream-rushing unit with an expansion chamber unit with intubation. In order to facilitate the test comparison, the chamber volume, length and internal diameter of the exhaust pipe of the coupled muffler for the diesel engine were all consistent with the original engine muffler. The design calculations of the internal structure parameters of the coupled muffler were completed by the design principle of muffler and multi-unit coupling theory. In order to reduce the exhaust resistance, according to the characteristics of the fluid, each cross-sectional area of the exhaust airflow flowing through the interior of the muffler was greater than or equal to the inlet cross-sectional area of the muffler. The structural optimization model of the coupled muffler was obtained by calculations. The structure diagram of the coupled muffler was shown in Fig.1.

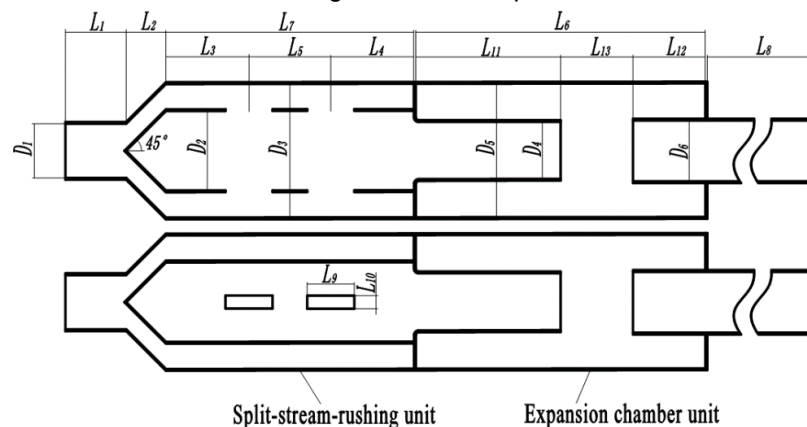


Fig. 1 - Dimensional diagram of coupled muffler models

As shown in figure 1, the length of the front tube of the muffler  $L_1=65$  mm, the diameter of the front tube of the muffler  $D_1=58$  mm, the length of the conical ring of the split-stream-rushing muffler unit  $L_2=42.5$  mm, the inner diameter of the annular cavity of the split-stream-rushing muffler unit  $D_2=85$  mm, the outer diameter of the annular cavity of the split-stream-rushing muffler unit  $D_3=143$  mm, the length of the annular cavity of split-stream-rushing muffler unit  $L_7=267.5$  mm, location dimension of the two sets of rushing holes  $L_3=L_4=89$  mm, the distance between the two sets of rushing holes  $L_5=89.5$  mm, the Length dimension of rectangular rushing holes  $L_9=50.5$  mm, width dimension of rectangular rushing holes  $L_{10}=14$  mm, outlet diameter of split-stream-rushing muffler unit  $D_4=62$  mm, total length of split-stream-rushing muffler unit  $L'=310$  mm, diameter of expansion chamber unit  $D_5=143$  mm, the length of expansion chamber unit  $L_6=310$  mm, the length of intubation at the entrance of expansion chamber unit  $L_{11}=155$  mm, the length of intubation at the exit of expansion chamber unit  $L_{12}=77.5$  mm, the length of straight tube in the middle of the expansion chamber unit  $L_{13}=77.5$  mm, diameter of tail pipe  $D_6=65$  mm, outlet length of tail pipe  $L_8=700$  mm.

Based on the structural model of the coupled muffler, the new muffler of diesel engine was trial-produced. The four-cylinder diesel engine was used as a prototype to carry out comparative tests of the acoustic performance and exhaust resistance performance of the new muffler and the original muffler.

## EXHAUST NOISE TEST

### Noise test method

The insertion loss which is widely used in field measurement to test and evaluate the acoustic performance (Zhenlin Ji, 2016) of the coupled muffler was used in exhaust noise tests of the tractor in this research. The prototype of DF 900 tractor equipped with LR 4M5-23 four-cylinder diesel engine was used to complete the comparison test verification of the new muffler and the original muffler, including acoustic performance tests and exhaust resistance performance tests.

The required equipment includes: LR 4M5-23 diesel engine (rated power 66.2 KW, rated speed 2300r/min, fuel consumption rate  $\leq 235$ g/KWh), the coupled muffler, alternative straight pipe, lateral exhaust conversion tube, microcomputer multifunctional fuel consumption meter (JWY-1, China) and non-contact photoelectric tachometer (DT2234B, China), opacity meter (NHT-6, China), 2250 handheld noise analyser (B&K, Denmark), 4189 microphone (B&K, Denmark), 4231 calibrator (B&K, Denmark), tripod, heat-resistant silencer cotton, disassembling tools.

Putting the tractor indoors was equivalent to shielding the noise of the diesel engine and its auxiliary equipment to achieve the separation of exhaust noise and other noise sources. The exhaust pipe was outdoors, there were no other sources of interference noise outside, and there were no reflectors within 5 meters around the exhaust pipe interfering with the exhaust noise test. The test environment was similar to the free sound field, and the exhaust noise of the muffler was tested. The coupled muffler, the original muffler and the straight pipe were installed to the lateral exhaust conversion pipe of the LR 4M5-23 diesel engine in order. The measurement point of the BK2250 sound level meter was kept at  $45^\circ$  from the axial direction of airflow from the exhaust tailpipe, the distance was 0.8m. The height measuring point from the ground was 1.25m, and the distance to the attenuator was 0.57m and the same position of measuring point was maintained in all noise tests.

The exhaust noise tests of the new muffler, the original muffler and the straight pipe were completed at idle speed of 750 r/min, intermediate speed of 1500 r/min, and rated speed of 2300 r/min. Photos of mufflers for DF 900 tractor were shown in Fig.2.



a) Original muffler

b) Coupled muffler

Fig. 2 - Photos of mufflers for DF 900 tractor

## RESULTS

### Comparison tests of insertion loss

From the 1/3 octave exhaust noise spectrum of the original muffler, coupled muffler and alternative straight pipe at three rotation speeds, the insertion losses of the original muffler and coupled muffler were obtained respectively. The exhaust noises of the original muffler and the new muffler in tests were all more

than 10 dB higher than the background noise at the corresponding speed. Therefore, no background noise corrections were required in the exhaust noise tests (Zhenlin Ji, 2016). Photos of insertion loss test were shown in Fig.3.



a) Exhaust noise test of coupled muffler



b) Exhaust noise test of original muffler

**Fig. 3 - Photos of insertion loss test for mufflers**

### ***Exhaust noise spectrum analyses at each speed***

The frequency spectrums of 1/3 octave of the same measuring point at three rotation speeds of the coupled muffler and the original muffler were shown in Fig.4-Fig.6. At 750 r/min, 1500 r/min, and 2300 r/min, the average sound pressure levels of the coupled muffler within 2000Hz were lower than that of the original muffler.

The average sound pressure levels of the coupled muffler within 2000Hz at three speeds were 60.52 dB, 63.22 dB, 70.29 dB, the corresponding average sound pressure levels of the alternative straight pipe were 86.24dB, 90.01 dB, 94.01 dB, and the average sound pressure levels of the original muffler at three speeds were 64.88 dB, 67.34 dB, 74.16 dB, so the average sound pressure levels of the coupled muffler at each speed within 2000 Hz were reduced by 25.72 dB, 26.79 dB, 23.75 dB compared to the straight pipe and the coupled muffler reduced the average sound pressure levels within 2000 Hz at three speeds by 4.36 dB, 4.12 dB, 3.87 dB compared with the original muffler.

Moreover, the coupled muffler significantly reduced low-frequency noises. The average sound pressure levels of the coupled muffler at three speeds within 200 Hz were 71.68 dB, 72.19 dB, 76.67 dB, while the average sound pressure levels of the original muffler were 77.67 dB, 79.70 dB and 83.73 dB. The average sound pressure levels of the coupled muffler within 200 Hz at three speeds were reduced by 5.99 dB, 7.51 dB, and 7.06 dB respectively compared to the original muffler. It could be seen that the attenuation of low-frequency noise by the coupled muffler at each speed was significantly better than that of the original muffler.

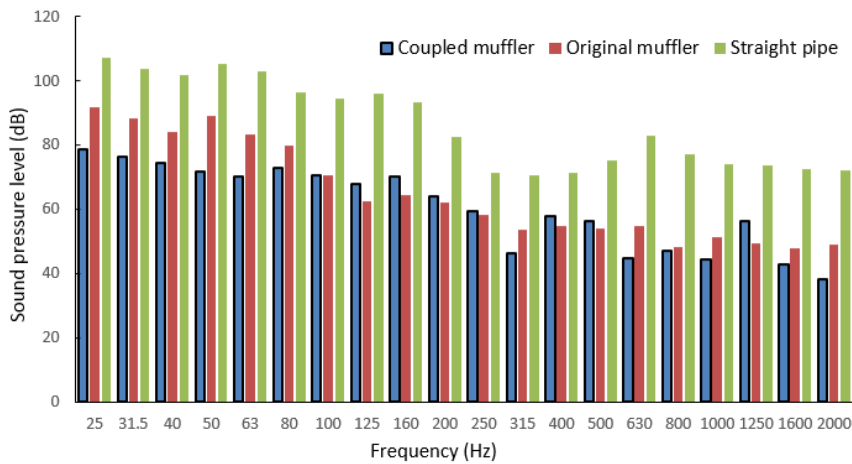


Fig. 4 - Comparison of noise spectrum at idle speed

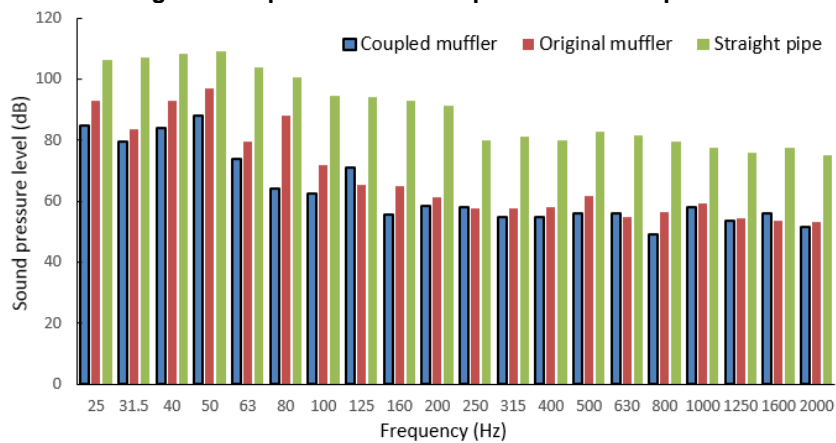


Fig. 5 - Comparison of noise spectrum at 1500r/min

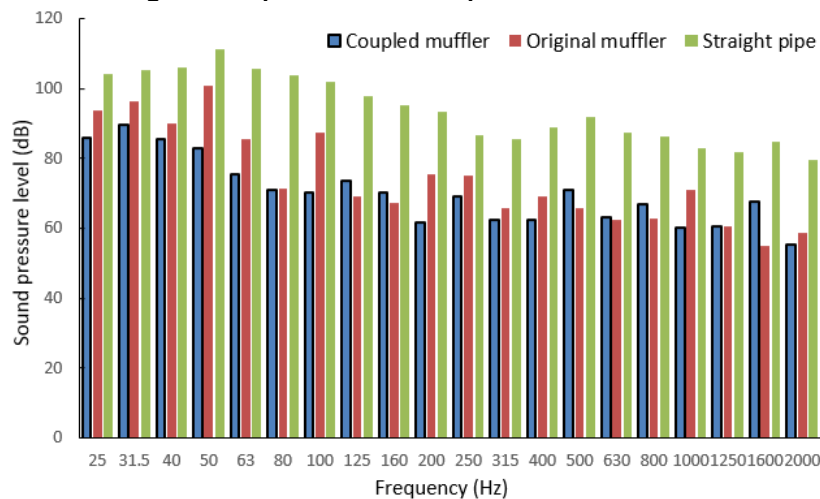


Fig. 6 - Comparison of noise spectrum at 2300 r/min

Since the exhaust pressure pulsation noise appears as periodic low-frequency noise, the control of the fundamental frequency noise can reflect the acoustic performance of the exhaust muffler. According to the calculation formula of the fundamental frequency of exhaust noise,  $f_1 = nZ / 60 \tau$ , where:  $n$  is the engine speed (r/min);  $Z$ -the number of cylinders;  $\tau$ -the stroke coefficient, 4 stroke  $\tau = 2$  (Zhihua Zhang et al., 1999).

From this, the exhaust noise fundamental frequencies of the LR 4M5-23 diesel engine at idle speed, intermediate speed and rated speed could be obtained respectively, and then the corresponding exhaust noise conditions at three speeds could be analyzed. At idle speed 750 r/min, the fundamental frequency  $f_1$  of the exhaust noise was 25 Hz, and the sound pressure level corresponding to this fundamental frequency was the low frequency noise peak of the diesel exhaust noise spectrum of the diesel engine, which was 107.04 dB, so the control of fundamental frequency noise at 25 Hz at idle speed was a key to reflect the

noise reduction performance of the muffler. The sound pressure level of the original muffler at the fundamental frequency of 25 Hz was 91.83 dB, which was still the peak of the noise in the spectrum. The average value of the sound pressure level of the original muffler within 50 Hz was relatively high, which was 88.39 dB, so its attenuation effect of low-frequency target noise was limited. The noise sound pressure level of the new muffler corresponding to the fundamental frequency of 25 Hz was 78.82 dB, which was 13.01 dB lower than that of the original muffler.

In the same way, the fundamental frequency  $f_1$  of the exhaust noise of the diesel engine at 1500 r/min and rated speed of 2300 r/min was calculated as 50 Hz and 76.67 Hz, and the corresponding low-frequency noise peaks at these two speeds appeared at 50 Hz in exhaust noise tests, and the noise peaks were 109.03 dB and 111.25 dB respectively. The sound pressure levels of the coupled muffler at the fundamental frequency of 50 Hz were 88.16 dB and 82.96 dB, which were 6.87 dB and 17.92 dB lower than that of the original muffler. The new muffler greatly attenuated the low-frequency noise peaks. The new type muffler was also superior to control the fundamental frequency noise at each speed compared with the original muffler.

**Analyses of insertion loss at each speed**

The comparison curves of the insertion losses at three rotation speeds between the coupled muffler and the original muffler were shown in Fig.7-Fig.9.

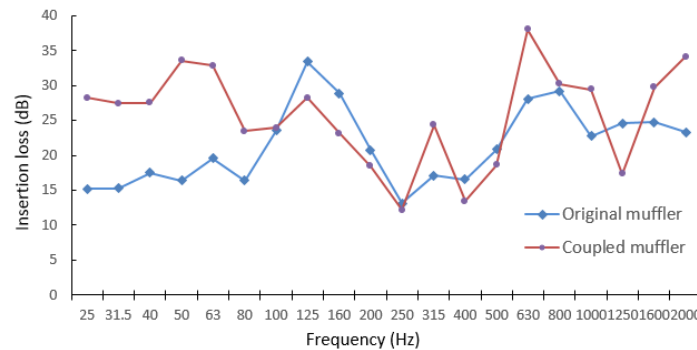


Fig. 7 - Contrast curve of insertion loss at idle speed

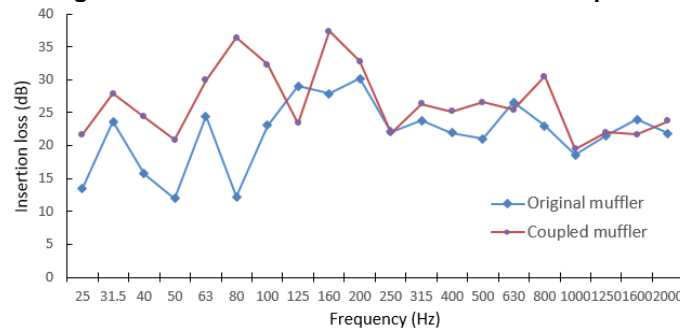


Fig. 8 - Contrast curve of insertion loss at 1500r/min

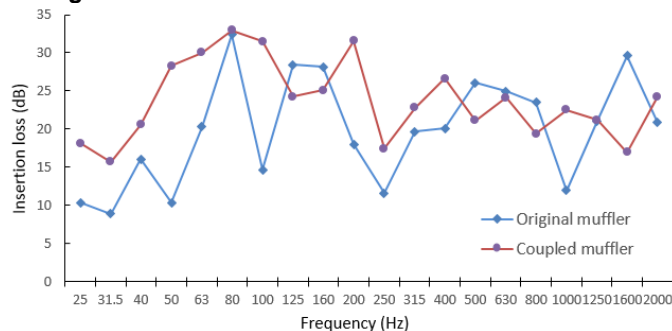


Fig. 9 - Contrast curve of insertion loss at 2300r/min

It could be seen from the insertion loss comparison curves of the new muffler and the original muffler at three rotation speeds that the insertion loss of the low frequency band of the new muffler within 200 Hz was better than that of the original muffler, and noise reduction of rest frequency band in 2000 Hz was also good compared to the original muffler, and the insertion losses at the fundamental frequency noise at each speed had been significantly improved. It could be found that the coupling structure of the new muffler was

conducive to the improvement of the acoustic performance of the diesel engine. The average insertion losses of the coupled muffler within 2000 Hz at 750 r/min, 1500 r/min and 2300 r/min were 25.72 dB, 26.80 dB, 23.72 dB. Compared with the original muffler, the average insertion loss of the new muffler was increased by 4.35 dB, 4.98 dB and 3.88 dB. The insertion losses of the new muffler at three speeds within 200 Hz of target frequency band were 26.69 dB, 29.30 dB, 25.81 dB respectively, which were 5.99 dB, 8.11 dB and 7.06 dB higher than that of the original muffler. The average insertion losses of the coupled muffler at three speeds within 50 Hz were 29.19 dB, 24.08 dB, and 20.67 dB, which were 13.08 dB, 7.85 dB, and 9.25 dB higher than that of the original muffler. The insertion losses of the coupled muffler about the fundamental frequency noise at three rotation speeds were 28.22 dB, 20.87 dB and 28.29 dB, which were 13.01 dB, 8.87 dB and 17.92 dB higher than that of the original muffler.

The comparison data of the average sound pressure levels (SPL) and the average insertion losses (IL) of the new muffler and the original muffler at each speed were shown in Table 1 and Table 2 below.

Table 1

Analyses of insertion loss at different speeds

Testing object	750 r/min			1500 r/min			2300 r/min		
	SPL [dB] (A)	IL in 2000Hz [dB] (A)	IL in 50Hz [dB] (A)	SPL [dB] (A)	IL in 2000Hz [dB] (A)	IL in 50Hz [dB] (A)	SPL [dB] (A)	IL in 2000Hz [dB] (A)	IL in 50Hz [dB] (A)
Straight pipe	86.24	-	-	90.01	-	-	94.01	-	-
Original muffler	64.88	21.37	16.11	68.19	21.82	16.23	74.16	19.84	11.42
Coupled muffler	60.53	25.72	29.19	63.22	26.80	24.08	70.29	23.72	20.67

Table 2

Analyses of insertion loss at different speeds

Speed [r/min]	IL within 200Hz [dB] (A)		Growth rate of IL [%]
	Original muffler	Coupled muffler	
750	20.70	26.69	28.94
1500	21.19	28.70	35.44
2300	18.75	25.81	37.65

The growth rate of the insertion loss of the coupled muffler within 200 Hz of target muffling frequency band at three rotation speeds were 28.94%, 35.44% and 37.65% respectively. The growth rate of insertion loss increased with the engine speed, because the higher the engine speed, the higher the airflow velocity at the muffler inlet, the greater the contribution of reduction of the internal velocity through the coupling structure, and the more obvious the effect of controlling the airflow regeneration noise, the acoustic performance of the diesel engine at high speeds was improved.

Compared with the original muffler, the average growth rate of insertion loss of the new muffler within 2000 Hz was 20.77 %, and the average growth rate of insertion loss of the target muffler frequency band within 200 Hz was 34.01 %. The average insertion loss within 50 Hz at three speeds was 68.95% higher than that of the original muffler. It could be seen that the full-band noise reduction performance and low-frequency noise reduction performance of the coupled muffler were significantly better than that of the original muffler, which was more suitable for the attenuation of low-frequency target noise for diesel engines.

### COMPARISON TESTS OF EXHAUST RESISTANCE PERFORMANCE

In the comprehensive performance analysis of the coupled muffler, the exhaust resistance performance of the new muffler at each speed of the actual diesel engine needs to be evaluated. The variation in fuel consumption can be used to assess the pressure loss of the muffler. The fuel consumption is directly related to the power loss and the exhaust back pressure (*Wu Guipei et al., 2008*). The fuel consumption of a diesel engine equipped with a new muffler can reflect the overall change in its aerodynamic performance.

In this research, the diesel fuel consumption meter was used to test the fuel consumption index of LR4M5-23 four-cylinder diesel engine at various speeds, and the effects of the coupled muffler and the original muffler on the exhaust resistance of the four-cylinder diesel engine were analyzed.

### Experimental approach of fuel consumption

JWY-1 microcomputer multifunctional fuel consumption meter was connected to the fuel circuit of the diesel engine. The test devices of fuel consumption meter were shown in Fig.10. The resolution of the fuel consumption meter is 0.1mL, the maximum flow rate is 60 L/h, and the measurement uncertainty is  $\pm 1\%$ .

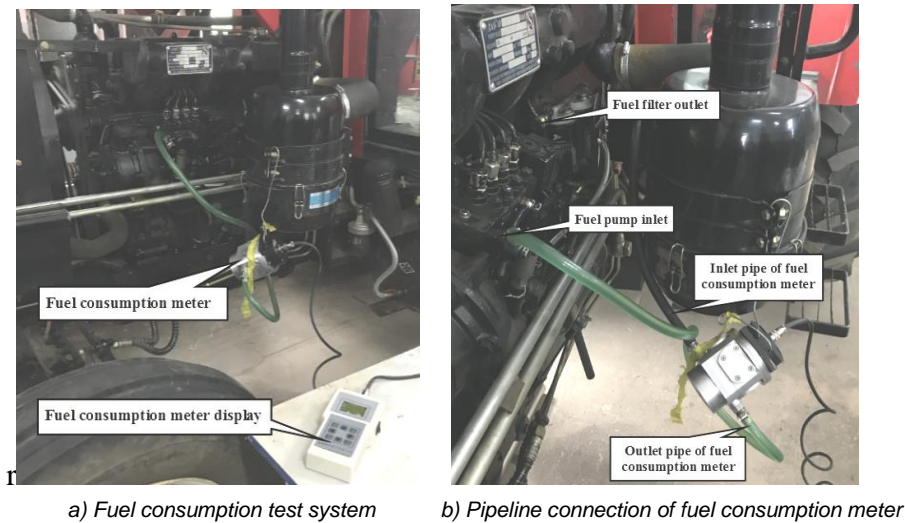


**Fig. 10 - Photos of fuel consumption test**

After the fuel consumption meter is connected to the fuel pipeline, it is necessary to press the manual fuel pump several times to eliminate the air in fuel circuit of the diesel engine, so that the engine can start normally. After 15 minutes of stable operation, the fuel consumption records are started to ensure the accuracy of the fuel consumption tests. The JWY-1 microcomputer multi-function fuel consumption meter is a digital display that can display and record three test parameters, including test time, fuel consumption  $L$  within the test time  $t$ , and fuel consumption per hour  $G$ . The test time  $t$  was set to 60 s, and the fuel consumption  $L$  (mL) and fuel consumption per hour  $G$  (L/h) were recorded, the fuel consumptions at each speed were recorded in three times, and the average value was taken.

The fuel consumption rate (specific fuel consumption) is the mass of fuel consumed (in units of g) in one hour for every 1 kW of effective power from the engine, and its unit is g/(kW·h). Specific fuel consumptions of the diesel engine equipped with the new muffler and the original muffler at the rated speed were further calculated. Based on the density of No. 0 diesel, which is 0.835 g/ml, the effective power  $P_e$  corresponding to 2300 r/min of the rated speed of LR4M5-23 four-cylinder engine is 66.2 kW.

The conversion formula of  $G$  and  $b_e$  is as follows:

$$b_e = 1000 \times 0.835 \times G/P_e = 835G/66.2 \quad (1)$$

where:  $G$  is fuel consumption per hour, L/h;  $P_e$  is effective power, kW.

The fuel consumption rate of diesel engines is generally 200...260 g/kWh, and the economy is better when the fuel consumption of the engine is lower. The fuel consumption rate of LR4M5-23 four-cylinder diesel engine is no more than 235 g/kWh.

### Comparison results of fuel consumption

The average values of fuel consumption  $L$  at 60 seconds and fuel consumption per hour  $G$  of the diesel engines equipped with the coupled muffler and the original muffler at idle speed of 750 r/min, intermediate speed of 1500 r/min, and rated speed of 2300 r/min were shown in Table 3.

**Table 3**

Speed $n$ [r/min]	Comparison of fuel consumptions				
	L [mL]		G [L/h]		
	Original muffler	Coupled muffler	Original muffler	Coupled muffler	Reduction rate of G
750	223.92	162.50	13.44	9.75	27.46%
1500	233.51	191.34	14.01	11.48	18.06%
2300	272.04	239.36	16.32	14.36	11.96%

The effective fuel consumption rate (specific fuel consumption) of the diesel engine equipped with the original muffler was:  $b_e = 835G/66.2 = 835 \times 16.32/66.2 = 205.85$  g/(kW·h).

The effective fuel consumption rate of a diesel engine equipped with the new muffler was:

$$be = 835G/66.2 = 835 \times 14.36/66.2 = 181.13 \text{ g/(kW}\cdot\text{h)}$$

Furthermore, the effective fuel consumption rate of the diesel engine equipped with the new muffler at the rated speed was calculated to be 19.16% lower than that of the original muffler.

From the statistical results above, it could be seen that the fuel consumption  $L$  and  $G$  of the diesel engine with new muffler at three different speeds were both lower than that of the original muffler. And the lower the engine speed, the higher the reduction rate of fuel consumption, fuel consumption decreased the most at idle speed, and the effective fuel consumption rate at rated speed had also been significantly reduced. Compared with the original muffler, the fuel consumptions of the diesel engine equipped with the coupled muffler were significantly reduced, indicating that the pressure loss and power loss of the diesel engine with the new muffler were smaller than that of the diesel engine equipped with the original muffler. The new muffler can achieve the goals of good noise reduction performance and low exhaust resistance by reducing the airflow velocity in the muffler, and improve the overall performance of the muffler.

### Simulation verification of the flow field in the muffler

Through the simulation analyses of the aerodynamic performance of the new muffler, the changes of the flow field in the new muffler under the common inlet airflow velocity of 0-50 m/s in diesel engines were discussed, and the velocity field and pressure field of inlet velocity at 50 m/s were shown as an example. It was verified that the pressure loss could be effectively controlled by reducing the airflow velocity in new muffler, thereby achieving an improvement in fuel consumption. The velocity cloud diagram and the full pressure cloud diagram of the new muffler at an inlet velocity of 50m/s were shown in Fig.11 and Fig.12.

From the analysis of Figure 11 and Figure 12, it could be seen that the inlet pressure was about 4500Pa at the inlet velocity of 50 m/s, and there was a partial pressure loss when the airflow velocity was slightly increased at the first bend of the conical ring.

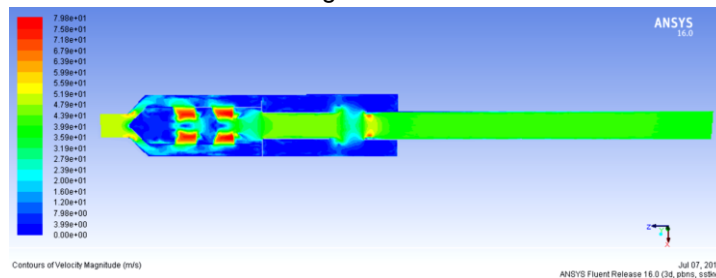


Fig. 11 - Velocity contours at inlet velocity of 50 m/s

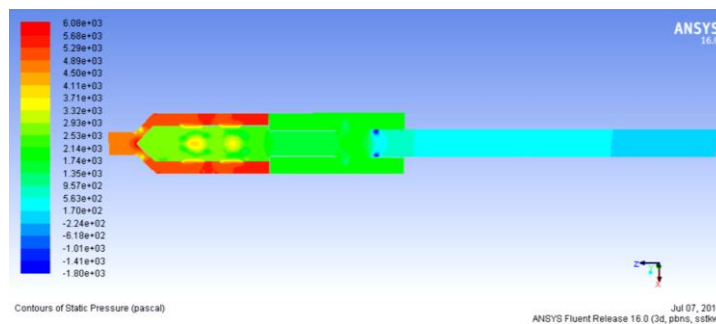


Fig. 12 - Total pressure contours in the muffler unit at inlet velocity of 50 m/s

After the airflow entered the two sets of opposing holes, the reverse airflow accelerated to rush at a velocity of about 71.8 m/s, and the pressure value dropped from 3320 Pa to 1740 Pa. After the rushing, the velocity in the central area decreased significantly to about 3.99 m/s, and the pressure returned to about 3500 Pa. There was a short acceleration after the airflow changed into an axial flow. The velocity at the junction of the front and rear muffler units was about 31.9 m/s, and the pressure here was reduced to 1740Pa. There was a brief acceleration phenomenon at the inlet of the inner cannula from the rear section, and then the velocity dropped to 35.9 m/s and this velocity was maintained to reach the outlet of the tail pipe. The outlet pressure was about -224 Pa, therefore, the total pressure loss of the new muffler at an inlet velocity of 50 m/s was 4724 Pa, and the pressure loss was well controlled.

It is verified that the airflow velocity of the coupling structure in the new muffler can be quickly reduced, which effectively controls the pressure loss, exhaust back pressure and fuel consumption.

## CONCLUSIONS

The acoustic performance, exhaust resistance and economy of the new muffler are superior to the original muffler. It can be seen that the new muffler is more conducive to the attenuation of low-frequency noise of diesel engines. The use of the new muffler reduces the engine exhaust back pressure and power loss. The coupled muffler can achieve the comprehensive goal of good acoustic performance and low exhaust resistance by reducing the airflow velocity in the muffler. It is verified that the design of the coupled muffler based on the split-stream rushing principle and multi-unit coupling theory is reasonable and feasible.

## ACKNOWLEDGEMENT

Special thanks are due to the National Natural Science Foundation of China (11464036), Science and Technology Plan Project of Inner Mongolia Autonomous Region (201802032), "Grassland Talents" Industrial Innovation Talent Team Project of Inner Mongolia Autonomous Region ([2014] No. 27), and the Natural Science Foundation of Inner Mongolia Autonomous Region (2019MS05004) for supporting authors' research.

## REFERENCES

- [1] Fei Xue, Beibei Sun, (2018), Experimental study on the comprehensive performance of the application of U-shaped corrugated pipes into reactive mufflers, *Applied Acoustics*, Vol.141, pp.362-370;
- [2] He Su, Pei Wu, Jing Xue, et al., (2020), Analysis of flow field characteristics and structure optimization of the split-stream rushing muffler for diesel engine, *Noise Control Engineering Journal*, Vol.68, Issue 1, pp.101-111;
- [3] He Su, Pei Wu, Yanhua Ma et al., (2018), Simulation on air-flow characteristics of a new split-stream-rushing exhaust muffler, *Transactions of CSICE*, Vol.36, Issue 2, pp.159-165;
- [4] Hua X., Jiang C., Herrin D.W. et al., (2014), Determination of transmission and insertion loss for multi-inlet mufflers using impedance matrix and superposition approaches with comparisons, *Journal of Sound and Vibration*, Vol.333, Issue 22, pp.5680-5692;
- [5] Longyang Xiang, Shuguang Zuo, Xudong Wu et al., (2017), Study of multi-chamber micro-perforated muffler with adjustable transmission loss, *Applied Acoustics*, Vol.122, pp.35-40;
- [6] Pei Wu, Yingli Shao, Yanhua Ma et al., (2010), Development of a diesel engine muffler using mixing of out-of-phase split exhaust streams, *Noise Control Engineering Journal*, Vol.58, Issue 6, pp.621-626;
- [7] Rong Guo, Wen-bo Tang, Wei-wei Zhu, (2016), Comparison of 1D transfer matrix method and finite element method with tests for acoustic performance of multi-chamber perforated resonator, *Applied Acoustics*, Vol.112, pp.140-146;
- [8] Sang-Myeong Kim, (2018), Turning a loudspeaker into an active Helmholtz resonator: Underlying law, principle and design methodology, *Journal of Sound and Vibration*, Vol.432, pp.373-386;
- [9] Wu Gupei, Hao Zhiyong, Jia Weixin, (2008), Exhaust muffler design based on CFD, *Noise and Vibration Control*, Issue 1, pp.115-118;
- [10] Xiaotian Bai, (2016), Study on Acoustic and Aerodynamic Performance of Semi-active Impedance Compound Muffler, Shenyang University of Technology, Shenyang/China;
- [11] Yawei Zhu, Fawang Zhu, Yanshan Zhang et al., (2017), The research on semi-active muffler device of controlling the exhaust pipe's low-frequency noise, *Applied Acoustics*, Vol.116, pp.9-13;
- [12] Yiliang Fan, Zhenlin Ji, (2019), Three-pass mufflers with perforated inlet/outlet tubes, *Applied Acoustics*, Vol.156, pp.217-228;
- [13] Yongan Zhang, Pei Wu, Yanhua Ma, et al., (2018), Analysis on acoustic performance and flow field in the split-stream rushing muffler unit, *Journal of Sound and Vibration*, Vol.430, pp.185-195;
- [14] Yongan Zhang, Yanhua Ma, Pei Wu et al., (2017), Prediction and analysis on acoustic properties of a specially-structured muffler unit, *Transactions of CSICE*, Vol.35, Issue 4, pp.362-368;
- [15] Zhenlin Ji, (2016), Acoustic theory and design of muffler. *Science Press*, Beijing/China;
- [16] Zhihua Zhang, Song Zhou, Su Li, (1999), Internal combustion engine emissions and noise control, *Harbin Engineering University Press*, Harbin/China;
- [17] Zhu Congyun, Li Xiaojuan, Lu Fujie, et al., (2015), The Working Principle of an Active Muffler Analysis, *Journal of Zhongyuan University of Technology*, Vol.26, Issue 6, pp.21-26.

# DESIGN OF TEMPERATURE AND HUMIDITY CONTROLLER OF AGRICULTURAL INTELLIGENT TOBACCO HOUSE BASED ON STM32

## 基于 STM32 的农业智能烤烟房温湿度控制仪的设计

He Hong <sup>1</sup>

College of Electronic Engineering, Xi'an Aeronautical University, Shaanxi, 710077 / China

Tel: 15789652896; E-mail: nwpuheh@163.com

DOI: <https://doi.org/10.35633/inmateh-62-04>

**Keywords:** STM32, automation, tobacco room, temperature and humidity, control

### ABSTRACT

The quality of tobacco baking is one of the important factors affecting the economic benefits of tobacco enterprises. Because of the low efficiency of traditional manual baking methods and the poor quality of tobacco, the economic benefits of tobacco enterprises and tobacco farmers are also greatly affected. In view of this, this research takes the temperature and humidity control as the research object, and proposes an agricultural intelligent tobacco house temperature and humidity controller based on STM32. Firstly, the general design scheme, hardware circuit design scheme and software design scheme of the control system are described, in which the human-machine interface circuit design of the hardware circuit design is emphatically analysed, and finally, the design of this research is applied. The agricultural intelligent temperature and humidity controller measures the temperature and humidity of the flue-cured tobacco house, and verifies the control effect. The results show that the temperature control accuracy based on STM32 is significantly higher than that of traditional control method, which is conducive to the improvement of tobacco baking quality. It is hoped that this study can provide a significant reference for the research of temperature and humidity control in tobacco industry in China.

### 摘要

烤烟的质量是影响烟草企业经济效益的重要因素之一。由于传统的手工烘烤方法效率低下以及烟草质量差,烟草企业和烟农的经济利益也受到很大影响。有鉴于此,本研究以温湿度控制为研究对象,提出了一种基于 STM32 的农用智能烟房温湿度控制器。首先介绍了控制系统的总体设计方案,硬件电路设计方案和软件设计方案,着重分析了硬件电路设计的人机界面电路设计,最后应用了本研究的设计。农业智能温湿度控制器测量烤烟房的温度和湿度,并验证控制效果。结果表明,基于 STM32 的温度控制精度明显高于传统控制方法,有利于提高烤烟质量。希望这项研究能为我国烟草工业的温湿度控制研究提供一定的参考和参考。

### INTRODUCTION

China is a big country of tobacco planting, and tobacco industry plays an important role in our national economy. According to statistics, the tobacco industry accounts for 10% of China's annual tax revenue, and the tobacco industry has become an important source of China's financial revenue (Enrico, Corti, Michele. 2017). With the improvement of the quality of life of Chinese residents, the public demand for tobacco products is also higher and higher, which requires that tobacco enterprises can bake high-quality tobacco products. However, due to the backward baking equipment and the low professional level of the staff in the remote mountainous areas, China's tobacco planting areas generally fail to bake out high-quality tobacco products (Yasser Abdelaziz, 2017). Therefore, it is necessary to improve the technology of tobacco baking to further improve the income of tobacco enterprises and farmers. Due to the low efficiency of the traditional artificial baking method and the poor quality of tobacco leaves, the economic benefits of tobacco enterprises and tobacco farmers have been greatly affected, which is not in line with the development trend of intelligence. Although some tobacco baking equipment has appeared in China, the temperature and humidity control of tobacco houses is often accompanied by coupling, non-linear and time-varying factors, resulting in the temperature and humidity control poor accuracy (Khan et al., 2015). In this study, STM32 microcontroller is introduced into the temperature and humidity automatic control technology, which takes the system control accuracy as the core, and optimizes the integration degree of the control system.

<sup>1</sup> He Hong, As. PhD. Lec.

Aiming at the control of temperature and humidity in the flue-cured tobacco house, STM32 microcontroller is introduced in this study. This technology belongs to an integrated circuit chip, and uses VLSI technology to integrate the original parts with data processing ability, and integrates these functional elements on the silicon chip to form a microprocessor. STM32 microcontroller is widely used in various fields because of its small size, simple structure and relatively cheap price.

The innovation of this study is to use the real-time measurement method of tobacco surface temperature, which cannot test the current situation of tobacco leaf surface temperature in the flue-cured tobacco house, and use the real-time detection method of leaf temperature to measure the surface temperature of tobacco leaf. In the process of baking experiment, the temperature difference between the environment of the flue-cured tobacco house and the surface temperature of tobacco leaf is measured, which provides reliable detection data for this research work.

This study is divided into four parts. The second part is about the research status of the application of temperature and humidity intelligent control technology in various fields at home and abroad; the third part mainly introduces the research method, the first section introduces the overall design scheme of the temperature and humidity controller based on STM32 intelligent flue-cured tobacco house, the second section introduces the hardware circuit design method of the control system, the third section introduces the software of the control system design method. In the fourth part, the control system is tested and analysed. The results show that the temperature control accuracy based on STM32 is significantly higher than that of traditional control method, which is conducive to the improvement of tobacco baking quality.

In recent years, people attach great importance to the intelligent control technology of temperature and humidity, which has a profound impact on the future direction of social development.

Researchers at home and abroad also conduct in-depth research on this technology.

*Wei Zheng et al.* proposed a Multivariable Decoupling Fuzzy logic control method, which designed two kinds of fuzzy controllers based on fuzzy logic theory. Fan, heater and humidifier are used to control the temperature and humidity. The temperature and humidity drop caused by ventilation is compensated by heater and humidifier respectively, which realizes multivariable decoupling. The results show that the power consumption of this method is 19% lower than that of manual regulation (*Wei-Zheng et al., 2019*).

*Elkhayat et al.* studied the prediction method of temperature and humidity by capacitive humidity sensor, and analysed the change of temperature and humidity by using circuit temperature control method. The results show that the prediction accuracy is very high, and it is suitable for self-diagnosis of humidity sensor (*Elkhayat et al., 2016*).

*Yan and others* developed the capacity controller of the three-evaporator air conditioning system to realize the analogue controllability of the capacity controller. According to the operation characteristics of the three-evaporator air conditioning (TEAC) system, the capacity controller was further improved and an improved controller was developed. The results show that the improved controller can realize the indoor temperature and humidity synchronous control of TEAC system (*Yan H et al., 2017*).

*Mirzaee Ghaleh et al.* monitored indoor climate management of typical poultry farms in Iran, and compared fuzzy logic with switch controller. Three fuzzy controllers were developed and tested by LabVIEW software. The results show that the fuzzy controller has a good response to temperature and humidity (*Mirzaee-Ghaleh et al., 2015*).

Infant incubators such as *Singla et al.* provide a controlled environment for premature infants in need of special care. The results show that the temperature and humidity controller of infant incubator based on microcontroller is very important for the normal growth of newborns (premature) (*Singla S. and Singh V., 2015*).

*Mien T.L.* analysed the indoor air, established the nonlinear interactive mathematical model of indoor air, proposed the design method of traditional PI controller, decoupling controller and parameter self-tuning PI controller based on the combination of fuzzy logic principle and decoupling controller in the process of indoor air heating and humidification, and simulated and tested the proposed temperature and humidity process controller on MATLAB (*Mien T.L., 2016*).

*Li Shujiang et al.* proposed a control algorithm based on genetic algorithm (GA) to optimize PID controller parameters. The predictive decoupling method was used to decouple the temperature and humidity. The objective function was used as the evaluation value of the controller. Through the selection, crossover and variation of genetic algorithm, the optimal solution of PID control parameters was obtained. The simulation experiment was carried out with MATLAB.

The results show that GA-PID control algorithm can effectively decouple the temperature and humidity, and the control system has better control performance (Li Shujiang, et al., 2017).

Shigang Cui and others have developed a temperature and humidity monitoring system based on embedded technology. This system uses STM32 microprocessor as the core controller to realize the accurate collection, display and control of environmental factors (including temperature and humidity) in the plant growth box through the monitoring system. According to the principle of optimal weight distribution, each layer of sensor data is adaptively weighted and fused to get accurate temperature and humidity values. The results show that the system can accurately monitor and display the temperature and humidity in the plant growth box (Shigang Cui et al., 2017).

Nurainaa Elias et al. designed a fuzzy logic controller to simulate the control system based on user's expected temperature, user's expected humidity and deviation from expected parameters. The results will be described by the speed of the output actuator varying with the input temperature and humidity (Nurainaa Elias et al, 2018).

Juliana D.S.G.B. et al. used two kinds of temperature control technology to evaluate the spatial distribution of farm thermal environment variables, evaluated the climate variables such as dry bulb temperature (TBS), relative air humidity (RH), temperature and humidity index (THI) and enthalpy, and drew the spatial distribution diagram of these variables by Kriging method. The results show that the resistance heating system with PID controller improves the thermal comfort conditions of pig farm in the coldest time, and maintains the spatial distribution uniformity of indoor air temperature (Juliana de Souza Grand Barossa et al., 2017).

Ou K et al. proposed a multi input multi output (MIMO) fuzzy controller, and proved its real-time control ability to the strong nonlinear power fuel cell system, constructed a five input two output fuzzy logic controller, which is used to adjust the temperature and relative humidity of the open cathode fuel cell in real time. The results show that the fuzzy controller effectively improves the output power of PEM fuel cell (Ou K, Yuan W.W. and Choi M., 2017).

Yan et al. introduced the development of a capacity controller of three-evaporator air conditioning (TEAC) system, which is used to improve indoor air humidity control. The results show that the controller can improve the indoor humidity control and energy efficiency (Yan H. et al., 2016).

Through the analysis and research of temperature and humidity intelligent control technology, it can be seen that STM32 microcontroller is the main carrier of temperature and humidity control technology, but the research work in this field in China is still in the initial stage, and the research of temperature and humidity control technology based on STM32 needs to be expanded. Therefore, this study mainly aims at the control of temperature and humidity in the flue-cured tobacco house. STM32 microcontroller is introduced into the temperature and humidity automatic control technology.

## **MATERIALS AND METHODS**

### **The overall design of the temperature and humidity controller in the tobacco house**

The main control object of this research system is the circulating fan, air door and combustion supporting fan, and the controlled object is the temperature and humidity measured in the flue-cured tobacco room. The system consists of five parts, including power supply, RS485 communication interface, man-machine interface, control output, STM32F103 microcontroller. The core component of the control system is STM32F103 chip, and the LCD screen is installed on the field controller, so that the indoor temperature and humidity changes can be known by the field staff at any time, and the system can be debugged in real time according to the changes. The temperature and humidity sensor is used to import the temperature and humidity collected in the flue-cured tobacco room into the STM32 controller, and the data is imported into the upper computer monitoring system by the field bus, and the temperature and humidity data is displayed on the LCD screen in real time. The control system adjusts the driving module through the internal stored expert curve and the preset temperature and humidity curve, so as to control the revolving speed of the circulating fan, the start and stop of the combustion supporting fan and the opening of the air door, and realize the adjustment of the indoor temperature and humidity. In case of phase loss, circuit failure, open circuit of sensor, abnormal temperature and humidity, the control system will give voice alarm through the upper computer and voice chip at the same time.

The controller is irregularly attached to the bus through the system interface, and the network bus is connected to the data adapter through the system interface, and then the data adapter is connected to the upper machine monitoring by the USB interface, and finally the data is received and sent. As shown in Figure 1.

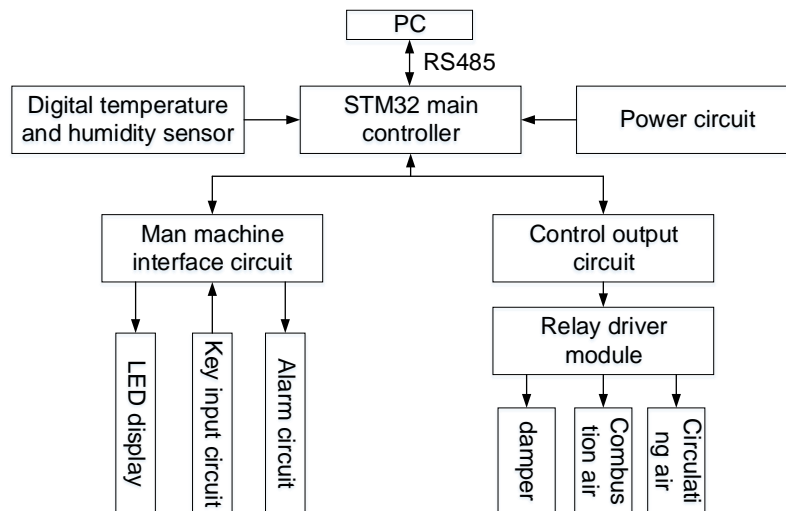


Fig. 1 - General structure of controller design

### Hardware design of temperature and humidity controller in tobacco room

The system in this study not only needs to collect the temperature and humidity data of the flue-cured tobacco house, but also provides the detection signals needed for system alarm. The detection signals include the detection signals of system voltage, working state of the circulating fan, phase loss overload and so on. Among them, the phase loss overload signal is the most special, which is supported by the double current transformer. Because STM32F103 is embedded with a digital simulator and there are 16 ADC channels, the analogue signals collected are processed by means of filtering and voltage dividing, and the processed data are input into the system. The circuit design of this study is relatively simple and will not be described too much. Because the key work of the system is to collect the temperature and humidity in the flue-cured tobacco room, the sensor selected by the system should have the characteristics of accurate measurement and convenient use. In addition, the system needs to measure the temperature of four test points in the flue-cured tobacco room, two temperature and humidity measurement points in the upper and lower shed. The digital temperature sensor of the control system is a series of HSTL sensors, which adopts a single interface mode and applies the mode of one wire bus. There are only three pins DQ, GDN and VDD in the sensor, which have fast conversion rate and stable performance. Moreover, the output of the measured data is also the interface directly applying the mode. Therefore, the control system only needs simple noise reduction for data, which can be directly connected to the input and output interfaces of STM32, improving the anti-interference ability of the system, and reducing the frequency of circuit components and input and output ports. The temperature range of HSTL series sensor is  $[- 55, + 125]$  °C. If it is between  $[- 10, + 85]$  °C, the accuracy error of measurement is about 0.5°C, and the voltage is  $[3.0, 5.5]$  V. The control system directly allocated four groups of input and output ports, PB3, PB11, PB12 and PB10, and connected these ports to the sensor at the same time. Generally, in the detection circuit, if the resistor R21 has a certain current limiting protection function, the single bus is pulled high through the pull-up resistor R22 to reach the receiving mode, and it is kept between  $[15,60]$   $\mu$ s. The capacitor C28 controls the electric frequency of the host at the level of not less than 480 $\mu$ s to form a reset pulse.

In order to enable the staff to adjust and control the controller conveniently on site, the man-machine interface circuit system in this study mainly includes key input, LCD display drive, voice alarm and other circuits, as shown in Figure 2. The display screen of the control system is pen Segment LCD, which has a backlight control mode of low brightness and high brightness. Low brightness indicates the normal operation of the control system, and high brightness indicates the operation of the control system. When the control system works normally, the LCD display shows the calendar clock, control curve data, working time, measured temperature in the flue-cured tobacco room, target temperature and humidity, etc. Set 8 keys of the control system, and drive ls165m by pb0, PC4 and PC5 ports of STM32, so as to achieve the function

realization purpose of the control system in the stop or operation state, such as alarm end, data record query, baking curve modification and other functions. On the basis of the pull-up resistance, the system also adds the anti-shake capacitance, which greatly increases the reliability of the system data in the input. In this study, wtv170-16p chip is selected as the chip of voice alarm.

The data converter of the chip is 16bitsdac, voice duration is 170s, frequency is 6KHz, and the chip belongs to one-time programmable burning chip. In this study, the serial port control mode is applied, and the voltage is 3.4V.

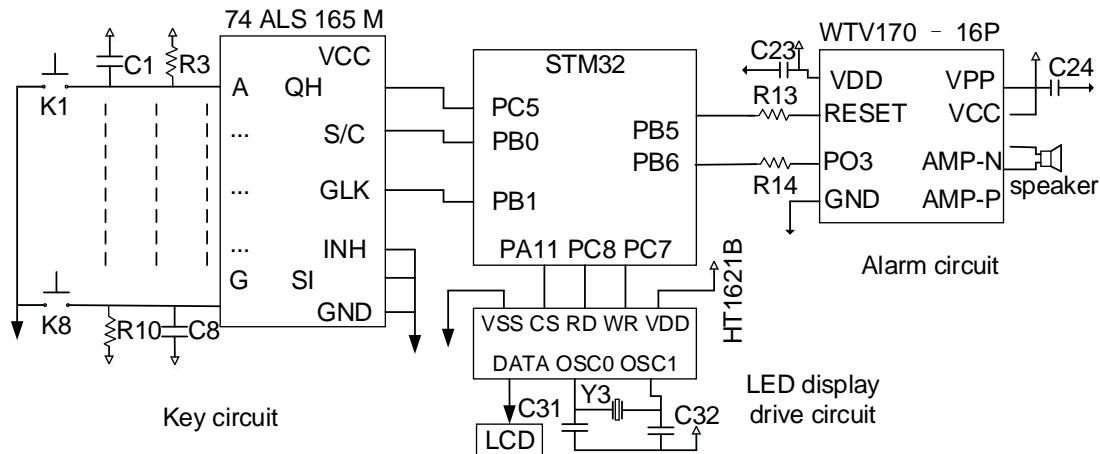


Fig. 2 - Design of human-machine interface circuit of the system

In the control system, RS485 bus communication interface is selected, sp485ee chip is applied, and Modbus RTU communication protocol is added, which can read the memory record in PC port. In the memory, the relevant historical data are recorded, such as the power failure, data setting, baking time and temperature and humidity in the baking room, so as to provide reference for the staff. In the system, the controller has designed the circulation fan with manual and automatic control. When the controller is under automatic control, the system can realize the communication between the external inverter and the controller through the frequency conversion communication interface, and realize the automatic control of the rotation speed of the circulation fan. When the controller is under manual control, the rotation speed of the circulation fan can be controlled according to the speed regulating switch. The communication interface circuit of this study is shown in Figure 3.

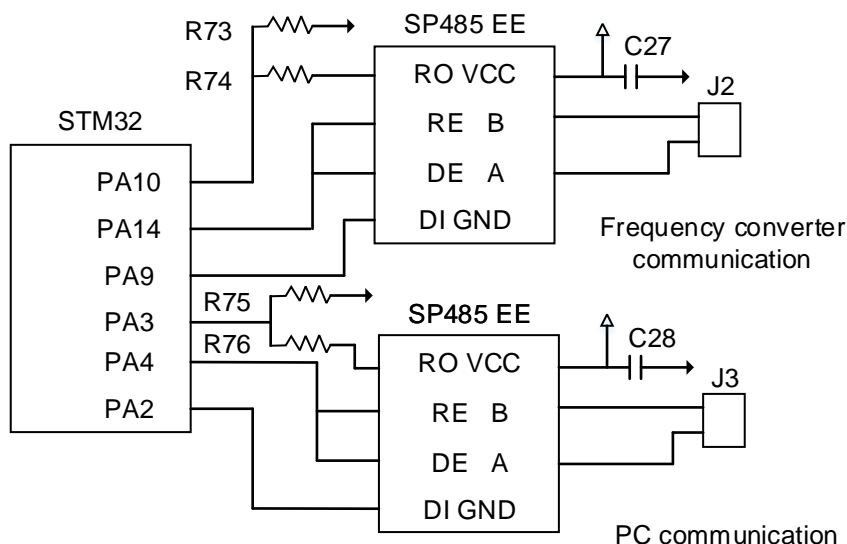


Fig. 3 - Design of system communication interface circuit

### Software design of temperature and humidity controller in tobacco house

The realization of the specific control task of the control system needs to be realized by the system software. The software design of this study is divided into the upper computer and the lower computer. The composition of the lower computer software corresponds to the design of the system hardware. The control system includes communication, algorithm, voice alarm, display driver, key processing, temperature and

humidity acquisition and other subroutines. The normal operation of the system depends on whether the software design is reasonable. The flow chart of the main control system is shown in Figure 4, including control output, fuzzy adaptive algorithm, temperature and humidity collection, key subprogram, interrupt program, initialization configuration, etc.

After the control system is powered on and reset, initialize the system, scan the on-site controller, determine whether the data has been input into the key, and display it on the on-site LCD screen; at this time, the upper computer starts to collect the data, successively receives the data on the keyboard and the sensor, stores the received data in the RAM controller, and makes it in the RAM controller through data conversion. The bus can realize the transmission of data frame. If the command of the upper machine is transmitted to the system, the data frame will be sent through the controller until the end of data receiving and sending, and there is no data conflict in the process of receiving and sending, then the algorithm subroutine will run.

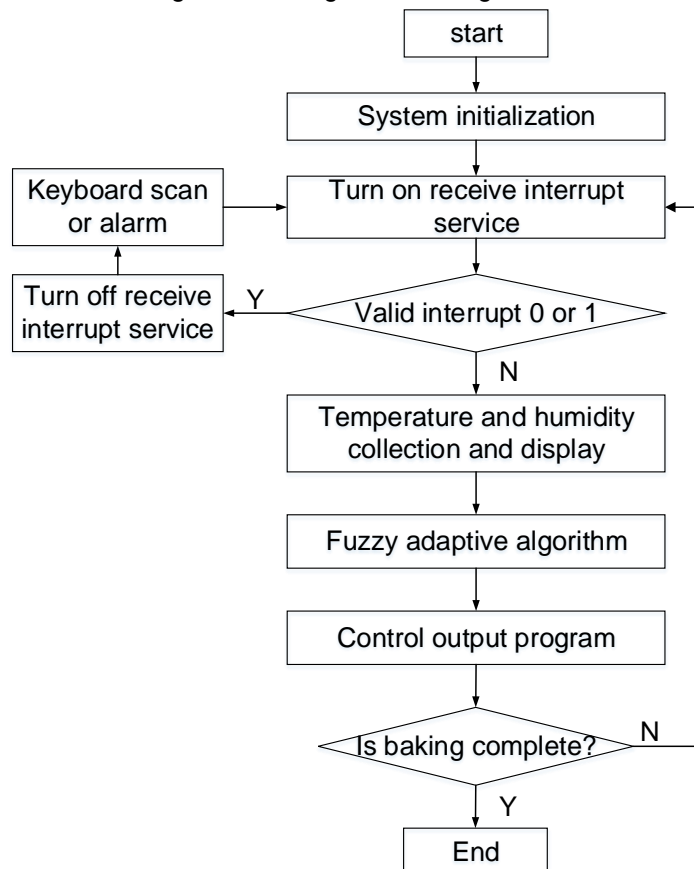


Fig. 4 - System main control flow chart

Two external interrupts 0 and 1 are designed in the system. The external interrupt 0 is used to process the alarm request. When the temperature and humidity are too high or too low, or lack of equal faults, the system will give a voice alarm and stop the system work as required. External interrupt 1 is used for key request. If it is a query key or a set key request, the system will enter the temperature and humidity setting subroutine or query record subroutine to make corresponding settings, and press the OK key to jump back to the main program after the end of setting data or query history. The flow chart is shown in Figure 5.

## RESULTS

### Experimental design of temperature and humidity measurement in flue-cured tobacco room

The agricultural intelligent temperature and humidity controller designed in this study was used to measure the temperature and humidity of flue-cured tobacco house, and the control effect was verified. According to the different targets, the experimental scheme is designed. The first is to compare the test results of this design with the traditional test methods. Before the test, fix the tobacco leaf and sensor on the fixture, use the instrument to monitor the temperature and indoor humidity of the tobacco leaf during the baking process, record the data every 4 hours, and use the dry and wet bulb thermometer to measure the temperature of the tobacco leaf surface until the end of the baking. Compare the room temperature monitored by the dry and wet bulb thermometer and the instrument, and analyse the results of comparison;

second, verify the control effect of the control design proposed in this study, compare the whole measurement process of the experiment, and experiment twice in the same flue-cured tobacco room. In the first experiment, we did not use the control design scheme proposed in this study, but only used the traditional manual adjustment method to control the temperature and humidity of the baking room. In the second experiment, according to the same technological process, we used the control design scheme proposed in this study to control the equipment of the baking room. The measurement object in the experiment is shown in Figure 5.



Fig. 5 - Physical picture of measurement experiment

### Experimental results and analysis

As shown in Table 1, the room temperature and tobacco surface temperature after the first experiment are obtained. It can be seen from table 1 that when the surface temperature of leaves on several bulb thermometers is heated to [34, 36] °C, and when the room temperature is heated to [34,38] °C, the difference between them is small. When the room temperature of some bulb thermometers is above 38°C, and the surface temperature of the blade is [38, 48]°C, the dry bulb temperature is in direct proportion to the surface temperature of the blade, and the difference between them is significant, and the temperature difference is fixed between [2.5, 3.5]°C. When the room temperature on several bulb thermometers is heated to [48, 68] °C, the temperature difference between the dry bulb thermometer and the blade temperature is relatively stable, and the temperature difference is fixed between [2, 4] °C. When the leaf temperature is fixed between [34, 36] °C, the humidity in the room is within [98.6, 90.2] %. If the leaf temperature increases gradually in [36, 48] °C, the room temperature in the baking room will also decrease gradually. When the humidity in the baking room is 42°C, the leaf temperature is 46.3°C. If the temperature of the leaves is [48, 66] °C, the humidity in the oven is within [42.0, 9.9] %.

Table 1

Comparison of room temperature and leaf temperature data from the first experiment

Time (h)	Traditional measurement (°C)	Instrument measurement (°C)	Difference (°C)	Time(h)	Traditional measurement (°C)	Instrument measurement (°C)	Difference (°C)
0	21.8	20.1	1.7	64	46.3	40.3	6.0
4	33.9	33.9	0	68	45.6	41.8	3.8
8	36.1	34.0	2.1	72	45.6	41.3	4.3
12	36.2	34.6	1.6	76	49.0	44.2	4.8
16	37.1	34.9	2.2	80	49.1	46.1	3.0
20	38.0	36.8	1.2	84	49.6	46.1	3.5
24	37.9	36.6	1.3	88	49.2	46.2	3.0
28	37.5	35.8	1.7	92	53.2	51.0	2.2
32	37.4	35.1	2.3	96	53.1	51.2	1.9
36	39.7	35.0	4.7	100	54.1	52.3	1.8
40	39.6	35.1	4.5	104	57.0	54.7	2.3
44	41.9	36.2	5.7	108	59.5	57.5	2.0
48	42.6	36.9	5.7	112	60.0	57.8	2.2
52	42.7	37.0	5.7	116	66.6	62.8	3.8
56	42.4	37.2	5.2	120	68.3	65.4	2.9
60	45.7	37.3	8.4	124	68.1	66.2	1.9

As shown in Table 2, the room temperature and tobacco surface temperature after the second experiment are obtained. It can be seen from table 2 that the second time is higher than the first time. In the process of flue-cured tobacco, when the surface temperature of the leaves on several bulb thermometers is heated to [34,37] °C, and when the room temperature is heated to [34,45] °C, the difference between them is small. When the room temperature of some bulb thermometers is above 45°C, and the surface temperature of the blade is at [45, 60] °C, the dry bulb temperature is in direct proportion to the surface temperature of the blade, and the difference between them is significant, and the temperature difference is fixed between [2.5, 3.5] °C. When the room temperature on several bulb thermometers is heated to [60, 68] °C, the temperature difference between the dry bulb thermometer and the blade temperature is relatively stable, and the temperature difference is fixed between [2, 4] °C. When the leaf temperature is fixed between [34, 37.3] °C, the humidity in the room is within [99.9, 75.0] %. If the leaf temperature increases gradually within [37.3, 57.8] °C, the room temperature in the baking room will also decrease gradually. When the humidity in the baking room is 22.8%, the leaf temperature will be 57.8°C. If the leaf temperature is [57.8, 66.2] °C, the humidity in the baking room is within [22.9, 12.8] %.

Table 2

Comparing the data of room temperature and leaf temperature in the second experiment

Time (h)	Traditional measurement (°C)	Instrument measurement (°C)	Difference (°C)	Time (h)	Traditional measurement (°C)	Instrument measurement (°C)	Difference (°C)
0	30.4	27.9	2.5	88	46.1	41.6	4.5
4	34.6	31.7	2.9	92	46.4	42.4	4.0
8	36.3	35.6	0.7	96	46.4	43.2	3.2
12	36.4	36.0	0.4	100	46.2	43.4	2.8
16	36.4	35.5	0.9	104	46.1	43.7	2.4
20	36.2	34.5	1.7	108	48.1	45.1	3.0
24	37.4	36.1	1.3	112	49.7	46.3	3.4
28	37.1	36.3	0.8	116	48.6	46.3	2.3
32	37.4	36.2	1.2	120	49.2	46.4	2.8
36	38.2	35.6	2.6	124	48.7	46.5	2.2
40	37.6	32.4	5.2	128	51.9	48.0	3.9
44	38.7	34.5	4.2	132	52.1	49.6	2.5
48	38.1	36.0	2.1	136	55.3	51.7	3.6
52	37.2	34.7	2.5	140	56.2	53.9	2.3
56	41.0	36.6	4.4	144	60.1	56.4	3.7
60	40.4	37.1	3.3	148	60.1	57.1	3.0
64	41.1	37.0	4.1	152	59.6	57.0	2.6
68	42.7	38.7	4.0	156	65.1	61.7	3.4
72	43.0	38.9	4.1	160	67.9	65.3	2.6
76	43.2	39.1	4.1	164	68.3	66.2	2.1
80	42.9	39.0	3.9	168	67.9	65.8	2.1
84	44.4	40.0	4.4				

In order to verify the control system proposed in this study, two baking experiments with different control modes were carried out, and the results were compared. According to the results of three-stage baking process and measurement, the comparison curve before and after adding the controller is obtained, as shown in Figure 6. Figure (a) shows the comparison curve between the baking process temperature and the results measured by the traditional measurement method. The temperature difference is relatively obvious, and overshoot is formed at some temperature points, such as 68°C, 60°C, 50°C, 48°C, 46°C, 37°C, 34°C, with poor control effect. Figure (a) shows the comparison curve between the results of the temperature control experiment based on STM32 and the measured temperature. The results show that the curve is consistent. Even if there are some places with obvious temperature difference, such as 60°C, 48°C and 37°C, it can be seen that the overshoot phenomenon is significantly reduced from the comparison curve, reflecting that the temperature control accuracy based on STM32 is significantly higher than that of the traditional control methods. It is conducive to the improvement of tobacco baking quality.

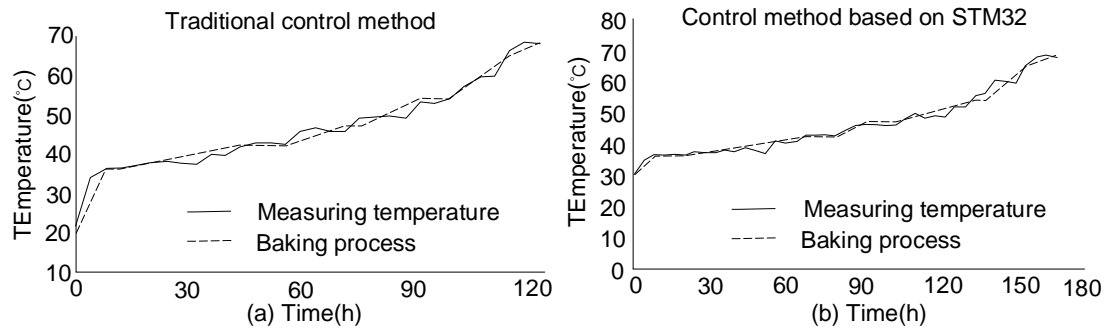


Fig. 6 - Comparison between STM32 based control method and traditional control method

## CONCLUSIONS

Aiming at the problem of temperature and humidity control in the flue-cured tobacco house, STM32 microcontroller is introduced into the temperature and humidity automatic control technology, and the temperature and humidity controller of the agricultural intelligent flue-cured tobacco house based on STM32 is designed. Finally, the designed system scheme is tested. The test results show that the temperature difference between the baking process temperature and the results measured by the traditional measurement method is obvious, and the overshoot is formed at some temperature points, such as 68°C, 60°C, 50°C, 48°C, 46°C, 37°C, 34°C, which has poor control effect; the comparison curve between the temperature control experiment and the measured temperature based on STM32 is consistent. Even if there are some places with obvious temperature difference, such as 60°C, 48°C and 37°C, we can see that the overshoot phenomenon is significantly reduced from the comparison curve, reflecting that the temperature control precision based on STM32 is significantly higher than the traditional control method, which is conducive to the improvement of tobacco baking quality. There are also some shortcomings in this study, because in the field measurement in the flue-cured tobacco room, the temperature points vary greatly. In order to reduce the measurement error, in the future research, the number of detection points will be increased to reduce the experimental error.

## ACKNOWLEDGEMENTS

The study was supported by “New Engineering Research and Practice Project at University Level” (Grant No. 18XGK002)”.

## REFERENCES

- [1] Elkhayat M., Mangiarotti S., Grassi M., (2016), Capacitance Humidity Micro-sensor with Temperature Controller and Heater Integrated in CMOS Technology, Vol.431, pp.383-387, USA;
- [2] Enrico Corti Michele., (2017), Model Based Control of Intake Air Temperature and Humidity on the Test Bench. *Energy Procedia*, Vol.126, pp.899-906, Netherlands;
- [3] Juliana de Souza Grand Barossa, Rossi L.A, Zigomar M.D.S., (2017), PID temperature controller in pig nursery: spatial characterization of thermal environment. *International Journal of Biometeorology*, Vol.62, pp.773–781, USA. DOI: 10.1007/s00484-017-1479-x
- [4] Khan M.W., Choudhry M.A., Zeeshan M., (2015), Adaptive fuzzy multivariable controller design based on genetic algorithm for an air handling unit. *Energy*, Vol.81, pp.477-488, England;
- [5] Li Shujiang, Zhao Chen, Su Xihui, (2017), Temperature and humidity control for environmental test chamber based on genetic algorithm optimized parameters of PID controller. *Journal of Nanjing University of Science & Technology*, Vol.41, Issue 4, pp.511-518, China;
- [6] Mien T.L., (2016), Design of Fuzzy-PI Decoupling Controller for the Temperature and Humidity Process in HVAC System. *International Journal of Engineering and Technical Research*, Vol.5, Issue 01, pp.589-594, USA;
- [7] Mirzaee-Ghaleh E, Omid M, Keyhani A., (2015), Comparison of fuzzy and on/off controllers for winter season indoor climate management in a model poultry house. *Computers and Electronics in Agriculture*, Vol.110, pp.187-195, England;
- [8] Nurainaa Elias, Nafrizuan Mat Yahya, Er Hong Sing., (2018), Numerical Analysis of Fuzzy Logic Temperature and Humidity Control System in Pharmaceutical Warehouse Using MATLAB Fuzzy Toolbox, pp.623-629, Singapore;

- [9] Ou K, Yuan W, Choi M., (2017), Performance increase for an open-cathode PEM fuel cell with humidity and temperature control. *International Journal of Hydrogen Energy*, Vol.42, Issue 50, pp.29852-29862, England;
- [10] Shigang Cui, Kun Liu, Xingli Wu., (2017), Design of a Temperature and Humidity Monitoring System for Plant Growth Cabinets Based on Data Fusion, Vol.458, pp.377-383, Singapore;
- [11] Singla S, Singh V., (2015), Design of a Microcontroller Based Temperature and Humidity Controller for Infant Incubator. *Journal of Medical Imaging & Health Informatics*, Vol.5, Issue 4, pp.704-708, USA;
- [12] Wei-Zheng S, Si-Yuan Z, Yan-Ling Y., (2019), Study on Multi-variables Decoupled Fuzzy Controller for Confined Pig House in Northern China. *Journal of Northeast Agricultural University*, Vol.026, Issue 001, pp.73-85, China;
- [13] Yan H, Deng S, Chan M., (2016), A novel capacity controller for a three-evaporator air conditioning (TEAC) system for improved indoor humidity control. *Applied Thermal Engineering*, Vol.98, pp.1251-1262, England;
- [14] Yan H., Xia Y., Deng S., (2017), Simulation study on a three-evaporator air conditioning system for simultaneous indoor air temperature and humidity control. *Applied Energy*, Vol.207, Issue 1, pp.294-304, England;
- [15] Yasser A Abdelaziz., (2017), Low Cost Humidity/Temperature Calibration System. *Journal of Scientific and Engineering Research*, Issue 410, pp.305-311, USA.

## INNOVATIVE MAINTENANCE AND FEEDING OF WEANING PIGLETS BASED ON NEW TECHNICAL MEANS

### ИННОВАЦИОННОЕ СОДЕРЖАНИЕ И КОРМЛЕНИЕ ПОРОСЯТ-ОТЪЕМЫШЕЙ НА ОСНОВЕ НОВЫХ ТЕХНИЧЕСКИХ СРЕДСТВ

**Nikolai Mikhailovich Morozov, Leonid Maksimovich Tsoy, Aleksander Nikolaevich Rasskazov**<sup>1</sup>

Institute of livestock mechanization–filial of Federal state budget scientific institution

"Federal research centre of agricultural engineering VIM" (IMJ –filial of FNAC VIM);

Tel: +7 916 9240844; E-mail: rassk49@mail.ru Ryazanovskoe settlement, the village of Znamya Oktyabrya, 31, Moscow. Russia

DOI: [https:// doi.org/10.35633/inmateh-62-05](https://doi.org/10.35633/inmateh-62-05)

**Keywords:** technology, feeding, postweaning piglets, small-group nested housing, piglet management pen, self-feeder, vibrating feeder.

#### ABSTRACT

A set of equipment for an innovative animal management system based on advanced technological solutions is presented. The equipment set includes a pen for housing postweaning piglets, a vibration feed distributor, and a self-feeder. Rationale behind the use of the small-group nested housing technique for postweaning piglets is presented, and the viability of development of a new feed distributor and self-feeders is discussed. Information on experimental studies of a new (vibration-based) type of feed distributor is presented to demonstrate its operating efficiency and adequate performance.

#### РЕЗЮМЕ

Представлен комплект оборудования для инновационной системы содержания на базе использования современных технических средств. Комплект оборудования включает в себя станок содержания поросят-отъемышей, вибрационный раздатчик кормов и самокормушку. Дано обоснование необходимости применения технологии мелкогруппового погнестного содержания поросят-отъемышей, показана целесообразность разработки нового типа раздатчика кормов и самокормушки. Представлены материалы экспериментальных исследований нового (вибрационного) раздатчика кормов, подтверждающие его работоспособность и достаточную производительность.

#### INTRODUCTION

In 2018, Russia has reached threshold values of the food self-sufficiency target of the Russian Federation in terms of meat production; meat output grew (mainly owing to pig farming) by 14.4%. The industry is actively employing advanced machinery and industrial digital technologies (Izmailov A. Yu., 2019; Latruffe et al., 2017; Wasserstein R. L., Lazar N.A., 2016).

Livestock and poultry production volumes amounted to 10,629.4 thousand tons (Table 1).

**Table 1**

**Production volumes of main types of livestock products and pig farming products in the Russian Federation (thousand tons)**

Product name	1990	2000	2010	2016	2017	2018
<i>All categories of producers</i>						
Slaughtered livestock and poultry (slaughter weight)	10111.6	4445.8	7166.8	9800.2	10391.4	10629.4
including pigs	3480.0	1578.2	2330.8	3368.2	3537.6	3744.2
<i>Agricultural organizations</i>						
Slaughtered livestock and poultry (slaughter weight)	7603.5	1786.5	4342.3	7515.2	8043.9	8349.7
including pigs	2290.6	435.8	1228.0	2716.8	2917.3	3186.4

<sup>1</sup> N. Morozov, Academician of RAS; L. Tsoy, Doctor of Economic Sciences; A. Rasskazov, Candidate of Economic Sciences

Product name	1990	2000	2010	2016	2017	2018
<i>Household farms</i>						
Slaughtered livestock and poultry (slaughter weight) including pigs	2507.0	2579.5	2612.6	2045.3	1973.3	1911.8
	1188.9	1107.2	1040.1	590.9	558.7	514.1
<i>Family-operated farms, farming enterprises and self-employed entrepreneurs</i>						
Slaughtered livestock and poultry (slaughter weight) including pigs	1.1	79.8	209.9	292.2	305.3	321.9
	0.5	35.2	69.0	47.2	44.2	43.7

Source: Federal State Statistics Service for 2010-2017, includes data of the All-Russian Agricultural Census of 2016.

A major area where resource saving technologies are being introduced is the sphere of comfortable animal housing and reduction of feed consumption that, on the average, account for 60% of total pork production costs. Optimal and biologically sound management of pigs with consideration to their genotype, is the basis for efficient use of resources (Kostlivý V., Fuksová Z., 2019; Laure Latruffe et al., 2017; Madau Fabio A. et al. 2017).

Comprehensive feeding of pigs with well-balanced feed is a critical factor in effective utilization of the genetic potential of animals. One of the particularities of pig feeding is that these animals have a very high growth rate, as compared to other livestock species. Thus, careful preparation of feed, as well as providing animals with high quality and safe feeding compounds, is required. All of the nutrients of the feed should be balanced not only in terms of the required consumption volume, but also in terms of balance of the nutrients, which should be optimized with respect to the proteins/calories composition of the diet (Syrovatka V. I. et al., 2019).

Affected by adverse factors during the piglet rearing stage, animals may become overstressed which may result in stock underdevelopment, disorders, and, consequently, high death level.

The adverse effects mentioned above are the most crucial for the initial stage of a pig's development, i.e., for postweaning piglets. For the above-mentioned reasons, pig breeding enterprises should strive to create comfortable housing and feeding conditions, most importantly – in rearing pens. According to the existing technological process, piglets are moved into houses where they are grouped in three or four nests, with up to 30 animals in a pen. This results in stress. When feeding a large group of piglets, there is not enough space to accommodate all of them, which leads to conflicts between animals.

## MATERIALS AND METHODS

Based on studies of various sources when researching the issue of eliminating the drawbacks of the postweaning piglet feeding process, it was determined that the nested small-group rearing method of piglets should be used, with the number of animals not exceeding 10 to 12 per one pen. To achieve this objective, a set of equipment was developed which uses a conceptually new type of distributor and self-feeder.

This study uses the methods of system analysis, mathematical statistics, regulatory documents; it also reviews the trends in technology and facilities used for management and feeding pigs; uses the technique of summarization of ranking scores. Some information in this study is presented in the form of tables (Choi L., 2016; Ivanov, Yu. Mironov V.V., 2018; Morozov N.M., Rasskazov A.N., 2019).

## STUDY RESULTS

Figure 1 shows the flow chart of the innovative system of postweaning piglets' housing and feeding based on advanced technological solutions.

The basis of the innovative system of housing and feeding postweaning piglets is the equipment providing small-group nested stress-free housing of animals. The conceptually new process solution for feed distribution and the self-feeder are technologically and structurally integrated into the pen system.

The pen for small-group nested housing of postweaning piglets accommodating up to 12 animals has the area of 6.9 m<sup>2</sup> (Fig. 1, Item 1), and is equipped with a self-feeder, a brooder intended as the piglet rest area, and suckle feeders. To ensure ease of animal management, the entrance gate is located within the front wall of the pen, close to the self-feeder. There is some free space in the pen near the self-feeder sufficient for at least four piglets. The brooder is located in the left part of the pen, and is adjacent to the rear wall. It accommodates up to 12 piglets. Floor area of the brooder is at least 1.2 m<sup>2</sup>.

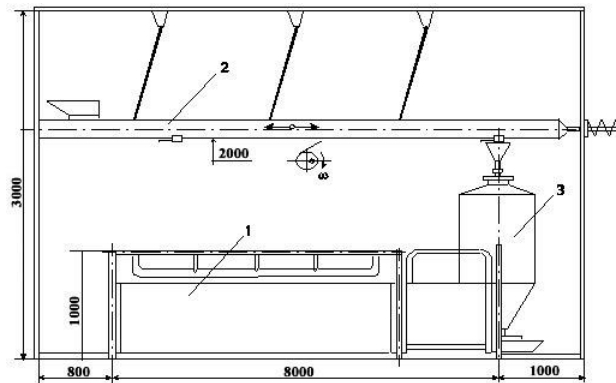


**Fig. 1 - Process scheme of the innovative system of postweaning piglets' housing and feeding based on advanced technological solutions**

1- pen for small-group nested housing of postweaning piglets; 2 – feed distributor; 3-self-feeder

General view of the pen for small-group nested housing of postweaning piglets is shown in Figure 2.

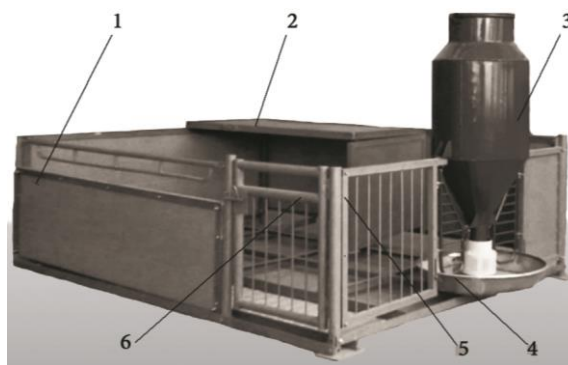


**Fig. 2 - Pen for nested housing of postweaning piglets**

1-pen front wall; 2-pigged brooder cover; 3-feed supply hopper; 4-round self-feeder trough; 5-contact grille; 6-gate

Pen fencing is made of 200 mm wide and 35 mm thick plastic panels. The top of the panels has a locking profile, and their bottom has the respective slot. The design of the panel ensures its durability, and makes it possible to treat the panels with disinfectants. Panels comprising a wall are assembled into panes of the required height: 600 mm high in the front, and 800 mm high on the sides and in the rear. The panels are reinforced along the perimeter by a metal frame made of angle bars with the dimensions of 45x45x5 mm, and a 40x45 mm plate. The frame has four bolt holes for securing the walls to the support poles.

In order to improve the efficiency, the self-feeder (Fig. 1, item 3) is located at the partition between two adjacent pens, and supplies both of them. The self-feeder is equipped with a supply hopper which holds two days' worth volume of feed; a round trough divided into four partitions is located in each of the pens. Beside the self-feeder, there are two suckle feeders.

The structural diagram of the self-feeder is shown in Figure 3.

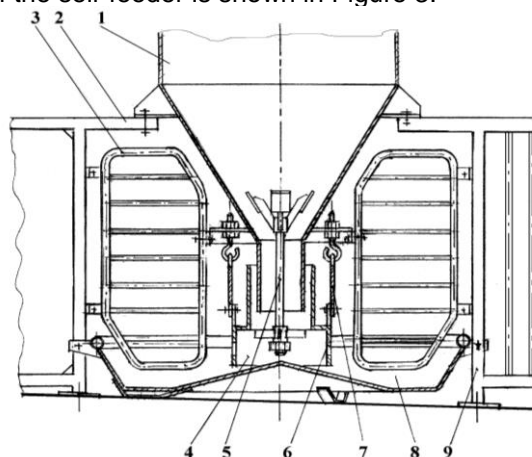


**Fig. 3 - Mechanism of the self-feeder**

1-hopper; 2-pen partition; 3-removable partitions; 4-discharge neck, 5-agitator; 6-slots; 7-flexible suspension; 8-round trough; 9-contact grille

Hopper 1 is intended for storage of a certain reserve volume of dry feed; the discharge neck 4, being a movable part, makes it possible to regulate the rate of feed supply from the hopper into the round trough 8.

The discharge neck 4 is the main working body of the self-feeder. Animals actuate its slotted shell ring (by moving the ring within the gap between the cylindrical pipes) and thus the feed in the trough 8 is replenished. To achieve this, the discharge neck unit is attached to the hopper using flexible elements to allow movement, and there is an adjustable gap between the discharge neck and the bottom of the trough.

The upper part of the discharge neck has the same form as the matching part of the hopper, while the neck internal diameter is 30 mm larger. This gap makes it possible for the discharge neck to move in all directions, and ensures that feed is always present in the trough 8. To prevent bridging of feed within the cone-shaped bottom part of the hopper, the discharge neck 4 is equipped with the flap agitator 5.

To attract animals to the self-feeder, the lower part of the discharge neck has a slotted shell ring. The ring slots fill with feed, but their width is not sufficient for feed to spill into the trough 8 spontaneously.

The conceptually new vibration feed distributor (Fig. 1, item 2) was developed to deliver feed to self-feeders. This device has a number of advantages over the existing feed conveyors.

Presently, the main method of feed distribution mechanization lies in the use of stationary feed transportation and distribution systems, based on various engineering solutions.

Systems employed to transport feed from bunkers to pig houses and distribute it within include chain-disc conveyors and screw-type (spiral) conveyors.

A common drawback of these technologies is that they employ a working body (a chain with discs, a helix or a screw), which forces the feed to the pig feeding location. The chain-disc, helix or screw system operate under a high load and are prone to intensive wear due to active interaction with the feed.

Alternative technologies to transport feed within the pig breeding facility are thus required that would have none of these disadvantages.

Research dedicated to the development of equipment for the transportation and distribution of feed based on new technological solutions resulted in the development of a conceptually new system of feed delivery to piglets.

A promising line of development of feed distribution systems is the vibrating transportation system.

Unlike chain-disc or screw (spiral) conveyors, the vibrating feed delivery chute has no moving parts.

Main requirements to vibrating conveyors are the capacity to prevent sticking of the feed, as well as to select parameters of vibration and the angle of inclination of suspension links and the piston.

Main advantages of vibrating conveyors as compared to chain-disc or screw (spiral) type conveyors are: improved working conditions in the pig house, reduced soiling owing to the fact that this feed delivery system is enclosed, absence of contamination of the feed and its loss to spillage, low wear of the feed delivery chute due to the absence of rubbing parts and simple design. Apart from the above advantages, metal needed to manufacture them and their energy consumption are lower, reliability of the system is higher while its operational costs are reduced.

A study of principles of this granular material transportation method enabled us to develop a valid process scheme and determine the location of the actuating mechanism of the feed distributor.

According to the theory of vibration-based transportation of granular materials, the line of the shaking force which sets the system in vibration, should pass through the centre of the system's mass (centre of attraction) to exclude secondary torsional oscillations that affect the material transportation process adversely.

The process scheme of the vibration piglet feed distributor was developed with due account to these requirements.

The process scheme is shown in Figure 4.

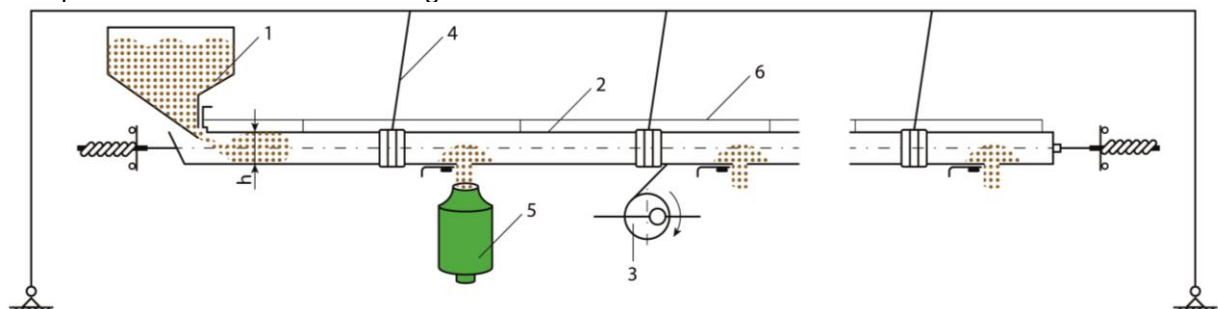


Fig. 4 - The technological scheme of the modernized vibrating feed distributor

The feed distributor includes intake hopper 1; feed delivery chute 2; actuator 3; suspension links 4; self-feeder 5; and rectangular reinforcement tube 6.

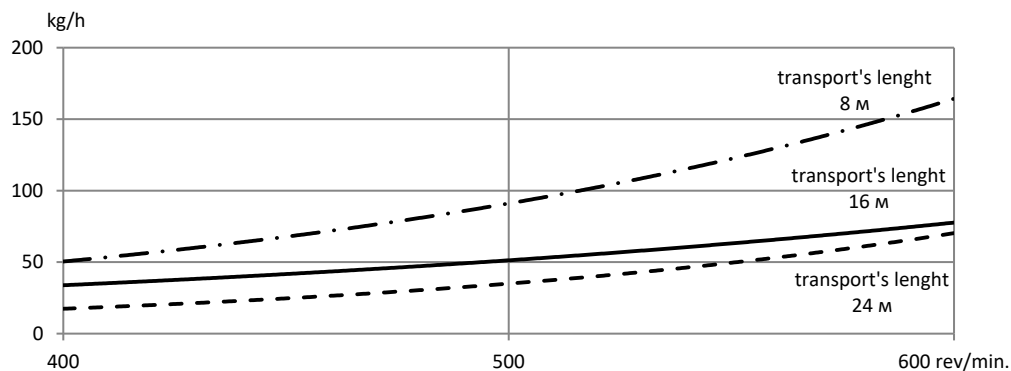
The intake hopper is intended to deliver feed into the delivery chute, which has the form of a cylindrical pipe 24 m long and 100 mm in diameter. The actuating mechanism is comprised of a cam which rotates to create vibration with a certain amplitude (in our particular case, two cams (10 and 20 mm) were used). Suspension links are located at a certain angle to the vertical line, and facilitate feed shaking within the feed supply chute.

The advance of dry feed into the self-feeder hopper is achieved by the feed distributor of the new design by means of vibrating feed delivery chute.

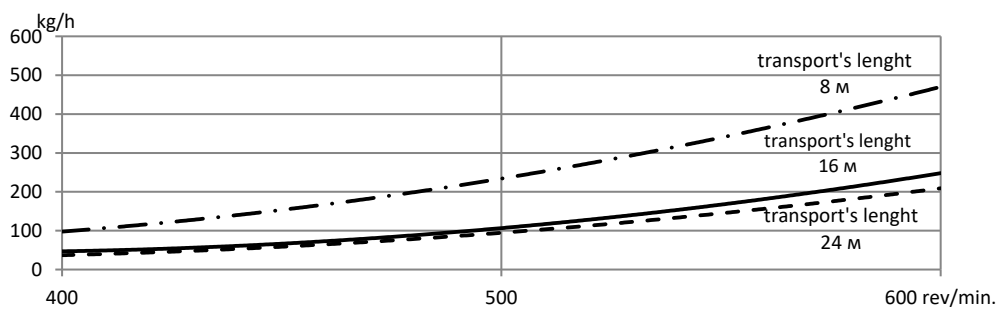
Dry feed is transported within the vibrating feed chute throwing up tossed granules and moving them towards discharge apertures.

On the basis of the process scheme of the vibrating feed distributor, design documentation was developed, and the feed distributor was manufactured and assembled. This enabled experimental studies of the vibration feed distributor.

These studies, conducted on loose and pellet feed, enabled us to determine the dependency of the feed distributor performance from the speed rate of the electric motor, the feed transportation distance, and the amplitude of the vibration mechanism oscillation (Fig. 5 a and b).



a) loose feed



b) pellet feed

**Fig. 5 - Dependence of the vibrating feed distributor’s capacity on the number of electric motor’s revolutions (eccentricity of 10 mm)**

The diagram demonstrates that, in case of loose feed (Fig. 5 a), the transportation distance of 8 m, and the electric motor’s speed within the range of 400 to 600 rpm, the performance of the feed distributor increases more than threefold, with the transportation distance of 16 m -- just over twofold, and with the transportation distance of 24 m it is more than four times higher.

For pellet feed (Fig. 5 b), the change of performance with the change of the electric motor speed rate at various feed transportation distances is as follows.

With the electric motor speed rate changing from 400 to 600 rpm and the transportation distance of 8 m, the performance is four times higher; with the transportation distance of 16 and 24 m, the performance is more than five times higher.

Similar experimental studies with an eccentricity equal to 20 mm were carried out. The vibrations' amplitude increasing due to a larger eccentricity using contributes to an overall vibrating feed distributor capacity increasing. Similar experiments were carried out with the eccentricity equal to 20 mm. The increased oscillation amplitude due to the higher eccentricity results in a more intensive increase of performance of the vibration feed distributor.

## CONCLUSIONS

The set of process equipment for the stress-free nested postweaning piglet management and feeding system would make it possible to minimize stress-related phenomena, ensure livability of piglets, improve average daily weight gain, and stabilize piglet development.

The expected results of application of the equipment are: an increase of postweaning piglet survivability of up to 98%, and achieving 30 to 32 kg of body weight in 85 to 90 days. The experimental studies have shown that the developed vibration feed distributor provides stable feed delivery and the required performance.

Stress-free small-group (up to 12 animals) housing of postweaning piglets improves livability of rearers up to 90 or 93%, and average daily weight gain during the rearing to no less than 400 g per animal per day.

## REFERENCES

- [1] Choi L. M., (2016), Development and investigation of vibrating dry food distributor for feeding weaned piglets (Разработка и исследование вибрационного раздатчика сухих кормов для кормления поросят-отъемышей). *Bulletin of VNIIMZH (ВЕСТНИК ВНИИМЖ)*. 1 (21), pp. 80-86.
- [2] Ivanov Yu.A., Mironov V.V., (2018), Test results of in-vessel composting system at the cattle farm located in the central part of Russia. *AMA, Agricultural Mechanization In Asia, Africa And Latin America*. Т.49. № 3, pp. 86-90.
- [3] Izmailov A.Yu., (2019), Smart technologies and robotic tools in agricultural industry. (Интеллектуальные технологии и роботизированные средства в сельскохозяйственном производстве), *Bulletin of the Russian Academy of Sciences*, Vol. 89, № 5, pp. 536-538. DOI: <https://doi.org/10.31857/S0869-5873895536-538>.
- [4] Kostlivý V., Fuksová Z., (2019), Technical efficiency and its determinants for Czech livestock farms. *Agric. Econ. – Czech*, 65: pp. 175-184.
- [5] Latruffe L., Bravo-Ureta B., Carpentier A., Desjeux Y., Moreira V., (2017), Subsidies and technical efficiency in agriculture: evidence from European dairy farms. *American Journal of Agricultural Economics*, Volume 99, Issue 3, April, pp. 783–799.
- [6] Latruffe L. et al., (2017), Subsidies and Technical Efficiency in Agriculture: Evidence from European Dairy Farms, *American Journal of Agricultural economics*. Vol. 99, Issue 3, pp. 783–799. DOI:<https://doi.org/10.1093/ajae/aaw077>.
- [7] Madau Fabio A., Furesi Roberto, Pulina Pietro, (2017), Technical efficiency and total factor productivity changes in European dairy farm sectors. *Agricultural Economics Review*, 8, pp. 5–21.
- [8] Morozov N.M., Rasskazov A.N., (2019), Russian livestock production competitiveness directions increasing // IOP Conference Series: *Earth and Environmental Science*. V. 403. С. 012117.
- [9] Syrovatka V.I. et al., (2019), Barothermal processing of compound feed ingredients (Баротермическая обработка ингредиентов комбикормов). *Engineering technologies and systems (Инженерные технологии и системы)*. Vol. 29, № 3, pp. 428-442. DOI: <https://doi.org/10.15507/2658-4123.029.201903.428-442>.
- [10] Wasserstein R. L., Lazar N. A., (2016), The Asa's Statement on P-Values: Context, Process and Purpose, *The American Statistician*. Vol. 70, № 2, pp. 129–133. DOI: <https://doi.org/10.1080/00031305.2016.1154108>.

# RELATIONSHIP BETWEEN SOIL MOVEMENT AND POWER CONSUMPTION IN A FURROW-OPENING ROTARY BLADE

## 圆盘式开沟刀土壤移动规律与功耗关系研究

Kuan Qin, Xiaolong Liang, Chengmao Cao<sup>1)</sup>, Liangfei Fang  
 College of Engineering, Anhui Agricultural University, Anhui Province, Hefei 230036, China  
 Corresponding author, Tel: +8615205111399; E-mail address: caochengmao@sina.com  
 First author, Tel: +8618855102551; E-mail address: qinkuan@ahau.edu.cn  
 DOI: <https://doi.org/10.35633/inmateh-62-06>

**Keywords:** rotary blade, tracer method, soil movement, movement distance, power consumption

### ABSTRACT

Small, handheld furrow openers using rotary blades usually have limited power, making it necessary to minimise their operating power consumption, which mainly occurs with the soil throwing and movement of rotary blades. To this end, it is necessary to investigate the power consumption of such tillage implements, particularly the relationship between their power consumption and operating conditions based on soil movement patterns. In this study, we performed a field test of a furrow-opening rotary blade using round, physical tracers to monitor soil movement. The total power consumption of the rotary blade was positively related to the operating depth of the blade but was not related to the soil movement distance. The total power consumption peaked at 6.677 kW at a forward speed of 0.3 m/s, which was negatively related to the forward speed, but positively related to the soil movement distance. At a blade rotational speed of 340 rpm, the total power consumption peaked at 4.385 kW and was positively related to the blade rotational speed and soil movement distance. Therefore, it was concluded that by decreasing the rotary blade rotational speed and operating depth and increasing the forward speed, the power consumption of the unit working length can be reduced.

### 摘要

小型手扶式开沟机对所使用的旋转式开沟刀具有动力限制，因此需要减小开沟刀作业过程中抛撒与移动土壤的阻力，为了达到减小作业阻力的目的，对开沟刀作业过程中的土壤移动规律与开沟功耗进行研究。通过圆形示踪颗粒代替土壤，通过追踪示踪颗粒达到测定土壤移动规律的目的，再此过程中同时测定作业功耗，得到土壤移动规律与旋转式开沟刀作业功耗之间关系。通过试验可知，开沟刀作业功耗和开工深度呈正相关，与土壤移动距离无关。开沟刀在作业速度 0.3 m/s 时，作业功耗最大为 6.677 kW；开沟刀在作业速度 340 rpm 时，作业功耗最大为 4.385 kW。通过试验结果可知，当减小开沟刀旋转速度和开沟深度，增加开沟刀前进速度时，可使单位工作距离下，旋转式开沟刀作业阻力最小。

### INTRODUCTION

Small, handheld furrow openers are widely used for preparing small field patches, particularly those in hilly and mountainous regions, owing to their better manoeuvrability in small spaces, lower power consumption, and greater slope-climbing capability as compared with large furrow openers. These furrow openers usually use disc-type rotary blades fixed to a rotating shaft (Figure 1a). To reduce the power consumption of such furrow openers, the resistance force on their rotary blades needs to be minimised (Matin *et al.*, 2015), making it necessary to investigate the occurrence mechanism of the resistance. The resistance on rotary blades is the reacting force of their soil-cutting force (Kataoka *et al.*, 2002; Ani *et al.*, 2018). The occurrence mechanism of the resistance has been investigated using various methods. Li *et al.* (2018) investigated the occurrence mechanism of the resistance on rotary blades using smoothed particle hydrodynamics and Taguchi methods. Asl *et al.* (2009) developed a mathematical model for predicting the power requirement of rotary blades and equations for quantifying blade surface area per unit volume of soil tilled, thereby optimising blade structure for resistance minimisation. Salokhe *et al.* (2002) experimentally investigated the resistance on reverse and traditional rotary blades operating at different rotational speeds in clay soil. Yang *et al.* (2015) developed a soil-cutting model of rotary blades using a finite element method, observing that the power consumed during soil cutting mainly consisted of kinetic and internal power, with a ratio of kinetic power to internal power of 1:9.5. Chertkiattipol *et al.* (2010) investigated the resistance on rotary blades at different temporal phases by measuring their coordinates at various time points. In addition,

past research into the effect of the structure of rotary blades on their cutting force has also been investigated (Ahmadi *et al.*, 2017; Fajardo *et al.*, 2014; Mollazade *et al.*, 2009). Furrow opening using rotary blades involves moving soil outside of the furrow (Lee *et al.*, 2003), with the kinetic and potential energies required for moving soil provided by the rotary blades. Thus, soil movement patterns affect the energy consumption of rotary blades (Shibusawa, 1993). Ucgul *et al.* (2017; 2018b) investigated the soil movement and tillage force of a mouldboard plough and rotary spader through discrete element modelling. Li *et al.* (2019) marked soil layers using physical tracers and analysed soil movement using a digital image processing technique. Haas *et al.* (2018) measured soil movement using different corpuscular metal tracers and a metal detector. Grayling *et al.* (2018) traced particle movement in soil using X-ray micro computed tomography. He *et al.* (2016) investigated the penetration force of a shovel-type furrow opener using a finite element method. The soil movement and cutting force of various tillage implements have been investigated. Traction-type implements involve only *in-situ* soil movement (Qin *et al.*, 2018). In contrast, furrow-opening rotary blades involve soil cutting, crushing, and throwing (Harrison, 1978). This process involves both short- and long-distance movement of scattering soil (Figure 1b), thereby moving soil from inside the furrow to targeted positions outside of the furrow. The power consumption of this process constitutes the majority of the power consumed by the furrow-opener. Thus, the soil movement patterns are key to the occurrence mechanism of the resistance on rotary blades.

In this study, the relationship between furrow-opening rotary blades and operating conditions was investigated based on soil movement pattern, and an optimal level of energy consumption of the furrow-opening rotary blade under different operating conditions was determined.

Physical tracers are most appropriate for tracing the soil movement and throwing operations of furrow-opening rotary blades. However, tracers used in previous experiments were large, heavy, and mostly polyhedral, features which are not appropriate for tracing the soil movement and throwing of furrow-opening rotary blades (Rahman *et al.*, 2005; Viktor *et al.*, 2018; Solhjou *et al.*, 2012). In this study, a small-diameter round tracer similar to a soil pellet was used to investigate the soil throwing and movement produced by furrow-opening rotary blades, and their power consumption was investigated in relation to the operating conditions and soil movement pattern.

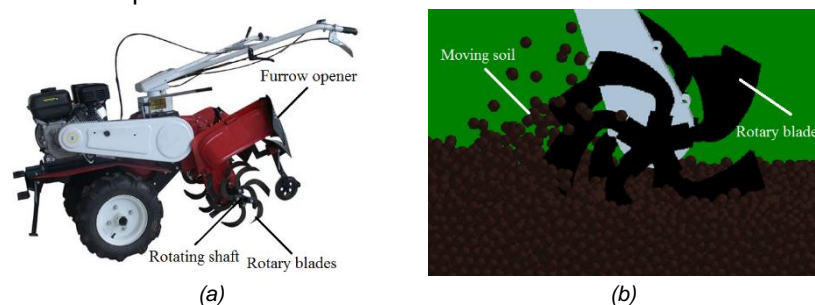


**Fig. 1 - Furrow-opening rotary blade**

(a) Small handheld furrow-opening rotary blades and soil movement during operation;  
 (b) Soil throwing and movement of furrow opening rotary blades

## MATERIALS AND METHODS

### Field test platform

A field test platform was established to measure the soil movement and cutting force of furrow-opening rotary blades when the rotary blades were operating (Figure 2). The platform consisted of a frame, 48-V power source, forward drive motor, motor speed controller, gasoline engine, gear box, chain drive for driving the rotary blades, shaft for mounting the disc blades, torque sensor, computer, furrow-depth adjustment unit, traction wheels, and depth roller. The power source provided power to the driving motor, which drove the traction wheel to move forward. The forward movement speed of the platform was adjusted through the motor speed controller. The gasoline engine drove the shaft (on which the discs blades were mounted) through the gear box and chain drive. The output speed of the gear box could be adjusted to four different levels. The shaft rotated at high speeds to drive the furrow-opening rotary blades. The torque sensor was fixed to a position between the gasoline engine and shaft for measuring in real-time the rotational speed and power consumption (torque and power, respectively) of the rotary blades; torque and power measurements were collected every second. Measurements were inputted into the computer through a wireless transmitter and were displayed on the computer screen. The data acquisition software (Labview) collected torque and power measurements according to the current frequency, and automatically output the total power

consumption for a given period. The soil cutting depth of the rotary blades was adjusted by modifying the distance between the frame and depth roller through the operating depth adjustment unit.

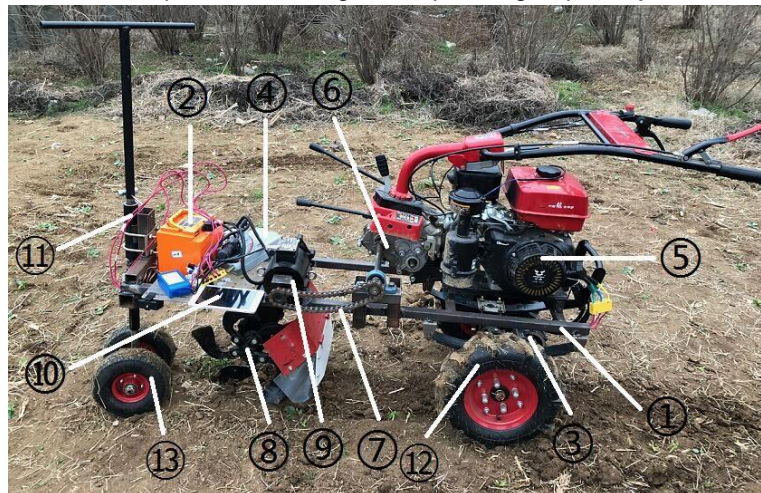


**Fig. 2 - Field test platform**

1 - Frame; 2 - Power source; 3 - Forward drive motor; 4 - Motor speed controller; 5 - Gasoline engine; 6 - Gear box; 7 - Chain drive; 8 - Shaft for mounting blade discs; 9 - Torque sensor; 10 - Computer; 11 - Operating depth adjustment unit; 12 - Traction wheel; 13 - Depth roller

**Rotary blade**

The rotary blade used for the test had lateral and forward cutting edges (Fig. 3a). The cutting edges were in different spatial planes, with the lateral cutting edge represented using coordinate system  $oxyz$  and the forward cutting edge represented using coordinate system  $obx_b y_b z_b$ . The radius of gyration of the rotary blade,  $R$ , measured 260 mm. The lateral and forward cutting edges were in-plane isometric spirals. The lateral cutting edge was represented in plane coordinate system  $oxyz$  and can be described using Eq. (1):

$$\rho = 168 + 3.7\theta \tag{1}$$

where:  $\theta$  represents the polar angle of the spiral, with the polar angle at the starting point of the spiral  $\theta_0 = 0^\circ$  and at the ending point  $\theta_n = 22.3^\circ$ ; and  $\rho$  is the polar radius of the spiral, with the polar radius at the starting point of the spiral  $\rho_0 = 168$  mm and at the ending point  $\rho_n = 250$  mm.

The plane of the forward cutting edge deflected around line  $l$  at an angle of  $\psi = 74^\circ$ , with the angle between line  $l$  and x-axis  $\beta = 58^\circ$ . The forward cutting edge was represented in plane coordinate system  $obx_b y_b$  and can be described using Eq. 2:

$$r = 214 + 3.2\delta \tag{2}$$

where:  $\delta$  is the polar angle of the spiral, with the polar angle at the starting point of the spiral  $\delta_0 = 0^\circ$  and at the ending point  $\delta_n = 12.6^\circ$ ; and  $r$  is the polar radius of the spiral, with the polar radius at the starting point of the spiral  $r_0 = 184$  mm and at the ending point  $r_n = 212$  mm.

The widths at the root, deflection, and tip of the blade,  $h_1$ ,  $h_2$ , and  $h_3$ , measured 32, 47, and 56 mm, respectively. Five blades were arranged circumferentially at an equal angular distance to form a disc (Figure 3b). The radius of gyration of the disc measured 300 mm. The blades were made using 65 Mn steel, which had a density of  $7.83 \times 10^3$  kg·mm<sup>-3</sup>, modulus of elasticity of  $2.06 \times 10^{11}$  Pa, and Poisson ratio of 0.35.

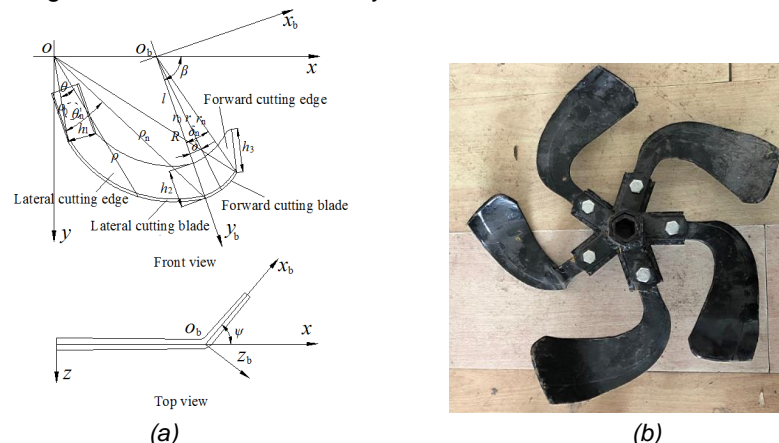


**Fig. 3 - Rotary blade**

(a) Illustration of the structure of the rotary blade; (b) Rotary blade disc

*Physical tracers*

Small, physical tracers made from silica gel were used, each measuring 0.6 g in weight, 6 mm in diameter, 5.3 g/cm<sup>3</sup> in density, and an elasticity modulus of 1.2 GPa (Figure 4). Owing to similar material properties found within soils, the tracers were mixed into soils to monitor the soil movement of the furrow-opening rotary blade. Tracer pellets were numbered (1–30), and their movement was used to represent soil displacement.



Fig. 4 - Tracer pellets

*Methods*

*Configuration of tracer pellets in soil*

An area of farming field measuring 5 × 1 m was randomly selected for the test. Numbered tracer pellets were then placed in the test area as follows: tracer pellets for each 5 cm soil layer (altogether five rows of tracer pellets; Fig. 5), with the distance between tracer pellets measuring 4 cm in the width direction and 100 cm in the travel direction length (four lines of tracer pellets in the width direction and six columns of tracer pellets in the travel direction; Fig. 5). To present the position of the tracer pellets, a coordinate system XYZ was established, with the X-, Y-, and Z-coordinates representing the travel, width, and depth directions, respectively. A total of 120 tracer pellets were used for this configuration, with each pellet representing the soil volume around it. Thus, movement of the tracer pellets represented the soil movement of the furrow-opening rotary blade.

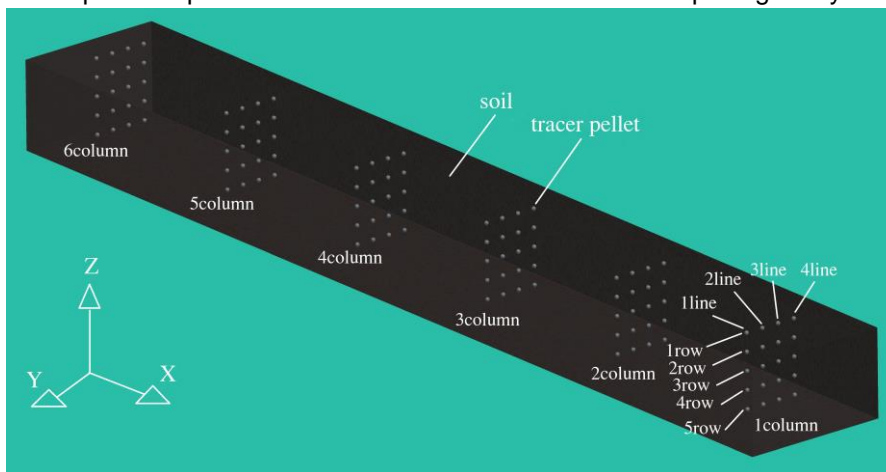


Fig. 5 - Illustration of tracer pellet configuration

*Definition of test variables*

The experiment was performed at the four operating depths of the furrow-opening rotary blade (5, 10, 15, and 20 cm), three forward speeds of the platform (0.3, 0.5, and 0.7 m/s), and three rotational speeds of the rotary blade (170, 255, and 340 rpm). Only one of the three variables was varied at a time. Thus, the test was performed at a total of ten levels, so that the effect of each of the variables on the soil movement and power consumption of the rotary blade was investigated. Table 1 shows the soil parameters.

Table 1

Main soil parameters of test field	
Parameters	Value
Bulk density [t·m <sup>-3</sup> ]	1.31
Wet density [t·m <sup>-3</sup> ]	1.8
Soil texture	Clay loam (23.60% clay, 40.82% silt, 35.55% sand)
Dry basis soil moisture content [%]	28.98
Soil cohesion [kPa]	45.01(0-2 cm), 53.44(4-6 cm), 64.16 (8-10 cm)
Soil con index [kPa]	695(0 cm), 994(5 cm), 1207(10 cm)

### Experimental procedure and data collection

Tracer pellets were buried in holes drilled in the soil according to the configuration in Figure 6(a). The rotary blade discs were fixed onto and driven by the rotating shaft of the field test platform for furrow opening (Figure 6(b)). For each level of the experiment, the platform was operated for furrow opening along the first line of tracer pellets in the width direction (because the rotary blades threw soil to the two sides symmetrically, soil movement at only one side was measured). Thus, the first line of tracer pellets was the centre of action of the rotary blade. Each level of the experiment was performed five times, with the measurements averaged for subsequent analyses. Measurements of the movement distance of the tracer pellets (Figure 6(c)), instantaneous torque (instantaneous power), and total power consumption (Figure 6(d)) were obtained from the experiment.



**Fig. 6 - Illustration of test procedure**  
(a) Tracer pellets set; (b) Platform; (c) Data measurements; (d) Power consumption collected

### Methods for obtaining measurements of tracer pellet movement

Measurements of tracer pellet movement in the travel, width, and depth directions ( $i$ ,  $j$ , and  $z$ , respectively) represented in the coordinate system defined above were obtained from the experiment and used to compute overall tracer pellet movement distance,  $L$ , using Equation 3:

$$L = \sqrt{i^2 + j^2 + z^2} \quad (3)$$

### Methods for obtaining measurements of instantaneous torque (instantaneous power) and total power consumption

Measurements of instantaneous torque obtained by the torque sensor were collected every second and were then used to compute instantaneous power using Equation 4:

$$P = \frac{T \cdot n}{9550} \quad (4)$$

where:

$P$  is the power (kW),  $T$  is the torque (N·m), and  $n$  is the rotational speed of the rotary blade (rpm).

At the end of each level of the test, the computer provided the output of the total power consumption for the entire length of travel (5 m) by analysing the measurement data using LabVIEW. Through the Origin8.5 software analysed the data and obtained the standard deviation of homogeneous data (error bars) and significant difference of inhomogeneous.

## RESULTS AND DISCUSSION

### Effect of operating depth on soil movement

When the blade rotational speed (225rpm) and forward speed (0.5m/s) were held constant, the movement distances of the first and second lines of tracer pellets were larger than those of the third and fourth lines, with the movement distance of the fourth line being the smallest. The first line was located at the centre of action of the rotary blade, the second line was close to the centre of action, and the third and fourth lines were gradually farther away from the centre of action. This indicates that the soil movement distance was the largest at the centre of action and decreased as the distance from the centre of action increased (Figure 7-10).

In Figure 7 through 10, the tracer movement distance consisting of movement in the travel, width, and depth directions is presented by the line charts, and the proportional relationship between the three components is presented by the pie charts. The proportional relationship of the three components showed that, for all soil layers at all different operating depths, the movement distance in the travel direction is larger than that in the width direction, followed by that in the depth direction. This indicates that, at all blade operating depths, the soil movement distance in the travel direction is larger than that in the width direction, followed by that in the depth direction.

Additionally, the proportion between the soil movement distances in the travel, width, and depth directions was not related directly to the operating depth. At all operating depths, the proportion of movement distance in the depth direction to the overall movement distance of deeper tracer pellets was larger than that of shallower tracer pellets. This indicates that the proportion of soil movement distance in the depth direction to the overall soil movement distance increased as the depth of the soil layer increased.

At a blade operating depth of 20 cm, for all lines of tracer pellets, the movement distance of the second row was the largest, and that of the fifth row was the smallest. As the numbering of the tracer pellet row decreased, the proportion of the tracer movement distance in the width direction in the overall tracer movement distance exhibited an increasing trend. The proportion of the movement distance in the depth direction exhibited a decreasing trend. The proportion of the movement distance in the travel direction first decreased then stabilised but was > 50% in all cases (Fig. 7). This indicates that, at a blade operating depth of 20 cm, the soil movement distance was the largest at a soil layer depth of approximately 5 cm and was the smallest at a soil layer depth of approximately 20 cm. Additionally, a deeper soil layer had a larger proportion of soil movement in the depth direction, and a shallower soil layer had a larger proportion of soil movement in the width direction.

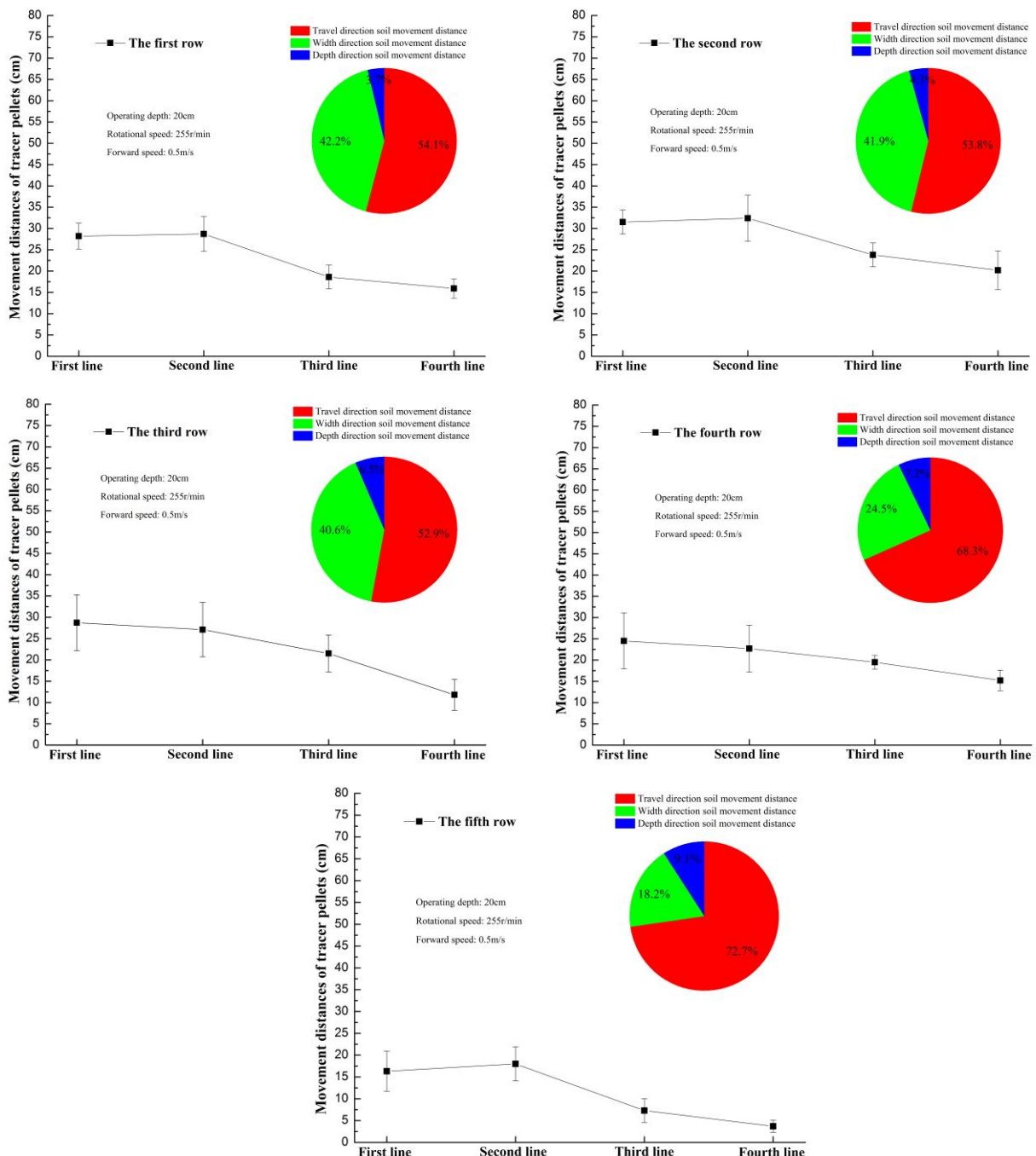


**Fig. 7 - Soil movement at operating depth of 20 cm**

At a blade operating depth of 15 cm, for all lines of tracer pellets, the tracer movement distance gradually decreased as the numbering of the tracer pellet row increased. Except for the fifth row, as the numbering of the tracer row decreased, the proportion of the tracer movement distance in the width direction to the overall tracer movement distance exhibited an increasing trend. The proportion of the tracer movement distance in the travel direction exhibited a decreasing trend but was > 50% in all cases (Figure 8).

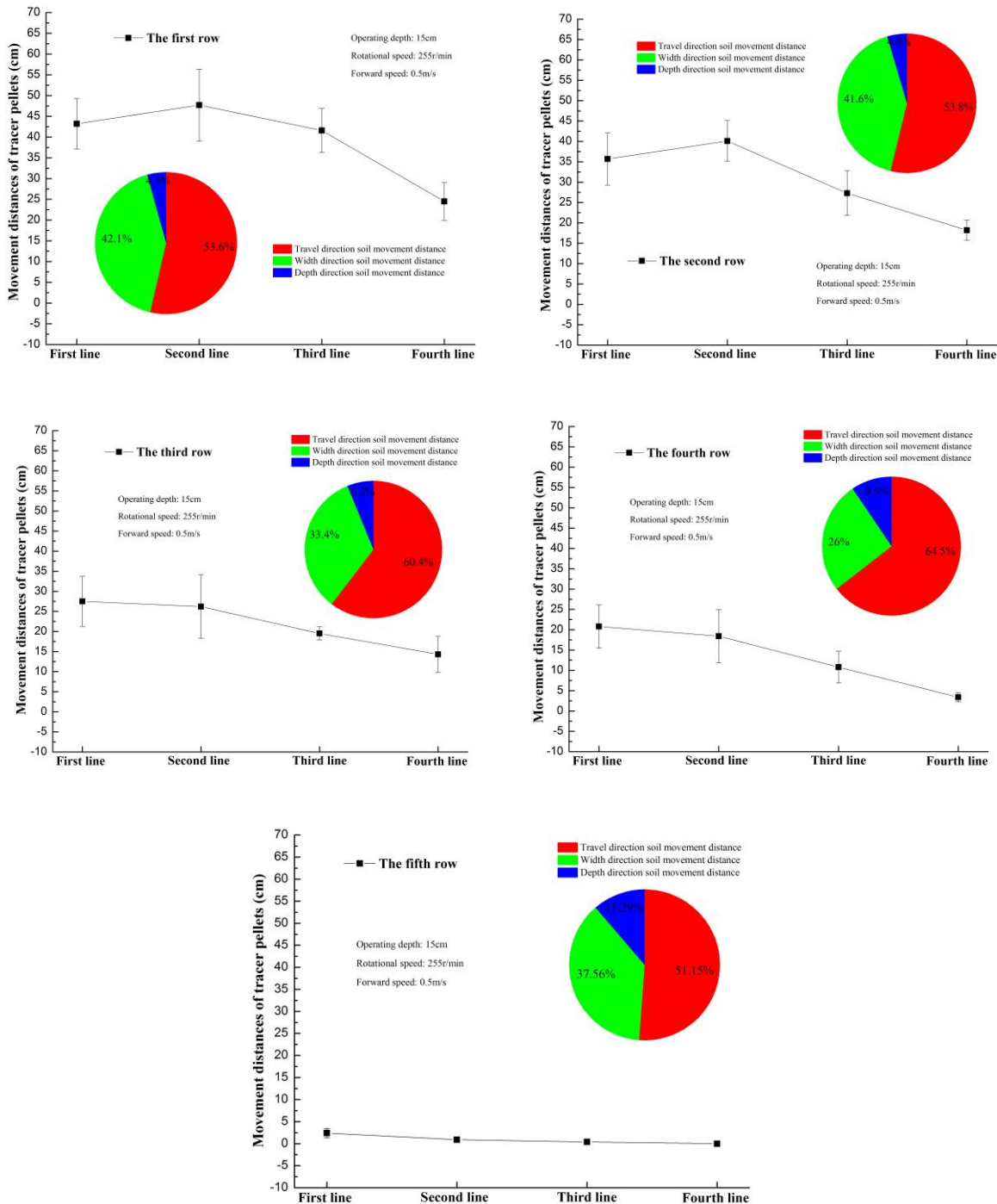


Fig. 8 - Soil movement at operating depth of 15 cm

This indicates that, at a blade operating depth of 15 cm, the soil movement distance was the largest in the surface soil layer and decreased as the soil layer depth increased. Additionally, except for the soil layer with a depth of approximately 20 cm, a shallower soil layer had a larger proportion of soil movement distance in the width direction, and a deeper soil layer had a larger proportion of soil movement distance in the travel direction.

At a blade operating depth of 10 cm, the movement distance of the tracer pellets in the second row of the first line was larger than that in the second row of the first line the difference was insignificant ( $p < 0.05$ ).

In all other cases, the tracer movement distance was the largest in the first row and decreased as the numbering of the tracer row increased (Figure 9). This indicates that, at a blade operating depth of 10 cm, the soil movement distance was the largest in the surface soil layer and decreased as the soil layer depth increased.

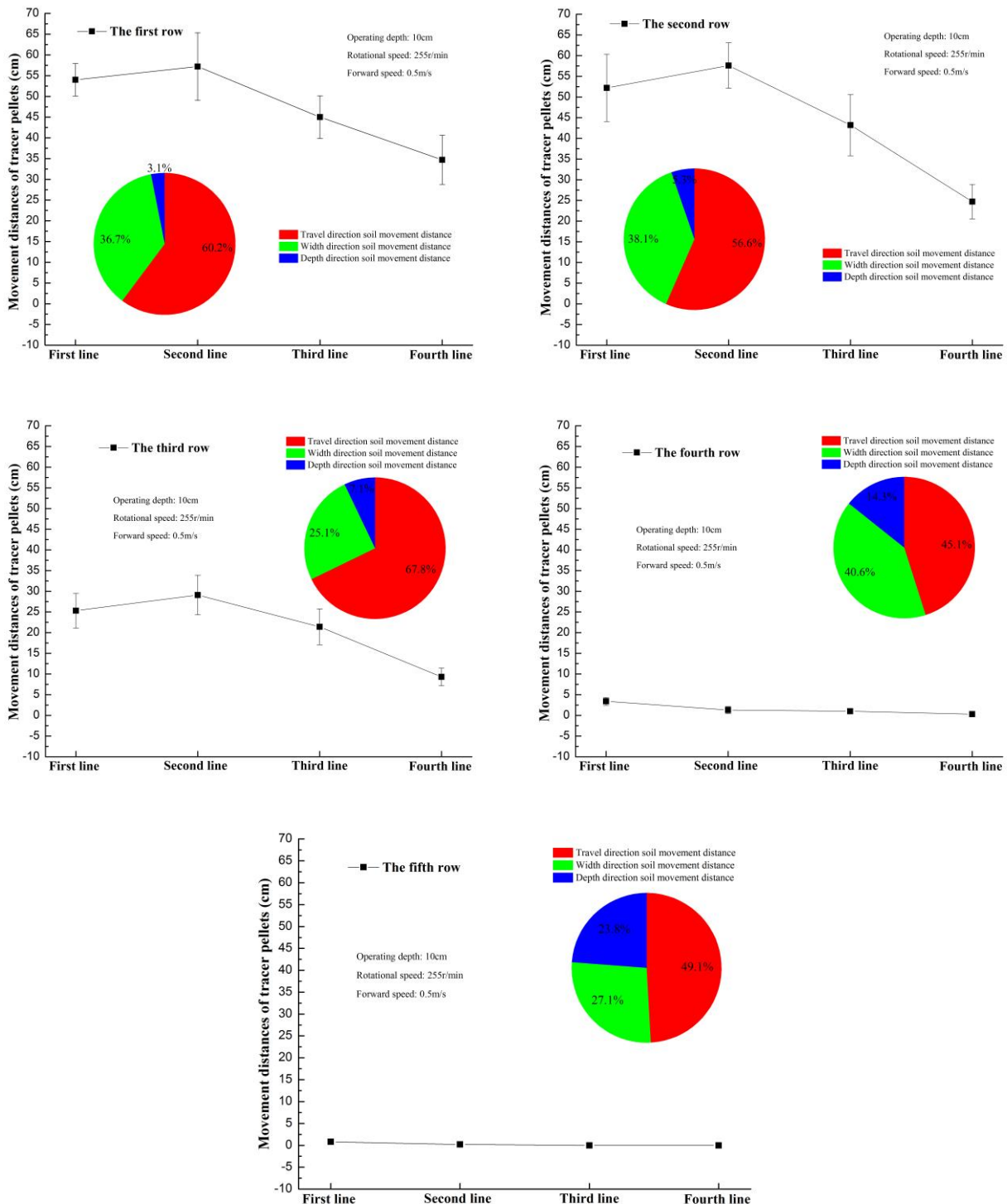


Fig. 9 - Soil movement distance at operating depth of 10 cm

At a blade operating depth of 5 cm, for all lines of tracer pellets, the tracer movement distance in the second row was the largest, followed by that in the first row; for all other rows, the tracer movement distance decreased as the numbering of the tracer row increased. In particular, the tracer pellets in the fifth row did not move (Figure 10). This indicates that, at a blade operating depth of 5 cm, the soil movement distance was the largest at a soil layer depth of approximately 5 cm, followed by that of the surface soil layer; and the soil layer with a depth of approximately 20 cm did not move.

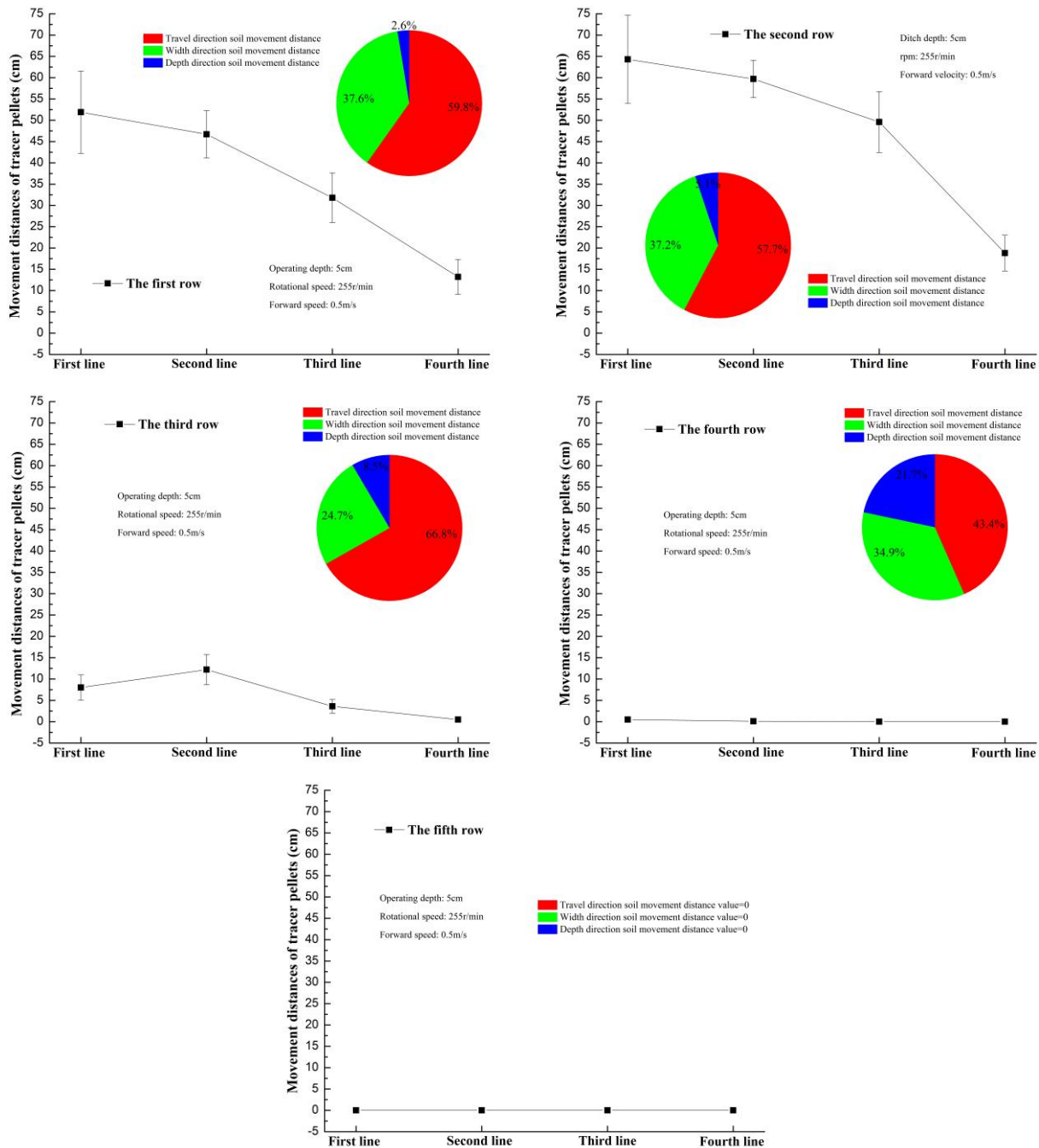


Fig. 10 - Soil movement at operating depth of 5 cm

The distance of the tracer movement by the tracer row was also analysed (Figure 7-10). The movement distance of the first row of the tracer pellet was the greatest at an operating depth of 10 cm and decreased as the operating depth increased or decreased from this level. This indicates that the soil movement distance was the greatest at an operating depth of 10 cm. At an operating depth of 5 cm, the movement distance of the first three lines in the second row of tracer pellets was the greatest, and it decreased as the operating depth increased. This indicates that the soil movement in the 5 cm depth soil layer was the greatest at an operating depth of 5 cm and decreased as the operating depth increased. At an operating depth of 20 cm, the movement distance of the third row of tracer pellets was smaller than that of the other rows, while at the other operating depths, the movement distance of the third row did not vary considerably. This indicates that the soil movement distance of the 10 cm depth soil layer did not vary considerably at operating depths of 5, 10, and 15 cm but smaller at an operating depth of 20 cm. The movement distance of the fourth and fifth rows of the tracer pellets increased as the operating depth increased. In particular, at an operating depth of 5 cm, the tracer pellets in the fifth row did not move. This indicates that the soil movement distance in the soil layers with depths of 15–20 cm was positively related to the operating depth. At an operating depth of 5 cm, the soil layers did not move.

Effect of forward speed and blade rotational speed on soil movement

Figure 11 shows the soil movement patterns at different forward speeds and blade rotational speeds. For a constant operating depth (15 cm) and blade rotational speed (255 rpm), the movement distance of the second line in the fifth row of the tracer pellets first decreased, and then increased as the forward speed increased. The movement distance of the fourth line in the fourth row peaked at a forward speed of 0.3 m/s and 0.5 m/s were equal to that at the forward speed of 0.7 m/s. The movement distance of all other rows and lines of the tracer pellets decreased as the forward speed increased (Figure 8). This indicates that soil movement distance generally increased as the forward speed decreased in the normal range. At a forward speed of 0.3 m/s, the movement distance of the second line in the second row of tracer pellets was greatest (57.9 cm).

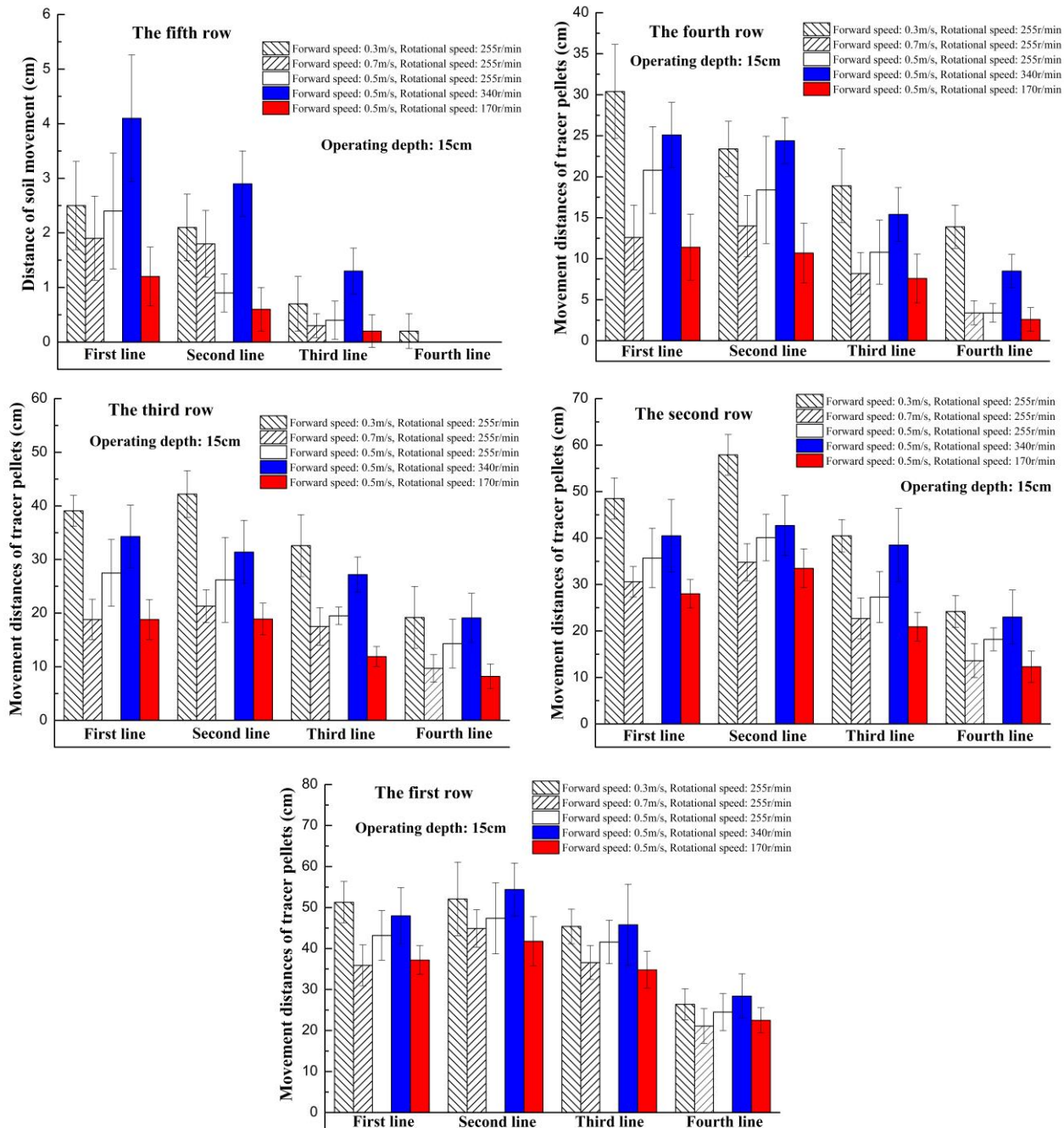


Fig. 11 - Soil movement pattern at different forward speeds and blade rotational speeds

At an operating depth of 15 cm and a forward speed of 0.5 m/s, the movement distance of the tracer pellets in all rows and lines increased as the blade rotational speed increased. This indicates that the soil movement distance increased as the blade rotational speed increased in the normal range. At a blade rotational speed of 340 rpm, the movement distance of the second line in the first row of tracer pellets was the greatest (54.4 cm).

*Overall soil movement pattern and its relationship with power consumption*

Table 2 summarises the tracer movement pattern at all positions and its relationship with power consumption. Under all the testing conditions, the tracer movement distance in the travel direction accounted for 55–64% of the overall tracer movement distance; along the width, it accounted for 30–37% and along the depth for 5–11%. This indicates that, under all the testing conditions, the soil movement distance in the travel direction accounted for more than half of the overall soil movement distance, followed by the width and depth directions.

For a constant operating depth (15 cm) and blade rotational speed (255 rpm), at a forward speed of 0.5 m/s, the proportions of tracer movement distance in the width and depth directions to the overall tracer movement peaked, whereas the proportion of the tracer movement distance in the travel direction minimised. At a forward speed of 0.3 m/s, the proportions of the tracer movement distance in the width and depth directions to the overall tracer movement were minimised, whereas the proportion of the tracer movement distance in the travel direction peaked. This indicates that the proportions of the soil movement distance in the width depth direction to the overall soil movement distance peaked at a forward speed of 0.5 m/s, whereas the proportion of the soil movement distance in the travel direction peaked at a forward speed of 0.3 m/s.

For a constant operating depth (15 cm) and forward speed (0.5 m/s), at a blade rotational speed of 255 rpm, the proportions of the tracer movement distances along the width and depth directions peaked, whereas the proportions of the tracer movement in the travel direction were minimised. At a blade rotational speed of 340 rpm, the proportions of the tracer movement distances in the width and depth directions were minimised, whereas the proportion of the tracer movement in the travel direction peaked. This indicates that the proportions of the soil movement distance in terms of width and depth to the overall soil movement distance peaked at a blade rotation speed of 255 rpm, whereas the proportion of the soil movement distance in the travel direction peaked at a blade rotation speed of 340 rpm.

**Table 2****Overall tracer movement pattern and power consumption**

Operating conditions	Overall soil movement distance [cm]	Proportions of soil movement distances in the travel, width, and depth direction to the overall soil movement [%]	Instantaneous torque [N · m]	Instantaneous power [kW]	Total power consumption [kW]
Operating depth: 5 cm, Rotational speed: 255 r/min, Forward speed: 0.5 m/s	360.9	33.60, 56.92, 9.48	8.7813	0.234	1.233
Operating depth: 10 cm, Rotational speed: 255 r/min, Forward speed: 0.5 m/s	460.7	33.63, 55.67, 10.70	15.0369	0.402	2.280
Operating depth: 15 cm, Rotational speed: 255 r/min, Forward speed: 0.5 m/s	422.6	36.13, 56.69, 7.18	26.3127	0.703	3.538
Operating depth: 20 cm, Rotational speed: 255 r/min, Forward speed: 0.5 m/s	415.4	33.48, 60.36, 6.16	47.3212	1.264	6.677
Forward speed: 0.3 m/s, Operating depth: 15 cm, Rotational speed: 255 r/min	571.5	33.50, 60.68, 5.82	22.8753	0.611	5.116
Forward speed: 0.7 m/s, Operating depth: 15 cm, Rotational speed: 255 r/min	349.7	31.04, 63.58, 5.38	38.4716	1.027	3.505
Rotational speed: 170 r/min, Operating depth: 15 cm, Forward speed: 0.5 m/s	323.1	35.82, 58.48, 5.70	33.9634	0.605	3.461
Rotational speed: 340 r/min, Operating depth: 15 cm, Forward speed: 0.5 m/s	515.0	30.88, 63.98, 5.14	28.8791	1.028	4.385

With the forward speed (0.5 m/s) and blade rotational speed (225 rpm) constant, the overall tracer movement distance peaked at 460.7 cm at an operating depth of 10 cm, followed by the movement distances at operating depths of 5, 15, and 20 cm. This indicates that soil movement distance peaked at an operating depth of approximately 10 cm. The instantaneous torque (instantaneous power) and total power consumption of the rotary blade increased with the operating depth. This finding is consistent with those obtained by Zhang et al. (2019) and Fujii et al. (2015). This indicates that the instantaneous torque and total power consumption were positively related to the operating depth; however, they were not related to the soil movement distance.

With the operating depth (15 cm) and blade rotational speed (225 rpm) constant, the overall tracer movement distance decreased as the forward speed increased (0.3, 0.5, and 0.7 m/s). The instantaneous torque exhibited an increasing trend with the forward speed, which agrees with the results obtained by Ahmadi (2017). This indicates that the instantaneous torque is positively related to the forward speed; however, it is negatively related to the soil movement distance. The total power consumption exhibited a decreasing trend with the forward speed, which is consistent with the results obtained by Salokhe et al. (2001). This indicates that the total power consumption was negatively related to the forward speed; however, it was positively related to the soil movement distance.

With the operating depth (15 cm) and forward speed (0.5 m/s) constant, the overall tracer movement distance increased with the blade rotational speed (170, 255, and 340 rpm). The instantaneous torque was the largest at a blade rotational speed of 170 rpm and was the smallest at a blade rotational speed of 255 rpm, which is consistent with the results obtained by Gupta and Pandey (1996) and Matin et al. (2015) that is, instantaneous torque first decreased then increased. This indicates that the instantaneous torque was not related to the blade rotational speed and soil movement distance. The total power consumption exhibited an increasing trend with the blade rotational speed, which was consistent with the results obtained by Tiwari and Gite (2006). This indicates that the total power consumption was positively related to the blade rotational speed and soil movement distance.

When other operating conditions were held constant, the total power consumption peaked at 6.677 kW at an operating depth of 20 cm and reached a minimum at 1.233 kW at an operating depth of 5 cm. With other operating conditions constant, the total power consumption peaked at 6.677 kW for a forward speed of 0.3 m/s and reached a minimum at 3.505 kW for a forward speed of 0.7 m/s. With other operating conditions constant, the total power consumption peaked at 4.385 kW at a blade rotational speed of 340 rpm and reached a minimum at 3.467 kW at a forward rotational speed of 170 rpm (Table 2).

Based on the investigations on soil movement, changes in the relationship between the operating conditions and power consumption of the rotary blade during furrowing were obtained. Although Jumin et al. (2014) and Thakur and Godwin (1989) performed similar studies, they only investigated the relationship between operating conditions and power consumption of the rotor blade. As the soil movement is essence that the operating conditions effect the furrowing power consumption. The study researched the correlation soil movement between furrowing power consumption further and could apply to analysing the furrowing power consumption of rotary blade based on soil movement.

## CONCLUSIONS

Rotary blades fixed to small handheld furrow openers for preparing small field patches involve soil throwing/movement and energy consumption. This study investigated the relationship between soil movement and power consumption and that between soil movement and operating conditions of such a blade. We draw the following conclusions:

- 1) The soil movement distance at or closer to the centre of action of the rotary blade was larger than that farther away.
- 2) Under all testing conditions, the proportion of the soil movement distance in the travel direction to the overall soil movement distance was the largest, with the value larger than 50%, followed by that in the depth direction and then that in the width direction.
- 3) The soil movement distance of the soil layers with depths of 0–5 cm was the largest at all operating depths. Moreover, soil movement distance decreased as the soil layer depth increased.
- 4) Generally, soil movement distance increased as the forward speed decreased in the normal range. The soil movement distance increased with the blade rotational speed in the normal range.
- 5) For constant forward and blade rotational speeds, the instantaneous torque and total power consumption were positively related to the operating depth, however, not related to the soil movement distance.

For constant operating depth and blade rotational speed, the instantaneous torque was positively related to the forward speed, however, negatively related to the soil movement distance; the total power consumption was negatively related to the forward speed, however, positively related to the soil movement distance. With the operating depth and forward speed constant, the instantaneous torque was not related to the blade rotational speed and soil movement distance; the total power consumption was positively related to blade rotational speed and soil movement distance.

Based on the results, it was concluded that by decreasing the operating depth and blade rotational speed and increasing forward speed, the power consumption of the unit working length can be reduced.

## ACKNOWLEDGEMENT

This research was supported by the Anhui Province Natural Science Foundation (No: 2008085QE270). The authors wish to thank Mr. Cai Lianhe for his support in adjusting the test platform.

## REFERENCES

- [1] Ahmadi I., (2017), A torque calculator for rotary tiller using the laws of classical mechanics. *Soil Tillage Res.* 165, 137-143.
- [2] Ahmadi I., (2017), A torque calculator for rotary tiller using the laws of classical mechanics, *Soil and Tillage Research*, vol. 165, ISSN: 0167-1987, pp. 137–143.
- [3] Ani O.A., Uzoejinwa B.B., Ezeama A.O., Onwualu P.A., Ugwu S.N., Ohagwu C.J., (2018), Overview of soil-machine interaction studies in soil bins. *Soil and Tillage Research*, vol. 175, ISSN: 0167-1987, pp. 13–27.
- [4] Asl J.H., Singh S., (2009), Optimization and evaluation of rotary tiller blades: Computer solution of mathematical relations, *Soil and Tillage Research*, vol. 106, no. 1, ISSN: 0167-1987, pp. 1–7.
- [5] Chertkiattipol S., Niyamapa T., (2010), Variations of torque and specific tilling energy for different rotary blades. *International Agricultural Engineering Journal*, vol. 19 no. 3, ISSN: 0858-2114, pp. 1–14.
- [6] Fajardo A.L., Suministrado D.C., Peralta E.K., Bato P.M., Paningbatan E.P., (2014), Force and puddling characteristics of the tilling wheel of float-assisted tillers at different lug angle and shaft speed, *Soil and Tillage Research*, vol 140, ISSN: 0167-1987, pp. 118–125.
- [7] Fujii T., Hasegawa H., Ohyama T., Sinegovskaya V.T., (2015), Evaluation of tillage efficiency and power requirements for a deep-placement fertilizer applicator with reverse rotational rotary, *Russian Agricultural Sciences*, vol. 41, no. 6, ISSN: 1068-3674, pp. 498 –503.
- [8] Grayling K.M., Young S.D., Roberts C.J., De Heer M.I., Shirley I.M., Sturrock C.J., Mooney S.J., (2018). The application of x-ray micro computed tomography imaging for tracing particle movement in soil. *Geoderma*, vol. 321, ISSN: 0016-7061, pp. 8-14.
- [9] Gupta J.P., Pandey K.P., (1996), Performance of rotary tiller tines under wetland condition. *Agricultural Mechanization in Asia, Africa and Latin America*, vol.27, no.1, pp.16–20.
- [10] Haas J., Fenner P.T., Schack-Kirchner H., Lang F., (2018.), Quantifying soil movement by forest vehicles with corpuscular metal tracers, *Soil and Tillage Research*, vol. 181, pp. 19–28.
- [11] Harrison H.P., (1978), Design of vertical rotary tiller blades for reforestation. *Transactions of the ASAE*, vol. 21, no. 6, ISSN: 0001-2351, pp. 1029–1033.
- [12] He C., You Y., Wang D., Wang G., Lu D., Kaji J.M.T., (2016), The effect of tine geometry during vertical movement on soil penetration resistance using finite element analysis, *Computers and Electronics in Agriculture*, 130, ISSN: 0168-1699, pp. 97–108.
- [13] Zhang J, He X., Xia J., Zhang S, Zhai J., Gui P., Zhang B., (2014), Design and field experiment of power consumption measurement system for high stubble returning and tillage machine, *Transactions of the Chinese Society of Agricultural Engineering*, vol. 30, no. 18, ISSN: 1002-6819, pp. 38–46.
- [14] Kataoka T., Shibusawa S., (2002), Soil-blade dynamics in reverse-rotational rotary tillage, *Journal of Terramechanics*, vol. 39, no. 2, ISSN: 0022-4898, pp. 95–113.
- [15] Lee K.S., Park S.H., Park W.Y., Lee C.S., (2003), Strip tillage characteristics of rotary tiller blades for use in a dryland direct rice seeder, *Soil and Tillage Research*, vol. 71, no. 1, pp. 25–32.
- [16] Li S., Chen X., Chen W., Zhu S., Li Y., Yang L., Xie S., Yang M., (2018), Soil-cutting simulation and parameter optimization of handheld tiller's rotary blade by smoothed particle hydrodynamics modelling and Taguchi method, *Journal of Cleaner Production*, vol. 179, ISSN: 0959-6526, pp. 55–62.

- [17] Matin M.A., Fielke J.M., Desbiolles J.M.A., (2015), Torque and energy characteristics for strip-tillage cultivation when cutting furrows using three designs of rotary blade. *Biosystems Engineering*, vol. 129, ISSN: 1537-5110, pp. 329–340.
- [18] Mollazade K., Ahmadi H., Alimardani R., (2009), Optimal design of rotary tiller's rotor and width proportionate to tractor power using energy method, *International Journal of Agricultural and Biological Engineering*, vol. 2, no. 2, ISSN: 1934-6344, pp. 1–7.
- [19] Qin K., Ding W., Ahmad F., Fang Z., (2018), Design and experimental validation of sliding knife notch-type disc opener for a no-till combine harvester cum seed drill, *International Journal of Agricultural and Biological Engineering*, vol. 11, no. 4, ISSN: 1934-6344, pp. 76–85.
- [20] Rahman S., Chen Y., Lobb D., (2005), Soil movement resulting from sweep type liquid manure injection tools, *Biosystems Engineering*, vol. 91, no. 3, ISSN: 1537-5110, pp. 379–392.
- [21] Salokhe V. M., Ramalingam N., (2001), Effects of direction of rotation of a rotary tiller on properties of Bangkok clay soil, *Soil and Tillage Research*, 63(1-2), ISSN: 0167-1987, pp. 65-74.
- [22] Salokhe V. M., Ramalingam N., (2002), Effect of rotation direction of a rotary tiller on draft and power requirements in a Bangkok clay soil, *Journal of Terramechanics*, vol. 39, no. 4, pp. 195–205.
- [23] Shibusawa S., (1993), Reverse-rotational rotary tiller for reduced power requirement in deep tillage, *Journal of Terramechanics*, vol. 30, no. 3, ISSN: 0022-4898, pp. 205–217.
- [24] Solhjoui A., Fielke J.M., Desbiolles J.M.A., (2012), Soil translocation by narrow openers with various rake angles, *Biosystems Engineering*, vol. 112 no. 1, ISSN: 1537-5110, pp. 65–73.
- [25] Thakur T.C., Godwin R.J., (1989), The present state of force prediction models for rotary powered tillage tools, *Journal of Terramechanics*, vol. 26, no. 2, ISSN: 0022-4898, pp. 121–138.
- [26] Tiwari P.S., Gite L.P., (2006), Evaluation of work-rest schedules during operation of a rotary power tiller. *International Journal of Industrial Ergonomics*, vol. 36, no. 3, ISSN: 0169-8141, pp. 203–210.
- [27] Ucgul M., Saunders C., Fielke J.M., (2017), Discrete element modelling of tillage forces and soil movement of a one-third scale mouldboard plough. *Biosystems Engineering*, vol. 155, pp. 44–54.
- [28] Ucgul M., Saunders C., Li P., Lee S.H., Desbiolles J.M.A., (2018), Analysing the mixing performance of a rotary spader using digital image processing and discrete element modelling (DEM), *Computers and Electronics in Agriculture*, vol. 151, ISSN: 0168-1699, pp. 1–10.
- [29] Viktor M., Munkholm L.J., Ying C., Tavs N., (2018), Modelling approach for soil displacement in tillage using discrete element method, *Soil and Tillage Research*, vol. 183, pp. 60–71.
- [30] Yang M.J., Niu P., Peng B., Yang L., Li Y.W., Chen X.B., Peng Z.M., (2015), Soil-cutting performance analysis of a handheld tiller's rotavator by finite element method (fem). *INMATEH – Agricultural Engineering*, vol. 47, no. 3, ISSN: 2068-4215, pp.13–20.
- [31] Zhang G.S., Zhang Z.Q., Xiao M.H., Bartos P., Bohata A., (2019), Soil-cutting simulation and parameter optimization of rotary blade's three-axis resistances by response surface method. *Computers and Electronics in Agriculture*, vol. 164, ISSN: 0168-1699, 104902.

# SIMULATION ANALYSIS ON THE PERFORMANCE OF SPLITTING AND PICKING DEVICES OF CORN HARVESTER

## 玉米收获机分禾与摘穗装置性能仿真分析

Tai Jianjian, Li Haitao <sup>\*)</sup>, Du Yuefeng, Mao Enrong, Guan Yunyi, Long Xinjian <sup>1</sup>

<sup>1)</sup>China Agricultural University, College of Engineering, Beijing/China

Tel: +86-18612925066; E-mail: h89533@cau.edu.cn

DOI: <https://doi.org/10.35633/inmateh-62-07>

**Keywords:** Corn harvester header; Splitting device; Vertical and horizontal picking roller; Simulation

### ABSTRACT

In the design of corn combine harvester, there is a high demand for customization and diversification in China. Aiming at the problems of backward design method, lack of design knowledge and long product development cycle, the discrete beam method is used to establish the corn plant model. The model of sub-device and the vertical and horizontal roller picking device is established by using UG, and the virtual prototype model is established by using ADAMS software. Meanwhile, the simulation experiments on the kinematics and dynamics performance of the separating device, the corn plant and the picking roller are carried out, and the simulation results are verified by field experiments. Through this method, the design parameters of the separating device and the picking roller are serialized, the method of evaluating the separating performance and the picking performance is provided, and the development and design cycle is shortened, which provides certain reference and theoretical basis for the development and design of the corn harvester header.

### 摘要

我国玉米联合收获机在设计过程中, 存在定制化、多样化需求高的特点, 针对其设计方法理论落后、设计知识匮乏, 产品开发周期长等问题, 采用离散梁法建立了玉米植株模型, 利用 UG 建立了分装置器和纵卧辊式摘穗装置模型, 运用 ADAMS 软件建立了其虚拟样机模型, 进行了分禾装置与玉米植株以及摘穗辊运动学和动力学性能仿真试验, 并通过田间试验验证了仿真结果的正确性。通过该方法实现了分禾装置和摘穗辊参数设计的系列化, 提供了评价分禾性能和摘穗性能的方法, 缩短了开发和设计周期, 为玉米收获机割台的研发和设计提供了一定的参考和理论依据。

### INTRODUCTION

Corn harvest is the most onerous link in corn production. The efficiency of artificial harvest is low and the labour volume is large, which requires a large number of labours (Aguayo et al, 2017). The input of corn harvest labour volume accounts for 55% of the whole corn production link (Zhang Xiru et al, 2019). At the same time, corn harvest has the characteristics of short time, heavy task and agricultural time. Mechanized harvesting of corn has the advantages of improving corn production efficiency, reducing operation time, reducing corn production cost and realizing production and farmers' income increasing (Cui Tao et al, 2019; Cook D. E. et al, 2014; Klopensein et al, 2013). China's mechanized corn harvest started late, due to the diversity of corn planting mode, the development speed of corn mechanization has been slow for quite a long time (Du Yuefeng et al, 2014). In 2017, China's mechanized corn harvest area reached 368 million mu, and the mechanized harvest level reached 69%, but it still lags behind the mechanized harvest level of wheat and rice (Chen Zhi et al, 2014). The low harvest level of corn mechanization is the main factor restricting the overall development level of corn mechanization in China (Geng Aijun et al, 2016; Geng Duanyang et al, 2017).

In the process of mechanical product research and development, generally through prototype design, trial production, test and improvement, the development process has a long cycle and high cost, and many parameters are determined by the experience of the designer, which has a serious impact on the quality of the product (Liu Hongxin et al, 2019; Alarcon R. Hunter et al, 2010).

As a new technology in the field of design and manufacturing, virtual prototype technology can be used

<sup>1</sup>Tai Jianjian, Ph.D. Eng.; Li Haitao, Prof. Ph.D. Eng.; Mao Enrong, Ph.D. Eng.; Guan Yunyi, Long Xinjian

to develop agricultural machinery products, which can significantly improve the above situation (Ming Zhe, 2014; Herman C. et al, 2011). In view of this, the three-dimensional model of the separating device and the vertical and horizontal roller picking device is constructed by three-dimensional software, and the motion simulation analysis is carried out by using ADAMS in order to provide theoretical basis and technical reference for further design of corn harvester.

## MATERIALS AND METHODS

### MODELING OF CORN PLANTS

When the header of corn harvester works, it is in direct contact with the corn plant, and there is mutual force between them (Zhang Xirui et al, 2019). Therefore, for the dynamic simulation of the main working parts of the corn harvester header, it is necessary to correctly model the corn plant and build an accurate virtual model of it, which plays a very important role in the process of simulation (Gupta S. et al, 2017; Ranum P. et al, 2014). Therefore, through the discrete beam method in ADAMS, the corn plant model is established; the corresponding binding force is defined, and finally the design and performance parameters of corn harvester are obtained.

In ADAMS, the method of discrete flexible connector is used to build the flexible body of corn plant. Firstly, two marker points are defined as the beginning and end of corn plant. The coordinates are Marker 1 (0,0,0) and Marker 2 (0,2200,0) respectively. Select [Build]→[Flexible Bodies]→[Discrete Flexible Link], and then the discrete flexible parts dialog box pops up, in which the parameters of corn plants can be set. After consulting the data, the Poisson ratio of straw is 0.33; the modulus is  $1.1 \times 10^{10}$  Pa; The density is  $450 \text{ kg/m}^3$ , and there are generally 10-20 knots on the corn plant. Taking Xianyu 508 corn plant as an example, according to the measured physical parameters of corn plant (Du Yuefeng et al, 2012), the height of corn plant is 2200 mm, the diameter of bottom end is 24mm and the diameter of ear point is 20 mm. During the simulation, 18 nodes are selected, and the diameter is gradually transiting, with the average height of 1050 mm. The established corn plant model is shown in Figure 1.

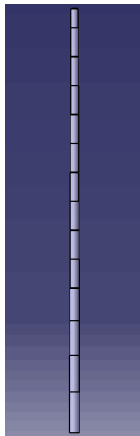


Fig. 1 - Discrete flexible connector model of corn plant

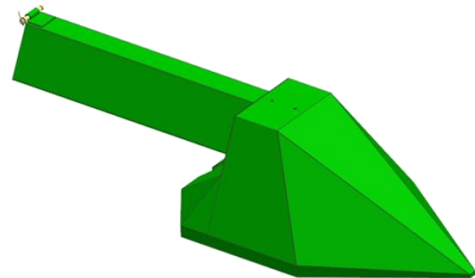


Fig. 2 - Three-dimensional model of the divider

### SIMULATION ANALYSIS OF THE SPLITTING DEVICE

When the header of the corn harvester is working, the main function of the splitting device is to feed the corn plants into the clamping and conveying mechanism, so that the corn plants cannot be harvested (Cui Tao et al, 2019). Therefore, whether the design of the separating device is reasonable directly affects the working performance of the header of the corn harvester. The specific creation method is as follows:

- (1) After consulting the relevant design methods and experience, the model of the splitting device is established in UG software, as shown in Figure 2. The model is imported into ADAMS in Para Solid format;
- (2) Add a moving pair for the divider device;
- (3) It is the initial forward speed of the harvester, and the initial speed in X direction is set as 2m/s;
- (4) Add Solid To Solid collision type for the separating device and corn plants;
- (5) Set the positive direction of X-axis as the forward direction of the harvester, the positive direction of Y-axis as the vertical downward direction of the ground, and the negative direction of Z-axis as the horizontal bending direction of corn straw when the separating device is working. The simulation plant starts to simulate

at the extreme position of the cutting edge of the splitting device, and the simulation process is shown in Figure 3. Figure 3.a shows the initial position of the corn plant and the splitting device, that is, the simulation starts at the extreme position of the cutting edge of the splitting device. Figure 3.b and 3.c show the position changes of corn plants and splitting devices in the progress of the harvester. Figure 3.d shows the moment when the splitting device is about to leave the corn plant, and the simulation is about to end. In the next process, the corn plant enters the picking device for picking.

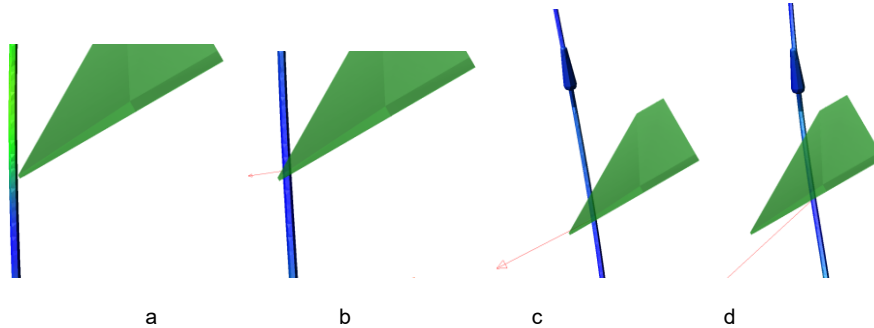


Fig. 3 -The motion simulation process of splitting device

**RESULTS**

**Action kinematical simulation of corn plant and its separating device**

According to the actual situation, set the divider 500mm away from the ground, the simulation times is 0.2s and select 1050mm on the corn stalk as the average ear height. When the moving speed of the splitting device is 2m/s, the displacement simulation curve of corn plant ear point along the X-axis, Y-axis, Z-axis and synthesis direction under the action of the splitting device is shown in Figure 4.

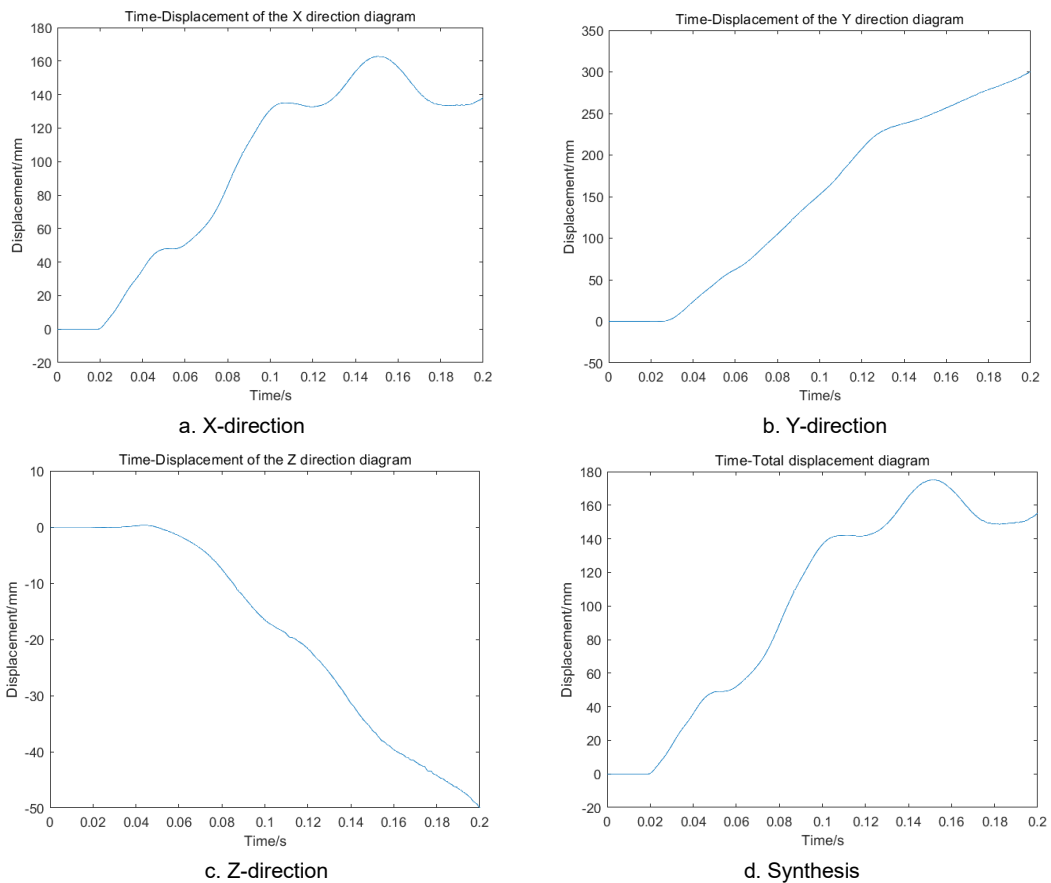


Fig. 4 - Time-varying curve of displacement in different directions of corn plant ear point

It can be seen from Figure 4.a that in the simulation process, in the X direction, i.e. in the direction of the harvester forward, the displacement at the ear point gradually increases, and the maximum displacement change is about 163mm, i.e. the bending amount at the ear point of the corn plant is 163mm. When the simulation reaches 0.15s, the displacement in X direction decreases suddenly.

This indicates that the corn plant is subject to large vibration and friction in the simulation process. It does not continue to move along the direction of the harvester, but in the opposite direction.

It can be seen from Figure 4.b that in the simulation process, the height from the ear point to the ground increases gradually in the direction of Y-axis, indicating that the height from the ear point to the ground decreases by 300 mm. When the simulation reaches 0.13s, the displacement suddenly increases, which shows that the corn straw is slightly vibrated in the simulation. It can be seen that there are some defects in the cone angle and shape design of the splitting device, which causes the corn plant to be pushed down when it is vibrated and affects the working performance of the splitting device.

Figure 4.c shows that in the simulation process, the displacement of the ear point of the corn plant increases gradually in the reverse direction of Z. Under the contact extrusion of the splitting device, there is a transverse bending in the negative direction of Z-axis, and the maximum displacement is 50 mm. Under the action of the splitting device, the corn device gradually moves inward without touching.

As shown in Figure 4.d, the maximum composite displacement is 178mm. The maximum bending angle between corn plant and the direction perpendicular to the ground is  $10.4^\circ$  in XY plane, and  $25.4^\circ$  in YZ plane. It can be concluded that the maximum angle between corn plant and vertical direction is  $26.4^\circ$ .

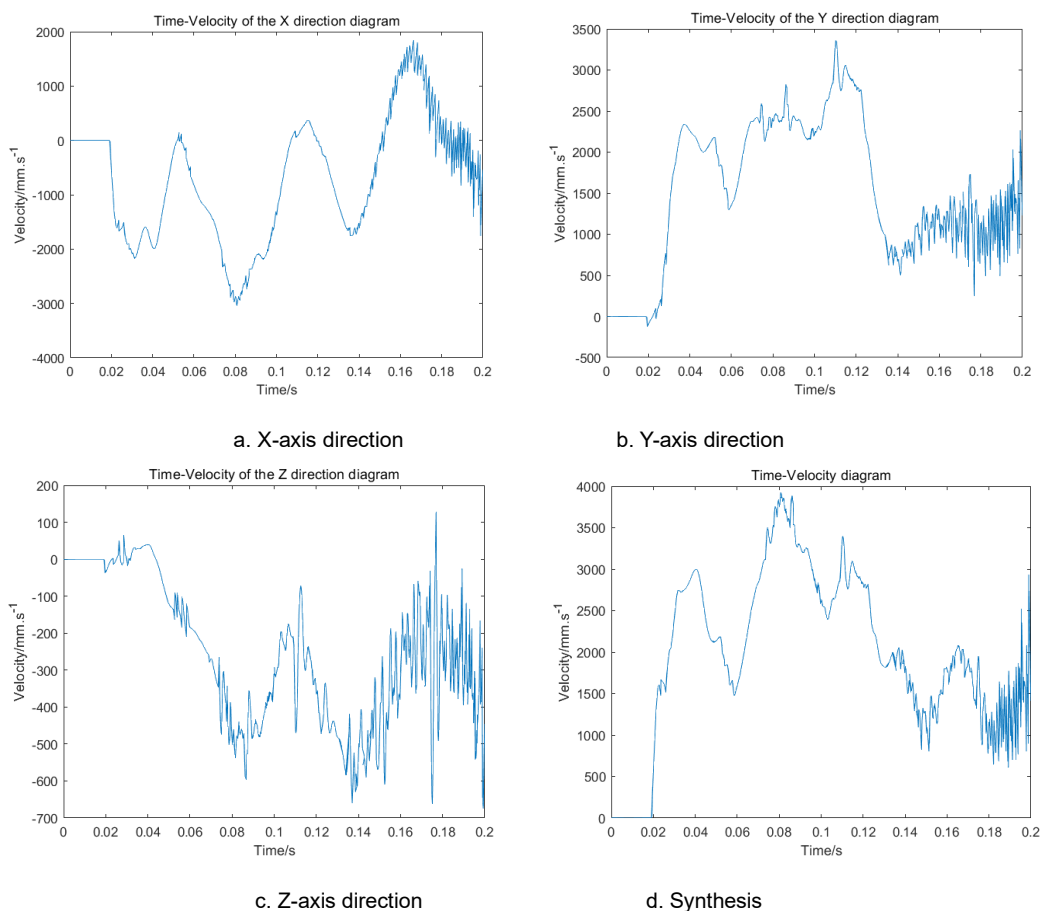


**Fig. 5 -Time-varying curve of speed in different directions of corn straw ear point**

The simulation curve of ear point speed of corn plant under the action of the splitting device is shown in Figure 5. In the whole simulation process, the forward direction of X-axis at the ear point is 2 m/s and the reverse direction is 3.03 m/s. The results show that there is a great friction and vibration in the plant of the splitting device when the header move forward, which causes the corn plant to swing back and forth. The ear point moves along the positive direction of Y-axis, the maximum speed appears at 0.11s with 3.41 m/s in the whole simulation process; the average velocity on the vertical Y-axis is 1.42 m/s. Before 0.02s, the movement speed of ear point on the z-axis is relatively stable, and the speed increases gradually. The speed decreases gradually between 0.14-0.18s. In the whole simulation process, the average speed on Z-axis is 0.283 m/s, and the direction is negative along Z-axis. In the whole process of dynamic simulation, it can be concluded from the speed synthesis curve that from 0.02s to 0.2s, the speed reaches the maximum at 0.08 s, and then decreases gradually.

### Dynamic simulation of the effect of corn plant and the splitting device

The main force of the splitting device is friction. When the speed of the device is 2m/s, the force simulation curve is shown in Figure 6.

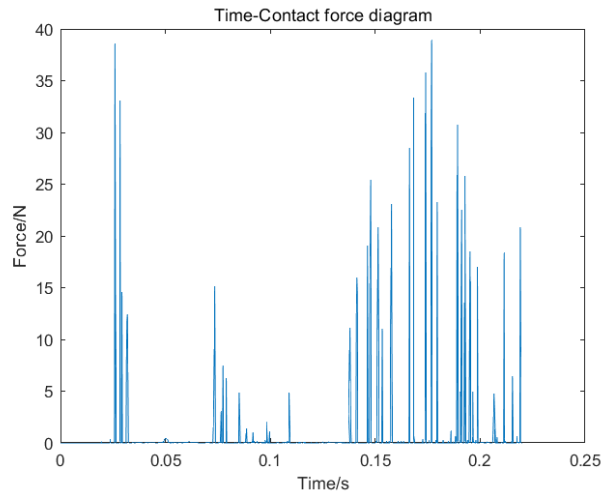


**Fig. 6 - Contact force curve of corn plant and divider**

Figure 6 shows the contact force curve between the corn plant and the splitting device. It can be concluded from the figure that at the beginning of the simulation, the contact force is large, reaching about 38N. When the simulation is at 0.25s, there are two big mutations in the contact force, indicating that the transition between the tip and the middle of the splitting device is not smooth, which hinders the movement of the corn plant. It is easy to break the plant at this time.

## ANALYSIS AND SIMULATION OF THE PICKING DEVICE

### Modeling of the picking device

The two rollers of the vertical and horizontal picking device are driven by gears, which are simplified when modeling, then imported into ADAMS software, and added some corresponding constraints, and then the dynamic simulation analysis can be carried out. When installing the stripping roller, the first is to ensure the accurate engagement position of the two gears, and the second is to consider that the retention time of the ear on the stripping roller is as short as possible, so as to reduce the loss of the ear (*Igathinathaneet et al, 2010*). Therefore, when installing, two picking rollers are not at the same height, and the inner picking roller is lower than the outer one. According to the design formula and experience, the model of the picking roller built in the 3D drawing software is shown in Figure 7.



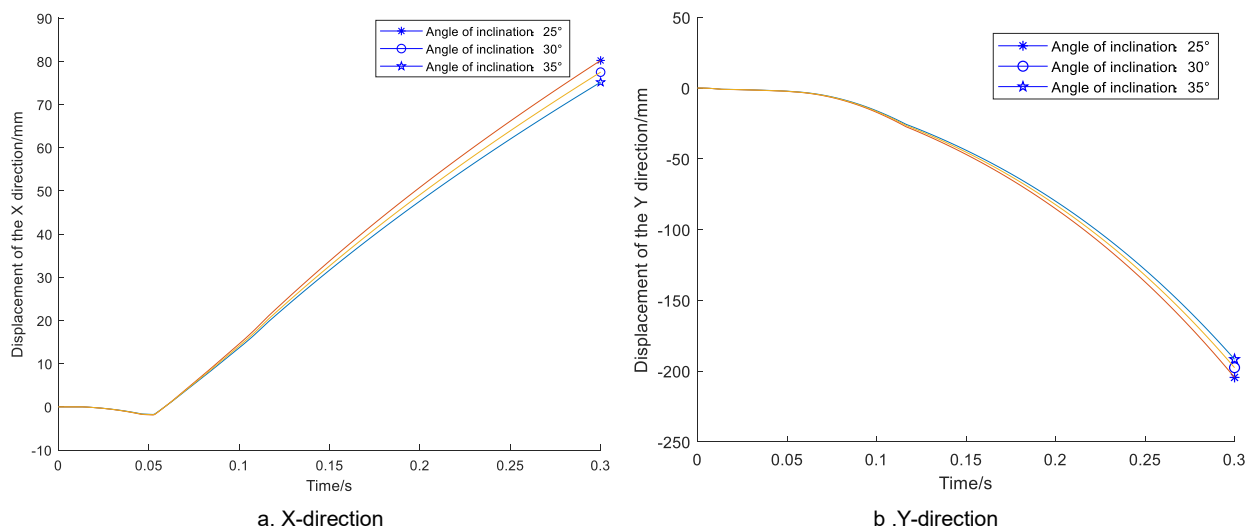
**Fig. 7 - Vertical and horizontal roller model of the picking roller**

### The effect of the angle of picking roller on corn harvest

The horizontal picking device is mainly composed of a pair of relatively rotating picking rollers. The axis of picking roller is generally  $25^\circ$  -  $35^\circ$  to the horizontal, and the plants are fed along the axis of the picking roller. This paper mainly simulated the effect of the picking roller on the corn harvest performance when the axis and the horizontal plane of the picking roller are  $25^\circ$ ,  $30^\circ$  and  $35^\circ$  respectively.

According to the actual situation, the average height of corn plant is 1050mm, the machine forward direction is X-axis, and the speed is 2 m/s. the positive direction of Y-axis is vertical and upward and Z-axis is transverse. Because the corn plant is clamped in the middle of the picking roller in the harvest, the displacement, speed and contact force of the ear point on the Z-axis are ignored. The speed of the picking roller is set to 1050r/min and the simulation time to 0.3s in order to simulate the working process of the picking roller.

Fig. 8 shows the time-varying curve of X and Y direction displacement at the ear point of corn plant under the action of picking roller when the angle between the picking roller and horizontal plane is  $25^\circ$ ,  $30^\circ$  and  $35^\circ$  respectively.



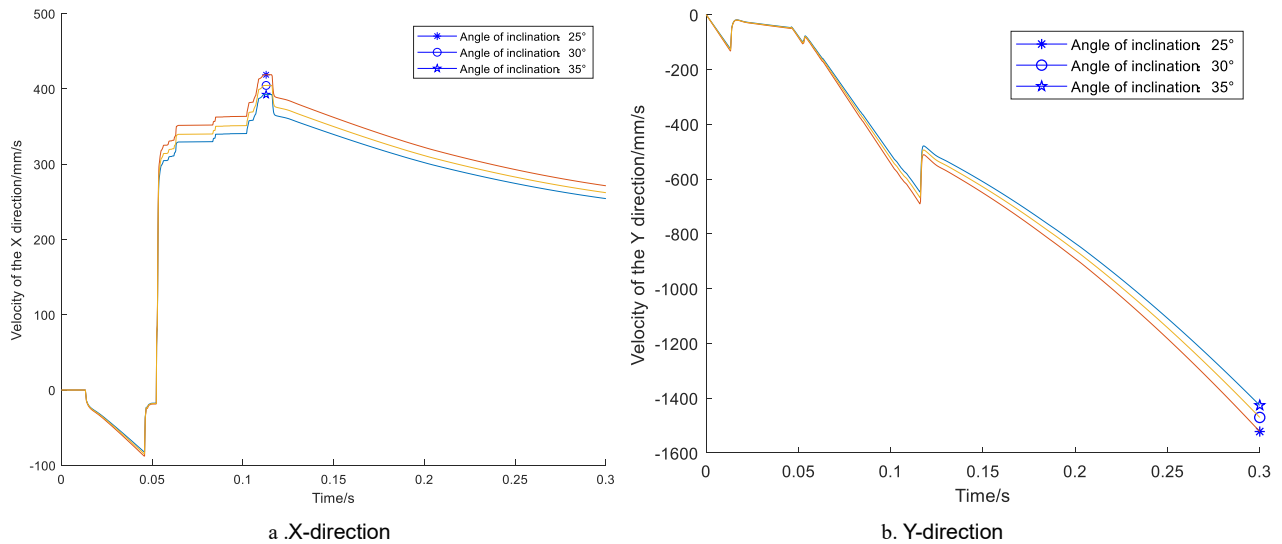
**Fig. 8 - Time-varying curve of displacement in different directions of ear point under different inclinations of the picking roller**

Fig. 8.a shows that the displacement of the corn plant heading point in the opposite direction of the machine is gradually increased over time, and with the increase of the inclination, the displacement is gradually reduced. It can be seen from Fig. 8.b that the displacement of the ear point of corn plant in the vertical downward direction increases gradually over time and the displacement decreases gradually with the increase of the inclination angle. Fig. 9 shows the time-varying curve of the speed in X and Y directions at the ear point of corn plant under the action of the picking roller when the angle between the picking roller and the horizontal plane is  $25^\circ$ ,  $30^\circ$  and  $35^\circ$  respectively.

It can be seen from Figure 9.a that at the moment of contact and rotation with the picking roller and under the rotation of the picking roller, the corn plant tends to move towards the rear of the machine. Then, under the action of the forward speed of the machine, the corn plant gradually moves to the positive X-axis direction. With the increase of the inclination angle, the speed of the point where the ear is formed decreases gradually, and the fluctuation of the speed change decreases gradually in the process of picking.

It can be seen from Fig. 9.b that with the advance of the harvester, the vertical downward speed of the ear point increases gradually; with the increase of the inclination angle, the speed decreases gradually, and the fluctuation of speed change decreases gradually in the process of picking.

Compared with the simulation results, it can be seen that when the angle between the stripping roller device and the horizontal ground is  $30^\circ$ , its performance is more stable. Therefore, it is better for the new type of corn harvester to choose the picking roller with an angle of  $30^\circ$  to the horizontal ground.

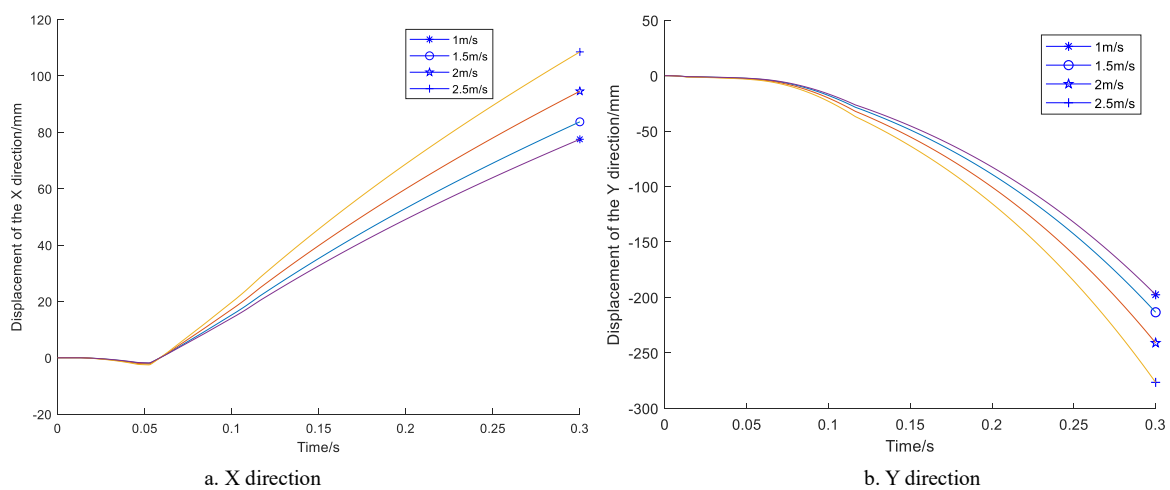


**Fig. 9 - Time-varying curve of speed in different directions of ear point under different rake angles of the picking roller**

**The effect of the forward speed of the harvester on the corn harvest**

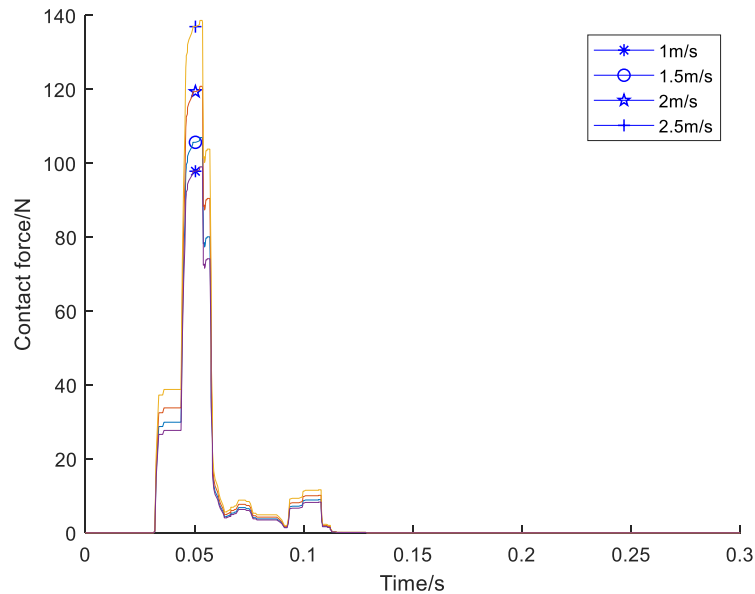
According to the actual situation, the average ear setting height is 1050 mm on the corn plant, and the forward direction of X-axis is the forward direction of the harvester; the positive direction of Y-axis is the vertical upward direction, and the Z-axis is the horizontal direction. The displacement, velocity and contact force of ear setting point on the Z-axis are ignored because the corn plant is clamped in the middle of the picking roller in the process of harvest. The rotation speed of the picking roller is 1050r/min, the inclination angle between the picking roller and the horizontal ground is 30°, and the simulation time is 0.3s. In this paper, the forward speed of harvester is selected as 1 m/s, 1.5 m/s, 2 m/s and 2.5 m/s to simulate the working process of the picking device.

Figure 10 shows the displacement curves of X and Y directions at the ear point of corn plant under the action of different forward speeds. It can be seen from Figure 10a at different forward speeds, with the advance of the harvester, the displacement of the heading point in the forward direction of the harvester increases uniformly, and the displacement at the same time also increases with the increase of the speed. From Figure 10.b, it can be seen that at different forward speeds, with the advance of the harvester, the displacement of the heading point in the forward direction of the harvester increases uniformly, and the displacement in the same time also increases with the increase of the speed.



**Fig. 10 - Time-varying curve of displacement in different directions of heading point under different forward speed conditions**

Fig.11 shows the varying curve of contact force with time between the ear point of corn plant and the picking roller under different forward speeds. It can be seen from Fig.11 that with the increase of forward speed, the numerical fluctuation of contact force between the ear point and the picking roller also increases. This is because when the machine speed increases, its inertia in the forward direction is large, and the force on the straw increases.



**Fig. 11 - Time-varying curve of the contact force between the ear point and the picking roller under different forward speed**

## FIELD TRIAL

### Test equipment and conditions

To verify the above simulation results, a field trial was conducted in Lingcheng District, Dezhou, Shandong Province, China in October 2019. In the test plot, the growth of corn plants was relatively uniform, and there was no lodging phenomenon and obvious drooping of ears. Zhengdan 958 was the corn in the experimental field. The moisture content of corn kernel and plant was 29.21% -33.64% and 76.63%-79.85% respectively. The planting row spacing was 580 mm, and the distance between adjacent horizontal roller picking mechanisms was 600 mm for harvest. The experimental equipment was a three row self-propelled horizontal roller ear harvester produced by China Wuzheng group. The test site is shown in Fig. 12.



**Fig. 12 - Field test site**

### Test scheme and result analysis

Taking the damage rate and loss rate of the harvester as the evaluation index, the speed of picking roller is set at 800 r/min, and the harvesting quality is evaluated with different forward speed of the harvester and the inclination angle between the picking roller and ground. Through experiments and calculation statistics, the results are shown in Table 1.

Table 1

Effect of ear picking in field experiment

Forward speed of harvester [m/s]	Dip angle between the picking roller and ground [°]	Harvest damage rate [%]	Harvest loss rate [%]
1	25	0.31	0.04
	30	0.27	0.03
	35	0.32	0.05
1.5	25	0.43	0.05
	30	0.32	0.04
	35	0.44	0.07
2	25	0.56	0.07
	30	0.43	0.06
	35	0.58	0.07
2.5	25	0.59	0.08
	30	0.51	0.08
	35	0.62	0.09

According to Table 1, the damage rate of harvest varies between 0.31-0.61, and the harvest loss rate varies between 0.03%-0.09%. The results show that the loss rate and damage rate increase with the increase of the forward speed of harvester; with the decrease of the angle between the picking roller and ground, the damage rate and loss rate of picking both decrease and then increase. When the angle between the picking roller and ground is 30°, the harvest damage and loss are the least and the harvest effect is the best. The correctness of the simulation theory is verified by field experiments.

### CONCLUSIONS

1. Based on the mechanical characteristics of corn plant, the flexible body model of corn stalk is established by using the method of discrete flexible connector, and the key connection parameters and contact parameters of simulation are determined;

2. Through the establishment of the model of the splitting device, the kinematics and dynamics simulation of the corn stalk and the splitting device are carried out respectively. A method of evaluating the splitting performance is obtained, which takes the displacement of the corn stalk in different directions, the speed of the ending point and the contact force between the splitting device and the plant in the splitting process as the index;

3. Through the establishment of the model of the vertical and horizontal roller picking device, taking the displacement, speed and acceleration of the ear point in different directions as the evaluation indexes, the effects of the different angle of the ear plucking roller and the different forward speed of the harvester on the picking performance are mainly studied;

4. Through the three-dimensional model of the main parts of the corn harvester header, and the dynamic and kinematic simulation analysis, a series of motion parameters of the harvester header can be obtained, which can shorten the development cycle of the harvester, reduce the development cost, and provide reference and theoretical basis for its further optimization design.

### ACKNOWLEDGEMENT

The work is supported by the National key R & D plan (2017YFD0700101).

### REFERENCES

- [1] Aguayo M., Sarin M., Subhash C. et al, (2017), A corn-stover harvest scheduling problem arising in cellulosic ethanol production. *Biomass and Bioenergy*, Vol.107, pp. 102-112, England / Britain.

- [2] Chen Zhi, (2014), Key technology and equipment of corn full value harvest. *China Social Sciences Press*, 2014. Beijing / China.
- [3] Chen J.Y., Zhou Q., Xu G., Wang R.T., Tai E.G., Xie L., Huang X., (2019), Non-invasive blood glucose measurement of 95% certainty by pressure regulated Mid-IR. *Talanta*. England / Britain doi:10.1016/j.talanta.2019.01.034.
- [4] Cheng Xianfu, Cong Yanyan, (2016), Rapid Design Method for Gantry Crane Based on Knowledge Reuse. *Machine Design & Research*, Issue 4, pp.145-148, Wuhan / China.
- [5] Cook D.E, Shinnars K.J., Weimer P.J. et al, (2014), High dry matter whole-plant corn as a biomass feedstock. *Biomass and Bioenergy*, Vol.64, pp.130-136, England / Britain.
- [6] Cui Tao, Fan Chenlong, Zhang Dongxing et al, (2019), Research Progress of Corn Mechanized Harvesting Technology. *Transactions of the Chinese Society for Agricultural Machinery*, Vol.50, Issue 12, pp.1-13, Beijing / China.
- [7] Du Yuefeng, (2014), Design method and experimental research of self-propelled corn harvester in Hilly Area. *China Agricultural University*, Beijing / China.
- [8] Du Yuefeng, Zhu Zhongxiang, Song Zhenghe et al, (2012), Simulation of Divider and Snapping Roll for Small-scale Corn Harvester. *Transactions of the Chinese Society for Agricultural Machinery*, Vol.43, Issue Z1, pp.100-105, Beijing / China.
- [9] Geng Aijun, Yang Jianning, Zhang Ji. et al, (2016), Analysis of Influencing Factors of Corn Ear Harvesting Machinery Damage. *Transactions of the Chinese Society of Agricultural Engineering*, Vol.32, Issue22, pp.56-62, Taian / China.
- [10] Geng Duanyang, Li Yuhuan, He Ke et al, (2017), Design and experiment of the gap clamping and conveying device for the header of vertical roller corn harvester, *Journal of Agricultural Machinery*, Vol.48, Issue 11, pp.130-136, Zibo / China.
- [11] Gupta S., Garsa V., Kumar P., Malik V., (2017), Measurement of Anthropometric parameters of Ilium of 100 human hip bones in North Indian region. *Journal of the Anatomical Society of India*, 66, S115. doi:10.1016/j.jasi.2017.08.367.
- [12] Herman C, Prochnow A, Heiermann M., (2011), Influence of chopping length on capacities, labour time requirement and costs in the harvest and ensiling chain of corn. *Biosystems Engineering*, Vol.110, Issue 3, pp.310-320, England / Britain.
- [13] Hunter Alarcon R., Chueco J. Rios, Perez Garcia J.M. et al, Fixture knowledge model development and implementation based on a functional design approach. *Robotics and Computer-Integrated Manufacturing*, Vol.26, Issue1, pp.56-66, England / Britain.
- [14] Igathinathane C., Womac A.R., Sokhansanj S., (2010), Corn stalk orientation effect on mechanical cutting. *Biosystems Engineering*, Vol.107, Issue 2, pp.97-106, England / Britain.
- [15] Liu Hongxin T.J., Erickson G.E., Berger L.L. et al, (2013), Corn is a critically important source of food, feed, energy and forage in the USA. *Field Crops Research*, Vol.153, pp.5-11, Netherlands.
- [16] Liu Hongxin, Zhou Xingyu, Jia Ru et al, (2019), Design and Reuse Technology of Mechanical Soybean Seed-metering Device Based on CBR. *Transactions of The Chinese Society of Agricultural Machinery*, Vol.50, Issue7, pp.39-50, Harbin / China.
- [17] Ming Zhe, (2014), Simulation analysis of main components of corn harvester based on ADAMS. *Journal of Agricultural Mechanization Research*, Vol.36, Issue10, pp.33-37, Jilin / China.
- [18] Ranum P., Pena-Rosas J.P., Garica-Casal M.N, (2014), Global corn production, utilization and consumption. *Ann NY AcadSci*, Vol.13 (12), pp: 105-112, New York / United States.
- [19] Wang Jianting, Li Yaoming, Ma Zheng et al, (2019), Structural characteristics and development trends of key devices of corn harvesting machinery. *Agricultural Mechanization Research*, Vol.41, Issue 09, pp.1-8, Zhenjiang / China.
- [20] Zhang Xirui, Wu Peng, Wang Kehenget et al, (2019), Design and experiment of 4YZT-2 type self-propelled fresh corn double ridges harvester. *Transactions of the Chinese Society of Agricultural Engineering (Transactions of the CSAE)*, Vol.35, Issue13, pp.1-9, Qingdao / China.

## MOVEMENT OF THE PARTICLE ON THE INTERNAL SURFACE OF THE SPHERICAL SEGMENT ROTATING ABOUT A VERTICAL AXIS

### РУХ ЧАСТИНКИ ПО ВНУТРІШНІЙ ПОВЕРХНІ СФЕРИЧНОГО СЕГМЕНТА, ЯКИЙ ОБЕРТАЄТЬСЯ НАВКОЛО ВЕРТИКАЛЬНОЇ ОСІ

Sergiy Pylypaka <sup>1)</sup>, Victor Nesvidomin <sup>1)</sup>, Tatiana Volina <sup>\*2)</sup>, Larysa Sirykh <sup>3)</sup>, Liudmyla Ivashyna <sup>3)</sup> <sup>1</sup>

<sup>1)</sup> National University of Life and Environmental sciences of Ukraine, Faculty of Design and Engineering, Kiev / Ukraine;

<sup>2)</sup> Sumy National Agrarian University, Faculty of Engineering and Technology, Sumy / Ukraine;

<sup>3)</sup> Sumy Regional Institute of Postgraduate Pedagogical Education, Faculty of Advanced Training and Retraining, Sumy / Ukraine

Tel: 0997233321; E-mail: t.n.zaharova@ukr.net

DOI: <https://doi.org/10.35633/inmateh-62-08>

**Keywords:** angular velocity, relative motion, particle movement, differential equations, kinematic parameters.

#### ABSTRACT

The particle relative motion on a spherical segment rotating about a vertical axis was considered in the article. The differential equations of the relative displacement of a particle were completed and solved by numerical methods. The relative and absolute trajectories of particle motion and graphs of relative and absolute velocity changes were constructed. The regularity of particle motion as it is lifted over the surface was found out. The conducted experimental research has confirmed the received theoretical results.

#### АНОТАЦІЯ

Розглянуто відносний рух частинки по сферичному сегменту, який обертається навколо вертикальної осі. Складено диференціальні рівняння відносного переміщення частинки, які розв'язано чисельними методами. Побудовано відносну та абсолютну траєкторії руху частинки та графіки зміни відносної і абсолютної швидкостей. З'ясовано закономірність руху частинки при її підйомі по поверхні. Проведені експериментальні дослідження підтвердили отримані теоретичні результати.

#### INTRODUCTION

The theory of particle motion on surfaces rotating about a vertical axis is used for designing centrifugal action devices (Lytvynenko *et al.*, 2019). In particular, it concerns devices for the dispersal of mineral fertilizers (Khan *et al.*, 2018), the extraction of juice from vegetables and fruits (Mushtaq *et al.*, 2017), the purification of air from dust particles in cyclones (Galins *et al.*, 2018) or in the process of designing the vortex type liquid-vapour jet apparatus (Merzliakov *et al.*, 2020).

It is common knowledge, that the particle performs a complex motion, which is the sum of two motions: the transportable movement of the surface and the relative movement of the particle on the surface, that is, it's sliding. A great deal is being written and said about the motion of particles on the surface of the cylinder (Pylypaka *et al.*, 2018; Pylypaka *et al.*, 2019) and on the surface of the cone (Carpena *et al.*, 2014). Importantly, the movement of particles on other rotating surfaces has its own peculiarities (Ivanov *et al.*, 2019; Liu *et al.*, 2019). Based on the foregoing, the aim of our research is the investigation of the regularities of motion of a material particle on a spherical segment, which rotates about a vertical axis with constant angular velocity.

#### MATERIALS AND METHODS

Generally, the parametric equations of a sphere with the origin in its lower pole are written:

$$\begin{aligned} X &= R \sin \varepsilon \cos \alpha \\ Y &= R \sin \varepsilon \sin \alpha \\ Z &= R(1 - \cos \varepsilon) \end{aligned} \quad (1)$$

<sup>1</sup> Sergiy Pylypaka, Dr.Sc. Prof.; Victor Nesvidomin, Dr.Sc. Prof.; Tatiana Volina, Ph.D. Assist.Prof.; Larysa Sirykh, Ph.D. Assist.Prof.; Liudmyla Ivashyna, Ph.D.

where:

$R$  is the radius of the sphere;

$\varepsilon, \alpha$  are the independent variables of the sphere (angles that define the position of a point on the sphere surface in the direction of the meridian and the parallel respectively).

Clearly, the angle  $\alpha$  varies within limits  $\alpha = 0 \dots 2\pi$ , the angle  $\varepsilon$  – within  $\varepsilon = 0 \dots \varepsilon_0$ , where the height of the spherical segment depends on the value of the angle  $\varepsilon_0$ . For example, at  $\varepsilon_0 = \pi/2$  the segment will be equal to half of the sphere.

Segment rotation will be considered regarding two coordinate systems: the fixed  $OXYZ$  and the moving  $Oxyz$ . The last one rotates with the segment. If the spherical segment (1) rotates about a vertical axis with an angular velocity  $\omega$ , then in time  $t$  the surface will turn to the angle  $\theta = \omega \cdot t$ . Let apply the known formulas of rotation of one coordinate system relative to another:

$$\begin{aligned} X &= R \sin \varepsilon \cos \alpha \cos \theta - R \sin \varepsilon \sin \alpha \sin \theta \\ Y &= R \sin \varepsilon \cos \alpha \sin \theta + R \sin \varepsilon \sin \alpha \cos \theta \\ Z &= R(1 - \cos \varepsilon) \end{aligned} \tag{2}$$

Taking into account  $\theta = \omega \cdot t$  after simplifications equations (2) can be written:

$$\begin{aligned} X &= R \sin \varepsilon \cos(\alpha + \omega t); \\ Y &= R \sin \varepsilon \sin(\alpha + \omega t); \\ Z &= R(1 - \cos \varepsilon). \end{aligned} \tag{3}$$

Firstly, at the initial moment ( $t = 0$ ) the two coordinate systems coincide, the spherical segment (or disk) does not rotate and the particle is at the meridian in the  $OYZ$  plane (Figure 1,a). For this particular case, the following forces are applied to the particle: the force of gravity  $mg$  ( $m$  is the mass of the particle,  $g=9.81 \text{ m/s}^2$  is the acceleration of gravity), surface reaction  $N$ , and the force of friction  $f \cdot N$  ( $f$  is the coefficient of friction), which prevents the particle movement down along the meridian toward the origin. Indeed, as the disc rotates at a constant angular velocity  $\omega$  during time  $t$ , it will rotate at an angle  $\theta = \omega \cdot t$  (Figure 1,b). If the particle would not slide on the disk, it would rotate with the disk to the corner  $\theta$  and would take a position on the same meridian after its rotation. As a result of sliding, the particle occupies an intermediate position (Figure 2,a). A particle sliding occurs in the opposite direction of rotation of the disk. So, the direction of relative velocity  $V_r$  is directed tangentially to the particle sliding trajectory (Figure 1,b).

The equation of particle motion should be derived from form  $m\bar{w} = \bar{F}$ , where  $\bar{w}$  is the vector of acceleration,  $\bar{F}$  is the resultant vector of applied forces to the particles. Hence, all vectors should be defined in the projections on the axis of the fixed coordinate system. The trajectory of the relative motion of a particle regarding the moving  $Oxyz$  coordinate system will be described by the dependency between curvilinear coordinates of the sphere  $\varepsilon$  and  $\alpha$ . Actually, this dependency can be set differently:  $\varepsilon = \varepsilon(\alpha)$ ,  $\alpha = \alpha(\varepsilon)$  or by means of a common variable  $t$ :  $\varepsilon = \varepsilon(t)$ ,  $\alpha = \alpha(t)$ . In our particular case, the common variable is time  $t$ .

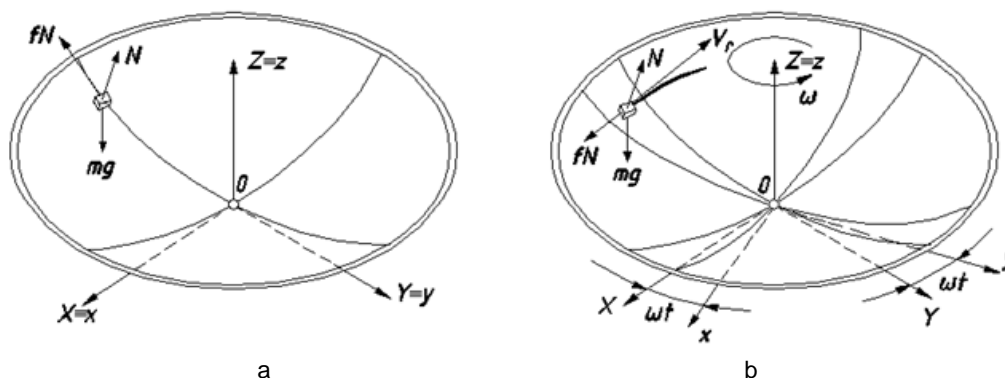


**Fig. 1 - The location of the particle in the spherical segment and the scheme of forces applied to it**  
 a) the fixed and moving coordinate systems coincide, the segment does not rotate;  
 b) the segment rotates, the particle slides on its surface

Thus, according to  $\varepsilon = \varepsilon(t)$  and  $\alpha = \alpha(t)$ , equation (1) defines the relative trajectory of particle motion and equation (3) – the absolute trajectory.

These dependencies are unknown and should be found. Besides, the vectors of relative and absolute velocities should be determined by differentiating expressions (1) and (3) by time  $t$ . Equations (1) and (3) in one case are the surface equations when  $\varepsilon$  and  $\alpha$  are the independent variables, and in the other, they are lines (particle trajectories which should be found) on the surface. For the surfaces the indication of the equations in uppercase letters was taken, as well as for the lines – the capital letters. For the relative trajectory the index "r" is used and for the absolute – "a". Therefore, by differentiating equations (1) the relative velocity of particle motion (sliding) on the surface of a spherical disk can be found:

$$\begin{aligned}\dot{x}_r &= R\dot{\varepsilon} \cos \varepsilon \cos \alpha - R\dot{\alpha} \sin \varepsilon \sin \alpha \\ \dot{y}_r &= R\dot{\varepsilon} \cos \varepsilon \sin \alpha + R\dot{\alpha} \sin \varepsilon \cos \alpha \\ \dot{z}_r &= R\dot{\varepsilon} \sin \varepsilon\end{aligned}\quad (4)$$

The geometric sum of the components (4) gives an opportunity to obtain the value of the sliding velocity of the particle on the spherical disk in the relative motion:

$$V_r = \sqrt{\dot{x}_r^2 + \dot{y}_r^2 + \dot{z}_r^2} = R\sqrt{\dot{\varepsilon}^2 + \dot{\alpha}^2 \sin^2 \varepsilon} \quad (5)$$

The unit vector  $T$  of the tangent to the trajectory of relative motion in projections on the axis of the OXYZ system is obtained by dividing the projections (4) to the value of the vector (5):

$$\begin{aligned}T_x &= \frac{\dot{\varepsilon} \cos \varepsilon \cos \alpha - \dot{\alpha} \sin \varepsilon \sin \alpha}{\sqrt{\dot{\varepsilon}^2 + \dot{\alpha}^2 \sin^2 \varepsilon}} \\ T_y &= \frac{\dot{\varepsilon} \cos \varepsilon \sin \alpha + \dot{\alpha} \sin \varepsilon \cos \alpha}{\sqrt{\dot{\varepsilon}^2 + \dot{\alpha}^2 \sin^2 \varepsilon}} \\ T_z &= \frac{\dot{\varepsilon} \sin \varepsilon}{\sqrt{\dot{\varepsilon}^2 + \dot{\alpha}^2 \sin^2 \varepsilon}}\end{aligned}\quad (6)$$

Let us find the direction of action of the surface reaction  $N$  (1). It is directed toward the normal  $P$  to the surface and is determined from the vector product of two vectors tangent to the coordinate lines of the surface. The projections of these vectors are partial derivatives of equations (1):

$$\begin{aligned}\frac{\partial X}{\partial \varepsilon} &= R \cos \varepsilon \cos \alpha; & \frac{\partial Y}{\partial \varepsilon} &= R \cos \varepsilon \sin \alpha; & \frac{\partial Z}{\partial \varepsilon} &= R \sin \varepsilon; \\ \frac{\partial X}{\partial \alpha} &= -R \sin \varepsilon \sin \alpha; & \frac{\partial Y}{\partial \alpha} &= R \sin \varepsilon \cos \alpha; & \frac{\partial Z}{\partial \alpha} &= 0.\end{aligned}\quad (7)$$

After vector multiplication of vectors (7) and transformation of the obtained vector into a unit one, projections of the vector of the normal  $P$  to the surface are:

$$P_x = -\sin \varepsilon \cos \alpha; \quad P_y = -\sin \varepsilon \sin \alpha; \quad P_z = \cos \varepsilon. \quad (8)$$

By differentiation of equations (3), the absolute velocity of motion of a particle with respect to a fixed coordinate system can be written:

$$\begin{aligned}\dot{x}_a &= R\dot{\varepsilon} \cos \varepsilon \cos(\alpha + \omega t) - R(\dot{\alpha} + \omega) \sin \varepsilon \sin(\alpha + \omega t) \\ \dot{y}_a &= R\dot{\varepsilon} \cos \varepsilon \sin(\alpha + \omega t) + R(\dot{\alpha} + \omega) \sin \varepsilon \cos(\alpha + \omega t) \\ \dot{z}_a &= R\dot{\varepsilon} \sin \varepsilon\end{aligned}\quad (9)$$

Then, the projections of the vector of absolute acceleration on the axis of the fixed coordinate system can be obtained by differentiation of expressions (9):

$$\begin{aligned} \ddot{x}_a &= R \left[ \ddot{\varepsilon} \cos \varepsilon - \dot{\varepsilon}^2 \sin \varepsilon - (\dot{\alpha} + \omega)^2 \sin \varepsilon \right] \cos(\alpha + \omega t) - \\ &\quad - R \left[ \ddot{\alpha} \sin \varepsilon + 2\dot{\varepsilon}(\dot{\alpha} + \omega) \cos \varepsilon \right] \sin(\alpha + \omega t) \\ \ddot{y}_a &= R \left[ \ddot{\varepsilon} \cos \varepsilon - \dot{\varepsilon}^2 \sin \varepsilon - (\dot{\alpha} + \omega)^2 \sin \varepsilon \right] \sin(\alpha + \omega t) + \\ &\quad + R \left[ \ddot{\alpha} \sin \varepsilon + 2\dot{\varepsilon}(\dot{\alpha} + \omega) \cos \varepsilon \right] \cos(\alpha + \omega t) \\ \ddot{z}_a &= R\ddot{\varepsilon} \sin \varepsilon + R\dot{\varepsilon}^2 \cos \varepsilon \end{aligned} \tag{10}$$

The unit vector  $T$  (6) of the relative velocity direction  $V_r$  and the unit vector (8) of the normal to the surface  $P$  are found for the fixed surface. Since the surface rotates at an angle  $\theta = \omega \cdot t$ , the vectors also should be rotated at this angle to correspond to the particle location. The rotation is carried out in the same way as the rotation of the surface according to formulas (2). After rotation, the projections of these vectors can be written:

- a unit vector of the tangent to the relative trajectory:

$$\begin{aligned} T_x &= \frac{\dot{\varepsilon} \cos \varepsilon \cos(\alpha + \omega t) - \dot{\alpha} \sin \varepsilon \sin(\alpha + \omega t)}{\sqrt{\dot{\varepsilon}^2 + \dot{\alpha}^2 \sin^2 \varepsilon}} \\ T_y &= \frac{\dot{\varepsilon} \cos \varepsilon \sin(\alpha + \omega t) + \dot{\alpha} \sin \varepsilon \cos(\alpha + \omega t)}{\sqrt{\dot{\varepsilon}^2 + \dot{\alpha}^2 \sin^2 \varepsilon}} \\ T_z &= \frac{\dot{\varepsilon} \sin \varepsilon}{\sqrt{\dot{\varepsilon}^2 + \dot{\alpha}^2 \sin^2 \varepsilon}} \end{aligned} \tag{11}$$

- a unit vector of the normal to the surface:

$$P_x = -\sin \varepsilon \cos(\alpha + \omega t); \quad P_y = -\sin \varepsilon \sin(\alpha + \omega t); \quad P_z = \cos \varepsilon. \tag{12}$$

At the same time, the vector equation  $m\overline{w} = \overline{F}$  in the projections on the axis of the fixed coordinate system OXYZ is written:

$$\begin{aligned} m\ddot{x}_a &= NP_x - fNT_x \\ m\ddot{y}_a &= NP_y - fNT_y \\ m\ddot{z}_a &= NP_z - fNT_z - mg \end{aligned} \tag{13}$$

The projections of unit directional vectors of tangent  $T$  to the relative trajectory and normal to the surface  $P$  are given in (11) and (12) accordingly, and the expressions of the second derivatives of the absolute trajectory are given in (10). As a result, substituting the expressions in (13) gives a system of three equations with three unknown dependencies:  $\alpha = \alpha(t)$ ,  $\varepsilon = \varepsilon(t)$ , and  $N = N(t)$ . It is essential to solve it regarding  $\ddot{\alpha}$ ,  $\ddot{\varepsilon}$  and  $N$ :

$$\begin{aligned} \ddot{\varepsilon} &= \left[ (\omega + \dot{\alpha})^2 \cos \varepsilon - \frac{g}{R} \right] \sin \varepsilon - f \frac{\dot{\varepsilon} B}{RA} \\ \ddot{\alpha} &= -2\dot{\varepsilon}(\omega + \dot{\alpha}) \operatorname{ctg} \varepsilon - f \frac{\dot{\alpha} B}{RA} \\ N &= mB \end{aligned} \tag{14}$$

where:  $A = \sqrt{\dot{\varepsilon}^2 + \dot{\alpha}^2 \sin^2 \varepsilon}$ ;  $B = g \cos \varepsilon + R \left[ \dot{\varepsilon}^2 + (\omega + \dot{\alpha})^2 \sin^2 \varepsilon \right]$ .

Actually, system (14) is the system of the first two equations relatively unknown dependencies  $\alpha = \alpha(t)$  and  $\varepsilon = \varepsilon(t)$ , and the dependence  $N = N(t)$  can be found after the solution of this system. The resulting system can be solved by numerical methods. It is necessary to substitute the found dependencies  $\alpha = \alpha(t)$  and  $\varepsilon = \varepsilon(t)$  into equation (1) in order to obtain the relative trajectory of particle motion on a spherical disk, that is, the sliding trajectory, and into equation (3) to obtain the absolute trajectory movement.

**RESULTS**

First of all, in Figure 2 by numerical methods the relative and absolute trajectories of particle motion on the disk for 2 s period were constructed with the following parameters:  $R=0.5$  m,  $\omega=20$  s<sup>-1</sup>,  $f=0.3$ .

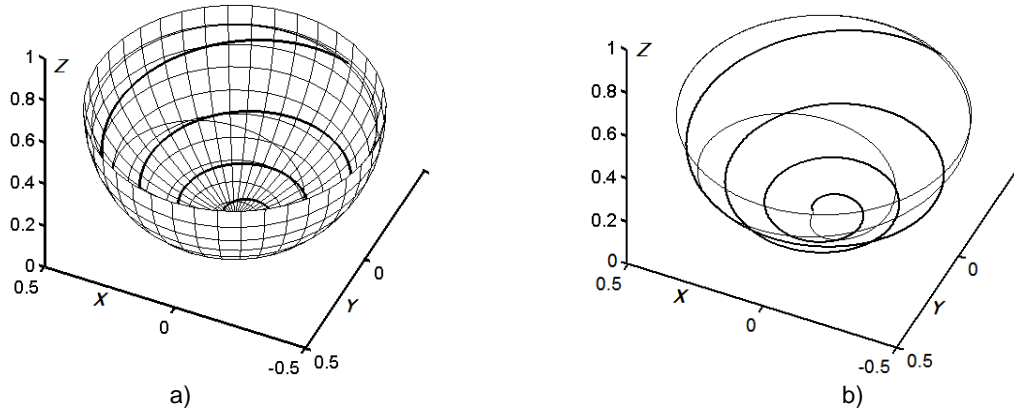


**Fig. 2 - The relative (thick line) and the absolute trajectory of particle motion**  
 a) on the surface of the spherical segment; b) the surface of the segment conventionally is not shown

After analysing the trajectory, it can be concluded that the particle slides on the sphere, rising to a certain position, then "sticks" and rotates with the surface. This case is shown on the graphs of the relative and absolute velocities of the particles (Figure 3). The absolute velocity of a particle  $V_a$  is defined as the geometric sum of its projections (9) by the formula (5).

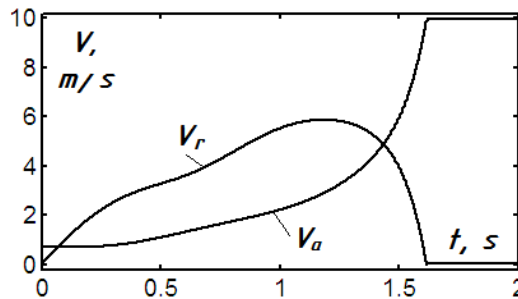


**Fig. 3 - Graphs of relative  $V_r$  and absolute  $V_a$  velocities of particle motion**

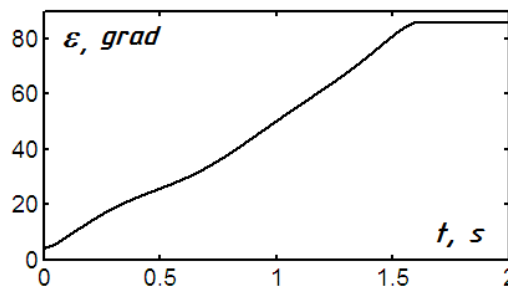


**Fig. 4 - Graph of the angle change  $\epsilon$**

Moreover, Figure 3 shows that after 1.6 s period after the start of the motion, the particle "sticks", so, its sliding speed becomes zero and the absolute speed becomes equal  $V_a = 10$  m/s. From the graph of change of angle  $\epsilon$  (Figure 4) it is seen that at the moment of particle sticking at  $t = 1.6$  s, it reaches the maximum value  $\epsilon = 85^\circ$ , so, the particle with a segment rotates by a circle that is almost equal to the equator of the sphere, that is, the radius of the sphere  $R$ . Based on the set values  $R = 0.5$  m and  $\omega=20$  s<sup>-1</sup>, one can find:  $V_a = \omega \cdot R = 10$  m/s, that is, the obtained velocity is consistent with the graph. If a particle begins the movement not from the lower point of the segment, but little higher (for example, at  $\epsilon_0 = 45^\circ$ , as shown in Figure 5), it reaches soon the upper boundary trajectory, beyond the hemisphere. It requires 0.2 s (Figure 6). Figure 7 shows a graph of the change of the surface reaction for a particle by mass  $m=0.01$  kg.

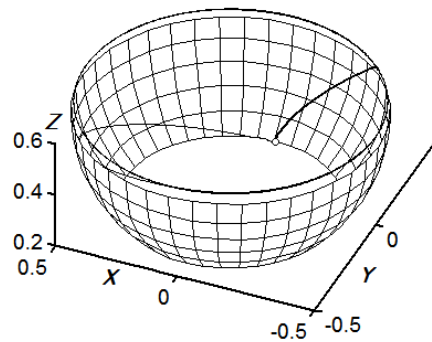


Fig. 5 - Relative (thick line) and absolute trajectory of motion on a bounded area of a segment

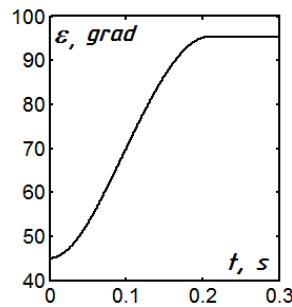


Fig. 6 - Graph of change of angle  $\varepsilon$  for initial value  $\varepsilon_0=45^\circ$

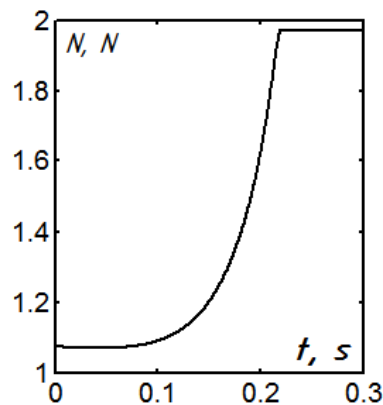


Fig. 7 - Graph of change of surface reaction for a particle with mass  $m=0.01 \text{ kg}$

For instance, the movement of the particle on the inner wall of the rotating surface takes place in devices for juice squeezing from fruits or vegetables. Usually, a cut cone with holes for the juice outlet is used there. Doubtless, the movement of the particle of technological material on the inner surface of the cone is different from a similar movement on the surface of the segment. Sliding on the surface of the cone, the particle will rise up and the speed will increase.

The segment of the sphere is characterized by the deceleration of the velocity  $V_r$  of the particle sliding as it rises up to the "sticking" in the vicinity of the equator (Figure 3). But the most intensive juicing process occurs in the braking zone, as evidenced by the sharp increase in pressure on the particle (Fig.7).

Of course, the nature of the movement of the technological material, such as the core, is different from that particle movement. The considered model does not take into account the obstacles to movement, which are holes in the wall surface. Obviously, as the cone rotates, some of the material moves up and out of bounds without giving all the juice. The other part "sticks" and is separated from the surface by a mechanical device with a manual drive. However, the behaviour of the individual particle gives a qualitative characterization of the movement, which can be transferred to the movement of the material particularly. In particular, the applying of a spherical segment makes it possible to prevent unauthorized abandonment of particles from the work area material.

In order to confirm the theoretical research, we have made a device for squeezing juice from grated fruits, vegetables and fruits (squash), in which a segment of a sphere with holes for removing juice was used as a working surface.

The research program consisted of determining the mass fraction of squash moisture after juice removal or the quality of juice release from the squash. The studies were performed according to GOST 13979.1-88, which establishes methods for determining the mass fraction of squash moisture in the range of values from 2 to 20%, and consisted of drying samples of boxes with the product and determining their weight before and after drying.

The mass fraction of moisture was determined by the formula:

$$W = \frac{m_1 - m_2}{m_1 - m} \times 100\%, \quad (15)$$

where:

$m$  is a mass of empty box;

$m_1$  is a mass of box with the product before drying;

$m_2$  is a mass of box with the product after drying.

The research was carried out by squeezing the juice from carrots, beets and apples squash both on a standard centrifugal juicer PHILIPS Viva Kompakt HR1832/02 and on a specially made device for squeezing juice with a segment of the sphere as a working surface.

It was found that the mass fraction of moisture in the squash squeezed in our experimental device is 8.1... 19.7 % less than in the squash squeezed by the PHILIPS juicer.

The results of experimental studies to determine the mass fraction of moisture in the squash of carrots, beets and apples are shown in Figure 8.

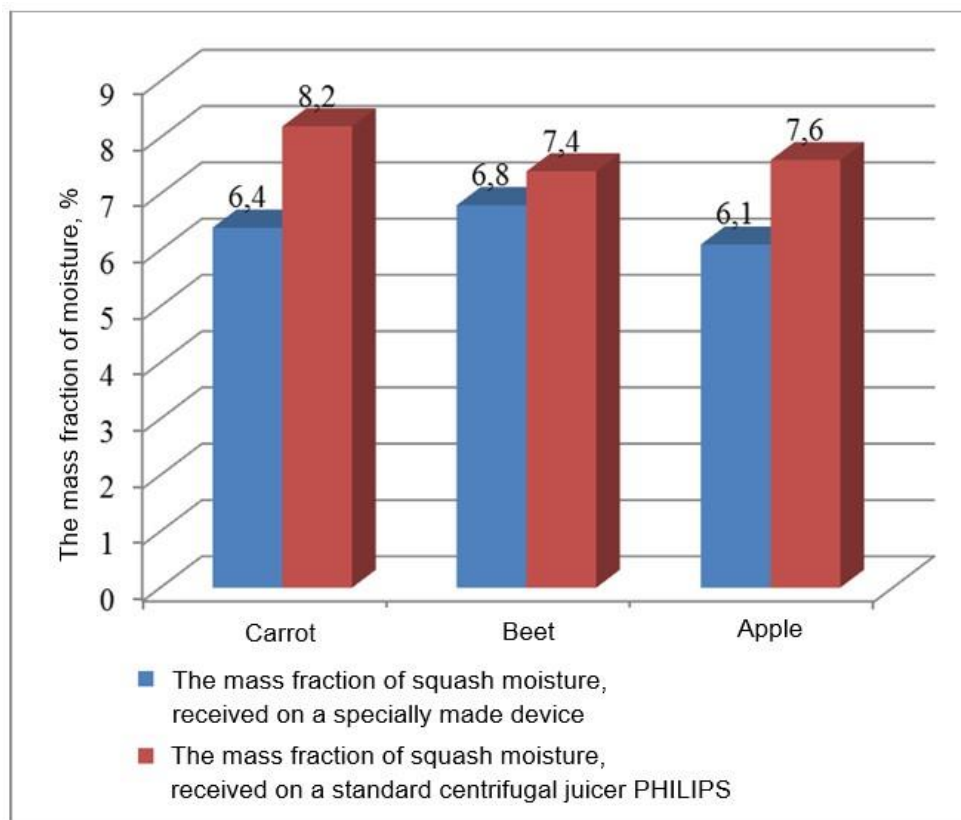


Fig. 8 - The results of experimental researches to determine the mass fraction of squash moisture

## CONCLUSIONS

The particle motion on the inner rough surface of a spherical segment has its own peculiarities. It relates to the nature of the particle sliding across the surface. When a particle hits the surface at the bottom of the segment, its acceleration occurs with a simultaneous upward movement.

Such motion is characterized by the change of two speeds: relative (the speed of sliding) and absolute. Firstly, the relative velocity increases and then decreases to zero at the time of a particle sticking. The

absolute velocity of a particle constantly increases and becomes constant after its "sticking". The "sticking" of the particle occurs at a height close to the equator of the sphere and it can stick both below and above depending on the initial conditions. The conducted experimental research has confirmed the received theoretical results.

## REFERENCES

- [1] Carpena P., Carretero C., Coronado Jiménez A.V., (2014), On the circular orbits of a particle sliding on the inside of a generic surface of revolution. *European Journal of Physics*, 35(1), DOI: 10.1088/0143-0807/35/1/015025;
- [2] Galins J., Laizans A., Galins A., (2018), Increasing cyclone efficiency by using a separator plate. *Rural and environmental engineering, landscape architecture*, Vol.1, pp.207–210, DOI: 10.22616/rrd.24.2018.032;
- [3] Ivanov V., Dehtiarov I., Pavlenko I., Kosov M., Hatala M., (2019), Technological assurance and features of fork-type parts machining. *Lecture Notes in Mechanical Engineering*, pp.114–125, DOI: 10.1007/978-3-030-22365-6\_12;
- [4] Khan M.N., Mobin M., Abbas Z.K. and Alamri S.A., (2018), Fertilizers and Their Contaminants in Soils, Surface and Groundwater. In: *Dominick A. DellaSala, and Michael I. Goldstein (Eds.). The Encyclopaedia of the Anthropocene*, Vol.5, pp.225–240, DOI: 10.1016/B978-0-12-809665-9.09888-8 225;
- [5] Liu N., Zhou J., Gao M., Cheng P., (2019), An experimental study on flow and heat transfer characteristics of binary hydrate slurries in a horizontal tube. *International Communications in Heat and Mass Transfer*, Vol.102, pp.34–41, DOI: org/10.1016/j.icheatmasstransfer.2019.01.009;
- [6] Lytvynenko A., Yukhymenko M., Pavlenko I., Pitel' J., Mižáková J., Lytvynenko O., Ostroha R., Bocko J., (2019), Ensuring the Reliability of Pneumatic Classification Process for Granular Material in a Rhomb-Shaped Apparatus. *Applied Sciences*, 9 (8), DOI: 10.3390/app9081604;
- [7] Merzliakov I., Pavlenko I., Chekh O., Sharapov S., Ivanov V., (2020), Mathematical modelling of operating process and technological features for designing the vortex type liquid-vapour jet apparatus. In: *Ivanov V. et al. (Eds.) Advances in Design, Simulation and Manufacturing. DSMIE 2018. Lecture Notes in Mechanical Engineering*. Springer, Cham, pp. 613–622 (2020), DOI: 10.1007/978-3-030-22365-6\_61;
- [8] Mushtaq M., (2017), Extraction of Fruit Juice: An Overview. *Fruit Juices*, 1(8), pp.131–159, DOI: 10.1016/B978-0-12-802230-6.00008-4;
- [9] Pylypaka S., Klendii M., Kremets T., Klendii O., (2018), Particle Motion over the Surface of a Cylinder, which Performs Translational Oscillations in a Vertical Plane. *Eng. J.*, 22 (3), pp.83–92, DOI: 10.4186/ej.2018.22.3.83;
- [10] Pylypaka S., Klendii M., Zaharova T., (2019), Movement of the particle on the external surface of the cylinder, which makes the translational oscillations in horizontal planes. *Lecture Notes in Mechanical Engineering*, F2, pp.336–345, DOI: 10.1007/978-3-319-93587-4\_35.

## DESIGN, ANALYSIS AND TEST OF SMALL ROTARY LAWN MOWER OF SINGLE-DISC TYPE

### 小型单元盘割草机设计、分析与试验

ShouYong Xie, Hang Zhao, ShangHong Yang, QiuJu Xie, MingJin Yang\*)<sup>1</sup>

Southwest University, College of Engineering and Technology, Chongqing Key Laboratory of Agricultural Equipment  
for Hilly and Mountainous Regions / P. R. China  
Tel: 8613883002509; E-mail: ymingjin@swu.edu.cn  
DOI: <https://doi.org/10.35633/inmateh-62-09>

**Keywords:** rotary lawn mower, single-disc, EDEM, modal analysis, field test

#### ABSTRACT

Machine quality, mowing efficiency and work reliability of lawn mowers are main issues concerned in hilly and mountainous regions. Taking a rotary lawn mower of single-disc type as research object, structure and parameter design of the mower was defined according to empirical formula, performance of grass cutting and modal analysis of the cutting blades were conducted by means of EDEM and Creo, and field test was conducted to verify the overall performance of the machine. Results showed that symmetrically installed 2 cutting blades with revolution speed 3500 r/min and forward speed 1.4 m/s showed good performance of grass cutting and stability. The velocity of grass particles of cut grass was mostly in the range of 1.1-1.5 m/s, and the velocity of broken grass was stable, which proved good harvest and gathering of grass. The height of remained stubbles was about 50 mm, and the length of cut grass was distributed in the range of 30-60 mm, which met requirements of forage production.

#### 摘要

丘陵山地割草机的机器质量、割草效率和工作可靠性广受关注。本研究以小型单圆盘式旋转割草机为研究对象，根据经验公式对其进行了结构和参数设计，基于 EDEM 和 Creo 对割草性能和切割刀片振动模态进行了分析，并割草机的整机性能进行了田间试验。结果表明，对称布置 2 把切割刀片，在旋转速度 3500r/min，前进速度 1.4m/s 的条件下，切草性能和稳定性俱佳。被切草粒子的速度值主要范围为 1.1-1.5m/s，且速度稳定，有利于牧草收割和拢草。割后草茬高度约为 50mm，割后草段长度范围 30-60mm，能满足牧草生产要求。

#### INTRODUCTION

China is rich in grass resource and ranks the 2nd largest country of grassland area after Australia, having nearly 4 million km<sup>2</sup> of natural grasslands (Yang L., 2019). Especially in the southwest of China, there are plentiful of rainfall and heat that benefit the growth of grass, which results in 4-6 times of natural grassland area higher than that in the north. However, the grasslands in the southwest are mostly distributed in hilly and mountainous regions, particularly in the range of 800 to 2000m above sea level, and they mainly consist of sparsely dispersed forest grassland and shrub grassland. As a result, the harvest and utilization of the grass are difficult by means of large lawn mower in these regions, with the effective utilization rate less than 50% (Fu M.Z., 2009). Therefore, it is necessary to develop small lawn mowers suitable for the mowing in these regions with good quality, high efficiency, and low cost (Yang H.W. and Zhang Y.H., 2016).

According to the working principle of cutters, lawn mowers can be divided into reciprocating lawn mowers and rotary ones (He Z.Q. et al, 2020; Fu M.Z. et al, 2018). As cutters of the rotary lawn mowers rotate with high revolution speed, they are suitable for grass harvest of high-yield forage with fast forward speed, and they show high reliability under harsh conditions, such as high humidity, high density, and severe lodging (Zhang N., 2014; Yang S.K. and Su Z.F., 2009). At present, the applicability of lawn mowers cannot fully meet the requirements of grass harvest in the southwest of China, especially in the hilly and mountainous regions. The main obstacles to the applicability are failures during mowing because of unreasonable design and unqualified manufacturing. With the advance of rectification of rural industrial structure, reforestation of

<sup>1</sup> SY Xie, Prof.; H Zhao, Ms.; SH Yang, Ms.; QJ Xie, Ms.; MJ Yang, Prof.

countryside, and agricultural mechanization of weak links in the hilly and mountainous regions of China, farmers' desires to purchase lawn mowers increased substantially (Xie Y.F. et al, 2020).

This study focused on development, analysis, and test of a small rotary lawn mower of single-disc, including explanation of working principle, design of main parameters, analysis of cutting process and vibration, performance evaluation by field test. The results could provide basis for the development and optimization of lawn mowers suitable for hilly and mountainous regions.

## MATERIALS AND METHODS

### Materials

A small rotary lawn mower of single-disc type was developed, as shown in Fig.1 (a). Configuration of grass box and cutting blade was shown in Fig. 1 (b). The external diameter of grass box  $D$  was 0.6 m. The dimensions of the cutting blade were length  $L$  0.5 m, width  $W$  0.08 m, thickness  $T$  0.05 m, and cutting-edge height  $h$  0.056m. There were 2 openings at the bottom edge of the grass box, one as entrance of growing grass, and the other as exit of cut grass. Both openings had opening angle  $\theta$   $60^\circ$ . The entrance was forward faced, and the exit was right-sided along forward direction of the mower. The cutting blade and grass box were made of carbon steel. Field test was conducted in a grassland in Beibei, Chongqing, China. Tape measure with precision of 1 mm was used to measure dimensions of growing grass, cut grass and stubble left.

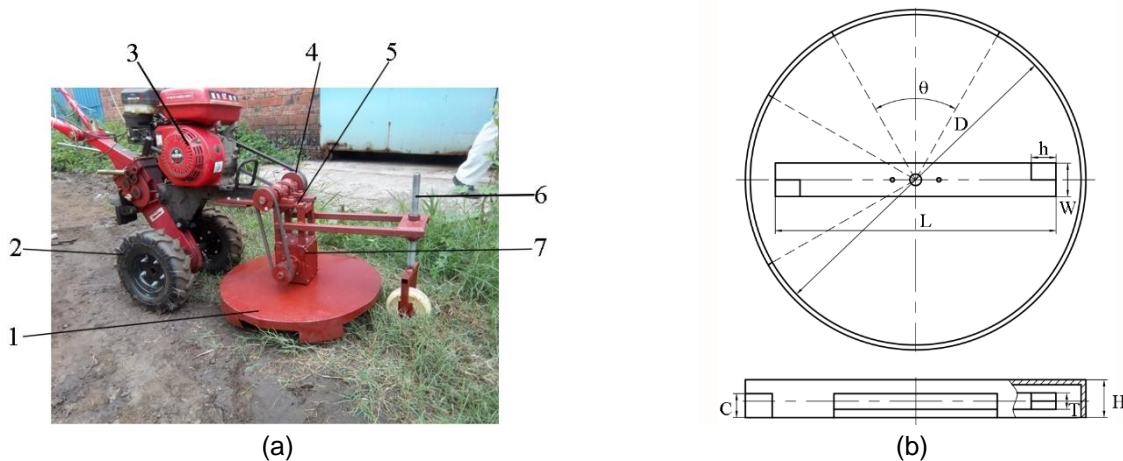


**Fig. 1 - Lawn mower: (a) outlook; (b) dimensions of grass box and cutting blades**

1- Grass box; 2- Walking wheels; 3- Diesel engine; 4- Pulley; 5- Frame; 6- Adjusting lever; 7- Gearbox

## Methods

### Cutting velocity

A coordinate system was defined as  $X$  along the right side, and  $Y$  along the forward speed, and the trajectories of end points a and b of cutting-edge of the cutting blade and composition of cutting velocity were plotted, as shown in Fig. 2. The move of the cutting blade was the combination of lawn mower walking and rotation of the blade, then a trochoid was formed for the blade (Ma X.C. 2005; Dong D.J. and Chen H. X., 2002). For the end points of the cutting-edge, their positions were expressed as (Fu, M. Z. et al, 2018):

$$\begin{cases} X_a = r \cos(\omega t + \beta) \\ Y_a = V_m t + r \sin(\omega t + \beta) \end{cases}, [m] \quad (1)$$

$$\begin{cases} X_b = R \cos(\omega t + \alpha) \\ Y_b = V_m t + R \sin(\omega t + \alpha) \end{cases}, [m] \quad (2)$$

Where

$(X_a, Y_a)$  – position of point a [m];  $(X_b, Y_b)$  – position of point b [m];  $\omega$  – angular velocity, [rad/s];

$r$  – radius of point a, [m];  $R$  – radius of point b, [m];  $t$  – time, [s];  $V_m$  – forward speed of lawn mower, [s];

$\beta$  – rotation angle of point a at time  $t$ , [rad];  $\alpha$  – rotation angle of point b at time  $t$ , [rad].

By applying differentiation to Eqs. (1) and (2), the cutting velocity of points a and b could be obtained. The cutting velocity can also be schematically plotted as combination of forward speed and rotational speed, and the velocity of point a, namely  $V_a$  was shown in Fig. 2 (b).

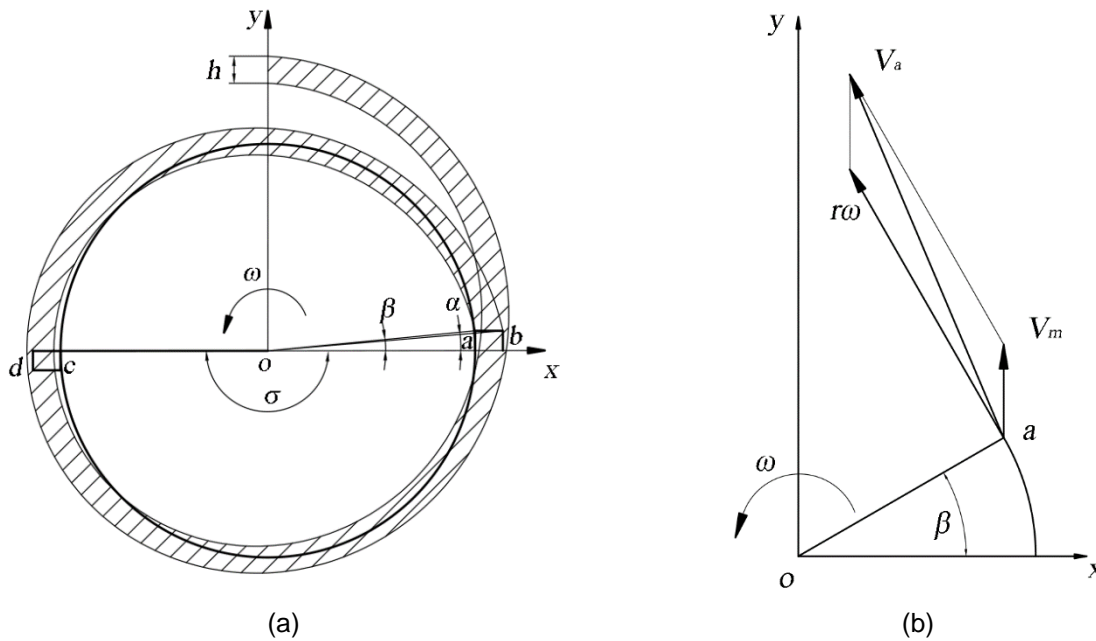


Fig. 2 – Trajectories of end points of cutting-edge and cutting velocity: (a) trajectory; (b) cutting velocity

For each cutting-edge with height  $h$ , there was a cutting width  $h$  along the forward direction, as shown in Fig. 2 (a). In order to cut grass without missing, the following requirement should be met:

$$\frac{V_a}{V_m} \geq \frac{2\pi r}{mh}, \text{ [dimensionless]} \quad (3)$$

Where  $m$ –number of cutting blades, [pieces].

### Power consumption

The walking wheels and cutting blades of the lawn mower were driven by the same diesel engine while with different transmission paths. As for the cutting blades, power of engine was transmitted to a gear box through belts. There was a vertical output via transmission of bevel gears. Then, the cutting blades in the grass box was driven by the vertical output. Therefore, the total power consumption of the lawn mower was expressed as (Stone and Gulvin, 2007):

$$P = P_1 + P_2 + P_3, \text{ [kW]} \quad (4)$$

Where  $P$ – total power consumption, [kW];  $P_1$  – power consumption in transmission, [kW];

$P_2$  – power consumption in grass cutting, [kW];  $P_3$ – power consumption for forward move, [kW].

The power consumption in transmission was expressed as:

$$P_1 = P_u B, \text{ [kW]} \quad (5)$$

Where  $P_u$  – power consumption for unit cutting width, [kW/m];  $B$  – cutting width of lawn mower, [m].

For flat grassland, the power consumption in grass cutting was expressed as (Chinese Academy of Agricultural Mechanization Sciences, 2007):

$$P_2 = \frac{V_m B W_0}{102}, \text{ [kW]} \quad (6)$$

Where  $W_0$  – work for unit area of grass cutting, [J/m<sup>2</sup>].

### Numerical method

For forage grass cutting, stalks of the grass are regarded as structure of slender pipes. The contact, collision between stalks and other motions of the stalks can be treated as function by particles with corresponding parameters. Then, stems and leaves of the forage grass can be filled in the grass box and bonded each other as particles in discrete element method analysis. Software of EDEM was employed in the numerical analysis. As there was cohesion force while grass cutting, Hertz-Mindlin adhesive contact model was selected.

Particles became bonded at a certain time  $t_{\text{BOND}}$ , namely bond time. Before  $t_{\text{BOND}}$ , particles interacted through default Hertz-Mindlin contact model. The adhesive normal and tangential forces  $F_n, F_t$  and torques  $T_n, T_t$  increased from zero with time (Wang G.Q. et al, 2010). For bonded particles, when normal and tangential stresses exceeded a certain value, the bond was destroyed. Therefore, the maximum values of normal and tangential stresses were defined as:

$$\sigma_{\text{max}} < \frac{-F_n}{A} + \frac{2T_t}{J} R_B, [\text{N}] \tag{7}$$

$$\tau_{\text{max}} < \frac{-F_t}{A} + \frac{T_n}{J} R_B, [\text{N}] \tag{8}$$

Where  $R_B$  – bond radius, [m];  $A$  – contact area, [m<sup>2</sup>], and  $A = \pi R_B^2$ ;  $J$  – parameter, [m<sup>4</sup>], and  $J = \frac{1}{2} \pi R_B^4$ .

The standard Hertz-Mindlin forces increased with the process of bonding, and bonding forces and moments increased as well. When bonding forces were introduced into the contact model, particles were no longer in natural contact. Then the contact radius should be set larger than actual contact radius of the spherical particles (Yao Y.P. et al, 2015; Shimizu and Cundall, 2001).

Simplified model of grass box with cutting blades and forage grass was created in Creo software, as shown in Fig. 3. According to the actual situation, the height of the forage grass was set to 60 mm, and diameter 10 mm. Some suitable amount of grass was added into the model during simulation.

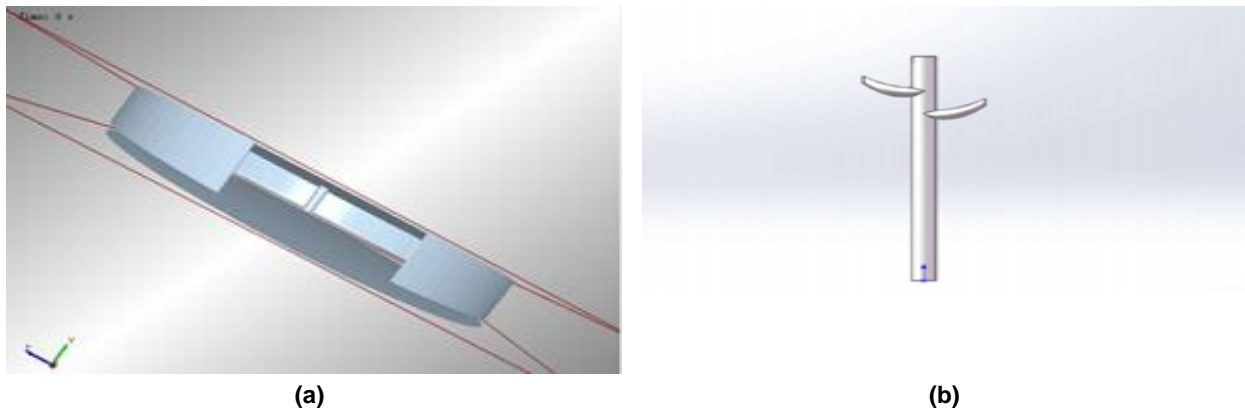


Fig. 3 – Geometric model: (a) Grass box and cutting blades; (b) Grass

Forage grass was automatically meshed in software of Gambit with minimum mesh size 0.26 mm. According to real problem of forage grass cutting, the minimum mesh size was manually set as 10.4 mm, 40 times of original 0.26 mm, in order to reduce computing time and save computing resources. 9555 particles were created to form a stalk of forage grass, as could be extracted in the file of API (Application Programming Interface). Similarly, only a small amount of grass stalks was considered in this study, as treated by a previous work (Moyley and Thompson, 2005). There were 2 types of particles for the grass, namely fraction particles and whole particles. A grass stalk was filled with fraction particles, and fraction particles combined as whole particle subsequently. Particle replacement method was adopted in the simulation. The material of cutting blades and grass box is defined as steel. The basic parameters for the DEM simulation were adopted, as shown in Tab. 1.

Table 1

Basic parameters of material and contact

Items	Material		Contact	
	Grass	45 steel	Grass-grass	Steel-grass
Poisson's ratio	0.4	0.3	/	/
Shear modulus [MPa]	1	10000	/	/
Density [kg/m <sup>3</sup> ]	100	7800	/	/
Restitution coefficient	/	/	0.2	0.5
Static friction coefficient	/	/	0.5	0.01
Dynamic friction coefficient	/	/	0.5	0.01

The grass cutting plane was a circular plane, with the same diameter as rotation diameter of the cutting blades. When grass particles of a stalk were replaced, grass model was re-generated at centre of whole

particle of the stalk. The lower plane of grass cutting machine was defined as 150 mm, equal to the radius of whole particle of a stalk.

The total number of whole particles was 15, equal to the number of the grass stalks (Chen, J. et al, 2011). The Rayleigh time-step was determined by Rayleigh's method (Owen and Cleary, 2010):

$$T = \frac{\pi R_p \left(\frac{\rho}{G}\right)^{\frac{1}{2}}}{(0.1631\nu + 0.8766)}, [\text{s}] \quad (9)$$

Where  $\nu$  – Poisson's ratio, [dimensionless];  $R_p$  – radius of fraction particles, [m];

$G$  – shear modulus, [MPa];  $\rho$  – particle density, [kg/m<sup>3</sup>].

Rayleigh time-step was set as 0.01 s, 0.02% of the fixed time-step. Particles were replaced at 0.01 s. The maximum velocity of particles flying out were limited to 0.5 m/s, which was better to bonded particles. After running for a period, the limitation was removed. The rotation of the cutting blades was set as 3500 r/min, which was consistent with field test.

## RESULTS AND DISCUSSIONS

### Machine design

For forage grass, the work for unit area of grass cutting was  $W_0 = 200\text{-}300 \text{ J/m}^2$ . While cutting width of the lawn mower  $B = 0.5 \text{ m}$  and forward speed  $V_m = 1.4 \text{ m/s}$ . The minimum power consumption in grass cutting should be  $P_2 = 2.06 \text{ kW}$ . For small lawn mowers, power consumption for unit cutting width was  $P_b = 0.44\text{-}1 \text{ kW}$ , then the minimum power consumption in transmission should be  $P_1 = 0.5 \text{ kW}$ . When the lawn mower moved forward with speed 1.4 m/s, about 5 km/h, power consumption for the unit mass of machine was 1-2.3 kW/1000kg. The mass of lawn mower was 350 kg, then the minimum power consumption for forward move should be  $P_3 = 0.805 \text{ kW}$ . Therefore, without considering power consumption in transmission, the minimum total power consumption of lawn mower  $P$  should be the sum of  $P_1$ ,  $P_2$ , and  $P_3$ , namely 3.365kW.

The revolution speed of cutting blades  $n$  were calculated as:

$$n = \frac{30(V_m + V_b)}{\pi R}, [\text{r/min}] \quad (10)$$

Where  $V_b$  – linear velocity of point b, [m/s], and  $V_b = 90 \text{ m/s}$ .

While forward speed  $V_m = 1.4 \text{ m/s}$ , linear velocity of point b,  $V_b = 90 \text{ m/s}$ , and radius of point b,  $R = 0.25 \text{ m}$ , the revolution speed of cutting blades was calculated as 3491 r/min. For practical application, the revolution speed of cutting blades was defined as 3500 r/min.

For grass cutting without stalk support, the limited velocity should be higher than 30 m/s (Wang et al, 2003). As for the grass cutting in the present study, the lowest velocity occurs at point a of the cutting-edge. The velocity of point a was expressed as:

$$V_a = \sqrt{r^2 \omega^2 + 2r\omega V_m \cos(\omega t + r) + V_m^2}, [\text{m/s}] \quad (11)$$

When  $\omega t + r = \pi + 2k\pi$  ( $k = 0, 1, 2, \dots, i$ ), the lowest velocity of point a was obtained as  $V_{\text{amin}} = r\omega - V_m$ , and it was 69.7 m/s, which met the limited velocity of 30 m/s, then the transmission scheme of the lawn mower was rational.

To meet the requirement of no-missing grass cutting, the number of cutting blades  $m$  should be larger than  $60 V_m / (hn)$ , namely 1.58 in the present case. Considering stability of blade move and production feasibility, the number of cutting blades was defined as 2.

### Numerical analysis

#### Cutting process analysis by means of EDEM

The grass cutting process was simulated by means of EDEM, and the contour of velocity of typical particles was obtained and plotted, as shown in Fig. 4. Particles were in state of grass after being cut and broken by cutting blades. The velocity of particles after being cut and broken was between 0.3-3.75 m/s.

The bottom and top of the grass stalk had the slowest velocity, and the cutting parts had the fastest velocity. In addition, the grass stalks could be cut multiply, which resulted in the great change of particle velocity.

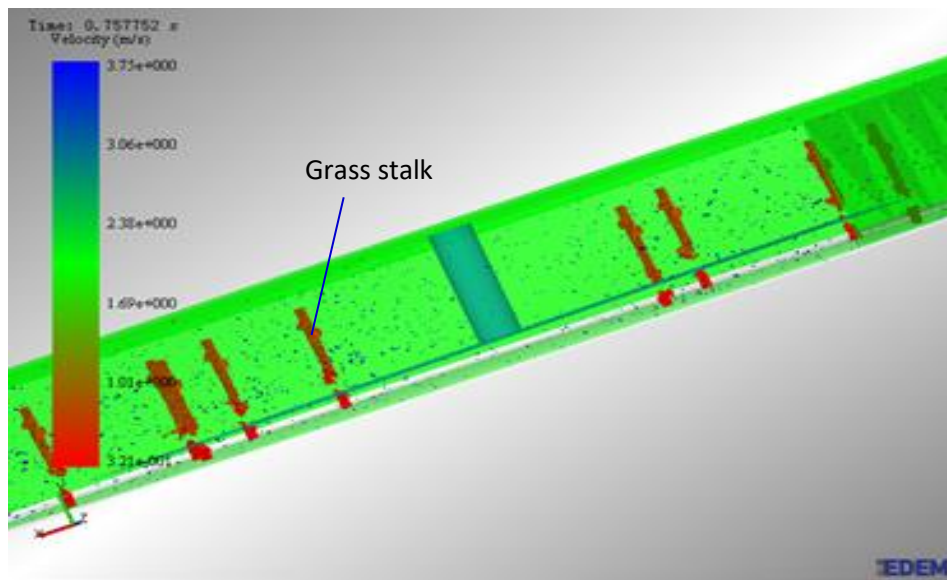


Fig. 4 – Contour of velocity of typical particles of grass

The broken grass moved in the grass box in all directions. The trajectory of grass particles was plotted by means of streamline, as shown in Fig. 5 (a). The relative move of grass and cutting blades formed circulating particle flow in the grass box. The distribution of grass particles revealed relatively uniform and lots of grass particles located in cutting zone, which showed the structure design and parameters defined were reasonable for the forage grass cutting. On conditions of revolution speed of cutting blades 3500 r/min and forward speed of lawn mower 1.4 m/s, the velocity of grass particles was mostly in the range of 1.1-1.5 m/s, and the velocity of broken grass was stable, which proved good harvest and gathering effect for the lawn mower. Fig. 5 (b) showed the typical curve of velocity of a grass particle vs. time in the Y direction. The grass particles obtained acceleration after being cut, and their velocity peaked afterwards, which agreed with real application.

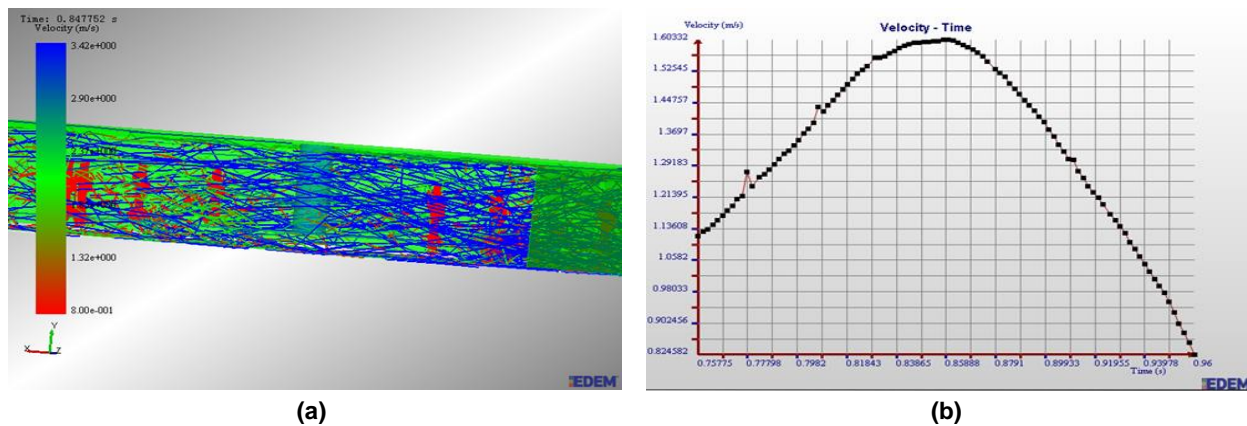


Fig. 5 – Typical particle move: (a) Grass trajectory; (b) Velocity vs. time

**Modal analysis of vibration of cutting blades**

Cutting blades are important for a lawn mower, and their vibration performance have a great influence on safety, reliability and efficiency of the grass cutting work. The modal analysis of vibration of cutting blades was conducted by Creo Simulate. The 3-D model of the cutting blade was built in Creo, as shown in Fig. 6. The material of the cutting blade was 45 steel, with elastic modulus 210 GPa, density 7800 kg/m<sup>3</sup> and Poisson's ratio 0.3. The vibration mode and natural frequency at different orders of the cutting blades could be obtained.

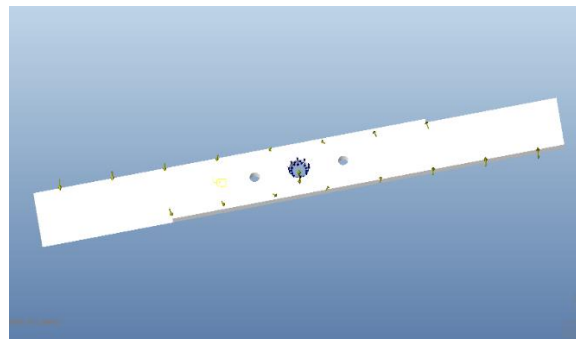


Fig. 6 – 3-D model of the cutting blades

The vibration patterns of cutting blades were shown in Fig. 7. According to vibration patterns of the first six orders, the vibration mainly occurred at locations of cutting edge of the blades. In the first-order and second-order modals of vibration, the cutting blades swung up and down in the vertical direction. In the third-order and fourth-order modals, the vibration was further strengthened, and a concave curved surface appeared between blade edges and the centre of rotation. And in the fifth-order and sixth-order vibration modals, the vibration was transmitted to the entire blade. The blade twisted back and forth along the X direction, and swung up and down along the vertical direction.

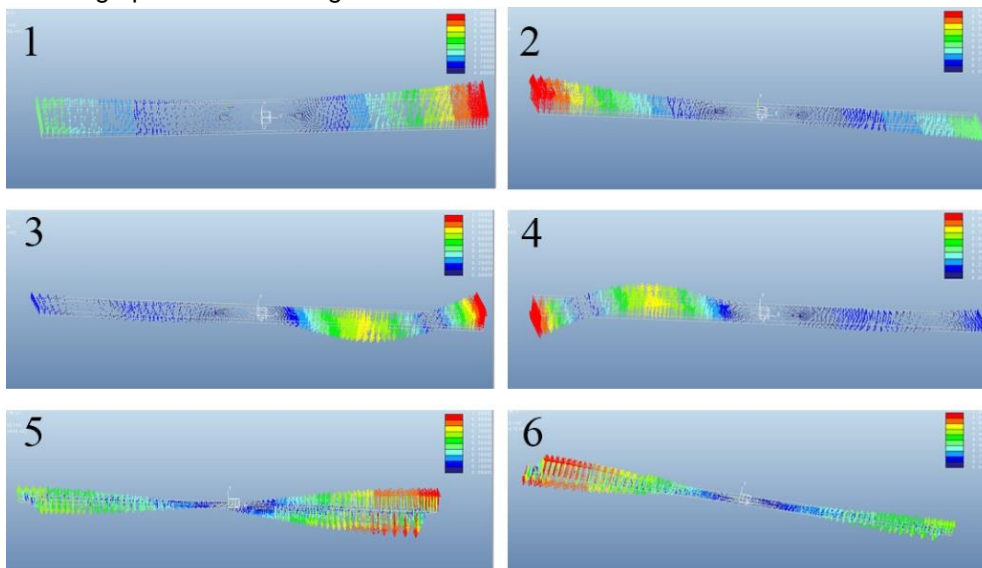


Fig. 7 – Vibration patterns of cutting blades

Since the main shaft that fixed the cutting blades was well installed with gearbox, the vibration increased gradually with the radius of the cutting blades. Therefore, the cutting edges of the blades were susceptible to damage of bending due to vibration, and the natural frequency and limited velocity of the first six orders were obtained by the modal analysis, as shown in Tab. 2. The minimum limited velocity of cutting blades among these orders was 5506.566 r/min, which corresponded to natural frequency of the first order. As for the present study, revolution speed of cutting blades was 3500 r/min, and it was far below the minimum limited velocity. Therefore, no resonance would occur during the grass cutting with the parameter design, and the safety and reliability of lawn mower could be guaranteed.

Table 2

Vibration modal orders	Frequency	Limited velocity
	[HZ]	[r/min]
1	91.7761	5506.566
2	92.1708	5530.248
3	322.952	19377.12
4	324.990	19499.40
5	463.691	27821.46
6	466.466	27897.96

### Field test

A small rotary lawn mower was developed according to the structure and parameter design. The field test was conducted in a grassland near Southwest University. The outlook of grassland for test was shown in Fig. 8, and the quality of the grass cutting was shown in Fig. 9. The height of grass stalks was about 200 mm, the height of remained stubbles was about 50 mm, and the length of cut grass was distributed in the range of 30-60 mm. The performance of the grass cutting met the requirements of forage production. At the same time, the small rotary lawn mower showed good passing ability and adaptability in the test grassland.



Fig.8 – Grassland for test: (a) before mowing; (b) after mowing



Fig. 9 – Measurement of grass stalk, stubble and cut grass

### CONCLUSIONS

In this study, the structure and parameter design of a small rotary lawn mower single-disc type was defined according to empirical formula, performance of grass cutting and modal analysis of the cutting blades were conducted by means of EDEM and Creo, and field test was conducted to verify the overall performance of the rotary lawn mower. Main conclusions were drawn as follows:

- Rotary lawn mower single-disc type is suitable for forage grass cutting in hilly land areas. Two cutting blades with revolution speed 3500 r/min and forward speed 1.4 m/s showed good performance of grass cutting and stability of the mower.
- The distribution of grass particles revealed to be uniform that proved good harvest and gathering effect of the lawn mower. The move of grass particles agreed with real application. The revolution speed of 3500 r/min was far below the limited velocity from modal analysis, and resonance could be avoided for the lawn mower.
- Field test of the rotary lawn mower showed good performance of grass cutting, good passing ability and adaptability. The height of remained stubbles was about 50 mm, and the length of cut grass was distributed in the range of 30-60 mm, which met requirements of forage production.

## ACKNOWLEDGEMENTS

The study was funded by Fundamental Research Funds for the Central Universities, China (No. XDJK2018AC001).

## REFERENCES

- [1] Chen, J., Zhou, H., Zhao, Z., Li, Y. M. and Gong, Z. Q., (2011), Analysis of Rice Seeds Motion on Vibrating Plate Using EDEM (基于 EDEM 的振动种盘中水稻种群运动规律研究), *Transactions of the Chinese Society for Agricultural Machinery*, vol. 42, issue 10, pp. 79-83, 100, Ed. Chinese Society for Agricultural Machinery, Beijing / P.R.C.; <http://doi.org/10.3969/j.issn.1003-188X.2009.06.069>
- [2] Chinese Academy of Agricultural Mechanization Sciences, (2007), Agricultural Machinery Design Manual (农业机械设计手册), *China Agricultural Science and Technology Press*, Beijing / P.R.C.;
- [3] Dong, D. J., Chen, H. X., (2002), Analysis of Blade Line of Hob Mower (滚刀式铡草机刀片刃线分析), *Journal of Agricultural Mechanization Research*, issue 2, pp. 41-42, Ed. Heilongjiang Society of Agricultural Machinery, Harbin / P.R.C.; <http://doi.org/10.3969/j.issn.1003-188X.2002.02.015>
- [4] Fu, M. Z., (2009), Current Situations and Trends of Forage Grass Harvester (牧草收割机械的现状和发展趋势), *Journal of Agricultural Mechanization Research*, vol. 31, issue 6, pp. 237-239, Ed. Heilongjiang Society of Agricultural Machinery, Harbin / P.R.C.; <http://doi.org/10.3969/j.issn.1003-188X.2009.06.069>
- [5] Fu, M. Z., Tian, J. W., Chen, D. J. and He, Y., (2018), Design of a Small Rotary Mower (小型旋转式割草机研究设计), *Journal of Agricultural Mechanization Research*, vol. 40, issue 7, pp. 116-119+130, Ed. Heilongjiang Society of Agricultural Machinery, Harbin / P.R.C.; <http://doi.org/10.3969/j.issn.1003-188X.2018.07.021>
- [6] He, Z. Q., Guo, Z. P., Li, F. W., Yang, L. and Dong, Z. Y., (2020), Experimental Study on Working Characteristics of Cutting Knives of Wide Mower (宽幅割草机割刀工作特性试验研究), *Journal of Agricultural Mechanization Research*, vol. 42, issue 10, pp. 122-129, Ed. Heilongjiang Society of Agricultural Machinery, Harbin/ P.R.C.; <http://doi.org/10.13427/j.cnki.njyi.2020.10.022>
- [7] Ma, X. C., (2005), *Design and Dynamic Research of Mower (割草机的设计与动态特性研究)*, Master dissertation, Northeast Forestry University, Harbin / P.R.C.;
- [8] Moysey, P. A., Thompson, M. R., (2005), Modelling the solids inflow and solids conveying of single-screw extruders using the discrete element method, *Powder Technology*, vol. 153, issue 2, pp. 95-107, Ed. Elsevier Sci Ltd, Oxford/England; <http://doi.org/10.1016/j.powtec.2005.03.001>
- [9] Owen, P. J., Cleary, P. W., (2010), Screw conveyor performance: comparison of discrete element modelling with laboratory experiments, *Progress in Computational Fluid Dynamics*, vol. 10, issue 10, pp. 327-333, Ed. Inderscience Enterprises Ltd, Geneva / Switzerland; <http://doi.org/10.1504/PCFD.2010.035366>
- [10] Shimizu, Y., Cundall, P. A., (2001), Three-Dimensional DEM Simulations of Bulk Handling by Screw Conveyors, *Journal of Engineering Mechanics*, vol. 127, issue 9, pp. 864-872, Ed. American Society of Civil Engineers, VA/ U.S.A.; [https://doi.org/10.1061/\(ASCE\)0733-9399\(2001\)127:9\(864\)](https://doi.org/10.1061/(ASCE)0733-9399(2001)127:9(864))
- [11] Stone, A. A., Gulvin, H. E., (2007), *Machines for Power Farming*[J]. John Wiley & Sons, New York / U.S.A
- [12] Wang, G. Q., Hao, W. J. and Wang, J. X., (2010), *Discrete element method and its application in EDEM (离散单元法及其在 EDEM 上的实践)*, Northwestern Polytechnical University Press, Xi'an/P.R.C.;
- [13] Wang, D. Z., Wang, D. J., Qi, S. W. and Wang, H. Z., (2003), A Design of 9GYS-0.85 Type Tray Style Throw Falchion Grass Cutter (9GYS-0.85 型盘式甩刀割草机的设计), *Journal of Agricultural Mechanization Research*, issue 1, pp. 90-92, Ed. Heilongjiang Society of Agricultural Machinery, Harbin/ P.R.C.; <http://doi.org/10.3969/j.issn.1003-188X.2003.01.037>
- [14] Xie, Y. F., Yao, S. B., Deng, Y. J., Jia, L., Li, Y. Y. and Gao, Q., (2020), Impact of the 'Grain for Green' Project on the Spatial and Temporal pattern of Habitat Quality in Yan'an City, China, (延安市退耕还林(草)工程对生境质量时空格局的影响), *Chinese Journal of Eco-Agriculture*, vol. 28, issue 4, pp. 575-586, Ed. Institute of Genetics and Developmental Biology, Beijing / P.R.C.; <http://doi.org/10.13930/j.cnki.cjea.190762>

- [15] Yang, L., (2019), Research situation and development tendency of herbage mower (牧草割草机研究现状与发展趋势), *Journal of Chinese Agricultural Mechanization*, vol. 40, issue 11, pp. 35-40, Ed. Nanjing Institute of Agricultural Mechanization, Ministry of Agriculture and Rural Affairs, Nanjing / P.R.C.; <http://doi.org/10.13733/j.jcam.issn.2095-5553.2019.11.06>
- [16] Yao, Y. P., Meng, W. J., Liao, Z. C. and Niu, S. S., (2015), Study on horizontal screw conveyors efficiency of flat bottomed bins based on EDEM simulation (平底仓系统水平螺旋输送机效率 EDEM 仿真研究), *Modern Manufacturing Engineering*, issue 2, pp. 6-11, 29, Ed. Beijing Mechanical Engineering Society, Beijing/P.R.C.; <http://doi.org/10.3969/j.issn.1671-3133.2015.02.003>
- [17] Yang, S. K., Su, Z. F., (2009), *Forage production machinery and equipment* (饲草生产机械与设备), China Agriculture Press, Beijing / P.R.C.;
- [18] Yang, H. W., Zhang, Y. H., (2016), Development Situation of Lawn Mower at Home and Abroad (国内外割草机械发展概况), *Agricultural Engineering*, vol.6, issue 4, pp. 19-20, Ed. Beijing Prominion Publishing Co., Ltd, Beijing/P.R.C.; <http://doi.org/10.3969/j.issn.2095-1795.2016.04.006>
- [19] Zhang, N., (2014), *Kinetic Analysis and Virtual Prototype Design of the Dual Disc Mower Crucial Components* (双圆盘割草机关键部件的虚拟样机设计及动力学分析), Master dissertation, Inner Mongolia Agricultural University, Hohhot / P.R.C.

## MOVEMENT STABILITY OF A SECTION OF THE MACHINE FOR BLACK FALLOW CULTIVATION IN A LONGITUDINAL-VERTICAL PLANE

/

### СТІЙКІСТЬ РУХУ СЕКЦІЇ МАШИНИ ДЛЯ ОБРОБКИ ПАРІВ В ПОЗДОВЖНЬО-ВЕРТИКАЛЬНІЙ ПЛОЩИНІ

V. Bulgakov<sup>1</sup>, S. Ivanovs<sup>2</sup>, V. Nadykto<sup>3</sup>, V. Kaminskiy<sup>4</sup>, L. Shymko<sup>1</sup>, H. Kaletnik<sup>5</sup>

<sup>1</sup>National University of Life and Environmental Sciences of Ukraine,

<sup>2</sup>Latvia University of Life Sciences and Technologies, Latvia,

<sup>3</sup>Dmytro Motornyi Tavria State Agrotechnological University Ukraine,

<sup>4</sup>National Science Centre "Institute of Agriculture of NAAS", Ukraine,

<sup>5</sup>Vinnitsia National Agrarian University, Ukraine

\*Correspondence: Tel.+37129403708, e-mail: [semjons@apollo.lv](mailto:semjons@apollo.lv)

DOI: <https://doi.org/10.35633/inmateh-62-10>

**Keywords:** soil, black fallow, harrow, stability of movement

#### ABSTRACT

One of the tasks of using the black fallow in agricultural production is the weed control and the moisture conservation in the soil. Application of the most advanced soil cultivation technologies ensures preservation of no more than 75% of precipitations in the soil. To improve the state of this issue, we have developed a special machine for processing the black fallow. A mathematical model has been developed that describes the dynamics of the movement of the harrow section in a longitudinal-vertical plane, and its solution is given, which allows investigation of the impact of this or that design parameter upon the dynamics of the angle of rotation in time. The adequacy of the developed mathematical model is confirmed by special laboratory and field investigations of the created experimental machine. With rational design parameters the rotation angle of the harrow section in a longitudinal-vertical plane will not exceed – 3°, and the time of its exit to the equilibrium position will not exceed 16...17 s.

#### АНОТАЦІЯ

До основних завдань застосування парів в сільськогосподарському виробництві є боротьба з бур'янами та збереження ґрунтової вологи. Застосування найсучасніших технологій обробки ґрунту забезпечує збереження в ґрунті не більше 75% вологи. Для поліпшення стану у даному питанні нами розроблена спеціальна ґрунтообробна машина для обробки парів та проведено її дослідження. Розроблено математичну модель, що описує динаміку руху боронувальної секції в поздовжньо-вертикальній площині і приведено його розв'язування, яке дозволяє визначати вплив того чи іншого конструктивного параметра на динаміку зміни в часі кута її повороту. Адекватність розробленої математичної моделі підтверджено спеціальними лабораторно-польовими дослідженнями на створеній експериментальній установці. Встановлено, що при раціональних конструктивних параметрах значення кута повороту боронувальної секції в поздовжньо-вертикальній площині не перевищить – 3°, а час її виходу в рівноважний стан не перевищить 16...17 с.

#### INTRODUCTION

The main objectives of the use of the fallow in agricultural production are the weed control and the conservation (or even accumulation) of the soil moisture. Under arid farming conditions the second objective comes to the first place (Chang *et al.*, 1990). The lack of moisture in the sowing layer of the soil leads to a delay in sowing the crops. And this inevitably leads to a decrease in their productivity (Donaldson *et al.*, 2001).

But practice shows that even the application of modern soil cultivation technologies ensures the preservation in it of no more than three quarters of the precipitations falling over the entire period of the fallow treatment (Masse *et al.*, 1978). The remainder moisture, according to these and other researchers (Riar *et al.*, 2010), evaporates from the soil. In addition, they emphasise that the period of the soil retention in the state of the fallow lasts approximately 21 months. And, if at least 1/10 of the lost moisture could be additionally saved during this time, the yield of the cultivated crops could increase up to 25% (Adamchuk *et al.*, 2020).

There are several ways how to reduce the soil moisture loss when cultivating the black fallow. One of them is the use of such a soil cultivation system in which at least 30% left from the previous crop remain on its surface (Schillinger, 2001; Schillinger et al., 2006).

The second way is mechanical treatment of the fallow combined with chemical treatment of the weeds with herbicides (Smith and Young, 2000; Smith et al., 1996).

A fairly common method of reducing the moisture evaporation during the fallow processing is to create an upper mulching layer from the loosened soil (Al-Mulla et al., 2009; Massee et al., 1978; Schillinger and Papendick, 1997).

The unifying aspect of the above ways of reducing the soil moisture loss when processing the fallow is the tillage depth at a level of at least 10 cm (4 in.). And this is quite natural if we take into account the form and parameters of the working tools of the tillage machines to be used. As a rule, these are the disk harrows and heavy cultivators (Lindwall and Anderson, 1981), machines with V-shaped blades of working tools with the operating width of 75 cm or more (Schillinger and Papendick, 1997; Smith et al., 1996).

At the same time, already in 1909, the Russian scientist and practitioner I. Ovsinskiy convincingly proved that the depth of the mulching layer of the soil should not exceed two inches (2 in.), that is, it should be equal to 5...6 cm (Ovsinskiy, 2014). But, as established by our studies, it is in this layer that the most intensive evaporation of moisture from the treated soil occurs.

Hence it follows that, when processing the fallow field to a depth of 2 in., the degree of mixing of the soil, and especially bringing its moisture to the day surface of the field should be minimal. As practice shows, the above-mentioned working tools of the currently used tillage machines cannot satisfy such requirements. Even the use of single row disc tools or bar harrows (Schillinger and Papendick, 1997), in principle, capable of cultivating the soil to a depth of 2 in., does not solve the problem. First of all, because they (especially the disk harrows) mix the cultivated soil layer sufficiently intensively.

Based on the foregoing, we have developed a special machine for the treatment of the fallow, consisting of several harrow sections of a new design (Fig. 1).

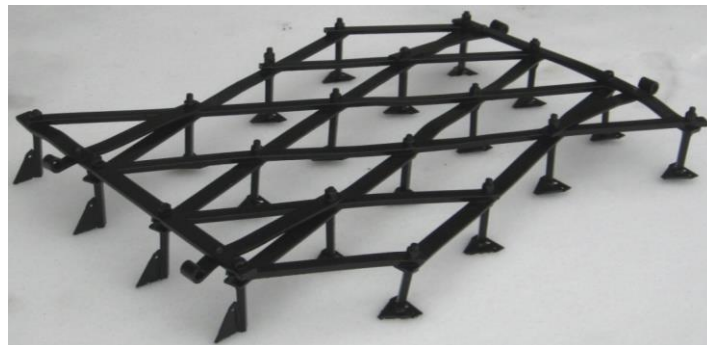


Fig. 1 - The harrow section of a new design

Each of them has 20 working tools (5 rows of 4 tools in a row) mounted on a frame according to the law of a “zigzag” harrow.

The working tool of the section is a flat rod (tooth), 8 mm thick, with a flat blade, welded to it, with the operating width of 80 mm. The front row of the working tools of the section may be equipped with vertically mounted blades. By means of two links each section is attached to a beam, which, in turn, is connected to the aggregating tractor. One of the problematic issues of the operation of such a section is the stability of its movement in the longitudinal-vertical plane.

Properly selected design parameters of the section should provide a minimum deviation of its frame from the horizon. Besides, the duration of the transition of the section as a dynamic system from one steady state to another should be as small as possible. These are the problems the solution of which is the objective of the research, the results of which are presented in this article.

## METHODS AND MATERIALS

First, we will consider theoretically the conditions for stable movement of the tillage (harrow) section in the longitudinal-vertical plane, for which we construct an equivalent scheme 2).

In the process of the working movement, caused by the action of force  $P$ , the deviation of the harrow section from a stable position can manifest itself in the form of its rotation angle by an angle  $\beta$  relative to the axis which is perpendicular to the longitudinal-vertical plane  $XOY$  and passes through point  $O$ .

Derivation of differential equations of such angular oscillations of the tillage section was carried out taking into account the following assumptions.

1. The gravity force of the harrow section  $G$  is concentrated at point  $C$  (see Fig. 2) which is located in the plane of the middle row of its teeth.

2. The traction resistance of the section is represented by the horizontal  $R_{xc}$  and vertical  $R_{yc}$  components applied in its “centre of resistance” (point  $D$ ).

3. The rotation angle of the harrow section  $\beta$  is such that for it the following relations are true:  
 $\sin \beta \approx \beta$ ;  $\cos \beta \approx 1$ .

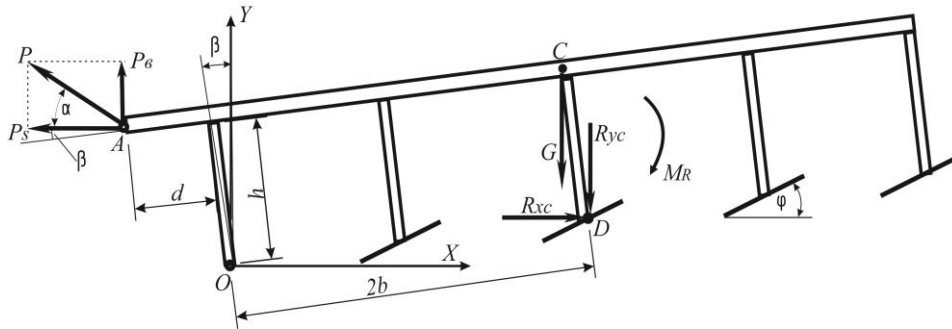


Fig. 2 - An equivalent scheme of forces acting upon the harrow section in a longitudinal-vertical plane

In its final form, the mathematical model describing the dynamics of the harrow section movement in a longitudinal-vertical plane has the form:

$$\ddot{\beta} + K_2 \cdot \dot{\beta} + K_1 \cdot \beta = K_o, \tag{1}$$

where  $K_2 = 30 \cdot K_s \cdot b^2 \cdot J_o^{-1}$

$$K_1 = [P_s \cdot (d + 1.6b + \tan \alpha \cdot h) - G \cdot h] \cdot J_o^{-1}$$

$$K_o = -0.4b \cdot P_s \cdot \cot(\varphi + \varphi_o) \cdot J_o^{-1}$$

$J_o$  – the inertia moment of the harrow section relative to the axis that is perpendicular to the  $XOY$  plane and passes through point  $O$ , [N·m·s<sup>2</sup>] (see Fig. 2);

$K_s$  – the coefficient of resistance to the vertical movement of the working tools of the harrow section in the soil, [N·s·m<sup>-1</sup>];

$\alpha$  – the inclination angle of the harrow, [deg.];

$\varphi$  – the angle of installation of the harrow tooth segment to the horizon, [deg.];

$\varphi_o$  – the angle of the soil friction along steel or the soil, [deg.];

$b, d, h$  – the design parameters of the harrow section, as understood from Fig. 2.

The solution of equation (1) has the following form:

$$\beta = \frac{K_o}{K_1} + e^{\frac{1}{2}(-K_2 + \sqrt{K_2^2 - 4K_1})t} \cdot \frac{K_o \cdot (-K_2 - \sqrt{K_2^2 - 4K_1})}{2K_1 \cdot \sqrt{K_2^2 - 4K_1}} - e^{\frac{1}{2}(-K_2 - \sqrt{K_2^2 - 4K_1})t} \cdot 2 \cdot \frac{K_o \cdot (-K_2 + \sqrt{K_2^2 - 4K_1})}{2 \cdot K_1 \cdot \sqrt{K_2^2 - 4K_1}}. \tag{2}$$

Equation (2) allows investigation of the impact of one or another design parameter of the harrow section upon the dynamics of the time variation of its rotation angle  $\beta$  in a longitudinal-vertical plane. In addition, the vector (or direction) of mathematical simulation determines such a value of the corresponding structural

parameter that will provide the shortest possible time for the dynamic system (i.e., the harrow section) to reach stable equilibrium, provided that its rotation angle  $\beta$  is as small as possible.

To test the mathematical model (2) for adequacy, special laboratory and field experimental investigations were performed. As a physical object there was chosen an aggregate consisting of an electrified minitractor, aggregated with one harrow section (Fig. 3).



Fig. 3 - The harrow aggregate, composed on the basis of an electrical mini tractor

The harrow section of this aggregate was attached to a minitractor, using tensometric fingers. On the axis of one of them (3, Fig. 4), sensor 2 was installed in the form of a variable resistance SP-3A (Ukraine) with a linear characteristic and a nominal resistance of 470 Ohm. The rotor of this resistance was connected to leash 1, which was constantly in contact with the frame of the harrow section. The rotation of the latter in the longitudinal-vertical plane through leash 1 carried out the corresponding rotation of the resistance stator 2. The corresponding electrical signal, generated from sensor 2, was transmitted to an analogue-to-digital converter (ADC), which, together with the power supply and the computer, was mounted on the minitractor (Fig. 5).

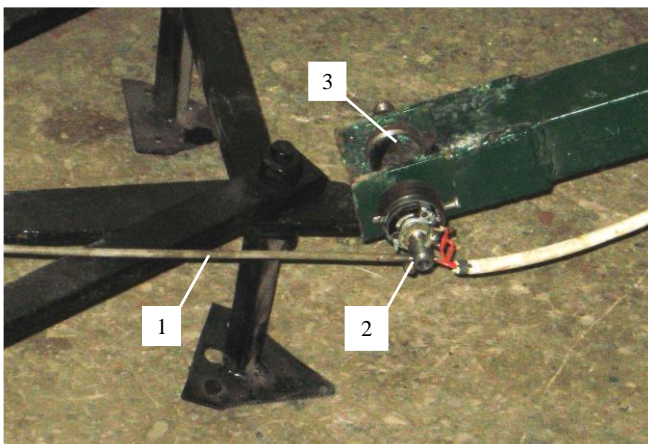


Fig. 4 - Installation of leash (1) and the angle sensor (2) of the harrow turn on its tensometric finger (3)



Fig. 5 - Installation of the ADC (1), the power supply (2) and the computer (3) on the tractor

The ADC digitalised data array in the form of the rotation angle of the harrow  $\beta$  entered the computer and was formed as an array, suitable for being processed by a graphical software environment (in this case, the Grapher 7 program).

The graphical dependence  $\beta = f(t)$ , constructed in this case, was compared with the calculated one, obtained in Mathcad 15.0 from equation (2).

Along with the signal from the SP-3A sensor, signals from the tensometric fingers of the harrow section were sent to the computer via the ADC (position 3, Fig. 4). These data were also generated in the form of digital arrays and were used to determine force  $P_s$  (Fig. 2).

To calculate equation (2), the following values of the parameters included in it were taken:  $b = 0.15 - 0.45$  m ;  $h = 0.08 - 0.14$  m ;  $d = 0 - 0.20$  m ;  $\alpha = 0 - 20^\circ$  ;  $\varphi = 5^\circ$  .

Considering the fact that the initial stage of using this tillage machine usually occurs when the soil moisture is 20...24%, the friction angle for it ( $\varphi_o$ ) and the resistance coefficient of the vertical movement of the working tools in it ( $K_s$ ) were assumed to be constant and equal to:  $\varphi_o = 60^\circ$   $K_s = 5000 \text{ N} \cdot \text{s} \cdot \text{m}^{-1}$ .

In order to determine the inertia moment of the harrow section in the longitudinal-vertical plane, it (the section) was regarded as a rectangle, the height of which was taken equal to the height of the tooth  $h$ .

The inertia moment of the section was calculated using the following expression:

$$J_o = \frac{G}{g \cdot 12} \cdot (52 \cdot b^2 + 12 \cdot h^2), \quad (3)$$

where  $g = 9.81 \text{ m} \cdot \text{s}^{-2}$  – the acceleration of gravity;  $G$  – the force of weight of the harrow section, variable within 250...450 N.

The laboratory and field investigations of the aggregate took place in spring against an agrotechnical background, where the precursor was sunflower. After harvesting this crop, the stubble was twice (with an interval of two weeks) traversed with a disk harrow to the depth of 12...14 cm.

At the time of the laboratory and field experimental studies, in addition to the above parameters, the soil moisture and density in the layer of 0...10 cm, as well as the speed of the movement of this harrow aggregate, were measured.

To measure the soil moisture, an MG-44 electronic device (MirAgro, Ukraine) was used with a measurement accuracy of  $\pm 0.1\%$ .

The soil density was measured by means of an instrument the electronic scale of which allows immediate display of the value of the measured parameter in  $\text{g} \cdot \text{cm}^3$ .

The time ( $t_a$ ) for the aggregate to pass the test section with a length of  $L = 250 \text{ m}$  was recorded using an FS-8200 electronic stopwatch with a measurement accuracy of 0.1 s. The speed of the movement of this harrowing machine-and-tractor aggregate  $V_a$  was calculated according to the formula:

$$V_a = L \cdot (t_a)^{-1}. \quad (4)$$

All the measurements in the process of the laboratory and field research were performed in triplicate.

## RESULTS AND DISCUSSION

The conditions for experimental laboratory and field investigations of the harrow aggregate are presented in Table 1.

Table 1

The conditions for experimental laboratory and field investigations of the harrow aggregate	
Indicator	Value
Type of the soil	Dark chestnut chernozem (black soil)
Relief	Flat
Microrelief	Levelled
Agricultural background	Disc-harrowed sunflower stubble
Soil humidity in a layer of 0...10 cm, %	21.5
Soil density in a layer of 0...10 cm, $\text{g} \cdot \text{cm}^{-3}$	1.14

As already emphasised above, in the process of checking the adequacy of a mathematical model of the plane-parallel movement of the harrow section, its traction resistance and the angle of rotation in a longitudinal-vertical plane were recorded. The investigated aggregate moved in the same gear in all experiments.

The analysis of the experimental data showed that the speed of the aggregate in all the experiments varied within the range of  $2.00 \pm 0.01 \text{ m} \cdot \text{s}^{-1}$ , the average traction resistance of the harrow section  $P_s$  being equal to 1500 N. It is this value of force  $P_s$  that was used in the calculation of equation (2).

The rotation angle of the harrow section varied in the confidence interval  $\beta = -2.80 \pm 0.03 \text{ deg}$ . The dispersion of the fluctuations of this angle was 0.0422 square degrees, and the coefficient of variation was 7.3%.

Comparison of the theoretical [calculated, using expression (2)] and theoretical processes of changing the angle of rotation of the harrow section in a longitudinal-vertical plane in time showed that the maximum difference between the analytical and the field data is not constant (Fig. 6).

Within the transient process of the movement of the considered dynamic system ( $t=0\ldots 0.7$  s) this difference may reach 40% (for  $t=0.2$  s, for example). At the same time, outside this rather short-term range ( $t>0.7$  s, Fig. 6), the difference between the calculated and the experimental data does not exceed 20%. Besides, it should be borne in mind that the condition of a steady-state movement of the harrow section, in contrast to the short-term transitional one, is decisive. With this in mind, the indicated difference (<20%) between the field data and the results of mathematical simulation points to the adequacy of the developed mathematical model of plane-parallel movement of the harrow section. And this gives the right to use it (i.e., the model) for further mathematical simulation in order to justify reliable design parameters of the developed tillage machine.

The results of such modelling show that the fluctuations of the angle of rotation of the harrow section in the longitudinal-vertical plane relative to point O (see Fig. 2) are of an aperiodic nature (Fig. 7).

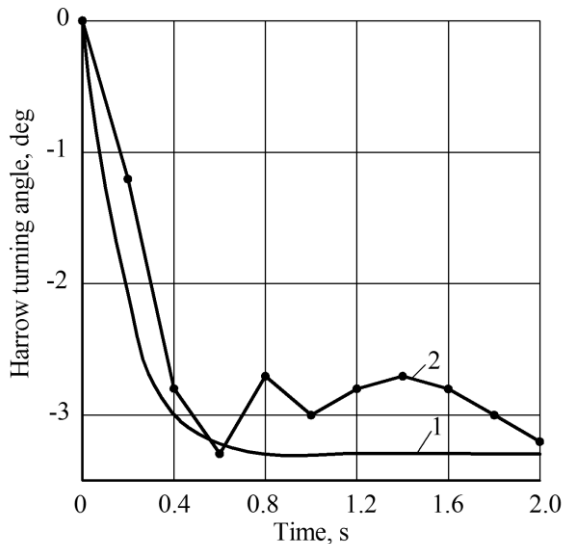


Fig. 6 - Theoretical (1) and experimental (2) dynamics of angle  $\beta$  changes in time

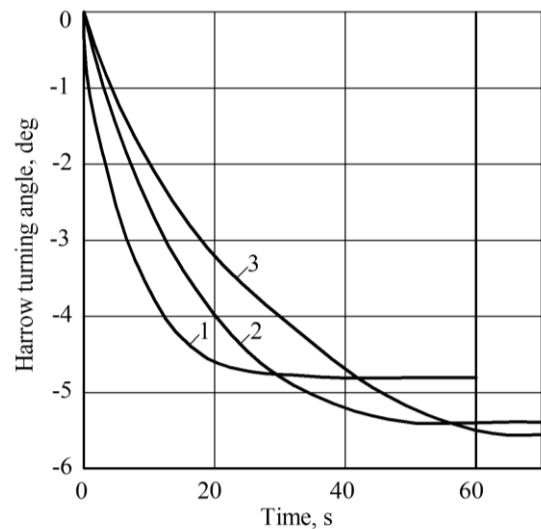


Fig. 7 - Dynamics of changes in the angle of rotation of the harrow section at different distances between the rows of its teeth: 1 –  $b = 0.15$  m; 2 –  $b = 0.30$  m; 3 –  $b = 0.45$  m

In the process of the movement the harrow makes angular clockwise deviations. From Fig. 2 it follows that such a direction of its rotation is negative, which is reflected by the corresponding sign of the parameter  $\beta$ .

Analysis of the data, presented in Fig. 7, shows that the larger the longitudinal distance between the rows of the teeth of the harrow section (parameter  $b$ ), the longer the time it takes for it to reach the steady-state position. So, if at a value  $b = 0.15$  m the steady-state movement of the harrow occurs after 20 s (Curve 1, Fig. 7), then at  $b = 0.45$  m this state of the dynamic system takes place not earlier than 65 s (Curve 3).

Moreover, if in the first case the harrow deviates by an angle of  $-4.8^\circ$ , then in the second case this indicator increases to  $-5.8^\circ$ . Although the difference between the values of angle  $\beta$  is only  $1^\circ$ , the tendency of the behaviour of the considered dynamic system changes. In this case it is the following: the smaller the value of the parameter  $b$ , the smaller the amplitude of the deviation of the tillage section from the horizontal position, and the shorter the time period for it to reach the condition of equilibrium.

The opposite (in the quality terms) impact upon the angle of rotation of the harrow section in the longitudinal-vertical plane is made by the coordinate of the offset of its leashes' attachment point. So, when establishing them with the offset  $d = 0$  (see Fig. 2), the steady movement of the harrow occurs only after 70 s, and it is characterised by a negative slope (rotation) of the tillage section by angle  $\beta = -6.5^\circ$  (Curve 1, Fig. 8).

Increasing the value of parameter  $d$  to 0.10 m, the steady-state movement of the harrow section starts approximately at the same time (that is, 70 s), yet the angle of its deviation decreases to  $-5.7^\circ$  (Curve 2, Fig. 8).

At the same time, increasing the offset of the attachment point of the harrow section leashes to  $d = 0.20$  m, the transition time to its steady movement starts after 38 s, i.e., it increases practically two times (compared with the previous two versions). The deviation angle of the harrow from its horizontal position also decreases, and it is  $-4.6^\circ$  (Curve 3, Fig. 8). It is clear that this is a positive factor.

In contrast to the structural parameters, analysed above, the inclination angle of the harrow section leashes  $\alpha$  has little impact upon its rotation dynamics in the longitudinal-vertical plane. Changing this parameter from 0 to  $20^\circ$  helps reducing angle  $\alpha$  by only  $0.5^\circ$  (Fig. 9).

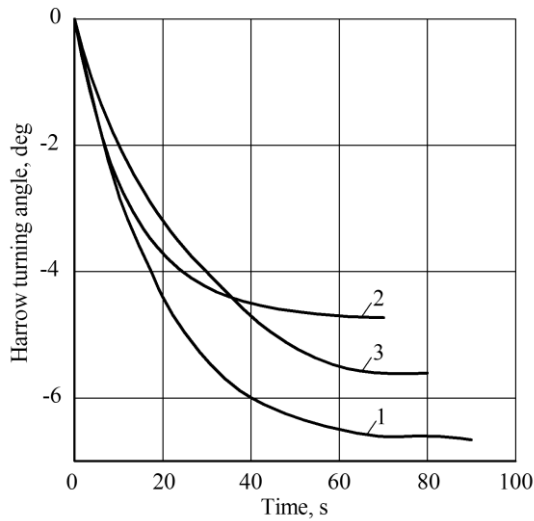


Fig. 8 - Dynamics of the angle of rotation of the harrow section with different offsets of its leashes' attachment point: 1 –  $d = 0$ ; 2 –  $d = 0.10$  m; 3 –  $d = 0.20$  m

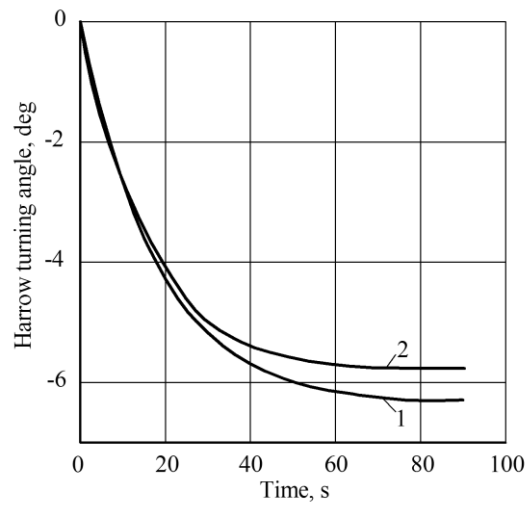


Fig. 9 - Dynamics of changes in the angle of rotation of the harrow section at different inclination angles of its leashes: 1 –  $\alpha = 0$ ; 2 –  $\alpha = 20^\circ$

An even smaller impact upon the angle of deviation of the harrow section from the horizontal position is exerted by its force of gravity  $G$  and the height of the teeth  $h$ . When changing these design parameters within the above ranges, the angle of rotation of the harrow  $\beta$  changes within the range  $0.15...0.20^\circ$ .

The analysis of the above material allows choosing such values of the structural parameters which cause a decrease in the angle of deviation of the harrow from the horizontal position and the time it takes to reach a new equilibrium state. Thus, the calculations show that at  $P_s = 1500$  N ,  $G = 300$  N ,  $\varphi = 5^\circ$  ,  $\varphi_o = 60^\circ$  ,  $\alpha = 25^\circ$  ,  $h = 0.14$  m ,  $b = 0.15$  m and  $d = 0.25$  m, the value of the rotation angle of the harrow section in the longitudinal-vertical plane  $\beta$  will not exceed  $-3^\circ$  (Fig. 10).

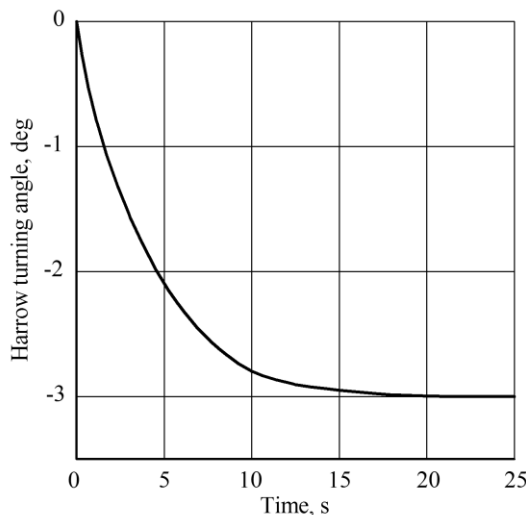


Fig. 10 - Dynamics of the angle of rotation of the harrow section with rational values of its design parameters

The exit of the section from the transition mode to the mode of a new equilibrium state does not exceed 16...17 s, and it is of a purely aperiodic nature.

## CONCLUSIONS

1. The smaller is the distance between the rows of teeth of the harrow section  $b$ , the smaller is the amplitude of its deviation from the horizontal position, and the less time it takes to reach the steady-state position. It has been established by calculations that reducing parameter  $b$  three times (from 0.15 to 0.45 m) with a smaller angle of rotation of the tillage section, the time period for its entry into equilibrium decreases from 65 to 20 s (i.e., 3.25 times).

2. Increasing the offset coordinate of the attachment point of the harrow section leashes from 0 to 0.2 m, the angle of its deviation from the horizontal position and the time to reach the new equilibrium position decreases by almost half, which is the desired result.

3. At the values of parameters  $P_s = 1500 \text{ N}$ ,  $G = 300 \text{ N}$ ,  $\varphi = 5^\circ$ ,  $\varphi_o = 60^\circ$ ,  $\alpha = 25^\circ$ ,  $h = 0.14 \text{ m}$ ,  $b = 0.15 \text{ m}$  and  $d = 0.25 \text{ m}$ , the value of the rotation angle of the harrow section in the longitudinal-vertical plane will not exceed  $-3^\circ$ , and the time of its entry into the equilibrium position will not exceed 16...17 s.

## REFERENCES

- [1] Adamchuk, V., Bulgakov, V., Nadykto, V., Ivanovs, S. (2020). Investigation of tillage depth of black fallow impact upon moisture evaporation intensity. *Engineering for rural development*, Vol. 19: pp. 377-383.
- [2] Al-Mulla, Y.A., Wu, J.Q., Singh, P., Flury, M., Schillinger, W.F., Huggins, D.R., Stöckel, C.O. (2009). Soil water and temperature in chemical versus reduced-tillage fallow in a Mediterranean climate. *Appl. Eng. Agric.*, 25: pp. 45–54.
- [3] Chang, C., Sommerfeldt, T.G., Entz, T., Stalker, D.R. (1990). Long-term soil moisture status in Southern Alberta. *Can. J. Soil Sci.*, 70: pp.125–136.
- [4] Donaldson, E., Schillinger, W.F., Dofing, S.M. (2001). Straw Production and Grain Yield Relationships in Winter Wheat. *Crop Sci.*, 41: pp.100–106.
- [5] Lindwall, C.W., Anderson, D.T. (1981). Agronomic evaluation of minimum tillage systems for summer fallow in Southern Alberta. *Can. J. plant Sci.*, 61: pp.247–253.
- [6] Massee, T.W., Cary, J.W., Plains, G., Desert, A. (1978). Potential for reducing evaporation during summer fallow. *J. Soil Water Conserv.*, 33: pp.126–129.
- [7] Moreno, M.M., Lacasta, C., Meco, R., Moreno, C. (2011). Rainfed crop energy balance of different farming systems and crop rotations in a semi-arid environment: Results of a long-term trial. *Soil Tillage Res.*, 114: pp.18–27. <https://doi.org/10.1016/j.still.2011.03.006>
- [8] Nadykto, V., Kotov, O. (2015). *Method for determining soil bulk density (in Ukrainian: Sposib viznachennya shchilnosti gruntu)*. UA 97828, G 01N 1/00.
- [9] Ovsinskiy, I. (2014). *New Farming System*. Moscow (in Russian).
- [10] Riar, D.S., Ball, D.A., Yenish, J.P., Wuest, S.B., Corp, M.K. (2010). Comparison of fallow tillage methods in the intermediate rainfall inland Pacific Northwest. *Agron. J.*, 102: pp.1664–1673. <https://doi.org/10.2134/agronj2010.0054>.
- [11] Schillinger, W.F. (2001). Minimum and Delayed Conservation Tillage for Wheat-Fallow Farming. *Soil Sci. Soc. Am. J.*, 65: pp.1203–1209. <https://doi.org/10.2136/sssaj2001.6541203x>
- [12] Schillinger, W.F., Papendick, R.I. (1997). Tillage Mulch Depth Effects during Fallow on Wheat Production and Wind Erosion Control Factors. *Soil Sci. Soc. Am. J.*, 61: pp.871–876.
- [13] Schillinger, W.F., Papendick, R.I., Guy, S.O., Rasmussen, P.E., Van Kessel, C. (2006). *Dryland Cropping in the Western United States. Dryland Agriculture*. 2nd Ed., Agronomy Monograph, 23. ASA, CSSA, and SSSA, Madison, WI: pp. 365–393.
- [14] Smith, E.C., Young, D.L. (2000). Requiem for summer fallow. *Choices*: pp. 24–25.
- [15] Smith, E.G., Peters, T.L., Blackshaw, R.E., Lindwall, C.W., Larney, F.J. (1996). Economics of reduced tillage fallow-crop systems in the dark brown soil zone of Alberta. *Can. J. soil Sci.*, 76: pp.411–416. <https://doi.org/10.4141/cjss96-049>
- [16] Zhuk, A.F. (2013). Work Wedge with Soil Growths. *Mech. Electr. Agric.*, 97: pp.148-161 (in Russian).

## EXPERIMENTAL CHECKING OF MATHEMATICAL MODELS DESCRIBING THE FUNCTIONING ADEQUACY OF BRIDGE SYSTEMS IN AGRICULTURAL TRACK SYSTEM

### TILTU VEIDU UZBŪVES MATEMĀTISKĀ MODEĻA ATBILSTĪBAS EKSPERIMENTĀLA PĀRBAUDE PRAKTISKAI IZMANTOŠANAI LAUKSAIMNIECĪBAS TRANSPORTA SISTĒMĀ

Ivanovs S.<sup>1)</sup>, Bulgakov V.<sup>2)</sup>, Kuvachov V.<sup>3)</sup>, Kaletnik H.<sup>4)</sup>, Shymko L.<sup>2)</sup>, Ihnatiev Y.<sup>3)</sup> <sup>1</sup>

<sup>1)</sup> Latvia University of Life Sciences and Technologies, Latvia,

<sup>2)</sup> National University of Life and Environmental Sciences of Ukraine,

<sup>3)</sup> Dmytro Motorny Tavsia State Agrotechnological University, Ukraine,

<sup>4)</sup> Vinnytsia National Agrarian University, Ukraine

\*Correspondence: Tel. +37129403708, e-mail: [semjons@apollo.lv](mailto:semjons@apollo.lv)

DOI: <https://doi.org/10.35633/inmateh-62-11>

**Keywords:** agriculture, bridge equipment, adequacy, simulation, technology.

#### ABSTRACT

The article exposes the results of the mathematical simulation of the agricultural bridge equipment functioning. The mathematical models describing the functioning of the agricultural bridge equipment were checked for adequacy by comparing the theoretical and experimental amplitude-frequency characteristics of the oscillations of its heading angle and lateral displacement. It was established by the result of investigated characteristics' quantitative assessment that a satisfactory coincidence of the theoretical and experimental results, as well as a positive result of checking the adequacy of the mathematical models of the vertical and the horizontal oscillations of the agricultural equipment indicate a possibility of their further use for solving scientific and practical problems.

#### ABSTRACT

Rakstā aprakstīta metodika, kas paredzēta lauksaimniecības tiltu veida aprīkojuma funkcionēšanas matemātiskās modelēšanas rezultātu atbilstības pārbaudei, izmantojot dinamisko sistēmu automātiskās regulēšanas teoriju. Lauksaimniecības tiltu veida aprīkojuma darbību raksturojošo matemātisko modeļu atbilstība tika pārbaudīta, salīdzinot teorētiskos un eksperimentālos amplitūdas frekvences raksturlielumus tā virziena leņķa svārstībām un sānu pārvietojumam. Ar izpētīto kvantitatīvā novērtējuma rezultātiem tika noskaidrots, ka ir apmierinoša teorētisko un eksperimentālo rezultātu sakrītība, kā arī pozitīvs rezultāts, pārbaudot lauksaimniecības tehnikas vertikālo un horizontālo svārstību matemātisko modeļu piemērotību, norāda uz iespēju tos turpmāk izmantot zinātnisku un praktisku problēmu risināšanai.

#### INTRODUCTION

Contemporary development of science and technology cannot be imagined without a wide use of the mathematical simulation methods. In recent years, mathematical simulation as a method of studying complex technical systems in agriculture has been widely used to solve various problems. They include investigations of the new agricultural bridge equipment in order to ensure its operation by the principle of gauge and bridge farming (Chamen et al., 1994; Bochtis et al., 2010; Onal, 2012; Bulgakov et al., 2017a). According to many scientists, such agricultural bridge equipment is a prospect for the transition from the traditional tractor-harvester technologies to more modern farming. And their functioning allows solving the main contradiction in the “mover-soil” system the essence of which is that, in order to achieve high traction and adhesion properties by the energy tool, its movers must be in contact with a dry and dense base while normal growth of the cultivated plants needs an optimally moist and fluffy soil environment (Nadykto, 2017; Adamchuk et al., 2016). This is possible only if the plant growth zone (the agrotechnical zone of the field) and the track of the movers of energy tools (the technological or engineering zone) are clearly separated in the field. In such a case the movement of the energy tools becomes strictly regulated (routed), and it is provided for exclusively pre-formed tracks – constant tramlines.

<sup>1</sup> Ivanovs S., Ph.D. Eng.; Bulgakov V., Ph.D. Eng.; Kuvachov V., Ph.D. Eng.; Kaletnik H., Ph.D. Eng.; Shymko L., Ph.D. Eng.; Ihnatiev Y., Ph.D. Eng.

At the first stage of the theoretical research of the agricultural bridge tools, the mathematical simulation of their functioning, using the software and algorithmic tools and the PC, provides valuable scientific information about the dynamics of their plane-parallel movement, and much more. In this case one main circumstance should be considered that taking advantage of the methodology of mathematical simulation to study the functioning of such new technical systems is possible only if the physical reality is adequately reflected in the mathematical and computer models.

Provided that modern software environments are used (for example, Mathematica, Statistica, Mathcad, MS Excel, and the like), checking the regression mathematical models for adequacy is a formalised procedure (Nadykto, 2017).

However, this formalised methodological approach for checking mathematical models in terms of adequacy is not always acceptable and possible to be implemented. So, for example, when simulating the behaviour of complex dynamic systems, such as agricultural bridge tools, the most informative is the use of statistical dynamics methods and the theory of automatic regulation of linear dynamic systems when they reproduce statistically random control and disturbing input actions. According to this methodology, based on the constructed differential equations, transfer functions are compiled, and then the amplitude-frequency characteristics are calculated (Chamen, 2015; Bulgakov et al., 2016a; Bulgakov et al., 2018). At the same time, assessment of the adequacy of the theoretical amplitude-frequency characteristics of the development of the input disturbance by the dynamic system to be studied is a rather complicated task. Its complexity is determined by the impossibility to apply a formalised programmatic checking procedure for adequacy.

In scientific publications (Bulgakov et al., 2016b; Bulgakov et al., 2017b), a methodology for checking the adequacy of mathematical models is described, the solution of which is represented by the amplitude-frequency characteristics of the development of external disturbances acting upon it by a machine-tractor aggregate. But the algorithm itself of the hardware search and formalisation of the input and output parameters is not sufficiently presented in the indicated scientific works.

The purpose of the research is to test the methodology for checking the results adequacy of the mathematical simulation of the agricultural bridge equipment functioning, using the provisions of the theory of dynamic systems' automatic regulation to improve the quality of this procedure.

## MATERIALS AND METHODS

There were tested for adequacy a mathematical model of the agricultural bridge tools functioning in a vertical and a horizontal plane, obtained by us as a result of theoretical investigations and described in detail in the scientific papers (Bulgakov et al., 2017c; Bulgakov et al., 2019).

We will test the mathematical model of horizontal oscillations of the agricultural bridge equipment for adequacy by comparing the theoretical  $A_T(\omega)$  and experimental  $A_E(\omega)$  amplitude-frequency characteristics of oscillations of its heading angle  $\varphi$  and lateral displacement  $x_s$  (as the output values) when it (the agricultural means) works out the input control action. As the last one, the driving force of the wheels of one of the sides  $P_{0i}$  of the agricultural tool was used with the onboard power method of turning it.

The mathematical model of vertical oscillations of the agricultural bridge equipment was checked for adequacy by comparing the theoretical  $S_{Td}(\omega)$  and the experimental  $S_{Ed}(\omega)$  normalised spectral densities of its vertical oscillations. For the input parameter we took the oscillations in the irregularities of the longitudinal profile of traces of a constant tramline along which the agricultural tool is moving, and for the output parameter – the oscillations of its frame. The theoretical amplitude-frequency characteristics of the oscillations of the heading angle  $\varphi$  and the lateral displacement  $x_s$  of the agricultural bridge equipment, when it worked out the control action with the power control method, as well as when it worked out the oscillations of the irregularities of the path profile, were calculated using the corresponding transfer functions (Bulgakov et al., 2017; Bulgakov et al., 2019, Pascuzzi et al., 2020, Ivanovs et al., 2020). To determine the experimental amplitude-frequency characteristic under the laboratory and field conditions, we studied the agricultural bridge equipment in an aggregate with the tooth harrows (type BZSS-1.0) (Fig. 1), which are structurally made like harrow (Nadykto, 2013).

To conduct research under the laboratory conditions, a constant tramline was artificially created on the soil, the longitudinal profile of the irregularities of which was finally formed by multiple passes of the wheels of the agricultural tool along it. The control of the agricultural bridge equipment was carried out by the operator in a manual mode. The principle of its control was, when the agricultural bridge equipment deviates from rectilinear movement along the tracks of a constant tramline, the operator monitors the movement of a

special device. In this role was the centre of the wheel of one of the sides of the agricultural tool at the level of the supporting surface passing through the central line of the tire track. The task of the control of the agricultural tool was to ensure that the centre of its wheel at the level of the supporting surface is as close as possible to the axis of symmetry of the constant tramline.



Fig. 1 - Agricultural bridge equipment as part of a harrowing aggregate, during the research

The operator corrected deviation of the trajectory of the sighting point by reducing (almost to zero) the tangential traction force  $P_{\partial x}$  on the wheels of the agricultural tool from one of its sides. In particular, if there was a right-hand deviation of the agricultural tool from the direction of its movement, then the tangential traction force decreased on the left side wheels, and vice versa. As a result of this operator's action the agricultural tool changed its heading angle accordingly. Acceptable controllability of the movement of the agricultural bridge equipment was achieved when the duration of the control action was sufficient so that it was able to compensate for the amplitude of its heading angle or lateral displacement without leaving the wheels beyond the established constant tramline width.

In the process of experimental tests of the agricultural bridge equipment by means of an analogue-to-digital converter, a PC and a mobile communicator, there were simultaneously recorded:

- the heading angle  $\varphi$  (deg.);
- the vertical accelerations  $Z$  ( $\text{m}\cdot\text{s}^{-2}$ ) of the frame of the agricultural tool;
- duration  $\tau_{P_{\partial x}}$  (s) of the control action to restore its rectilinear movement as a result of deviation from it.

The first two parameters during experimental investigations were recorded using a mobile communicator with the Android operating system. In this software environment, using a special Accelerometer Meter application (version 1.32), there were recorded in time the digitised output signals and their frequency spectrum from the accelerometer sensors, built into the mobile communicator (Fig. 2).



a)



b)

Fig. 2 - A mobile communicator (a) and Android-based Accelerometer Meter interface (b) for measuring vertical acceleration  $Z$  and heading angle  $\varphi$  of the agricultural bridge equipment

Also, in the process of experimental investigations of the agricultural bridge equipment there was measured the amplitude  $x_s$  of its lateral deviation from the axis of symmetry of the constant tramline. For this purpose, the shortest distance from the axis of symmetry of the constant tramline to the midpoints of the trajectories of its front and rear wheels from one side with a step of 0.2 m was measured (Fig. 3).

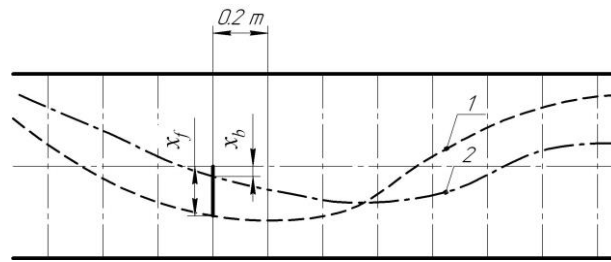


**Fig. 3 - A scheme for the determination of the agricultural tool lateral displacement:**  
1, 2 – respectively, the middle points of the trajectories of its frontal and rear wheels within the tramline

Since the amplitude of the heading angle  $\varphi$  of the agricultural bridge equipment did not exceed 6...8 degrees, the amplitude  $x_s$  of the transverse displacement of its mass centre was calculated with sufficient accuracy according to Fig. 3 by expression:

$$x_s = \frac{x_f - x_b}{2}, \quad (1)$$

where  $x_f$ ,  $x_b$  – the distances (m) from the axis of symmetry of the constant tramline to the middle of the trajectories of the frontal and rear wheels of the agricultural equipment, respectively.

The characteristics of irregularities' oscillations of the longitudinal profile of constant tramline traces were recorded using an automated profilograph with an analogue-to-digital converter and a PC (Fig. 4) according to the method, described in detail in (Bulgakov et al., 2019).



**Fig. 4 - A hardware-measuring complex for profiling the irregularities of a constant tramline traces**

From the obtained arrays of realisations of the input and output parameters, such statistical characteristics as standard deviations and normalised spectral densities were determined using the technique, presented in (Nadykto, 2017; Gmurman, 2016).

The experimental amplitude-frequency characteristic of the functioning of the agricultural bridge equipment was calculated according to expression (Nadykto, 2017):

$$A(\omega) = \frac{\sigma_y}{\sigma_x} \cdot \left( \frac{S_y(\omega)}{S_x(\omega)} \right)^{\frac{1}{2}} \quad (2)$$

where:

- $\sigma_x$ ,  $S_x(\omega)$  – the mean-square deviation and normalised spectral density of the input quantity;
- $\sigma_y$ ,  $S_y(\omega)$  – the mean-square deviation and normalised spectral density of the output quantity;
- $\omega$  – the frequency of oscillations of the control impact,  $s^{-1}$ .

The theoretical spectral density of the output parameter oscillations was found according to expression (Nadykto, V., 2017):

$$S_T(\omega) = \frac{A_T(\omega)^2 \cdot S_x(\omega) \cdot D_x}{D_y} \quad (3)$$

where:

- $S_x(\omega)$ ,  $D_x$  – the normalised spectral density and dispersion of oscillations of the input value;
- $D_y$  – dispersion of oscillations of the input value.

Dispersions of the characteristics of random processes at the output of a linear dynamic system were found according to expression:

$$D_y = \int_{\omega_{st}}^{\omega_{zr}} S_y(\omega) d\omega \quad (4)$$

where:

$\omega_{st}$ ,  $\omega_{zr}$  – the initial value of the frequency range of the spectral characteristics and the cut-off frequency.

Since the ordinate of the spectral density of oscillations of the agricultural tool frame vertical accelerations has a unit of measurement  $m \cdot s^{-2}$ , which is the implementation of the signals from the accelerometer sensors, in order to pass to the linear amplitude  $z_y$  (m), the ordinate of the points of the indicated spectral density, were recounted with some assumption and with sufficient accuracy as follows:

$$z_y = \frac{Z \cdot T^2}{2} \quad (5)$$

where:

$Z$  – acceleration of vertical oscillations according to the data of the Accelerometer Meter software environment,  $m \cdot s^{-2}$ ;

$T$  – the time, equal to the length of the correlation of the density of accelerations of the agricultural tool vertical oscillations, s.

A quantitative statistical assessment of the compared theoretical and experimental data adequacy was done by testing the null hypothesis on the equality of the compared dispersions of the initial value fluctuations according to the Fisher F-test. If the calculated value of the Fisher F-test was less than the critical value, then the zero hypothesis on the equality of the compared variances was not rejected (at a certain statistical significance level). Besides, the number of the degrees of freedom was taken equal to 10, since the graphs of the spectral density of fluctuations of the considered input and output parameters were calculated from such a number of points. In such a case the critical value of the Fisher F-criterion at a statistical significance level of 0.05 was 2.97, and at a level of 0.01, it was 4.84, respectively.

## RESULTS AND DISCUSSION

As the analysis of the obtained and processed experimental data showed, the fluctuation spectrum of the control impact of the agricultural bridge equipment with the onboard power method of its control is of low-frequency nature (Fig. 5). The main dispersion spectrum of this parameter is concentrated in the frequency range  $0 \dots 2 \text{ s}^{-1}$ , which corresponds to  $0 \dots 0.32 \text{ Hz}$ . Almost in the same frequency range, the dispersion of fluctuations of the output parameter, that is, the heading angle  $\varphi$  of the agricultural tool is also concentrated (Fig. 5). The standard of fluctuations of this parameter was  $\pm 0.014 \text{ rad}$ .

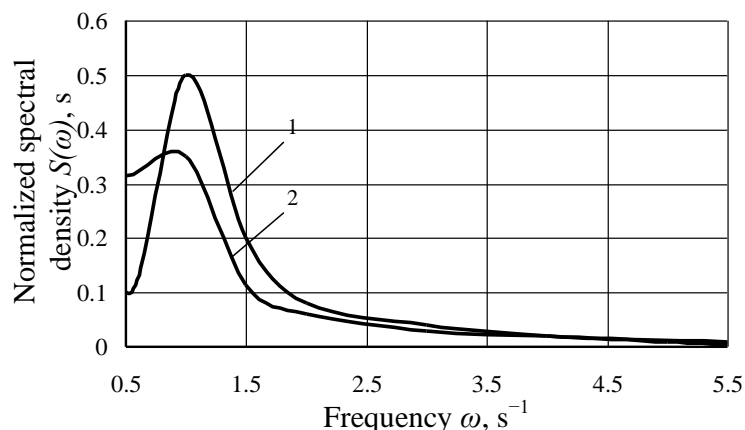


**Fig. 5 - Normalised spectral densities of fluctuations of the tangential traction force (1) of the agricultural tool and its heading angle (2)**

Further calculation of the experimental amplitude-frequency characteristic of the agricultural bridge equipment and its comparison with the theoretical characteristic (Fig. 6) showed that in the operating frequency range  $0 \dots 2 \text{ s}^{-1}$ , the difference between the fluctuations of the input and the output signals does not exceed 15%.

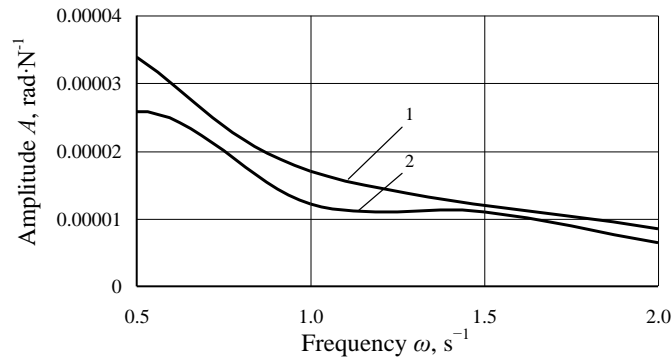


**Fig. 6 - Theoretical (1) and experimental (2) amplitude-frequency characteristics of the fluctuations in the heading angle  $\varphi$**

The result of a quantitative assessment of the characteristics in Fig. 6 showed that, according to the Fisher F-test, the null hypothesis about the equality of the compared dispersions ( $1.57 \text{ s}^2$  and  $1.67 \text{ s}^2$ ) does not deviate neither at the static significance level of 0.05 nor at the level of 0.01.

Fluctuations of the lateral displacement of the agricultural bridge equipment as part of a harrowing aggregate are also of a low-frequency nature (Fig. 7). The main spectrum of dispersions is concentrated in the frequency range  $0 \dots 2 \text{ s}^{-1}$ . The standard of fluctuations of this parameter is  $\pm 0.05 \text{ m}$ .

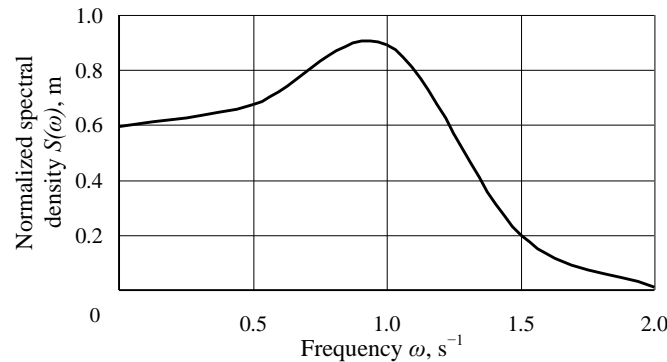


**Fig. 7 - Normalised spectral densities of fluctuations of the linear transverse displacement  $x_s$  of the agricultural bridge equipment**

Calculation of the experimental amplitude-frequency characteristic according to (2) and its comparison with the theoretical one showed (Fig. 8) that in the operating frequency range of  $0 \dots 2 \text{ s}^{-1}$  oscillations of the input signal, the greatest difference between the theoretical and the experimental data does not exceed 15%.

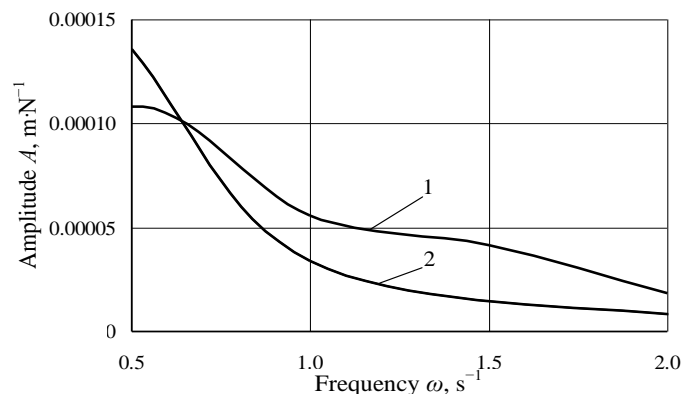


**Fig. 8 - Theoretical (1) and experimental (2) amplitude-frequency characteristics of the fluctuations of the linear transverse displacement  $x_s$  of the agricultural equipment as part of the harrowing aggregate when working out the control impact**

As a result of measuring the characteristics of the irregularities of the constant tramline tracks' longitudinal profile, a graph of the normalised spectral density of the amplitudes of their fluctuations was obtained (Fig. 9).

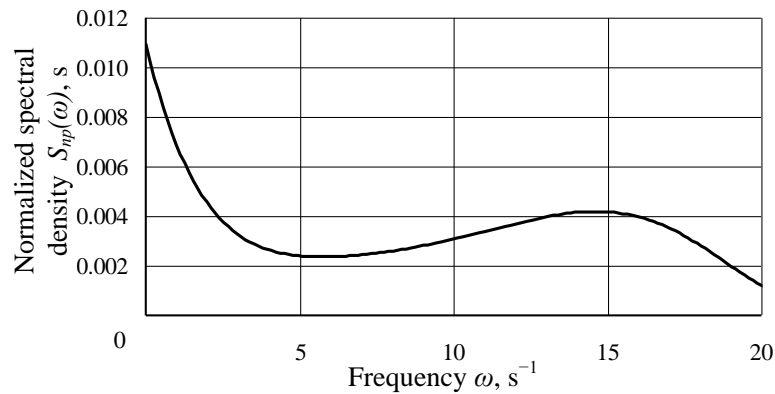


**Fig. 9 - The normalised spectral density of irregularities of the constant tramline traces' longitudinal profile, according to the hourly argument**

From the analysis of Fig. 9 it follows that the working frequency range of fluctuations in the irregularities of the constant tramline traces' profile is  $0 \dots 20 \text{ s}^{-1}$  (or  $0 \dots 3.2 \text{ Hz}$ ). In this frequency range a mathematical model of the dynamics of vertical fluctuations of the agricultural bridge equipment in a vertical plane was checked.

A comparison of the theoretical  $S_{Ta}(\omega)$  and the experimental  $S_{Ea}(\omega)$  normalised spectral densities of vertical oscillations of the frame of the agricultural bridge tool shows (Fig. 10) that both processes are characterised by approximately the same nature of the change in the frequency range.

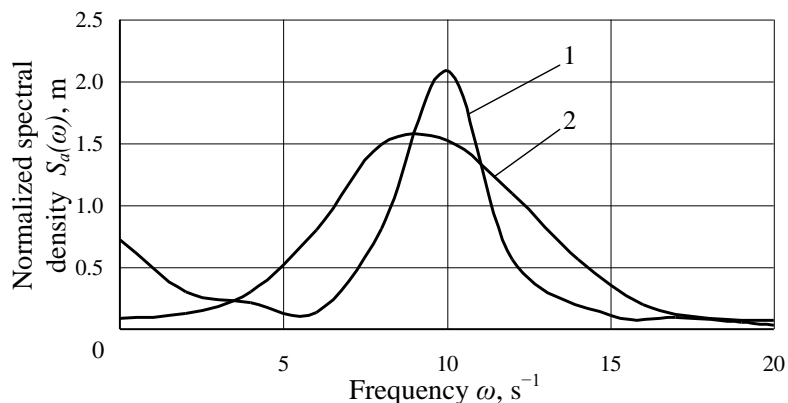


**Fig. 10 - Theoretical (1) and experimental (2) normalised spectral densities of vertical oscillations of the frame of the agricultural bridge tool**

The difference in the maximum theoretical dispersion (see Fig. 10) attributed to  $\omega_T = 10 \text{ s}^{-1}$  and the experimental one  $\omega_T = 9 \text{ s}^{-1}$  is  $1 \text{ s}^{-1}$ . As testing of the null hypothesis about the equality of the theoretical dispersion  $D_{Ta} = 1.21 \text{ sm}^2$  and the experimental dispersion  $D_{Ta} = 1.56 \text{ sm}^2$  according to the Fisher F-test showed, it does not deviate at the static significance levels of 0.05 and 0.01.

The satisfactory agreement of the above theoretical and experimental results, as well as the positive result of checking the mathematical models of the agricultural bridge equipment for adequacy, indicates the possibility of their further use for solving scientific and practical problems.

## CONCLUSIONS

Thus, the adequacy of the conducted investigations confirms the fact that mathematical simulation of functioning of the agricultural bridge tools, using the theory of automatic regulation of dynamic systems, is quite effectively verifiable. At the same time, for experimental registration of such parameters of the agricultural bridge tool as the characteristics of its heading angle and vertical movements, a mobile Android-based communicator with accelerometer sensors and the Accelerometer Meter application integrated in it is sufficient.

A positive result of checking for adequacy the functioning of the mathematical models of the TSATU agricultural bridge equipment that we developed earlier indicates the possibility of their further use for solving scientific and practical problems.

## REFERENCES

- [1] Adamchuk, V., Bulgakov, V., Nadykto, V., Ihnatiev, Y., Olt, J., (2016), Theoretical research into the power and energy performance of agricultural tractors. *Agronomy Research*, 14(5), pp.1511–1518.
- [2] Bochtis, D.D., Sørensen, C.G., Green, O., Moshou, D., Olesen, J., (2010), Effect of controlled traffic on field efficiency. *Biosystems Engineering*, 106 (1), pp. 14-25.
- [1] Bulgakov, V., Adamchuk, V., Arak, M., Nadykto, V., Kyurchev, V., Olt, J., (2016a), Theory of vertical oscillations and dynamic stability of combined tractor-implement unit. *Agronomy Research*, Vol. 14(3), pp. 689–710.
- [2] Bulgakov, V., Ivanovs, S., Adamchuk, V., Nadykto, V., (2016b), Theoretical investigation of turning ability of machine and tractor aggregate on basis of ploughing and intertilling wheeled tractor. *Engineering for Rural Development*, Vol. 15, pp.1077–1084.
- [3] Bulgakov, V., Adamchuk, V., Kuvachov, V., Ivanovs S., (2017a), Research of possibilities for efficient use of wide span tractor (vehicle) for controlled traffic farming. *Engineering for rural development*, Vol. 16, pp.281–287.
- [4] Bulgakov, V., Holovach, I., Bandura, V., Ivanovs, S., (2017b), A theoretical research of the grain milling technological process for roller mills with two degrees of freedom. *INMATEH - Agricultural Engineering*. Vol. 52(2), pp. 99-106.
- [5] Bulgakov, V., Ivanovs, S., Pascuzzi, S., Boris, A., Ihnatiev, Y., (2019). A mathematical model of the cutting process of the sugar beet leafy tops without a tracer. *INMATEH - Agricultural Engineering*, Vol. 59, pp.33–40.
- [6] Bulgakov, V., Kuvachov, V., Nozdrovický, L., Krocko, V., Findura, P., Smolinsky, S., Ihnatiev, Y., (2018), The study of movement of the wide span tractor–based field machine unit with power method of its control. *Acta Technologica Agriculturae*, 4, pp.163–168.
- [7] Bulgakov, V., Pascuzzi, Adamchuk, V., Kuvachov, V., Nozdrovicky, L., (2019), Theoretical study of transverse offsets of wide span tractor working implements and their influence on damage to row crops. *Agriculture*, 9 (144), art.10.
- [8] Chamen, T., (2015), Controlled traffic farming - From worldwide research to adoption in Europe and its future prospects. *Acta Technologica Agriculturae*, 18 (3), pp. 64-73.
- [9] Chamen, W.C.T., Dowler, D., Leede, P.R., (1994), Design, operation and performance of a gantry system: Experience in Arable Cropping. *Journal of Agricultural Engineering Research*, 59, 45–60.
- [10] Gmurman, V.E., (2016), Probability theory and mathematical statistics. Moscow: *Yurayt Publishing House*, 479 p.
- [11] Ivanovs, S., Bulgakov, V., Nadykto, V., Ihnatiev, Y., Smolinskyi, S., Kiernicki, Z. (2020), Experimental study of the movement controllability of a machine-and-tractor aggregate of the modular type. *INMATEH - Agricultural Engineering*, Vol. 59, pp.9-16.
- [12] Nadykto, V., (2013), Nadykta-Ayubov harrow for tillage under steam: patent of Ukraine. No UA201311396.
- [13] Nadykto, V., (2017), Fundamentals of scientific research: a textbook. Kherson: OLDI-PLUS, 268 p.
- [14] Onal, I., (2012), Controlled traffic farming and wide span tractors. *Agricultural Machinery Science*, Vol. 8, No 4, pp.353–364.
- [15] Pascuzzi, S., Bulgakov, V., Santori, F., Aniatis, A.S., Ivanovs, S., Holovach, I., (2020), A study on the drift of spray droplets dipped in airflows with different directions. *Sustainability (Switzerland)*, Vol. 12 (11), art. 4644.

# RESEARCH ON MAXIMUM POWER POINT TRACKING'S ALGORITHM OF PHOTO-VOLTAIC CELL ARRAY FOR GREENHOUSE

## 用于农业大棚的光伏阵列最大功率点跟踪算法研究

Liming Wei<sup>1)</sup>, Yangyun Wu<sup>1)</sup>, Nan Ji<sup>1)</sup>, Boheng Li<sup>2)</sup>, Xiujuan Guo<sup>1)</sup>, Bin Li\*<sup>1, 3)</sup>

<sup>1)</sup> Institute of Electrical & Computer, Jilin Jianzhu University, Changchun 130012, P.R. China;

<sup>2)</sup> School of Electrical Engineering and Telecommunications, University of New South Wales, Sydney, Australia;

<sup>3)</sup> College of Computer Science and Technology, Jilin University, Changchun 130012, P.R. China

Tel: +86-043184566184; E-mail: 870731919@qq.com

DOI: <https://doi.org/10.35633/inmateh-62-12>

**Keywords:** PV cell array, power prediction algorithm, MPPT, variable-step conductance increment algorithm

### ABSTRACT

In order to enhance the utilization of solar energy in photovoltaic greenhouse, this paper takes the optimization strategy of photovoltaic array's maximum power point tracking algorithm as research object. According to the changing rule of the slope of photovoltaic array's output P-U curve, this paper proposes a new variable-step conductance increment method to track the maximum power point. When the working point is located on the left side of maximum power point, the logarithmic function value of curve's slope is adopted as the voltage step to adjust the position of working point. When the working point is located on the right side of maximum power point, the exponential function value of curve's slope is adopted as the voltage step to adjust the position of working point. Through the MPPT modelling and simulation in MATLAB/Simulink and the corresponding circuit test, the result shows that comparing with the traditional variable-step conductance increment method, the proposed algorithm can find the maximum power point faster, and it can effectively reduce the power loss caused by step oscillation in the searching process, which achieves the goal of enhancing conversion efficiency of photovoltaic power generation.

### 摘要

为了提高光伏农业大棚对太阳能的利用率，本文对光伏阵列最大功率点跟踪算法的优化策略进行了深入研究。根据光伏阵列输出 P-U 曲线斜率的变化规律，文章提出一种新型的变步长电导增量法对 MPP 点进行追踪，当工作点位于 MPP 点左侧时，采用曲线斜率的对数函数值作为电压步长调整工作点的位置，当工作点位于 MPP 点右侧时，采用曲线斜率的指数函数值作为电压步长调整工作点的位置。通过在 MATLAB/Simulink 中进行 MPPT 建模与仿真，并对相应的电路进行测试，结果表明该算法相较于传统的变步长电导增量法，能够更快地寻找到 MPP 点，且有效降低了寻找过程中由步长振荡造成的功率损失，提高了光伏发电转换效率。

### INTRODUCTION

Greenhouse with solar energy system has been world widely developed in recent years. These greenhouses are integrated with solar cell array, digital control system, power-conversion module and data communication system to perform sustainable development functions (Aznar-Sánchez *et al.*, 2020; Riahi *et al.*, 2020; Zialo *et al.*, 2019). For instance, solar cell array has been fixed on the top of greenhouse that leads to the result of land saving. In addition, the solar panels have numerous levels of transmittance and they can be used as a part of the luminous system for different plants. The generated electrical power can be consumed by the intelligent greenhouse including the irrigation system, ventilation system and heating system (Chen *et al.*, 2013; Wang *et al.*, 2011; Zhang *et al.*, 2020). The extra energy generated during the high luminous period can be sold to the state grid for further financial benefit. The utilization of solar energy system for greenhouse has been studied by many researchers (Azaizia *et al.*, 2019; Cuce *et al.*, 2016; Ravishankar *et al.*, 2020).

However, the efficiency of the solar energy system for greenhouse has been a challenge due to the fluctuation of luminous intensity, temperature and other environmental factors (Gil *et al.*, 2019; Loik *et al.*, 2017; Tiwari *et al.*, 2017; Thaker *et al.*, 2019; Zhang *et al.*, 2019).

<sup>1</sup> Liming Wei, Prof.; Yangyun Wu, Stud.; Nan Ji, Stud.; Boheng Li, Stud.; Xiujuan Guo, Prof.; Bin Li, Ph.D.

The solar panels are impacted by these factors and the output power cannot meet the maximum power point. This not only results in energy loss but also leads to the instability of the system.

Therefore, corresponding algorithm is required to deploy on the solar systems to track the maximum power point (Carbone, 2017; He et al., 2015; Liu, 2015; Radjai et al., 2015; Tajuddin et al., 2015).

In this paper, an incremental conductance with variable step size MPPT control method has been proposed. This improved algorithm is superior to the traditional method for better stability and fast response. Its fundamental principle is to adopt logarithmic function and exponential function to modulate the output voltage for achieving higher tracking efficiency. Compared to our previous algorithm based on the fuzzy control theory (Wei et al., 2019), this proposed method has much faster response time which can result in less power loss in the solar energy systems. Experimental tests have been performed by using MATLAB Simulink to evaluate the performance of the proposed algorithm and results suggest good tracking efficiency.

## SYSTEM STRUCTURE AND THEORY

### System structure

The functional block diagram of the MPPT system for greenhouse is shown in Figure 1. The solar cell panel array system has been mounted on the greenhouse for electricity generation. The output voltage is detected by the main control board through ADC module. The proposed algorithm is processed by the high-performance processor, which is TMS320F28335 in this system, and the output PWM is adjusted according to the detected working point. A boost circuit is deployed in the system to perform DC-DC voltage modulation. Then, the stabilized DC power will be converted to be AC power by the inverter system. The output AC power has been consumed by the electrical devices in the greenhouse and the extra power will be sent to the national grid for further commercial benefit. During the process, modulation of the fluctuated voltage is crucial not only for the system's stability but also results in less power waste. In this way, the performance of the voltage detection and modulation has been researched and optimized in different ways. The improved algorithm based on variable-step incremental conductance principle has been adopted and experiments have been carried out to optimize the system.

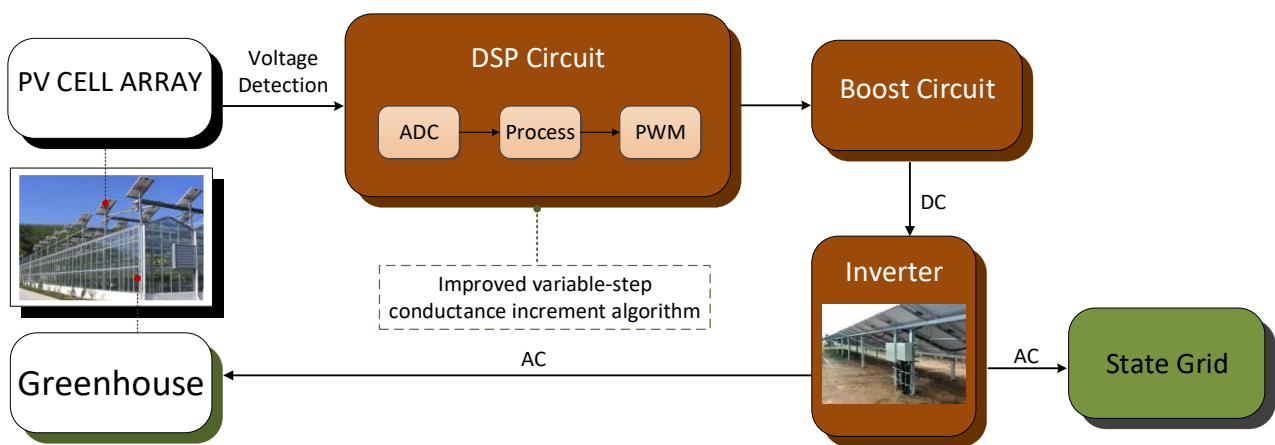


Fig. 1 - Block diagram of the MPPT adopted solar cell array system for greenhouse

### MPPT control method of incremental conductance with variable step size

The fundamental of MPPT control theory is briefly summarized here to guide audience. The MPPT control method of incremental conductance with variable step size, which is similar to the fuzzy control method proposed in our previous research paper, is also required to detect real-time voltage and current of solar cell. Then, calculation is performed to obtain the opposite number of the output conductance and the instantaneous conductance. The results are compared in order to evaluate the MPPT location. Meanwhile, the slope of  $P-U$  can be adopted as reference step size coefficient to adjust the output voltage. The equation below shows the derivation expansion of solar cell output power towards voltage.

$$\frac{dP}{dU} = \frac{d(UI)}{dU} = I + U \frac{dI}{dU} \quad (1)$$

As shown in Equation (1), the working point located at the left side of maximum power point when  $I+U(dI/dU)>0$ , which can also be expressed as  $dI/dU>-I/U$ . In this way, the output voltage should be modulated from the positive direction. On the contrast, the output voltage should be modulated from the negative direction if the working point located at the right side of the maximum power point when  $I+U(dI/dU)<0$ , which can also be expressed as  $dI/dU<-I/U$ . The last situation is  $I+U(dI/dU)=0$ , which is  $dI/dU=-I/U$  when the working point is exactly located at the maximum power point. Under this situation, the solar cell is at its maximum power point.

The incremental conductance with variable step size equation can be expressed as Equation (2).

The output voltage can be shown as Equation (3).

$$d = \frac{dP}{dU} \tag{2}$$

$$U(k) = U(k - 1) + d \tag{3}$$

In order to establish models for analysis, parameters of solar cells are applied in this paper. These parameters include short current  $I_{sc}$ , short voltage  $V_{oc}$ , optimum operating voltage  $V_m$ , optimum operating current  $I_m$  and are provided by project companies. In this way, the model of solar cell can be expressed in Equations (4) – (6).

$$I = I_{sc} \{1 - C_1 \left[ \exp\left(\frac{V}{V_{oc}C_2}\right) - 1 \right]\} \tag{4}$$

$$C_1 = \exp\left[-\frac{V_m}{V_{oc}C_2}\right] \left(1 - \frac{I_m}{I_{sc}}\right) \tag{5}$$

$$C_2 = \left(\frac{V_m}{V_{oc}} - 1\right) \left[\ln\left(1 - \frac{I_m}{I_{sc}}\right)\right]^{-1} \tag{6}$$

As shown in Equations (4) – (6), C1 and C2 are project variables that can be obtained considering two situations. The first situation is that the output voltage is located at the maximum power point. The second situation is that the output is under short condition. The two situations can also be expressed as shown in Equations (7) and (8) respectively.

$$V = V_m, I = I_m \tag{7}$$

$$V = V_{oc}, I = 0 \tag{8}$$

By using this MPPT control method, the output voltage can be adjusted to achieve optimum output power. However, this method can also be improved to reduce the fluctuation of output power and to minimize response time. Therefore, the improved MPPT control method of incremental conductance with variable step size is adopted in this paper. In contrast with the traditional method, which adopts P-U slope to adjust output voltage, the improved method adopts the asymmetry of P-U curve with modulation strategy for the left side and right side of the maximum power point in order to achieve better tracking performance.

## MATERIALS AND METHODS

### Improved simulation of Incremental conductance with variable step size MPPT control method

The proposed algorithm model of improved incremental conductance with variable step size MPPT control method is shown in Figure 2. In this figure, there are two input ports which are the output voltage and current of the solar cell system. The output of the model is the voltage step which is adopted to modulate the working voltage at the most efficient value. In this way, the maximum power generation of the solar system can be achieved. The model can be divided into three parts. Firstly, the output voltage of the solar cell system is measured and compared with zero and then suitable modulation strategy will be selected by the switch block. Secondly, if the instantaneous voltage is zero, fixed step will be applied to modulate the output voltage and the instantaneous current will be measured and its direction will be adjusted by using the sign block. Finally, if the instantaneous voltage is not zero, its working point will be compared with the maximum power point and corresponding algorithm will be adopted to modulate the output voltage.

In contrast with the original algorithm model, there are two additional approaches implemented in this improved model. The P-U slope is determined and suitable calculations are performed by using logarithmic function and exponential function accordingly.

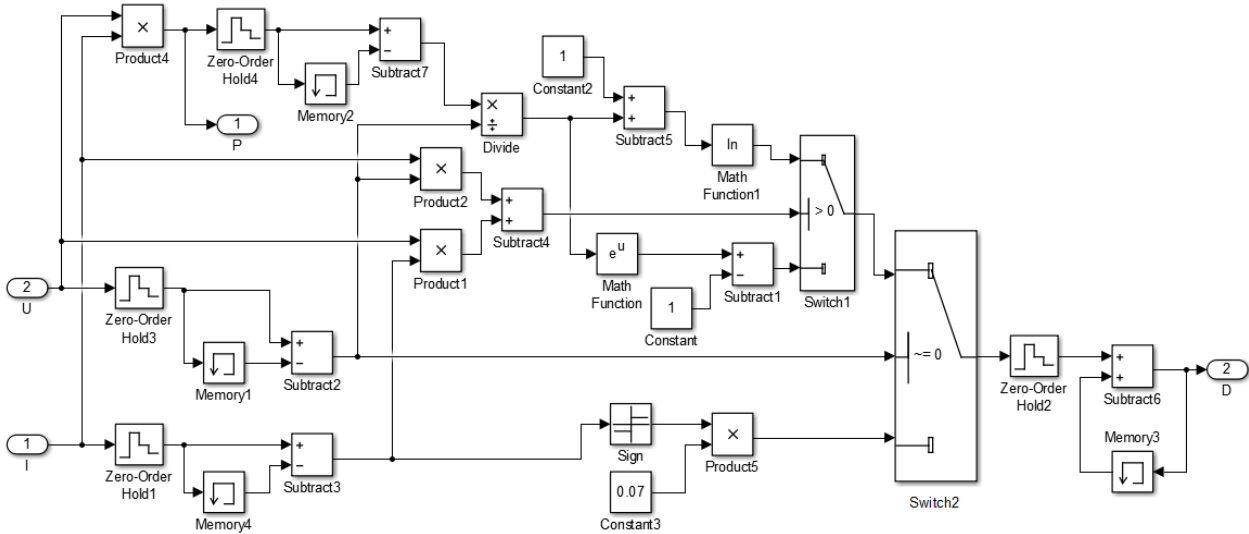


Fig. 2 – Diagram of improved MPPT control method with incremental conductance with variable step size

**Optimized algorithm**

The P-U curve can be obtained by using MATLAB simulation with equations and algorithm proposed in the theory part. The simulated curve is shown in Figure 3. In this figure, the parameters are provided as  $V_{oc} = 21.8V$ ,  $V_m = 17.6V$ ,  $I_{sc} = 4.23A$  and  $I_m = 4.05A$ . As shown in the figure, the P-U curve of solar cell presents unipolar asymmetry feature. The left side of the curve is linearly increased and the right side of the curve drops sharply. This feature leads to further analysis of two conditions. On the one hand, when the output voltage is zero,  $dP/dU$  is positive and the absolute value is relatively small. It increases slowly at the left side of the maximum power point. On the other hand, when the output voltage is short,  $dP/dU$  is negative and the absolute value is relatively big. It decreases sharply at the right side of the maximum power point. Therefore, further modulation can be performed based on this feature.

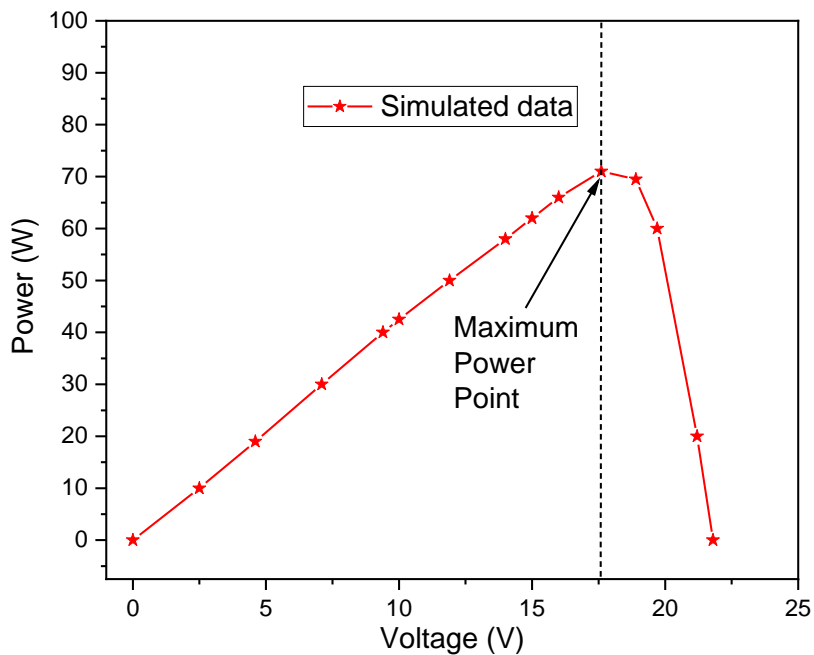


Fig. 3 – Variation curve of the P/U data by using MATLAB simulation

According to the features proposed above, the variations features of logarithmic function  $\ln(x+1)$  within the scope  $(0, +\infty)$  and exponential function  $\exp(x)-1$  within the scope  $(-\infty, 0)$  are combined to optimize the traditional incremental conductance with variable step size MPPT control method in two ways. Firstly, if the  $P-U$  slope is positive, which is  $dP/dU > 0$ , the output voltage is modulated by using  $\ln[(dP/dU)+1]$  as its reference step. Then, if the  $P-U$  slope is negative, which is  $dP/dU < 0$ , the output voltage is modulated by using  $\exp(dP/dU)-1$  as its reference step. The plotted curve is shown in Figure 4. In this figure, the relationship between the step and slope are shown for traditional method and improved method in Figure 4 (a) and Figure 4 (b) respectively.

As shown in Figure 4 (a), the  $P-U$  curve has a steep slope by adopting the traditional method. The advantage is fast response for region far away from the maximum power point. However, the asymmetry of the curve is not considered by using this method. Therefore, the improved method divides the whole scope into two regions to achieve better tracking performance and the advantage of the traditional method can be kept as well. Relatively big step and small step are applied for working point located at the left side and right side of the maximum power point respectively.

In this paper, the instantaneous  $PV$  output voltage is measured and calculated firstly. Then, if the measured voltage has positive or negative value, the output voltage will be adjusted accordingly. If  $dI/dU > -I/U$ , the output voltage will be increased with the step of  $k1\ln[(dP/dU)+1]$ . Otherwise the output voltage will be decreased with the step of  $k2[\exp(dP/dU)-1]$ . In addition, the output voltage remains its value without adjustment if  $dI/dU = -I/U$ . The coefficient  $k1$  and  $k2$  are valued as 2 and 1 respectively in the experiments. In this way, accurate detection of output voltage is crucial for obtaining precision calculations and results for carrying out experiments.

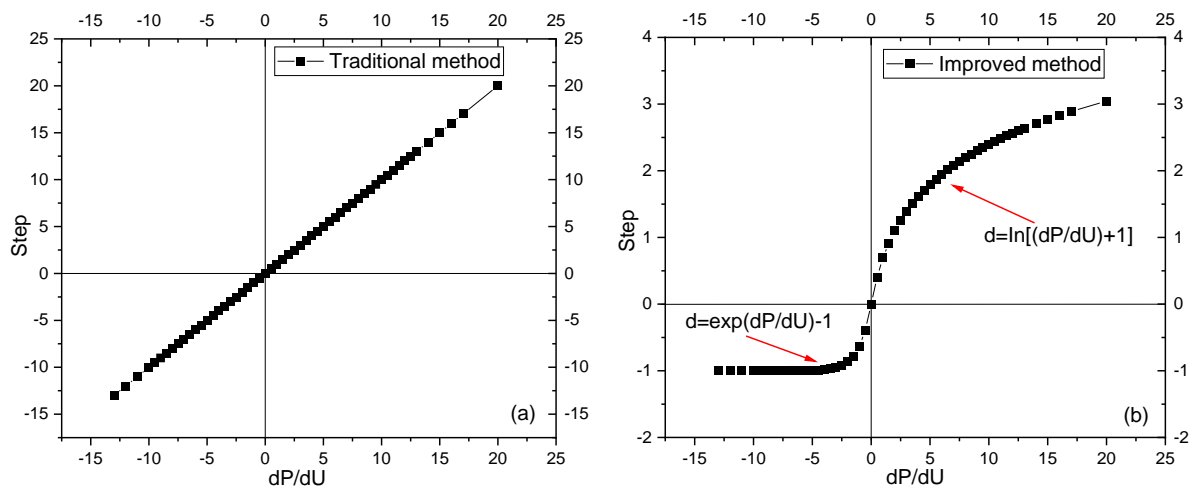


Fig. 4 – Traditional incremental conductance with variable step size MPPT control method (a) and the improved method (b)

### Optimized Circuits

In order to accurately measure the output voltage of solar cell system, the main control circuit has been optimized and the schematic diagram is shown in Figure 5 (a). Compared to our previous circuit, the boost circuit remain the same but the main controlling chip has been replaced as TMS320F28335 which is shorter as DSP28335 (Digital Signal Processing). The photo of the main control board is shown in Figure 5 (b).

The output voltage is measured by the DSP28335 chip with its own analog-to-digital converter (ADC). There are 16 ADC channels available for voltage measurement. The conversion accuracy is 12 bit which is suitable for applications including solar system. The on-chip ROM of DSP28335 is 256K 16-bit and there is an extensional FLASH chip embedded on the board for data storing as well. This processor has powerful computing ability so that the floating computing speed is 150 MHz. The board is able to detect multiple channels of output voltage and then perform the calculations for generating PWM to control the MOSFET circuit. Meanwhile, there is also a serial port on the board for communicating with computer. In this way, the voltage measurement can be performed accurately by using the high-performance hardware based on DSP circuit and further simulation experiments can be performed to evaluate the algorithm proposed previously.

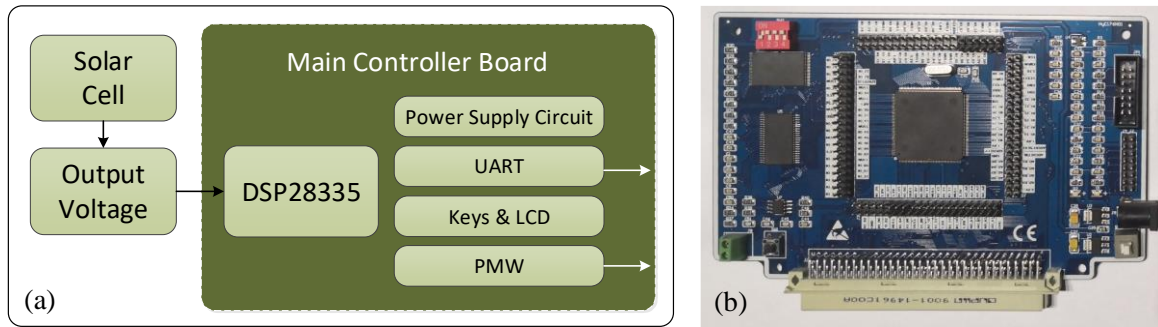


Fig. 5 – Schematic diagram of voltage measurement by using DSP28335 (a) and the photo of DSP board (b)

## RESULTS AND DISCUSSIONS

### Simulation circuit

The simulated circuit is shown in Figure 6 for evaluating the performance of the proposed algorithm. In this model, a typical boost circuit has been established with solar cell module, MPPT module, PWM generator, MOSFET, resistor, capacitor, inductance and I/O ports. According to the simulation demonstrated in the last section, the PWM module can be adjusted by the proposed algorithm to modulate the charge-discharge status of the boost inductance. Based on the principle of conservation of energy, the average output current of solar cell is equal to the current flowed through the boost inductance. In this model, the inductance is set as  $11 \mu\text{H}$ . Considering the impact of ripple and the stability of the circuit, the ripple is set as 1%, which is relatively big enough compare to the realistic applications, and the corresponding filter capacitors have been deployed to minimize the impact. There are two filter capacitors, C1 and C2, deployed to stable the circuit and set as  $300 \mu\text{F}$  and  $100 \mu\text{F}$  respectively. The PWM frequency is set as 30 kHz and is adjustable.

The MOSFET, IRF640 type, is applied to perform the on-off functions for this high-frequency and low-voltage application. In addition, the maximum power capacity of solar cell is 70 W and the environmental luminous intensity, temperature and load resistor are  $100 \text{ W/m}^2$ ,  $25^\circ\text{C}$  and  $50\Omega$  respectively. Experiments have been carried out to evaluate the performance of the circuit with the corresponding parameters.

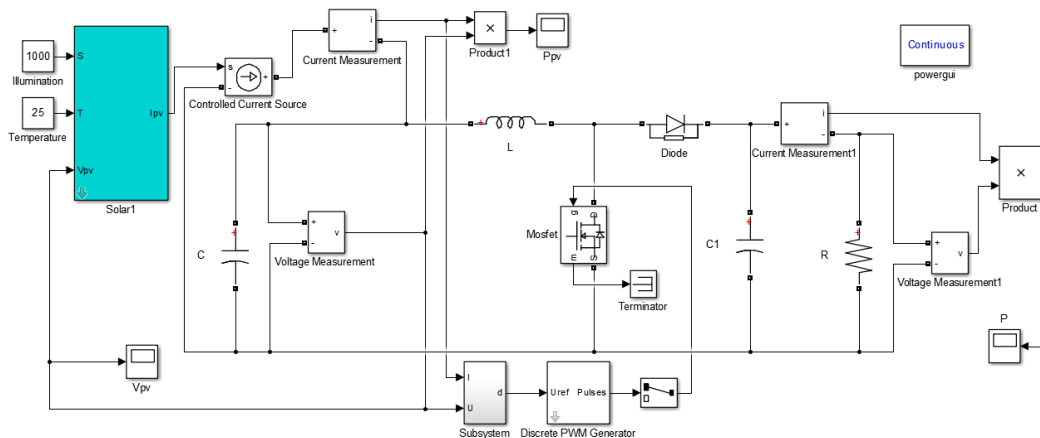


Fig. 6 – Circuit of improved MPPT control algorithm by using MATLAB Simulink

### Comparison between the improved method and the traditional method

The performance between the traditional method and the improved method of incremental conductance with variable step size has been separately executed and the results are shown in Figure 7. The parameters were set according to the circuit and simulation solver was set as ODE45. The period, environmental temperature and luminous was set as 0.1 s,  $25^\circ\text{C}$  and  $1000 \text{ W/m}^2$ . The result of the traditional and improved method are shown in Figure 7 (a) and Figure 7 (b) respectively. As shown in Figure 7 (a), it can be seen that the curve reaches the maximum power point at 70 W very quickly but it keeps rising until the peak point around 80 W. Then it drops and maintains at 70 W. The total process takes about 0.04 s from the beginning to the stable status. This result demonstrates that the output voltage varies rapidly and there is a fluctuation in the system until the output becomes stable.

On the other hand, the curve in Figure 7 (b) which adopts the improved method has a less vibration than the first one. Also, it costs about 0.03 s from the begging to the stable status at the maximum power point. This experiment demonstrates that the proposed method has a quicker response time and more stable performance during the begging period of the system.

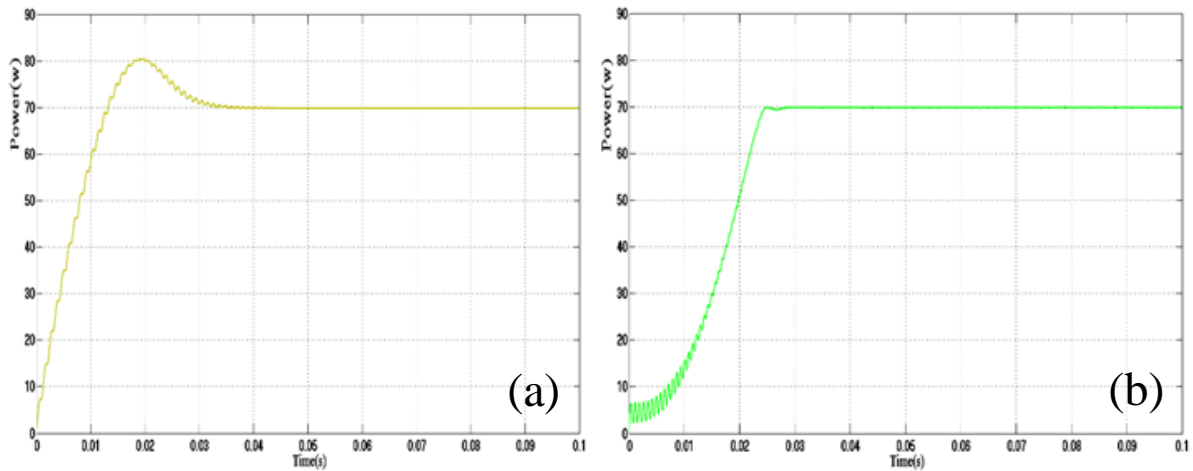


Fig. 7 –Response test of the traditional method (a) and the improved method (b)

The performance of the two algorithms was evaluated by using a robust test as shown in Figure 8. The intensity of luminance and temperature drops from 1000 W/m<sup>2</sup> and 25°C to 900 W/m<sup>2</sup> and 15°C at 0.06 s respectively. As shown in Figure 8 (a), the curve drops deeply and there is a regain process. On the other hand, the curve in Figure 8 (b) drops quickly and there is no fluctuation between the two steady statuses.

In this way, it can be seen that the proposed method has a better robust performance. The system that adopts this algorithm will be more stable and less energy loss will be achieved.

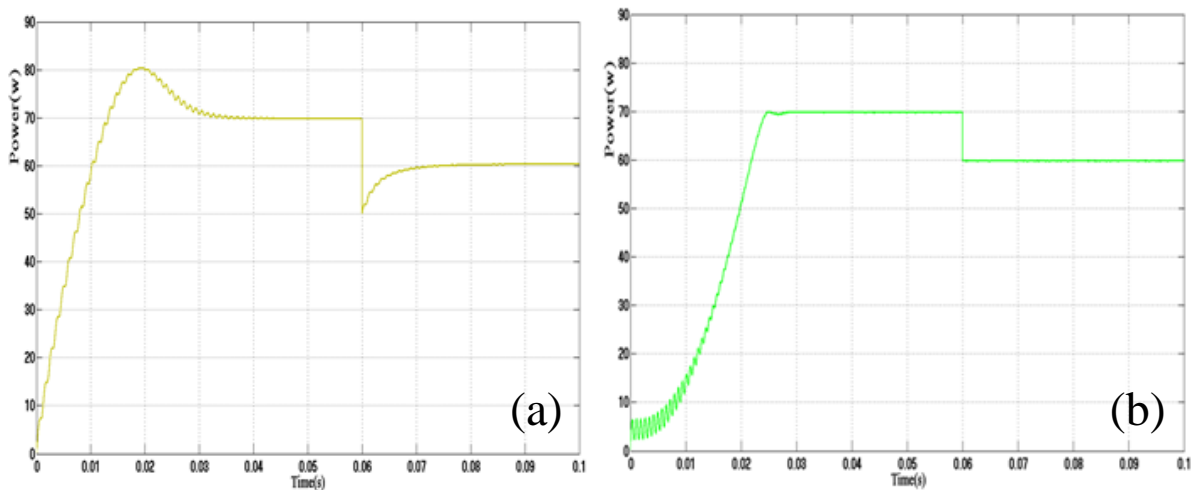


Fig. 8 – Robust test of the traditional method (a) and the improved method (b)

The tracking performance was evaluated by carrying out comparison experiments as shown in Figure 9. The target output power has been set as 70 W as well, but other environmental factors have been changed to see the general tracking performance between the two algorithms. In Figure 9 (a), it can be seen that the output power can be adjusted to the maximum power point after a period of fluctuation. On the other hand, the curve in Figure 9 (b) still present faster response and more stable status than the first one. This general tracking test suggests good efficiency of the proposed method.

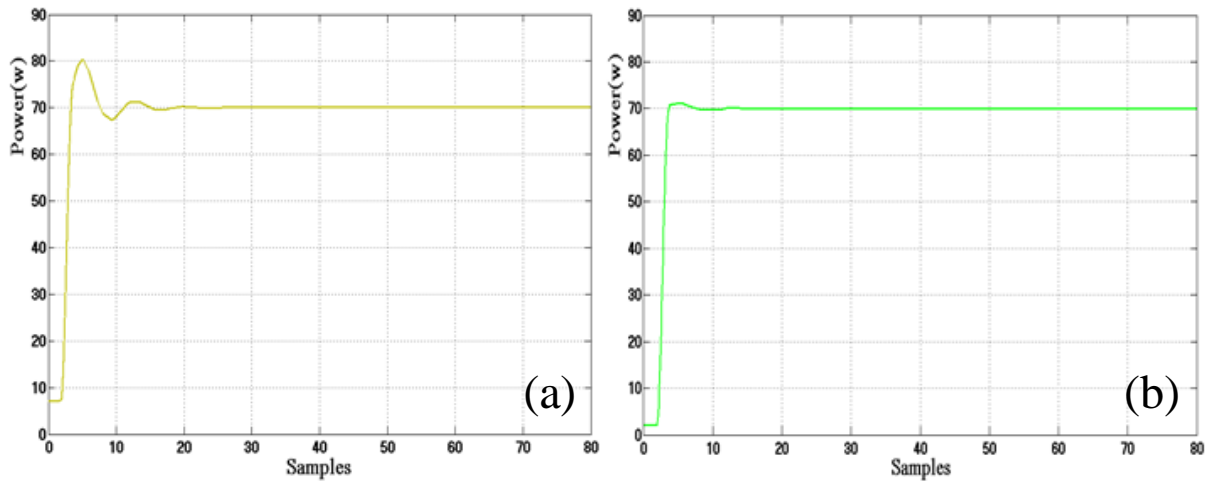


Fig. 9 – Tracking performance test of the traditional method (a) and the improved method (b)

**Comparison between the proposed method and the fuzzy control method**

The comparison experiment was carried out between the proposed method and the fuzzy control method which was demonstrated in our previous paper. The result of the experiment is shown in Figure 10. It can be seen that the two methods are both capable to track the maximum power point which is at 64 W. The fuzzy control curve fluctuated in the begging stage and reached the target point after about 0.04 s. The response time was slower than the second one which was about 0.02 s.

The advantage of the fuzzy control method is that there is no oscillation zone when it reaches the target point. The curve in Figure 10 (b) apparently has a very fast response time compared to the first one. This not only results in good stability of the system but also saves much energy for the solar systems. Therefore, the result of the comparison test demonstrates that the proposed method is superior to the fuzzy control method for its fast response time and system stability.

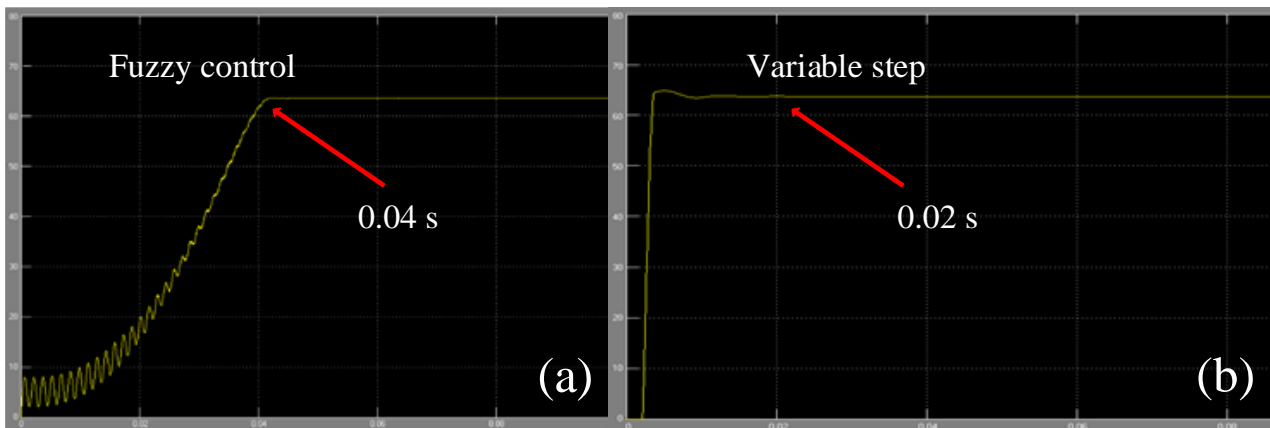


Fig. 10 – Performance comparison between the fuzzy control method (a) and the proposed method (b)

**CONCLUSIONS**

In this paper, an improved MPPT tracking algorithm based on the variation step method has been proposed. This algorithm has been tested and has been compared with the traditional variation step algorithm. In this process, models have been established and relative parameters have been obtained experimentally. The working point and output voltage of the system are measured firstly and then corresponding strategy are deployed. Logarithmic function and exponential function are adopted to achieve better response time for MPP tracking. The PWM signal can be modified according to the environmental change based on the proposed method. The output power can reach its peak value quicker than traditional method and the power loss can also be minimized. In this way, the solar energy system can be optimized to generate more electricity for greenhouse. In the future, further experiments will be conducted to evaluate the performance in the greenhouse to optimize the system.

## ACKNOWLEDGEMENT

The authors wish to express their gratitude to Jilin Jianzhu University (201810191114), the National Key Technology R&D Programme of the Ministry of Science and Technology of China, Province of China and the Education Department of Jilin Province of China (JJKH20180573KJ, JJKH20170240KJ) the Science and Technology Department of Jilin (20180201052SF, 20180201063SF, 20190303114SF), for the generous support of this work.

## REFERENCES

- [1] Azaizia Z., Kooli S., Hamdi I. et al., (2019), Experimental study of a new mixed mode solar greenhouse drying system with and without thermal energy storage for pepper. *Renewable Energy*, vol.145, pp.1972-1984, England; <https://doi.org/10.1016/j.renene.2019.07.055>
- [2] Aznar-Sánchez J., Velasco-Muñoz J.F., López-Felices B. et al., (2020), An analysis of global research trends on greenhouse technology: towards a sustainable agriculture. *International Journal of Environmental Research and Public Health*, vol.17, 17020664, Switzerland, <https://doi.org/10.3390/ijerph17020664>
- [3] Carbone R., (2017), PV plants with distributed MPPT founded on batteries. *Solar Energy*, vol.122, pp.910-923, U.S.A., <https://doi.org/10.1016/j.solener.2015.10.017>
- [4] Chen J.L., Kang S.Z., Du T.S. et al., (2013), Quantitative response of greenhouse tomato yield and quality to water deficit at different growth stages. *Agricultural Water Management*, vol.129, pp.152-162, Holland; <https://doi.org/10.1016/j.agwat.2013.07.011>
- [5] Cuce E., Harjunowibowo D., Cuce P. M., (2016) Renewable and sustainable energy saving strategies for greenhouse systems: A comprehensive review. *Renewable and Sustainable Energy Reviews*, vol.64, pp.34-59, Holland; <https://doi.org/10.1016/j.rser.2016.05.077>
- [6] Gil J.D., Ivarez J.D. Á, Roca L. et al., (2019), Optimal thermal energy management of a distributed energy system comprising a solar membrane distillation plant and a greenhouse. *Energy Conversion and Management*, vol.198, pp.1-12, England; <https://doi.org/10.1016/j.enconman.2019.11.1791>
- [7] He W., Wang Y., Shaheed M.H., (2015), Maximum power point tracking (MPPT) of a scale-up pressure retarded osmosis (PRO) osmotic power plant. *Applied Energy*, vol.158, pp.584-596, England; <https://doi.org/10.1016/j.apenergy.2015.08.059>
- [8] Liu X.S., (2015), A highly efficient ultralow photovoltaic power harvesting system with MPPT for internet of things smart nodes. *IEEE Transactions on Very Large Scale Integration (VLSI) Systems*, vol.23, pp. 3065-3075; <https://doi.org/10.1109/tvlsi.2014.2387167>
- [9] Loik M.E., Carter S.A., Alers G. et al., (2017), Wavelength-selective solar photovoltaic systems: powering greenhouses for plant growth at the food-energy-water nexus. *Earth's Future*, vol.5, pp.1044-1053, England; <https://doi.org/10.1002/2016EFO00531>
- [10] Radjai T., Gaubert J.P., Rahmani L. et al., (2015), Experimental verification of P&O MPPT algorithm with direct control based on Fuzzy logic control using CUK converter. *International Transactions on Electrical Energy Systems*, vol.15, pp. 3492-3508, England; <https://doi.org/10.1002/etep.2047>
- [11] Ravishankar E., Booth E.R., Saravitz C. et al., (2020), Achieving net zero energy greenhouses by integrating semitransparent organic solar cells. *Joule*, vol.4, pp.1-17; <https://doi.org/10.1016/j.joule.2019.12.018>
- [12] Riahi J., Vergura S., Mezghani D., et al., (2020), Intelligent control of the microclimate of an agricultural greenhouse powered by a supporting PV system. *Applied Sciences*, vol.10, pp.10041350; <https://doi.org/10.3390/app10041350>
- [13] Tajuddin M.F.N., Arif M.S., Ayob S.M., Salam Z., (2015), Perturbative methods for maximum power point tracking (MPPT) of photovoltaic (PV) systems: a review. *International Journal of Energy Research*, vol.39, pp. 1153-1178, England; <https://doi.org/10.1002/er.3289>
- [14] Thaker S., Oni A.O., Gemechu E. et al., (2019), Evaluating energy and greenhouse gas emission footprints of thermal energy storage systems for concentrated solar power applications. *Journal of Energy Storage*, vol.26, pp.1-12; <https://doi.org/10.1016/j.est.2019.100992>
- [15] Tiwari S., Tiwari G.N., (2017), Energy and exergy analysis of a mixed-mode greenhouse-type solar dryer, integrated with partially covered N-PVT air collector. *Energy*, vol.128, pp. 183-195, England; <https://doi.org/10.1016/j.energy.2017.04.022>
- [16] Wang F., Kang S.Z., Du T.S. et al., (2011), Determination of comprehensive quality index for tomato and its response to different irrigation treatments. *Agricultural Water Management*, vol.98, pp. 1228-1238, Holland; <https://doi.org/10.1016/j.agwat.2011.03.004>

- [17] Wei L.M., Luo J.X., Li B.H. et al., (2019), Modelling and measurement of a photovoltaic cell array maximum power point tracking system for greenhouse. *INMATEH- Agricultural Engineering*, vol.59, pp.285-292, Romania, <https://doi.org/10.35633/INMATEH-59-31>
- [18] Zhang T.F., Zhou W.W, Meng F. et al., (2020), Efficiency analysis and improvement of an intelligent transportation system for the application in greenhouse. *Electronics*, vol.8, pp.8090946; <https://doi.org/10.3390/electronics8090946>
- [19] Zhang X.D, Lv J., Dawuda M.M. et al., (2019), Innovative passive heat-storage walls improve thermal performance and energy efficiency in Chinese solar greenhouses for non-arable lands. *Solar Energy*, vol.190, pp.561-575, U.S.A.; <https://doi.org/10.1016/j.solener.2019.08.056>
- [20] Zialo M., Kluza K., Spoz A., (2019), Impact of sustainable financial and economic development on greenhouse gas emission in the developed and converging economies. *Energies*, vol.12, 12234514, Switzerland, <https://doi.org/10.3390/en12234514>

## EXPERIMENTAL STUDY OF LIQUID SLOSHING FORCE CHARACTERISTICS IN RECTANGULAR TANK OF SPRAYER UNDER HARMONIC EXCITATION

### 简谐激励下喷雾机矩形药箱内液体晃动力特性实验研究

Jizhou Zheng<sup>1,2)</sup>, Xiang Han<sup>1)</sup>, Haoran Guo<sup>1)</sup>, Jialin Hou<sup>1,2)</sup>, Xinyu Xue<sup>3) 1</sup>

<sup>1)</sup> Shandong Agricultural University, College of Mechanical and Electronic Engineering / China

<sup>2)</sup> Shandong Provincial Key Laboratory of Horticultural Machineries and Equipment / China

<sup>3)</sup> Nanjing Research Institute for Agricultural Mechanization of Ministry of Agriculture and Rural Affairs / China

Tel: 02584346243; E-mail: [735178312@qq.com](mailto:735178312@qq.com)

DOI: <https://doi.org/10.35633/inmateh-62-13>

**Keywords:** liquid sloshing, sprayer, rectangular tank, experiment, liquid sloshing force

#### ABSTRACT

The stability of the boom system of sprayers is easily affected by the liquid sloshing force and the uniformity of droplet deposition deteriorates. Therefore, the liquid sloshing forces in the rectangular tank were measured through experiments. Three main factors affecting the sloshing forces were examined. Experimental results reveal that the sloshing forces measured fit well with the theoretical curve and the maximum sloshing force is independent of the excitation amplitude for a violent sloshing. Based on these characteristics, a practical method was proposed which can approximately calculate the maximum sloshing force based on the linear model, and can be used for the sprayer chassis design and active and passive control of boom attitude.

#### 摘要

喷雾机喷杆系统的稳定性易受液体晃动力的影响，导致液滴沉积均匀性变差。因此，实验测量了矩形药箱中的液体晃动力。探讨了影响晃动力的三个主要因素。实验结果表明，测得的晃动力与理论曲线吻合很好，大幅晃动时最大晃动力与激励幅值无关。基于晃动力的这些特点，提出了一种近似计算最大晃动力的实用方法，可用于喷雾器底盘设计及喷杆姿态的主被动控制。

#### INTRODUCTION

Sloshing is fluctuation of a free liquid surface. The distribution of the liquid in a tank will change if the sloshing occurs. At the same time, the liquid applies a large impact pressure on the vessel wall. The sloshing force of the liquid is the result of these two factors. Sloshing may cause bad effects such as fatigue, damage, and instability of the container and external structure. Therefore, sloshing has been studied in many engineering fields, involving aerospace (Miao Li and Wang, 2017; Chiba and Magata, 2017), ships (Zhao et al., 2011; Vieira et al., 2018), transportation (Kolaei, Rakheja and Richard, 2014; Touni, Bouazara and Richard, 2009), water conservancy (Li Di and Gong, 2012; Li and Wang, 2012) and so on. Apart from theoretical analysis and numerical simulation, experiment is also an important means to research the problem of sloshing (Ishikawa et al., 2016; Yan, Rakheja and Siddiqui, 2009; Cavalagli et al., 2017).

With the development of the agricultural mechanization, boom sprayers and plant protection UAVs are widely used today. The weight of the liquid in tanks tends to be 1/3 of the total or more in sprayers. Usually, the tank is placed on the upper part of the sprayer and a high chassis is used in order not to damage crop. Therefore, the centre of gravity is high and the tread is narrowly relative to the vehicle height. When the sprayer drives on the uneven ground, vibration in the vertical direction and sway in the longitudinal and lateral directions will occur because of the fluctuation of land. Moreover, the attitude of sprayers is also influenced by the driving conditions such as start, stop, acceleration, deceleration and turning. The liquid sloshing is easily induced by these factors. The liquid sloshing force whose value and direction are constantly changing directly acts on the sprayer, and the attitude of the sprayer will be affected in turn. Not only does the stability of the sprayer deteriorate, but also the balance of the boom is influenced, which thereby reduces the application effect of the pesticide. So, the liquid sloshing in the tank has begun to attract

<sup>1</sup> Jizhou Zheng, Prof. Ph.D. Eng.; Xiang Han, M. A. Eng.; Haoran Guo, M. A. Eng.; Jialin Hou, Prof. Ph.D. Eng.; Xinyu Xue, Prof. Ph.D. Eng.

attention (Jeon, 2003). The stability and safety of the crop protection UAV are also affected by the liquid sloshing caused by the change of attitude (Li et al., 2017).

The change of the sprayer's driving state during operation has great uncertainty, and the ground unevenness is also a kind of low-frequency large-amplitude random excitation. Therefore, the change of the attitude of the tank is also random. The posture of the tank randomly changes with time during the whole operation process, and the attitude of the tank may be any combination of translation and rotation at a certain moment. Obviously, it is difficult to establish a correspondence between the liquid sloshing and such a random excitation, so the sloshing mechanism and the control strategy cannot be discussed further.

Although pure harmonic excitation is less likely to occur than periodic or other types of excitation, understanding the behaviour of a system undergoing harmonic excitation is essential in order to comprehend how the system will respond to more general types of excitation (Thomson and Dahleh, 2013). Therefore, the rectangular tank commonly used in sprayers was chosen in this paper, and the harmonic excitation with known frequency and amplitude was applied to study the sloshing characteristics of the liquid in the tank. The lateral force generated by liquid sloshing was measured by force sensors, and the factors that influence the sloshing force were analysed.

## MATERIALS AND METHODS

To measure the force generated by the sloshing, the liquid must be placed in a tank with certain shape and size. In other words, the force needs to be measured indirectly by means of the tank. However, under the external excitation, the inertial force of the box itself also acts on the force sensor at the same time. Therefore, it is essential to correctly measure and to distinguish the inertia force of the box from the liquid sloshing force in the experiment. A suspension system was designed in order to reduce the influence of friction, as shown in Fig. 1.

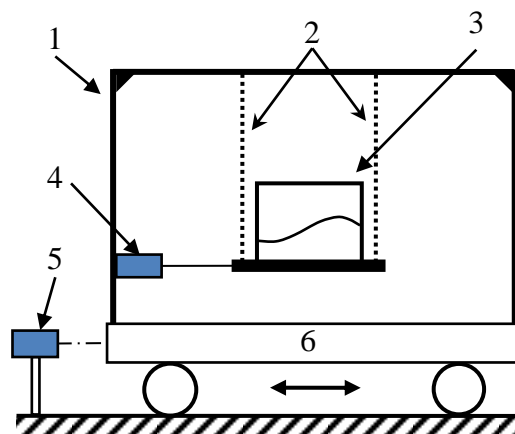


**Fig. 1 - Schematic diagram of experiment**

1. Frame 2. Steel wire 3. Tank 4. Load cell 5. Laser displacement sensor 6. Shake table

A frame like a door was fixed to the shake table and moves together with it. The tank made of transparent plexiglass was fixed to a steel plate, and the steel plate was suspended from the frame by thin steel wires. The uniaxial force sensor was placed horizontally with the steel plate and the frame attached at each end. Therefore, the weight of the steel plate, the tank and the liquid in the tank is borne by the wire ropes, and the force sensor measures only the force in the horizontal direction. In order to reduce the influence of the shake table's motion, the laser displacement sensor used for measuring the displacement of the tank was horizontally placed on the ground. The force and displacement signals from these sensors were recorded using a high-speed data acquisition instrument.

The horizontal displacement of the shake table is transmitted to the tank through the frame, the force sensor and the steel plate, causing the liquid in the tank to sway. The force generated by the sloshing of the liquid acts on the tank and is transmitted to the force sensor through the steel plate. In addition, during the reciprocating motion, the acceleration of the steel plate and the tank is not constant, and so the corresponding inertial force also acts on the force sensor. Therefore, the force sensor simultaneously measures the liquid sloshing force and the inertial force of the steel plate and the tank. In other words, the sloshing force should be the force measured by the force sensor minus the inertial force of the steel plate

and the tank. The inertial force can be calculated through the mass of the steel plate and the tank, the amplitude and frequency of shake table's motion.

The complete test system is shown in Fig. 2. The horizontal displacement excitation is produced by a shake table whose frequency and amplitude can be adjusted according to the need. The frequency range is 0 - 2Hz and the frequency resolution is 0.02Hz. The force sensor is piezoelectric force sensor (CA-YD-303) and associated charge amplifier (YE5853), produced by Jiangsu Lianneng Electronic Technology Co., Ltd. The measurement range of the force sensor is 0-2kN. The laser displacement sensor (IL-300) is produced by Keyence Corporation with a measuring range of 300 mm. The data acquisition system is high-speed data acquisition card (4492) and the corresponding controller (8820) produced by National Instruments Corporation. The tank is made of plexiglass and has an internal dimension of 500x100x500 mm, corresponding to length, width and height, respectively. A large amount of water is used to dilute chemical pesticides during the application. In other words, majority of the liquid in the tank of sprayers is water. So, dyed water was used in the experiment.

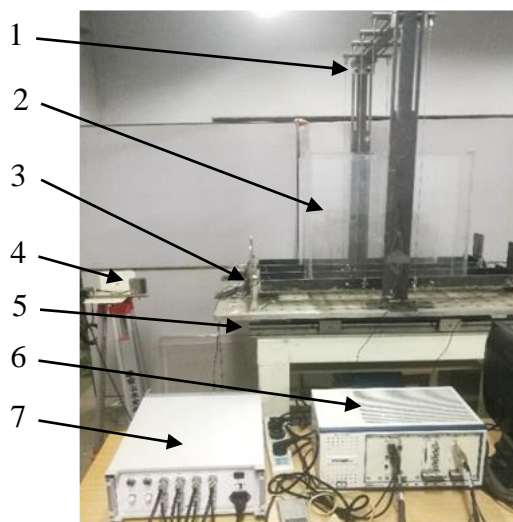


**Fig. 2 - Experiment system**

1. frame; 2. tank; 3. load cell; 4. laser displacement sensor; 5. shake table;  
6. dynamic signal acquisition instrument; 7. charge amplifier

The length and width of the tank have been fixed, so other factors that affect the sloshing force were considered, namely liquid depth, frequency and amplitude of the excitation. The experiment was performed in the following order. Firstly, the amplitude of excitation was kept constant, and harmonic displacement excitations with different frequencies were applied to the tank with a certain liquid depth, and then the above process was repeated by changing the liquid depth. Secondly, the liquid depth was kept constant, and harmonic displacement excitations with different frequencies were applied on the tank with the same amplitude, and then the process was repeated by increasing the amplitude. The values of each factor are shown in Tab. 1. Where,  $f$  is the first natural frequency determined by length and depth of liquid, [Hz].

**Table 1**

**Parameters in the experiments**

Parameters	Ranges	Increments
Excitation frequency [Hz]	0.5f - 1.8f	0.05f
Excitation amplitude [mm]	5 - 30	5
Liquid depth [mm]	100 - 500	25

## RESULTS

### *Influence of liquid depth on sloshing force*

The quantity of the liquid in the tank gradually reduced as the liquid is continuously consumed during the pesticide spraying operation, which can be reflected directly by the liquid depth for the rectangular tank.

The sloshing force with different liquid depths is shown in Fig. 3. When the liquid depth does not exceed 400 mm, there is no significant difference in the tendency of the sloshing force. So, only parts of

the results are shown for the sake of clarity, as shown in Figures (a) and (b). When the liquid depth is large, the sloshing force varies differently, so all the results are given, as shown in Figures (c) and (d). Please note that the excitation amplitude is 10mm in all of these cases.

If the excitation amplitude and the liquid response are small, the sloshing force for a rectangular tank under harmonic excitation  $x_0 \sin \omega t$  can be written as (Ibrahim, 2005)

$$F = \rho L w h x_0 \omega^2 \sin \omega t \cdot \left\{ 1 + \sum_{n=0}^{\infty} \left[ \frac{8 \tanh(k_n h)}{k_n^3 L^2 h} \frac{\omega^2}{\omega_n^2 - \omega^2} \right] \right\} \quad [\text{N}] \quad (1)$$

Where:

$\rho$  is the density of the liquid, [kg.m<sup>-3</sup>];

$L, w, h$  is the length, width and depth of the liquid respectively, [mm];

$x_0$  is the amplitude of excitation, [mm];

$\omega$  is the circle frequency of excitation, [rad/s];

$\omega_n = \sqrt{g k_n \tanh(k_n h)}$  is the natural circle frequency of liquid sloshing, [rad/s];

$k_n = (2n + 1)\pi / L$ , [m<sup>-1</sup>];

$g$  is the gravity acceleration, [ms<sup>-2</sup>];

$t$  is time, [s].

The sloshing force can be calculated according to given parameters mentioned above and was drawn in solid or dash line in the following figures.

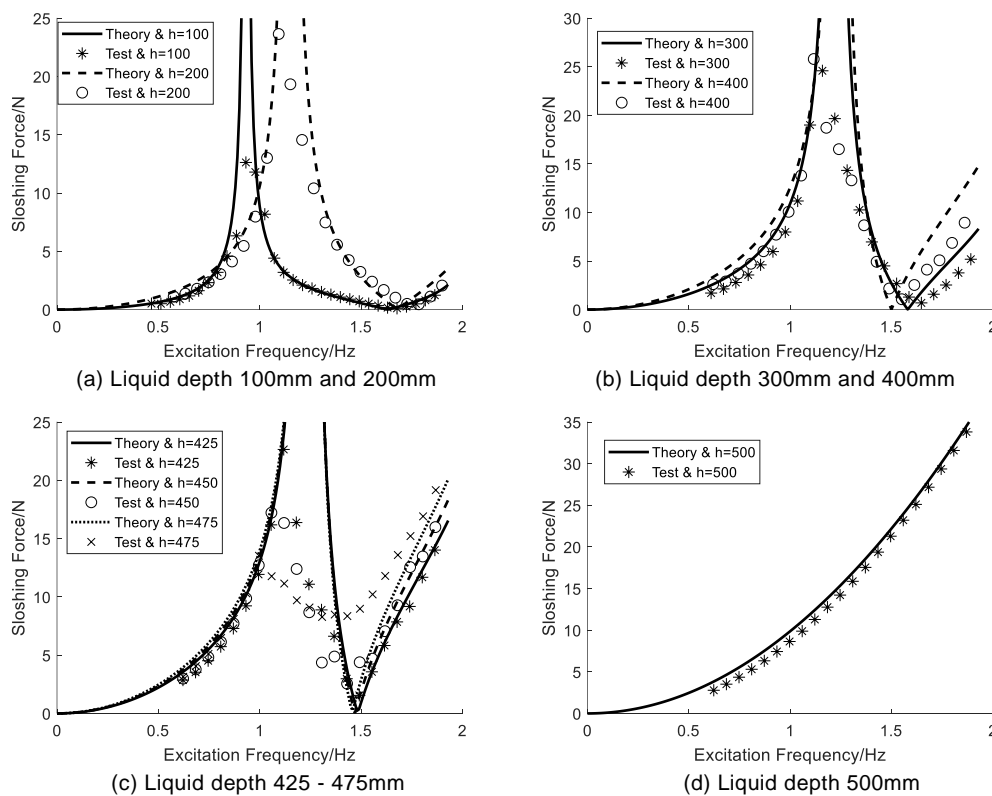


Fig. 3 - Liquid sloshing force with different liquid depth

It can be seen that in the case of small liquid depth (i.e., 100mm), the experimental results are basically consistent with the theoretical ones over the entire frequency range. The biggest difference occurs at the natural frequency. The sloshing force at this frequency is infinity according to the formula (1), but the experimental result is a finite value. The reason lies in the fact that the liquid sloshing force expression (1) is based on the premise of the ideal fluid, without considering the viscosity of the fluid. For the actual fluid, there is friction between the fluid and the tank wall due to the presence of viscosity, which hinders the movement of the liquid. Therefore, the sloshing force is finite.

For the medium liquid depth (i.e., 200 and 300mm), the forces measured are slightly smaller than the theoretical ones when the excitation frequency is lower than the frequency where the maximum sloshing force occurs. Different from the small depth, the maximum sloshing force appears at a lower frequency (i.e.,  $0.95f$ ). The sloshing forces at the following one or two frequencies successively reduce. Thus, the forces measured have a relatively large discrepancy with the theoretical results. Then, the differences are small again with the frequency increases. The frequency corresponding to the maximum sloshing force further lowers for the larger liquid depth (400mm), which is only  $0.9f$ . The reason is analysed as follows. When the liquid depth is small, the free surface of liquid can keep as flat at almost whole frequency range, apart from the natural frequency, so the movement of liquid satisfies the condition of the linear model. The relatively flat surface can also be gotten at the lower frequency range for the medium or larger liquid depth. So, the discrepancy between the sloshing force measured and the theoretical one is not distinct. But, when the excitation frequency is larger than the natural frequency, the surface of liquid presents multiple standing waves or travelling waves with shorter wavelength for the medium or larger liquid depth. In other words, the surface of liquid is not flat but curved. More crests appear at the middle positions along the length direction and less liquid impacts on the side wall of the tank. So, the sloshing force measured is less than the theoretical one.

The frequency where the maximum sloshing force occurs for the 450 and 475mm liquid depth is  $0.85f$  and  $0.8f$ , respectively. For the latter, the sloshing forces decrease slowly and then gradually increase at the subsequent frequencies, showing relatively large discrepancies with the theoretical model. The reason is that the distance between the free surface of the liquid and the top cover of the tank is small (only 2 - 5cm), and the liquid impact not the side wall but the cover even if the sloshing is small. On the other hand, large amount of liquid in the lower part does not participate in the sloshing, but moves along with the tank. Therefore, inertial force plays a more important role than the sloshing force in this case. Based on this attribute, horizontal baffle can be placed on the side wall to reduce the liquid sloshing force.

If the tank is completely filled with liquid, they will move together. Sloshing will no longer occur due to the absence of free liquid surface. The sloshing force increases as the excitation frequency increases since it is actually the inertial force, as shown in Figure (d).

The experimental results near the natural frequency differ greatly from the theoretical curve, mainly due to the non-linearity of the large amplitude sloshing. The typical waveform of the free liquid surface is shown in Fig. 4 for better understanding.

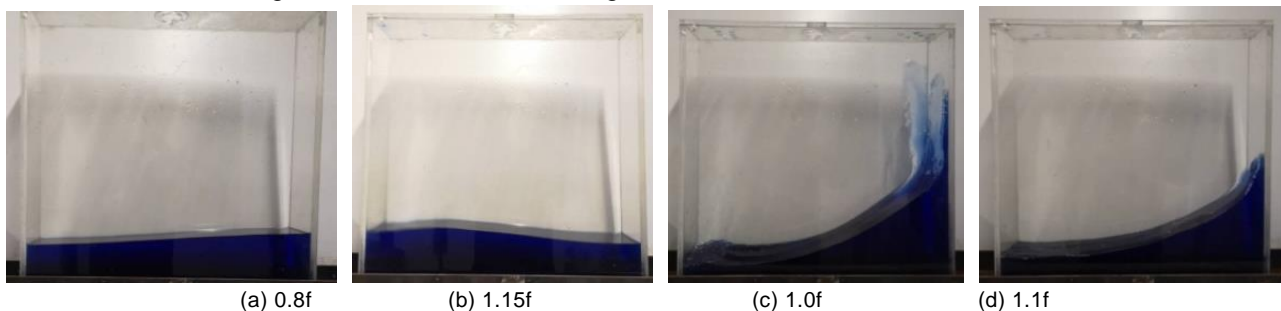


**Fig. 4 - Waveform of liquid surface under different excitation frequency**

(Note: the liquid depth is 100mm)

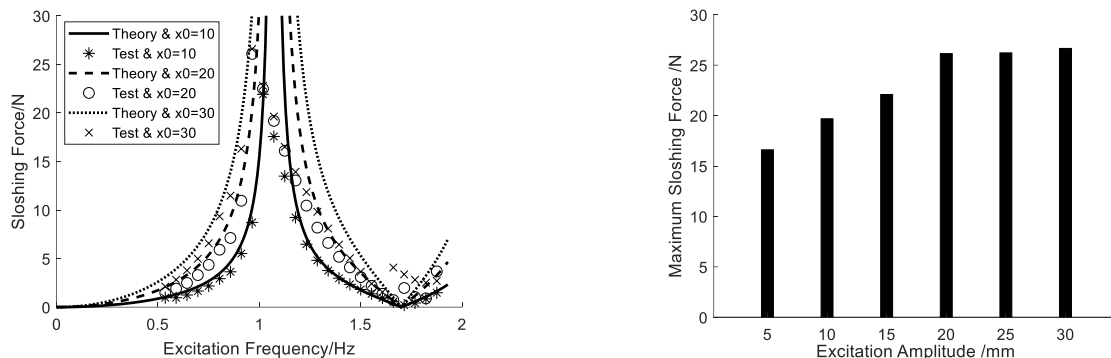
It can be seen that the liquid sloshing amplitude is small and the liquid surface is flat when the excitation frequency is far from the resonance frequency of the liquid (i.e., below  $0.8f$  or above  $1.15f$ ), as shown in Figures (a) and (b). In this circumstance, the precondition of linearization can be basically satisfied, so the experimental result is in good agreement with the linear model. However, violent sloshing occurs near the natural frequency of the liquid. During the large amplitude sloshing, the liquid climbs rapidly along the tank wall, then tends to slow down, and finally falls quickly. At the same time, the rolling and breaking of the liquid surface often occurs. In addition, the movement of the liquid is also not limited to the excitation direction. Not only is the waveform a curved surface in the longitudinal direction, but also the surface is no longer flat in the width direction. The maximum wave height appears at a certain corner and then alternates among the four corners. This means that the motion of the liquid contains one or more waves that rotate around the vertical axis of the tank. Obviously, the liquid

sloshing amplitude does not satisfy the premise of the linear model, and so it is inevitable that the experimental results greatly deviate from the theoretical value.

### **Influence of excitation amplitude on sloshing force**

Boom sprayers are widely used in the South China paddy field, where the height of hard bottom ranges from 58mm to -40mm (Zhu *et al.*, 2016). Taking a certain boom sprayer as an example, the wheelbase is 1.5m and the distance between the bottom of the tank and the ground is 1.3m. Therefore, the maximum displacement of the tank in horizontal plane is about 40mm due to the ground unevenness excitation. The liquid in the tank is prone to sloshing violently under such large an excitation. So, it is necessary to discuss the effects of the excitation amplitude on the liquid sloshing force.

The sloshing force corresponding to different excitation amplitude is shown in Fig. 5. Please note that the liquid depth is 150mm.



(a) Sloshing force under different excitation frequency with 10, 20 and 30mm excitation amplitude (b) Maximum sloshing force with different excitation amplitude

**Fig. 5 - Liquid sloshing force with different excitation amplitude**

It can be seen that the sloshing force is in good agreement with the theoretical model in the lower frequency range, and the excitation amplitude has almost no influence. However, in the higher frequency range, the larger the excitation amplitude is, the more the sloshing force deviates from the theoretical value. In addition, the frequency at which the maximum sloshing force occurs is also affected by the excitation amplitude, that is, the larger the excitation amplitude is, the lower the frequency is. The reason is analysed as follows. The larger excitation amplitude is more likely to cause a violent sloshing of the liquid, so that the maximal sloshing force can be gotten at a lower frequency. Furthermore, the larger excitation amplitude is more likely to form a short-wavelength traveling wave in the high frequency range, and the impact pressure of the liquid is smaller. So, the sloshing force is less than the theoretical one.

Figure (b) shows the maximum sloshing force at different excitation amplitudes. It can be seen that when the excitation amplitude is equal to or more than 20 mm, the sloshing force is basically unchanged, showing a feature of saturation. The reason lies in the fact that the amplitude of the liquid sloshing has reached the limit and thus the sloshing force is not increased any longer. In other words, the sloshing amplitude cannot be further increased even if the excitation amplitude is increased.

### **Approximate calculation of maximum sloshing force**

During the pesticide application operation of the sprayer, the continuous excitation from irregular ground and unstable driving may cause large amplitude sloshing of the liquid in the tank, and thus the sloshing force occurs.

According to the analysis in the former section, the maximum sloshing force does not depend on the excitation frequency and amplitude any longer but tends to be fixed, once large amplitude sloshing occurs. This makes it possible to obtain the maximum sloshing force by means of the theoretical model. The sloshing force measured with different liquid depth in the experiment was carefully analysed and an obvious law can be found. If the entire frequency range is divided into two parts by the frequency at which the maximum sloshing force occurs, in the higher frequency range the discrepancies between the experimental results and the theory model are relatively large and depend on the liquid depth at a certain extent. However, in the lower frequency range the difference between the experimental results

and the theoretical ones is small and stable regardless of the change of the liquid depth. Therefore, the maximum sloshing force with different liquid depth may be approximately calculated by the formula (1).

When the liquid depth is small, the maximum sloshing force is obtained at  $1.0f$  or  $0.95f$ , so  $0.95f$  is taken to calculate the sloshing force for the liquid depth of 100-175 mm. The maximum sloshing force generally appears at  $0.95f$  as the liquid depth further increases, but it is slightly smaller than the corresponding theoretical result. So,  $0.94f$  and  $0.93f$  is taken to calculate the sloshing force for the liquid depth of 200 - 225mm and 250 - 275mm, respectively. The frequency can be further decreased to  $0.92f$  for the liquid depth of 300-375mm. The maximum sloshing force is basically the same as the theoretical value of the corresponding frequency for the liquid depth above 400mm, and thus the frequency is taken as  $0.9f$ ,  $0.85f$  and  $0.8f$ , respectively. The theoretical results corresponding to the frequencies mentioned above are compared with the experimental ones, as shown in Fig. 6(a). The maximum relative error is equal to 6.4% within the whole liquid depth range.

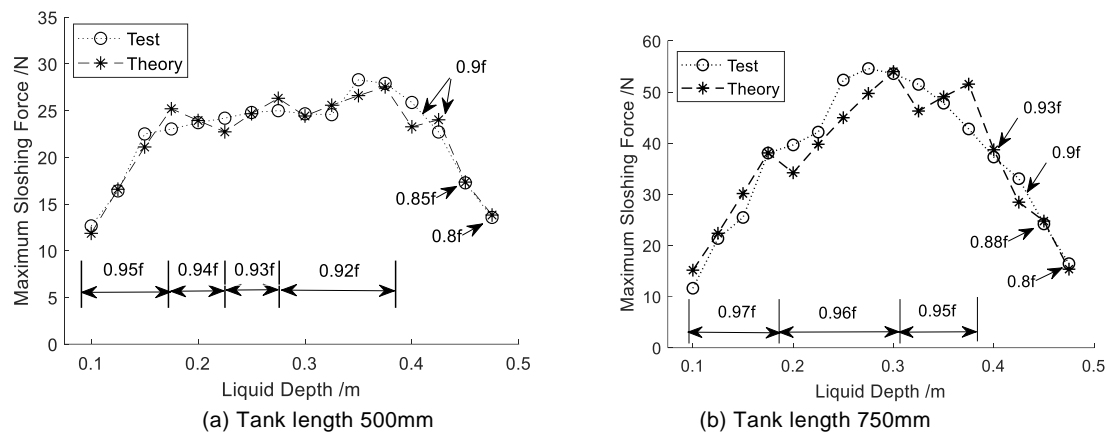


**Fig.6 - Maximum sloshing force tested with different liquid depth and theoretical value at different frequencies**

It can be seen from Fig. 3 and Fig. 5(a) that the experimental results of the sloshing force are always slightly smaller than the theoretical ones in the lower frequency range. It may originate from the force sensor itself because the measure range of the sensor is far larger than the actual sloshing force. Taking this fact into consideration, the frequency for calculating the theoretical value can be appropriately increased. That is, it is taken as  $0.97f - 0.96f$  for the small liquid depth,  $0.96f - 0.94f$  for the medium liquid depth, and  $0.93f - 0.8f$  for the large liquid depth, respectively. In general, the greater the liquid depth is, the lower the frequency is.

As verification, the experimental results of a tank with 750mm length and 100mm width were compared with the theoretical values. The frequencies used to calculate the theoretical value are shown in Fig. 6(b).

It can be seen that the theoretical value calculated fits well with the experimental one. The maximum relative error is 23.3%, which occurs at the 100 mm liquid depth. But the actual difference is only 3.5N.

It should be pointed out that the frequency at which the maximum sloshing force occurs is  $1.1f$  or  $1.05f$  for the 750mm length tank when the liquid depth is less than 175mm, which is different from the 500mm length tank. But the conclusions mentioned above are not affected by the changes of these frequencies. In other words, the conclusions can be applied to different length rectangular tank and have good robustness.

## CONCLUSIONS

Harmonic displacement excitation was applied to the rectangular tank commonly used in sprayers in order to make the inside liquid sloshing. The effects of liquid depth, frequency and amplitude of the excitation on the liquid sloshing force were studied.

(1) When the liquid depth is relatively small and the excitation frequency is far from the natural frequency of the liquid sloshing, the experimental result of sloshing force is in good agreement with the

theoretical one. However, in the vicinity of the natural frequency, especially in the case of large liquid depth, a relatively large deviation between the test and the theory occurs.

(2) Larger excitation amplitude is more likely to cause violent sloshing of the liquid, but the maximum sloshing force does not increase linearly with the excitation amplitude, showing a characteristic of saturation.

(3) The maximum sloshing force can be approximately calculated by the linear model. It can be used for the sprayer dynamics analysis, chassis design and active and passive control of boom. It is also helpful for the flight control system design for plant protection UAVs.

(4) Based on the experiments and results in this paper, field tests can be better performed.

## ACKNOWLEDGEMENT

This work was supported financially by the Key Laboratory of Modern Agricultural Equipment, Ministry of Agriculture and Rural Affairs, P. R. China (HT20160351), and the National Key Research and Development Program of China (2017YFD0700905).

## REFERENCES

- [1] Cavalagli N., Biscarini C., Facci A. L., Ubertini F., Ubertini S. (2017), Experimental and numerical analysis of energy dissipation in a sloshing absorber, *Journal of Fluids and Structures*, Issue 68, pp. 466-481;
- [2] Chiba M., Magata H. (2017), Influence of liquid sloshing on dynamics of flexible space structures, *Journal of Sound and Vibration*, Issue 401, pp. 1-22;
- [3] Ibrahim R. A. (2005), *Liquid Sloshing Dynamics*, Cambridge: Cambridge University Press;
- [4] Ishikawa S., Kondou T., Matsuzaki K., Yamamura S. (2016), Analysis of nonlinear shallow water waves in a tank by concentrated mass model, *Journal of Sound and Vibration*, Issue 371, pp. 171-182;
- [5] Jeon H. Y. (2003), Instrumented Self-Propelled Sprayer to Determine Dynamic Boom Effects on Droplet Application Uniformity, Master's Thesis, University of Tennessee, USA;
- [6] Kolaei A., Rakheja S., Richard M. J. (2014), Effects of tank cross-section on dynamic fluid slosh loads and roll stability of a partly-filled tank truck, *European Journal of Mechanics B/Fluids*, Issue 46, pp. 46-58;
- [7] Li X., Zhang J. X., Qu F., Zhang W. Q., Wang D. S., Li W. (2017), Optimal design of anti-sway inner cavity structure of agricultural UAV pesticide tank, *Transactions of the Chinese Society of Agricultural Engineering*, Vol. 33, Issue 18, pp. 72-79;
- [8] Li Y., Di Q., Gong Y. (2012), Equivalent mechanical models of sloshing fluid in arbitrary section aqueducts, *Earthquake Engineering and Structural Dynamics*, Issue 41, pp. 1069-1087;
- [9] Li Y., Wang J. (2012). A supplementary, exact solution of an equivalent mechanical model for a sloshing fluid in a rectangular tank. *Journal of Fluids and Structures*, Issue 31, pp. 147-151;
- [10] Miao N., Li J., Wang T. (2017), Equivalent mechanical model of large-amplitude liquid sloshing under time-dependent lateral excitations in low-gravity conditions, *Journal of Sound and Vibration*, Issue 386, pp. 421-432;
- [11] Thomson W. T., Dahleh M. D. (2013), *Theory of Vibrations with Applications* (5th Edition), New York: Pearson Education Limited;
- [12] Toumi M., Bouazara M., Richard M. J. (2009), Impact of liquid sloshing on the behaviour of vehicles carrying liquid cargo, *European Journal of Mechanics A/Solids*, Issue 28, pp. 1026-1034;
- [13] Vieira D. P., Mello P. C., Dotta R., Nishimoto K. (2018), Experimental investigation on the influence of the liquid inside the tanks in the wave behaviour of FLNG vessels in side-by-side offloading operations, *Applied Ocean Research*, Issue 74, pp. 28-39;
- [14] Yan G., Rakheja S., Siddiqui K. (2009), Experimental study of liquid slosh dynamics in a partially-filled tank, *Journal of Fluids Engineering*, Issue 131, pp. 1-14;
- [15] Zhao W. H., Hu Z. Q., Yang J. M., Wei Y. F. (2011), Investigation on sloshing effects of tank liquid on the FLNG vessel responses in frequency domain, *Journal of Ship Mechanics*, Vol. 15, Issue 3, pp. 227-237;
- [16] Zhu S. H., Ma J. F., Yuan J. Q., Xu G., Zhou Y. Q., Deng X. T. (2016), Vibration characteristics of tractor in condition of paddy operation, *Transactions of the Chinese Society of Agricultural Engineering*, Vol. 32, Issue 11, pp. 31-38.

# FOOD LOSSES IN PRIMARY CEREAL PRODUCTION. A REVIEW

## /

## RISIPA ALIMENTARA LA NIVELUL PRODUCTIEI AGRICOLE PRIMARE. REVIEW

Oana-Mihaela Dumitru<sup>1</sup>, Sorin Iorga<sup>\*1</sup>, Nicolae-Valentin Vlăduț<sup>2</sup>, Carmen Brăcăcescu<sup>\*2</sup> <sup>1</sup>

<sup>1</sup> National Research and Development Institute for Food Bioresources -IBA Bucharest / Romania;

<sup>2</sup> National Institute for Research-Development of Machines and Installations Designed for Agriculture and Food Industry - INMA Bucharest / Romania

Tel: +0743046536, e-mail: [soriniorga@gmail.com](mailto:soriniorga@gmail.com)

DOI: <https://doi.org/10.35633/inmateh-62-14>

**Keywords:** losses, cereal grains, harvest, postharvest

### ABSTRACT

The food waste and losses (FW) became one of the most impacting aspects in modern society. This review article presents an overview of various aspects linked to the phenomenon of food losses in primary cereal production and its consequences. From the analysis of reviewed specific literature, it resulted that the losses are found both in the harvesting process and in the post-harvest processes (conditioning, separation, sorting, chemical treatment, transport etc.) these representing the primary processing of agricultural products, especially seeds. The review focuses on the new technologies' influence in reducing FW in harvesting and post-harvesting process, highlighting the contribution of agricultural engineering studies on this specific topic.

### REZUMAT

Deșeurile și pierderile alimentare (PA) au devenit una dintre problemele de mare impact din societatea modernă. Acest articol de revizuire prezintă o imagine de ansamblu a diferitelor aspecte legate de fenomenul pierderilor de alimente în producția primară de cereale și consecințele acestuia. Din analiza literaturii specifice revizuite a rezultat că pierderile se găsesc atât în procesul de recoltare, cât și în procesele post-recoltare (condiționare, separare, sortare, tratare chimică, transport etc.) acestea reprezentând prelucrarea primară a produselor agricole, în special semințe. Revizuirea se concentrează asupra influenței noilor tehnologii în reducerea pierderilor alimentare în procesul de recoltare și post-recoltare, subliniind contribuția studiilor de inginerie agricolă pe acest subiect specific.

### INTRODUCTION

The technical progress, social awareness campaigns and dietary evolution, the need of assessing and quantifying the food waste and losses (FW) remain of main interest for the scientific community (*Bräutigam et al., 2014; Mesterhazy et al., 2020; Mirzaadeh et al., 2015*). There are a lot of efforts of specialists around the world on developing FW reduction methods on the entire food chain, starting from seed to fork. According to a recent definition food waste is the difference between the amount of food produced and the sum of all food employed in any kind of productive use, whether food or nonfood (*Bandinelli et al., 2020*).

In the acreage structure of world agriculture, cereal crops occupy more than half. Their main areas are in Asia, North America, Europe, Australia and Africa. Of these, rice and wheat are the most important food crops in the world. Likewise, wheat is food crop with the highest yield and ranks first among cereals (*Fu et al., 2018*).

On the other hand, grains are the main food items in agriculture. Grains like maize, wheat and rice account for 43% of all food calories and 87% of all grain production worldwide. Maize is the most consumed food in the world. Over 42% of the world's population depends on maize to fulfill its food requirements. About 87% of the whole maize output is consumed and produced in developing countries (*Khan et al., 2018*).

*Mar'in and Vereshchagin (2016)* considers that adverse effects on the grain may occur during cultivation, harvesting and post-harvesting handling or storage. During grain cultivation problems may be caused by edaphoclimatic conditions, affected grains, dead-ripe stage or overwintering in the field. During the harvest problems may be caused by mechanical damage, prolonged storage in heaps and waiting for post-harvest treatment. During post-harvest handling or storage problems may be caused by pests and microorganisms. High values of humidity and impurities can lower grain value by affecting their technological advantages.

<sup>1</sup> Dumitru O.M., Eng.SR III, Ph.D.Eng.; Iorga C.S., Ph.D.Eng.; Vlăduț V., Ph.D.Eng.; Brăcăcescu C., Ph.D.Eng.

Wheat sowing mechanization technologies were also analyzed in detail by *Creț et al. (2018)*.

The Postharvest Losses (PHL) through deterioration of the grain quantity and quality that occurs in the time interval between harvesting and marketing or when it reaches the consumer, lead to loss of nutritional and monetary values as well as limited access to particular market segments. In many developed countries, postharvest losses of cereals account to 10-15%. Qualitative and quantitative post-harvest losses are mainly due to insect infestation. In search of food and shelter, they contaminate the grains with their by-products, making them unfit for consumption. Tropical and wetlands are most prone to pest infestation of stored grain (*Gach and Chlebowski, 2016; Mostafavand and Kamgar, 2014; Nkurunziza et al., 2015*).

Minimizing post-harvest losses through efficient post-harvest handling, primary processing, storage and marketing can contribute substantially to reducing production volumes needed to feed a growing population, resulting in improved food and nutrition security (*Odendo et al., 2017*).

One of the underestimated aspects of capacity building to reduce post-harvest losses is the personnel level of knowledge and their ability to manage grain stocks throughout their value chain. In general, the emphasis is on the introduction of state-of-the-art technologies and a little on the training of operating personnel (*Ileleji et al., 2017*).

Nowadays, the introduction of new technologies into the agricultural production requires constant upgrades of the machines. So, the present article is a part of the research that assesses the FW impact on primary production, by focusing on the technological influence in reducing FW in harvesting and post-harvesting process.

## **MATERIAL AND METHOD**

The selection of articles was made by Elsevier search which included criteria related to the grain primary production, harvesting techniques' efficiency, food waste reduction. An initial 300 articles addressed some of the criteria. The final assessment selected 69 articles that considered food waste reduction in grain primary production process. The selection includes researches conducted in some of the main agricultural areas: SE Europe, France, sub-Saharan Area, China, India and South America. Many of them are international cooperation projects that reunite researchers from USA, UE together with colleagues from Africa, or SE Asia.

From the analysis of reviewed specific literature, it resulted that in agriculture sector the losses are found both in the harvesting process and in the post-harvest processes (conditioning, separation, sorting, chemical treatment, transport etc.) these representing the primary processing of agricultural products, especially seeds.

The dynamics of mechanization and automation of agriculture is constantly growing: the current focus is on increasing the number of agricultural machinery and equipment and improving their performance.

### **1. Harvesting**

Cereal harvesting is the final part of the agricultural production process and represents it's fulfilment. Nowadays, the demand for food is constantly increasing and because of this fact it is important to use proper technology that not only increases production on the same land area, but also preserves the biodiversity and the environment (*Ilea et al., 2013*).

The main problem about harvesting is to ensure timely collection and obtain minimum loss of grain production. In the same time, harvesting is also the process that requires the greatest weight in terms of resources (labour consumption and material costs), others than the mechanization technology.

Taking into account these aspects, the cereal harvesting combines are among the most complex machines, which are used in agriculture, as they are made up of different gears and specialised operating parts, but also of a lot of auxiliary technical and checking systems. Due to the reduction of the existing combine harvester park, physical depreciation of the machines, their obsolescence, increase in number of the broken machines, as well as an increase in the average load on the machine, it is important to choose the combine harvester that meets the conditions in the sector best. Upgrading the machines brings long-term positive results in technical and economic areas, so when choosing a combine harvester, one needs to analyse both the technical characteristics and the results of field trials (*Popa et al., 2010; Prístavková et al., 2016; Redlingshöfer et al., 2017; Shvedyk, 2015; Mahmoodi et al., 2007*).

A performant combine harvester needs to be a high-tech one in order to deliver high productivity with minimal crop losses, damage and minimal expenses on maintenance (*Zubko et al., 2018*).

It is known that the combine productivity depends both on the technical parameters of the machine, and on the logistics factors. Such a factor is the place of unloading the full grain tanks (*Delchev et al., 2016*).

### 1.1. Straw harvesting combines

Straw grain harvesting is a very important operation that must be performed at the optimal time and with the lowest possible losses. On the other hand, the maintenance of combine harvesters is considered by the specialist as the main condition for a successful harvesting campaign (Popa et al., 2010; Zubko et al., 2018).

The evolution in the field of construction of agricultural machines has led to the emergence of *self-propelled straw harvesting combines* much better in terms of productivity, reliability, with a high degree of automation, ensuring an increased quality of harvested crop and increased operating comfort. To determine losses upon harvesting straw cereals operation, it is necessary to evaluate yield before harvesting. In straw grain harvesting the main losses depend on field state, on the flow of the thresher, on self-propelled combine components tightness, etc. Losses are presented quantitatively and as percentage depending on the yield evaluated being determined for each case apart. A higher power flow than optimal for straw harvesting combines can cause higher losses. Optimum feeding flow is established in accordance with the type of the harvesting combine and the field state, so that grain losses range within admitted limits. So, using straw grain harvesting combines rationally and at the optimum time ensures minimum loss and low expenses (Duma-Copcea et al., 2017).

In modern agriculture, combine harvester is a crucial farm machine which it is mainly used for the harvest of cereal crops (wheat, corn, oat, barley, etc.), soybean and sunflower.

Current modern combine harvester is a fully automated self-propelled farm machine that carries out multiples task s during its operation (Figure 1). The operation starts with gathering and cutting the crop by the header unit, then material is conveyed into threshing unit which processes it. Finally, the mixture of grain and chaff goes to the cleaning unit and the straws are sent to the separation unit (straw walker).

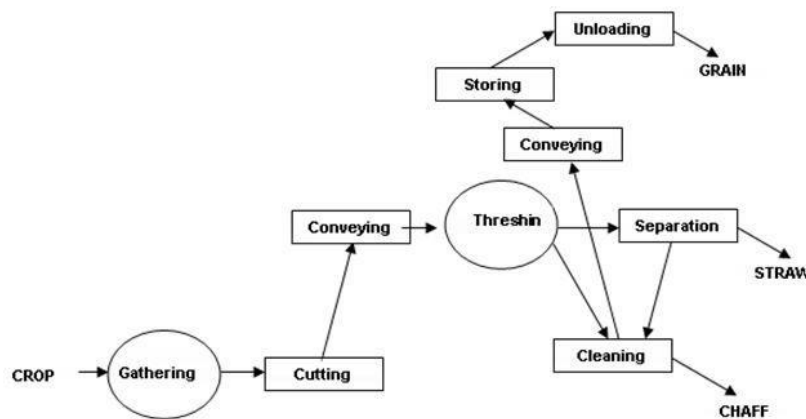


Fig. 1 - A simplified flow chart of the internal tasks of a combine harvester (Keskin and Şekerli, 2018)

The straw and chaff are dumped out of the harvester onto the field ground while the clean grain material is conveyed to the storage tank. When the tank is full, the grain is unloaded to a trailer through the unloading auger (Keskin and Şekerli, 2018).

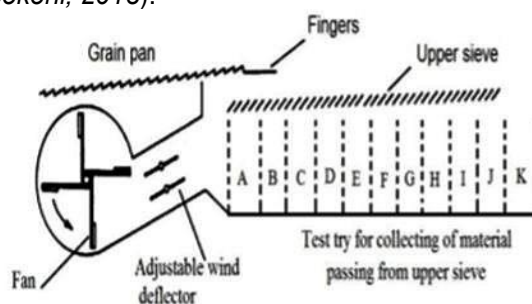


Fig. 2 - A schematic diagram of a cleaning mechanism (Mirzazadeh et al., 2015)

Bumbar et al (2018) consider as the most effective way to improve the harvesting process in general and increase the efficiency necessary for obtaining agricultural products to use a rational adjustment of the parameters of the threshing-separating device of a combine harvester and an optimization of the operation of the crop-harvesting equipment fleet, depending on the physical and mechanical properties of the harvested crops and the calendar time of harvesting.

The most important function of grain harvester is threshing, so grain damage and loss are significantly related to threshing theory and harvesting technology. Many researchers put their efforts to study grain-threshing devices, the results of these research have been the developing of different kinds of grain threshers or threshing components (Alatürk and Şal, 2018; Tihanov, 2017; Tihanov 2019; Tang et al., 2015; Upadhayay et al., 2018).

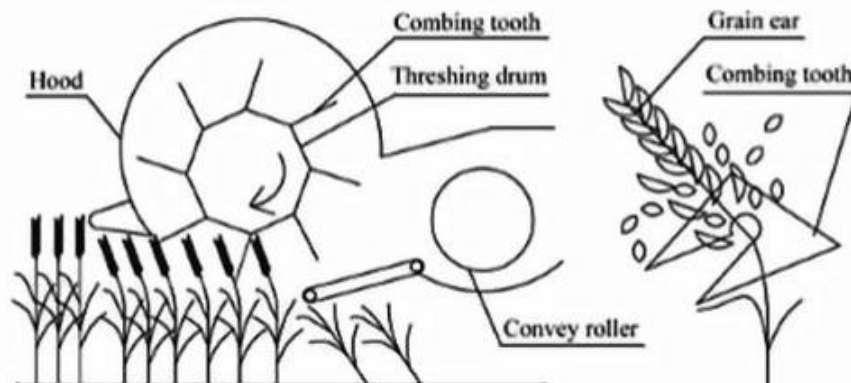


Fig. 3 - Pre-cut combing threshing harvester (Fu et al., 2018)

There are four kinds of threshing principles (impact, rubbing, combing and grinding) which led to the construction of four correspondently types of contact models between grain and threshing components. Grain damage can be regarded as a function of peripheral velocity and contact pattern of impacting, while grain loss can be regarded as a function of contact pattern of rasp bars. Grain loss coming in the subsequent process (cleaning and separation) of combing threshing was significantly decreased. Tangential and axial threshing technologies have been widely applied in modern grain threshing system. Research has shown that in the combined application, tangential rolls accelerate grain flow, and axial rolls increase threshing quality especially lower loss and damage. Also, conical concave may take the place of the traditional cylindrical one. With the development of sensor, digital technology and artificial intelligence, harvesting robot and automatic threshing system will be integrated together to improve grain quality, productivity and operator comfort (Fu et al., 2018).

In harvesting grain loss and damage are significantly affected by threshing performances so, higher level of threshing theory and technology are still the unswerving pursuit. A major parameter to evaluate the performance of grain threshing is loss rate. To improve quality of grain threshing, reducing the mechanical loss become a more practicable means. Another direct index of grain threshing which negatively affects the market value and storage is damage rate. Typical kinds of grain damage are mechanical and chemical damage. Mechanical grain damage comes from the impact of grain kernels and rigid surface of threshing unit of high relative speed (Tang et al., 2017). To find the morphological and textural characteristics of three views of grain when grain kernels free fall and impact, the method of high-speed digital imaging has been used. When grain is harvested during the rainy season, chemical damage is due to a complex of fungi. Previous research indicates that the grain chemical damage could decrease to the minimum level if grain crops are harvested at physiological maturity and then dried artificially.

In terms of harvesting machine performance in grain threshing system are widely applied tangential and axial threshing technologies. T-series of John Deere, four drums of New Holland and Fendt of Agco apply tangential threshing technology on threshing drum independently, while S-series of John Deere, Twin rotor of New Holland, APS of CLAAS, Axial-Flow of CASE IH, Challenger and Gleaner of AGCO apply tangential and axial threshing technologies together. Experimental research shows that in the combined application, tangential rolls accelerate grain flow, and axial rolls raise threshing quality indicators.

Fu et al., (2018), conclude that grain loss and damage are the result of mechanical action of threshing, so, the best solution for threshing quality is an intelligent threshing system. Manual intervention of farmers is difficult to be efficient during the grain harvesting process.

Because of the fact that material properties (moisture content, planting density, etc.) are diverse, the threshing system's of speed and clearance should be controlled intelligently.

The development of sensors and hydromatic system contributed to the development of intelligent control system and mechanical threshing system to ensure improvement of grain quality and operator comfort.

### 1.2. Grain maize harvesting combines

Maize harvesting is a most important field operations on which maize production largely depends. The accelerating development of maize industry determined that mechanized maize harvesting to be widely accepted and used by farmers all over the world. The shortening of the harvesting period and the increasing of labour productivity depends of the scientific organisation of harvesting grain maize. Also, to obtain high yields per area unit with low expenses, it is necessary to strictly observe the cultivation technologies corroborated with the use of innovative aggregates with the highest efficiency possible (*Petrovska and Valkova, 2018; Li et al., 2016*).

Self-propelled combines for the harvesting of grain maize are made up of two main components: maize cob cropper and maize stem thrasher. The maize cob cropper has the role of detaching the maize cobs from the stems, carrying the leafless maize cobs to the thrasher and chopping the stems. The chopped stems can be loaded into a means of transport or they can be spread over the soil to be later incorporated into the soil. The maize stem thrasher thrashes the maize cobs, separates the grains from impurities, and carries the grains to the bunker (*Duma-Copcea et al., 2018*).

As the mechanized maize harvesting works have become more widespread worldwide lately, the choice of the optimal operating parameters of the harvesting aggregates are determining factors in increasing the productivity and quality of the harvested material and in reducing costs. Analysis of literature leads to highlighting of scientific research regarding the improvement of self-propelled grain maize harvesting combines and cob collectors parameters to meet increasing qualitative and quantitative requirements in work. Besides choosing the most efficiency variants of mechanisation technology in harvesting grain maize, for reducing costs other factors are important (periodical technical maintenance, optimum feeding flow of the thrasher, working speed correlating with field yield, movements of the combine during the day from one plot to another, daily working norm for each combine, the equipment adjusting depending on the maize cultivar being harvested, etc.). In order to obtain high yields per unit area with low costs, complex aggregates with high production capacity must be used (*Creț et al., 2018; He et al., 2017*).

According to the harvesting methods, maize harvesters could be classified into two types: maize-for-grain harvesters (including pickers and grain harvesters) and whole plant harvesters (including forage harvesters and combined grain-stover harvesters). Large size farms require big horsepower engines with working efficiency, automation and intelligence devices. Grain combine harvesters will take a large scale in the future with maize breeding development and with implementation of great varieties that are suitable for grain harvesting.

The purpose of mechanized maize harvesting is to replace manual labour to harvest maize from fields in time with minimum loss while maintaining high quality. The harvesting method and equipment depend upon planting pattern, agronomy and climate conditions. The entire harvesting operation may be divided into gathering, snapping, husking, cutting, threshing and cleaning (Figure 1). These functions are performed by different equipment, or can be performed by one equipment in a single pass depending on the method employed for harvesting. Among the biggest advantages of mechanized maize harvesting are increasing of productivity and reducing of human drudgery. The development of maize harvesting machinery can be traced back to the successful development of field operation machine of snapping, husking and stalk cutting. The emerging of new maize varieties with the ability of dense planting and high yield will cause the change of cultivation modes, especially plant row spacing. It is required to study new harvesting technologies and harvesters with higher adaptability; and at the same time, maize dense planting puts forward a higher request for picking ears and threshing technology. The research and development of new efficient picking ears, threshing and separation device will become the emphasis for improving the production efficiency and reducing the yield loss (*Milkias et al., 2018*).

*Marek et al. (2019)*, performed experimental measurement during maize harvesting, cleaning and drying with grain moisture 23 - 35%. The purpose of coarse and light trash analysis was the next step to find out the losses of grain quality. The analysis of the internal grain quality from the starch, fats and proteins was then conducted.

### 1.3. Soybean harvesting and threshing

In soybean production, harvesting and threshing are the most important operations and for their optimization the knowledge of the physical- mechanical properties of soybean stem and seeds are therefore particularly important, as it is reflected into minimization of losses and mechanical damage (*Faggion et al., 2017*). As it is known, soybean is usually harvested in the autumn season with high air relative humidity and

possibility of rainfall. Because of this, the moisture content of soybean pods and stems are high, so during the harvesting and threshing operations, can occur some problems such that the conventional combine harvester can't harvest the stem, thresh and separate the bean from its pod properly. For a proper designing and manufacturing pre-threshing dryer on combine harvester, determination of physical and mechanical properties of soybean pod is needed. Due to the distribution of pods along the plants, it is necessary to cut the entire crop using existing combine harvesters before threshing, separating and cleaning. About 40% of the combine engine power is used by the threshing cylinder who is located at a high level because it processes the stem in addition to the pods. As the moisture content of soybeans decreases, so does the amount of energy needed to shatter soybeans. To open soybean pods at impact velocities similar to those imported by the reel and cutter-bar of a combine a small amount of energy is necessary. So, the energy required to shatter soybean pod is correlated with moisture content and impact velocity. More information on the physical and mechanical properties of soybean is necessary for the efficient use of energy in soybean harvesting and threshing. To reduce harvesting losses, mainly due to pod shattering, especially designed equipment was developed. Also, to reduce impact on soybean pods and to reduce the cutting height, header components were modified. Shear force and shear strength of stems are important data in the design of harvesting and threshing machine (Öztürk *et al.*, 2017).

#### 1.4. Canola harvesting

Asoodar and Izadinia, (2012,) considers that in canola harvesting with common combine platforms, considerable losses is due by some mechanized harvesting systems. The amount of losses in combine harvester could decrease with the header extension through the increasing of the distance between platform auger and cutter bar. Also, it could be able to reduce grain loss by improving the conditions before harvesting and by using the hydraulic system instead of mechanical system and double knife cutter bar instead of the single cutter bar.

#### 1.5. Rice harvesting

Harvesting techniques have a significant economic input. Results demonstrated that a harvester cutting and straw chopping combination was the harvesting method with the lowest operating cost, high yield, time savings and high net income (Latif *et al.*, 2018). The rice crop harvesting time is an important parameter in respect of yield as well as in economic terms. A suitable time of rice harvesting and a suitable storage after harvesting allow to obtain a production with 10-15% higher. An early harvest can lead to a low yield and a long delayed harvest can lead to an increased percentage of broken grains and a decrease in yield (Jewel *et al.*, 2016).

Rice with pericarp in various colours began to gain popular interest and increased consumption (Promsomboon, 2018). Promsomboon, (2019) considers that Kum Bangpra variety had greater yield than Riceberry under the same cultivation conditions. It was found that in lowland condition Kum Bangpra variety had straw-coloured husk, round grain with a dark purple color, a gelatinization temperature at 67°C which causes the cooked rice to become soft and sticky.

Present trend in the field of rice combine harvester is to increase harvesting capacity, reducing harvester losses, resulting in large combines with a high level of automation with high cost which is also resulting in soil compaction problem with modern farming system. Adisa *et al.*, (2016), determined optimal operating parameters of a self-propelled stripper harvester prototype developed for Nigeria's small farm size and intercropping farming pattern.

Postharvest losses to "stacks" of harvested rice in the rice-pulse systems are a major concern. The harvested rice is stacked before threshing for 2-5 weeks. Drying of grain and seed typically relies on sun drying. Gummert *et al.*, in 2016, considers that late threshing and poor postharvest management practices by stacking rice in improper conditions can reduce both the quantity and quality of rice grain.

#### 1.6. Hemp harvesting

A simple technological hemp harvesting solutions with practical applications in Latvia is harvesting of the hemp stalks in spring. The disadvantages of this technology are that there is a significant loss of product mass and a decrease in its quality. The possible solution for reducing these losses is raising the cutting height of the stalks when the seedy part of the yield is harvested (Ivanov *et al.*, 2015).

#### 1.7. Paddy harvesting

During production of paddy crop, harvesting is one of the major operations among all other operations which plays significant role in realizing the full benefit of raised crop.

*Bhanage et al., (2016)* conclude that in the range of field operations, the most important operations are paddy harvesting and threshing. These operations are laborious, involving human effort, requiring approximately 150-200 man-h / ha to harvest paddy alone. The main advantages of the paddy stripper harvester are: increased harvesting capacity, reduced power requirement and more time available for harvest. However, most of the straw is un-harvested and left in the field.

Stripper harvesting technology, which strips only seeds and keeps straw high in the field, has the bright prospects for mechanizing the harvesting operation in small and fragmented land. Specialists believe that for mechanization of the harvesting operation on small and fragmented lands is appropriate the technology of harvesting the stripper, which only strips the seeds and keeps the straw high in the field. This technology has the advantage of reducing the time required for threshing operation with the light mechanism and with a lesser power compared to conventional cutter bar combine harvester (*Bhanage et al., 2017*).

#### 1.8. *Lupinus albus* harvesting

Of particular interest is the possibility of harvesting large grains of *Lupinus albus* by harvesters with axial rotary threshing and separating device. Their constructive peculiarity consists in the fact that the gaps between the rotor and a concave are large and allowing to work on light modes providing low damage of seed. So, the area of grain separation has improved more than the classic combines harvesters ensuring the allocation of grain from the heap. Experimental results has shown that the use of axial rotary combines or *Lupinus albus* harvesting allow reducing the seeds loss and damage (*Aldoshin and Didmanidze, 2018*). Another advantage is that the casing in the threshing and separating parts can rotate in the passing or counter direction with the rotor. The locking elements provides the possibility of using the system with a fixed casing.

## **2. Postharvest**

Postharvest cereal loss is the loss of grains between harvest and consumption. A poor post-harvest storage management can lead to postharvest cereal losses due to rodents, grain weevils and microorganisms (*Agwang and Okiki-Lating, 2017; Stathers et al., 2017; Westerman and Werf, 2007; Zaica et al., 2018*). Adoption of improved postharvest storage modern facilities (e.g. open drums, metal silo, hermetic bags/ drums, etc.) or various preservation methods are major approaches towards loss reduction (*Ndiritu and Ruhinduka, 2019; Egessa et al., 2017; Ahmed, 1983; Njoroge et al., 2017*).

In Africa the level of knowledge of the operating personnel and their capacity to manage grain stocks through the grain value-chain is one of the understated aspects of capacity building to reduce postharvest losses. Most of the time, emphasis is placed on the provision of modern technologies that aid in improving grain quality and reducing losses during grain handling and storage, with little emphasis on training of personnel (*Ileleji et al., 2017*).

#### 2.1. Storage

Efficient design for long term storage is impose by seasonal fluctuations in the harvesting of grains because the grains quality will be retained by proper storage. The qualitative and quantitative losses of grains in postharvest processing and storage at a particular geographical location are influenced by a lot of factors such as temperature, humidity, aeration, insect infestation, rodents, fungus etc. (*Loganathan et al., 2018; Jatkauskas and Vrotniakiene, 2006*).

Cereals proper storage must not be neglected because of the importance and high demand of cereals for consumption. The postharvest grains damage caused during storage is mainly due to infestation by storage pest which causes huge quality losses in food grains and last but not least financial losses. This damage may be due to microbiological agents like fungi and bacteria or to direct feeding of grains by insects and pests.

The above storage losses can be minimized through use of proper pest management practices. Moulds and insects are different causative agents which cause economic and quality losses during storage.

The main reasons of fungal infection are humidity and non-aerated storage space. The only solution to avoid the infection is a proper drying of the stored product because due to their strong viability even a high aeration at the place of storage do not completely kill the spores (*Katagi and Malashetti, 2014*).

Postharvest losses (PHLs) are crop/product specific and occur at many stages in the supply chain (harvesting, drying, storage, market, transport, etc.). They are evident as loss of weight and loss of quality and are compounded by subsequent losses of market opportunity and lost production resources such as land, water, labour, agricultural inputs and soil fertility. By improving PHL estimates it will be possible to target loss-reduction interventions at the most affected areas (geographically), the most affected links in the postharvest chain or those links that would be most cost effective to address.

Suitable initiatives underpinned by modern rapid approaches to loss assessment are required to strengthen the ability of developing countries to collect relevant data, in the format needed by the system (Hodges *et al.*, 2010).

The main physical factors that affect grain in storage are climate variables such as temperature, moisture content and relative. They influence insect and mould development, which lead to deterioration and loss of quality of stored grain. Higher or very low temperatures and low level of humidity are less likely to support the development of most of the pests and insects (Ndiritu and Ruhinduka, 2019).

The lack of centralized storage and the non-performance of grain conditioning leads to the fact that producers cannot perform a proper post-harvest handling and storage, not having grain drying units, pre-cleaning equipment and the required number of granaries. In addition, a proper grain storage requires higher financial costs, so not every producer can meet the necessary technological requirements of grain receiving and post-harvest primary processing. Also, the processing of the incoming grain mixture with another moisture content, hard-separable impurities and content of germinated grains using standard practice is costly or this grain is used for animal feeding purposes (Mar'in and Vereshchagin, 2016).

Because infection spread through the spores, which are present in the atmosphere everywhere and move by insect and wind it is very difficult in stored grains to identify the stage of fungal infection. Some of the obvious indicators of fungi infestation are blackening of grains and pungent smell. Improper storage spaces lead to fungal infection who completely altered grain quality, texture, and taste. Also food items acquire bad taste and have decreased nutritious quality. The main reasons of fungal infection are humidity and non-aerated storage space. The only solution to avoid the infection is a proper drying of the stored product because even high temperature at the place of storage does not completely kill the spores due to their strong resistance (Katagi and Malashetti, 2014).

Chen *et al.*, (2018) considers that to ensure grain security in China reducing post-harvest grain loss represents one of the most realistic and effective ways. The results of their survey show that grain storage conditions followed by transportation have the greatest impact on post-harvest grain loss. To analyse the main factors affecting post-harvest grain loss during sales was used the Tobit regression model. The findings suggest that the seller's education level, experince of working as a seller, the conditions of grain storage, and the supply and management level of public facilities in the market were negatively correlated with grain loss in the sales process, whereas the seller's age, the separation of sales shops and storage warehouses, and the fall season were positively correlated with grain loss.

## 2.2 Seed treatment technology

Within primary processing and post-harvest technologies, cereal and seed treatment technology represents an area of great interest with high impact on environmental and food industry. Establishing a suitable seed and grain crops coating technology involves a thorough analysis of all the factors involved in the coating seed process (seed quality, special characteristics depending on the variety of seed, destination, etc.). "Seed treatment" means any process that seed have undergone before sowing in order to obtain high and stable yields.

Success in growing cereal seed starts with efficient treatment, so one of the criteria for seed quality assessing is chemical treatment with major implications for future crop development. Achieving a proper seed treatment technology of cereals requires a thorough analysis of all the factors involved in the process of seed coating.

To perform a proper seed treatment operation are used complex machines which are composed of rotating disc system for the spreading of the substance to treat and screw conveyor brush for better uniformity of coating substance on the surface of seeds. For the determination of the degree of coverage, speed rotating disc and screw conveyor speed are two basic parameters (Zaica *et al.*, 2016).

*Fusarium graminearum* is the major causal agent of Fusarium Head Blight (FHB) of wheat and other cereals, a devastating disease responsible of yield and quality losses worldwide. It is actually able to produce a wide range of mycotoxins highly resistant to thermal and chemical treatments. Consequently, they cannot be removed from the crops and therefore, efforts to control FHB should be made before harvesting.

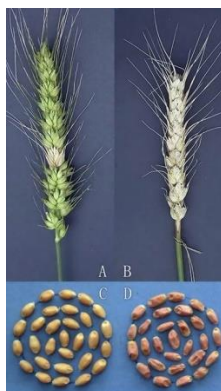


**Fig. 4 - Wheat reaction to *Fusarium graminearum* A, PI 672538 spike, B, L661 spike, C, PI672538 seed, and D, L661 seed (Li et al., 2017)**

Various studies demonstrated the importance of cultural practices and fungicides in the management of FHB but these methods are not sufficient enough to ensure high quality grains at harvest. Thus, it is important to find effective alternatives and the use of antagonistic microorganisms against *Fusarium graminearum* could become one of them (Legrand et al., 2015).

It is reckoned that a sizeable quantity of world's food production is lost due to damage caused by bacteria, mould, insects and other pests. One of the major cause of postharvest loss encountered in stored grains is the presence of larvae and adults of several insects.

Many of the postharvest chemical fumigants currently in use for control of insect infestation, such as methyl bromide (MB), ethylene dibromide (EDB) and ethylene oxide (ETO) are either banned or to be phased out because of their danger and adverse impact on human health and environment. There are also reports of development by major grain pests of higher levels of resistance to phosphine, the other major grain fumigant used worldwide.

Therefore, a long-term proper storage of agricultural products may be at risk as the traditional fumigants are phased out and/or due to development of increased insect resistance. Practical control of insect pests, regardless of species or stage of development is possible by low dose irradiation in the dose range of 0.2 to 0.5 kGy. The advantages include short treatment time, no undesirable chemical residues in the food, no resistance developed by the insects and no significant changes in the physicochemical and functional properties or the nutritive value of the product (Thomas, 2001).

### 2.3. Drying

Specialists believe that by taking away of water contents from agricultural product, drying provides extended period of shelf life. Solar energy is used by the solar air heaters to heat air and it can be engaged in many applications, for example heating of spaces and drying of crop material. The drying is carried out in two processes. In the first process, the vaporization of moisture hooked on the atmosphere from surface of the substance at stable rate of drying takes place. In the second process, drying rate decreases because it decreases with moisture content or decreases with increase in air humidity.



**Fig. 5 - Comparative test of multipurpose solar dryer (left), drying tray in open-air (centre), and tarp in open-air (right) (Ileleji et al., 2017)**

Solar dryers are the machines that organize the drying practice and prevent the agriculture product from being destroyed by insect pest, rain and dust. *Khan et al., 2018*, designed and developed the solar collector for air heating and evaluated the energy requirements for the drying of grains. Blower was used to scatter the air that strike the grains. A solar collector was joined with the bin in which grains were kept. The solar collector was 6m long, 4 m wide and 0.3 m deep. The material used for absorber plate was steel metal sheet. For glazing, a single glass with 6 mm thickness was used. They used plywood as an insulating material for the body of the solar collector. They tested the performance at seven different convective air flow rates. They found that the drying efficiency of the solar collector was 10% higher than all previous conventional methods. Statistical analysis was also done to check the performance of the solar collector and showed that the flow rate of hot air increased its performance (*Khan et al., 2018*).

*Cardoso et al., (2015)* evaluates the influence of the moisture and type of drying applied to grains on the level of carotenoids in yellow maize. Based on the results, they recommended that the harvest be done preferably when the grains present 22% humidity, followed by drying in a dryer or in shade.

## CONCLUSIONS

Considering the system or the agro-food chain as a whole, harvesting can be seen as the connecting operation or binder between the pre-harvest operation, corresponding to production activity and the post-harvest operation, extending from harvesting to marketing and consumption.

For the purpose of business development, producers of agricultural products from all countries focus on determining the ways to increase the gross harvesting of products, and improve its quality indicators. In order to deliver high productivity with minimal crop losses, damage and minimal expenses on maintenance, the combine harvester needs to be a high-tech one.

Postharvest loss is a complex problem and it vary for different crops, climatic conditions, agriculture practices, and the degree of industrialization and economic development of each country. Therefore, reducing food losses contributes to global food demand satisfaction and to continuously improving food security and increasing resource use efficiency.

In postharvest operations more than one-third of agriculture production is lost or wasted while fulfilling the food demand of an increasing population remains a major global concern. In developing countries, especially, reducing the postharvest losses, could become a reliable solution to increase food availability, eliminate hunger, reduce pressure on natural resources and last but not least to improve farmers' livelihoods. Modern technologies and improved storage structures can successfully reduce postharvest losses and increase farmers' revenues in the same time. Using the sealed waterproof bags or structures (hermetic storage creates an automatic modified atmosphere of high carbon dioxide concentration) lead to significant reduction of losses due to insect infestations. With the help of properly sealed hermetic storage structures storage losses reduced by 98%, maintaining the quality and long-term viability of stored seeds.

Using the latest agricultural practices and adequate innovative technologies on primary cereal production farmers all over the world can significantly reduce the losses, help strengthening food security and at the same time to increase their profit.

## ACKNOWLEDGEMENT

This study was supported by Romanian Ministry of Agriculture and Rural Development, through ADER Programme - Grant no. 18.1.2., Project "Methods for reducing food waste at national level in the agrifood chain, in order to prevent and reduce the socio-economic impact by 2030".

## REFERENCES

- [1] Adisa, A.F., Ndirika, V.I.O., Yiljep, Y.D., Mohammed, U.S., (2016), Determination of optimum critical operating parameters of stripping rice harvester in a rural area, *CIGR-AgEng conference, Aarhus/Denmark*;
- [2] Agwang, F., Okiki-Lating, P., (2017), Selection of appropriate chilli drying technologies using analytical hierarchy process: a case of northern Uganda, *1st All Africa Postharvest Congress*, pp.33-35, Nairobi/Kenya;
- [3] Ahmed, H., (1983), Losses incurred in stored food grains by insect pests - A review, *Pakistan Journal of Agricultural Research*, Vol 3(4), pp.198-207, Faisalabad/Pakistan;

- [4] Alatürk, M., Şal., Y.S., (2018), A study on the feasibility of double production (seed and hay) in triticale with different height and number of harvestings, *COMU J. Agric. Fac* 6, pp.235-241, Ankara/Turkey;
- [5] Aldoshin, N., Didmanidze, O., (2018), Harvesting Lupinus albus axial rotary combine harvesters, *Research in Agricultural Engineering*, vol. 64 (4), pp.209-214, Prague/Czech Republic;
- [6] Asoodar, M.A., Izadinia, Y., (2012), Benefits of harvester front extension in reducing canola harvest losses, *International Agricultural Engineering Journal*, Vol 21(2), pp.32-37, Ramin/Iran;
- [7] Bendinelli, W.E., Su C.T., Pera, T.G., Caixeta, J.V.(2020), What are the main factors that determine post-harvest losses of grain?, *Sustainable production and consumption*, vol. 21, pp.228-238;
- [8] Bhanage, G.B., Shahare, P.U., Aware, V.V., Dhande, K.G., Deshmukh, P.S., (2016), Laboratory testing of paddy stripping header mechanism, *Agriculture Update*, Vol. 11(2), pp.139-144, Ashram/India;
- [9] Bhanage, G.B., Sharare, P.U., Aware, V.V., Dechale, J.S., (2017), Development of paddy stripper header mechanism, *International Journal of Agricultural Engineering*, vol. 10(1), pp.179-185, Bangkok/Thailand;
- [10] Bräutigam, K-R, Jörissen, J., Priefer, C., (2014), The extent of food waste generation across EU-27: Different calculation methods and the reliability of their results, *Waste Management & Research*, Vol. 32(8) pp.683 –694, Sunway/Malaysia;
- [11] Bumber, I.V., Epifantsev, V.V., Shchegorets, O.V., Singovskaya, V. T., Kuznetsov, E.E., Kuvshinov A.A., Lontseva, I.A., Kapustina, N.A., (2018), Optimization of agrotechnical terms of harvesting of crops, design and operating parameters of crop harvesting machines under conditions of the Amur Region, Russian Federation, *Plant Archives* Vol. 18(2), pp.2567-2572, Uttar Pradesh/India;
- [12] Cardoso, W.S., Borem, A., Karam, D., Rios, S.D., Paes, M.C.D., (2015), Influence of the moisture at harvest and drying process of the grains on the level of carotenoids in maize (*Zea mays*), *Food Science and Technology*, vol.35(3), pp 481-486, Brazil;
- [13] Chen, XJ, Wu, LH, Shan, LJ, Zang, OX., (2018), Main Factors Affecting Post-Harvest Grain loss during the Sales Process: A Survey in Nine Provinces of China, *Sustainability*, vol.10 (3);
- [14] Creț, C., Șerban, P., Duma-Copcea, A., MiHuț, C., Țigriș, N., Ilea, R., (2018), Mechanisation technology in sowing wheat in Chișineu-Criș, Arad County, *Research Journal of Agricultural Science*, 50 (4), Timișoara/Romania;
- [15] Creț, C., Șerban, P., Duma-Copcea, A., MiHuț, C., Țigriș, N., Ilea, R., (2018), Harvesting grain maize with a Case-IH 7088 self-propelled combine, *Research Journal of Agricultural Science*, 50 (1), pp.158-161, Timișoara/Romania;
- [16] Delchev, K., Trendafilov, K., Tihanov, G., Stoyanov, Y., (2016), Grain combines productivity according to various unloading methods – in the field and at the edge of the field, *Agricultural Science and Technology*, vol. 9, no 2, pp.221-226, Stara Zagora/Bulgaria;
- [17] Duma Copcea, A., Ilea, R., Crîsta, I., (2017), Studies regarding grain loss in straw cereals, *Research Journal of Agricultural Science*, Vol 49 (2), Timișoara/Romania;
- [18] Duma-Copcea, A., Ilea, R., Popa, D., Sîrbu, C., (2018), Mechanisation technology for the harvesting of grain maize with a self-propelled combine, *Research Journal of Agricultural Science*, 50 (1), pp.45-50, Timișoara/Romania;
- [19] Egessa, J., Olupot, M., Deppeler, A., Dischl, R., Vodouhe, S., Cossa, L., (2017), Experiences with business models and dissemination techniques for sustainable postharvest management among smallholder farmers, 1st *All Africa Postharvest Congress*, pp.159-160, Nairobi/Kenya;
- [20] Faggion, F., Melara, D.F., Correia, T.P., Pereira, E.A., (2017), Lost in harvester soybean by two depreciated combines, *Brazilian Journal of Applied Technology for Agricultural Science*, vol. 10, no.2, pp.89-95, Guarapuava/Brazil
- [21] Fu, J., Chen, Z., Han, L., Ren, L., (2018), Review of grain threshing theory and technology, *Int J Agric & Biol Eng*, Vol 11(3), pp.12-20, Beijing/China;
- [22] Gach, S., Chlebowski, J., (2016), Technological, economic and methodological aspects of corn grain harvesting and preservation, *Annals of Warsaw University of Life Sciences – SGGW, Agriculture No 67 (Agricultural and Forest Engineering)*, pp.49–61, Warsaw/Poland;
- [23] Gummert, M., Htwe, N., Cabardo, C., Thu, A., Aung, Y., Thant A., Maw M., Quilloy R., Singleton G., (2016), Loss assessment from harvesting to milling of rice in traditional and best practice postharvest systems in Myanmar, <https://www.cabdirect.org/cabdirect/FullTextPDF/2016/20163227405.pdf>, pp.59-62;

- [24] He, W., Xiaopng, B., Hongbin, L., (2017), Proportional distribution method for estimating actual grain flow under combine harvester dynamics, *Int J Agric & Biol Eng*, pp.158-164, Beijing/China;
- [25] Hodges, R. J., Bernard, M., Knipschild, H., Rembold, F., (2010), African postharvest losses information system - a network for the estimation of cereal weight losses, *10th International Working Conference on Stored Product Protection*, pp.957-962, Estoril/Portugal"
- [26] Ilea, R., Bungescu, S., Popa, D., Caba, I., (2013), Studies regarding the harvesting of grain corn, *Research Journal of Agricultural Science*, Vol 43 (3), pp.94-97, Timișoara/Romania
- [27] Ileleji, K., Opit, G., McNeil, S., Omobowale, M., Ala, A., Otitodun, G., Nwaubani, S., Tarver, H., Solorio E., Ayodele M., (2017), Stored grain protection and management capacity building in Nigeria – review of 7 years of experience, *1st All Africa Postharvest Congress*, pp.132-134, Nairobi/Kenya;
- [28] Ileleji, K.E., Shrestha, R., Sarr, I., Diop, P., Ketiém, P., De Groote, H., (2017), Field testing of a multipurpose solar dryer for small farm holders, *1st All Africa Postharvest Congress*, pp.45-48, Nairobi/Kenya;
- [29] Ivanovs, S., Adamovics, A., Rucins, A., (2015), Investigation of the technological spring harvesting variants of the industrial hemp stalk mass, *Agronomy Research* 13(1), pp.73–82, Tartu/Estonia;
- [30] Jatkauskas, J., Vrotniakienė, V., (2006), An evaluation of alternative grain processing and storage methods (storage and nutrition value), 9th International Working Conference on Stored Product Protection, PS 1-13-6325, pp.99-106, São Paulo/Brazil;
- [31] Jewel, M.H., Rahman, R., Rahman, M.M., Islam, J., (2016), Effect of variety and date of harvesting on yield performance of Boro rice, *Fundamental and Applied Agriculture* 1(2), pp.66-69, Mymensingh/Bangladesh;
- [32] Katagi, A., Malashetti I., (2014), Use of plant products for safe and economic storage of food grains, *Advance Research Journal of Crop Improvement*, Vol5(1), pp.53-56
- [33] Keskin, M., Şekerli, Y.E., (2018), An evaluation of combine harvester accidents in Turkey, *Journal of Agricultural Faculty of Mustafa Kemal University*, 23(2), pp.137-147, Hatay/Turkey;
- [34] Khan, F.A., Munir, A., Ghafor, A., Murtaza, G., (2018), The design, fabrication and performance evaluation of solar sustained batch type maize dryer for valuation addition, *International Journal of Agriculture, Environment and Food Sciences* 2(2), pp.50-56, Diyarbakir/Turkey;
- [35] Latif, M.T., Sher, F., Hussain, M., Asghar, M., (2018), Economics of different harvesting techniques of wheat in rice-wheat cropping pattern of Punjab, Pakistan, *Azarian Journal of Agriculture*, vol. 5(3), pp.103-107, Maragheh/Iran;
- [36] Legrand, F., Picot, A., Cor, O., Barbier, G., le Floch, G., (2015), Reduction of the incidence of fusarium graminearum on cereals (triticales) by application of biocontrol agents and stimulation of endemic fungal communities, *AFPP-Fifth International Conference on Alternative Methods of Plant Protection*, pp.385-306, Lille/France;
- [37] Li, X., Xiang, Z.P., Chen, W.Q., Huang, Q.L., Liu, T.G., Li, Q., Zhong, S.F., Zhang, M., Guo, J.W., Lei L., Luo, P.G., (2017), Re-evaluation of Two Quantitative Trait Loci for Type II Resistance to Fusarium Head Blight in Wheat Germplasm PI 672538, *Phytopathology*, 107, pp. 92-99;
- [38] Li, Y., Tao, C., Zhe, Q., Kehong, L., Xiaowei, Y., Dandan, H., Bingxin, Y., Dongyue, Z., Dongxing Z., (2016), Development and application of mechanized maize harvesters, *International Journal of Agricultural and Biological Engineering*, vol. 9, no 3, pp.15-28, Beijing/China;
- [39] Loganathan, M., Akash, U., Durgalakshmi, R., Anandharamakrishnan, C., (2018), Constraints in Grain quality management: A warehouse journey, *12th International Working Conference on Stored Product Protection (IWCSPP)*, pp.98-100, Berlin/Germany;
- [40] Mahmoodi, E., Jafari, A., Mobli, H., (2007), A new idea for construction of a flexible cutter bar mower for listed lands, *4th International Automotive Electronics Congress*, Bangkok/Thailand;
- [41] Marek, A., Kristof, K., Michalm A., Jobbagy, J., (2019), The effect of postharvest processing in model line at food maize grains external and internal quality, *Proceeding of 7<sup>th</sup> International conference on trends in agricultural engineering (TAE)*, pp.32-39, Prague/Czech Republic;
- [42] Mar'in, V.A., Vereshchagin, A.L., (2016), Physical principles of processing off-grade buckwheat, *Foods and Raw Materials*, vol. 4, no. 1, pp.51-60, Kamerevo/Russia;
- [43] Mesterhazy, A., Olah, J., Popp, J., (2020), Losses in the Grain Supply Chain: Causes and Solutions, vol. 12(6);

- [44] Milkias, A., Tadesse, T., Zeleke, H., (2018), Evaluating the effects of in-situ rainwater harvesting techniques on soil moisture conservation and grain yield of maize (*Zea mays* L.) in Fedis District, Eastern Hararghe, Ethiopia, *Turkish Journal of Agriculture - Food Science and Technology*, 6(9), pp.1129-1133, Sivas/Turkey;
- [45] Mirzazadeh, A., Abdollahpor, S., Vahed, M.M., (2015), Incorporating skewness and kurtosis in improvement of combine harvester cleaning system performance, *International Journal of Agriculture Innovations and Research*, Vol 3(5), pp.1412-1416, Bhopal/India;
- [46] Mostafavand, H., Kamgar, S., (2014), The effect of grain moisture content and forward speed on grain losses of three varieties of chickpea in mechanical harvesting using feeder and cutter mechanism, *International Journal of Agriculture Innovations and Research*, 3(3), pp.860-865, Bhopal/India
- [47] Ndiritu, S.W., Ruhinduka, D., (2019), Climate variability and post-harvest food loss abatement technologies: evidence from rural Tanzania, *Studies in Agricultural Economics* 121, pp.30-40, Budapest/Hungary
- [48] Njoroge, A.W., Affognon, H., Mutungi, C., Richter, U., Hensel, O., Rohde, B., Mankin, R.W., (2017), Acoustic survey and detection of pests in Kenya's grain storage facilities, *1st All Africa Postharvest Congress*, pp.121-123, Nairobi/Kenya
- [49] Nkurunziza, L., de Toro A., Von Rosen D., Ackersten, H., (2015), Effects of extreme weather on yields of major cereal crops in Sweden: Analysis of long-term experiment data, *Aspects of Applied Biology*, pp.165-172, Warwick/UK;
- [50] Odendo, M., Muyekho, F., Onyango, E., (2017), Farmers' awareness and adoption of improved grain storage technology in western Kenya, *1st All Africa Postharvest Congress*, pp.135-136, Nairobi/Kenya;
- [51] Öztürk, F., Pekitkan, G., Esgici, R., Eliçin, A.K., (2017), Some mechanical properties of soybean (*Glycine max*) stems and seeds, *Scientific Papers. Series A. Agronomy*, Vol. LX, pp.352-355, Bucharest/Romania;
- [52] Petrovska, N., Valkova V., (2018), Knezha, 461 - A new maize hybrid from the middle early group, *Agricultural Science and Technology*, vol. 10, no.4, pp.275-278, Stara Zagora/ Bulgaria;
- [53] Popa, D., Tonea, C., Ilea, R., Drăgoi, Gh., Piloca, L., Tonea, E., Becherescu, A., (2010), Research on tracking technology indices perform operational work by different combine harvesters, *Research Journal of Agricultural Science*, Vol 42 (1), pp.659-662, Timișoara/ Romania;
- [54] Prístavková, M., Žitňák M., Lendelová, J., (2016), Hazard analysis in operating of the post-harvest lines, *Research in Agricultural Engineering*, vol. 62, pp.53-60, Prague/Czech Republic;
- [55] Promsomboon, P., Promsomboon, S., (2018), Evaluation of yield traits between 15 purple-pericarp rice lines (*Oryza sativa* L.), *International Journal of Agricultural Technology* Vol. 14(5), pp.741-750, Bangkok/ Thailand;
- [56] Promsomboon, P., Promsomboon, S., (2019), Environmental responsibility of rice var. Kum Bangpra and Riceberry in lowland and upland conditions, *International Journal of Agricultural Technology*, Vol. 15(5), pp.747-752, Bangkok/ Thailand;
- [57] Redlingshöfer, B., Coudurier, B., Georget, M., (2017), Quantifying food loss during primary production and processing in France, *Journal of Cleaner Production* 164, pp.703-714;
- [58] Shvedyk, M., (2015), Researches results of grain pneumatic collector which is knocked out by reel palletes, *ISB-INMA TEH'*, pp.529-538, Bucharest/Romania;
- [59] Stathers, T., Tran, B., Bernad, M., Rembold, F., Mvumi, B., Priebe, J., Sonntag, F., Block, R., (2017), Expanding the African postharvest losses information system - APHLIS+, *1st All Africa Postharvest Congress*, pp.156-158, Nairobi/Kenya;
- [60] Tang, Z., Li, Y., Cheng, C., (2017), Development of multi-functional combine harvester with grain harvesting and straw baling, *Spanish Journal of Agricultural Research* 15(1), pp.1-10, Madrid/Spain;
- [61] Tang, Z., Li, Y., Zhao, Z., Sun, T., (2015), Structural and parameter design of transverse multi-cylinders device on rice agronomic characteristics, *Spanish Journal of Agricultural Research* 13(4), pp.1-12, Madrid/Spain
- [62] Tihanov, G., (2017), Study on the process of unloading grain harvesters at the end of the field, *Agricultural Science and Technology*, vol. 9, no 2, pp.129-131, Stara Zagora/Bulgaria;
- [63] Tihanov, G.,(2019), A grain harvester performance according to unloading time and modes, *Agricultural Science and Technology*, vol. 11, no.1, pp.59-62, Stara Zagora/ Bulgaria;

- [64] Thomas, P., (2001), Control of post-harvest loss of grain, fruits and vegetables by radiation processing, Proceedings of International Conference on Ensuring the Safety and Quality of Food through Radiation Processing, pp93-102, Antalya, Turkey
- [65] Upadhayay, A.K., Singh, V., Moses, S.C., (2018), To study of effective speeds for harvesting of wheat straw by straw combine, *International Journal of Agricultural Engineering*, vol. 11(1), pp.54-59, Bangkok / Thailand
- [66] Westerman, P.R., Van der Werf W., (2007), Annual losses of weed seed due to predation on cereal fields, *2007 Congress of the Spanish Society of Malherbología*, pp.17-20, Toledo / Spain;
- [67] Zaica, A., Ciupercă, R., Nedelcu, A., Zaica, Al., Popa, L., Anghel, A., Ștefan, V., Cristescu, A.C., (2018), Aspects regarding the flattened installation for the drying cereals in a wet condition, *International Symposium ISB-INMA TEH' 2018*, pp.395-400, Bucharest / Romania;
- [68] Zaica, A., Visan, A.L., Păun, A., Găgeanu, P., Bunduchi, G., Zaica, A., Ștefan, V., Manea, D., (2016), The coating process of corn grains using a treatment machine with brush screw conveyor, 44. *Symposium "Actual Tasks on Agricultural Engineering"*, pp.333-345, Opatija / Croatia;
- [69] Zubko, V., Roubik, H., Zamora, O., Khvorost, T., (2018), Analysis and forecast of performance characteristics of combine harvesters, *Agronomy Research* 16(5), pp.2282- 2302, Tartu/Estonia.

# TESTING, ANALYSIS AND COMPARISON FOR CHARACTERISTICS OF AGRICULTURAL FIELD AND ASPHALT ROAD ROUGHNESS

/

## 农田地面与沥青路面不平度特征的测试、分析与比较

Lijuan Wang, Jianguo Yan\*, Shengshi Xie, Chunguang Wang

Inner Mongolia Agricultural University, College of Mechanical and Electrical Engineering, Hohhot, China

Tel: +86 13624713647; E-mail: yanyjg@126.com

DOI: <https://doi.org/10.35633/inmateh-62-15>

**Keywords:** Field and road surface roughness, Power Spectral Density, Root Mean Square, Waviness, Roughness index

### ABSTRACT

Measuring and analysing the roughness of agricultural field and road have great significance for studying the characteristics of tractor dynamic response. This study was designed to analyse and compare the roughness characteristics of agricultural field and asphalt road profiles. A profiling apparatus was developed to measure field and road surface profiles of parallel tracks. The profile measurements were conducted in a grass field, a corn stubble field, a harvested potato field and on an asphalt road. The root mean square value and two spectrum parameters of surface profiles were calculated and analysed to investigate the roughness characteristics of fields and asphalt road. The results of the study indicate that for the values of the agricultural field and asphalt road surface roughness, waviness and roughness index are both positive associated with the root mean square value. Most of the waviness values of all measured field profiles were less than 2 with the average of 1.8, while the waviness values of all measured asphalt road profiles were greater than 2 with the average of 2.08. The roughness of both field and asphalt road profiles can be distinguished by the power spectral density fitting method. However, it has better performance in characterizing asphalt road profiles than characterizing field profiles with the power spectral density fitting method.

### ABSTRACT

测量和分析农田和路面的不平度对研究拖拉机动态响应特性具有重要意义。本文为分析和比较农田地面与沥青路面的不平度特征，研制了一种地面不平度测量装置，分别在田间草地、玉米茬地、马铃薯收获地和沥青路面上开展了不平度测试试验。通过分析测试地面不平度的均方根及两个频谱特征参数，研究了农田地面和沥青路面的不平度特性。结果表明，农田地面和沥青路面的不平度频率指数和不平度系数均与不平度均方根呈正相关；测试的三种农田地面不平度频率指数多数都小于 2，其平均值为 1.8，而沥青路面不平度频率指数都大于 2，其平均值为 2.08；利用功率谱密度拟合方法可以有效识别农田地面与沥青路面的不平度特征，但用于沥青路面的不平度特征识别具有更好的效果。

### INTRODUCTION

The road surface roughness is the main source of kinematic excitation of a moving vehicle, which plays an important role in ride comfort evaluation, dynamic load analysis and vehicle vibration simulation (Cutini *et al.*, 2017; Zhang *et al.*, 2018). Agricultural field and asphalt road can be considered as off-road and on-road conditions for dynamic analysis of tractor. There is a significant difference in the amplitude of tractor vibration when it travels on the different roads with the same speed (Yiliyasi *et al.*, 2016). Thus, an accurate dynamic simulation of tractor is only possible if the terrain or road profiles tractor traversing on should be accurately acquired and modeled.

A detailed report on how to measure and interpret road surface profiles was introduced in Sayers and Karamihas (1998). Road surface roughness, which plays a major role in vehicle ride dynamics, can be specified with the use of the Root Mean Square (RMS) elevation in the time domain or the Power Spectral Density (PSD) in the frequency domain (Gorsich *et al.*, 2003). Some approaches based on RMS or spectrum parameters of typical roads and terrains were proposed in the past (Lu *et al.*, 2005; Phillip *et al.*, 2014; Johannesson *et al.*, 2016).

However, limited research has been conducted on analysing the relationship between the profile parameters in characterizing the road surface roughness. An early research on measuring and modeling road surface roughness on bridge in spectral characteristics showed the integral of a filtered profile's *PSD* was the profile's *RMS* (Honda et al., 1966). A study about predicting *RMS* surface roughness using fractal dimension and spectrum parameters was carried out in (Phillip et al., 2011).

This study was intended to derive a proposal for comparing the roughness characteristics of agricultural field and asphalt road by measuring and analysing *RMS* and *PSD* parameters of surface profiles. The effect of characterizing field and asphalt road roughness with *PSD* fitting method was evaluated from the perspective of analysing the relation between the time-domain *RMS* and the spectrum parameters.

## MATERIALS AND METHODS

### Instrumentation

A surface profiling apparatus (profilers), which was mounted on the front counterweight of a tractor shown in Figure 1, was developed for the measurement of agricultural terrain and road profiles with parallel tracks. The surface profiles can be measured dynamically during tractor driving. The design and validation of the profiler was presented in a previous study (Yan et al., 2019) in detail. The overall accuracy of the profiler, expressed by the root mean square error (*RMSE*) value, was 3.6-4.7 mm and 4.5-5.1 mm with profiling speeds of 1.02 km/h and 2.56 km/h, respectively.



Fig. 1 - Profiling apparatus mounted on the front counterweight of a tractor

### Profile measurements of agricultural field and asphalt road

The location of the profiling tests was situated at 40.21°N latitude and 111.34°E longitude in Hohhot, China, and the test was completed on October 7, 2019.

The profiling tests took place in a grass field, a corn stubble field (average stubble height of 10 cm), a harvested potato field and an asphalt road, as shown in Figure 2. During all profiling tests, the tractor was maintained at constant forward speeds of 2.56 km/h, which was verified by the RTK-GNSS system. The measurements for each type of field included five treatments, which were conducted on different tracks with test distances of around 100 meters. The average values of the field surface soil penetration resistance of the grass field, corn stubble field, harvested potato field were 187.6 N·cm<sup>-2</sup>, 246.3 N·cm<sup>-2</sup> and 130.2 N·cm<sup>-2</sup>, respectively, while the average values of the field surface soil moisture content of the grass field, corn stubble field, harvested potato field were 3.24%, 1.82% and 4.26%, respectively (soil penetration resistance and soil moisture content were determined using a digital soil compaction meter and a digital soil moisture meter).



Fig. 2 - Agricultural field and asphalt road profiling measurement

## THEORY

### **Spectrum parameters of profile PSD**

The *PSD* representation is widely used either to assess the road roughness or as an input to vehicle dynamics (Ma *et al.*, 2013). Previous proposals suggest the vertical displacement *PSD* of road or off-road terrain profiles can be represented by equation (1) in assumption that profiles are considered to be stationary random signals with a Gaussian distribution and zero value (prEN, 2015; Múčka, 2016).

$$G(n) = Cn^{-W} \quad (1)$$

where:

$G(n)$  is the *PSD* of vertical road profile displacement, [ $m^3$ ];

$C$  is the roughness index, [ $m^{3-W}$ ];

$n$  is the spatial frequency, [ $m^{-1}$ ];

$W$  is the wavelength distribution, named waviness, which is the exponent of the fitted *PSD*.

According to Eq. (1), the distribution of road surface *PSD* in spatial frequency domain can be approximated by means of a straight line in the log-log chart, which can be called the *PSD* fitting method. Two spectrum parameters, waviness  $W$  and roughness index  $C$  of vertical profiles can be determined by the *PSD* fitting method.

From Eq. (1), two spectrum parameters, roughness index  $C$  and waviness  $W$ , determine the characteristics of road surface roughness. Parameter  $C$  is proportional to the roughness variance, while  $W$  quantifies the distribution of the road profile wavelength content between particular spatial frequency bands.

### Relation among RMS and two spectrum parameters

According to Parseval's relation (Steven, 1999), since the time and frequency domains are equivalent representations of the same signal, they must have the same energy. When the mean value of road profile sample is zero, the variance of the profile is equal to the mean square value. Also, the RMS of road profile is equal to the standard deviation, which determine the relationship between the *RMS* and the *PSD* of the road surface profile. That is the *RMS* of the vertical displacement of the profile and the square root of the area under the displacement *PSD* should result in the same value, which represent the energy of the vertical profile. The calculation formulas are as follows:

$$RMS = \left( \int_{n_1}^{n_2} G(n) dn \right)^{1/2} \quad (2)$$

Eq.(1) can be substituted into Eq.(2), resulting in Eq.(3).

$$RMS = \sqrt{\frac{C(n_2^{(1-W)} - n_1^{(1-W)})}{1-W}} \quad (3)$$

where:  $n_1$  is lower spatial frequency;

$n_2$  is upper spatial frequency.

The relation among the  $W$ ,  $C$  and *RMS* determined by the Eq. (3) is simulated in Figure 3. The spatial frequency is selected from  $0.011 \text{ m}^{-1}$  to  $2.83 \text{ m}^{-1}$  according to the ISO 8608 standard (ISO 8608, 1995). The coordinate variable  $C$  in the Figure 6 covers the range of eight roughness index grades which is from  $16 \times 10^{-8}$  to  $262144 \times 10^{-8}$  in the ISO 8608 standard, while coordinate variable  $W$  changes from 1 to 3.5 which covers a wide range of road profiles (Múčka and Kropáč, 2009). Figure 3 shows *RMS* is positive related with  $C$  and  $W$ , which codetermine the energy of road roughness. Therefore,  $W$  is an important parameter which should be investigated in the testing and analysis of road surface roughness, although the ISO 8608 suggests  $W = 2$  in the road classification.

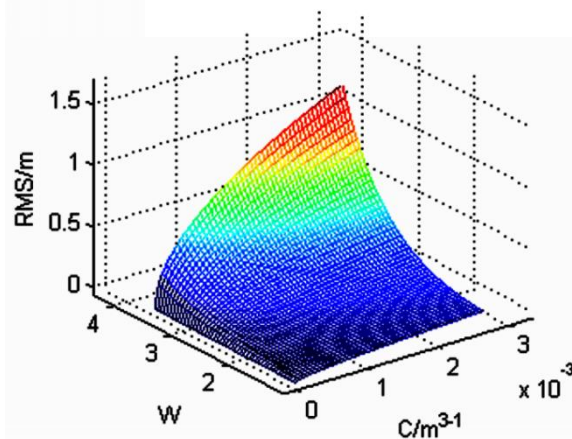


Fig. 3 - The relation between the  $W$ ,  $C$  and *RMS*

Relation between *RMS* and two spectrum parameters of surface profile is established by Eq. (3). Theoretically, root mean square of measured profile ( $RMS_m$ ) and root mean square calculated ( $RMS_c$ ) by  $W$  and  $C$  according to Eq. (3) should be equivalent with the assumption of *PSD* characterization fulfilled. However, the profiles of road or terrain can't totally meet the assumption, which cause the deviations between  $RMS_m$  and  $RMS_c$ . Therefore, it can be concluded that the closer the  $RMS_c$  is to  $RMS_m$ , the better profile data meets the assumption condition of *PSD* characterization, which can be used to check the effect of characterizing the profiles with the *PSD* fitting method.

## RESULTS

### Comparison on the profile values between the agricultural field and asphalt road

The measured data of profile displacements from both wheel tracks were analysed and transformed into the *PSD* of agricultural field and asphalt road roughness by use of the Fourier analysis. Calculated *PSD* curves of tested field profiles are illustrated in Figure 4-6 (Take one group of test data as an example in each kind of the field terrains).

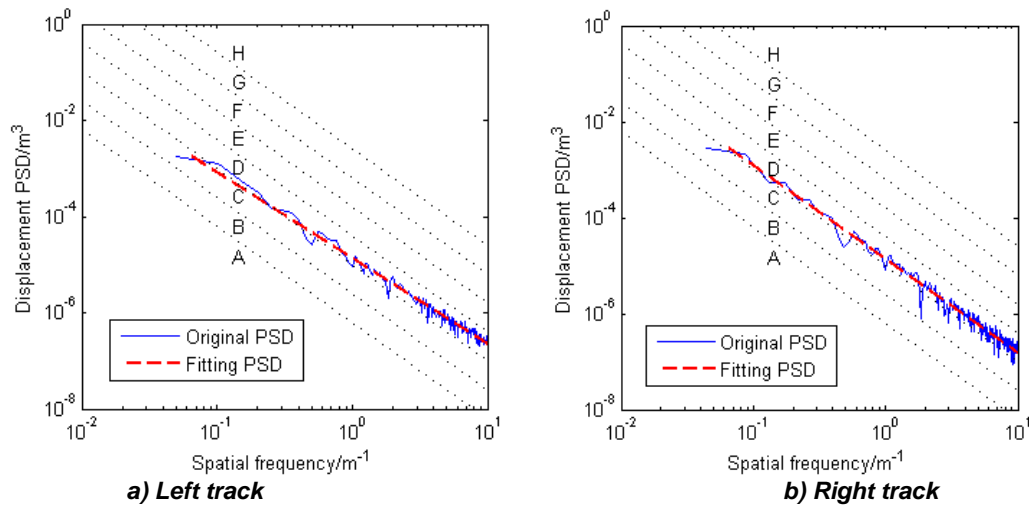


Fig. 4 - PSD of the measured profiles from one test treatment in the grass field

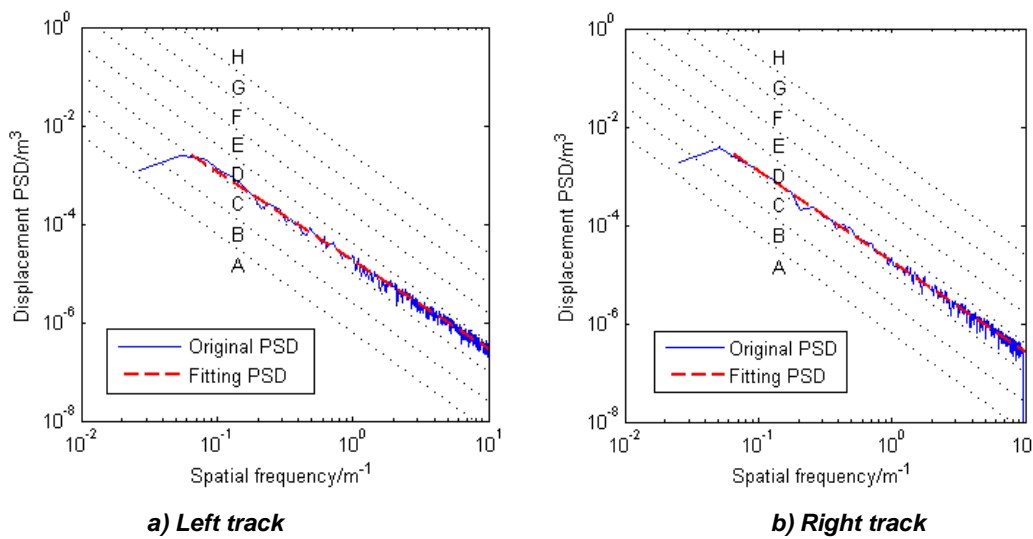


Fig. 5 - PSD of the measured profiles from one test treatment in the corn stubble field

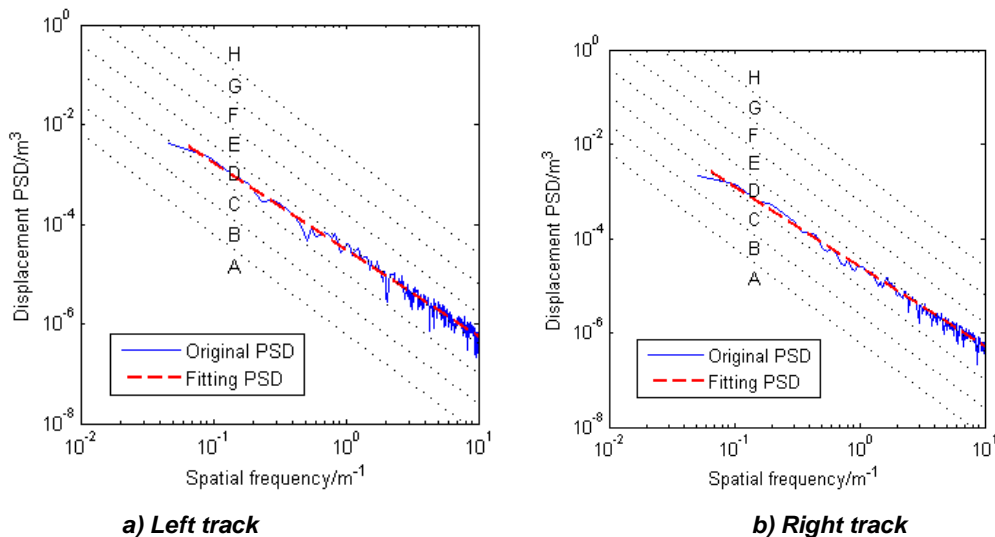


Fig. 6 - PSD of the measured profiles from one test treatment in the harvested potato field

In Figure 4, the roughness index  $C$  of the grass field profiles at the left and right wheel tracks are  $1182 \times 10^{-8}$  and  $1254 \times 10^{-8}$  respectively, and the waviness  $W$  values are 1.78 and 1.95 respectively. In Figure 5, the roughness index  $C$  of the corn stubble field profiles at the left and right wheel tracks are  $1687 \times 10^{-8}$  and

$1625 \times 10^{-8}$  respectively, and the waviness  $W$  values are 1.8 and 1.84 respectively. In Figure 6, the roughness index  $C$  of the harvested potato field profiles at the left and right wheel tracks are  $2866 \times 10^{-8}$  and  $2568 \times 10^{-8}$  respectively, and the waviness  $W$  values are 1.74 and 1.69 respectively.

ISO 8608 suggests waviness  $W = 2$ . However, according to  $W$  values of Figure. 4-6, it was found that the  $W$  values of the three measured field profiles from both tracks were less than 2 with the average of 1.8. In the case of the asphalt road,  $PSD$  shown in Figure 7, the irregularities of measured profiles in the asphalt road measurement seem to be close to each other.

Figure 7 shows the  $PSD$  curves of the tested asphalt road profiles. On each of these figures, the limits of eight roughness levels according to ISO 8608 are also shown for reference. Each  $PSD$  was fitted with a straight line in log-log scale using the least-mean-square method, then two spectrum parameters  $W$  and  $C$  of each profile were obtained according to Eq. (1).

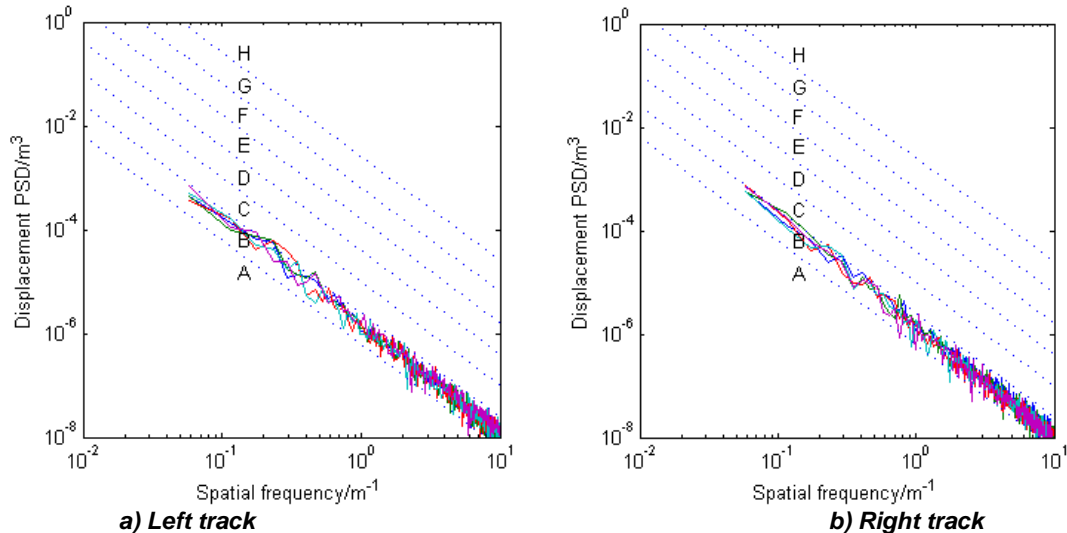


Fig. 7 -  $PSD$  of the measured profiles from five test segments on the asphalt road

The spectrum parameters of all measured field profiles and asphalt road profiles were summarized in Table 1. Time-domain profile values  $RMS_m$  and  $RMS_c$  were also investigated and presented in the Table 1.  $RMS_m$  is the root mean square of the measured profile calculated from the test data, while  $RMS_c$  is the root mean square calculated by the waviness  $W$  and the roughness index  $C$  according to the Eq. (3).

By comparing the characteristics of the field surface profiles and asphalt road surface profiles (Table 1), it was found that the differences between the left and right track parameters of field surface roughness, such as  $W$ ,  $C$ ,  $RMS_m$  and  $RMS_c$  were greater than that of the asphalt road in most cases. Meanwhile, most of the  $W$  values of all measured field profiles were less than 2 with the average of 1.8, while the  $W$  values of all measured asphalt road profiles were greater than 2 with the average of 2.08, which indicates that the ratio of the short wave energy to the all wavelength energy of the field profile is greater than that of the asphalt road. Also, a relatively obvious difference was found in the  $W$  values of the same type of field with different test routes or left and right track of the same route, which was particularly evident in the harvested potato field test results. However, no obvious differences could be found between the  $W$  values of the asphalt road profiles for different treatments or two tracks with the same treatment. In addition, the  $W$  values of the same tested asphalt road were close to each other.

It can be observed from the Table 1 that the roughness values of field profiles including roughness index  $C$ ,  $RMS_m$  and  $RMS_c$ , which were tested on the parallel tracks, are significantly higher than those of the asphalt roads. The results show roughness energy of field surface is much larger than that of asphalt road surface. Meanwhile, it was also found that the  $RMS_m$  which is positively associated with the roughness energy of surface profile increased with the increase of  $W$  and  $C$  values. This corroborates the simulation result of Figure 3.

#### **Effect of characterizing the field and asphalt road profiles by the $PSD$ fitting method**

In order to check the effect of characterizing the field and asphalt road profiles by the  $PSD$  fitting method, the percentage differences between the  $RMS_m$  and  $RMS_c$  of the same track profiles were calculated and

presented in Table 1. The range of the percentage difference between the  $RMS_m$  and  $RMS_c$  of the same track field profiles was 0.3%-41.9%, and the mean values of the left and right tracks were 13.1% and 15.8%, respectively. The range of the percentage difference between the  $RMS_m$  and  $RMS_c$  of the asphalt road profiles was 2.2%-10.6%, and the mean values of the left and right tracks were 6.7% and 6.2%, respectively. Therefore, the percentage difference between the  $RMS_m$  and  $RMS_c$  of the field profiles is much larger than that of the asphalt road profiles, which illustrates it has better performance in characterizing asphalt road profiles than characterizing field profiles with the  $PSD$  fitting method.

Table 1

The waviness  $W$ , roughness index  $C$ ,  $RMS_m$  and  $RMS_c$  values of profile in each test

Test code	Waviness $W$		Roughness index $C$ [ $10^{-8} m^3 \cdot W$ ]		$RMS_m$ [ $10^{-3} m$ ]		$RMS_c$ [ $10^{-3} m$ ]		Percentage difference between the $RMS_m$ and $RMS_c$ [%]	
	Left track	Right track	Left track	Right track	Left track	Right track	Left track	Right track	Left track	Right track
A1	1.78	1.95	1182	1254	24.7	26	22.5	30.9	8.9	15.8
A2	1.91	2.25	931	945	22	26.7	24.8	46	11.3	41.9
A3	2.05	1.83	878	968	25.2	26.2	30.8	22.1	18.1	15.6
A4	1.76	1.66	1147	1194	24.1	25.8	21.4	18.6	11.2	27.9
A5	1.68	1.77	1081	1031	21.6	22.3	18.3	20.6	15.3	7.6
B1	1.8	1.84	1687	1625	27.9	29.2	27.7	29.1	0.7	0.3
B2	1.79	1.99	1142	1096	20.7	22.9	22.4	31	7.6	26.1
B3	1.88	1.83	1166	1161	22.4	21.5	26.4	24.2	15.2	11.2
B4	2	1.91	1695	1704	32.1	29.7	39.2	33.6	18.1	11.6
B5	1.77	1.82	1650	1520	26.5	25.7	26.1	27.2	1.5	5.5
C1	1.74	1.69	2866	2568	36.4	35.3	32.7	28.6	10.1	19
C2	1.4	1.57	3541	3063	31.3	30.3	21.9	25.9	30	14.5
C3	1.83	1.98	2290	2114	32	34.9	34	42.2	5.9	17.3
C4	1.29	1.69	3265	1577	23.9	26.7	18.3	22.4	23.4	16.1
C5	1.65	1.85	1428	1044	24.6	25.5	20	23.7	18.7	7
D1	2.1	2.13	20	17	4.8	4.8	5.1	5	5.9	4
D2	2.08	2.14	18	16	4.2	4.4	4.7	4.9	10.6	10.2
D3	2.12	2.09	16	20	4.4	4.6	4.7	5	6.4	8
D4	2.06	2.02	19	20	4.3	4.3	4.6	4.4	6.5	2.2
D5	2.03	2.07	22	17	4.5	4.1	4.7	4.4	4.3	6.8

Different test code letters A, B, C, D indicate the grass field, the corn stubble field, the harvested potato field and the asphalt road, respectively. Different numbers 1, 2, 3, 4, 5 indicate five segments of each profile test.

## CONCLUSIONS

Based on the measured data and analysis presented above, the following conclusions have been developed.

For the values of the agricultural field and asphalt road surface roughness,  $W$  and  $C$  are both positive associated with the  $RMS$ . Most of the  $W$  values of all measured field profiles were less than 2 with the average of 1.8, while the  $W$  values of all measured asphalt road profiles were greater than 2 with the average of 2.08, which indicates the ratio of the short-wave energy to the all wavelength energy of the field profile is greater than that of the asphalt road. The differences between the left and right track values of the field surface roughness, such as  $W$ ,  $C$ ,  $RMS_m$  and  $RMS_c$  are greater than that of the asphalt road in most cases, while these values of the same tested asphalt road with different treatments are close to each other.

The effect of characterizing the field and asphalt road roughness by  $PSD$  fitting method was evaluated from the view of analysing the relation between the time-domain  $RMS$  value and the spectrum parameters. The result shows the roughness of both field and asphalt road profiles can be distinguished by the  $PSD$  fitting

method. However, it has better performance in characterizing asphalt road profiles than characterizing field profiles with the PSD fitting method.

## ACKNOWLEDGEMENT

Special thanks are due to the Research Program of Science and Technology at Universities of Inner Mongolia Autonomous Region (NJZY20046), the National Natural Science Foundation of China (31901409), and the Natural Science Foundation of Inner Mongolia Autonomous Region (2019BS05012) for supporting authors' research.

## REFERENCES

- [1] Cutini M., Brambilla M., Bisaglia C., (2017), Whole-body vibration in farming: background document for creating a simplified procedure to determine agricultural tractor vibration comfort, *Agriculture*, 7(10), 1-20. <https://doi.org/10.3390/agriculture7100084>
- [2] Gorsich D. J., Chaika M., Gunter D., Karlson R., Hauelsen B., Sun T., Ferris J., (2003), Terrain roughness standards for mobility and ultra-Reliability prediction, *SAE World Congress & Exhibition*, Detroit, MI, USA, March 3. <https://doi.org/10.4271/2003-01-0218>
- [3] Honda H., Kajikawa Y., Kobori T., (1966), Spectra of road surface roughness on bridges, *Journal of the Structural Division.*, 108(9), 1956-1966.
- [4] International Organization for Standardization. (1995). *Mechanical Vibration-Road Surface Profiles-Reporting of Measured Data*, 30(ISO Standard No. 8608:1995). <https://www.iso.org/standard/15913.html>
- [5] Johannesson P., Podgórski K., Rychlik I., (2016), Modelling roughness of road profiles on parallel tracks using roughness indicators, *International Journal of Vehicle Design*, 70(2), 1-28. <https://doi.org/10.1504/IJVD.2016.074421>
- [6] Lu Z. X., Nan C., Perdok U. D., Hoogmoed W. B., (2005), Characterisation of soil profile roughness, *Biosystems Engineering*, 91(3), 369-377. <https://doi.org/10.1016/j.biosystemseng.2005.04.004>
- [7] Ma R., Chemistruck H., Ferris J. B., (2013), State-of-the-art of terrain profile characterisation models, *International Journal of Vehicle Design*, 61(1-4), 285-304. <https://doi.org/10.1504/IJVD.2013.050850>
- [8] Múčka P., (2016), Proposal of road unevenness classification based on road elevation spectrum parameters, *Journal of Testing and Evaluation*, 44(2), 930-944. <https://doi.org/10.1520/JTE20150179>
- [9] Múčka P., Kropáč O., (2009), Sensitivity of road unevenness indicators to road waviness, *Journal of Testing and Evaluation*, 37(2), 1-11. <https://doi.org/10.1520/JTE102005>
- [10] Phillip J. D., George L. M., Burney M., Alex B., (2011), Predicting RMS surface roughness using fractal dimension and PSD parameters, *Journal of Terramechanics*, 48(2), 105-111 <https://doi.org/10.1016/j.jterra.2010.05.004>
- [11] Phillip J. D., Alex B., Burney M., (2014), A general model for inferring terrain surface roughness as a root-mean-square to predict vehicle off-road ride quality, *International Journal of Vehicle Design*, 64(2/3/4), 137-152. <https://doi.org/10.1504/IJVD.2014.058481>
- [12] European Committee for Standardization (CEN). (2015). *Surface Characteristics of Road and Airfield Pavements-Test Methods-Part 5: Determination of Longitudinal Unevenness Indices* (prEN Standard No. 13036-5: 2015). Brussels, Belgium.
- [13] Sayers M.W., Karamihas S.M., (1998), *The Little Book of Profiling - Basic Information about Measuring and Interpreting Road Profiles*, (9). University of Michigan.
- [14] Steven W. S., (1999), *The Scientist and Engineer's Guide to Digital Signal Processing* (Second Edition), California Technical Publishing San Diego, California, USA, 208
- [15] Yan J. G., Wang C. G., Xie S. S., Wang L. J., (2019), Design and validation of a surface profiling apparatus for agricultural terrain roughness measurements, *INMATEH Agriculture Engineering*, 59(3), 169-180. <https://doi.org/10.35633/inmateh-59-19>
- [16] Yiliyasi Y., Zhu S. H., Do M. C., Nie X. T., Xu G., (2016), Study on vibration characteristics of tractor travel at the condition of marshy paddy soil (湿软水田土壤行驶工况下拖拉机振动特性研究), *Journal of Nanjing Agricultural University*, 39(6), 1062-1068. <https://doi.org/10.7685/jnau.201512001>
- [17] Zhang Z. M., Sun C., Bridgelallb R., Sun M. X., (2018), Road profile reconstruction using connected vehicle responses and wavelet analysis, *Journal of Terramechanics*, 80(12), 21-30. <https://doi.org/10.1016/j.jterra.2018.10.004>

## USING CFD SIMULATION TO INVESTIGATE THE IMPACT OF FRESH AIR VALVES ON POULTRY HOUSE AERODYNAMICS IN CASE OF A SIDE VENTILATION SYSTEM

## ВИКОРИСТАННЯ CFD МОДЕЛЮВАННЯ ДЛЯ ОЦІНКИ ВПЛИВУ ПРИПЛИВНОГО КЛАПАНА НА АЕРОДИНАМІКУ ПТАШНИКА ПРИ БОКОВІЙ СИСТЕМІ ВЕНТИЛЯЦІЇ

Trokhaniak V.I.<sup>1)</sup>, Rogovskii I.L.<sup>1)</sup>, Titova L.L.<sup>1)</sup>, Dziubata Z.I.<sup>2)</sup>, Luzan P.H.<sup>3)</sup>, Popyk P.S.<sup>1)</sup> <sup>1</sup>

<sup>1)</sup> National University of Life and Environmental Sciences of Ukraine / Ukraine;

<sup>2)</sup> Separated Subdivision of National University of Life and Environmental Sciences of Ukraine Berezahny Agrotechnical Institute / Ukraine;

<sup>3)</sup> Central Ukrainian National Technical University / Ukraine

Tel: +380673513082; E-mail: [Trohaniak.v@gmail.com](mailto:Trohaniak.v@gmail.com)

DOI: <https://doi.org/10.35633/inmateh-62-16>

**Keywords:** CFD, aerodynamics, poultry house, side ventilation system, fresh air valves

### ABSTRACT

*Exposure and the outbreak of diseases result in significant losses in large scale poultry operation. New ventilation systems are necessary to provide safe and homogenous internal environment at large enterprises, especially under the changeable climatic conditions of global warming. Within the framework of this investigation, computational fluid dynamics (CFD) simulation of a side ventilation system in a poultry house during winter seasons has been conducted. As results, 3D temperature fields, current lines and pressures in a poultry house have been found. It has been determined that fresh air valves arranged at a height of 200 mm from flooring work better than those traditionally arranged at a height of 400 mm. The erection of walls on the inside of a poultry house framework as well as the decrease in the height of flooring improve poultry house aerodynamics.*

### РЕЗЮМЕ

*Переохолодження і спалах хвороби призводять до значних втрат при великомасштабному виробництві птиці. З метою забезпечення безпечного і однорідного внутрішнього середовища для великих виробництв необхідні нові системи вентиляції, особливо в умовах мінливого клімату глобального потепління. В рамках цього дослідження було проведено моделювання обчислення гідродинаміки (CFD) бокової системи вентиляції в пташнику у зимовий період року. В результаті отримано поля швидкостей, ліній току і тисків у пташнику в 3D постановці. Знайдено, що припливні клапана які розміщуються на висоті 200 мм від перекриття працюють значно ефективніше ніж в традиційній постановці на висоті 400 мм. Монтаж стін із внутрішнього боку каркасу пташника, а також зменшення висоти перекриття покращують аеродинаміку в пташнику.*

### INTRODUCTION

The paper of Saraz J.A.O. *et al.*, (2012), was aimed at the development of the modern level of using CFD models in the internal broiler house environment and the investigation of their current limitations. It was based on the assumption that CFD models can provide knowledge about the distribution of velocities, the temperatures of air, gases and solid particles in case of natural ventilation, mechanical ventilation and adiabatic pad-and-fan cooling systems.

The results of the paper written by Tong, X. J. *et al.*, (2019) show that an upward airflow displacement ventilation system makes it possible to increase the efficiency of air exchange in cages for 46% -129% as well as to provide more homogenous thermal environment with the heat stress of 9.4% in summer and the cold stress of 68% in winter compared to a tunnel ventilation system.

The paper published by Cheng Q.Y. *et al.*, (2018), analyses the influence of the height (0.4 m, 0.55 m, 0.7 m, 0.85 m and 1 m) and the intervals (6 m, 9 m, 12 m, 15 m and 18 m) of deflectors on the velocity and air distribution in cage areas. The investigation shows that deflectors can significantly direct air flow

<sup>1</sup> Trokhaniak V.I., Assoc. Prof. Ph.D. Eng.; Rogovskii I.L., Prof. Ph.D. Eng.; Titova L.L., Assoc. Prof. Ph.D. Eng.; Dziubata Z.I., Assist. Lect. PhD; Luzan P.H., Assoc. Prof. Ph.D. Eng.; Popyk P.S., Senior Lect., PhD Eng.

downwards, increase air velocity in cage and pass-through areas for 0.66 m/s and 0.91 m/s respectively, compared to the lack of deflectors, in case of deflectors being 1 m tall and with the interval of 6 m.

Some authors' results, suggested a new cooling system to be applied in a poultry house with the use of heat-exchangers of a special design (Gorobets V.G. et al., 2018; Gorobets V. et al., 2019). CFD simulation of air flows and heat-and-mass exchange in a poultry building is presented. Here, water from subterranean wells is used as a cooler. There are recommendations provided for choosing the design of ventilation systems in poultry houses. In their follow-up studies Gorobets V.G. et al., (2018), optimize the height of extractor-type fan arrangement. It is shown that it is to the point to arrange ventilation equipment at a height of 1.5 m. Here, the area of dead-air zones and the inequality of air velocity distribution close to poultry decrease.

Aimed at the decrease of energy cost and the increase of quality indices of air environment when providing the necessary conditions for poultry management, some authors conducted experimental research and numerical simulation. In the process of investigation, the decrease of energy expenditures for establishing microclimate during broiler management has been obtained. The quality of air environment in poultry houses has been increased. It makes it possible to decrease the disposal of feeding stuffs and the loss of poultry stock and, as a result, increase the economic efficiency of production and product quality. (Trokhaniak V.I. et al., 2019)

Bustamante E. et al., (2017), consider the methods of side mechanical ventilation to be more efficient compared to other methods. Their CFD simulation shows a wide range of the values of air flow velocity. According to the indoor air velocity, two main conclusions have been drawn: 1 – there is excess inhomogeneity in the area of animal presence; and 2 – the movement of air is insufficient to contribute to bird thermoregulation.

Shurub Yu.V. et al., (2018), Shurub Yu. et al., (2019) presented the description of loading of various ventilator engines and a combined connection diagram.

Zajicek M. and Kic P., (2012), Pourvosoghi N. et al., (2018) presented in their paper a CFD solution for various flow configurations and poultry house forms. The effects of cross and longitudinal ventilation are combined with the change of inlet air flow directions as well as various forms of the cross-sectional area obtained with the help of valves. This paper considers the design of a poultry house in such a way that the walls are arranged on the outside of a concrete framework. Such a design makes aerodynamics inside a poultry house worse. There are a lot of dead-air zones. Due to high flooring, warmth during winter season is concentrated above poultry, which results in the increase of energy costs to heat the building.

Fig. 1 presents a traditional poultry house design. The walls are arranged on the outside of a concrete framework. The flooring is not lowered. Thus, the paper is aimed at the improvement of a poultry house design, finding the most effective way to arrange fresh air valves and the improvement of the aerodynamic indices of a poultry house environment with the help of CFD.

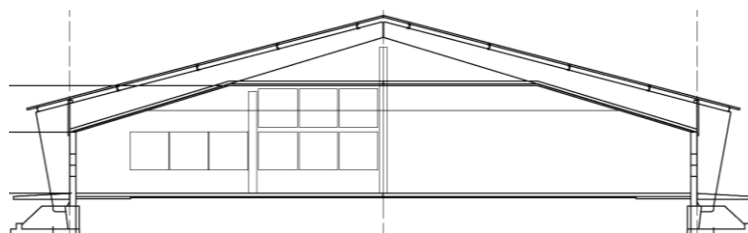


Fig. 1 - Extract of traditional poultry house design with fresh air valves of side ventilation

## MATERIALS AND METHODS

According to the set technical task, the engineering calculation of air exchange during winter season was conducted. In order to remove carbon dioxide, moisture vapour and harmful substances, it was necessary to provide air expenditure being about 155 ths m<sup>3</sup>/h at the outside temperature being -10°C.

The geometrical pattern was constructed in actual size. In order to decrease the estimate time inside along the building, symmetry was applied. That is to say, simulation was conducted for half of a poultry house building only. The calculation was conducted at the air expenditure being 30 kg/s. Outside air temperature was taken to be equal to -10°C and the parameters of heat emission were introduced. The walls were made of concrete and were insulated by expanded foam being 35 kg/m<sup>3</sup> thick: 60/150/60 mm, respectively. The building was coated by polyurethane being 100 mm thick, 45 kg/m<sup>3</sup>. The floor was

insulated by expanded polystyrene being  $45 \text{ kg/m}^3$  thick, 100 mm for the width of 2 m from the wall around the perimeter of the poultry house, 50 mm for the rest of the area. The length of the poultry house was 120 m, the width was equal to 22.36 m (see Fig. 2). Floor-managed poultry in the building was 41 ths in number, poultry weight was equal to 3.3 kg. It was a heat source and corresponded to  $+41^\circ\text{C}$ . Ventilation valves Wlotpowietrza 857x337 mm 3000-VFG Przepustowocs 2900  $\text{m}^3/\text{h}$  were applied. They were arranged on the side walls being 79 pcs in total (Fig. 5a). The first ten ventilation valves were arranged at a height of 0.2 m from flooring (see Fig. 3b, Fig. 5a). The rest of the valves were arranged at a height of 0.4 m from flooring (see Fig. 3a, 4, 5a (H5)). One of the design concepts was to install a spoiler at a slope angle being  $75^\circ$  from a vertical line above fresh air valve (see Fig. 4 (A20)). The length of the spoiler was 0.8 m (L9). Munters EM50 1.5 Hp extraction fans were used, 18 pcs. in total. During winter season 6 pcs were specifically arranged (see Fig. 5b). As a rule, they are arranged in the upper row displaced closer to the centre. Such ventilators can undertake the maximum long-term loading up to 56 Pa.

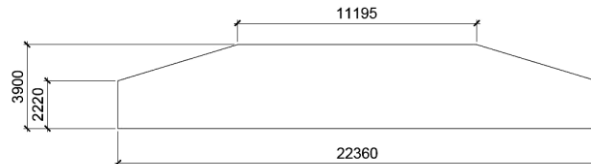


Fig. 2 - Suggested cross sectional diagram of poultry house structural dimensions

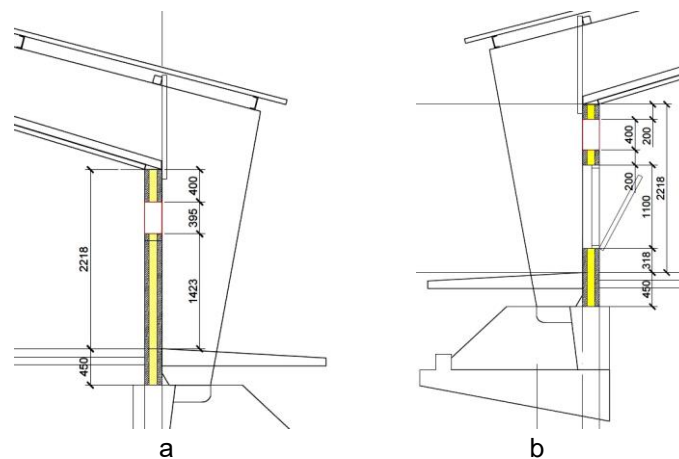


Fig. 3 - Arrangement of valves along longitudinal walls

a – small valves, b – tunnel ventilation valves

Fig. 4 schematically presents valve angle side view.

The ventilation scheme was constructed in such a way that air flow reached the centre of the building in winter season in order to normalize the aerodynamic parameters of a poultry house. Such a method made it possible to reduce the loss of fresh air pressure in the poultry building. Thus, the following structural alterations were made: the width of the building was increased from 21 m, which was typical in a traditional design, to 22.36 m in a new design. Fig. 4 presents the maximum valve opening of 0.1 m (H16). Numerical simulation was conducted at valve opening being 0.1 m, 0.066 m and 0.049 m, respectively.

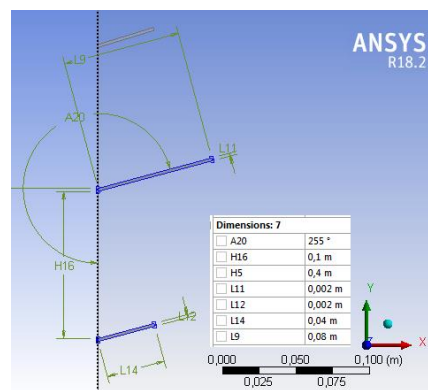


Fig. 4 - Fresh air valves and spoiler angles

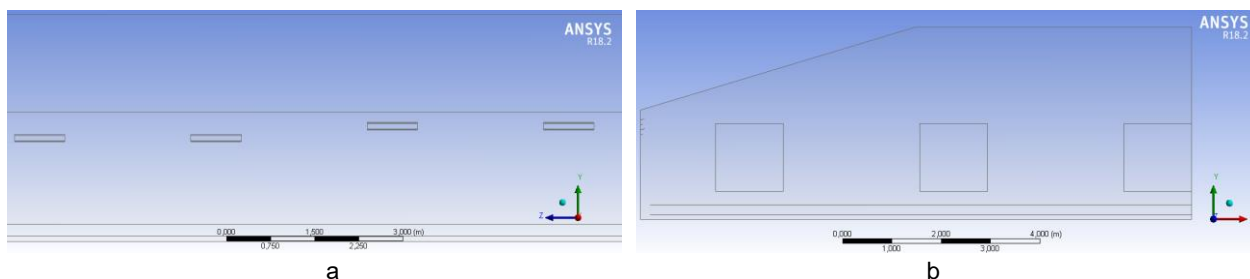


Fig. 5 - Side (a) and back end (b) walls of a poultry house

The number of elements and faces was quite numerous (Table 1). Taking into account great building dimensions, the size of an element and a face was not significantly increased because of the limitations of computer productive and design capacity.

Table 1

Parameters of mesh generation for a poultry building.

Settings	Measure units	Measure
Mesh quality index (orthogonal quality)	–	0.24
Number of elements	pcs	3813129
Number of mesh points	pcs	4005901
Method	–	CutCell
Maximum face size	m	0.11
Minimum face size	m	0.0275
Minimum size of fresh air valve element	m	0.0276
Minimum size of extraction fan element	m	0.05

Fig. 6 presents frontal and side views of the generated mesh of a poultry building, fresh air openings and an entry gate. The mesh was a little decreased relative to the rest of the wall area. Such measures were applied in order to obtain better hydrodynamics calculation. In addition, the mesh was condensed close to the floor, since poultry was placed there.



Fig. 6 - Side view (a) and back end view (b) of a poultry house wall

Having applied the finite-element method, 3D computational mesh was constructed in ANSYS Meshing software complex aimed at solving the tasks of hydrodynamics and heat transfer in a poultry house. The construction of various meshes for CFD models resulted in choosing the most optimal and the best-quality ones that made it possible to obtain trustworthy and exact results of the calculation of poultry house ventilation. The simulation was performed without using any additional heating system.

The flow of viscous fluid or gas (air) was described by the system of equations, which included the continuity equation and the momentum equation in the projections on the coordinate axis. If the medium flow was followed by heat transfer, the energy conservation equation (the heat transfer equation) was added to the above-mentioned system of equations.

The mathematical model was based on Navier-Stokes equations (Khmelnik S.I., 2018; Trokhaniak V. and Klendii O., 2018) and energy transfer equation for convective currents. Spalart-Allmaras turbulence model (Allmaras S.R. et al., 2012) and Discrete Ordinates radiation model (ANSYS, 2017) were applied in the calculation.

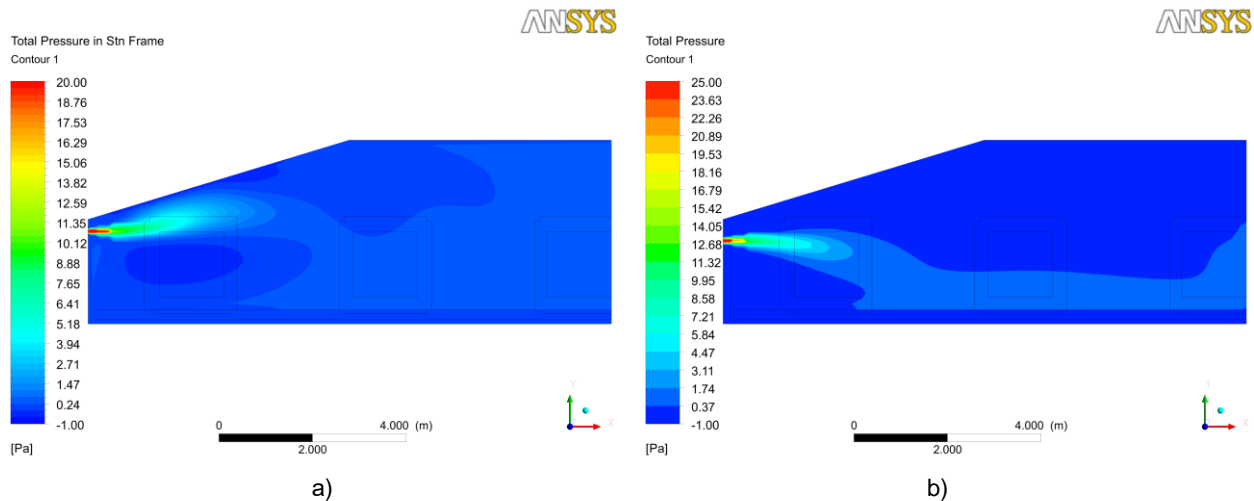
**RESULTS**

The results of CFD 3D simulation of a poultry house has made it possible to compare three modifications of valve opening in case of side poultry house ventilation system. Prior to conducting numerical simulation, 3D mesh has been generated applying the finite-element method in ANSYS Meshing.

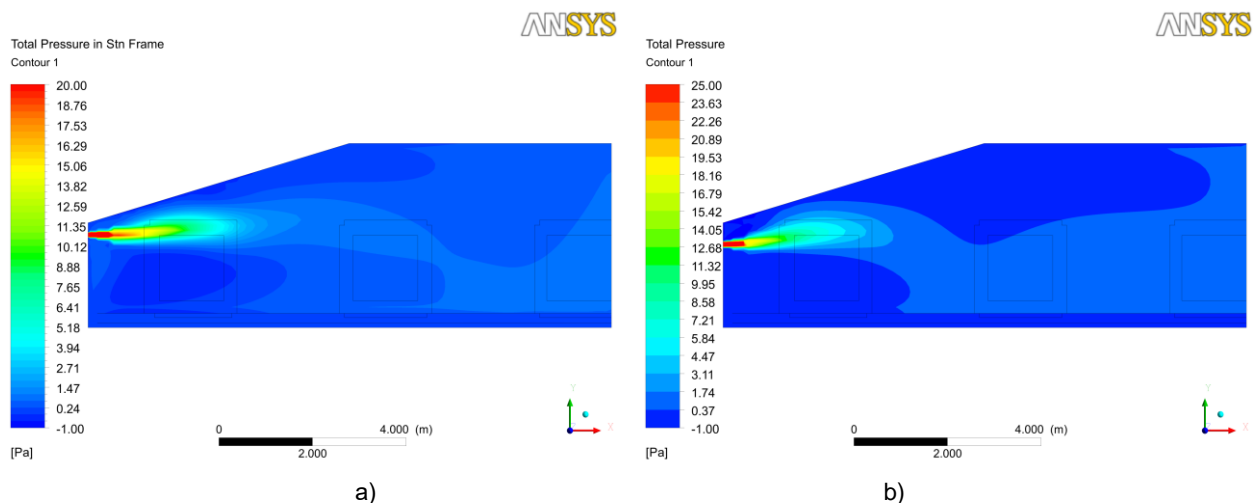
Fig. 7-15 present the results of CFD simulation of a poultry house in two areas along the length of the building – 10.3 m. and 52.3 m. at various valve opening ranging from 0.1m to 0.049 m.

Fig. 7-9 present pressure loss values in fresh air valves. The least pressure loss is shown to be 24.3 Pa at valve opening being 0.1 m and the greatest one – 55.68 Pa at 0.049 m, respectively.

Fig. 10-15 present air flow hydrodynamics in a poultry house. As it has been already mentioned, air flow is directed upwards by fresh air valves. However, due to low entry pressures and velocities, after passing the third of the building the air falls down. The valves are arranged at a height of 200 mm from the flooring (Fig. 12a, Fig. 15a). The air smoothly moves close to the flooring area and is directed to the centre of the building. The valves that are arranged at a height of 400 mm from flooring cannot provide the same impact. This can be caused by perturbation due to large building airspace. The average entry velocity at various air expenditures ranges from 6.39 m/s to 9.62 m/s.



**Fig. 7 - Pressure loss (Pa) in a fresh air valve of a poultry building at valve opening being 0.1 m at a distance from the front-end wall of:**  
*a – 10.3 m; b – 52.3 m*



**Fig. 8 - Pressure loss (Pa) in a fresh air valve of a poultry building at valve opening being 0.066 m at a distance from the front-end wall of:**  
*a – 10.3 m; b – 52.3 m*

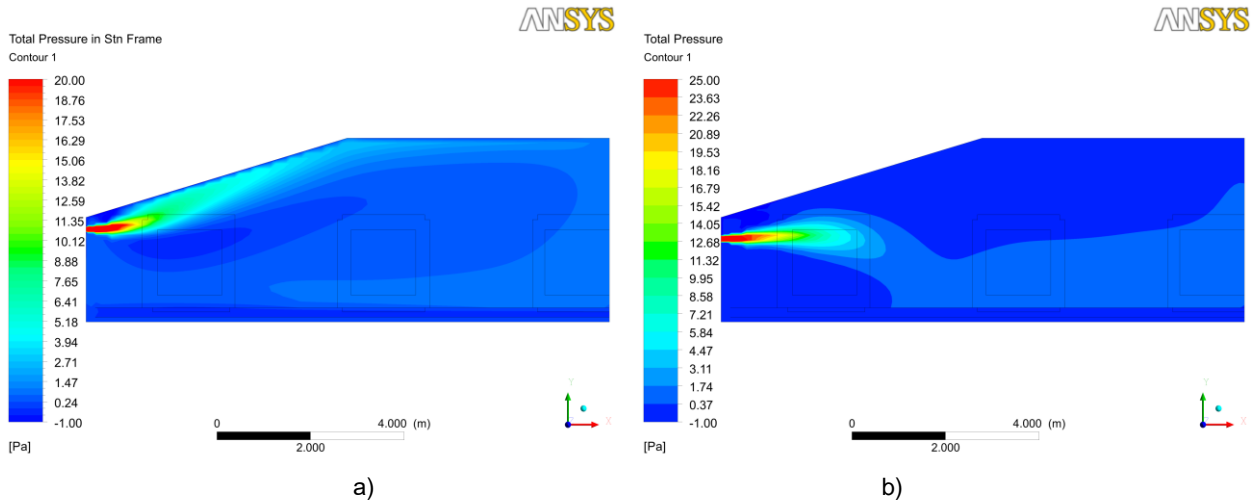


**Fig. 9 - Pressure loss (Pa) in a fresh air valve of a poultry building at valve opening being 0.049 m at a distance from the front-end wall of:**  
*a – 10.3 m; b – 52.3 m*

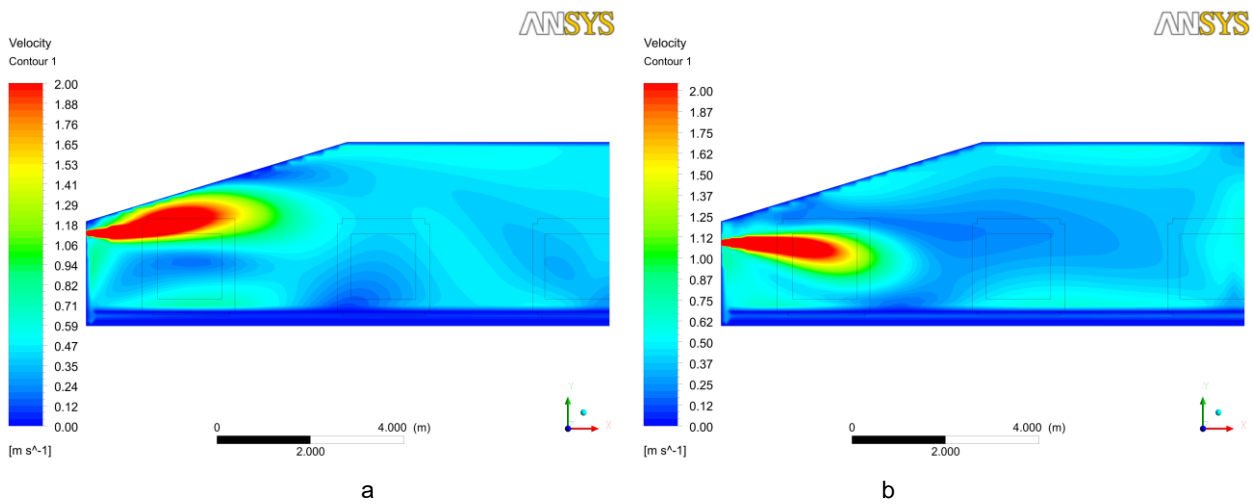


**Fig. 10 - Field of velocities (m/s) in a poultry house at valve opening being 0.1 m at a distance from the front-end wall of:**  
*a – 10.3 m, b – 52.3 m*

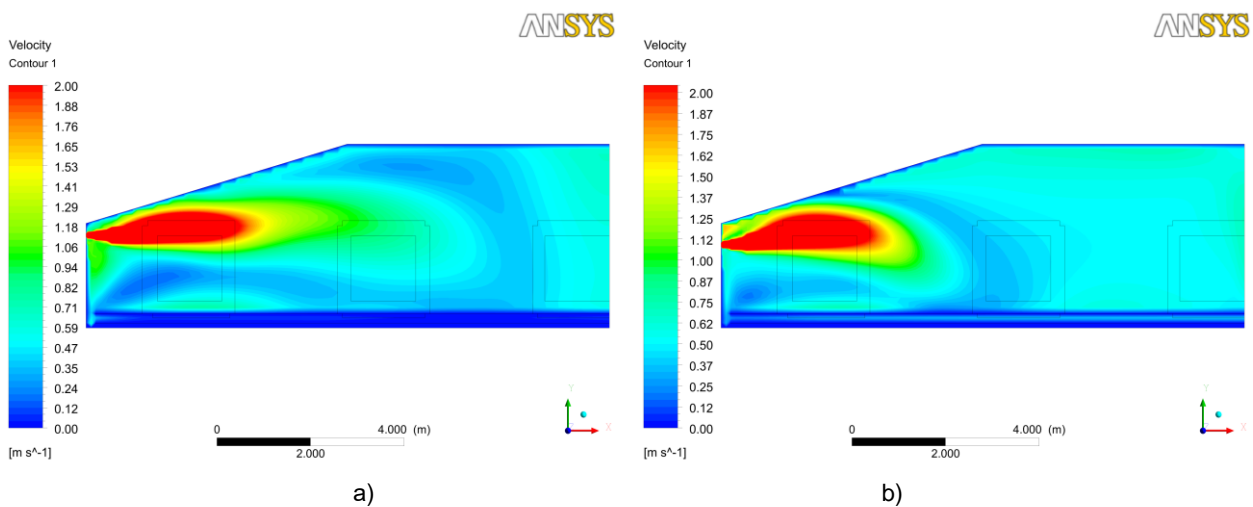


**Fig. 11 - Field of velocities (m/s) in a poultry house at valve opening being 0.066 m at a distance from the front-end wall of:**  
*a – 10.3 m; b – 52.3 m*

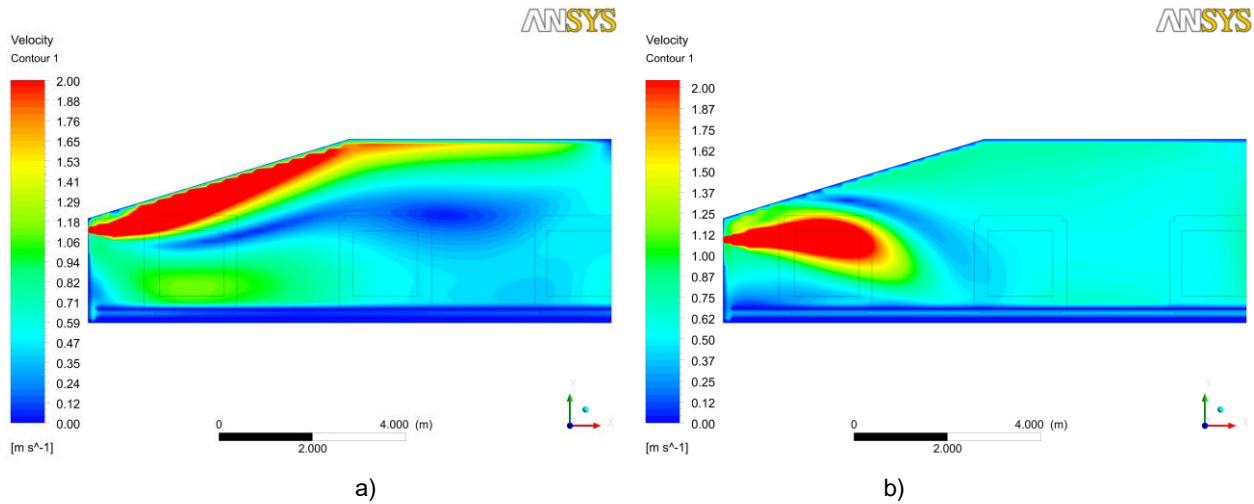


**Fig. 12 - Field of velocities (m/s) in a poultry house at valve opening being 0.049 m at a distance from the front-end wall of:**  
*a – 10.3 m; b – 52.3 m*

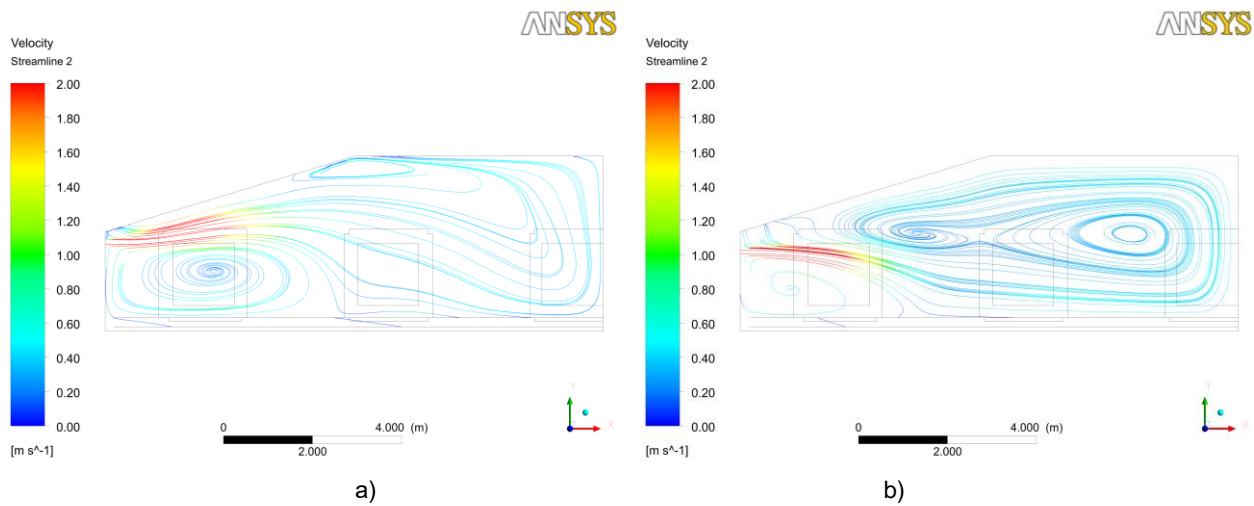


**Fig. 13 - Stream lines (m/s) in a poultry house at valve opening being 0.1 m at a distance from the front-end wall of:**  
*a – 10.3 m; b – 52.3 m*

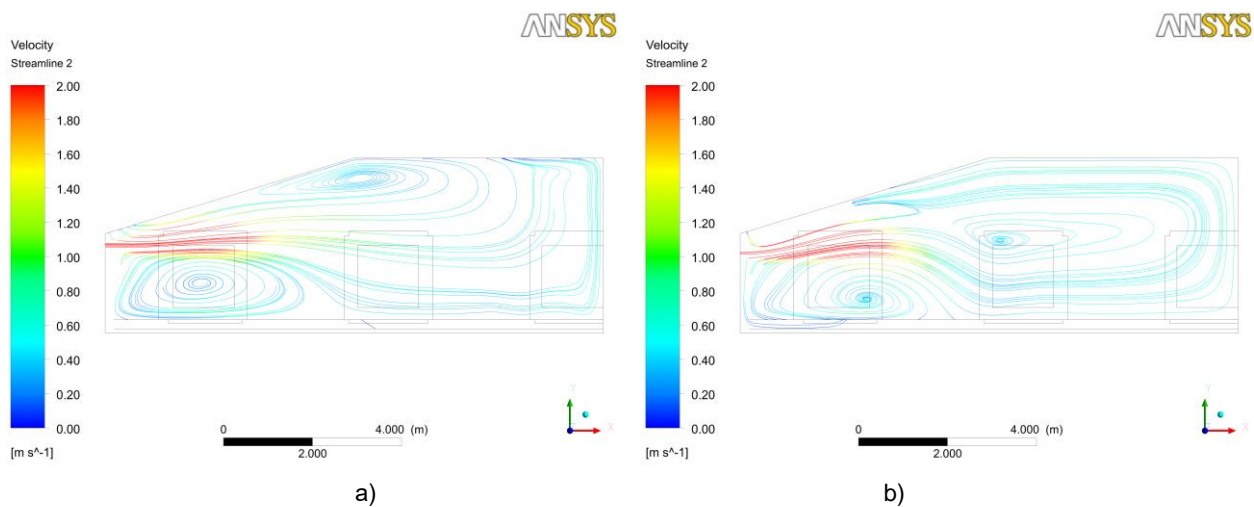


**Fig. 14 - Stream lines (m/s) in a poultry house at valve opening being 0.066 m at a distance from the front-end wall of:**  
*a – 10.3 m; b – 52.3 m*

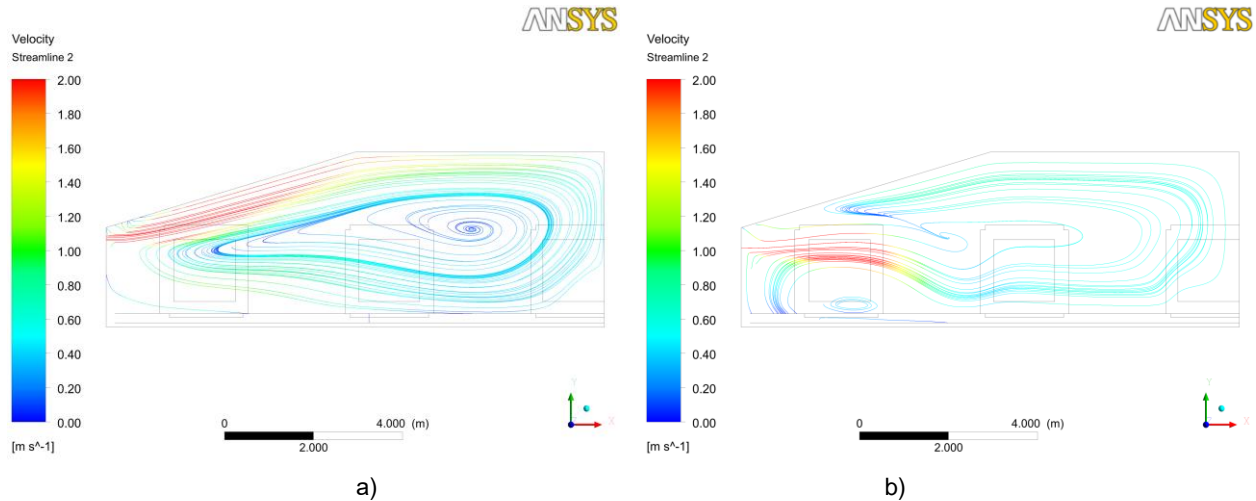


**Fig. 15 - Stream lines (m/s) in a poultry house at valve opening being 0.049 m at a distance from the front-end wall of:**  
*a – 10.3 m; b – 52.3 m*

Fig. 16 presents the field of velocities around the building area at a height of 0.7 m from the floor level. These results can help to estimate air velocity above poultry. The average air velocity ranges from 0.54 m/s to 0.66 m/s. Only close to extraction fans the velocity is a little higher, which is 2 m/s. The main body of poultry does not discomfort.

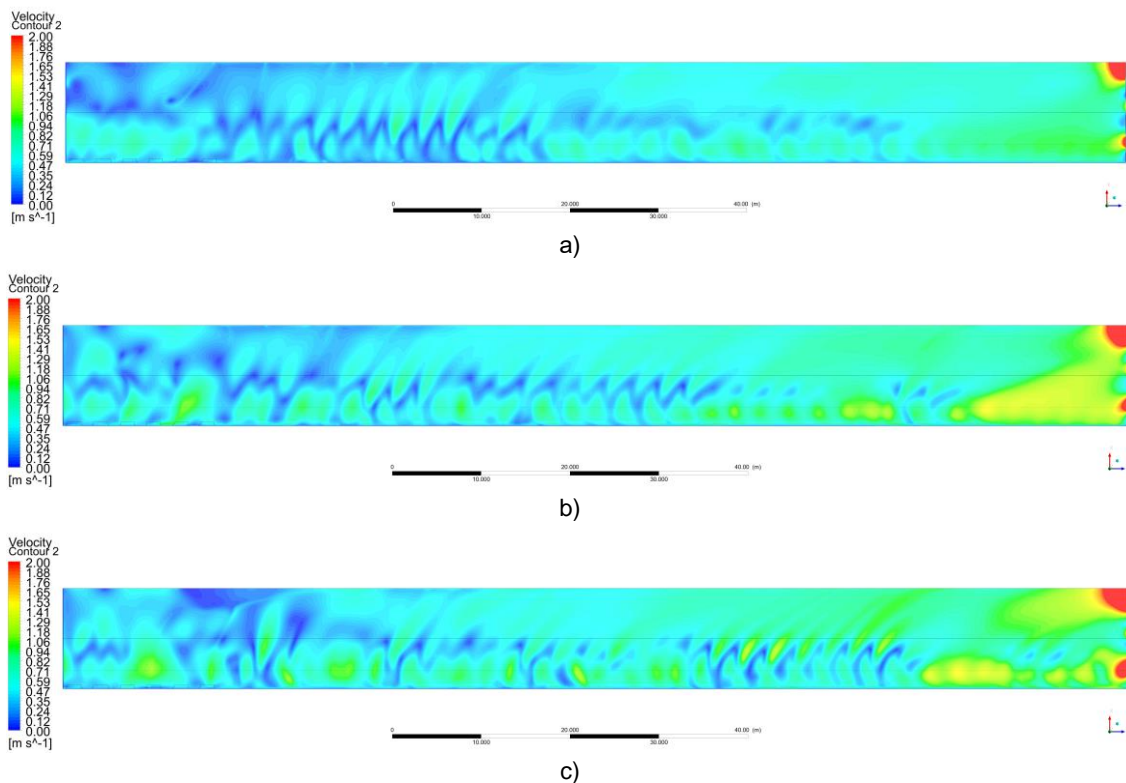


**Fig. 16 - Field of velocities (m/s) in a poultry house at a height of 0.7 m from the floor level at valve opening being:**  
*a – 0.1 m; b – 0.066 m; c – 0.049 m*

Fig.17 presents 3D current lines in a poultry house. The results show that the valves, which are arranged at a height of 400 mm are not effective. The middle extractor fan is practically not utilized. A great load is put on the side fan, which is arranged close to the wall. The main load is taken by the fan, which is located in the centre of the building.

In winter seasons, fresh air density is greater than in summer seasons. Thus, in case of side ventilation system, it is difficult to perform air transfer to the centre of a poultry house. At the next stage of

designing a side ventilation system, the authors suggest taking into account that fresh air valves should be arranged at a height of not less than 200 mm from the flooring level.

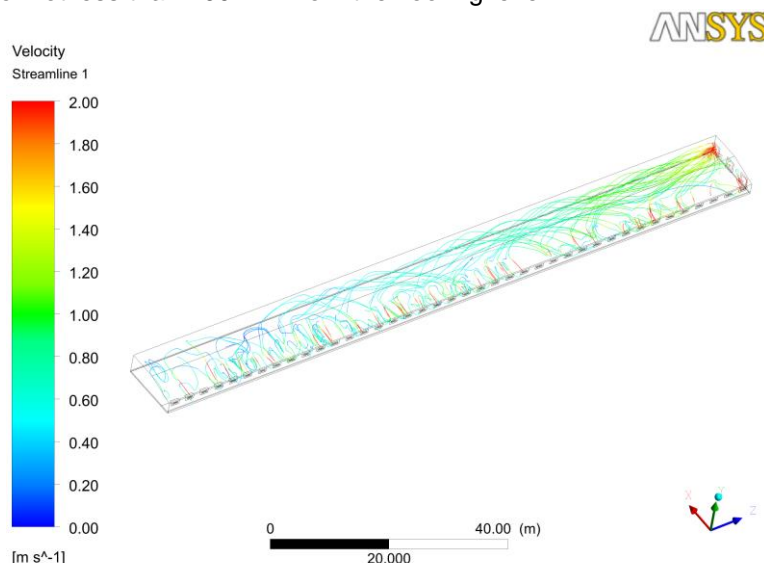


Fig. 17 - 3D stream lines (m/s) in a poultry house at valve opening being 0.049 m

Table 2 presents more detailed information on the results of CFD simulation.

Table 2

Averaged air measures in a poultry house

Parameter	Measure units	Result		
		0.1	0.066	0.049
Distance of valve opening	m	0.1	0.066	0.049
Entry air expenditure for half of a poultry house	kg/s	30	30	30
Valve-inlet pressure	Pa	24.332	43.41	55.684
Fan-outlet pressure	Pa	-1.23	-2.215	-3.132
Valve-inlet air temperature	K	263.947	263.927	263.975
Fan-outlet air temperature	K	273.778	273.91	273.148
Valve-inlet air velocity	m/s	6.388911	8.518548	9.625959
Fan-outlet air velocity	m/s	5.904209	7.946565	9.010783
Air velocity at a height of 0.7 m from flooring level	m/s	0.54181	0.63328	0.657591
Valve-inlet air density	kg/m <sup>3</sup>	1.337423	1.337529	1.337287
Fan-outlet air density	kg/m <sup>3</sup>	1.289433	1.288785	1.292457

## CONCLUSIONS

The design of a poultry house has been improved. It has been suggested arranging spoilers above fresh air valves at an angle of 75° from a vertical line; mounting outside walls on the inside of a concrete framework; increasing the width of a poultry house up to 22.36 m; decreasing the height of flooring up to 3.9 m above the floor level.

Effective arrangement of fresh air valves and the improvement of aerodynamic characteristics in a poultry house building have been investigated applying CFD. It has been determined that the least pressure loss is 24.3 Pa at valve opening being 0.1 m and the greatest loss is 55.68 Pa at 0.049 m, respectively.

The conducted research shows that the valves, which are arranged at a height of 200 mm from flooring are much more effective. The valves, which are arranged at a height of 400 mm from flooring cannot provide the same impact.

## ACKNOWLEDGEMENT

Supported by Affiliate «Poultry Complex» LLC Vinnitsa Poultry Farm (Ladyzhyn), Project No. 4/80.

## REFERENCES

- [1] Allmaras S.R., Johnson F.T., Spalart P.R., (2012), Modifications and Clarifications for the Implementation of the Spalart-Allmaras Turbulence Model, *7th International Conference on Computational Fluid Dynamics*, pp. 9-13, Big Island/Hawaii;
- [2] ANSYS, (2017), ANSYS Fluent Theory Guide. Release 18.2, Published in the USA, 832 p.;
- [3] Bustamante E., Calvet S., Estelles F., Torres A.G., Hospitaler A., (2017), Measurement and numerical simulation of single-sided mechanical ventilation in broiler houses, *Biosystems Engineering*, vol. 160, pp. 55-68, San Diego/USA;
- [4] Cheng Q. Y., Li H., Rong L., Feng X. L., Zhang G. Q., Li B. M. (2018), Using CFD to assess the influence of ceiling deflector design on airflow distribution in hen house with tunnel ventilation. *Computers and Electronics in Agriculture*, vol. 151, pp. 165-174. doi:10.1016/j.compag.2018.05.029, Netherlands;
- [5] Gorobets V., Bohdan Y., Trokhaniak V., Antypov I., Masiuk M., (2019), Summarizing of Nusselt numbers and Euler numbers depending on Reynolds number for the compact tube bundle of small diameter tubes by experimental and numerical methods of researches. *E3S Web of Conferences*, vol. 128, p. 04003. <https://doi.org/10.1051/e3sconf/201912804002>, Rome/Italy;
- [6] Gorobets V.G., Bohdan Yu.O., Trokhaniak V.I., Antypov I.O., (2018), Experimental studies and numerical modelling of heat and mass transfer process in shell-and-tube heat exchangers with compact arrangements of tube bundles, Paper presented at the *MATEC Web of Conferences*, vol. 240, p. 02006. <https://doi.org/10.1051/mateconf/201824002006>, Cracow/Poland;
- [7] Gorobets V.G., Trokhaniak V.I., Antypov I.O., Bohdan Yu.O., (2018), The numerical simulation of heat and mass transfer processes in tunneling air ventilation system in poultry houses, *INMATEH - Agricultural Engineering*, vol. 55, no. 2, pp. 87-96, Bucharest/Romania;
- [8] Gorobets V.G., Trokhaniak V.I., Rogovskii I.L., Titova L.L., Lendiel T.I., Dudnyk A.O., Masiuk M.Y., (2018), The numerical simulation of hydrodynamics and mass transfer processes for ventilating system effective location. *INMATEH - Agricultural Engineering*, vol. 56, no 3, pp. 185-192, Bucharest/Romania;
- [9] Khmelnik S.I., (2018), Navier-Stokes equations. On the existence and the search method for global solutions, *Mathematics in Computers – MiC*, 134 p., Bene-Ayish/Israel;
- [10] Pourvosoghi N., Nikbakht A. M., Sharifian F., Najafi R., (2018), Numerical analyses of air velocity and temperature distribution in poultry house using computational fluid dynamics. *INMATEH - Agricultural Engineering*, vol. 56, no. 3, pp. 109-118, Bucharest/Romania;
- [11] Saraz J. A. O., Martins M. A., Marin O. L. Z., Damasceno F. A., Velasquez H. J. C., (2012), A review about the use of computational fluid dynamics (CFD) in broiler house. *Dyna-Colombia*, vol. 79 no. 175, pp.142-149, Medellin/Colombia;
- [12] Shurub Y., Dudnyk A., Vasilenkov V., Tsitsyurskiy Y., (2019), Simulation of Random Loads Applied to Statistical Optimal Synthesis of Electric Drives. *Proceedings of the International Conference on Modern Electrical and Energy Systems (MEES 2019)*, pp. 354-357, doi: [10.1109/MEES.2019.8896464](https://doi.org/10.1109/MEES.2019.8896464), Kremenchuk/Ukraine;
- [13] Shurub Yu.V., Vasilenkov V.Y., Tsitsyurskiy Yu.L., (2018), Investigation of properties of combined scheme of single-phase switching of induction electric drive of pumping plants. *Tekhnichna Elektrodynamika*, vol. 6, pp. 50-53. <https://doi.org/10.15407/techned2018.06.050>, Kyiv, Ukraine
- [14] Tong X. J., Hong S. W., Zhao L. Y. (2019), Using CFD simulations to develop an upward airflow displacement ventilation system for manure-belt layer houses to improve the indoor environment. *Biosystems Engineering*, vol. 178, pp. 294-308. doi:10.1016/j.biosystemseng.2018.08.006, San Diego/USA;
- [15] Trokhaniak V., Klendii O., (2018), Numerical simulation of hydrodynamic and heat-mass exchange processes of a microclimate control system in an industrial greenhouse. *Bulletin of the Transilvania University of Brasov, Series II: Forestry, Wood Industry, Agricultural Food Engineering*, vol. 11 (60), no. 2., 171-184, Brasov/ Romania;
- [16] Trokhaniak V.I., Rutylo M.I., Rogovskii I.L., Titova L.L., Luzan O.R., Bannyi O.O., (2019), Experimental studies and numerical simulation of speed modes of air environment in a poultry house. *INMATEH - Agricultural Engineering*, vol. 59, issue 3, pp. 9-18. doi: 10.35633/INMATEH-59-01, Bucharest/Romania;
- [17] Zajicek M., Kic P., (2012), Improvement of the broiler house ventilation using the CFD simulation, *Agronomy Research*, vol. 10, Special Issue 1, pp. 235–242, Tartu/Estonia.

## INVESTIGATION OF OPERATIONAL PARAMETERS OF COATINGS FOR REBUILDING WORN-OUT CAST-IRON PARTS OF SELF-PROPELLED AGRICULTURAL MACHINES

### ИЗСЛЕДВАНЕ НА ЕКСПЛОАТАЦИОННИ ПАРАМЕТРИ НА ПОКРИТИЯ ЗА ВЪЗСТАНОВЯВАНЕ НА ИЗНОСЕНИ ЧУГУНЕНИ ДЕТАЙЛИ ОТ САМОХОДНИ ЗЕМЕДЕЛСКИ МАШИНИ

Bekana D. L.<sup>1)</sup>, Kolev Z. D.<sup>1)</sup>, Kadirova S. Y.<sup>2)</sup>, Nenov T. R.<sup>2)</sup>, Kadikyanov G. P.<sup>3)</sup> <sup>1</sup>

<sup>1)</sup> Ruse University "Angel Kanchev", Agrarian – Industrial Faculty / Bulgaria

<sup>2)</sup> Ruse University "Angel Kanchev", Faculty of Electrical Engineering, Electronics and Automation / Bulgaria

<sup>3)</sup> Ruse University "Angel Kanchev", Faculty of Transport / Bulgaria

Tel: +359 877 089537; E-mail: skadirova@uni-ruse.bg

DOI: <https://doi.org/10.35633/inmateh-62-17>

**Keywords:** operational parameters, coatings for rebuilding, cast iron parts, agricultural machines

#### ABSTRACT

*This paper presents investigation of some operational parameters of coatings for rebuilding, deposited on worn-out cast-iron parts of self-propelled agricultural machines. The coatings have been realized by applying a combined technology comprising deposition of electrochemical coating of non-ferrous metal and subsequently deposition of welding coating. The parameters for deposition of the electrochemical coatings and the parameters for deposition of the welding coatings have been presented. The results of the investigation of the following coatings' operational parameters are presented: removed material in friction process, friction torque, micro-hardness and roughness. Based on the results obtained, the relative wear resistance of the coatings has been calculated.*

#### РЕЗЮМЕ

*В публикацията е разгледано изследване на някои експлоатационни параметри на възстановителни покрития, нанесени върху износени чугунени детайли от самоходни земеделски машини. Възстановителните покрития са реализирани чрез прилагане на комбинирана технология, включваща нанасяне на електрохимично покритие от цветен метал и последващо нанасяне на наваръчно покритие. Представени са параметрите за нанасяне на електрохимичните покрития и параметрите за нанасяне на наваръчните покрития. Представени са резултатите от изследване на следните експлоатационните параметри на покритията: големина на износване при процеса на триене, момент на триене, микротвърдост и грапавост. На база на получените резултати е изчислена относителната износоустойчивост на възстановителните покрития.*

#### INTRODUCTION

In the agricultural machinery cast iron parts are wide spread. They are structural parts - cylindrical blocks, cylindrical sleeves, housings, plates, shells, caps, etc. (Souza T. et al, 2014; Vasilev T. et al, 2012) as well as dynamically and heavily loaded parts - camshafts, crankshafts, gears, worm wheels, flywheels, belt pulleys, valves, sprockets, brake drums, clutch discs, etc. (Mallikarjuna V. et al, 2014; Song L., 2015; Vasilev T. et al, 2012).

The cast iron material is suitable for casting complex shape parts. The density of cast iron is lower than the steel's density. On the other hand, the cast iron parts have high damping capacity under dynamic loads which leads to less accumulation of mechanical stresses (Golovin S., 2012; Vasilev T. et al, 2012).

The loss of metal of the parts' surfaces limits the reliability and serviceability of the agricultural machines (Popovych P. et al, 2017).

The rebuilding of worn-out parts increases their resource, and saves money for buying spare parts, and also ensures positive environmental effect. The rebuilding of worn-out parts from agricultural machinery has a positive impact in terms of reducing the production costs in agriculture (Lorencowicz E., Uziak J., 2015).

<sup>1</sup> Bekana D. L., Assoc. Prof. Ph.D. Eng.; Kolev Z. D., Lecturer Ph.D. Eng.; Kadirova S. Y., Lecturer Ph.D. Eng.; Nenov T. R., PhD Student; Kadikyanov G. P., Lecturer Ph.D. Eng.

One of the most common methods for rebuilding machine parts is by applying welding coating on the worn surface (Afanasyev V. et al, 2018; Kenchi Reddy K., Jayadeva C., 2012; Vasilev T. et al, 2012). There are a number of difficulties in the deposition of welding coatings on cast iron parts due to certain reasons related to the structure and properties of the cast iron material (Dametew A., 2015; Vasilev T. et al, 2012; Zuk M. et al, 2017).

The investigation of the tribological parameters of the rebuilt machine parts allows to determine their wear resistance comparing to non-rebuilt parts. The results obtained from the tribological investigations can be used to optimize the processes of worn-out parts rebuilding (Nikolov M., Kangalov P., 2014; Nikolov M. et al, 2015; Nikolov M. et al, 2015; Todorov I., Nikolov M., 2014).

The experimental investigations in the current research are based on specific methodology related to similar studies (Kadikyanov G., et al, 2010; Nikolov M., Kangalov P., 2014; Nikolov M. et al, 2016; Nikolov M. et al, 2015; Nikolov M. et al, 2015; Todorov I., Nikolov M., 2014).

The aim of the paper is to determine some operational parameters of coatings deposited on specimens. The investigation is needed for selection of the most appropriate coating in rebuilding process of worn-out cast-iron parts of self-propelled agricultural machines.

## MATERIALS AND METHODS

### OBJECT OF INVESTIGATION AND METHODOLOGY

#### Object of investigation

The objects of investigation are two types of coatings for rebuilding, realized by a combined technology applied on cast iron specimens. This technology involves the deposition of a transient electrochemical coating of non-ferrous metal (nickel and/or copper) and subsequent deposition of a welding coating. The welding coating has been realized by a process of automatic arc welding in a carbon dioxide protective medium using low-carbon steel thin wire. The reason for applying the non-ferrous metal transition coating is to improve the welding properties of the cast iron in order to realize a welding coating with sufficient parameters, as well as to provide stress relaxation, i.e. to prevent cracks. The rebuilt surfaces are in friction process with sliding bearings in the conditions of liquid, semi-liquid and boundary friction (Vasilev T. et al, 2012).

Table 1 presents the parameters of deposited transient electrochemical coatings. The treated specimens are called coating "A" and coating "B".

Table 1

Parameters of the transient electrochemical coatings

Coating for rebuilding	Type of transient electrochemical coating	Thickness of the electrochemical coating $h_{el.chemical\ coating}$ , [mm]
coating "A"	Cu	0.3
coating "B"	Ni + Cu	total thickness 0.2 (0.1 – Ni; 0.1 – Cu)

Table 2 presents the parameters of the welding deposition process for the investigated coatings for rebuilding.

Table 2

Welding deposition parameters

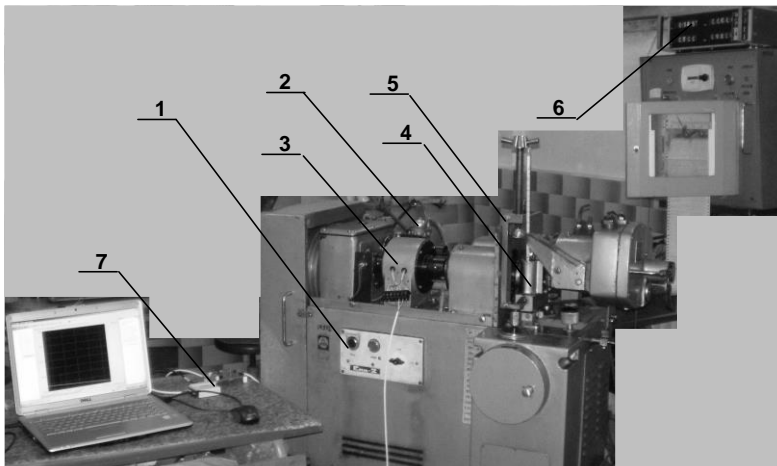
Coating for rebuilding	$d_{wire}$ [mm]	$l_{wire}$ [mm]	$\dot{V}_{CO_2}$ [l/min]	$n$ [min <sup>-1</sup> ]	$S_{weld}$ [mm/min <sup>-1</sup> ]	$V_{wire}$ [m/min]	$V_{weld}$ [m/min]	$U_{weld}$ [V]	$I_{weld}$ [A]
coating "A"	1	15	20	0.79	4.50	2.60	0.12	23	90
coating "B"	0.8	12	20	0.79	5.30	6.35	0.12	25	90

The parameters in the table are as follows:  $d_{wire}$  – welding wire diameter, mm;  $l_{wire}$  – length of the welding wire out of contact nozzle, mm;  $\dot{V}_{CO_2}$  – volume flow rate of the carbon dioxide, l/min;  $n$  – rotational speed of the cylindrical specimen, min<sup>-1</sup>;  $S_{weld}$  – step of welding deposition, mm/min<sup>-1</sup>;  $V_{wire}$  – welding wire feed rate, m/min;  $V_{weld}$  – welding deposition speed, m/min;  $U_{weld}$  – welding deposition voltage, V;  $I_{weld}$  – welding deposition current, A.

### Methodology for determination of the operational parameters

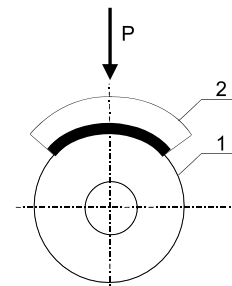
The investigated operational parameters can be divided into three types: tribological parameters (removed material in friction process and friction torque), mechanical parameter (micro-hardness), and micro-geometric parameter (roughness).

Figure 1 presents the experimental installation for investigation of liquid friction processes. The physical model of the friction pair "shaft–sliding bearing" is the pair "roll–sector" with corresponding parameters of geometric and physical similarity (Figure 2).



**Fig. 1 - Experimental installation:**

1 – tribometer for tribological investigations; 2 – oil mixing system; 3 – friction torque sensor; 4 – water-cooled chamber; 5 – loading mechanism; 6 – electronic recording system; 7 – electronic board of "National Instruments"



**Fig. 2 - Physical model of the friction pair**

1 – roll; 2 – sector

The tribometer for tribological investigations is equipped with additional devices, which have ensured: continuous mixing of the oil; cooling the chamber with oil to maintain a constant temperature; measuring the rotation speed of the roll (the friction path travelled) and duration of the experiment.

The friction pair has been loaded by a spring and a worm gear, by counting the divisions of the graduated flywheel.

The friction torque between the roll and the sector has been measured by an inductive sensor positioned between the reducer and the machine spindle. At the output of the inductive sensor for the friction torque, two electrical voltages have been obtained. The difference between the two voltages increases by increasing of the friction torque. To measure the output of the sensor and convert it into units for friction torque (N.cm), an USB electronic circuit board of „National Instruments" and the "LABVIEW" software have been used. The friction torque data has been continuously recorded during the experiment and visualized on the PC screen in digital or graphical form.

The rotational speed of the roll has been measured by electronic system, which receives the signal from another inductive sensor mounted between the reducer and the friction torque sensor.

The friction process between the roll and the sector has been implemented in an oil chamber with volume of 0.15 l. The chamber is water-cooled. The oil is being stirred by air fed from a three-way tap located in the bottom of the chamber. For temperature control in the chamber is used a thermostat.

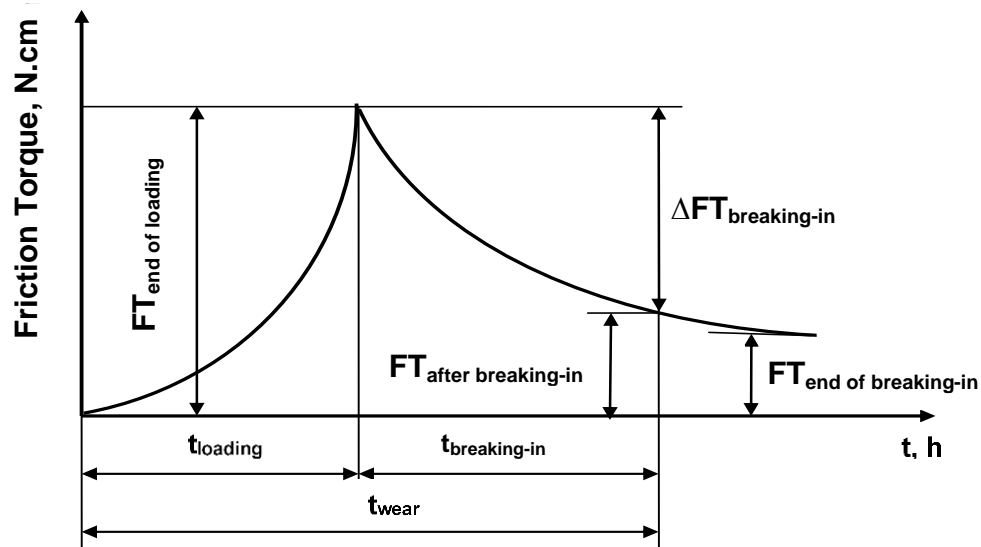
The parameters of friction and wear of the investigated specimens have been determined by liquid friction conditions in engine oil environment. The oil is with standard parameters and used in the breaking-in process of the internal combustion engines from agricultural machinery.

Figure 3 presents the variation of the friction torque in breaking-in and wear processes, in conditions of stepless loading.

The amount of material removed from the friction elements (roll and sector) during the wear process has been determined by the weighing method. Analytical weighing scale with accuracy of 0.05 mg has been used. The specimens have been cleaned with gasoline, dried and weighted before and after each fixing to the tester.

The roughness of the roll and the sector has been determined before and after each experiment of breaking-in and wear processes. The roughness parameter  $R_a$  in different planes and sections has been measured with roughness meter.

The micro-hardness of the surfaces has been measured with hardness meter. The measurements have been implemented with loading by weight of 100 g for the roll, and 50 g for the sector respectively.



**Fig. 3 - Variation of the friction torque in breaking-in and wear processes**

$FT_{end\ of\ loading}$  – friction torque at the end of the loading;  $FT_{after\ breaking-in}$  – friction torque after the breaking-in process;  
 $\Delta FT_{breaking-in}$  – friction torque during the breaking-in process;  $FT_{end\ of\ breaking-in}$  – friction torque at the end of breaking-in process;  
 $t_{loading}$  – loading period;  $t_{breaking-in}$  – breaking-in period;  $t_{wear}$  – wear period

The specimens are two types sectors and rolls. The sectors for the friction pair are with steel base on which a bearing lining with a thickness of  $0.1 \div 0.5$  mm in radius has been deposited (Figure 4). Respectively, the material of investigated rolls is ferrite-pearlite grey cast iron (Figure 5).

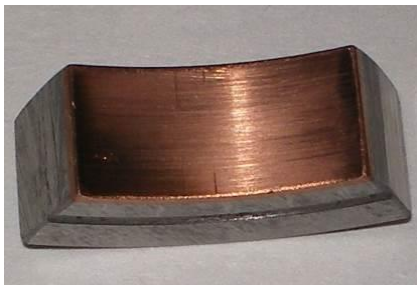


**Fig. 4 - Sector for investigation of coatings for rebuilding**

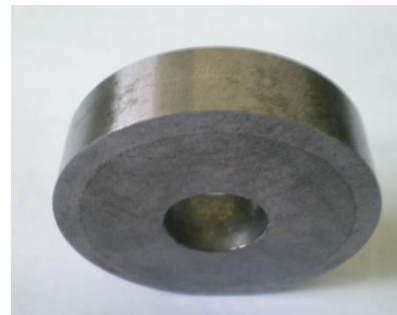


**Fig. 5 - Roll with deposited coating for rebuilding**

The friction pair has been loaded up uniformly. The loading parameters are: loading speed – 1 MPa/min, loading duration – 5 minutes, and a value of load – 100 daN, as the accuracy of the loading mechanism is 1 daN. The applied load of 100 daN provides a pressure of 5 MPa between the roll and the sector. This pressure value is close to the boundary conditions and can be applied for different types of materials and coatings without fretting of the surfaces.

The rolls' rotation speed is  $540\ min^{-1}$ , the roll diameter is 50 mm. At these conditions the wear of specimens is measurable. The calculated parameters for these conditions are: a sliding speed – 1.41 m/s, and a tribological characteristic  $PV = 7.05\ MPa/s$ . These values have been accepted in accordance to the admissible load limits of the sliding bearings.

During the experiments, the oil temperature in the low-volume chamber for friction and wear investigations, has been maintained in the range of  $30 \div 40\ ^\circ C$ . These temperatures are typical for the processes of agricultural machinery's engines cold starting, where the wear process is intensive.

RESULTS

Results obtained from the investigation of the wear process of the friction pair elements

Figure 6 presents the variation in the quantity of the removed material in friction process  $J_i$  of the rolls: with coating "A" (the friction surface is welding coating with transient layer of Cu), with coating "B" (the friction surface is welding coating with transient layer of Ni+Cu), and "NO" coating (the friction surface is ferrite-pearlite grey cast iron) during the investigation.

In all three types of friction surfaces of the rolls, the highest wear has been observed in the interval from the beginning to the first hour. Then the process of breaking-in between the surfaces of the friction pair is more intensive. After the second hour of the investigation, during the steady wear process, the value of  $J_i$  has decreased significantly. This is due to the cutting of most of the micro-irregularities on the friction surfaces. Generally, the highest wear in the process of investigation has been observed in the roll without deposited coating for rebuilding. The least wear has occurred in the roll, with deposited coating "B".

Figure 7 presents the variation in the quantity of the removed material in friction process of the sectors. Analogically to the rolls, the highest wear of the sectors has been observed in the first hour of the investigation. As a whole, the biggest wear has the sector involved in the friction process with the roll "NO" coating. The least wear has the sector involved in the friction pair with the roll type coating "B".

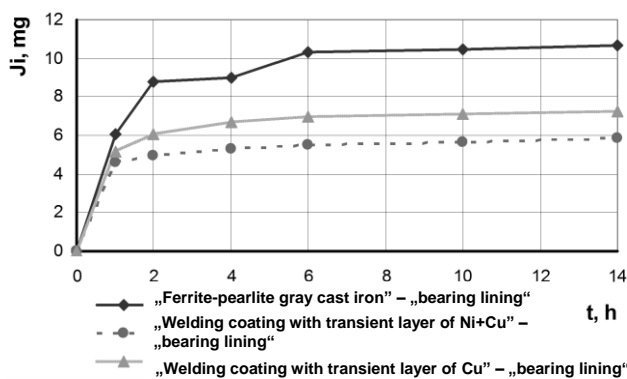


Fig. 6 - The quantity of the removed material from the rolls at different friction surfaces

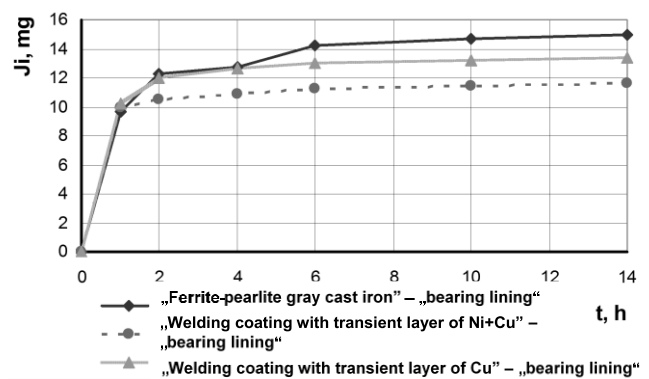


Fig. 7 - The quantity of the removed material from the sectors at different friction surfaces of the rolls

Results obtained from the investigation of the friction torque between the friction pair elements

The variation of the friction torque at the end of the loading during the investigation is presented in Figure 8. It can be seen that for all three types of rolls that the friction torque at the end of the loading has decreased during the investigation in the transition from the breaking-in process between the elements from the friction pair to the process of steady wear. The smallest value of  $FT_{end\ of\ loading}$  has the pair, in which the roll has been deposited with coating „B”. Therefore, in this case the best breaking-in process with the bearing alloy deposited on the sectors has been observed.

Figure 9 presents the variation of the friction torque after the breaking-in process. Based on the results, it can be concluded that at the rolls with deposited coating for rebuilding, the friction torque after the breaking-in process has decreased. The lowest value of  $FT_{after\ breaking-in}$  has been obtained at the roll deposited with coating "B".

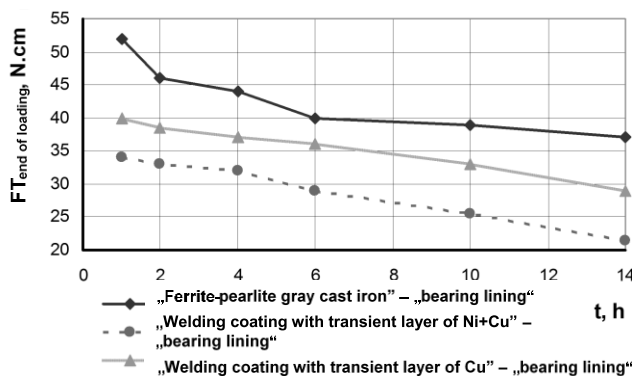


Fig. 8 - Variation of the friction torque at the end of the loading

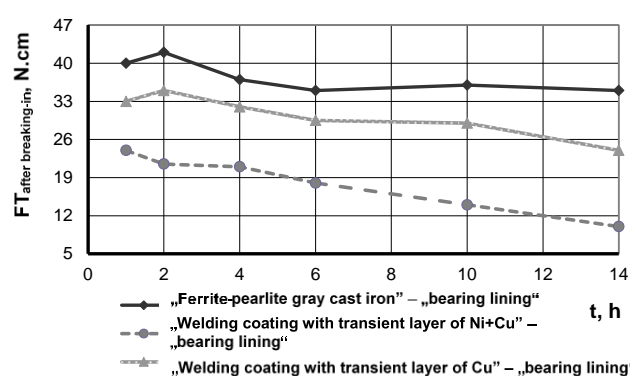


Fig. 9 - Variation of the friction torque after the breaking-in process

The variation of the friction torque at breaking-in process has been presented in Figure 10. The lowest values of the friction torque at breaking-in process have been obtained at the roll deposited with coating "A" and at the roll without deposited coating.

The friction torque reducing during the tests is due to the smoothing of the friction surfaces' microroughness, which reduces their direct contact.

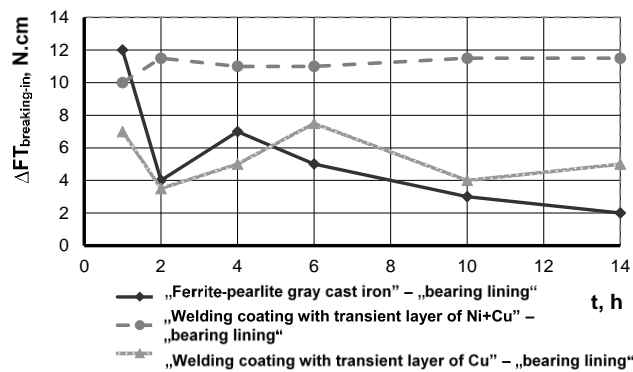


Fig.10 - Variation of the friction torque at breaking-in process

**Results obtained from the investigation of the roughness of pair elements' friction surfaces**

Figure 11 presents the variation of the friction surfaces' roughness of the rolls, during the investigation. The diagram presents that the lowest roughness has the roll with not deposited coating. The rolls with deposited coatings have almost the same roughness values.

Figure 12 presents the variation of the friction surfaces' roughness of the sectors at different friction surfaces of the rolls. The roughness of the sectors, involved in the friction pair with the rolls with deposited coating, has decreased during the breaking-in process, to reaching almost constant value in the steady wear process.

Due the transfer of microparticles against each other surfaces the roughness increases during breaking in process. This phenomenon is typical of this process. The general tendency to reduce the roughness of the friction surfaces after breaking-in process is generated by the reduction of the height of the microroughness.

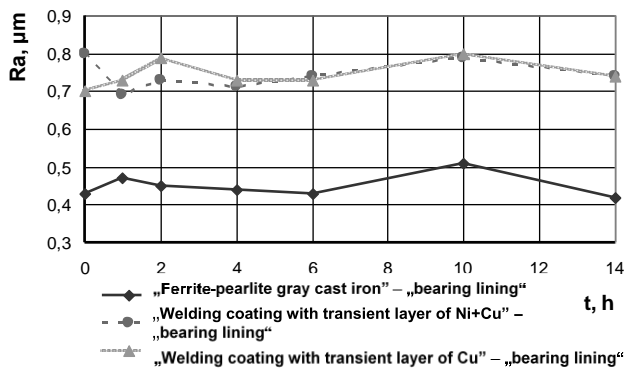


Fig. 11. Variation of the friction surfaces' roughness of the rolls

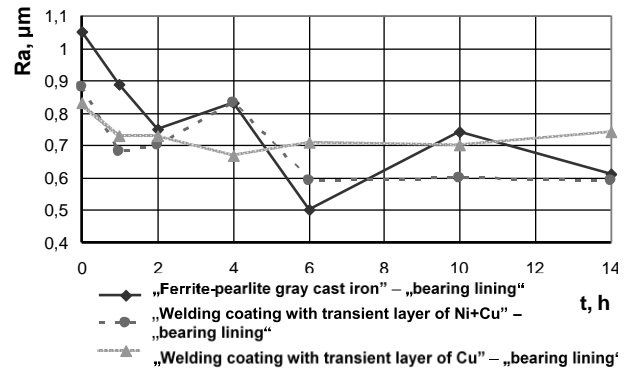


Fig. 12. Variation of the friction surfaces' roughness of the sectors

**Results from micro-hardness investigation of friction surfaces of the friction pair elements**

The variation of the friction surfaces' micro-hardness of the rolls during the investigation is presented in Figure 13. The highest micro-hardness of the friction surface has the roll deposited with coating "B". At the three types of rolls, the micro-hardness of the friction surface has changed in wide boundaries in the breaking-in process compared to the steady wear process.

Figure 14 presents the variation of the micro-hardness of the sectors' friction surfaces at different friction surfaces of the rolls. The micro-hardness of the friction surfaces of the sectors has changed significantly. The sector with the highest micro-hardness values is the sector with coating "A" (friction surface - welding coating with copper transient layer).

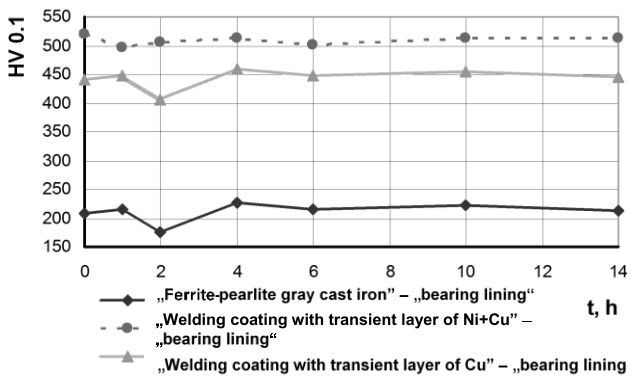


Fig. 13 - Variation of the friction surfaces' micro-hardness of the rolls

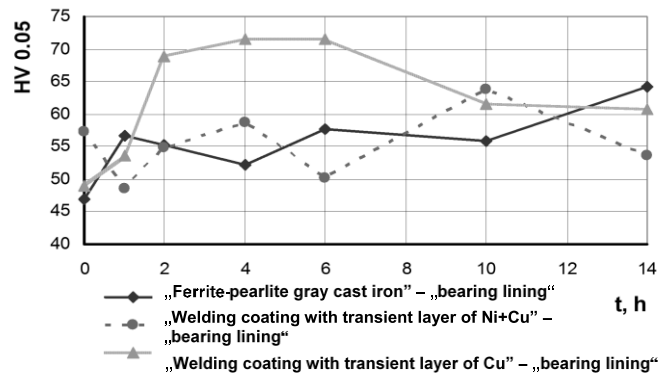


Fig. 14 - Variation of the micro-hardness of the sectors' friction surfaces

**Determination of the relative wear resistance of the coatings for rebuilding**

The relative wear resistance of the coatings for rebuilding has been determined by the equation:

$$\varepsilon = E/E_E \tag{1}$$

where:  $E$  is wear resistance of the friction surface of a roll with deposited coating for rebuilding, m/g;

$E_E$  – wear resistance of the friction surface of a roll without deposited coating for rebuilding, m/g.

The wear resistance is a reciprocal parameter of the wear intensity  $v$ :

$$E = 1/V \text{ [m/g]} \tag{2}$$

The wear intensity of the friction surface,  $V$  of the rolls has been determined by the equation:

$$V = J_i/S \text{ [g/m]} \tag{3}$$

where  $S = 71215.2$  m is the path of the friction surface of the roll, during the investigation.

Table 3 presents the values of calculated relative wear resistance of the rolls' friction surfaces.

Table 3

Relative wear resistance of the rolls' friction surfaces

Type of roll's friction surface	Micro-hardness, HV 0.1	Removed material in wear $J_i$ [g]	Wear intensity $V$ [g/m]	Wear resistance $E$ [m/g]	Relative wear resistance $\varepsilon$
Coating "A"	472	$7.25 \times 10^{-3}$	$10.1 \times 10^{-6}$	99009.90	1.485
Coating "B"	525	$5.83 \times 10^{-3}$	$8.1 \times 10^{-6}$	123456.79	1.852
"NO" coating	232	$10.70 \times 10^{-3}$	$15 \times 10^{-6}$	66666.67	1

Based on the results in the Table 3, it can be concluded that coating "B" is with the highest relative wear resistance. The value of the wear resistance means that the resource of the rebuilt machine part with this coating will increase 1.852 times, compared to non-rebuilt machine part.

**CONCLUSIONS**

The rebuilding of machine parts is a way of achieving a positive economic, environmental and social effect in many fields. The presented investigations of the coatings for rebuilding allow determining the achieved wear resistance of the rebuilt parts. It is directly related to the calculation of the savings, for not buying of spare parts.

The results from the investigations can be used to analyse the qualities of the coatings for rebuilding. Based on current results, the most appropriate coatings can be selected. On the other hand, the results can be used for optimization of the methods and technologies for rebuilding of worn-out machine parts.

Last but not least, it can be summarized that the coating "B" is better than coating "A". Coating "B" is characterized with higher micro-hardness, lower quantity of removed material in friction process, respectively higher wear resistance, less friction torque at the end of the loading process and less friction torque after the breaking-in process.

## REFERENCES

- [1] Afanasyev V., Chernysh A., Dolgova, S., (2018). Restoration of agricultural machines surfaces by white cast iron with the formation of technological repair units. *Materials Science Forum*, Vol.927, pp.43-47;
- [2] Dametew A., (2015). Experimental investigation on weld ability of cast iron. *Science Discovery*, 3(6), ISSN 2331-0642 (print), ISSN 2331-0650 (online), pp.71-75;
- [3] Golovin S., (2012). On the damping capacity of cast irons. *The Physics of Metals and Metallography*, Vol.113, Issue 7, pp.716–720;
- [4] Kadikyanov G., Stoyanov V., Bekana D., Marinov E., (2010). Study of friction coefficient between parts of aluminium and iron containing alloys. *Quality and Reliability of Technical Systems*, ISBN 978-80-552-0390-4, pp.337-341, Nitra / Slovakia;
- [5] Kenchi Reddy K., Jayadeva C. T., (2012). The effects of welding processes on microstructure and abrasive wear resistance for hardfacing deposits. *Bonfring International Journal of Industrial Engineering and Management Science*, Vol.2, №2, pp.28-34;
- [6] Lorencowicz E., Uziak J., (2015). Repair cost of tractors and agricultural machines in family farms. *Agriculture and Agricultural Science*, Vol.7, pp.152-157;
- [7] Mallikarjuna V., Jashuva N., Nagaraju G., Rama Bhupal Reddy B., (2014). Design manufacturing and cost estimation of camshaft used in two-wheeler. *IOSR Journal of Mechanical and Civil Engineering (IOSR-JMCE)*, Vol.11, Issue 1, e-ISSN 2278-1684, p-ISSN 2320-334X, pp.53-67;
- [8] Nikolov M., Kangalov P., (2014). Research methods for tribological properties of restorative and preventive coatings in different lubricating media at sliding friction. *Acta Technologica Agriculturae*, №3, ISSN 1335-2555, pp.70-74;
- [9] Nikolov M., Kangalov P., Kerekov S., Gospodinova N., (2016). Investigation of the tribological characteristics of complex ester of adipic acid as a friction modifier for engine oils on SMC-2 tribotester. *Journal of the Balkan Tribological Association*, №22, 3A-II, ISSN 1310-4772, pp.3412-3419;
- [10] Nikolov M., Máchal P., Mareček J., (2015). Dynamics of change in the roughness due to friction of the sliding surfaces of vibroarc weld overlaid coatings against steel and cast-iron parts. *Acta Universitatis Agriculturae et Silviculturae Mendelianae Brunensis*, №63, ISSN 1211-8516, pp.107-111;
- [11] Nikolov M., Todorov I., Zach M., Máchal P., Mareček J., (2015). A research about wear-resistance of applied layers obtained by gas metal arc overlaying process with increased wire electrode vibrating frequency. *Acta Universitatis Agriculturae et Silviculturae Mendelianae Brunensis*, №63, ISSN 1211-8516, pp.101-105;
- [12] Popovych P., Lyashuk O., Shevchuk O., Tson O., Poberezhna L., Bortnyk I., (2017). Influence of organic operation environment on corrosion properties of metal structure materials of vehicles. *INMATEH Agricultural Engineering*, Vol.52, №2, pp.113-118, Bucharest / Romania;
- [13] Song L., (2015). Foundry and development of ductile iron crankshaft. *The Open Mechanical Engineering Journal*, №9, pp.791-796;
- [14] Souza T., Nogueira R., Franco F., Aguilar M., Cetlin P., (2014). Mechanical and microstructural characterization of nodular cast iron (NCI) with niobium additions. *Materials Research*, 17(5), pp.1167-1172;
- [15] Todorov I., Nikolov M., (2014). A research about coefficient and moment of friction during interaction of deposited layers obtained through increased wire electrode vibrating frequency. *Machines Technologies Materials*, №8, ISSN 1313-0226, pp.44-46;
- [16] Vasilev T., Bekana D., Kolev Zh., (2012). Research on the possibility of recovery of worn and defective cast iron parts from agricultural machinery. *Proceedings of University of Ruse*, Vol.49, Series 1.1, ISSN 1311-3321, pp.66-71, Ruse / Bulgaria;
- [17] Zuk M., Górká J., Dojka R., Czupryński A., (2017). Repair welding of cast iron coated electrodes. *IOP Conference Series: Materials Science and Engineering*, Vol.227, Issue 1, Article number 012139.

## RESEARCH ON SEED SEPARATION PROCESS ON A GRAVITY-CASCADE SEPARATOR

### ДОСЛІДЖЕННЯ ПРОЦЕСУ СЕПАРУВАННЯ НАСІННЯ НА СЕПАРАТОРІ ГРАВІТАЦІЙНО-КАСКАДНОГО ТИПУ

Igor Dudarev<sup>\*)</sup>, Lyudmyla Zabrodotska, Vasyl Satsiuk, Iryna Taraymovich, Vasyl Olkhovskyi

Lutsk National Technical University / Ukraine

<sup>\*)</sup>Tel: +38(096)0403755; E-mail: i\_dudarev@ukr.net

DOI: <https://doi.org/10.35633/inmateh-62-18>

**Keywords:** separation process, gravity separator, seed flow rate, quality index of separation process, sieve

#### ABSTRACT

Different designs of separators are used for separating seeds. The principle of separator operation is based on various physical, mechanical and aerodynamic properties of seeds. Gravitational separators are promising because energy is not spent on separation process in this type of separators. A gravity-cascade separator was proposed, in which the separator sections are connected like “scissors”. The sieve length was theoretically justified, taking into account the condition for passing a small fraction of seeds into the sieve holes. The influence of sieves tilt angle and seed flow rate from hopper on the quality index of separation process was studied experimentally.

#### АНОТАЦІЯ

Для сепарування насіння використовуються різні конструкції сепараторів. Принцип роботи сепараторів заснований на різних фізико-механічних та аеродинамічних властивостях насіння. Перспективними є гравітаційні сепаратори, оскільки в них енергія не витрачається на процес сепарування. Був запропонований сепаратор гравітаційно-каскадного типу, в якому сепарувальні секції з'єднані по типу “ножиці”. У статті теоретично обґрунтована довжина решета сепаратора із урахуванням умови проходження дрібної фракції насіння в отвори решета. Також експериментально досліджено вплив кута нахилу решіт та подачі насіння з бункера на показник якості процесу сепарування.

#### INTRODUCTION

After harvesting crops, the collected seed mass is cleared of impurities, and the seeds are separated into fractions by size. Technological processes of separation and cleaning seeds are extremely important (Dong et al., 2013; Wang et al., 2017), since seed quality and cost depend on these processes. The seed separation and cleaning processes are carried out on separators of various types (Kugbei et al., 2018): air-screen cleaner, grader, horizontal and vertical screen cylinders, indent disk separator, indent cylinder separator, gravity separator, air separator, velvet roll separator, spiral separator, magnetic separator, vibrator separator, electrostatic separator, fluidized bed separator and colour separator. In addition, engineers and scientists have developed original designs of seed separators, such as separating conveyor (Vasylykovskiy et al., 2019), belt-type electrostatic separator (Basiry and Esehaghbeygi, 2012), solar grain separator machine (Nagesh and Lakshminarasimhan, 2014), pneumatic separator (Panasiewicz et al., 2012) and universal air-screen seed cleaner (Giyevskiy et al., 2018).

Seed separators differ in the principle of operation. The separator design is conditioned by a large number of factors, in particular, the physical-mechanical and aerodynamic properties of the seed mass, the level of cleaning accuracy, efficiency of a technological line (Panasiewicz et al., 2012). The seed separation process occurs according to the physical and mechanical properties of the components of seed mass (Bracacescu et al., 2016): seed size (length, width, and thickness), mass, shape, density, surface texture, electrical conductivity, humidity, colour, aerodynamic properties (Li et al., 2002; Voicu et al., 2008). The operation principle of the most common seed separators provides the separation of seed mass by size and aerodynamic properties of the mass components. According to the seeds shape and size, seeds are separated by sieves with round or oblong holes (Badretdinov et al., 2020). Also, sieves with a different shape of holes are used in agricultural industry. The aerodynamic properties of seed mass components are used when using the airflow to separate light impurities from the seeds.

To describe the seed separation process, scientists use a method of mathematical modelling, which allows us to better understand the complex flow of seed mass particles on the sieve and optimize the sieve parameters (Wang *et al.*, 2017). Most mathematical models of the separation process are phenomenological models (Dong *et al.*, 2009). Also, discrete element method (DEM) is widely used for modelling the separation process of bulk materials (seed mass) and justifying the operation mode of the separator (Chen and Tong, 2009; Zhao *et al.*, 2011). This method gives results, which are in good agreement with experimental data (Dong *et al.*, 2013) and allow us to simulate the separation process of bulk materials with spherical and non-spherical particles (Delaney *et al.*, 2012; Kruggel-Emden and Elskamp, 2014). While using this method, it is established that one of the most influential factors in the separation process is height of the bulk material layer on the sieve (Li *et al.*, 2002). The height of the seed layer on the sieve depends on the seed flow rate from the hopper. The flow rate depends on the unloading velocity of the seed mass and the area of the hopper unloading orifice. In addition to the physical and mechanical seeds properties, the hopper geometry has a significant impact on the flow rate of seed mass during hopper unloading (Albaraki and Antony, 2014). To determine the flow rate of bulk materials in different parts of the hopper during unloading, scientists use a simulation method. This method allows us to determine the dependence of the flow rate of bulk material on hopper opening angle and orifice size (Magalhaes *et al.*, 2016). DEM is also used to determine the flow rate of bulk materials at the unloading orifice of various shaped hoppers (plane-wedged hopper, space-wedged hopper, and flat-bottomed hopper) (Balevicius *et al.*, 2011). The velocity of bulk material unloading from the hopper side orifice can be calculated according to the equation (Sergeev and Nicolaev, 2010):

$$V_0 = \lambda \sin \varepsilon \sqrt{2g \left( 2.1R - \frac{3.4\Theta_0}{\rho g} \right)} \quad (1)$$

where:

$V_0$  – velocity of bulk material flow at the hopper unloading orifice, m·s<sup>-1</sup>;  $\lambda$  – coefficient of bulk material outflow;  $\varepsilon$  – tilt angle of the hopper bottom, rad;  $R$  – hydraulic radius ( $R = F/L_p$ ), m;  $\Theta_0$  – initial shear resistance, Pa;  $\rho$  – bulk material density, kg·m<sup>-3</sup>;  $g$  – gravitational acceleration, m·s<sup>-2</sup>;  $F$  – area of the unloading orifice, m<sup>2</sup>;  $L_p$  – perimeter of the unloading orifice, m.

Reducing energy consumption for the seed separation process is the main direction of developing new designs of seed separators. Gravity separators are the most promising in this direction, since these separators do not spend energy directly on the separation process, but only on loading and/or dosing of the seed mass. In gravity separators, the movement of the seed mass on the working surfaces is due to the forces of gravity, which act on the particles of the seed mass. Thus, studies that provide justification for the parameters of a new design gravity separator, in which the separation process occurs without energy consumption, are relevant. Therefore, the research purpose is to study the seed separation process on a gravity-cascade separator and substantiate its parameters.

## MATERIALS AND METHODS

The study of the seed mass separation process took place on an experimental gravity-cascade separator. The separator contains a seed mass hopper, seed fractions containers and system of separation sections that are connected crosswise (like "scissors") (fig. 1, a). Flat sieves and pallets are located on the frames of the separation sections. The seed fractions gutters are located at the end of each sieve and pallet. The gutters direct seed fractions to the beginning of the next sieve or pallet, which are located below. The screw-nut transmission is connected to the lower separation section, which makes it possible to adjust the tilt angle  $\alpha$  of the sieves and pallets.

Separating of vetch (*Vicia sativa*) seeds into two fractions (a large fraction with a seed size > 4 mm; a small fraction with a seed size ≤ 4 mm) was experimentally studied on the proposed separator. Sieves with round holes with a diameter of 4 mm were used for separating the vetch. Characteristics of separator sieves are sieve width 0.15 m, sieve length 0.2 m, sieve area 0.03 m<sup>2</sup>, and area of all sieves 0.36 m<sup>2</sup>. The study of the vetch separation process was carried out using the two-factor experiment method (Montgomery, 2017). The study involved determining the quality index of vetch separation process  $\mu_s$  depending on the tilt angle  $\alpha$  of the sieves and the flow rate  $Q$  of vetch seeds from the hopper.

Experiments were performed for the following cases: 1) the seed mass was separated with two sieves (total sieves length was  $2L_s = 0.4$  m); 2) the seed mass was separated with four separator sieves (total

sieves length was  $4L_s = 0.8$  m); 3) the seed mass was separated with six sieves (total sieves length was  $6L_s = 1.2$  m). The single sieve length ( $L_s = 0.2$  m) was determined depending on the maximum allowable length  $S$  of the sieve. According to the method (Sologubik et al., 2013), a study on the friction angle  $\varphi$  of vetch seeds on a steel surface was carried out to justify the range of sieve tilt angle variation. Also, the static coefficient of friction was calculated based on the results of this study  $f = \text{tg}(\varphi) = \text{tg}(0.331) = 0.344$ .

The interval of variation of the sieve tilt angle  $\alpha = 0.349\dots 0.419$  rad was justified taking into account the results of vetch seed friction angle study. All experiments were conducted for the vetch seed moisture content  $W = 14\%$ , which was determined by the experimental method (Sologubik et al., 2013).

The interval for varying the flow rate  $Q = 120\dots 140$  kg·h<sup>-1</sup> of vetch seeds from the hopper was justified taking into account that the seed layer height on the sieve did not exceed two seeds.

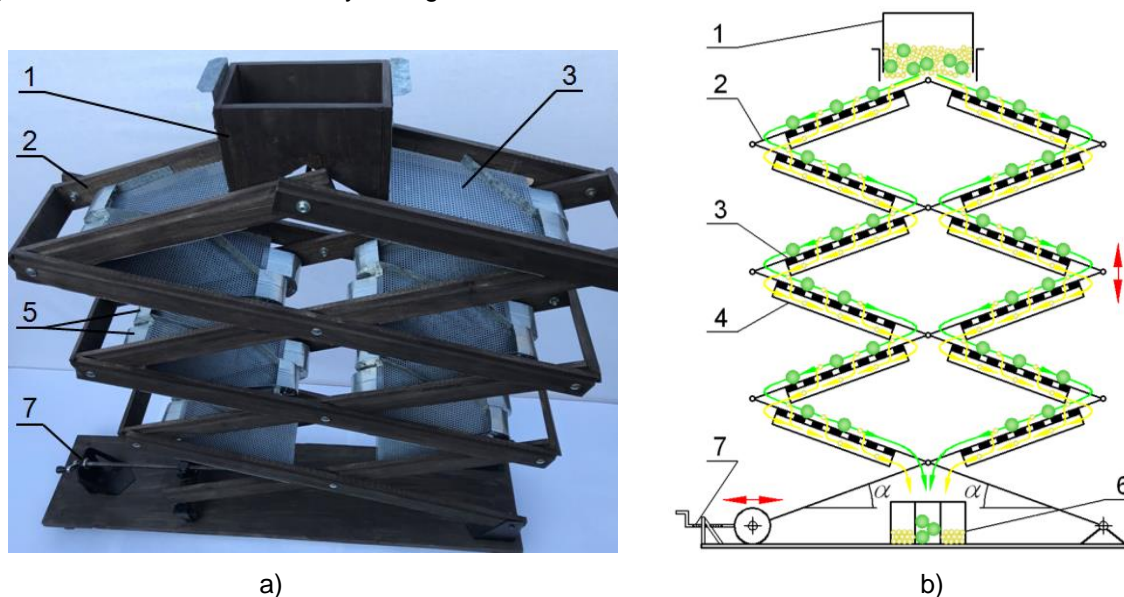


**Fig. 1 - Gravity-cascade separator (a) and scheme of seed fractions flows (b)**

1 – hopper; 2 – separator sections; 3 – sieve; 4 – pallet; 5 – gutters of seed fractions; 6 – containers; 7 – screw-nut transmission

During the study, a portion of vetch seeds weighing 1 kg was loaded into the separator hopper. After that, the hopper flaps were raised to the required height, which regulated the seed flow rate, and the vetch seeds were fed to the sieves of the upper separation sections. The vetch seeds moved through the separator in two separate symmetrical flows (fig. 1, b). The separated fractions of vetch seeds were fed to the seed fractions containers. Each vetch seed fraction was weighed after the separation process. Vetch seeds from a large fraction container were additionally sifted on a laboratory sieve with round holes with a diameter 4 mm using the sieve method of grain-size analysis (Lopez, 2016). According to the results of such sifting, the mass of a small seed fraction, which was not separated by separator, was determined. According to the obtained data, the quality index of separation process was calculated:

$$\mu_s = \frac{m_{f1}}{m_{f1} + m_{f2}} \cdot 100\% \quad (2)$$

where:  $\mu_s$  – quality index of separation process, %;  $m_{f1}$  – mass of small seed fraction, which was separated by separator, g;  $m_{f2}$  – mass of small seed fraction, which was not separated by separator, g.

## RESULTS

The proposed gravity-cascade separator separates the seed mass into two fractions: a large one (in fig. 1, b and fig. 2, b the seed fraction is indicated in green), which does not pass into the sieve holes, and a small one (in fig. 1, b and fig. 2 the seed fraction is indicated in yellow), which passes into the sieve holes.

The most important factor, which determines the passage of seeds of small fraction into the sieve holes, is the velocity of seeds movement along the sieve. The probability of seed passing into the sieve holes decreases with increasing seed velocity. The seed velocity increases with increasing seed move path along the sieve and sieve tilt angle  $\alpha$ .

Let the seed of small fraction have a spherical shape and diameter  $d$ , and its centre of gravity is centred at point  $C$  (the sphere centre). At the initial moment of passing into the sieve hole, the seed has a velocity  $V_{max}$ . The sieve hole length along the direction of seed movement is  $L$  ( $L > d$ ). The length  $L$  is not greater than the size of seeds of large fraction. The sieve is fixed and installed at tilt angle  $\alpha$ . The coordinate system  $xy$  is located as shown in fig. 2, a. The movement of seed of small fraction during its passage into the sieve hole can be described by equations:

$$\left. \begin{aligned} m\ddot{x} &= mg \sin \alpha; \\ m\ddot{y} &= -mg \cos \alpha, \end{aligned} \right\} \quad (3)$$

where:  $m$  – mass of small fraction, kg;  $\ddot{x}$ ,  $\ddot{y}$  – projections of seed acceleration on  $x$  and  $y$  axes,  $m \cdot s^{-2}$ ;  
 $g$  – gravitational acceleration,  $m \cdot s^{-2}$ ;  $\alpha$  – sieve tilt angle, rad.

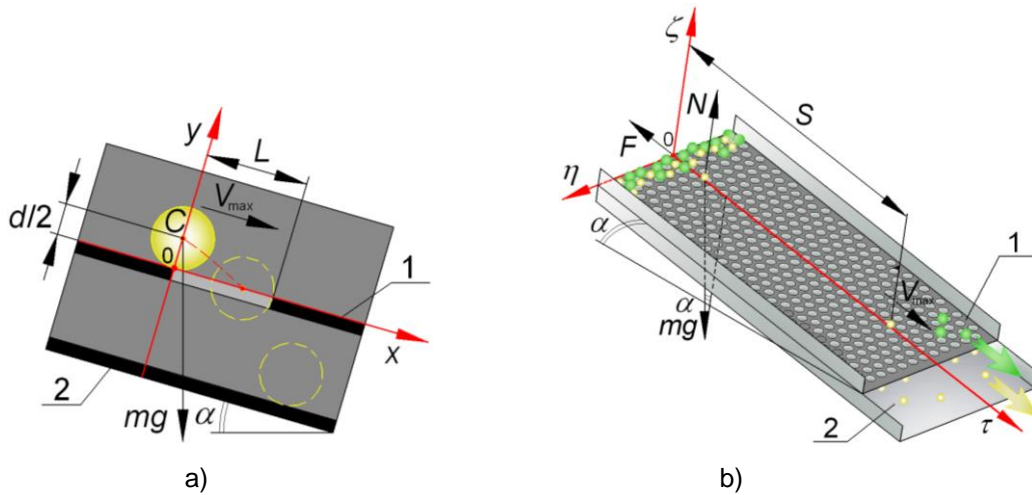


Fig. 2 - Scheme of the passage of seed of small fraction into the sieve hole (a) and scheme of the movement of seed of small fraction along the sieve (b)  
 1 – sieve; 2 – pallet

The equations of the system (3) were integrated twice under the initial conditions: time  $t_0 = 0$ ; the initial coordinates of the seed centre of gravity are  $x_0 = 0$  and  $y_0 = d/2$ ; the initial projections of the seed velocities along  $x$  and  $y$  axes are  $\dot{x}_0 = V_{max}$  and  $\dot{y}_0 = 0$ . After integration, the following equations were obtained:

$$\left. \begin{aligned} x &= \frac{gt^2}{2} \cdot \sin \alpha + V_{max} t \\ y &= -\frac{gt^2}{2} \cdot \cos \alpha + \frac{d}{2} \end{aligned} \right\} \quad (4)$$

where:

$x, y$  – coordinates of the seed centre of gravity  $C$ , m;  $d$  – seed diameter, m;  $t$  – time, s.

The seed of small fraction will pass into the sieve hole when the conditions  $x \leq L - (d/2)$  and  $y \leq 0$  for the coordinates of the seed centre of gravity  $C$  are implemented. Otherwise, the seed will not pass into the sieve hole and will be pushed out by the seed flow. From the second equation of the system (4), for the case  $y = 0$ , the time  $t_{d/2}$  was determined by equation:

$$t_{d/2} = \sqrt{\frac{d}{g \cdot \cos \alpha}} \quad (5)$$

The time  $t_{d/2}$  was used in the first equation of the system (4):

$$x = \frac{d}{2} \tan \alpha + V_{max} \sqrt{\frac{d}{g \cdot \cos \alpha}} \quad (6)$$

If coordinate  $x$  obtained in equation (6) satisfies the condition  $x \leq L - (d/2)$ , then the seed will pass into the sieve hole.

The extreme case ( $x = L - (d/2)$ ) for the seed passage into the sieve hole will be considered below. For this case, after substituting  $x = L - (d/2)$  in equation (6), an equation for determining the maximum allowable initial velocity of seed, after which the seed will pass into the sieve hole, was obtained:

$$V_{\max} = \left( L - \frac{d}{2}(1 + \operatorname{tg} \alpha) \right) \sqrt{\frac{g \cos \alpha}{d}} \quad (7)$$

where:

$V_{\max}$  – maximum allowable initial velocity of seed of small fraction, m·s<sup>-1</sup>.

Let the seed mass flow with a height of one seed move down along the sieve. The movement of the small fraction seed selected from seed flow along the tilt sieve will be considered below (fig. 2, b). If the seed slides down a tilt sieve with the initial velocity  $V_0$ , then the equations of its movement in a fixed coordinate system  $\tau\zeta\eta$  will have the form (the seed movement along the axis  $\eta$  does not occur ( $\eta = 0$ )):

$$\left. \begin{aligned} m\ddot{\tau} &= mg \sin \alpha - F \\ m\ddot{\zeta} &= -mg \cos \alpha + N \\ m\ddot{\eta} &= 0 \end{aligned} \right\} \quad (8)$$

where:  $m$  – mass of small fraction seed, kg;  $\ddot{\tau}$ ,  $\ddot{\zeta}$ ,  $\ddot{\eta}$  – projections of seed acceleration on  $\tau$ ,  $\zeta$  and  $\eta$  axis, m·s<sup>-2</sup>;  $F$  – friction force, N;  $N$  – normal reaction of the sieve surface, N.

If the seed moves along the tilt sieve without leaving its surface ( $\ddot{\zeta} = 0$ ), then from the second equation of the system (8) the normal reaction of the sieve surface  $N$  and friction force  $F$  can be obtained:

$$N = mg \cos \alpha \quad (9)$$

$$F = fN = fmg \cos \alpha \quad (10)$$

where:  $f$  – static coefficient of friction.

After substituting equation (10) into the first equation of the system (8), the equation can be obtained:

$$\ddot{\tau} = g(\sin \alpha - f \cos \alpha) \quad (11)$$

The equation (11) was integrated twice under the initial conditions: time  $t_0 = 0$ ; initial seed coordinate along the  $\tau$  axis was  $\tau_0 = 0$ ; initial projection of the seed velocity along the  $\tau$  axis was  $\dot{\tau}_0 = V_0$  (the velocity  $V_0$  was calculated from the dependence (1)). After integration, the following equations were obtained:

$$\dot{\tau} = gt(\sin \alpha - f \cos \alpha) + V_0 \quad (12)$$

$$\tau = \frac{gt^2}{2}(\sin \alpha - f \cos \alpha) + V_0 t \quad (13)$$

where:  $\dot{\tau}$  – projection of the seed velocity on the  $\tau$  axis, m·s<sup>-1</sup>;  $\tau$  – coordinate of the seed, m;  $t$  – time, s.

Let us define the time  $t_V$ , during which the seed, moving along the sieve down, reaches the velocity  $V_{\max}$ . After substituting velocity  $\dot{\tau} = V_{\max}$  into the equation (12), the equation was obtained:

$$t_V = \frac{V_{\max} - V_0}{g(\sin \alpha - f \cos \alpha)} \quad (14)$$

The move path  $S$ , which the small fraction seed will pass along the sieve during time  $t_V$ , can be determined by equation (13):

$$\tau = S = \frac{V_{\max}^2 - V_0^2}{2g(\sin \alpha - f \cos \alpha)} \quad (15)$$

where:  $S$  – path, which the seed of small fraction will pass along the sieve during time  $t_V$ , m.

Thus, the maximum sieve length of the proposed separator, on which it is possible to pass the seed into the sieve hole, is equal to  $S$ . To increase the sieve length  $S$ , on which the seed mass is separated, is possible by reducing the angles  $\alpha$  and  $\varepsilon$ , as evidenced by the analysis of the graph (fig. 3). Complete separation of seed mass on the sieves of the gravity separator cannot always be provided by reducing the angles  $\alpha$  and  $\varepsilon$ . Also, the slowing down of the seed mass on the separator sieves (reducing seed flow speed) improves the condition of seed mass separation. The slowing down of the seed mass can be achieved by design changes in the separator. In the proposed separator the sieves are arranged in a cascade, so the seed flow slowdown occurs at the stage of the transition of the seed flow from one sieve to another sieve, due to a change in the direction of the seed flow. In case of separating vetch seeds into two fractions, the maximum sieve length should be  $L_s \leq S = 0.203$  m (the sieve length was calculated for the parameters:  $\alpha = 0.349$  rad,  $\varphi = 0.331$  rad,  $\varepsilon = 0.349$  rad,  $\lambda = 0.6$ ,  $F = 7.5 \cdot 10^{-4}$  m<sup>2</sup>,  $L_p = 0.31$  m,  $d = 1.2 \cdot 10^{-3}$  m,  $L = 4 \cdot 10^{-3}$  m).

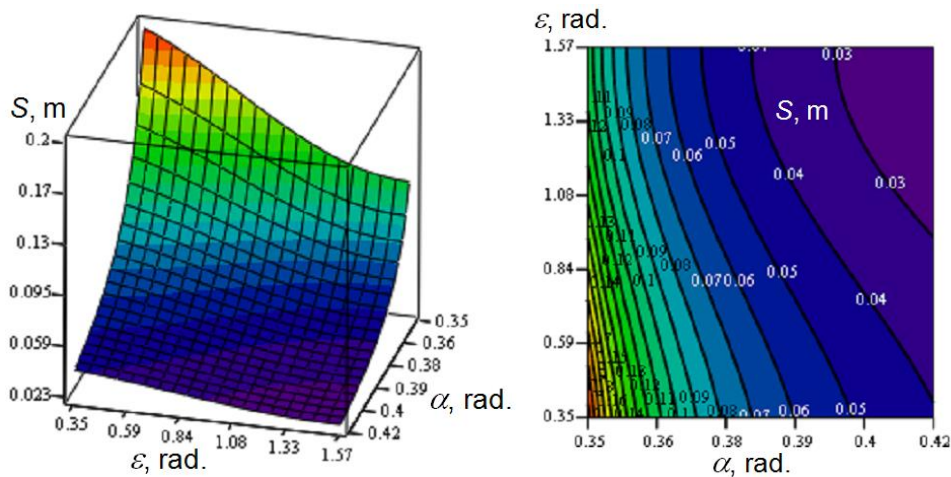


**Fig. 3 - The maximum sieve length  $S$ , on which the separation of the seed mass is possible, depending on the angles  $\alpha$  and  $\varepsilon$**

( $f = 0.344$ ,  $\lambda = 0.6$ ,  $F = 7.5 \cdot 10^{-4} \text{ m}^2$ ,  $L_p = 0.31 \text{ m}$ ,  $d = 1.2 \cdot 10^{-3} \text{ m}$ ,  $L = 4 \cdot 10^{-3} \text{ m}$ )

The influence of the sieve tilt angle  $\alpha$  and seed flow rate  $Q$  on the quality index of separation process  $\mu_s$  of vetch seed was studied on the proposed gravity-cascade separator. According to the result of experimental study, equations were obtained for the following cases (fig. 4):

- 1) the seed mass was separated with two separator sieves ( $2L_s = 0.4 \text{ m}$ ):

$$\mu_s = 161.81 - 185.71\alpha - 0.3Q \quad (16)$$

- 2) the seed mass was separated with four separator sieves ( $4L_s = 0.8 \text{ m}$ ):

$$\mu_s = 200.97 - 195.23\alpha - 0.4Q \quad (17)$$

- 3) the seed mass was separated with six separator sieves ( $6L_s = 1.2 \text{ m}$ ):

$$\mu_s = 176.78 - 140.48\alpha - 0.308Q \quad (18)$$

where:

$\mu_s$  – quality index of separation process, %;  $\alpha$  – sieve tilt angle, rad.;  $Q$  – vetch seeds flow rate,  $\text{kg} \cdot \text{h}^{-1}$ .

Data analysis shows that the quality index of separation process  $\mu_s$  decreases with increasing sieve tilt angle  $\alpha$  and vetch seeds flow rate  $Q$ . With increasing sieve tilt angle from  $\alpha = 0.349 \text{ rad}$  to  $\alpha = 0.419 \text{ rad}$  and increasing seed flow rate from  $Q = 120 \text{ kg} \cdot \text{h}^{-1}$  to  $Q = 140 \text{ kg} \cdot \text{h}^{-1}$  the quality of separation process is reduced: 1) the seed mass was separated with two separator sieves ( $2L_s = 0.4 \text{ m}$ ) – from  $\mu_s = 61.0\%$  to  $\mu_s = 42.0\%$  (fig. 3, a, b); 2) the seed mass was separated with four separator sieves ( $4L_s = 0.8 \text{ m}$ ) – from  $\mu_s = 84.8\%$  to  $\mu_s = 63.2\%$  (fig. 3, a, c); 3) the seed mass was separated with six sieves ( $6L_s = 1.2 \text{ m}$ ) – from  $\mu_s = 90.8\%$  to  $\mu_s = 74.8\%$  (Fig. 3, a, d). Such research results can be explained by the fact that with increasing sieve tilt angle  $\alpha$  probability of small fraction seed passage into the sieve holes decreases due to the high velocity of seed movement. The increasing of seed flow rate  $Q$  also creates unfavourable conditions for the separation process, as the thickness of the seed layer on the sieves increases.

Analysis of research results also indicates that the quality index  $\mu_s$  increases with the increase in the number of sieves into which the seed flow passes. It should be noted that the intensity of the separation process is the highest during the seed passage of the first two sieves, but the intensity of the process decreases on the next sieves. So, in the case of  $2L_s = 0.4 \text{ m}$  (the first and second sieves), the quality index of separation process is within  $\mu_s = 42.0 \dots 61.0\%$ ; in the case of  $4L_s = 0.8 \text{ m}$  –  $\mu_s = 63.2 \dots 84.8\%$  (only 21.2...23.8% small seed fraction was separated on the third and fourth sieves); in the case of  $6L_s = 1.2 \text{ m}$  –  $\mu_s = 74.8 \dots 90.8\%$  (only 6.0...11.6% small seed fraction was separated on the fifth and sixth sieves).

It was also found that individual seeds flew out from the sieves during seed separation on the proposed separator. This is the result of changing the direction of seed movement during the transition from one sieve to another sieve. During the research, the percentage of such seeds was 0.2% of the initial seed mass. Installing the covers over the separator sieves allows eliminating this disadvantage.

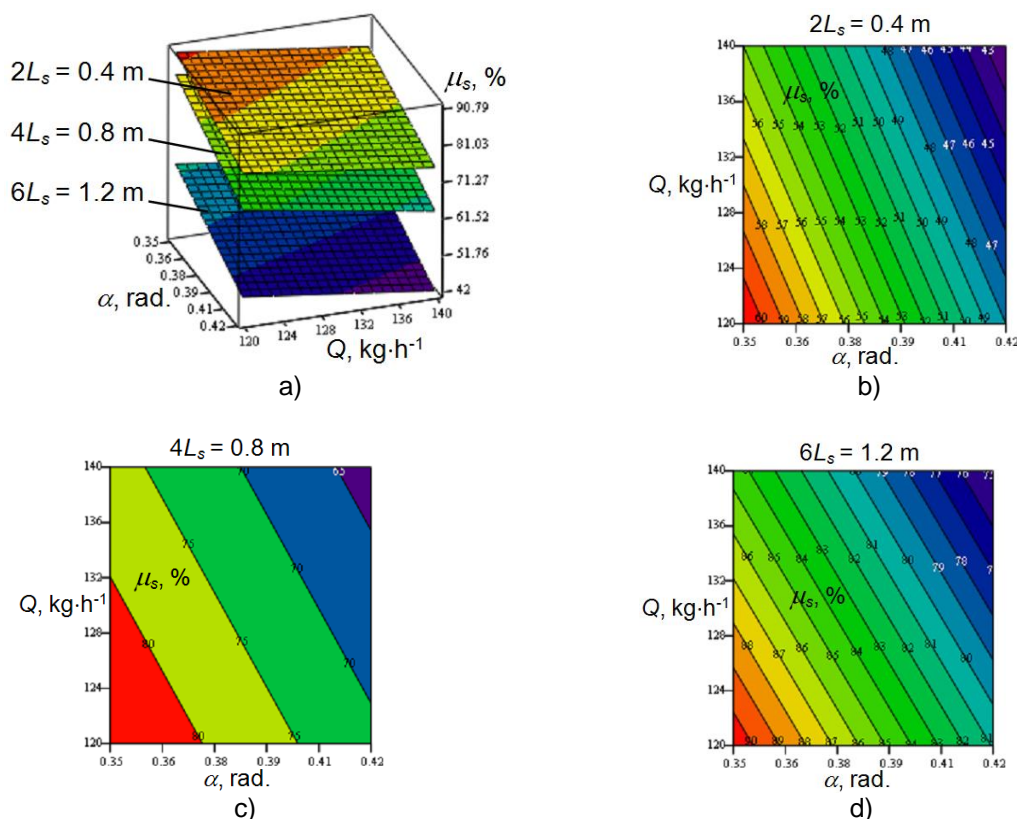


**Fig. 4 - The quality index of separation process  $\mu_s$  depending on the sieve tilt angle  $\alpha$  and seed flow rate  $Q$**   
 a – three cases ( $2L_s$ ,  $4L_s$ ,  $6L_s$ ); b –  $2L_s = 0.4$  m; c –  $4L_s = 0.8$  m; d –  $6L_s = 1.2$  m

## CONCLUSIONS

The obtained theoretical equations allow us to justify the maximum sieve length on which it is possible to separate the seed mass. It was found that as the sieve tilt angle  $\alpha$  increases, the sieve length, on which it is possible to pass the small fraction seeds into the sieve holes, decreases. For the case of vetch seed separation in the proposed separator the recommended sieve length is  $S = 0.203$  m (the sieve length was calculated for the parameters:  $\alpha = 0.349$  rad and  $\varepsilon = 0.349$  rad). As the results of experimental study show, the sieve length  $S$  is not sufficient for complete separation of the seed mass. It is recommended that the sieves be arranged in a cascade, as in the proposed design of a gravity-cascade separator. This arrangement of sieves allows us to slow down the seed flow by changing the direction of its movement between sieves and, accordingly, increase the number of sieves on which it is possible to pass the small fraction seeds into the sieve holes. Thus, increasing the total length of the sieves contributes to an increase of the quality index of separation process. The design of the proposed separator also allows us to easily adjust the sieve tilt angle, depending on the physical and mechanical properties of the seed mass components. As a result of experimental studies, it was found that with the increase in the sieve tilt angle the percentage of separated seeds of small fraction  $\mu_s$  decreases. The quality index of separation process also decreases with the increase in the seed flow rate from the hopper. It was experimentally found that the percentage of separated small seed fraction increases with increasing the number of sieves. However, the intensity of separation process decreases on each subsequent sieve.

## REFERENCES

- [1] Albaraki S., Antony S.J. (2014). How does internal angle of hoppers affect granular flow? Experimental studies using digital particle image velocimetry. *Powder Technology*, 268, 253–260.
- [2] Badretdinov I., Mudarisov S., Lukmanov R., Ibragimov R., Permyakov V., Tuktarov M. (2020). Mathematical modelling and study of the grain cleaning machine sieve frame operation. *INMATEH – Agricultural Engineering*, 60(1), 19–28. <https://doi.org/10.35633/inmateh-60-02>
- [3] Balevicius, R., Kacianauskas, R., Mroz, Z., & Sielamowicz, I. (2011). Analysis and DEM simulation of granular material flow patterns in hopper models of different shapes. *Advanced Powder Technology*, 22, 226–235. <https://doi.org/10.1016/j.apt.2010.12.005>

- [4] Basiry M., Esehaghbeygi A. (2012). Cleaning and charging of seeds with an electrostatic separator. *Applied Engineering in Agriculture*, 28(1), 143–147. <https://doi.org/10.13031/2013.41274>
- [5] Bracacescu C., Gageanu I., Popescu S., Selvi K.C. (2016). Researches concerning impurities separation process from mass of cereal seeds using vibrating sieves in air flow currents. *Engineering for Rural Development*, Jelgava, 364–370.
- [6] Chen Y., Tong X. (2009). Application of the DEM to screening process: a 3D simulation. *Mining Science and Technology (China)*, 19(4), 493–497. [https://doi.org/10.1016/s1674-5264\(09\)60092-2](https://doi.org/10.1016/s1674-5264(09)60092-2)
- [7] Delaney G.W., Cleary P.W., Hilden M., Morrison R.D. (2012). Testing the validity of the spherical DEM model in simulating real granular screening processes. *Chemical Engineering Science*, 68(1), 215–226. <https://doi.org/10.1016/j.ces.2011.09.029>
- [8] Dong K. J., Yu A. B., Brake I. (2009). DEM simulation of particle flow on a multi-deck banana screen. *Minerals Engineering*, 22(11), 910–920. <https://doi.org/10.1016/j.mineng.2009.03.021>
- [9] Dong K.J., Wang B., Yu A. B. (2013). Modelling of particle flow and sieving behaviour on a vibrating screen: from discrete particle simulation to process performance prediction. *Industrial & Engineering Chemistry Research*, 52(33), 11333–11343. <https://doi.org/10.1021/ie3034637>
- [10] Giyevskiy A.M., Orobinsky V.I., Tarasenko A.P., Chernyshov A.V., Kurilov D.O. (2018). Substantiation of basic scheme of grain cleaning machine for preparation of agricultural crops seeds. *IOP Conf. Ser.: Mater. Sci. Eng.*, 327 042035. <https://doi.org/10.1088/1757-899X/327/4/042035>
- [11] Kruggel-Emden H., Elskamp F. (2014). Modelling of screening processes with the discrete element method involving non-spherical particles. *Chemical Engineering & Technology*, 37(5), 847–856.
- [12] Kugbei S., Avungana M., Hugo, W. (2018). *Seeds Toolkit. Module 2: Seed processing: principles, equipment and practice*. The Food and Agriculture Organization of the United Nations and AfricaSeeds, Rome.
- [13] Li J., Webb C., Pandiella S. S., Campbell G. M. (2002). A numerical simulation of separation of crop seeds by screening – effect of particle bed depth. *Food and Bioprocess Processing*, 80(2), 109–117. <https://doi.org/10.1205/09603080252938744>
- [14] Lopez G.I. (2016). Grain size analysis. *Encyclopedia of Earth Sciences Series*, 341–348. [https://doi.org/10.1007/978-1-4020-4409-0\\_18](https://doi.org/10.1007/978-1-4020-4409-0_18)
- [15] Magalhaes F. G. R., Atman, A. P. F., Moreira, J. G., & Herrmann, H. J. (2016). Analysis of the velocity field of granular hopper flow. *Granular Matter*, 18(33). <https://doi.org/10.1007/s10035-016-0636-y>
- [16] Montgomery D. C. (2017). *Design and analysis of experiments* (9<sup>th</sup> ed.). John Wiley & Sons, Limited.
- [17] Nagesh S., Lakshminarasimhan S. N. (2014). Development of grain separator machine. *International Journal of Engineering Research – Online*, 2(6), 161–167.
- [18] Panasiewicz M., Sobczak P., Mazur J., Zawislak K., Andrejko D. (2012). The technique and analysis of the process of separation and cleaning grain materials. *Journal of Food Engineering*, 109, 603–608. <https://doi.org/10.1016/j.jfoodeng.2011.10.010>
- [19] Sergeev N. S., Nicolaev V. N. (2010). Outflow of loose feeds from bunker of multicomponent vibratory measuring hopper (Истечение сыпучих кормов из бункера многокомпонентного вибрационного дозатора). *Achievements of Science and Technology of AIC (Достижения науки и техники АПК)*, 10, 65–67.
- [20] Sologubik C. A., Campanone L. A., Pagano A. M., Gely M. C. (2013). Effect of moisture content on some physical properties of barley. *Industrial Crops and Products*, 43, 762–767.
- [21] Vasylovskiy O., Vasylovskaya K., Moroz S., Sviren M., Storozhyk L. (2019). The influence of basic parameters of separating conveyor operation on grain cleaning quality. *INMATEH – Agricultural Engineering*, 57(1), 63–70.
- [22] Voicu G., Casandroiou T., Tarcolea C. (2008). Testing stochastic models for simulating the seeds separation process on the sieves of a cleaning system, and a comparison with experimental data. *Agricultural Conspectus Scientificus*, 73(2), 95–101.
- [23] Wang Y., Yu J., Yu Y., Fu H. (2017). Numerical simulation of the particular flow on an agricultural screen with a complex motion based on the coupling model of PMBK with DEM. *Proceedings of the 7<sup>th</sup> International Conference on Discrete Element Methods*, 188, 687–695.
- [24] Zhao L., Zhao Y., Liu C., Li J., Dong H. (2011). Simulation of the screening process on a circularly vibrating screen using 3D-DEM. *Mining Science and Technology*, 21(5), 677–680.

# INTELLIGENT CONTROL TECHNOLOGY OF AGRICULTURAL GREENHOUSE OPERATION ROBOT BASED ON FUZZY PID PATH TRACKING ALGORITHM

/

## 基于模糊 PID 路径跟踪算法的农业温室作业机器人智能控制技术

Ren Qun <sup>1</sup>

Bozhou University, Department of Electronic and Information Engineering, Bozhou, Anhui, 236800 / China

\*Tel: 13006396137; E-mail: gtukhx35@sina.com

DOI: <https://doi.org/10.35633/inmateh-62-19>

**Keywords:** path tracking, fuzzy PID, robot, greenhouse operation

### ABSTRACT

With the development of agricultural automation, applying intelligent algorithms to the navigation control of agricultural work vehicles has important practical significance for improving vehicle navigation accuracy and operation efficiency. In view of the complexity of the agricultural greenhouse environment, this study proposed a fuzzy PID path tracking algorithm based on the traditional vehicle PID control system. This algorithm uses a fuzzy controller to improve the PID control system, thereby realizing the online setting of PID control parameters. In order to verify the effectiveness of the fuzzy PID path tracking algorithm, the improved control system was applied to the tracked vehicle robot of Beijing Forestry University, and the operation performance of the vehicle robot was tested. The research results show that the absolute error rate of vehicle robot distance measurement is less than 1%; the error of the man-machine follow-up test is between 4 and 7 cm, and the measured follow-up distance is slightly less than the safe follow-up distance; the maximum error of the vehicle's fixed-point parking is 0.3 cm; The linear position tracking control has a lateral position deviation of  $\pm 3\text{cm}$ , and the vehicle's linear driving control and steering effects are better. The fuzzy PID path tracking algorithm designed this time shows good control performance, which has reference significance for the practical application of agricultural robots.

### 摘要

随着农业自动化的发展, 将智能算法应用于农业作业车辆的导航控制, 对于提高车辆导航精度和作业效率具有重要的现实意义。针对农业温室环境的复杂性, 本文在传统车辆 PID 控制系统的基础上, 提出了一种模糊 PID 路径跟踪算法。该算法采用模糊控制器对 PID 控制系统进行改进, 从而实现 PID 控制参数的在线整定。为了验证模糊 PID 路径跟踪算法的有效性, 将改进后的控制系统应用于 S 大学履带式车辆机器人, 并对其运行性能进行了测试。研究表明, 车载机器人测距的绝对误差率小于 1%; 人机跟踪试验的误差在 4~7cm 之间, 实测跟踪距离略小于安全跟踪距离; 车辆定点停车最大误差为 0.3cm; 直线位置跟踪控制具有  $\pm 3\text{cm}$  的横向位置偏差, 车辆的线性驾驶控制和转向效果较好。本次设计的模糊 PID 路径跟踪算法具有良好的控制性能, 对农业机器人的实际应用具有参考意义。

### INTRODUCTION

The in-depth research and development of modern science and technology and control theory have guided the intelligent transformation of agricultural production technology. The traditional agricultural production method mainly relies on manpower. This method has low production efficiency and is greatly affected by the environment and weather. The application of automation technology has fundamentally liberated the agricultural labour force. Blake T. discussed the impact of the development of automation, robotics, and the Internet of Things on the transformation of agricultural production technology, and proposed to apply modern factory control experience to agricultural technology to improve agricultural productivity (Blake T., 2016). Auat Cheein F. proposed an intelligent sampling technology for automatic vehicle tracking path. The probability frame was used to predict and avoid obstacles. Finally, the working performance of the controller was tested on agricultural machinery.

<sup>1</sup> Ren Qun, As. PhD. Eng.

The results show that this technology significantly improves agricultural machinery, control performance and work efficiency (Auat C.F., 2016). Facility agriculture is the current mainstream modern agricultural production method. This technology is to carry out agricultural production activities, such as agricultural greenhouse production, in an artificially constructed facility environment. Facility agriculture is a labour-intensive industry. If a high level of equipment and technical automation cannot be achieved, the production efficiency of this method will be greatly limited. Agricultural vehicles are important cooperative operation equipment in facility agriculture. Improving the intelligent control technology of agricultural vehicles can effectively improve agricultural production's efficiency. Electromagnetic navigation is currently the main method of agricultural vehicle navigation, but the stability of electromagnetic sensors is poor, and it is susceptible to electromagnetic interference from other equipment. Path tracking is currently an important research direction in the navigation control of agricultural vehicles, but in facility agriculture, traditional control technology is greatly affected by the environment, and the navigation effect is unstable. This study uses intelligent algorithms to improve traditional control techniques in order to improve the stability and accuracy of agricultural vehicle navigation.

This study proposed the use of fuzzy PID control algorithm to improve the navigation performance of agricultural vehicles. This algorithm contains two aspects, namely fuzzy logic and PID control. PID control is a classic industrial control method, but this method has poor control performance for nonlinear and uncertain objects. Fuzzy control is the use of fuzzy rules for fuzzy reasoning, and the online setting of control parameters is achieved through the fuzzy control rule table. Combining fuzzy control with PID control can make up for the limitations of PID control technology.

For the optimization of the navigation technology of agricultural work vehicles, there are two innovations in this study. One is to use the weighted fusion algorithm to process the sensor distance value. This method assigns weights to the ranging information of different sensors to ensure full monitoring of the operating environment information. The second is to use fuzzy controller to improve the PID control technology. The fuzzy controller adjusts the PID control parameters and improves the accuracy of the control algorithm.

This research is mainly carried out from four parts. The first part analyses the relevant literature at home and abroad, and expounds the research status from the three perspectives of automated agriculture, PID control technology and fuzzy logic. The second part designs the navigation control algorithm of agricultural vehicles from two aspects: distance weighted fusion algorithm and fuzzy PID control technology. In the third part, the control algorithm designed above is used for field test application, and the performance of the fuzzy PID path tracking control algorithm is analysed according to the test results. Finally, the fourth part summarizes the method and results of this research, and reflects and explains the shortcomings of the research process.

Paul M. studied the relationship between sustainable agriculture and a fair economy in the United States, proposed the reconstruction of food sheds to create sustainable and safe local food systems, and discussed the feasibility of rebuilding food sheds from the perspective of mass participation (Paul M. and Philip A. L., 2016). According to the current situation of agricultural automation in India, Patel. A et al. proposed adaptive intelligent systems for the development of agriculture based on the complexity and nonlinear characteristics of biological systems, and analysed the role of various intelligent technologies in the transformation of agricultural technology (Patel A, Kadam P., 2016). Li J. applied intelligent robot technology to the cycle management of agriculture, and proposed key technologies such as robot vision modelling, pattern recognition, and human-computer interaction decision (Li J., Wei X. and Zhang G., 2017). Ishii K. and others discussed the application status and application prospects of robot technology in the primary industry, and gave a detailed introduction to the current research on advanced robot technology in order to improve the production and management efficiency of agriculture, forestry, fishery and the primary industry. (Ishii K., Hayashi E., Misron N.B., 2018)

Hamidi K E and others designed an adaptive control strategy. By combining PID fuzzy logic and particle swarm optimization algorithm, the stability and trajectory tracking problems of the aircraft system were solved, and the control was proved by robustness (Hamidi K. E. et al., 2019). Maurya S et al. proposed a neutral fuzzy PID controller and analysed the position tracking control performance of the neutral fuzzy PID controller through simulation experiments, proving that this method has better robustness (Maurya S., Jain V. K., 2016). Yan H. and others designed a processing system based on fuzzy logic and PID control, and analysed its processing performance in a single-axis solar tracking system.

The results show that this system can effectively reduce the influence of uncertain factors on system control (Yan H., Deng S. and Chan M., 2016). Peng L. et al. proposed a fuzzy PID control strategy based on variable domain in view of the characteristics of large inertia and large lag in the main steam temperature control system of thermal power plants, and proved the effectiveness and superiority of this strategy through simulation experiments. (Peng L, Zheng S. and Chai X., 2018).

Sabir M.M. and others designed an optimal PID controller and used a swarm intelligence algorithm to optimize the PID controller. The research shows that the Cuckoo search algorithm has the best optimization effect on the controller (Sabir M. M. and Ali. T., 2016). Kurniasih D. et al. used fuzzy logic method to study the potential development direction of the village of Bullejo based on the indicators of agricultural potential, large cattle farms, small livestock and poultry farms, and proved that this method is used to calculate the potential development direction of the village. (Kurniasih D, Jasmi K. A. and Basiron B., 2018). Morais P. has a good application effect (Morais P., Alberto Marchi, 2017). Yan H. et al. proposed an automatic control method for farmland irrigation based on sensor network technology, and used fuzzy logic technology to select the best cluster head to achieve the lowest energy consumption of sensor nodes. Research shows that this control strategy effectively extends the entire longevity of the network (Yan H., Xia Y. and Deng S., 2017). Rodriguez E. et al. used fuzzy logic to establish an agricultural soil dynamic quality index, and proved the response performance of the index by verification experiments (Rodriguez E., Peche R. and Garbisu C., 2016).

In summary, intelligent technology and robot technology have a huge impact on the sustainable development of agriculture; PID control technology has a lot of research and application in path tracking; the advantage of fuzzy logic lies in handling uncertainty, inaccuracy and Subjective question. Here, fuzzy PID control technology is applied to the operation of vehicle robots in agricultural greenhouses, in order to achieve intelligent control of vehicle robots in path tracking.

## MATERIALS AND METHODS

### Design of weighted fusion algorithm for target distance information processing

Agricultural greenhouses have a complex and changeable open production environment, so it is difficult to obtain complex environmental information with only a single sensor. (Na Y, Qing W and Shicao C., 2020) Due to the difference in working principle and equipment performance, the measurement range and accuracy of different sensors are different. Ultrasonic technology and infrared technology are currently commonly used sensor technology for agricultural greenhouses. Ultrasonic sensors have better measurement accuracy, but their measurement efficiency is lower, and multiple sets of measurements will reduce the real-time detection of equipment. Although the infrared sensor has a slightly lower measurement accuracy, it has a digital-to-analogue conversion function, which can ensure the real-time and efficiency of the device detection (LingXin B, ChengKun C, GuangRui H, Adilet S and Jun C., 2020). With the development of intelligent technology, multi-sensor fusion algorithms fuse the measurement information of different sensors to make up for the shortcomings of a single sensor (Yibo L., Hang L and Xiaonan G., 2020). The core idea of this technology is to use the measurement information of different sensors in accordance with the established time sequence and rules, so as to realize the comprehensive detection of environmental characteristic information. The current sensor information fusion technology mainly includes weighted average method, artificial neural network method, Bayesian estimation, etc. This research will use weighted fusion algorithm to process the sensor measurement information of infrared technology and ultrasonic technology.

$X_u$ ,  $X_r$  represents the ultrasonic and infrared sensor measurement values;  $X$  represents the true value;  $e$  represents the random detection error, and  $e_i \sim N(0, \sigma_i^2)$ . Then there is the following relationship.

$$\begin{cases} X_u = X + e_u \\ X_r = X + e_r \end{cases} \quad (1)$$

Based on the measured values and adaptive methods of the two sensors, the weights of the two sensors can be calculated. Combining weights and measurement values, the optimal value of the fusion detection system can be obtained. It is assumed that the optimal value is an unbiased estimate of the true value, and it has a linear relationship with the measured value. Let  $X$  represent the optimal value, and its function expression is as follows, where  $W$  is the weight of the corresponding sensor.

$$\hat{X} = W_u X_u + W_r X_r \tag{2}$$

The difference between the true value and the optimal value represents the estimated error value of the sensor, then the total mean square error  $E[X^2]$  of the ranging module is shown below.

$$E[\tilde{X}^2] = E\left[(X - \hat{X})^2\right] \tag{3}$$

The optimal value  $X$  is an unbiased estimate of the true value  $X$ , and  $W_u + W_r = 1$  Combining equations (1), (2), and (3), the following relational expression can be calculated.

$$E[\tilde{X}^2] = W_u^2 e_u^2 + W_r^2 e_r^2 \tag{4}$$

According to the theory of seeking extremum of multivariate function, under the condition that the total mean square error  $E[X^2]$  is the smallest, the function expression of the weighting weights of the two sensors is shown in formula (5). By combining formula (2) and formula (5), the optimal value  $X$  after weighted fusion can be obtained.

$$\begin{cases} W_u = \sigma_u^2 \left( \frac{1}{\sigma_u^2} + \frac{1}{\sigma_r^2} \right)^{-1} \\ W_r = \sigma_r^2 \left( \frac{1}{\sigma_u^2} + \frac{1}{\sigma_r^2} \right)^{-1} \end{cases} \tag{5}$$

**Design of vehicle robot control system based on fuzzy PID**

The vehicle operating state is easily affected by the vehicle's own structural characteristics and external road conditions, so the vehicle's operating system exhibits characteristics of nonlinearity and inaccuracy. PID control is also called proportional integral differential control. Because of its simple algorithm and good robust performance, it is widely used in industrial process control. In the vehicle operation control system, the traditional PID control technology mainly adjusts the movement state of the vehicle through the position, speed, and heading angle of the vehicle. However, in practical applications, this control strategy reflects some limitations, such as the difficulty of setting control parameters and the lack of flexibility in control. Considering the complexity of the ground environment of agricultural greenhouses and the inaccuracy of environmental information, fuzzy control technology is used here to set the PID control parameters online, thereby improving the stability and control accuracy of the traditional PID control technology.

The core design of the fuzzy PID controller has three main parts, namely, determining the model structure, determining the membership function, and establishing the fuzzy control rule table. The key to determining the model structure of the fuzzy PID controller is to determine the structure of the fuzzy controller. The commonly used fuzzy controller is a dual-input single-output structure, but in this study, the three control parameters of the PID controller need to be jointly tuned, so the dual-input three-output model structure is selected here. After the input variables are fuzzified, the membership of the corresponding fuzzy subset will be obtained. Commonly used membership functions are triangle, trapezoidal, Gaussian and other types; the specific membership function selection needs to be considered in conjunction with practical problems. Fuzzy control rules are the basis for fuzzy inference and the core of fuzzy control algorithms. There are two forms of fuzzy rule control, one is a computer language form, such as "if...then..."; the other is a table form, the advantage of this form is that it is easy to read.

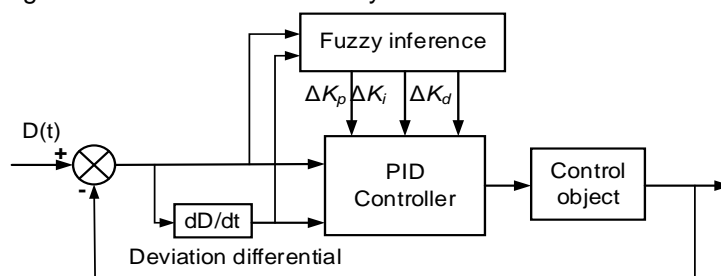


Fig. 1 - Structure diagram of fuzzy PID controller

Figure 1 shows the structure of the fuzzy PID controller. There are two important parameters in the running process of the vehicle. The lateral position deviation  $e$  refers to the deviation between the sensor centre and the preset path. The lateral deviation change rate  $e_c$  can be calculated from the lateral position deviation and the measured value. In the actual operation process, the greenhouse operation vehicle achieves the purpose of turning control by changing the speed of the left and right track wheels. The fuzzy PID controller uses a two-dimensional fuzzy controller before the traditional PID controller, so as to realize the online tuning of PID control parameters. The control method of fuzzy PID controller is incremental PID control. The characteristic of this method is to discretely sample the deviation to obtain discrete deviation data.

Under incremental PID control, the system only needs to calculate based on this and the previous two deviations, which greatly improves computational efficiency. The function expression of the incremental PID is as follows, where  $k$  represents the number of discrete samplings,  $k=1,2,\dots$ , and  $k_i = \frac{k_i T}{T_i}, k_d = \frac{k_d T}{T_d}$ ;  $T$  is the sampling period;  $e(k)$  represents the system deviation of the  $k^{th}$  order.

$$u = u(k) - u(k-1) = k_p(e(k) - e(k-1)) + k_i e(k) + k_d(e(k) - 2e(k-1)) + e(k-2) \tag{6}$$

The input of fuzzy PID controller is  $e_c, e$ , and the output parameter adjustment is  $\Delta K_p, \Delta K_i, \Delta K_d$ . When adjusting PID control parameters, three adjustment principles need to be followed. When the deviation value is a large value in the domain, in order to ensure the system response speed and avoid differential oversaturation, it is necessary to take a smaller value for  $K_p, K_d$ ; when the deviation value is an intermediate value, in the case of satisfying the system response speed, the value of  $K_p$  needs to be reduced; when the deviation value is a smaller value in the domain, in order to control the steady-state performance of the system, the value of  $K_p, K_i$  needs to be increased appropriately.

The greenhouse operation vehicle designed by this research is to use the magnetic navigation system to detect the degree of position deviation. There are 7 kinds of position deviation output, which are left large deviation ( $NB$ ), left centre deviation ( $NM$ ), left micro deviation ( $NS$ ), Zero offset ( $ZR$ ), right micro offset ( $PS$ ), right centre offset ( $PM$ ), right large offset ( $PB$ ). Therefore, the fuzzy definition of the position deviation can be defined as follows.

$$e = \{NB, NM, NS, ZR, PS, PM, PB\} \tag{7}$$

The deviation change rate is a measure of the change in the lateral position offset distance at different moments, so the function expression of the deviation change rate and the definition of fuzzy subset are as follows.

$$e_c = e_{i+1} - e_i \tag{8}$$

$$e_c = \{NB, NM, NS, ZR, PS, PM, PB\} \tag{9}$$

According to the correction range of the parameters, the change range of the position deviation and deviation change rate of the fuzzy PID control system is set, and the basic domain of the parameter adjustment amount  $\Delta K_p, \Delta K_i, \Delta K_d$  is  $[-0.3, 0.3], [-0.06, 0.06], [-3, 3]$  to define the fuzzy subset of each output. In this study, the description of fuzzy subsets will use a Gaussian membership function. The image of this function is shown in Figure 2. Among them, the abscissa represents the fuzzy universe, and the ordinate represents the degree of membership.

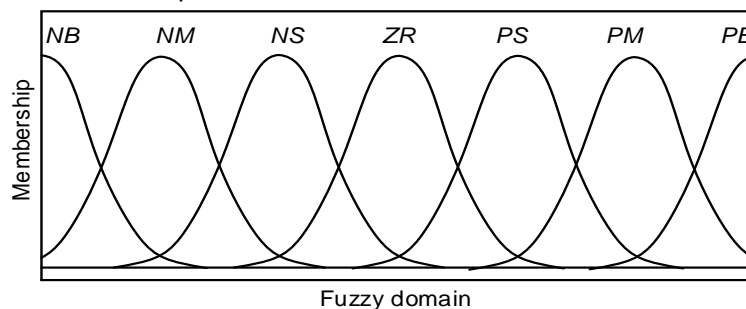


Fig. 2 - Gaussian membership function

Establishing a fuzzy control rule table is the key to fuzzy control. This process not only needs to consider the position deviation and deviation change rate, but also needs to comprehensively consider the role and correlation of the three parameter adjustments. Based on engineering design experience and vehicle operating conditions, this study established the fuzzy control rule table shown in Table 1 for the three output control parameter adjustments. Here, the fuzzy rule control table is described in computer language, and the general description form "if...then..." is used. Among them, the part of if describes the state of position deviation and deviation change rate, and the part of then describes the state of output in the control rule table. Therefore, under this method, 49 control rules can be obtained for each output control parameter adjustment.

**Table 1**

**Fuzzy control rules of  $\Delta K_p$**

Output	$EC$	$E$						
		$NB$	$NM$	$NS$	$ZR$	$PS$	$PM$	$PB$
$\Delta K_p$	$NB$	$PB$	$PB$	$PM$	$PM$	$PS$	$PS$	$ZR$
	$NM$	$PB$	$PB$	$PM$	$PM$	$PS$	$ZR$	$ZR$
	$NS$	$PM$	$PM$	$PM$	$PS$	$ZR$	$NS$	$NM$
	$ZR$	$PM$	$PS$	$PS$	$ZR$	$NS$	$NM$	$NM$
	$PS$	$PS$	$PS$	$ZR$	$NS$	$NS$	$NM$	$NM$
	$PM$	$ZR$	$ZR$	$NS$	$NM$	$NM$	$NM$	$NB$
	$PB$	$ZR$	$NS$	$NS$	$NM$	$NM$	$NB$	$NB$
$\Delta K_i$	$NB$	$NB$	$NB$	$NB$	$NM$	$NM$	$ZR$	$ZR$
	$NM$	$NB$	$NB$	$NM$	$NM$	$NS$	$ZR$	$ZR$
	$NS$	$NM$	$NM$	$NS$	$NS$	$ZR$	$PS$	$PS$
	$ZR$	$NM$	$NS$	$NS$	$ZR$	$PS$	$PS$	$PM$
	$PS$	$NS$	$NS$	$ZR$	$PS$	$PS$	$PM$	$PM$
	$PM$	$ZR$	$ZR$	$PS$	$PM$	$PM$	$PB$	$PB$
	$PB$	$ZR$	$ZR$	$PS$	$PM$	$PB$	$PB$	$PB$
$\Delta K_d$	$NB$	$PS$	$PS$	$ZR$	$ZR$	$ZR$	$PB$	$PB$
	$NM$	$NS$	$NS$	$NS$	$NS$	$ZR$	$NS$	$PM$
	$NS$	$NB$	$NB$	$NM$	$NS$	$ZR$	$PS$	$PM$
	$ZR$	$NB$	$NM$	$NM$	$NS$	$ZR$	$PS$	$PM$
	$PS$	$NB$	$NM$	$NS$	$NS$	$ZR$	$PS$	$PS$
	$PM$	$NM$	$NS$	$NS$	$NS$	$ZR$	$PS$	$PS$
	$PB$	$PS$	$ZR$	$ZR$	$ZR$	$ZR$	$PB$	$PB$

The process of solving the fuzzy control parameter adjustment according to the control rule table is to defuzzify. Defuzzifying not only needs to consider the prerequisites of approximate reasoning, but also needs to consider the inherent relationship between fuzzy rules. The output of defuzzification is a fuzzy set, which is generally segmented and irregular. In order to ensure the rationality of the output value, it is necessary to clarify the output fuzzy set and scale the processed value according to the scale factor. In this study, the weighted average method is used as the method of clarification, and the scale factor is calculated according to the physical range of the controlled object.

**RESULTS**

**Vehicle robot path tracking experiment based on distance information**

In order to verify the effectiveness of the target tracking control system for agricultural greenhouse work vehicles proposed in this research, here is a field test in the agricultural greenhouse with the crawler vehicle robot of Beijing Forestry University as the platform. Fig. 3 shows the shed operation of the tracked vehicle robot. The test is mainly divided into two parts, one is the path tracking test of the vehicle robot based on the ranging information, and the other is the fixed-point parking and linear tracking control test of the vehicle robot.



**Fig. 3 - Crawler-type greenhouse working vehicle robot**

The first part of the test is based on the sensor's ranging information, so here the ultrasonic sensor and infrared sensor's ranging information is first collected and weighted. The test equipment includes work vehicle, 1m precision steel tape measure, 1.2m × 0.45m foam board, and navigation magnetic stripe. Before the test starts, you need to select the preset route for vehicle operation and lay a navigation magnetic strip on the preset route. Place the foam board vertically on the preset route to calibrate the distance measured by the sensor.

**Table 2**

**Statistics of distance measurement after weighted fusion**

Statistics	Statistical results				
	100	90	80	70	60
Actual value	100	90	80	70	60
Weighted fusion value (cm)	100	89.9	79.8	70	59.8
Absolute error rate	0.00%	0.11%	0.25%	0.00%	0.33%
Actual value	50	40	30	25	20
Weighted fusion value (cm)	49.9	39.9	30	24.8	19.9
Absolute error rate	0.20%	0.25%	0.00%	0.80%	0.50%

During the test, it was found that between 10 and 20 cm, the measurement error of the ultrasonic sensor is relatively large, while the infrared sensor cannot measure. Between 20 and 100 cm, the absolute error of both sensors is relatively stable. Therefore, the experiment takes the distance measurement results between 20 and 100 cm as the effective information of weighted fusion. Table 2 shows the statistical results of the distance measurement information after weighted fusion. According to the statistical results in Table 2, it can be found that the absolute error rate of ranging between 30 and 100 cm is within 0.33%; the absolute error rate of ranging between 20 and 25 cm is controlled between 0.50% and 0.80%. Overall, the absolute error rate of the measured value after weighted fusion is less than 1%. Therefore, the ranging performance of the ranging sensor between 30 and 100 cm is relatively stable, and the weighted fusion algorithm has a better processing effect on the ranging information.

**Table 3**

**Statistical results of human-machine following test**

Statistics	Statistical results				
	200	190	180	170	160
Initial distance (cm)	200	190	180	170	160
Set following distance (cm)	100	100	100	100	100
Measured following distance (cm)	94	95	95	94	95
Initial distance (cm)	150	140	130	120	110
Set following distance (cm)	100	100	100	100	100
Measured following distance (cm)	94	93	95	96	93

In order to test the human-machine following ability of the vehicle robot, on the basis of the above test, the following distance of the vehicle robot is tested. Set the safe following distance to 100 cm and the vehicle speed to 1 m/s. Table 3 shows the statistical results of the man-machine following test. It can be seen from the statistical results in Table 3 that the error between the measured follow distance and the safe follow distance is between 4 and 7 cm, and the measured follow distance is slightly smaller than the safe follow distance. Combined with the vehicle operating state and the analysis of the results, it may be because of the inertia effect of the vehicle operation and the motor response characteristics, which causes the actual following distance of the vehicle robot to be slightly smaller than the safety distance. On the whole, under the fuzzy PID control system, the operating robot can basically meet the functional requirements of human-machine following and realizing the target tracking of the greenhouse operation.

**Vehicle robot's fixed-point docking performance and linear path tracking performance**

The vehicle robot mainly realizes the detection of the surrounding environment and the fixed-point cruising of the vehicle through the induction of the magnetic block around the magnetic navigation. The magnetic blocks of different magnetic poles are laid on the preset route and the guide path respectively, so that the vehicle robot travels at different speeds, and the parking distance of the vehicle at different speeds is tested.

**Table 4**

**Statistical results of vehicle robot parking distance at different speeds**

Speed (m/s)	1.0	0.8	0.7	0.6	0.5	0.4
Distance between vehicle and magnetic landmark (cm)	4.8	5.7	6.3	6.6	6.9	7.4
Distance error between vehicle and detection point (cm)	0.2	0.1	0.2	0.3	0.2	0.2

Table 4 shows the parking distance of vehicle robots at different speeds. Observing the statistical results in Table 4, it can be found that when the vehicle is traveling at a speed of 0.4 to 1.0 m/s, the distance error between the vehicle and the detection point does not exceed 0.3 cm. Therefore, the fixed-point parking performance of the vehicle robot can meet the parking needs.

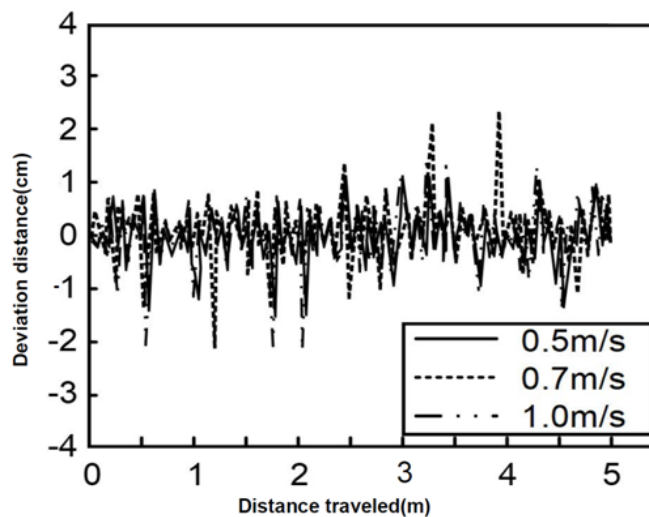


**Fig. 4 - Lateral deviation of vehicle running in straight line at different speeds**

Under the same test conditions, the linear path tracking performance of the vehicle robot is tested. In order to better record the running trajectory of the vehicle robot, an ink bottle is placed at the rear of the test vehicle, and the ink bottle is allowed to drip ink at a certain speed. Travel at 0.5 m/s, 0.7 m/s, 1.0 m/s to detect the position deviation of the vehicle in straight line tracking, and define the left deviation of the vehicle as positive and the right deviation as negative. Figure 4 shows the lateral deviation of the vehicle traveling straight at different speeds.

Observing Fig. 5, it can be found that the maximum lateral position deviation during the straight-line driving of the vehicle is  $\pm 2.5$  cm, which indicates that the straight-line path tracking stability of the vehicle is good.

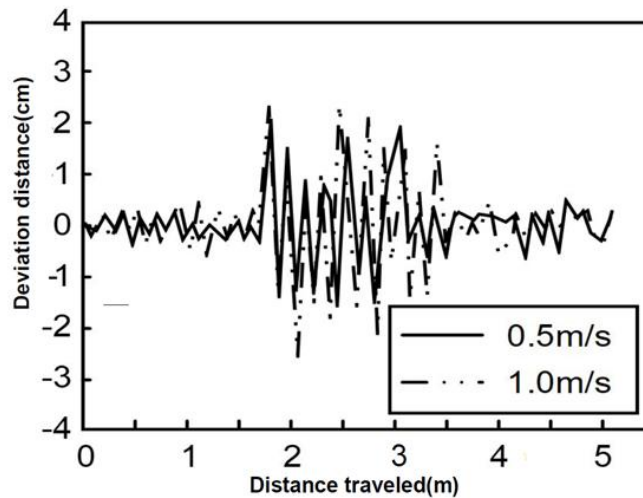


Fig. 5 - Lateral deviation of vehicle circle curve line running at different speeds

With reference to the experimental design of the linear path tracking performance, the circular curve path tracking performance of the vehicle is tested. Drive at a speed of 0.2 m/s and 0.3 m/s, and measure the lateral position deviation of the vehicle on a preset circular curve path. Figure 4 shows the results of the lateral deviation of the vehicle traveling on a circular curve at different speeds. Observing Figure 5, we can find that when the vehicle travel speed is 0.2 m/s, the lateral deviation of the circular curve path tracking is  $\pm 2.3$  cm; when the vehicle travel speed is 0.3 m/s, the lateral deviation of the circular curve path tracking is  $\pm 2.9$  cm; overall, the lateral deviation of the work vehicle is controlled within  $\pm 3$  cm, and the steering effect of the vehicle is better. Therefore, the vehicle's circular curve path tracking performance is good, which can meet the needs of agricultural greenhouse operations.

## CONCLUSIONS

The environmental information of agricultural greenhouses is uncertain and variable, so in the application of automation technology in agricultural greenhouses, traditional control strategies reflect poor control accuracy and efficiency. In view of the limitations of traditional PID control technology, this study proposed a fuzzy PID path tracking algorithm.

This algorithm uses a fuzzy controller to adjust the PID control parameters to improve the control accuracy and flexibility of the control system. Based on the crawler vehicle robot system of Beijing Forestry University as a platform, the fuzzy PID path tracking algorithm is tested.

The research results show that under the weighted fusion algorithm, the ranging error rate of the vehicle robot is less than 1%; in the man-machine follow-up test, the measured distance is slightly less than the safety distance, and the following error is up to 7 cm; in the fixed-point parking performance test of the vehicle, the maximum parking error is 0.3 cm; in the linear path tracking performance test, the lateral position deviation of the vehicle is  $\pm 3$  cm.

The fuzzy PID path tracking algorithm proposed in this research not only has good target tracking effect, but also reflects good linear driving and steering control performance. It is hoped that this research result can provide some data reference for path tracking research, and at the same time make a positive contribution to the development of agricultural intelligent technology. The research still has deficiencies, and in the future, the control algorithm will be further improved based on the actual operating environment of the agricultural greenhouse.

## ACKNOWLEDGEMENTS

This work was supported by the Anhui Province University excellent young talents support project (No. GXYQ2019119), Bozhou University scientific research (No. BYZ2018C05), the Key natural science projects of Anhui Province (No. KJ2018A0820)

## REFERENCES

- [1] Auat C.F., (2016), Intelligent Sampling Technique for Path Tracking Controllers. Control Systems Technology. *IEEE Transactions on Grid*, Vol.24, Issue 2, pp.747-755, USA;
- [2] Blake T., (2016), Agriculture: Robotics and automation. *Professional engineering*, Vol. 29, Issue 2, pp.54-56, England;
- [3] Hamidi K.E., Mjahed M., Abdeljalil E.K., (2019), Neural Network and Fuzzy-logic-based Self-tuning PID Control for Quadcopter Path Tracking. *Studies in Informatics and Control*, Vol.28, Issue 4, pp.401-412, Romania;
- [4] Ishii K., Hayashi E., Misron N. B., (2018), Special Issue on Advanced Robotics in Agriculture, Forestry and Fisheries. *Journal of Robotics & Mechatronics*, Vol.30, Issue 2, pp.163-164, Japan;
- [5] Kurniasih D., Jasmi K. A, Basiron B., (2018), The uses of fuzzy logic method for finding agriculture and livestock value of potential village. *International Journal of Engineering and Technology*, Vol.7, Issue 3, pp.1091-1095, Italy;
- [6] Li J, Wei X, Zhang G., (2017), An Extended Kalman Filter-Based Attitude Tracking Algorithm for Star Sensors. *Sensors*, Vol.17, Issue 8, pp.1921, Switzerland;
- [7] Maurya S, Jain V K., (2016), Fuzzy based energy efficient sensor network protocol for precision agriculture. *Computers and Electronics in Agriculture*, Issue 130, pp.20-37, England;
- [8] Morais P, Alberto Marchi., (2017), Cardiovascular magnetic resonance myocardial feature tracking using a non-rigid, elastic image registration algorithm: assessment of variability in a real-life clinical setting. *Journal of Cardiovascular Magnetic Resonance*, Vol.19, Issue 1, pp. 24, USA;
- [9] Patel A, Kadam P., (2016), An Ample Study of Numerous Intelligent Systems used for Agriculture: Review. *International Journal of Computer Applications*, Vol.143, Issue. 1, pp.20-24, USA;
- [10] Paul M, Philip A. L., (2016), Rebuilding the foodshed: how to create local, sustainable, and secure food systems. *Agriculture & Human Values*, Vol.33, Issue 4, pp.1011-1012, Netherlands;
- [11] Peng L, Zheng S, Chai X., (2018), A novel tangent error maximum power point tracking algorithm for photovoltaic system under fast multi-changing solar irradiances. *Applied Energy*, Vol.210, pp.303-316, England;
- [12] Rodriguez E, Peche R, Garbisu C., (2016), Dynamic Quality Index for agricultural soils based on fuzzy logic. *Ecological indicators*, Issue 60, pp.678-692, Netherlands;
- [13] Sabir M. M, Ali. T., (2016), Optimal PID controller design through swarm intelligence algorithms for sun tracking system. *Applied Mathematics & Computation*, Issue 274, pp.690-699, USA;
- [14] Yan H, Deng S, Chan M., (2016), A novel capacity controller for a three-evaporator air conditioning (TEAC) system for improved indoor humidity control. *Applied Thermal Engineering*, Vol.98, pp.1251-1262, England;
- [15] Yan H, Xia Y, Deng S., (2017), Simulation study on a three-evaporator air conditioning system for simultaneous indoor air temperature and humidity control. *Applied Energy*, Vol.207, Issue 1, pp.294-304, England;
- [16] Na Y, Qing W, Shicao C., (2020), Road recognition technology of agricultural navigation robot based on road edge movement obstacle detection algorithm. *INMATEH-Agricultural Engineering*, Vol.61, Issue 2, pp. 281-292, Romania;
- [17] LingXin B, ChengKun C, GuangRui H, Adilet S, Jun C., (2020), Technological development of robotic apple harvesters: a review. *INMATEH-Agricultural Engineering*, Vol.61, Issue 2, pp. 151-164, Romania;
- [18] Yibo L., Hang L., Xiaonan G., (2020), Online parameter identification of rice transplanter model based on IPSO-EKF algorithm. *INMATEH-Agricultural Engineering*, Vol.61, Issue 2, pp. 25-34, Romania.

# RECOGNITION TECHNOLOGY OF AGRICULTURAL PICKING ROBOT BASED ON IMAGE DETECTION TECHNOLOGY

## 基于图像检测技术的农业采摘机器人识别技术

Yujie Jin<sup>1</sup>

School of Information Science and Engineering, Changsha Normal University, Changsha, Hunan, 410199 / China

\*Tel: 13006254198; E-mail: uggzqp@163.com

DOI: <https://doi.org/10.35633/inmateh-62-20>

**Keywords:** visual servo, PID control, image, picking, robot

### ABSTRACT

As a kind of intelligent agricultural equipment, picking robots are of great significance for improving the efficiency of agricultural production. However, the main bottleneck restricting the development of picking robots today is the positioning and control in image recognition. Therefore, an agricultural picking control method based on visual servo technology is proposed. This method can accurately control the picking hand of the picking robot on the basis of building an eye-hand relationship model and an online identification system. With the tomato picking process as the background, the effectiveness of the method was verified. The test results of image feature points show that there is a small error between the stable feature points and the expected image feature points. In addition, the image plane trajectory of the picking robot is relatively smooth, and there is no vibration or overshoot. In addition, from its density distribution characteristics, it can be seen that the picking hand movement is a continuous acceleration stage at the beginning of the control, and at the end of the control, the characteristic points gradually tend to the desired characteristics, and the output of the control system is relatively stable. It can be seen from this that the model has better control performance. This method has certain practical significance for the improvement of agricultural picking efficiency.

### 摘要

采摘机器人作为一种智能农业设备，对提高农业生产效率具有重要意义。然而，目前制约采摘机器人发展的主要瓶颈是图像识别中的定位与控制。为此，提出了一种基于视觉伺服技术的农业采摘控制方法。该方法在建立眼-手关系模型和在线辨识系统的基础上，能够准确地控制采摘机器人的拣手。以番茄采摘过程为背景，验证了该方法的有效性。图像特征点测试结果表明，采摘机器人的稳定特征点与期望的图像特征点之间仅存在误差。另外，拾取机器人的像面轨迹比较平滑，没有振动和过冲现象。另外，从其密度分布特征可以看出，采摘手的运动在控制开始时是一个连续的加速阶段，在控制结束时，特征点逐渐趋向于期望的特性，控制系统的输出相对稳定。由此可见，该模型具有较好的控制性能。该方法对提高农业采摘效率具有一定的现实意义。

### INTRODUCTION

Agriculture industry is an important guarantee for food security in all countries in the world. Agricultural robots are widely used in agricultural production to improve the ability of agricultural robots to sense their work and precise control, which can not only improve agricultural modernization level, but also improve international status in agricultural production and technology exchange. Among them, the fruit and vegetable picking robot, as a key field of agricultural science and technology research, is of great significance to agricultural modernization. However, today's fruit and vegetable picking robots usually have poor picking results due to positioning errors and motion errors (Bao, Cai and Qi, 2016). In order to overcome the problem of low control accuracy of fruit and vegetable picking operations in complex environments, the article explores the control error of fruit and vegetable picking robots, and proposes a micro-control method of fruit and vegetable picking robots based on visual servo technology to effectively improve agricultural picking efficiency.

The micro-control of the picking robot achieves precise positioning in a small space by installing a monocular camera on the robot arm to adjust the image error (Bargoti et al, 2017). Its core lies in setting the control purpose of the robot, so as to automatically obtain image information and analyse it, and output the feedback information of the machine control in a short time to achieve a good effect on the control of the robot trajectory (Mehta et al, 2016).

<sup>1</sup> Yujie Jin, As. PhD. Eng.

According to the observable features on the plane and the texture target plane, a suitable control law is derived, and the estimated factors of unknown constant force disturbance are introduced into the control law, and then the effectiveness of the controller is proved through experiments. (Wang S. et al., 2018). In order to study the visual servo control of space-based space robots, Dong G. and his colleagues conducted an in-depth discussion on non-cooperative target pose and motion estimation algorithms. Finally, experiments prove the applicability of the control scheme (Dong et al., 2015). In order to effectively solve the problem of visual servo control for robots without degrees of freedom, the Tsai C.Y. research team proposed a new hybrid switched reactive visual servo control structure, which is derived from perception and reaction behaviour and does not require inverse interaction matrix calculations (Tsai et al., 2015). This control structure helps to simplify the realization process of the visual servo system and improve the control efficiency (Serra et al., 2016). Szymon Krupinski et al. proposed a visual servo control method for underwater robots based on non-linear inertial auxiliary images. This method uses the homomorphic matrix between two images of a plane scene as feedback information to control the system in a cascaded manner in the control design. The development of dynamics is more robust to the uncertainty and perturbation of the model than the traditional solution that only considers the traditional solution of system kinematics. (Szymon Krupinski et al., 2017). The research team of Silveira G discussed the problem of vision-based robot control and proposed a new strength-based non-metric visual servo technology. This technology does not consider the target characteristics of the observation object, the displacement of the camera and the relative attitude, and can achieve the dynamic decoupling of the translation control error. Finally, through corresponding experiments, the effectiveness of the technology is proved. (Silveira et al., 2020).

Combined with experiments to verify the effector, the results show that the effector has great potential in promoting kiwifruit harvest. The research team outlined the research and development activities of agricultural robots in recent years, and discussed some specific issues related to the precise control of weeds and fertilizer applications by robots. (Wang J, Zhou G and Wei X., 2019). With the development of picking robots, Tao Y and his colleagues proposed an apple automatic recognition method based on point cloud data in order to improve the robot's recognition ability and perception ability in three-dimensional space. (Tao Y., Zhou J., 2017). The research team introduced an intelligent machine that helps farmers pick lemons. The machine is a mechanical arm that can cut lemons from trees. This machine can help farmers complete their work effortlessly, greatly reducing labour (Yan H.J., Bai G. and He J.Q., 2010). In order to manage the precise application of fertilization and water in agriculture, Zavala-Yoe R et al. constructed an agricultural intelligent production model. The original model is equipped with a laser sensor, which can measure the content of water, fertilizer or any other nutrients in the crops. This is of great significance for improving the level of agricultural modernization. (Zavala-Yoe R. et al., 2017).

## MATERIALS AND METHODS

### Eye-hand relationship model building

The essence of robot visual servoing is the problem of nonlinear system control, which is generally described by the eye-hand relationship model. (Qingqing S., Bin W., Jiawei Y., Yizhi L. and Tongming Y., 2020) Therefore, the first task of constructing an agricultural picking robot model based on visual servo technology should be to establish an eye-hand relationship model, and then use an online identification system to set its real-time status, and finally establish a control strategy design plan, so the agricultural based on visual servo technology is obtained. (Changbin H, Yong Y, Decheng W, Hongjian W. and Bingnan Y., 2020). According to the positional relationship between the camera and the mechanical structure, the eye-hand configuration of the agricultural picking robot can be divided into an eye-on-hand configuration and an eye-fixed configuration. The two configurations are shown in fig.1.

The eye-fixed configuration refers to fixing the camera on a certain working scene of the agricultural picking system to ensure that the entire picking process is captured and it is convenient to integrate the image information into the visual control system. The image obtained by the eye-fixed configuration is clearer and the image resolution is higher. (Min J, Chunguang W, and Pengpeng W., 2020) The eye-on-hand configuration refers to fixing the camera on the moving arm of the agricultural picking robot so that the camera and the moving arm are synchronized. The main advantage is that the posture of the robot arm can be flexibly adjusted to minimize the distance between the camera and the target object, so as to ensure the accuracy of picking the target, and at the same time improve the image observation accuracy. Because the eye-on-hand configuration is more conducive to the precise positioning of the target picking object, this time the eye-on-

hand configuration is mainly used. In the process of building the relationship model, the most important thing is to define the coordinate relationship.

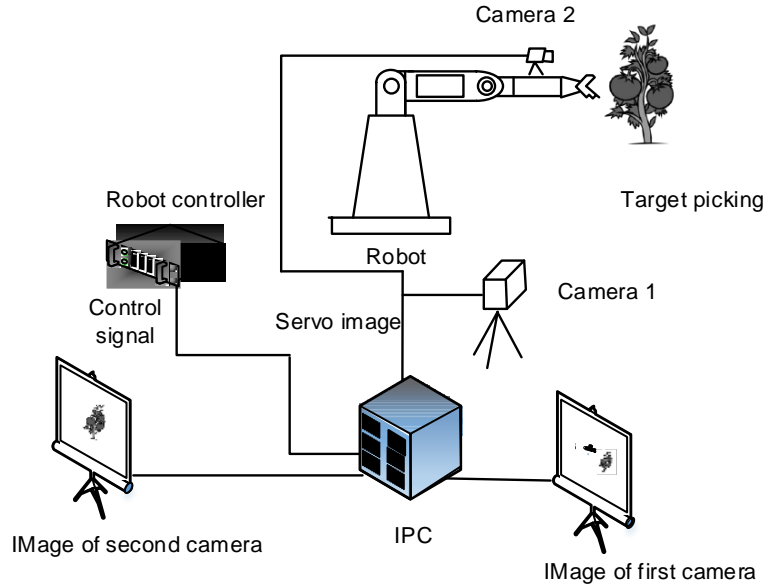


Fig. 1 – Eye-hand configuration of agricultural harvesting robot

This study uses the relationship structure shown in Figure 2 as the determination rule.

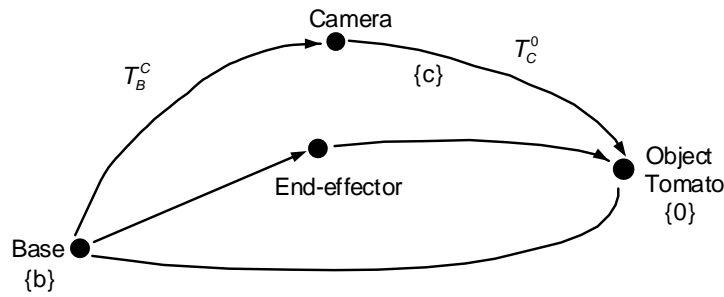


Fig. 2 – Eye-on-hand configuration coordinate diagram

Taking the plane centre of gravity of the target pick as the target  ${}^b p_a = [{}^b p_x, {}^b p_y, {}^b p_z]^T$ , and the spatial coordinate of the target pick under the camera coordinate system  $\{C\}$  is  ${}^c p_a = [{}^c p_x, {}^c p_y, {}^c p_z]^T$ ,  ${}^c P_z$  represents the depth information of the target pick, and the optical axis of the camera is integrated with the  $Z_c$  axis. In addition, the unit distance pixels in each direction on the image plane  $\{i\}$  are assumed, respectively denoted by  $N_x, N_y$ , the plane coordinates of the centre of the image plane are represented by  $(u_0, v_0)$ , and the pixel coordinates of the target plane after image processing are represented by  $f = [u, v]^T$ , which is obtained by formula (1) The projected coordinate of the target image is  ${}^i p = [x, y]^T$ , and the formula (1) is shown below.

$$\begin{cases} x = (u - u_0) / N_x \\ y = (v - v_0) / N_y \end{cases} \quad (1)$$

The plane coordinates of the target picking object obtained by the projection principle and the projection coordinates are converted according to the corresponding calculation model. The conversion principle is as follows.

$$\begin{cases} x = \lambda \cdot \frac{{}^c p_x}{{}^c p_z} \\ y = \lambda \cdot \frac{{}^c p_y}{{}^c p_z} \end{cases} \quad (2)$$

$\lambda$  in the above formula represents the focal length of the camera. Differentiating the formula (2) gives the results shown below.

$$\begin{cases} \dot{x} = -\lambda \cdot \frac{{}^c \dot{p}_x \cdot {}^c p_z - {}^c p_x \cdot {}^c \dot{p}_z}{({}^c p_z)^2} \\ \dot{y} = -\lambda \cdot \frac{{}^c \dot{p}_y \cdot {}^c p_z - {}^c p_y \cdot {}^c \dot{p}_z}{({}^c p_z)^2} \end{cases} \quad (3)$$

The above formula is written in matrix form, and the result is shown in formula (3). Formula (3) shows that there is a nonlinear relationship between the transformation of the plane coordinate position of the target picking and the transformation of the spatial coordinate position.

$$\begin{bmatrix} \dot{x} \\ \dot{y} \end{bmatrix} = \lambda \begin{bmatrix} \frac{1}{{}^c p_z} & 0 & -\frac{{}^c p_x}{{}^c p_z^2} \\ 0 & \frac{1}{{}^c p_z} & -\frac{{}^c p_y}{{}^c p_z^2} \end{bmatrix} \quad (4)$$

For the principle of coordinate conversion in each coordinate system, see formula (5).  ${}^c P_a$  in formula (5) represents the position vector of the origin of the camera coordinate system, and  ${}^c_b R$  represents the relative position of the two coordinate systems.

$${}^c P_a = {}^c_b R \cdot ({}^b p_a - {}^b p_c) \quad (5)$$

Differentiating formula (5) yields the results shown below.

$${}^c \dot{p}_a = {}^c_b \dot{R} \cdot ({}^b p_a - {}^b p_c) + {}^c_b R \cdot ({}^b \dot{p}_a - {}^b \dot{p}_c) \quad (6)$$

${}^b P_a$  in the above formula represents the coordinate translation speed of the target picking relative to the agricultural picking robot, and  ${}^b P_c$  represents the coordinate translation speed of the camera relative to the agricultural picking robot. Because the target picking is usually at rest, it is assumed that the translation speed is 0, that is,  ${}^b P_a = 0$ , and the formula (6) is rewritten using the relevant calculation model. The results are as follows.

$${}^c \dot{p}_a = {}^c_b \dot{R} \cdot ({}^b p_a - {}^b p_c) - {}^c_b R \cdot \dot{p}_c \quad (7)$$

The camera follows the robot arm to make a rotary motion  ${}^c \Omega = ({}^c w_x, {}^c w_y, {}^c w_z)$  and a translation motion  ${}^c T = ({}^c T_x, {}^c T_y, {}^c T_z)$ , and the calculation results shown below are obtained.

$${}^c \dot{p}_a = \begin{bmatrix} {}^c \dot{p}_x \\ {}^c \dot{p}_y \\ {}^c \dot{p}_z \end{bmatrix} = \begin{bmatrix} -1 & 0 & 0 & 0 & -{}^c p_z & {}^c p_y \\ 0 & -1 & 0 & {}^c p_z & 0 & -{}^c p_x \\ 0 & 0 & -1 & -{}^c p_y & {}^c p_x & 0 \end{bmatrix} \begin{bmatrix} {}^c T_x \\ {}^c T_y \\ {}^c T_z \\ {}^c W_x \\ {}^c W_y \\ {}^c W_z \end{bmatrix} \quad (8)$$

The two formulas (4) and (8) are integrated, and the results are shown in formula (9). Formula (9) shows that there is a close correlation between the change in the image plane of the target picking and the change in camera position. That is, the image Jacobian matrix as shown in (10).

$$J_{image} = \begin{bmatrix} -\frac{\lambda}{{}^c p_z} & 0 & \frac{x}{{}^c p_z} & \frac{xy}{\lambda} & -\frac{\lambda^2 + x^2}{\lambda^2} & y \\ 0 & -\frac{\lambda}{{}^c p_z} & \frac{y}{{}^c p_z} & \frac{\lambda^2 + y^2}{\lambda} & -\frac{xy}{\lambda} & -x \end{bmatrix} \quad (9)$$

The above formula is the conventional analytical formula of the image Jacobian matrix. The image Jacobian matrix is closely related to the image plane position and the target picking depth. The monocular camera cannot accurately measure the depth of the target picks, so it is necessary to use the image Jacobian matrix to convert the plane information and the base coordinate information of the target picks to overcome the depth measurement difficulty.

### Online identification design

In the process of using visual servo technology for micro-control, if the estimated value of the image Jacobian matrix cannot be corrected online, then the performance of the image feedback system cannot be controlled. In severe cases, the visual system will cause a greater degree of Shock. Existing image Jacobian matrix estimation methods usually introduce tentative motion, which will affect the operation of the visual servo system. In addition, there is a lot of noise interference in the image information processing link, and the identification algorithm should be able to have high robustness to effectively deal with the image processing link noise and avoid the degradation of matrix estimation performance. The online identification algorithm should not be too cumbersome, and the processing time should be reduced as much as possible. So as to effectively improve the response efficiency of the system. Based on the above analysis, this study uses Kalman filter to complete the online identification of the image Jacobian matrix. The founder of Kalman filter estimation method is Kalman. He proposed the algorithm in 1960. The core idea is to estimate the minimum state value of error variance. The spatial model of the linear discrete system of Kalman filter is shown below.

$$\begin{cases} x(k) = Ax(k) + \eta(k) \\ z(k) = Cx(k) + v(k) \end{cases} \quad (10)$$

There are  $Z \in R^m$ ,  $X \in R^n$  in the above formula, and these two represent the state vector and output vector of the visual system, respectively,  $\eta$ ,  $v$  is the noise vector, and  $A$ ,  $C$  represents the state equation coefficient matrix. In order to improve the efficiency of the linear discrete system state assessment, the corresponding prerequisites need to be set.

$$\begin{aligned} E(\eta(k)) &= 0, \text{cov}\{\eta(k), \eta(j)\} = R_\eta \delta_{kj} \\ E(v(k)) &= 0, \text{cov}\{v(k), v(j)\} = R_v \delta_{kj} \\ \text{cov}\{\eta(k), v(j)\} &= R_{\eta v} = 0, \forall k, j \\ Z_k &= (z(1) \ z(2) \dots \ z(k)) \end{aligned} \quad (11)$$

The Kalman filter estimation method can be used to evaluate the state of the visual system by using relevant expressions (Formulas (12)-(15)).

$$Q(k+1) = AP(k) + R_\eta \quad (12)$$

$$K(k+1) = Q(k+1)C^T [CQ(k+1)C^T + R_v]^{-1} \quad (13)$$

$$P(k+1) = [I - K(k+1)C]Q(k+1) \quad (14)$$

$$\hat{x}(k+1) = A\hat{x}(k) + K(k+1)[z(k+1) - CA\hat{x}(k)] \quad (15)$$

Based on the image Jacobian matrix of the eye-on-hand relationship model, the relevant definitions in the application of agricultural picking machines are as follows, where  $q$  represents the robot's hand  $n$  order vector, and  $f$  represents the current picking robot through the visual sensor, then the feature vector of  $m$ -dimensional image is obtained.

$$\dot{f} = J(q) \cdot \dot{q} \quad (16)$$

The above formula is discretized, and the result is shown in the following formula.

$$f(k+1) = f(k) + J(q(k)) \cdot \Delta q(k) \quad (17)$$

The Kalman filter is used to complete the online identification of the Jacobian matrix of the image, that is, the process of accurately estimating all the elements in  $J(q(k))$ , and the  $m \times 1$ -dimensional observation vector shown below is constructed.

$$x = \left( \frac{\partial f_1}{\partial q} \ \frac{\partial f_2}{\partial q} \ \dots \ \frac{\partial f_m}{\partial q} \right)^T \quad (18)$$

The vector of the image Jacobian matrix  $J(q)$  in row  $i$  is represented by  $\frac{\partial f_i}{\partial q} = \left( \frac{\partial f_i}{\partial q_1} \ \frac{\partial f_i}{\partial q_2} \ \dots \ \frac{\partial f_i}{\partial q_n} \right)$  ( $i=1, 2, \dots, m$ ) in the above formula. The state value of the visual system is defined by the observation vector of the image Jacobian matrix. The movement of the robot arm will cause the system output to change with the change of the image characteristics. That is, there is a corresponding linear relationship  $y(k) = f(k+1) - f(k)$  between the two, and the state equation shown below is obtained.

$$\begin{cases} x(k+1) = x(k) + \eta(k) \\ y(k) = C(k) \cdot x(k) + v(k) \end{cases} \quad (19)$$

The state noise vector and the image observation noise are respectively represented by  $\eta(k)$ ,  $v(k)$  in the above formula, and  $C(k)$  represents the diagonal matrix. For the corresponding expression form, see the following formula.

$$C(k) = \begin{pmatrix} \Delta q(k)^T & \dots & 0 \\ \vdots & \ddots & \vdots \\ 0 & \dots & \Delta q(k)^T \end{pmatrix}_{m \times n} \quad (20)$$

According to the Kalman filter estimation principle shown in (12)-(15), a recursive estimation model of the image Jacobian matrix is established.

$$\begin{cases} Q(k+1) = P(k) + R_\eta \\ K(k+1) = Q(k+1) \times C^T(k) \cdot [C(k) \cdot Q(k+1) \cdot C^T(k) + R_v]^{-1} \\ P(k+1) = [I - K(k+1) \cdot C(k)] \cdot Q(k+1) \\ \hat{x}(k+1) = \hat{x}(k) + K(k+1) \cdot [y(k+1) - C(k) \cdot \hat{x}(k)] \end{cases} \quad (21)$$

In the above formula,  $R_n$ ,  $R_v$  represents the noise variance matrix, and  $P(K)$  represents the state estimation error variance matrix. The corresponding initial value can be set to  $P(o)$  and expressed by the unit matrix  $I_{m \times n}$ . The initial value of state estimation can be calculated by least square method. When the hand of the agricultural picking robot is located at the initial position, the estimated value of the Jacobian matrix of the image can be obtained by calculating the estimated value of the Jacobian matrix of the image according to the trial motion  $\Delta q_1, \Delta q_2$  and the observation model. (Eq.22).

$$\hat{J}(0) = (\Delta f_1 \ \Delta f_2) \cdot (\Delta q_1 \ \Delta q_2)^{-1} \quad (22)$$

In order to avoid the tentative motion behaviour of agricultural picking robots, before iterative calculation of the image Jacobian matrix, the depth value needs to be estimated according to the image plane size of the picking target. Because the image Jacobian matrix will be continuously updated by iteration, this is a process of continuous convergence of depth estimation until the required requirements are met.

**Visual servo control design**

According to the form of visual feedback signals, agricultural picking robots can be divided into position-based visual servos and image-based visual servos. The position-based visual servo can estimate the position of the target by judging the image information of the target. This kind of estimation error is small and has high applicability. Image-based visual servos can feedback control visual information by judging the characteristics of target images. There is no need to estimate the position of the target. In the case where the eye-on-hand configuration is selected, the image-based visual servo control system is shown in fig. 3, the control amount is calculated according to the image feature error, and the robot's motion space is adjusted using the relevant transformation model to promote the machine. The arm approaches the picking target. When the difference between the image feature and the actual feature is small, it can be considered that the agricultural picking robot has a high visual servo accuracy.

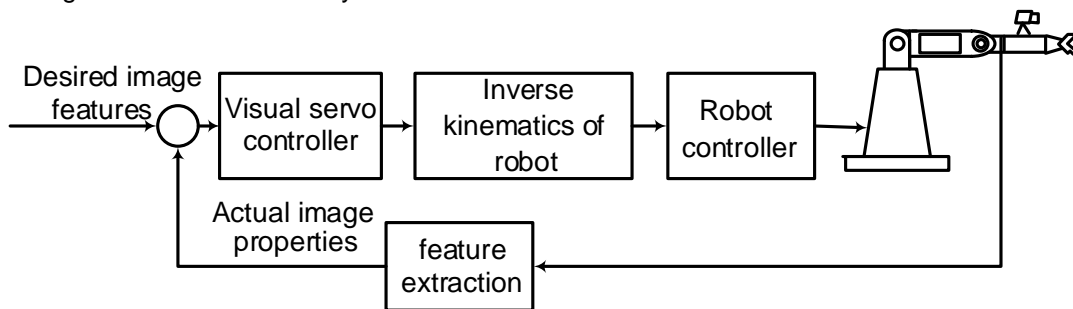


Fig. 3 - Visual servo control structure of agricultural picking robot based on image

According to the related performance of vision system of agricultural picking robot, PID control design is adopted to serve the controller vision. As the most typical controller design method, PID control is applied to the robot visual servo system with high frequency. This kind of control method can realize the arbitrary space representation of the error. The robot is controlled mainly through the Cartesian space instruction. The robot can build an appropriate PID controller based on the error information obtained by feedback. The construction model is shown below.

$$u(k) = K_p e(k) + K_I \sum_{i=1}^k e(k) + K_D (e(k) - e(k-1)) \tag{23}$$

In the above formula,  $U(k)$  represents the machine control input, while  $K_D, K_p, K_k$  represents the integral coefficient matrix, proportional and differential coefficient matrix, and  $e(k)$  represents the error display signal. In order to achieve the visual feedback effect of the eye-on-hand, the visual servo control must meet the requirement that the image features of the target picking material continue to approach the position of the image plane. Therefore, the image error  $e(t)$  is defined as a systematic error, and is handled by referring to the following formula.

$$e(t) = f^d - f(t) \tag{24}$$

$f^d$  in the above formula represents the image feature of the target picking, and there is  $f^d = (u_c, v_c)^T$ , which represents the position of the image plane. In addition, the control amount of the robot is defined, and the definition formula is as follows.

$$u(k) = \Delta q(k+1) = q(k+1) - q(k) \tag{25}$$

In order to ensure the micro-control effect, it is necessary to eliminate the system static error, and process the image processing noise. Using the PI control strategy, the visual servo control expression of the agricultural picking robot is obtained, see formula (14).

$$u(k+1) = J^{-1} \cdot \left( c_1 e(k) + c_2 \sum_{i=0}^k e(i) \right) \tag{26}$$

$C_1, C_2$  in the above formula respectively corresponds to the control ratio and integral processing coefficient of the PI controller. The visual servo control process of agricultural picking is shown in the following figure. The control process includes a total of six steps, which are the desired position of the target picking, visual servo control processing, the robot acquiring the target picking image, the visual servo system processing image, and the image Jacobian. The matrix estimates that these six steps cooperate with each other to complete the picking of agricultural products.

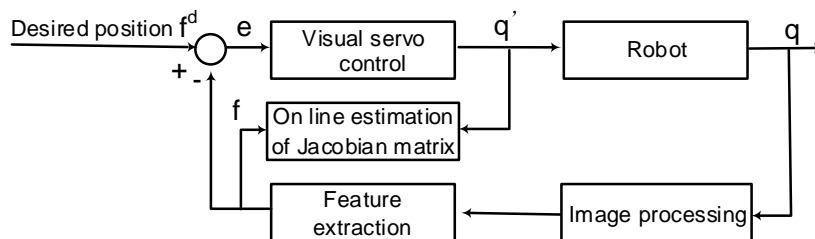


Fig. 4 - Visual servo control flow of agricultural picking robot image

**RESULTS**

**Experiment design and preparation**

In order to verify the effectiveness of the micro-control model of the agricultural picking robot constructed above, this experiment used tomatoes as the picking object. For the design of the experimental platform, see fig. 5. Before the experiment starts, the picking robot needs to be moved near the tomatoes to be picked. The right arm is set as an air suction picker to fix the target picking object. The waist coordinate system of the picking robot is set to the world coordinate system. The monocular camera is installed on the lower right side of the air-suction picking robot, and the two axes of the monocular camera coincide with the two axes of the cutting hand. The installation requirements of the monocular camera can ensure that the target picks appear in the image plane. The image plane of the monocular camera is set to 650×450 pixel, the feature point is set to the image centre of the target picking object, and it is recorded as  $p$ , and the corresponding image plane

coordinate is marked as  $(u, v)$ . The  $u$  axis is used as the main direction of movement of the shearing grip along the  $X$  axis, and the  $v$  axis is used as the main direction of movement of the shearing grip along the  $Z$  axis. These two axes respectively control the translation direction of the shearing grip. Due to the influence of the  $R$  type cutting hand's own attributes, the incision range of the target pick into the type  $R$  cutting hand cannot be accurately calculated, so it is necessary to use the teaching method to obtain the actual position of the target pick. It is generally believed that when the centre point of the target tomato is within the standard range  $(250, 270)$  or  $[190, 210]$ , the cutting position of the picker is more accurate.

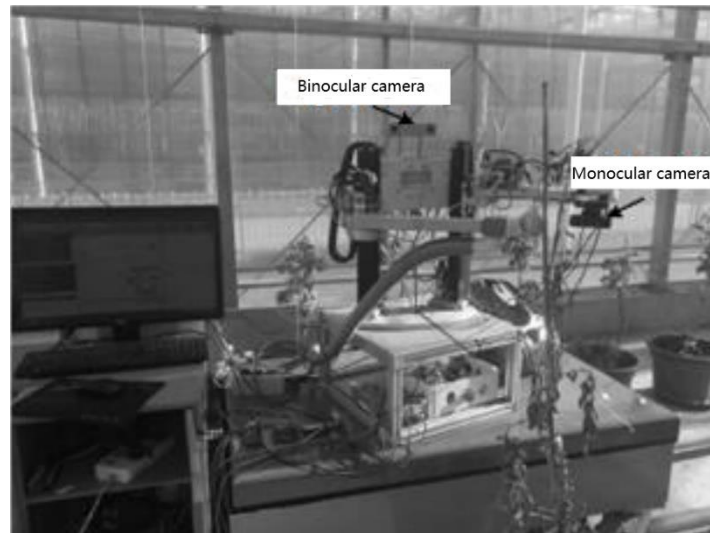


Fig. 5 - Visual servo test platform of agricultural harvesting robot

### Analysis of results

After completing the installation of the experimental instrument and parameter settings, the above model is officially applied, and the application results are shown in Figure 6. It can be seen from fig.6 that the initial feature plane coordinate of the target picking is  $(42, 148)$ , the final stable feature plane coordinate is  $(263, 198)$ , and the error from the expected image feature point is  $(3, -4)$ . It can be seen from this that the model has high accuracy for the image recognition of the picking target position.

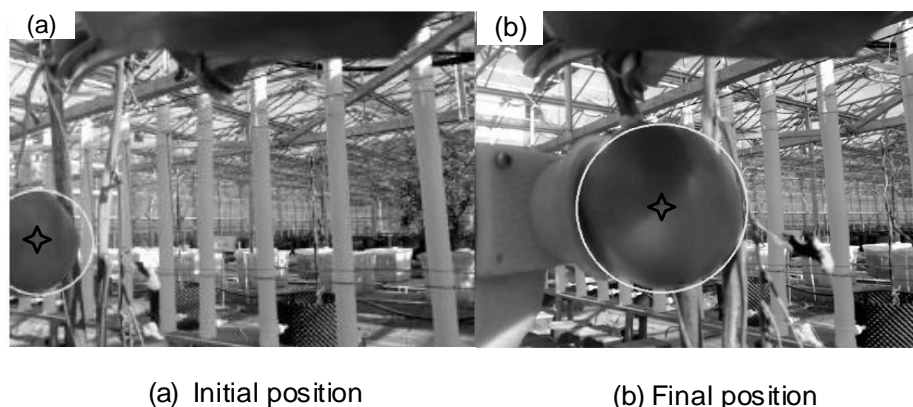


Fig. 6 - Image position comparison of target picking

In addition, the image characteristic deviation curve of the visual servo control system is obtained by the above method, as shown in fig. 7. It can be seen from fig. 7 that compared with the desired image feature points, the feature points at the final stable state are slightly lower, and there is a deviation of about 4 pixels between the two. Therefore, it can be considered that the visual servo micro-control model can meet the requirements of tomato picking.

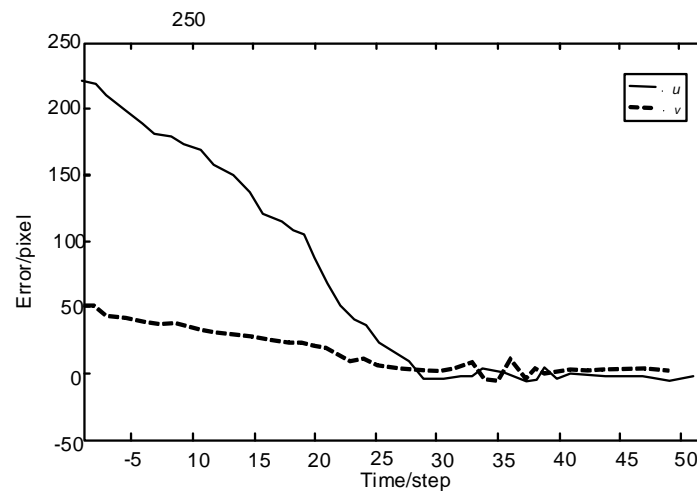


Fig. 7 - Image feature deviation curve

The movement path of the feature points of the target picking on the image plane can be seen in Fig. 8. It can be seen from fig. 8 that the movement trajectory of the image plane is relatively smooth and no significant vibrations and overshoots are found. It can be seen that the design of the visual servo micro-control model is more scientific and reasonable. When the feature point is close to the desired feature point, the speed of picking the hand gradually slows down, and the deceleration process will continue until the feature point enters the allowable control range. The movement path of the plane image of the feature point is more tortuous and is not the optimal route, but this is also the characteristic of visual servo control.

## CONCLUSIONS

In order to improve the efficiency of agricultural picking and solve the problems of positioning error and motion error during the picking process, this paper builds a micro-control model of agricultural picking robot based on visual servo technology. After the completion of the experimental platform construction and parameter settings, the validity of the model was verified. The experimental results show that the initial feature plane coordinates of the target picks are  $(42, 128)$ , and the final stable feature plane coordinates are  $(263, 198)$ . Compared with the expected image feature points, the error is only  $(3, -4)$ . In addition, according to the movement trajectory of the target picking object, the image plane movement trajectory of the picking robot generally looks smooth, without obvious vibration or overshoot, and it can be judged that the design of the visual servo micro-control model is reasonable. The characteristics of its density distribution indicate that the picking hand movement is higher in the initial stage of control and continues to increase. When the feature points gradually tend to the desired feature, the image error will decrease and the output of the control system will stabilize. In summary, the model can adapt to the complex environment of agricultural picking and effectively overcome binocular positioning errors and motion errors. Although this model can provide a method reference for the research of agricultural picking robot identification technology, there are still problems in the experiment that the simulation of picking times is small and the accuracy of the experiment is not high enough.

## ACKNOWLEDGEMENTS

This work was supported by the 2018 National Education Science Planning Project (No. DIA180393) 2019 Hunan Province Social Science Achievement Evaluation Committee Project (No. XSP19YBC221), 2018 Research Project of Teaching Reform in Hunan Universities (No.2018-926)

## REFERENCES

- [1] Bao G, Cai S, Qi L., (2016), Multi-template matching algorithm for cucumber recognition in natural environment. *Computers & Electronics in Agriculture*, Issue 127, pp.754-762, England;
- [2] Bargoti S, Underwood J P., (2017), Image Segmentation for Fruit Detection and Yield Estimation in Apple Orchards. *Journal of Field Robotics*, Vol.34, Issue 6, pp.1039-1060, USA;
- [3] Changbin H, Yong Y, Decheng W, Hongjian W, Bingnan Y., (2020), An experimental investigation of soil layer coupling failure characteristics on natural grassland by passive subsoiler- type openers. *INMATEH-Agricultural Engineering*, Vol.61, Issue 2, pp. 49-58, Romania;

- [4] Dong G, Zhu Z H., (2015), Position-based visual servo control of autonomous robotic manipulators. *Acta astronautica*, Issue 115, pp.291-302, England;
- [5] Mehta S, Burks T F., (2016), Adaptive Visual Servo Control of Robotic Harvesting Systems. *Ifac Papersonline*, Vol.49, Issue 16, pp.287-292, Netherlands;
- [6] Min J, Chunguang W, Pengpeng W., (2020), CFD Numerical simulation of temperature and airflow distribution in pigsty based on grid independence verification. *INMATEH-Agricultural Engineering*, Vol.61, Issue 2, pp. 241-250, Romania;
- [7] Qingqing S, Bin W, Jiawei Y, Yizhi L, Tongming Y., (2020), An omni-directional electric pruning saw for forest tending. *INMATEH-Agricultural Engineering*, Vol.61, Issue 2, pp. 35-40, Romania;
- [8] Serra P, Cunha R, Hamel T., (2016), Landing of a Quadrotor on a Moving Target Using Dynamic Image-Based Visual Servo Control. *IEEE Transactions on Robotics*, Vol.32, Issue 6, pp.1524-1535, USA;
- [9] Silveira G, Mirisola L, Morin P., (2020), Decoupled Intensity-Based Nonmetric Visual Servo Control. *IEEE Transactions on Control Systems Technology*, Vol.28, Issue 2, pp.566-573, USA;
- [10] Szymon Krupinski, Allibert G, Hua M D., (2017), An Inertial-Aided Homography-Based Visual Servo Control Approach for (Almost) Fully Actuated Autonomous Underwater Vehicles. *IEEE Transactions on Robotics*, Vol.33, Issue 5, pp.1041-1060, USA;
- [11] Tao Y, Zhou J., (2017), Automatic apple recognition based on the fusion of colour and 3D feature for robotic fruit picking. *Computers & electronics in agriculture*, Issue 142, pp.388-396, England;
- [12] Tsai C Y, Wong C C, Yu C J., (2015), A Hybrid Switched Reactive-Based Visual Servo Control of 5-DOF Robot Manipulators for Pick-and-Place Tasks. *Systems Journal, IEEE*, Vol.9, Issue 1, pp.119-130, USA;
- [13] Wang J, Zhou G, Wei X., (2019), Experimental characterization of multi-nozzle atomization interference for dust reduction between hydraulic supports at a fully mechanized coal mining face. *Environmental Science and Pollution Research*, Vol.26, Issue 10, pp.10023-10036, Germany;
- [14] Wang S, He X, Song J., Wang et al., (2018), Effects of xanthan gum on atomization and deposition characteristics in water and Silwet 408 aqueous solution. *International Journal of Agricultural and Biological Engineering*, Vol.11, Issue 3, pp.29-34, China;
- [15] Yan H J, Bai G, He J Q., (2010), Model of droplet dynamics and evaporation for sprinkler irrigation. *Biosystems Engineering*, Vol.106, Issue 4, pp.440-447, USA;
- [16] Zavala-Yoe R, Ramirez-Mendoza R A, Silverio García-Lara., (2017), A 3-SPS-1S Parallel Robot-based Laser Sensing for Applications in Precision Agriculture SCI-Journal. *Soft Computing*, Issue 21, pp.641-650, USA;

# EFFECTS OF DIFFERENT PLASTIC FILMS MULCHING ON SOIL TEMPERATURE AND MOISTURE AND FILM MECHANICAL PROPERTY

## 不同地膜覆盖对土壤温湿度及地膜力学特性的影响

Wang Long<sup>1, 2, 3)</sup>, Wang Xufeng<sup>2, 3)</sup>, Hu Can<sup>1, 2, 3)</sup>, He Xiaowei<sup>1, 2, 3)</sup>, Guo Wensong<sup>2, 3)</sup>, Hou Shulin<sup>1\*)</sup> <sup>1</sup>

<sup>1)</sup> College of Engineering, China Agricultural University, Beijing, 100083 / China;

<sup>2)</sup> College of Mechanical and Electronic Engineering, Tarim University, Alar Xinjiang, 843300 / China;

<sup>3)</sup> Key Laboratory of Colleges & Universities under the Department of Education of Xinjiang Uygur Autonomous Region, Alar Xinjiang 843300/ China

Tel: +86 13581711364; E-mail: hsl010@126.com

DOI: <https://doi.org/10.35633/inmateh-62-21>

**Keywords:** plastic mulch, soil moisture, soil temperature, breaking force

### ABSTRACT

The purpose of this research was to study heat and moisture retention and breaking force properties of different plastic mulches. The field experiments with different plastic mulches were carried. The results showed that, the fracture strength and the right-angle tear strength of reinforced mulch are superior to those of weather-resistant mulch and ordinary mulch. The soil moisture, humidity and daily mean temperature under plastic mulches were affected by the laying time at a 1% probability level. It was also found that the variety had no significant effect on daily mean temperature under plastic mulches. A strong correlation was found between breaking force and the laying time of plastic film. A multiple linear regression model was developed to determine the relationship between the heat and moisture retention properties and breaking force. The  $R^2$  values of three plastic mulch varieties regression model were 0.904, 0.913 and 0.931. The breaking force of reinforced mulch and weather-resistant mulch indicates that plastic mulch recovery should be conducted after autumn, before it is too weakened by exposure.

### 摘要

本研究旨在探讨不同塑料地膜的保热保湿性及破断力特性。进行了不同地膜覆盖的田间试验及破裂力试验。结果表明，加强型地膜的断裂强度和直角撕裂强度均优于耐候地膜和普通地膜。地膜覆盖对土壤水分、湿度和日平均温度受铺膜时间的影响十分显著 ( $P < 0.01$ )。不同品种对地膜覆盖下的日平均气温无显著影响。破断力与覆膜时间有较强相关性。建立了多元线性回归模型，确定了地膜下土壤温湿度与破断力的关系，三个地膜覆盖回归模型的  $R^2$  值分别为 0.904、0.913 和 0.931。以免地膜强度过低，地膜回收应在棉花收获后立即进行。

### INTRODUCTION

Plastic film mulching planting technology was introduced into China from Japan in the 1970s. Since then, it has become an important agricultural practice for increasing grain yields and crop productivity by conserving soil humidity, increasing soil temperature, and increasing the yields of crops by more than 20%, driving its widespread use (Hou S, et al., 2002; Hu C, et al., 2020; Liu E, et al, 2014). Plastic film mulching has been especially important in Xinjiang, considering its geographical location characterized by a dry climate and low spring temperatures. Film mulching has developed rapidly and has been widely used in Xinjiang since its introduction in 1983 (Yan C, et al, 2016). The area of mulched planting in Xinjiang exceeded 3 million ha by 2018, accounting for nearly 20% of China's total agricultural areas covered in plastic mulching (Gao W & Han R, 2019). However, despite the large amount of plastic mulches put into use, only a small fraction of these polyethylene films is currently recycled because of the expense and time required for its recycling (Gao, H, et al, 2019). Most of the mulch film residues remain in the soil owing to the lack of timely recovery of plastic film each year (Xue Y, et al., 2017), and the residue thus accumulates year by year. The physical structure of soil is also changed by film residue (Zhao Y, et al., 2017). The soil porosity and permeability are reduced, while the movement of water and fertilizer in the soil is impeded (Yang N, et al., 2015). It also hinders the movement of agricultural machinery in the soil (He C, et al., 2019).

<sup>1</sup> Wang Long, Ph.D. Stud.; Wang Xufeng, Prof. Ph.D.; Hu Can, Ph.D. Stud.; He Xiaowei, Ph.D. Stud.; Guo Wensong, A. Prof. Ph.D.; Hou Shulin, Prof. Ph.D.;

In addition, the residues can deteriorate the soil structure, become entangled with crop roots, and inhibit the absorption of water and nutrients. These issues directly affect the root length, root surface area, and vigour of crops (Yan C, *et al.*, 2008; Zhang K, *et al.*, 2020), resulting in reduced crop production and "White pollution", and the sustainable development of agriculture in China has thus been affected seriously (Qi Y, *et al.*, 2018). Heat and moisture retention are the main function of plastic mulch. The research on the performance of heat and moisture retention of film focuses on biodegradation film (Gao H, *et al.*, 2019; Kyrikou & Briassoulis, 2007). The effects of increasing soil moisture and temperature were present well at the early stage, biodegradation film is thus recommended as a viable option to the plastic film, but it should be carefully selected according to local environmental conditions (Zhang Y, *et al.*, 2018). Many studies have been conducted on the characteristics of mulch film. The changes in the tensile properties of mulch film are affected by the environment at different timescales, and studies of its thickness and position have shown that the tensile strength of plastic film is greatly affected by both natural conditions and covering time (Zhang J, *et al.*, 2015). Especially in the two months after mulching, the tensile strength decreases significantly, with the tensile strength of the mulch film near to cotton plants being higher than that of the mulch film far from cotton plants, and that of thick film being higher than that of thin film. Though there is much research related to the heat and moisture retention properties of biodegradation film in literature, there is limited information about heat and moisture retention properties of plastic film.

It has been observed that the reinforced mulch, weather-resistant mulch and ordinary mulch are used widely in Xinjiang, which were selected for the present study. The tensile and right-angle tear properties of new plastic films, as well as the relationship between mulching time, daily mean temperature and humidity under the film with breaking force were examined. The relationship between breaking force and these parameters of plastic films is a useful reference for the use and recovery of plastic film in Xinjiang and similar areas.

## MATERIALS AND METHODS

The field experiment was conducted in plot 10 of Alar Farm (40.61°N 81.28°E, 912.3 m above sea level) in 2019. Three kinds of plastic mulch, those that are presently used widely in Xinjiang, were selected for the experiment, namely reinforced mulch (RM), weather-resistant mulch (WM), and ordinary mulch (OM). The dimensions of the plastic mulch are 2050 mm × 0.01 mm (width × thickness), and all plastic mulches used were produced in 2018. Plastic mulch was laid down as shown in Figure 1, and the area of the testing field was 40 m<sup>2</sup> (20 m × 2 m). Local machine-picked cotton was planted in the experimental area, and the cultivation utilized three drip irrigation belts and six rows of cotton plants under plastic mulch. The distance between belts and rows were 660 mm and 100 mm, respectively, with a column spacing of 12.5 cm. The water and fertilizer management followed common local field management practices, with a top dressing applied.

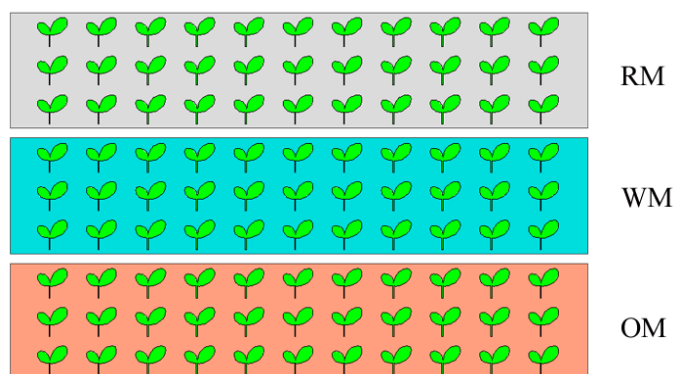


Fig. 1 - Diagram of plastic mulching experiment

To study the mechanical properties of plastic mulch, the three kinds of new plastic films were cut into 500 mm × 1000 mm samples using scissors. Sample surfaces were checked to be free of visible defects, including cracks, breakage, or other defects. The mechanical properties of plastic mulch including tensile and right-angle tear strength. The tensile strength test is common test methods for mechanical properties of materials. Then the right-angle tear strength test is a method for assessing tear resistance of plastic films. The specimen is ultimately torn at a right angle by stretching it. Therefore, the tear strength of the sample is

also an important index of the physical properties of the plastic film. The tear strength of different mulch films is obtained through the right-angle tear test, which provides some reference for the mechanized recovery of plastic film.

Based on the plastic-determination of tensile properties standards (GB/T 1040-2006), a special cutting tool was used to punch the sample into a type II strip sample, with a width and length of 10 mm and 150 mm, respectively (Committee, 2019). Test samples were placed on a 10 kN universal testing machine (model WWD-10J) for testing. During the test, the mulch sample was clamped at both ends with a special fixture, to ensure that the long axis of the specimen aligns with the centreline of the fixture to prevent the mulch sample from sliding relative to the fixture. Accordingly, the clamping force was checked to ensure it was not held in place too firmly or weakly in order to prevent failure of the specimen without it being properly tested. Tests were conducted with a tensile rate of 500 mm/min and initial distance of 50 mm. For materials with yield phenomena, the nominal fracture strain  $\varepsilon_t$  is expressed as shown in Formula (1) (Kassner, Kennedy, & Schrems, 1999):

$$\varepsilon_t = \frac{\Delta L}{L} \times 100\% \quad (1)$$

where,  $\varepsilon_t$  represents the nominal strain of fracture (as a ratio or percentage),  $L$  represents the initial distance between fixtures (in mm), and  $\Delta L$  represents the incremental distance between fixtures (in mm).

The right-angle tear test results provide the maximum load during the process of tearing the material with a right-angle tear load. The right-angle tear strength is expressed in  $\sigma_s$ , as shown in formula (2):

$$\sigma_s = \frac{P}{d} \quad (2)$$

where,  $\sigma_s$  represents the tight angle tear strength, [kN/m],  $P$  represents tear load, [N],  $d$  represents sample thickness, [mm].

Following the test method for right-angle tear properties of plastics standard (QB/T 1130-1991), films were cut in transverse directions into dovetail-shaped samples with a length of 100 mm and width of 20 mm using a special cutter, as shown in Figure 2. Specimens were aligned with the central direction of the two clamps and clamped into the fixture at a certain depth to ensure that the specimen was fully and evenly clamped in the parallel position. The initial distance between the two clamps was 50 mm, one end of which was fixed, while the other end was stretched by the testing machine, such that it moves to stretch the specimen in one direction at a tensile speed of 200 mm/min. Testing was conducted at 22°C and 43% relative humidity.

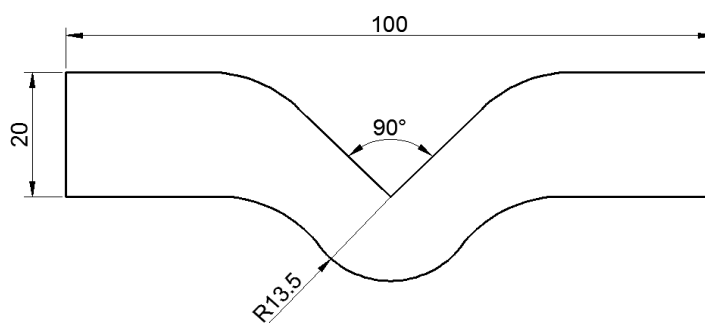


Fig. 2 - Rectangular tear samples

In order to study the heat and moisture retention properties of plastic mulch, during the cotton growing season from May to October, soil moisture, humidity, and daily mean temperature under the plastic mulch as well as ambient temperature were periodically measured. Soil humidity was measured with a MD783 humidity detector, and the measurement range was 2–60% relative humidity. The relative humidity resolution was 0.1%, while the measurement accuracy was  $\pm 1.5\%$ . Humidity in the plastic mulch was measured by a RH87 multifunctional environmental parameter recorder, with a humidity measurement range of 20–80%, a

resolution of 0.1%, and measurement accuracy of  $\pm 3\%$ . Daily mean temperature in the plastic mulch was measured by a buried-soil temperature and humidity sensor.

The breaking force of the plastic film was assessed in the process of it being picked up by the tillage parts of a residual film recovery machine. In order to simulate the mechanized recycling process of plastic mulches, a hook breaking force test was designed; the diagram of the test is shown in Figure 3. The tensile testing instrument was the AFG5 high precision tensile tester, which has a force measuring range of 0–20 N, force resolution of 0.1 N, and measurement accuracy of  $\pm 2\%$  FS. Each sample was stretched at 20 mm/min until the plastic mulch break-off. Each test was repeated 10 times.

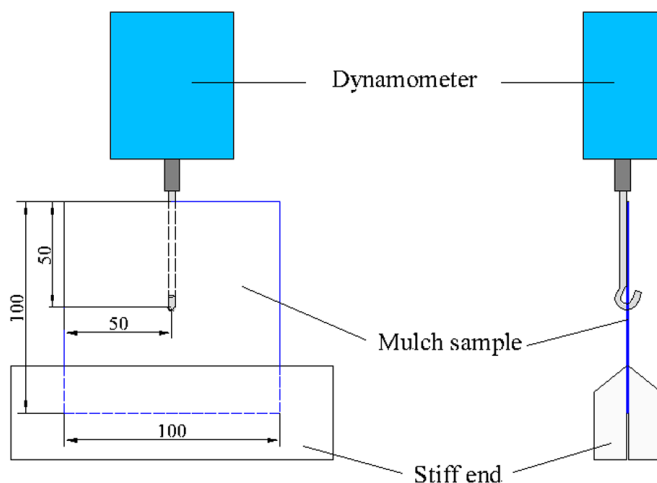


Fig. 3 - Breaking force test for plastic mulch

The data recorded in the field test and breaking force test were statistically analysed using a two-factor randomized complete block design to study the effects of six laying time and three varieties on some heat and moisture retention and breaking force properties explained in this section. Duncan's multiple range test was used to compare the means. Data processing Statistical analysis was done using SPSS 22.0 for Windows. The figures were prepared using the Origin 8.6 software program.

## RESULTS AND DISCUSSION

As shown in Figure 4, the strain-stress curve of plastic mulch exhibits a yield point and a fracture point. It shows that the plastic mulches are all ductile materials. The relationship between stress and strain is approximately linear in the initial loading stage. When the stress reaches the yield point, the stress decreased and then increased until the fracture point. It is generally believed that the yield point corresponds to the destruction of the microstructure. When the stress is lower than this value, the stress does not cause damage to the plastic mulch. The stress and strain continue to increase until the load reaches the maximum, that is, the fracture point shown in the figure. Therefore, the stress at fracture point is viewed as the maximum stress that the plastic mulch can bear.

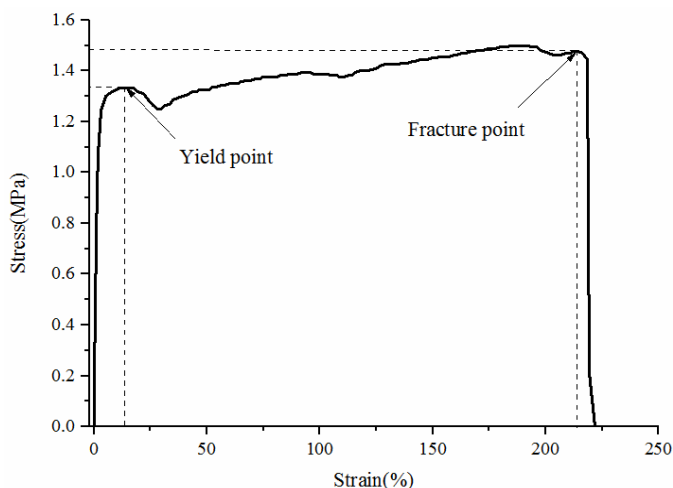
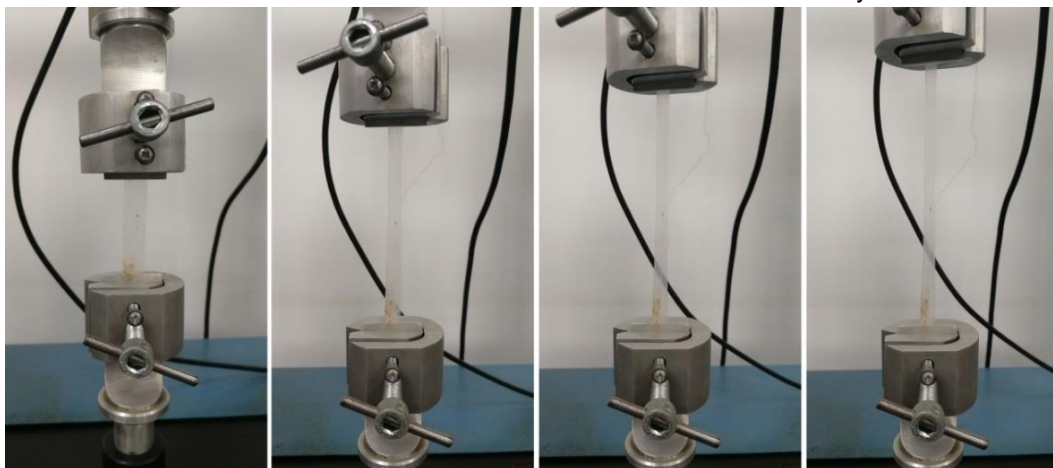


Fig. 4 - A typical strain-stress curve

The tensile testing process is shown in Figure 5, which shows that the film sample is continuously stretched in the images arranged from left to right. The width gradually narrows, and the light transmittance is obviously enhanced. The thickness of the film thins as it stretches until it eventually breaks.



**Fig. 5 - Tensile testing process**

A right-angle tear test sample before and after the test is shown in Figure 6, which demonstrates that the film sample gradually changes from a swallowtail shape to a strip shape in the process of stretching, from a right-angle notch to an eventual tear, and there is a small protuberance at the site of failure in the sample. This shows that the specimen first ruptures from the right-angle notch, then breaks to a certain extent and no longer tears, but instead bears the overall tensile force until fracturing.

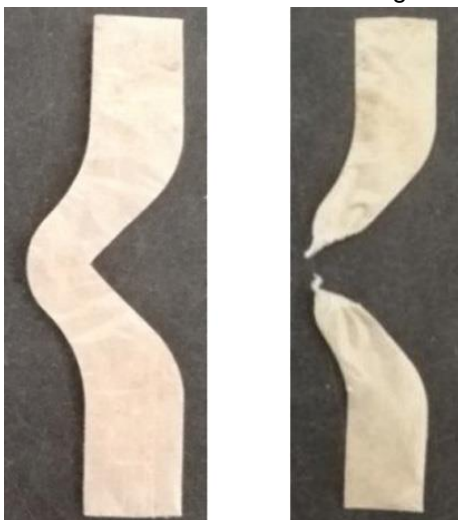


**Fig. 6 - A sample (a) before and (b) after right-angle tear testing**

As shown in Figure 7, the right-angle tear curve of plastic mulch exhibits a right-angle tear point. The relationship between force and displacement is approximately parabola distribution in the entire right-angle tear stage. When the force reached the right-angle tear point, the force decreases until the plastic mulch break-off. Therefore, the load at this point is viewed as the maximum right-angle tear force that the plastic mulch can bear.

The fracture stress, fracture strain, right-angle tear strength and strain for the plastic mulch varieties are shown in Table 1. The fracture strain and fracture stress of the reinforced mulch were also the highest, at  $284.60 \pm 10.86\%$  and  $1.66 \pm 0.12$  MPa, respectively. Meanwhile, the right-angle tear strength and strain value of the reinforced mulch were also the highest, at  $12.1625$  kN/m and  $57.51\%$ . The results of Duncan's multiple range tests showed that the difference among the fracture stress, fracture strain, right-angle tear strength and strain were statistically significant for plastic mulch variety. The test results show that the fracture strength and the right-angle tear strength of reinforced mulch are superior to those of weather-resistant mulch and ordinary mulch. The tensile lengths of the three plastic mulches at their breaking points are all satisfactory, with the fracture strain for each of them exceeding 200%.

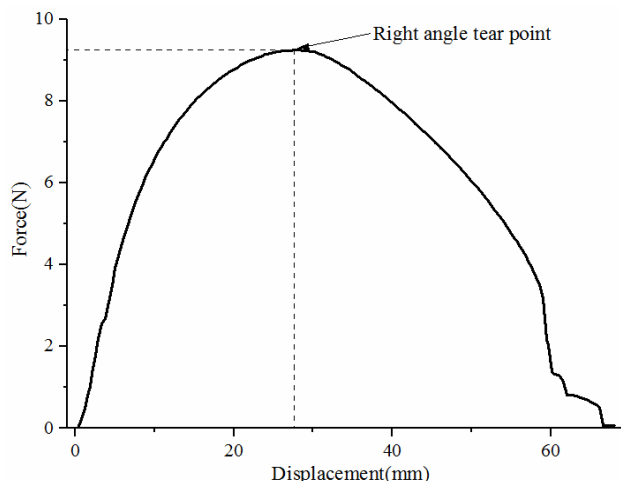


Fig. 7 - A typical right-angle tear curve

Table 1

The mechanical property test results

Variety	Fracture stress (MPa)	Fracture strain (%)	Right-angle tear strength (kN/m)	Right-angle tear strain (%)
RM	1.66±0.12 <sup>a</sup>	284.60±10.86 <sup>a</sup>	12.14±1.54 <sup>a</sup>	57.69±5.34 <sup>a</sup>
WM	1.44±0.15 <sup>ab</sup>	218.27±8.85 <sup>b</sup>	11.55±1.27 <sup>a</sup>	53.66±4.37 <sup>ab</sup>
OM	1.40±0.09 <sup>b</sup>	236.58±10.05 <sup>b</sup>	10.07±1.04 <sup>a</sup>	47.48±4.88 <sup>b</sup>

In each column, means with the same letters are not significantly different at the 0.01 level of significance using Duncan's multiple range test.

The soil moisture, humidity and temperature under each mulch for the plastic mulch varieties are summarized in Table 2.

Table 2

The heat and moisture retention performance test results

Time (D)	Variety	Soil moisture (%)	Humidity (%)	Daily mean temperature (°C)
0	RM	26.30	39.57	18.8
	WM	20.57	37.63	20.8
	OM	14.73	36.70	19.3
17	RM	32.53	68.63	24.5
	WM	22.27	65.37	24.9
	OM	21.70	61.53	23.5
45	RM	30.13	64.43	28.0
	WM	27.60	63.37	29.5
	OM	20.83	62.17	26.1
72	RM	43.43	59.60	23.5
	WM	39.43	60.63	25.2
	OM	38.63	58.37	23.1
91	RM	39.73	60.60	24.2
	WM	34.37	59.80	24.6
	OM	38.80	58.70	23.7
104	RM	42.33	64.50	24.3
	WM	39.40	62.70	23.7
	OM	38.97	62.30	23.2
Mean				
	RM	35.74 <sup>a</sup>	59.56 <sup>a</sup>	24.8 <sup>a</sup>
	WM	30.61 <sup>b</sup>	58.25 <sup>ab</sup>	23.9 <sup>a</sup>
	OM	28.94 <sup>c</sup>	56.63 <sup>b</sup>	23.1 <sup>a</sup>
P-value				
T		0.000 <sup>**</sup>	0.000 <sup>**</sup>	0.000 <sup>**</sup>
V		0.000 <sup>**</sup>	0.000 <sup>**</sup>	0.079 <sup>ns</sup>
T×V		0.000 <sup>**</sup>	0.356 <sup>ns</sup>	0.977 <sup>ns</sup>

\*, \*\*: Significant at the levels of 5% and 1%, respectively.

ns: Not significant.

In each column, means with the same letters are not significantly different at the 0.01 level of significance using Duncan's multiple range test.

The soil moisture and humidity under mulches increased as the time increased for plastic mulch varieties. The reason for this is that the test field began to drain water in late May. This relationship was found statistically significant at a 1% probability level. The differences among the humidity values under plastic mulch for varieties were found to be statistically insignificant. The overall soil moisture values varied between 26.30 % and 43.43 % for reinforced mulch, varied between 20.57 % and 39.43 % for weather-resistant mulch, and varied between 14.73 % and 38.97 % for ordinary mulch, respectively. This difference was also found to be statistically significant at a 1% probability level. According to the variance analysis results, the increase in soil moisture and humidity under plastic mulches with time was significant for varieties.

From Table 2, it can be observed that temperature under plastic mulch increased nonlinearly as the time increased. Considering the varieties together, the daily mean temperature values ranged from 18.8°C to 29.5°C. The effect of time on daily mean temperature was also statistically significant at a 1% probability level. However, it was found that daily mean temperature values for plastic mulch varieties were in the same group according to Duncan's multiple range test results.

There is a large area of plastic film coverage in Xinjiang, and there are many brands and types of mulch on the market. Three kinds of plastic mulch were tested for their heat preservation and moisture retention, and temperature and humidity are related to the location and depth of measurements. Accordingly, this testing was conducted in the middle of each cotton row, the temperature and humidity under the film were measured between the film and the soil, and the soil moisture was measured at a 5-cm soil depth. Reinforced mulch was found to have the best moisture retention effect, though the difference between the weather-resistant mulch and the ordinary mulch in this aspect was not large, and the heat retention effect of weather-resistant mulch was also the best. However, the climatic environment and soil conditions in the northern and southern regions of Xinjiang are quite different (Hu C, *et al.*, 2019). Therefore, even within Xinjiang, the test results are not universal, and suitable mulch should be selected according to the planting characteristics of each particular area.



**Fig. 8 - Breaking force test process**

The breaking force test process of the plastic film is shown in Figure 8. During the stretching process of the hook, the plastic film starts to break from the middle point. The rupture point of plastic film is related to the position of hook action. Breaking force of plastic mulch is summarized in Figure 9, which shows that as mulch covering time increased, the hook breaking force decreased gradually. The breaking force of reinforced mulch was the greatest, followed by that of weather-resistant mulch. As mulch covering time increased, the rate of decrease in mulch breaking force also decreased.

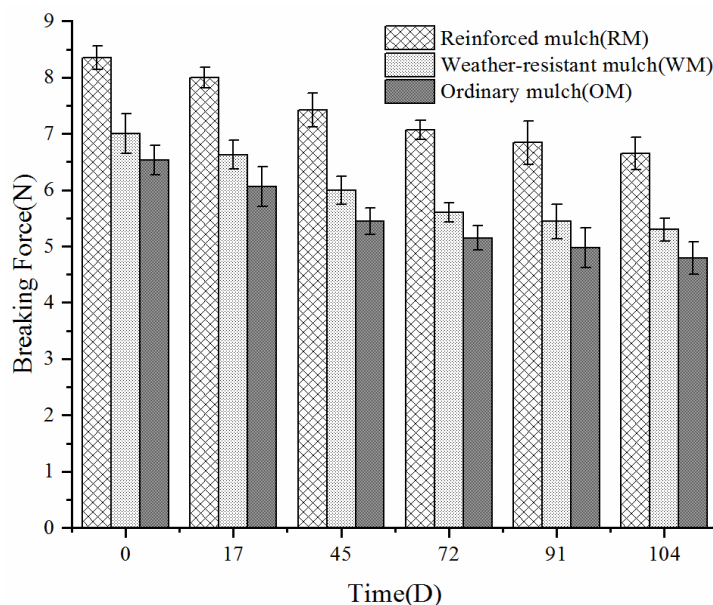


Fig. 9 - Breaking force of plastic mulch

Based on the relationship of mulch covering time, soil moisture, temperature, and humidity with mulch breaking force, the following mathematical model can be established:

$$\begin{bmatrix} y_1 \\ y_2 \\ y_3 \end{bmatrix} = \begin{bmatrix} a_{11} & a_{12} & a_{13} & a_{14} & a_{15} \\ a_{21} & a_{22} & a_{23} & a_{24} & a_{25} \\ a_{31} & a_{32} & a_{33} & a_{34} & a_{35} \end{bmatrix} \begin{bmatrix} x_0 \\ x_1 \\ x_2 \\ x_3 \\ x_4 \end{bmatrix} \tag{3}$$

Here,  $y$  represents the estimate of breaking force;  $a$  represents the regression coefficients;  $x_1$  represents the mulch covering time;  $x_2$  represents the soil moisture estimate;  $x_3$  represents the humidity estimate;  $x_4$  represents the daily mean temperature estimate.

Using multivariate linear analysis, coefficient value and significance of each variable was given in Table.3. The breaking force decreased as the time increased for plastic mulch varieties, this relationship was found statistically significant at a 1% probability level. That means that the application time of plastic mulches is the main factor that influence the breaking force.

Table 3

Coefficient value and significance of each variable

Variable	Time	Soil moisture	Humidity	Daily mean temperature
RM	-0.556**	0.712 <sup>ns</sup>	0.057 <sup>ns</sup>	-0.019 <sup>ns</sup>
WM	-0.414**	-2.924 <sup>ns</sup>	0.664 <sup>ns</sup>	-0.040 <sup>ns</sup>
OM	-0.344**	-3.031 <sup>ns</sup>	0.444 <sup>ns</sup>	-0.104*

\*, \*\*: Significant at the levels of 5% and 1%, respectively.  
 ns: Not significant

By substituting coefficient value into Formula (3), the following multiple linear regression model can be obtained:

$$\begin{bmatrix} y_1 \\ y_2 \\ y_3 \end{bmatrix} = \begin{bmatrix} 13.420 & -0.556 & 0.712 & 0.057 & -0.019 \\ 12.176 & -0.414 & -2.924 & 0.664 & -0.040 \\ 12.735 & -0.344 & -3.031 & 0.444 & -0.104 \end{bmatrix} \begin{bmatrix} x_0 \\ x_1 \\ x_2 \\ x_3 \\ x_4 \end{bmatrix} \tag{4}$$

The fitted values and Mann-Whitney U test results are tabulated in Table.4. As seen in Table.4, the  $R^2$ , Adjusted  $R^2$  and RMSE values all achieve significant effect, indicating that the regression equation obtained has a high degree of fitting. The Mann-Whitney U test values were greater than 0.05, therefore, there is no significant difference between the test data and the prediction data. Obviously, the regression model is suitable to describe the breaking force changes.

Table 4

Fitted values and Mann-Whitney U test results

Variety	$R^2$	Adjusted $R^2$	RMSE	Mann-Whitney U test
RM	0.904	0.875	0.3553	1.000 <sup>ns</sup>
WM	0.913	0.886	0.3296	0.938 <sup>ns</sup>
OM	0.931	0.909	0.3086	1.000 <sup>ns</sup>

*ns: Not significant*

The best time for plastic film recovery is after autumn when the cotton is harvested. At that time, the mulch covering has been in place for approximately 160 days, while the soil moisture, humidity and daily mean temperature under plastic mulches are approximately 32%, 48%, and 26°C, respectively. Based on the mathematical model, the breaking forces of reinforced mulch, weather-resistant mulch, and ordinary mulch are predicted to be 6.2263 N, 5.1061 N, and 4.9239 N, respectively. During the actual removal operation, most of the surface film can be recovered with a force above 5.0 N. The hook breaking force of the reinforced mulch and the weather-resistant mulch can thus meet the mechanical operation requirements. After the cotton harvest, the three types of surface mulch were recovered by a comb-tooth mulching recycling machine. The recovery rates for reinforced mulch were higher than that of weather-resistant mulch and ordinary mulch. The results are consistent with the model predictions.

Comparisons of the coefficients of the mathematical regression model show that mulch laying time has a much greater impact than the other parameters. Accordingly, the performance of mulch film is greatly affected by the mulch covering time period. This result is consistent with previous studies, in the early stage of the mulch covering time period, the performance of the cutting force decreased substantially. The hook breaking force performance of plastic film also decreases with the time of mulch covering. Therefore, plastic film should be recovered as soon as possible after the autumn harvest of each year. Otherwise, longer mulch covering time periods increases the difficulty of recycling.

## CONCLUSIONS

The mechanical properties, heat and moisture retention performance and breaking force for three typical plastic mulches widely used in Xinjiang were measured. A breaking force regression model was established by fitting the field experiment and breaking force data using multiple regression method. The results indicate that the fracture strength and the right-angle tear strength of reinforced mulch are superior to those of weather-resistant mulch and ordinary mulch. The different plastic mulches exhibited significant differences in soil moisture retention and breaking force, and insignificant differences in humidity and daily mean temperature under plastic mulches. The correlation analysis showed that soil moisture and humidity under plastic mulches were significantly correlated with the laying time and plastic mulch varieties, whereas the temperature under plastic mulch and breaking force were significantly correlated with the laying time at a 1% probability level. The significant factor of the breaking force was the laying time. The breaking force was predicted and evaluated based on the laying time, soil moisture, humidity and daily mean temperature under plastic mulches. The mathematical model predicts that the hook breaking force of the reinforced mulch and the weather-resistant mulch can meet the requirements of film recovery after autumn. This study evaluated the heat and moisture retention performance and breaking force of commonly used plastic mulches in Xinjiang and provides reference data to develop suitable conditions for plastic mulches use and recycling.

## ACKNOWLEDGEMENT

The work was supported by Young and middle-aged leaders of the Corps, under the Grant No.2020CB028, and the Major Scientific and Technological Projects of the Corps, under the Grant No.2018AA001/03.

## REFERENCES

- [1] Committee, N.S.M. (2019), GB/T1040.3-2018, *Plastics - determination of tensile properties - part 3: test conditions for films and thin sections* (塑料拉伸性能的测定第 3 部分: 薄膜和薄片的试验条件), Beijing: China Standards Press;
- [2] Gao, H., Yan, C., Liu, Q. et al, (2019). Effects of plastic mulching and plastic residue on agricultural production: A meta-analysis. *Science of the Total Environment*, 651, 484-492;
- [3] Gao, W., & Han, R, (2019), *Xinjiang statistical yearbook* (新疆统计年鉴), Beijing: China statistics press;
- [4] Hu, C., Wang, X., Chen, X. et al, (2019), Current situation and control strategies of residual film pollution in Xinjiang (新疆农田残膜污染现状及防控策略), *Transactions of the Chinese Society of Agricultural Engineering*, 35(24), 223-234;
- [5] Hu, C., Wang, X., Wang, S., et al, (2020), Impact of agricultural residual plastic film on the growth and yield of drip-irrigated cotton in arid region of Xinjiang, China, *International Journal of Agricultural and Biological Engineering*, 13(1), 160-169;
- [6] He C., You Y., Wang D. et al. (2019), Effect of tine geometry on penetration resistance during vertical movement on natural grassland, *INMATEH - Agricultural Engineering*, 59(02):19-26;
- [7] Hou, S., Hu, S., Kong, J., et al, (2002), Present situation of research on plastic film residue collector in China (国内残膜回收机研究的现状), *Transactions of the Chinese Society of Agricultural Engineering*, 18(3), 186-190;
- [8] Kassner, M.E., Kennedy, T.C., Schrems, K.K. (1999), The mechanism of ductile fracture in constrained thin films, *MRS Online Proceeding Library Archive*, 539:263-268;
- [9] Kyrikou, I., Briassoulis, D. (2007). Biodegradation of agricultural plastic films: A critical review. *Journal of Polymers and the Environment*, 15(3), 227-227;
- [10] Liu, E. K., He, W. Q., Yan, C. R. (2014), 'White revolution' to 'white pollution'—agricultural plastic film mulch in China. *Environmental Research Letters*, 9(9), 091001;
- [11] Qi, Y. L., Yang, X. M., Pelaez, A. M. et al, (2018), Macro- and micro- plastics in soil-plant system: Effects of plastic mulch film residues on wheat (*Triticum aestivum*) growth, *Science of the Total Environment*, 645, 1048-1056;
- [12] Xue, Y., Cao, S., Xu, Z. et al, (2017), Status and trends in application of technology to prevent plastic film residual pollution (地膜残留污染防治技术现状及发展趋势), *Journal of Agro-Environment Science*, 36(8), 1595-1600;
- [13] Yan, C., He, W., Xue, Y. et al, (2016), Application of biodegradable plastic film to reduce plastic film residual pollution in Chinese agriculture (生物降解地膜应用与地膜残留污染防治), *Chinese journal of biotechnology*, 32(6), 748-760;
- [14] Yan, C., Wang, X., He, W. et al, (2008), The residue of plastic film in cotton fields in Shihezi, Xinjiang, (新疆石河子地区棉田土壤中地膜残留研究), *Acta Ecologica Sinica*, 28(7), 3470-3474;
- [15] Yang, N., Sun, Z. X., Feng, L. S., et al, (2015), Plastic Film Mulching for Water-Efficient Agricultural Applications and Degradable Films Materials Development Research. *Materials and Manufacturing Processes*, 30(2), 143-154;
- [16] Zhang, J., Chen, J., Jia, R. M. et al, (2018), Selection and evaluation of microorganisms for biodegradation of agricultural plastic film. *3 Biotech*, 8(7), 308;
- [17] Zhang, J., Wang, X., Zhang, et al, (2015), Effects of mechanical tensile properties of plastic film on plastic recycling method (农田地膜拉伸性能变化对缠绕式回收的影响), *Transactions of the Chinese Society of Agricultural Engineering*, 31(20), 41-47;
- [18] Zhang, K., Sun Y., Liu, L. et al (2020), Design and test of variable diameter pneumatic drum type bean seed metering device, *INMATEH - Agricultural Engineering*, 60(021): 9-18;
- [19] Zhao, Y., Chen, X., Wen, H. et al, (2017), Research Status and Prospect of Control Technology for Residual Plastic Film Pollution in Farmland (农田残膜污染治理技术研究现状与展望), *Transactions of the Chinese Society for Agricultural Machinery*, 48(6), 1-14.

## EFFECT OF FAN'S PARAMETERSON ADHESION MECHANISM OF THRESHED RAPE MIXTURETO CLEANING SIEVE

### 风机参数对油菜脱出物与清选筛的粘附性影响

Zhang Tao<sup>1,2)</sup>, LiYaoming<sup>\*1,2)</sup>, XuLizhang<sup>1,2)</sup>, QingYiren<sup>1,2)</sup>

<sup>1)</sup> Key Laboratory of Modern Agricultural Equipment and Technology, Jiangsu University, Zhenjiang, 212013/China

<sup>2)</sup> School of agricultural equipment engineering, Jiangsu University, Zhenjiang, 212013/China

Tel: 13805283656; E-mail: ymli@ujs.edu.cn

DOI: <https://doi.org/10.35633/inmateh-62-22>

**Keywords:** Rape, Anti-adhesion Mechanism, Hot Airflow, Orthogonal Experiments

#### ABSTRACT

In order to reduce the adhesion of moist threshed rape mixture and cleaning sieve, a method named "Hot-airflow Cleaning" has been proposed. Firstly, the key factors influencing anti-adhesion property were obtained based on the theoretical analysis. They were temperature, wind speed and fan inclination. Then, based on the single-factor experiments, the proper temperature of the fan was 30-50°C, the proper wind speed and inclination of the fan were 2-4 m/s and 15-45°, respectively. Finally, the fan's parameters were optimized by Box-Behnken design. The results showed that the optimum technological parameters were temperature of 50 °C, a wind speed of 4 m/s and that fan inclination was 45°. This research could provide a reference for the improvement of cleaning system for rape combine harvesters.

#### 摘要

为了降低湿脱粒油菜混合料与清选筛的粘附性,提出了一种“热风清选”的方法。首先,在理论分析的基础上,得出了影响防粘性能的关键因素:温度、风速和风机倾角。通过单因素试验得出风机的适宜温度为30~50°C,适宜风速为2~4m/s,倾角为15~45°。最后,采用Box-Behnken设计对风机参数进行了优化。结果表明,最佳工艺参数为温度50°C,风速4m/s,风机倾角45°。本研究可为油菜联合收获机清洗系统的改进提供参考。

#### INTRODUCTION

Rape has high nutritional value and economic value. It is widely planted in northwest China, north China and the Yangtze River basin, and is one of the major oil crops in China (Ma Z. et al, 2011; Zhang M., et al, 2019; Chen X. et al, 2018). Air-and-screen cleaning equipment which were responsible for the separation of unnecessary or even harmful impurities from usable material, have high precision requirements for separation and cleaning and the ability to adjust in a wide range of operating parameters (Panasiewicz M. et al, 2012; Liu C. et al, 2018; Du H. et al, 2019; Ning X. et al, 2018). The purity of the grain determined by the percentage of impurities is the most important target for cleaning. However, when harvesting wet sticky rape, the components of the threshed rape mixture could be bond to each other, unable to disperse and stratify quickly because of the surface tension, grease and other binders on the threshed rape mixture, resulting in high impurity and loss rate of cleaning device. Therefore, it is very helpful to reduce the adhesion on the screen surface to improve the harvest performance.

Numerous scholars mainly study the adhesion mechanism of metal materials with soil, coal and other particles (Chen S. et al., 2018; Yang X. et al., 2000; Liu Q. et al., 2019; Chen X. et al., 2003; Chen C. et al., 2019), while few studies have been conducted on the adhesion mechanism of agricultural materials. In order to solve the problem of hole plugging of wet sticky rape materials, some commonly used methods include reducing the moisture content of materials, heating the screen surface, using the screen surface cleaning device had been proposed by Zuber and Eibs (1995), Chen C. et al. (2019) have adopted vibrating and heating anti-adhesion test. The results indicated that the increase of temperature effectively decreased the adhesion rate of the shaking plate surface, but this method can only destroy the adhesion interface after two heat exchanges, and the heat transfer efficiency was low. Li Y. et al (2013) applied the bionic non-smooth surface to the vibration screen of rape harvester, and the test proved that the bionic non-smooth screen surface has good stability and use effect, but the processing technology of the non-smooth screen is complex and the production cost was pretty high.

Air and screen cleaning device is currently widely used in rape harvesting machinery. Due to different floating speed, the threshed rape mixture can be dispersed and layered under the action of pneumatic force. However, rape is repeatedly impacted and kneaded in the threshing device, which will produce a large number of light impurities such as stem debris and pod diaphragm. These impurities are easy to interact with free water of stem and oil of broken rapeseed and then adhere to the surface of cleaning sieve. Some literature works have pointed out that heating is an important method to control the mechanical properties of adhesion interface, which can reduce the surface tension of water film and the adhesion force (Ren L., 2011; Liu G. et al, 2008; Peng X. et al, 2020). Hiraku et al. (2017) have studied the law of adhesion by varying the roughness and temperature of the wheel-rail surface. Results showed that the wheel-rail adhesion increases with the increase of water temperature. In this paper, the anti-adhesion mechanism of wet sticky rapeseed under the action of hot airflow and the influence of different fan's parameters on the adhesion characteristics of rapeseed and sieve interface were studied. The optimum operating parameters were revealed to provide references for improving the cleaning efficiency (Fei Liu et al, 2020).

## MATERIALS AND METHODS

Most of the wet sticky rape materials are the light impurities with large surface area, according to the reference (Chen C. et al, 2019), in the high humidity of cleaning chamber, the surface of the particles is uniformly covered with a layer of liquid film. When the particles collide, part of the liquid film will fuse together to form a liquid bridge. Due to the effect of liquid surface tension and pressure difference of gas-liquid interface, the particles and surface of cleaning sieve are affected by the liquid bridge force and would form adhesion-interface. When the particle size exceeds 20  $\mu\text{m}$ , the interaction force of surface water is much greater than van der Waals force and other intermolecular forces (Chen X. et al., 2002).

As shown in fig.1, rapeseed was taken as an example and the anti-adhesion model was constructed; the force on stable rapeseed is:

$$F = F_2 + G \quad (1)$$

Where:  $F$  represents normal wind force (N);  $F_2$  represents adhesion force (N);  $G$  represents gravity of rape. The normal wind force  $F$  on rapeseed was based on the following equation:

$$F = F_1 \sin \alpha = m \frac{g}{v_p^2} v^2 \sin \alpha \quad (2)$$

where:  $m$  represents the mass of rapeseed (kg),  $v_p$  represents the float speed of rapeseed (m/s),  $v$  represents wind speed (m/s);  $\alpha$  represents the fan inclination. From formula (1) and (2), the change of wind speed and fan inclination will cause the inequality between the left and right sides of the formula. The unbalanced force will make the rapeseed leave the sieve surface or slide along the sieve surface. In addition, the water molecules in the liquid bridge will move violently when heated, expressing phenomenon of vaporization. The water film between the material and the cleaning screen would absorb the heat of the hot airflow and the meniscus radius of the water film ( $r_1$ ) gradually decreases, resulting in the decrease of the adhesion force between the threshed rapeseed and the screen surface. Therefore, the fan's parameters that affect anti-adhesion properties are wind speed, temperature and fan inclination.

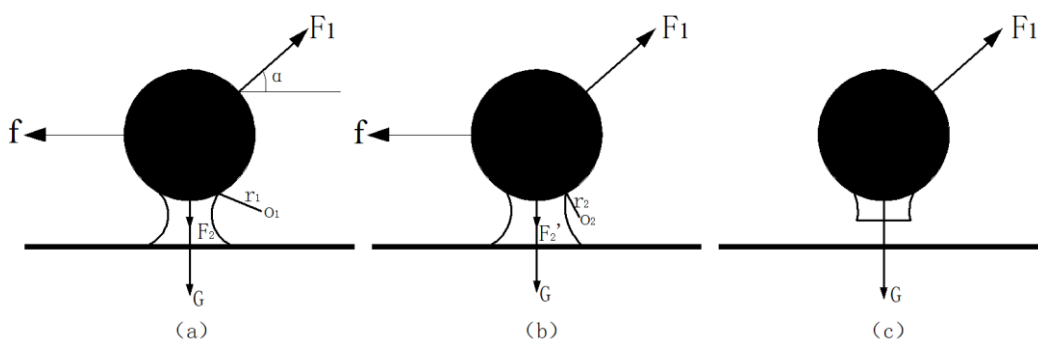


Fig. 1 - Anti-adhesion model

The wet and sticky rape materials were chosen as test subject with strong adhesion, including grains, husks, stems, stalks, horn beaks and other fine particles which were shown in Fig.2. The sealed wet sticky rape mixture was collected from the field, and then taken to the laboratory. The drying method was used to measure the moisture content in time (Bhupendra M., 2017; Ma Z. et al., 2011). Screening test was conducted by using 10 standard sieve with 0.1~6 mm aperture to determine size of adhesive materials, screening time was 5 minutes and the size proportion of the adherent of the rape sieve surface was obtained by dividing the mass of the adherent in each size range by the total mass of the sample. The screen test was repeated five times and average value was applied. The measured moisture content of the mixture was 19.4%, and 70% of the wet sticky rape mixture were 0.3~2.6 mm in size, 13% are over 2.6 mm, and the maximum size did not exceed 8 mm.



Fig. 2 - Wet sticky rape mixture

A type of PTC (Positive Temperature Coefficient) heating fan was designed to provide hot airflow. The PTC heating fan includes motor, PTC heating, voltage regulator, hot wire anemometer and thermostat, etc. PTC heating is a kind of electric heater with ceramic heating elements, which will not produce redness and avoid fire and scald. The type and parameter of these electronic devices was shown in Table 1. Before the test, the PTC heating fan was fixed on the fan inclination adjuster in front of the sieve. The range of the fan inclination adjuster was 0° to 90°. Temperature can be adjusted by the thermostat and the motor speed can be adjusted by the voltage regulator.

Table 1

Name and parameter of PTC heating fan

Name	Type
Motor	6030
Voltage regulator	BAT100-800B
Thermostat	EK-3010
Hot wire anemometer	AVM-07

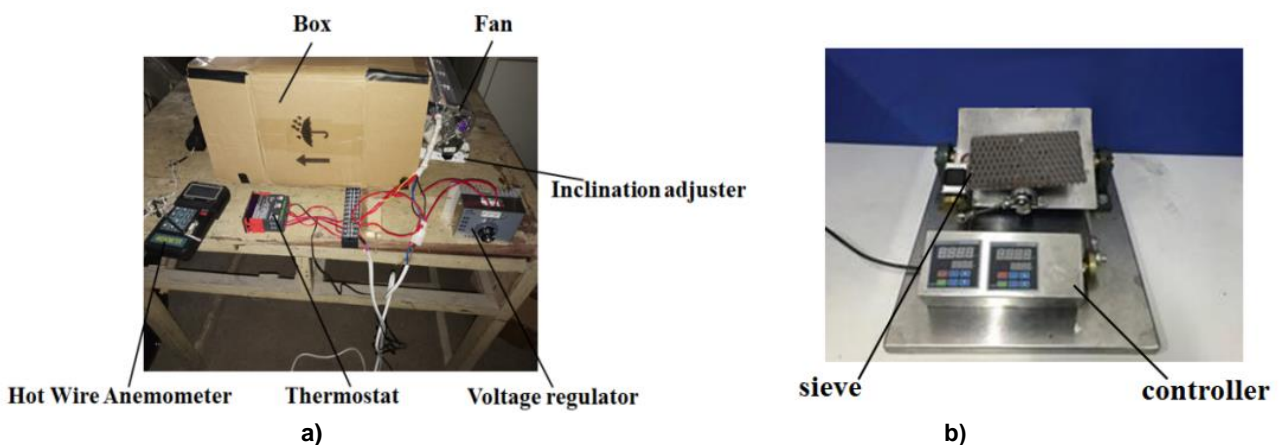


Fig. 3 - Test equipment

As shown in Fig.3, a square box was chosen as the cleaning room. A hot wire anemometer was used to measure temperature and wind speed of the fan outlet. A circular sieve with 200 mm length and 3 mm height was fixed on the vibration platform in the cleaning room and the vibration frequency and amplitude were 4 Hz and 30 mm, respectively. Round holes with a diameter of 5 mm are evenly distributed on the surface of circular sieve, so the rapeseed can pass through them when vibrating and the impurities were blown out of the box. The wet sticky rape materials were laid on the sieve evenly. Before the test, the mass of wet sticky rape mixture and sieve was weighed by the electronic scale, and it was weighed again when each test finished. Each test in different conditions was repeated three times and the average value was applied. At the end of each test, the surface of sieve was cleaned by towels. In this particle, the test procedure was named “hot-airflow cleaning”.

To quantify the effect of parameters of hot airflow on the anti-adhesion mechanism of wet sticky threshed rape mixture to adhesion interface, the escape rate was defined as:

$$\varphi = \frac{m - m_t}{m - m_s} \times 100\% \quad (3)$$

Where:  $\varphi$  represents the escape rate,  $m$  represents the mass of wet sticky rape mixture and sieve before each test (g),  $m_t$  represents the mass of wet sticky rape mixture and sieve after each test (g),  $m_s$  represents the mass of circular sieve (303 g).

## RESULTS AND DISCUSSION

The five levels of temperature were selected over a range of 26-60°C, the wind speed and the fan inclination were set at 4 m/s and 30°, respectively and the escape rate on the circular sieve as a function of temperature was shown in Fig.4. It can be seen that with the increase of temperature, the escape rate of threshed rape mixture shows an increasing trend as a whole. When the temperature is below 30°C, the escape rate does not exceed 30%, and the effect of reducing adhesion on the circular sieve is not significant. Because the adhesion force is far greater than wind force when the temperature is low, most of mixture cannot leave the sieve surface. In the range of 30-50°C, with the increase of temperature, the escape rate increases rapidly. When the temperature is 50°C, the escape rate exceeds 60%. The escape rate changes a little when the temperature ranges from 50-60°C, and the anti-adhesion property is gradually stable.

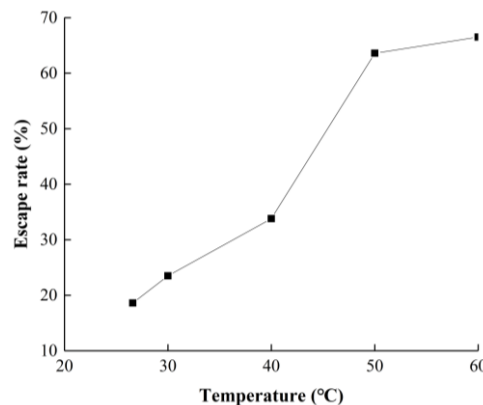


Fig. 4 - Escape rate on the circular sieve as a function of temperature

The five levels are determined over a range of 2-6 m/s, the temperature and the fan inclination are selected at 40°C, 30°C, respectively and the escape rate on the circular sieve with increase of wind speed is shown in Fig.5. It can be seen that when the wind speed is 2 m/s, the escape rate is less than 30% and the escape rate increases rapidly as wind speed increases from 2-4 m/s. In the range of 4-6m/s the escape rate increases slowly, with the increase of wind speed, and the effect of wind speed on the anti-adhesion is not significant. The reason may be that the increase of wind speed may cause turbulence in someplace of the square box, resulting in the local wind speed not reaching the actual measured wind speed, thus affecting the anti-adhesion property. Hence the proper value of wind speed is 2-4 m/s.

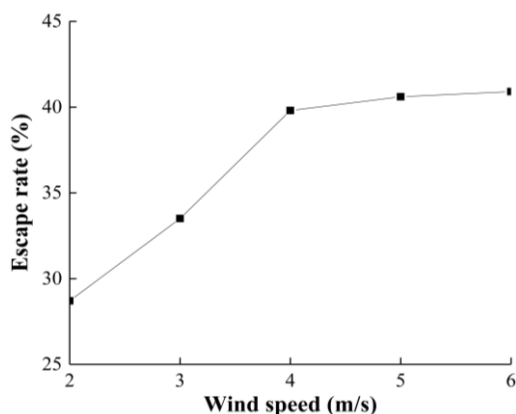


Fig. 5 - Escape rate on the circular sieve as a function of wind speed

Every test was carried out under the condition that the wind speed and temperature were 4 m/s, 30°C respectively. The five levels were selected in the range of 0-60° and the escape rate on the circular sieve with increase of fan inclination is shown in Fig.6. In the range of 0-60°, with the increase of fan inclination, the escape rate increases significantly and then decreases. When the fan inclination is below 15°, the value of the escape rate is less than 30%. There is an inflection point in the escape rate at a fan inclination of 45°, after which the escape rate decreases. The escape rate is more than 60% at the fan inclination of 45°. The reason is that when the fan inclination increases, the normal wind forces subsequently increases, resulting in the anti-adhesion of mixture on the sieve. However, when the fan inclination exceeds the critical value, the tangential wind force will reduce, which is not enough to overcome the friction resistance, resulting in the decrease of the escape rate. Consequently, a better anti-adhesion performance should be achieved from 15-45°.

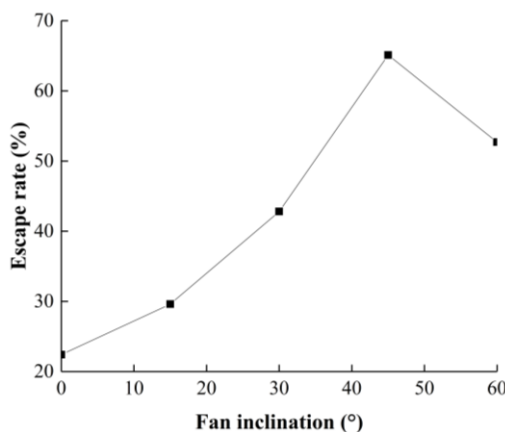


Fig. 6 - Escape rate on the circular sieve as a function of fan inclination

The suitable fan inclination, temperature and the wind speed of the circular sieve outlet were determined to be factors based on the results of the single-factor experiments. Subsequently, orthogonal experiments considering the three factors and three levels were conducted. The escape rate between the threshed rape mixture and sieve were chosen as the evaluation index to the analysis factors that affected the optimal parameter combination. The levels of the factors and results are shown in tables 2 and 3, respectively. Furthermore, ANOVA for response surface analysis was conducted to determine the effect of three factors on the escape rate, as shown in Table 4.

Table 2

Levels of the factors

Level	Factors		
	Temperature A [°C]	Wind speed B [m/s]	Fan inclination [°C]
1	30	2	15
2	40	3	30
3	50	4	45

Table 3

Results of the orthogonal experiments

No.	A	B	C	$\varphi$
1	50	4	30	64.2
2	30	3	45	50.7
3	40	3	30	42.2
4	50	3	15	58.6
5	40	4	45	66.1
6	40	3	30	34
7	50	3	45	59.3
8	40	4	30	64.2
9	40	2	45	35.2
10	50	2	30	47.1
11	30	2	30	12.6
12	30	3	15	10.9
13	40	2	15	28.5
14	30	4	30	20.7
15	40	4	15	30.4

Table 4

## ANOVA for response surface analysis

Difference source	Sum of squares	Df	Mean of squares	F	P-value
<b>Model</b>	4312.34	9	479.15	23.92	0.0014
<b>A</b>	2254.56	1	2254.56	112.54	0.0001
<b>B</b>	462.07	1	462.07	23.07	0.0049
<b>C</b>	859.05	1	859.05	42.88	0.0012
<b>AB</b>	20.25	1	20.25	1.01	0.3609
<b>AC</b>	382.20	1	382.20	19.08	0.0072
<b>BC</b>	210.25	1	210.25	10.50	0.0230
<b>Lack of fit</b>	66.55	4	16.64	0.49	0.7718
<b>Pure error</b>	33.62	1	33.62		

Values of "P Value" less than 0.0500 indicate model terms are significant. So, the regression model is reliable to optimize the escape rate of threshed rape mixture to cleaning sieve. The key factors affecting the escape rate are as follows: temperature, fan inclination, wind speed. Meanwhile, table 4 demonstrates that the interaction between temperature and fan inclination and between wind speed and fan inclination had significant effects on the anti-adhesion performance of threshed rape mixture. The best combination of parameters for the escape rate was obtained by the optimization of the regression model (software: Design-Expert 8.0.6), which was  $A_3B_3C_3$ . i.e. The temperature and air speed of the cyclone separator outlet were 50°C, 4 m/s, respectively and the fan inclination was 45°.

The above analysis shows that the hot airflow can effectively reduce the adhesion of the waste on the screen surface, while there was no 220V alternating current in the combine harvester when working in the field, so it is necessary to find a scheme to replace the electric heating. The effective work of output heat equivalent of diesel engine only accounts for 30~40% of the input heat equivalent and the rest of the heat is discharged into the air in the form of hot airflow of the radiator and exhaust, which causes heat loss and even more serious pollution to the environment. The waste heat recovery technology has been widely used in automobile, and its reliability and economy have been confirmed (Lin G. *et al.*, 1994). There are two modes of engine waste heat for heating: one is to use the heat of cooling water, the other is to use the heat of exhaust gas. Both of them could run without additional heating on the automobile, and the power consumption of the engine would not increase (Fen L. *et al.*, 2010). In order to save costs, the waste heat recovery technology has not been widely used in domestic harvesters. However, with the development of large-scale and intelligent combine harvesters, more and more combine harvesters begin to be equipped with air conditioning to provide a good working environment for farmers. The hot air cleaning system proposed in this paper requires high efficiency and low-cost heat source, so the feasibility analysis is carried out below. Radiator was considered as the heat source for "hot-airflow cleaning" firstly, the temperature and wind speed of radiator were measured when the engine was working in the field test, as shown in Fig.7, Table 5 and Table 6.



Fig. 7 - Field measuring

It can be seen that the temperature is from 47~51°C and wind speed ranged of 8~10 m/s, which indicate that the radiator can produce enough energy for the anti-adhesion between threshed rape mixture and cleaning sieve. Engine radiator is a good source of hot air, the next challenge is how to collect the hot air of radiator and import it into the cleaning room, which is not discussed here.

Table 5

Wind speed of radiator

Measuring points	Times[m/s]			Average
	1	2	3	
1	10.1	9.6	9.6	9.77
2	10.2	9.9	10.1	10.07
3	7.8	7.8	8.5	8.03
4	9.8	9.6	9.1	9.50
5	9.6	8.8	10.0	9.47

Table 6

Temperature of radiator

Measuring points	Times[°C]			Average
	1	2	3	
1	46.4	47.2	48.3	47.30
2	47.5	47.9	46.4	47.27
3	50.8	52.0	50.2	51.00
4	48.6	49.5	49.9	49.33
5	51.3	51.6	48.8	50.57

**CONCLUSIONS**

The adhesion interface model of wet sticky rape material and cleaning sieve surface was constructed. The force of wet sticky rape material on the circular screen surface was analysed and the mechanism of hot airflow on the adhesion interface was revealed. The analysis showed that the factors affecting the anti-adhesion performance were wind temperature, wind speed and fan inclination.

The single-factor experiments showed that hot airflow can effectively reduce the adhesion of wet sticky threshed rape mixture on the cleaning sieve. The escape rate is positively correlated with temperature and wind speed. When the fan inclination was 45°, the escape rate reached the peak. In addition, the proper temperature of ventilator was 30-50°C. The proper wind speed and inclination of ventilator were 2-4 m/s and 15-45°, respectively. The interaction between parameters of the fan was studied by orthogonal experiments. The results illustrated that the interaction between temperature and fan inclination had significant effects on the anti-adhesion performance of threshed rape mixture. The optimal working condition of ventilator occurred at a temperature of 50°C, a wind speed of 4 m/s and when fan inclination was 45°. Through the field test, the sufficient temperature and wind force for the anti-adhesion between moist threshed rape mixture and cleaning sieve could be provided by the engine radiator, which is a good source of hot air for “hot-airflow cleaning”.

**ACKNOWLEDGEMENT**

This research was financially supported by National Natural Science Foundation of China under Grant (31671590).

## REFERENCES

- [1] Bhupendra M.G.; Manish P.; Rohit N.; Gopal C., (2018), Calibration of discrete element model parameters: soybeans. *Computational Particle Mechanics*, vol.6, no.1, pp.3-10;
- [2] Chen C., Fu J. Tang X.L., Chen Z., Ren L.Q., (2019), Heating anti-adhesion experiments of jitter plate of rice harvesting machinery, *Transactions of the CSAE*, no.50, pp.110-118;
- [3] Chen X.M., Zhao Y.M., Zhu H., Gao Q.Y., (2003), Study on adhesive mechanism in screening fine moist material, *Applied Jiangsu Coal*, no.4, pp.38-40;
- [4] Chen S.F., Wang J.J., Jin Y.H., (2018), Model of Particle Deposition and Adhesion on Blade Surface of Flue Gas Turbine, *The Chinese Journal of Process Engineering*, vol.18, no.3, pp.447-453;
- [5] Chen, X.M.; Zhao, Y.M.; Zhu, H.; Gao, Q.Y.(2002), Adhesive Model of Moist Fine Material, *Journal of China University Mining & Technology*, vol.31, no.5, pp.70-73;
- [6] Chen X., Wu C.Y., Zhang M.,(2018), Development status and trend analysis of rapeseed combine harvester in China, *Journal of Chinese agricultural mechanization*, vol.39, no.10, 28-31;
- [7] Du H.Y., Wang Y.G., Zhang H., Sun H.B., Zhang G.H., (2019), Current status and development trend of centrifugal fan in cleaning device of combine harvesters, *Journal of Chinese agricultural mechanization*, vol.40, no.7, pp.73-77;
- [8] Fen L.M., (2010), *Theoretical and experimental study of waste heat recovery of engine based on Rankine cycle*, 基于朗肯循环的发动机废热回收理论与试验研究, PhD dissertation, Tianjin University, China;
- [9] Hiraku T., Yang Y.,(2017), Influence of surface roughness and temperature on wheel-rail adhesion in wet conditions, *Foreign rolling stock*, vol.54, no.4, pp.38-42;
- [10] Liu C.Y., Wang S.S., Shi Q.X. Gen L.X., Yang F., (2018), Design of peanut combine harvester cleaning system test bench, *Journal of Agricultural Mechanization Research*, vol.40, no.12, pp.91-95;
- [11] Liu G.M., Li J.Q., Zou M., Li Y.W., Tian X.M., (2008), Feature and the characteristic of sliding resistance reduction of the earthworm's non-smooth surface, *Transactions of the CSAE*. Vol.24, no.12, pp.62-65;
- [12] Liu Q., Qi C.L., Ma W.B., Hu C., Li F.,(2019), Experimental study of adhesion between deep-sea sediment and metal surface, *Rock and soil mechanics*, vol.40,no.2, pp.701-708;
- [13] Lin G.P., Yuan X.G., Mei Z.G., (1994): The feasibility study of the waste heat air-conditioning system for automobile, *Journal of Thermal Science*, vol.3, no.2, pp.126-129;
- [14] Li Y.M., Ma Z., Xu L.Z., (2012), Adhesion Property between Rape Mixture and Bionic Screen Matrix, *Transactions of the CSAE*, Vol.43, no.2, pp.75-78;
- [15] Ma Z., Li Y.M., Xu L.Z., (2011), Testing and analysis on rape excursion components characteristics in floating, friction and wettability, *Transactions of the CSAE*, vol.27, no.9, pp.13-17;
- [16] Ma Z., li Y.M., Xu L.Z., (2011), Micro flow field on adjacent screen of bionic non-smooth cleaning screen, *Transactions of the CSAE*, vol.42, pp.74-77+9;
- [17] Ning X.J., Jin C.Q., Yin X., Liu P., Li Q.L., (2018), Research status and development trend of air-and-screen cleaning device for cereal combine harvesters, *Journal of Chinese agricultural mechanization*, Vol.39, no.9, pp.05-10;
- [18] Panasiewicz M., Sobczak P., Mazur J., Zawi'slak K., Andrejko D., (2012), The Technique and Analysis of the Process of Separation and Cleaning Grain Materials, *Journal of Food Engineering*, vol.109, no.3, pp.603–608;
- [19] Peng X.Y., Ma C.D., Ji J.X., Li J., (2020), Underwater adhesion mechanisms and biomimetic study of marine life, *Applied Tribology*, pp.1-28;
- [20] Ren L.Q., (2011), *Soil Adhesion Mechanics*, Beijing, China Machine Press;
- [21] Yang X.D., Chai X.L., Cong Q., Ren L.Q., (2000), Adhesion law and adhesion mechanism analysis for tub, *Applied Natural Science Journal of Jilin University Technology*, no.4, pp.66-69;
- [22] Zhang M., Wu C.Y., Jin M., Mu S.L., Liang S.N., Tang Q., (2019), Effects of harvesting method and date on yield loss and seed quality of rapeseed, *Oil Crop Science*, vol.4, no.3, pp.166-174;
- [23] Zuber J, Eibs M., (1995), Screening of difficult materials on BIVITEC screens with flip-flow systems, *Aufbereitungs-Technic*, vol.36, no.7.
- [24] Fei Liu, Dapeng Li, Tao Zhang, Zhen Lin, Manquan Zhao, (2020), Analysis and calibration of quinoa grain parameters used in a discrete element method based on the repose angle of the particle heap, *INMATEH - Agricultural Engineering*, Volume 61 / No. 2 / pp: 77-86

# ANALYSIS OF VISUAL NAVIGATION EXTRACTION ALGORITHM OF FARM ROBOT BASED ON DARK PRIMARY COLOUR

## 基于暗原色的农田机器人视觉导航提取算法分析

Zhongkun Hou <sup>1</sup>

Department of Mechatronics and Information Engineering, Sichuan College of Architectural Technology,  
Deyang City, Sichuan Province / China

\*Tel: 15963582573; E-mail: [akun501@163.com](mailto:akun501@163.com)

DOI: <https://doi.org/10.35633/inmateh-62-23>

**Keywords:** dark primary colours, farmland, robot, visual navigation, extraction algorithm

### ABSTRACT

With the development of information technology, precision agriculture has also ushered in new development prospects. The use of farm robots to accurately identify the navigation path is of great significance for achieving accurate positioning of agriculture. In this study, when analysing the extraction algorithm of farm robot visual navigation based on dark primary colours, a method for pre-processing and edge detection of farmland images based on dark primary colours is proposed. At the same time, the least square method of linear fitting is used for the navigation path of agricultural robot, and then the fitting program is executed. On this basis, combined with the actual situation of outdoor farming and greenhouse cultivation of crops, the effectiveness of the robotic visual navigation extraction algorithm was verified. The research results show that for any form of farmland cultivation, image extraction technology based on dark primary colours can effectively distinguish between soil and crops, and the visual navigation path of farm robots fitted with least squares is basically linear, which is consistent with the commonly used crops for farm planting. The legal route is basically the same, and then the effectiveness of the extraction algorithm is verified. It is hoped that this study will provide a certain reference and reference for the analysis of the field navigation robot visual navigation extraction algorithm based on dark primary colours.

### 摘要

随着信息技术的发展, 精准农业也迎来了新的发展前景。使用农业机器人准确识别导航路径对实现农业的精确定位具有重要意义。本文在分析基于深色原色的农用机器人视觉导航提取算法的基础上, 提出了一种基于深色原色的农田图像预处理和边缘检测方法。同时, 线性拟合的最小二乘法用于农用机器人的导航路径。执行拟合。在此基础上, 结合野外耕作和温室大棚栽培的实际情况, 验证了机器人视觉导航提取算法的有效性。研究表明, 对于任何形式的农田耕作, 基于深色原色的图像提取技术都可以有效地区分土壤和农作物, 配备最小二乘法的农场机器人的视觉导航路径基本上是线性的, 这与通常的做法是一致的。用于农作物种植的农作物。合法路径基本相同, 然后验证了提取算法的有效性。希望这项研究为基于深色原色的野外导航机器人视觉导航提取算法的分析提供一定的参考和借鉴。

### INTRODUCTION

Agriculture is the basis for human survival, an important guarantee for human food and clothing, and plays an important role in economic prosperity and social stability. With the development of social economy, the development of agricultural modernization is steadily advancing. One of the most important signs of agricultural modernization is the increasing degree of agricultural mechanization (Teshome and Degu, 2019). With the rapid development of information technology, agricultural mechanization is moving to the next new development stage, namely, agricultural precision. The so-called precision agriculture refers to relying on information technology and computer technology such as artificial intelligence to achieve the precise development of agriculture. Among them, farmland cultivation is the most important and basic part of agriculture, and is a part of the vigorous development of precision agriculture (Srbnovska and al., 2015). Machine vision has been widely used in the development of precision farming technology. Field robot is of great significance for accurate identification of navigation path and accurate positioning.

---

<sup>1</sup> As. PhD. Lec. Zhongkun Hou

Machine vision refers to the use of cameras and other sensors to collect images, and to simulate human visual functions through image processors. After completing a series of image acquisition and simulation function operations, extract and understand relevant information from the images, and finally use the relevant information for monitoring and control (Sun T.H., Tien F.C. and Tien F.C., 2016). Farm robot visual navigation is relatively low in cost and easy to operate. It has no special requirements for operators and agricultural scale, and has good applicability, so it is widely used in farm cultivation. In addition, in the visual navigation of farm robots, the extraction of navigation lines is the most critical content, which is the key to determine the navigation accuracy and speed of farm robots.

In this study, when analysing the field navigation robot visual navigation extraction algorithm based on dark primary colours, a method for pre-processing and edge detection of farmland images based on dark primary colours is proposed. At the same time, the least square method in linear fitting is used to extract the navigation lines. Farm robot navigation path to fit. On this basis, combined with the actual planting conditions of outdoor farmland cultivation and greenhouse cultivation of crops, the effectiveness of the robot visual navigation extraction algorithm was verified.

The innovation of this research lies in the use of dark primary colour prior theory for grayscale pre-processing of farmland images, which can quickly perform grayscale processing on the image, and can effectively distinguish crops and soil in farmland images. At the same time, the research also focused on the practical application of extraction algorithms, combining the method with the actual farmland cultivation, and by combining the actual conditions of outdoor farmland cultivation and greenhouse cultivation of crops, the effectiveness of the robotic visual navigation extraction algorithm was verified.

This research mainly includes four parts. The first part is the application of the prior theory of dark primary colours by domestic and foreign scholars and the research of robot visual navigation. The second part is the research of the field navigation robot visual navigation extraction algorithm based on the dark primary grayscale processing, including the use of dark primary colour images for grayscale pre-processing and edge detection, and the least square method in linear fitting to extract the navigation path. The third part is to verify the effectiveness of the robotic visual navigation extraction algorithm in combination with the actual planting conditions of outdoor farmland cultivation and greenhouse cultivation.

Aimed at the inaccuracy of the Gaussian algorithm in the dark primary colour prior theories, Li A *et al.* proposed a method to improve the image clarity based on the dark channel, and verified this by analysing the factors affecting the image colour shift. Regarding the effectiveness of the method, the results show that this method can effectively solve the problem of image migration in light-coloured areas (Li A., Fang Z and Mi B., 2018). In the study of coal dust and smoke images, Mingben D.U *et al.* proposed an image enhancement algorithm based on dark primary color prior theory. Based on the image degradation model, the image denoising technology is realized. The experimental results show that the image denoising technology can optimize and enhance the image quality. (Mingben D.U., *et al.*, 2015). Xiao JS *et al.* proposed an image denoising algorithm based on the dark primary colour prior theory to overcome the colour distortion and halo effect of the sky, accurately estimate the overall atmospheric light in the sky area, and use the median filter technology to obtain detailed Edge information to effectively estimate the transmission image (Xiao J.S. *et al.*, 2017). Liu H.B. *et al.* proposed an image defogging method based on the a priori theory of dark primary colours, and changing the grey value of the image through linear mapping, thereby improving the medium transmittance in foggy and large sky areas. This method can achieve faster image processing speed (Liu H.B., Yang J. and Wu Z.P., 2015). When studying the single image denoising algorithm, Alharbi EM *et al.* proposed an atmospheric light estimation algorithm based on the dark primary colour prior theory. By improving the attenuation image contrast, etc., the effectiveness of the algorithm in estimating atmospheric light was verified (Alharbi E.M., Ge P. and Wang H., 2016).

When studying the visual navigation of autonomous mobile robots, Kurashiki K. *et al.* proposed an image-based road boundary tracking control law, and designed an interactive model of robot motion and image features. This method reduces a priori information and improves the map scalability (Kurashiki K, *et al.*, 2015). Rômulo T Rodrigues and others proposed a method of improving robot visual positioning based on artificial potential field when researching robot visual navigation, which connects the features in robot visual images with potential energy to promote the robot to advance. The research results show that this method has good performance (Rômulo T. Rodrigues, *et al.*, 2018). Phalak Y. *et al.*, when studying robot navigation, combined with the parabolic geometry in mathematical tools, proposed a method of navigation using image processing, and finally proposed a system expansion based on the actual experimental results

of the combination of static and dynamic (Phalak Y. et al., 2018). Kamaev A.N. et al. used the point cloud computing algorithm and the algorithm to establish the point cloud correspondence to provide navigation data for the aircraft when studying the navigation problem of the automatic launch vehicle. The test results show that this method can make the aircraft always follow the navigation trajectory (Kamaev A.N. and Karmanov D.A., 2018). When studying the visual navigation path of coloured cotton robots, Li D. et al. proposed a field navigation path extraction method based on horizontal spline segmentation, and obtained the connected domain of cotton valley by detecting the connected domain in the horizontal spline. Planning the navigation path for the coloured cotton robot finally verified the accuracy and effectiveness of the method (Li D., Xu S. and Zheng Y., 2017). Kumar B. et al. proposed a robot path navigation method using RF communication and wireless audio and video transmission when studying the mobile navigation of autonomous robots. By installing a navigation embedded system inside the robot, the robot can help the robot to achieve autonomous mobile navigation. The actual test verifies the effectiveness of the method (Yang H., Gao L. and Tang N., 2019). Delaune J. et al. proposed a vision-assisted inertial navigation system for autonomous space robot landing when studying the running path of autonomous space robot. Image processing is performed through data fusion to accurately control the navigation path of space robot (Delaune J. et al., 2016).

It can be seen that the relevant research at home and abroad mainly includes the application of dark primary colour prior theory in image processing and the application of related methods in robot navigation (Wang B., He J.L., Zhang S.J. and Li L.L., 2020). Among them, the dark primary colour prior theory is mainly used in image processing, and robot visual navigation also mainly depends on the research on related image features. The related researches are less concerned with the navigation research of farm robots, so this study analyses and studies the visual navigation of farm robots based on dark primary colours.

## MATERIALS AND METHODS

### Dark primary grayscale processing

In the process of visual navigation of farm robots, in order to quickly and accurately extract image features, it is necessary to pre-process the images in visual navigation. In general, for the visual navigation of farm robots, one of the main problems is that the farm environment is complex and changeable, the colours are complicated, the farm contains a lot of colour image information, and the amount of related data is huge. (Tai J.J., Li H.T., Du Y.F., Mao E.R., Zhang J.N. and Long X.J., 2020) Extracting relevant image information and pre-processing it is beneficial to quickly extract navigation information, so that farm robots can better perform farm operations.

In farmland images, the colours of most crops are more vivid colours such as green, and there are fewer crops that are darker. (Guo Y.B., Zhang X.G. and Zhang C., 2020). Therefore, according to the principle of dark primary colours, if the image includes objects with bright colours or bright surfaces, it also includes objects or surfaces with darker colours, for the three RGB values in the images of these objects or surfaces, there must be a channel with a very small value, and the corresponding dark primary colour image is also greyer. Therefore, for crop images or soil images in farmland, there must be a kind of grey state. In order to promote the application of farm robot visual navigation in agricultural operations, this study grey-scales the dark primary colours of the corresponding farm road images based on the grey-levelling rules and the principle of dark primary colours. First, a mathematical method is used to define the dark channel.

The dark channel of each pixel of the farmland image can be expressed as follows.

$$I^{dark}(x, y) = \min_{c \in \{r, g, b\}} I^c(x, y) \quad (1)$$

Among them,  $I^{dark}(x, y)$  represents the dark primary colour channel of the pixel coordinate  $(x, y)$ ;  $I^c(x, y)$  is the colour channel of the pixel coordinate  $(x, y)$ . On this basis, traverse all the pixels included in the farmland image  $I$ , and compare the size of the three colour channel values of each pixel; the three colour channels can be expressed as:  $I^r(x, y)$ ,  $I^g(x, y)$ ,  $I^b(x, y)$ , before comparing the three colour channel values. It is necessary to calculate the grey value of each pixel according to formula (1), and finally obtain the dark primary grey image  $I_{dark}$ . In order to evaluate the image processing effect in the visual navigation process of farm robots, MATLAB is used to process farm images, and the corresponding image running time and normalized histogram characteristics are obtained, as shown in Figures 1 and 2.



**Fig. 1 - Gary scale conversion results**

Figure 1 is a comparison between an unprocessed image and a grey-scale image, where Figure 1(a) is the original image of a typical crop, Figure 1(b) is a dark-primary grey-scale image, and Figure 1(c) is the image after 2G-R-B grayscale processing. It can be seen from the figure that the green crops and soil can be clearly distinguished from the original image of typical crops. The dark primary colour grayscale image processing time is only 0.532s, and compared to the original image, it can also be clearer. Crop and soil are distinguished from it. 2G-R-B grayscale processing image takes longer time than dark primary grayscale processing image, which is 4.267s. Compared with the original crop image and gray processing image, the difference between soil and green crop is not obvious. Although the two can be distinguished to some extent, the performance of the green crops is not obvious enough, and the reflection is not accurate enough.

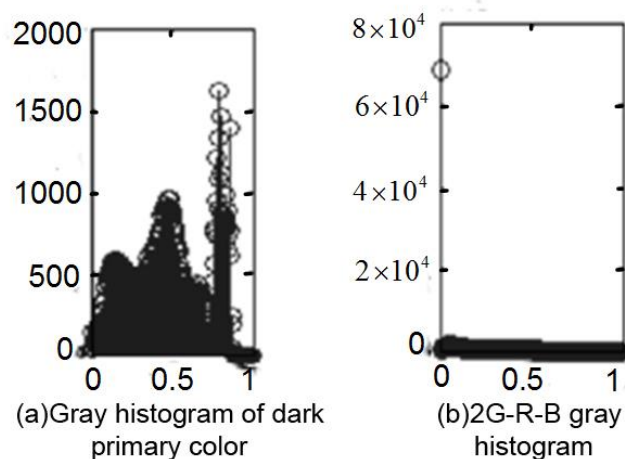


**Fig. 2 - Histogram features of grey level processing**

Figure 2 is a comparison of the normalized histogram features of agricultural image grey-scale processing. Figures 2(a) and 2(b) are the histogram characteristics of dark primary grayscale processing and the histogram characteristics of 2G-R-B grayscale processing, respectively. It can be seen from the figure that the histogram characteristics of agricultural crop images processed by the dark primary grayscale are more obvious, there are more obvious peaks and troughs, and they range from 0 to 2000; while for the 2G-R-B grayscale processing, as far as crop histograms are concerned, their characteristics are relatively insignificant, and there are no obvious fluctuations. The maximum value is between  $6 \times 10^4$  and  $8 \times 10^4$ , while the remaining small disturbances are mostly concentrated around zero.

### **Farmland image edge detection based on dark primary grayscale processing**

On the basis of grey-scale processing of crop images, edge detection is performed on the images in a derivation manner. For the crops in the farmland, the edges between them and the farmland background can reflect the trend of the crops to a certain extent. Therefore, the detection of the edge parts of the crops is helpful for the farmland robot to extract important navigation feature points, so as to better perform visual navigation. This study takes a binary image as an example.

The biggest feature of the edge of a binary image is that the pixel value along the edge of the image always remains the same, while the pixel value perpendicular to the edge of the image changes.

In general, the differentiation mainly uses differential algorithms, and for the processing of digital images, differential approximation is often used to solve differential operations. Commonly used edge detection differential operators include first-order differential operators and second-order differential operators. Among them, the binary image with different edges and its first derivative curve are shown in Figure 3. It can be seen from the figure that all different image forms obtain the maximum value of the first derivative at the edge, and edge detection can be performed on the crop image on this basis. This is the principle of the first-order differential operator used for edge detection, namely the correlation between the image gradient and the first derivative is used for detection.

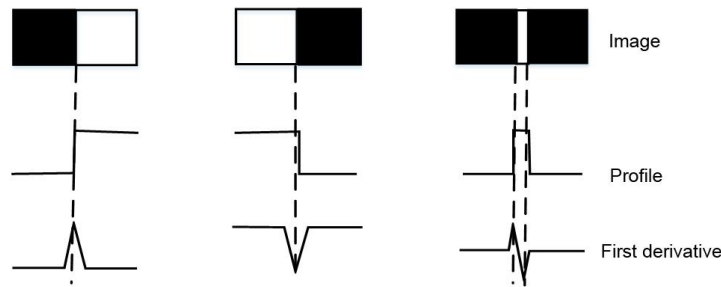


Fig. 3 - Image edge type and its first derivative curve

Assuming that the continuous image function is  $f(x, y)$ , the gradient at the point  $(x, y)$  can be defined as shown in the following formula.

$$\nabla f(x, y) = \left[ \frac{\partial f(x, y)}{\partial x} \quad \frac{\partial f(x, y)}{\partial y} \right]^T = [G_x \quad G_y]^T \tag{2}$$

Where  $G_x$  is the gradient in the  $x$  direction;  $G_y$  is the gradient in the  $y$  direction. Further, the gradient modulus corresponding to the gradient vector can be expressed by Euclidean distance, as shown in the following formula.

$$|G(x, y)| = \sqrt{G_x^2 + G_y^2} \tag{3}$$

Similarly, the gradient modulus can also be expressed as a checkerboard distance as follows.

$$|G(x, y)| = |G_x| + |G_y| \tag{4}$$

The gradient direction corresponding to the gradient vector can be expressed as follows.

$$\theta(x, y) = \arctan\left(\frac{G_y}{G_x}\right) \tag{5}$$

The main idea of the first-order differential operator to detect the edge of the crop image is to set a suitable modulus threshold. If there is a gradient modulus value in a certain part of the image that exceeds this threshold, you can set the pixel of the image as the edge point. If otherwise, it belongs to a non-edge point, and the related expression is shown in the following formula.

$$g(x, y) = \begin{cases} 1, & G(x, y) > T \\ 0, & \text{Others} \end{cases} \tag{6}$$

When performing edge detection on farm crop images, several differential operators are mainly used, namely Roberts operator and Sobel operator.

Among them, the Roberts operator belongs to one of the first-order differential operators, and its main idea is to use the difference to approximate the gradients  $G_x$  and  $G_y$  in the  $x$  direction and the  $y$  direction, and the related expressions are as follows.

$$\begin{aligned} G_x &= f(x+1, y+1) - f(x, y) \\ G_y &= f(x+1, y) - f(x, y+1) \end{aligned} \tag{7}$$

The Roberts operator includes corresponding convolution templates, as shown in Table 1 and Table 2.

Table 1

Convolution template 1 of Roberts operator

-1	0
0	1

Table 1 is a convolution template of Roberts operator. Among them, the two diagonal numbers are 0, 0, and -1, 1. When using Roberts operator to detect edge of farm crop image, calculating the gradient amplitude is actually calculating the adjacent pixel value on the diagonal difference between. The same is true for another convolution template of Roberts operator. It can be seen from Table 2 that the convolution template is a transpose of another convolution template, and the two diagonal numbers are 1, -1, and 0, 0, respectively. Therefore, Roberts operator can be used to detect vertical and horizontal edges of crop images, and then extract image edge information.

Table 2

Convolution template 2 of Roberts operator

0	-1
1	0

The Sobel operator is also one of the first-order differential operators, and the gradients  $G_x$  and  $G_y$  in the x direction and the y direction are approximated by the difference as shown in the following formula.

$$\begin{aligned}
 G_x &= [f(x-1, y-1) + 2f(x, y-1) + f(x+1, y-1)] \\
 &\quad - [f(x-1, y+1) + 2f(x, y+1) + f(x+1, y+1)] \\
 G_y &= [f(x+1, y-1) + 2f(x+1, y) + f(x+1, y+1)] \\
 &\quad - [f(x-1, y-1) + 2f(x-1, y) + f(x-1, y+1)]
 \end{aligned}
 \tag{8}$$

The convolution templates corresponding to the Sobel operator are shown in Table 3 and Table 4.

Table 3

Convolution template 1 of Sobel operator

-1	-2	-1
0	0	0
1	2	1

Table 3 is a convolution template of the Sobel operator. The convolution operator mainly includes -2, -1, 0, 1, and 2, and the three 0s are arranged horizontally. Table 4 is another convolution template of Sobel operator, which is transposed from template 1. The convolution operator in this template also includes -2, -1, 0, 1, and 2, the difference is that the operator's three 0s are arranged vertically. In the edge detection of farm crop images, the Sobel operator has a better effect when detecting the oblique edges of the image, and can effectively reduce or even suppress the image noise.

Table 4

Convolution template 2 of Sobel operator

-1	0	1
-2	0	2
-1	0	1

In order to enable the field robot to realize automatic navigation during visual navigation, the navigation curve is fitted on the basis of extracting corresponding navigation feature points. Generally, the seeding method is mostly used in agricultural planting, and its path is basically straight or straight in the local range of the direction of agricultural machinery. Therefore, the least square method in linear fitting is used in this study to achieve navigation fitting. Assuming that the coordinate of the navigation feature point is  $(x_i, y_i) (i=1, 2, \dots, n)$ , the fitting equation can be obtained as shown in the following formula.

$$f(x) = ax + b \quad (9)$$

Among them,  $a$  and  $b$  both represent fitting coefficients. The residual sum of squares of the fitted equation is further obtained as shown in the following formula.

$$E = \sum_{i=1}^n [f(x_i) - y_i]^2 = \sum_{i=1}^n (ax_i + b - y_i)^2 \quad (10)$$

To minimize the value of  $E$ , the fitting coefficient  $a$ ,  $b$  needs to satisfy the following conditions.

$$\begin{cases} \frac{\partial E}{\partial a} = 2 \sum (ax_i + b - y_i) x_i = 0 \\ \frac{\partial E}{\partial b} = 2 \sum (ax_i + b - y_i) = 0 \end{cases} \quad (11)$$

Further obtain the result shown in the following formula, and find the  $a$ ,  $b$  to obtain the corresponding navigation line equation.

$$\begin{bmatrix} \sum_{i=1}^n x_i^2 & \sum_{i=1}^n x_i \\ \sum_{i=1}^n x_i & n \end{bmatrix} \begin{bmatrix} a \\ b \end{bmatrix} = \begin{bmatrix} \sum_{i=1}^n x_i y_i \\ \sum_{i=1}^n y_i \end{bmatrix} \quad (12)$$

## RESULTS

Real agricultural robots play an important role in the visual navigation effect measurement of agricultural crops. Based on the grayscale processing of farmland crop images, the first-order differential operator is used for edge detection and feature point extraction to obtain the visual navigation effect of farm robots when planting crops in outdoor farmland and the visual navigation effect of farm robots when planting crops in Dapeng. The experiment also analyzes the measurement results of the agricultural robot in the corresponding crop vision navigation path.



Fig. 4 - Real agricultural robots

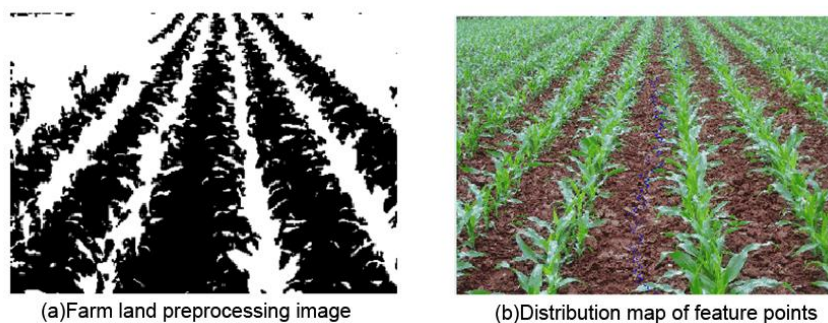
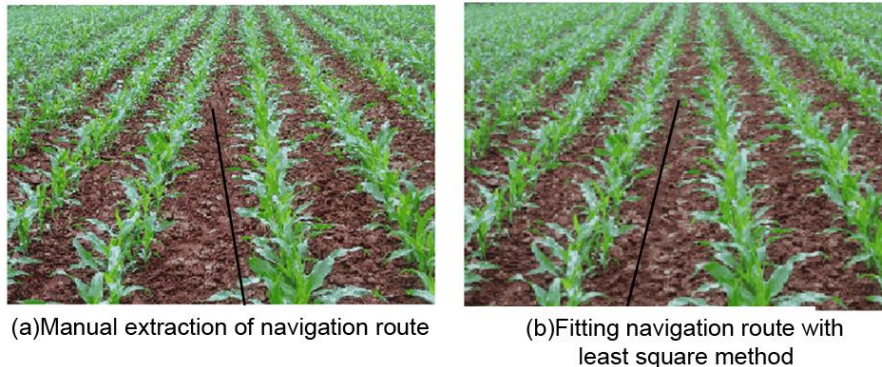


Fig. 5 - Processing of farmland crop lines

Figure 5 is the relevant situation of the green crops planted in a certain outdoor farmland. Figure 5(a) is the result of the dark primary grayscale pre-treatment of the green crops planted in the original farmland. It can be seen from the figure that in the image of the dark primary grayscale processing, the distinction between soil and green crops is more obvious, where green plants become black after grayscale processing,

and the soil becomes white after grayscale processing. On the basis of the grey processing of dark primary colours, the navigation feature points are extracted by linear fitting, and the distribution map of the navigation feature points as shown in Figure. 5(b) is obtained. As can be seen from the figure, most feature points fall in the navigation within the path. It is more in line with the straight path of the seeding method commonly used when planting crops.



**Fig. 6 - Comparison of navigation of farmland crops**

After extracting feature points from outdoor farmland plants, the least square method was used to extract the navigation route, and compared with the result of manually extracting the navigation route, the results shown in Figure 6 were obtained, both Figure 6(a) and Figure 6(b). The same piece of outdoor farmland is planted with the same green crops. Among them, Figure 6(a) is a manually extracted navigation route. As can be seen from the figure, the navigation line is basically located on the navigation path, but there are some routes that deviate from the navigation path. Figure 6(b) is the navigation route obtained by fitting the least squares method based on the grey processing of dark primary colours. As can be seen from the figure, compared to the manually extracted navigation line, the route is basically the same as the actual sowing method used in sowing is consistent with the navigation path, which is located at the edge of two rows of crops. This shows that using the least square method of linear fitting to determine the visual navigation path of the farm robot has a good effect.

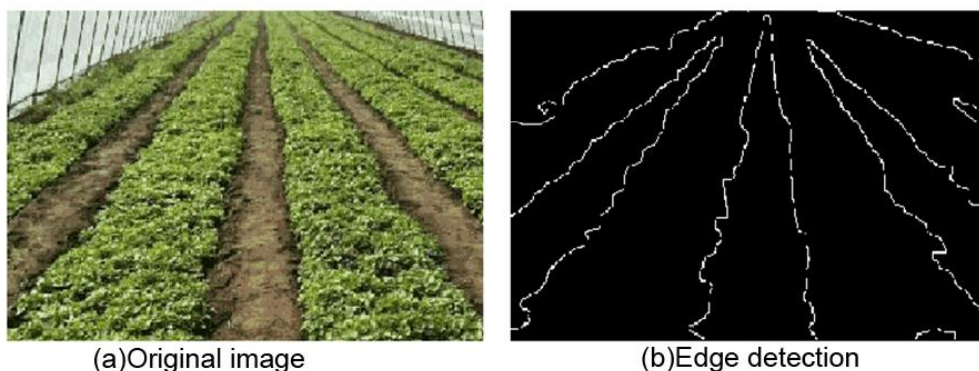


**Fig. 7 - Comparison of original farmland image and edge detection results**

Figure 6 is the relevant situation of the green crops planted in a greenhouse, and Fig. 7(a) is the crop image taken in the greenhouse environment. It can be seen from the figure that the light intensity in the greenhouse environment is very different from that in the normal environment. Compared with the light in the normal environment, the light in the greenhouse environment is darker, and the soil of the crops is also darker, so the brightness of the crop colour is closer to the soil colour. This kind of environment brings great difficulties to image recognition, which will directly affect the accuracy of image recognition during the navigation of agricultural machinery. This is also the focus of this research. Under the visual effect of agricultural robots, the edge detection results in the greenhouse are shown in Figure 7(b).

As can be seen from Figure 7(b), through edge detection, the image edge extraction algorithm based on dark primary colours proposed in this study successfully identified the boundary between crops and planting soil clearly, and this boundary is strict. According to the law of vision, the real display is carried out. As the distance of vision increases from near to far, the boundary between crops and planting soil gradually approaches. From this result, this study proposes that the image processing technology based on dark primary colour images can normally simulate the visual effect during the recognition process, and on this basis, it can further navigate the trajectory of the agricultural robot.

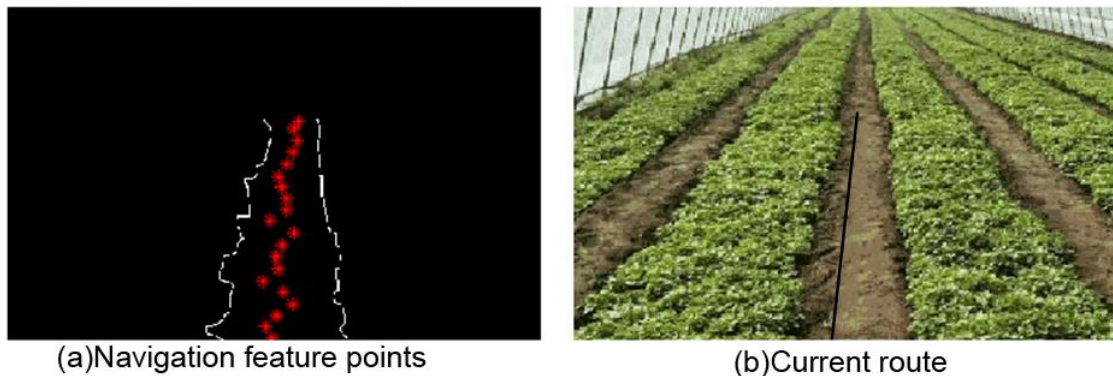


**Fig. 8 - Navigation lines extracted when the row spacing of crops is wide**

Figure 8 is the result of using linear fitting to route the crops in the greenhouse. The feature points need to be extracted before navigation. Among them, Figure 8(a) represents the feature points extracted by linear fitting at a wide line spacing, and only one line is used as the research object when extracting feature points. In order to distinguish from the results of edge detection, red is used when extracting feature points line. It can be seen from the figure that the feature points extracted by linear fitting are mostly distributed on the same straight line, which is basically consistent with the path when crops are planted by the seeding method in agricultural planting. Between the straight line where the feature points are located and the line spacing edge detection line there is a more obvious distinction. Figure 8(b) represents the visual navigation results of the farmland robot based on feature point extraction. It can be seen from the figure that the robot is completely advancing along the navigation line when performing agricultural planting operations, and is consistent with the straight line of the seed planting. This verifies the effectiveness of linear fitting for feature point extraction and farm robot visual navigation.

## CONCLUSIONS

In the visual navigation of the farm robot, extracting the navigation line is the most critical content, which determines the navigation accuracy and speed of the farm robot. Based on the analysis of vision navigation circuit of field robot, a vision navigation extraction algorithm based on dark primary color is proposed in this paper. After the dark primary colour grayscale processing of the farmland plant image, the image is edge detected, and the least square method in linear fitting is used to extract the farmland navigation feature points, and then the robot visual navigation path is formed. On this basis, combined with the actual situation of outdoor farming and greenhouse cultivation of crops, the effectiveness of the robotic visual navigation extraction algorithm was verified. The results show that the crop images of outdoor crops processed by dark primary colours are more clearly distinguished, and most of the feature points fall within the navigation path. Compared with the manually extracted navigation lines, the least square method is used to fit the farm robot the visual navigation route is basically the same as the navigation method of the sowing method used in actual planting. The navigation route is located at the edge of two rows of crops. When the crops are planted in the greenhouse, the edge detection effect of the crop image is relatively good, the crops and the soil are clearly separated, and the linearly fitted robot visual navigation line is basically a straight line. On the whole, the visual navigation route of the farm robot based on the dark primary colours is basically the same as the conventional planting route of the seeding method used in agricultural cultivation. This study verifies the effectiveness of the field navigation robot visual navigation extraction algorithm based on dark primary colours, but its wide applicability needs further study.

## REFERENCES

- [1] Alharbi E.M, Ge P., Wang H., (2016), A Research on Single Image Dehazing Algorithms Based on Dark Channel Prior. *Journal of Computer and Communications*, Vol.04, Issue 2, pp.47-55, USA;
- [2] Delaune J, Le Besnerais G, Voirin T., (2016), Visual-inertial navigation for pinpoint planetary landing using scale-based landmark matching. *Robotics & Autonomous Systems*, Vol.78, pp.63-82. Netherlands;
- [3] Guo Y.B., Zhang X.G., Zhang C., (2020), Adaptability test of dry farming tillage technique in northern China and study of key techniques. *INMATEH Agricultural Engineering*, Vol.61, Issue 2, pp. 273-280, Romania;
- [4] Kamaev A.N., Karmanov D.A., (2018), Visual navigation of an autonomous underwater vehicle based on the global search of image correspondences. *Computer Optics*, Vol.42, Issue 3, pp.457-467. Russia;
- [5] Kurashiki K., Aguilar M., Soontornvanichkit S., (2015), Visual Navigation of a Wheeled Mobile Robot using Front Image in Semi-Structured Environment. *Journal of Robotics and Mechatronics*, Vol.27, Issue 4, pp.392-400. Japan;
- [6] Li A., Fang Z., Mi B., (2018), An Improved Defogging Algorithm Based on Dark Colour Theory Combined with Self-Adaptive Threshold Mechanism. *Journal of Control Science & Engineering*, Issue 2, pp.1-10, USA;
- [7] Li D., Xu S., Zheng Y., (2017), Navigation Path Detection for Cotton Field Operator Robot Based on Horizontal Spline Segmentation. *International Journal of Information Technology & Web Engineering*, Vol.12, Issue 3, pp.28-41, USA;
- [8] Liu H.B., Yang J., Wu Z.P., (2015), A fast single image dehazing method based on dark channel prior and Retinex theory. *Zidonghua Xuebao/Acta Automatica Sinica*, Vol.41, Issue 7, pp.1264-1273. China;
- [9] Mingben D.U., Lichao C., Lihu P., (2015), Enhancement algorithm for fog and dust images in coal mine based on dark channel prior theory and bilateral adaptive filter. *Journal of Computer Applications*, Vol.35, Issue 5, pp.1435-1438, China;
- [10] Phalak Y., Charpe G., Paigwar K., (2018), Omnidirectional Visual Navigation System for TurtleBot Using Paraboloid Catadioptric Cameras. *Procedia Computer Science*, Vol.133, pp.190-196, Netherlands;
- [11] Rômulo T. Rodrigues, Basiri M, Aguiar A.P., (2018), Feature Based Potential Field for Low-Level Active Visual Navigation. *Third Iberian Robotics Conference*, Vol.693, pp.791-800, Switzerland;
- [12] Srbínovska M., Gavrovski C., Dimcević V., (2015), Environmental parameters monitoring in precision agriculture using wireless sensor networks. *Journal of Cleaner Production*, Vol.88, Issue 1, pp.297-307. Netherlands;
- [13] Sun T.H., Tien F.C., Tien F.C., (2016), Automated thermal fuse inspection using machine vision and artificial neural networks. *Journal of Intelligent Manufacturing*, Vol.27, Issue 3, pp.639-651, Netherlands;
- [14] Tai J., Li H.T., Du Y.F., Mao E.R., Zhang J.N., Long X.J., (2020), Rapid design of maize ear harvester header based on knowledge engineering. *INMATEH - Agricultural Engineering*, Vol.61, Issue 2, pp.263-272, Romania;
- [15] Teshome F.B., Degu Y.M., (2019), Design of Combined Press Tool for the Manufacturing of Rice Thresher Blade (Case Study at Amhara Agricultural Mechanization and Food Science Research Centre-Ethiopia). *International Journal of Engineering Science*, Vol.3, Issue 4, pp.90-107, England;
- [16] Wang B., He J.L., Zhang S.J., Li L., (2020), Non-destructive testing of soluble solids content in *Cerasus humilis* using visible / near-infrared spectroscopy coupled with wavelength selection algorithm. *INMATEH Agricultural Engineering*, Vol.61, Issue 2, pp.251-262, Romania;
- [17] Xiao J.S., Gao W., Zou B.Y., (2017), Image Dehazing Based on Sky-Constrained Dark Channel Prior. *Tien Tzu Hsueh Pao/Acta Electronica Sinica*, Vol.45, Issue 2, pp.346-352, China;
- [18] Yang H., Gao L., Tang N., (2019), Experimental Analysis and Evaluation of Wide Residual Networks Based Agricultural Disease Identification in Smart Agriculture System. *EURASIP Journal on Wireless Communications and Networking*, Vol.1, pp.292. USA.

# A MONITORING SYSTEM OF AGRICULTURAL EQUIPMENT FIELD POSITION BASED ON GPS AND GIS

## 一种基于 GPS 和 GIS 农业装备田间位置的监控系统

Zhenyu Yang<sup>1)</sup>, Zeqiu Chen<sup>2)</sup>, Ken Chen<sup>3)</sup> <sup>1</sup>

<sup>1)</sup>School of Earth and Space Sciences, Peking University, Beijing, 100871 / China

<sup>2)</sup>School of Information Engineering, China University of Geosciences (Beijing), Beijing, 100191 / China

<sup>3)</sup>School of Computer and Information Engineering, Heilongjiang University of Science and Technology, Harbin, 150027 / China

\*Tel: 18010596387; E-mail: 492323358@qq.com

DOI: <https://doi.org/10.35633/inmateh-62-24>

**Keywords:** GPS, GIS, agricultural equipment, field position, monitoring system

### ABSTRACT

With the development of communication technology and embedded technology, mobile intelligent terminals (mobile GIS) have become the key research direction of monitoring systems. In view of this, the study first constructed the structure frame of the agricultural monitoring system and the system mobile database, and designed the monitoring system terminal, combined with the .Net Compact Framework platform to implement the system functions, and finally the monitoring system based on GPS and GIS. The function of the system was tested. The results show that the system design of this study combines user needs' analysis, system framework and functional module division. The system design function realizes the function of creating a database, the entry and collection of attribute data and graphic data; and the editing and browsing of map data and management functions; it realizes the processing of data and the output of results, and displays in the form of graphs or reports; it realizes the functional modules of the monitoring system. It is hoped that this research can provide a certain reference and reference for the application of mobile intelligent terminals in our country's agriculture.

### 摘要

随着通信技术和嵌入式技术的发展, 移动智能终端 (mobile-intelligent terminals, mobile-GIS) 已成为监控系统的重点研究方向。鉴于此, 本研究首先构建了农业监测系统的结构框架和系统移动数据库, 并设计了监控系统终端, 结合 .Net 网站紧凑的框架平台实现了系统的功能, 最后对基于 GPS 和 GIS 的监控系统的功能进行了测试。结果表明, 本研究的系统设计结合了用户需求分析、系统框架和功能模块划分。系统设计功能实现了建库功能、属性数据和图形数据的录入与采集; 地图数据的编辑浏览和管理功能; 实现了数据的处理和结果的输出, 并以图形或报表的形式显示; 实现了监控系统的功能模块。希望本研究能为移动智能终端在我国农业中的应用提供一定的参考和借鉴。

### INTRODUCTION

With the increasing development of Internet technology, people have begun to be dissatisfied with the way to obtain information in fixed places, hoping that information can be obtained anytime, anywhere (Zhang Sui et al., 2016). The development in the field of mobile computing is also getting faster and faster. Mobile information systems such as tablets and smartphones are gradually replacing traditional PCs, workstations and other clients, promoting the application of GIS in mobile terminals (Holliday et al., 2017). Geographic information systems have also begun to gradually shift from indoor to outdoor mobile computing terminals. Mobile geographic information systems have become a research hotspot in the field of geographic information. Mobile GIS is a technology built on a limited level of processing and mobile computing terminals. This technology provides geographic information systems (Agbalagba et al., 2016) for entourage, mobile, and distributed information services. Based on GPS and GIS agricultural equipment field position monitoring system, which integrates GPS positioning and wireless technology, it is a monitoring system whose main purpose is to collect agricultural information. (Li Y.B. et al., 2020) The traditional geographic information system mainly collects and utilizes geographic information.

<sup>1</sup> Zhenyu Yang, As. PhD. Eng.; Zeqiu Chen, As. PhD.; Ken Chen, As. PhD.

Now that global positioning has developed to the stage of Mobile GIS, the real-time spatial location is added to the information collected by Mobile GIS. (Wei W *et al.*, 2020). The system integrates different data of location information and collects it. The application value of the system becomes higher (Xu Y.W. and Dong F., 2015). Nowadays, wireless communication has begun to be introduced into GIS systems. The wireless downloading, uploading and sharing of data has become a new field of GIS applications. The future research focus of Mobile GIS has become an information management system integrating collection, positioning and wireless.

Geographic Information System (GIS) is a multi-disciplinary integrated application subject, which involves map, geography, surveying, computer and other disciplines. With the support of computer software and hardware, systems engineering and information science are applied to three-dimensional space. Geographic information system can combine geographic attribute data with spatial data. Through data input, collection, operation, storage and other operations, the spatial information can be visually expressed, and various geographic information data can be detected at the same time. GIS has gradually become an indispensable facility in social information detection, and it has begun to penetrate all parts of life.

The innovation of this research is the combination of collected information and geographic images to build an efficient system based on GPS and GIS monitoring, so that users can get rid of the constraints of device location and transmission cables, users can apply various methods to the database, and this provides a reliable technical means for this study.

This study is divided into three parts. The first part is the research status of GPS and GIS monitoring technology at home and abroad. The second part is the design of agricultural equipment field position monitoring system based on GPS and GIS. The framework of agricultural monitoring system based on GPS and GIS is introduced in detail, including the construction of mobile database and the design of monitoring system terminal. The third part realizes and tests the main functions of the system. It includes map creation, data acquisition, data acquisition and data management. Data processing and result output are displayed in the form of graph or report. In addition, this part also includes the function modules of the monitoring system.

In recent years, the research based on GPS and GIS monitoring system has been highly valued by people. This technology has a profound impact on the future direction of social development. Researchers at home and abroad have also conducted in-depth research on this technology (Yan H.W. *et al.*, 2020). Barrile V. *et al.* established a processing tool that can perform a large amount of data processing and visualization by taking GPS measurements on the test bench, using GIS data processing tools, and combining traditional neural network artificial intelligence models (Barrile V. *et al.*, 2016). Issa ATE proposes a client/server solution, including two integrated databases, one for spatial data processing, and the other as a text database to store text coordinates of spatial data, and proposes a cache to improve system performance method (Grzelak A. *et al.*, 2019). Mert B.A. and others analysed the borehole data to generate digital map and table quality data, then used VISUALBASIC to write MapBasic computer application program in GIS environment, and finally combined the two. Finally, the digital monitoring of coal mining and extraction points was realized, and an inventory account and quality database were provided for coal production (Mert and Dag A., 2018). Cai M *et al.* used the speed-density relationship method to estimate the traffic volume of GPS data of floating vehicles, and automatically output the attributes of roads and buildings from the GIS, establishing a regional traffic noise calculation model that considers the attenuation of urban traffic noise. The accuracy of the algorithm was verified by conducting traffic noise monitoring experiments in several areas of different road types in Guangzhou. The results show that the average error between the estimated value and the measured value is less than 2.0dB (Cai M., Zou J. and Xie J., 2015). Shahini Shamsabadi and others introduced a road surface monitoring system PAVEMON based on GIS network. PAVEMON's Web-based GIS module was seamlessly integrated with the database to provide a reference for road surface survey data. Finally, information was obtained through PAVEMON, greatly increased pavement management capabilities (Cunha D.G.F., 2019). Tong Y. *et al.* designed a real-time monitoring system for vehicle detection based on MapX, and introduced the system architecture and functional framework. Experiments show that the system is stable and efficient (Tong Y. *et al.*, 2016).

Brasington J *et al.* proposed a new method to study the three-dimensional morphological dynamics of gravel reach, using global positioning system (GPS) to perform topographic surveys on the exposed and flooded areas of the reach. The results show that the overall large-scale river structure has little change (Brasington J., 2015). Mishra A. and others conducted a detailed soil fertility survey in the Bhadrak area of Odisha using global positioning system (GPS) and geographic information system (GIS) tools.

Using ArcGIS software to compile the soil fertility map of Bhadrak area, the soil fertility status was evaluated (Mishra A. et al., 2017).

Choosumrong S. and others discussed the implementation of an open-source mobile geographic information system framework that uses a client-server model to meet the current need for data assimilation using smartphones. The entire system is implemented through free open-source software and open geospatial standards. Finally, it demonstrates the tracking and management of emergency medical service (EMS) vehicle driving conditions (Choosumrong S. et al., 2016). Zeybek M. et al. combined resistivity tomography measurement, global navigation satellite system and ground laser scanning technology to monitor the landslide. The results show that the integrated technology provides a better means for monitoring the landslide process and collecting data to predict future movements (Zeybek M. et al., 2015). Akanwa A.O. and others used remote sensing technology in the field of geographic information systems to determine the degree of impact of quarrying activities on vegetation coverage in the study area. The visual interpretation of the satellite image confirmed that the white patches on the image are areas affected by quarrying activities, and the dark green colour indicates no human activities observed in the forest (Akanwa A.O. et al., 2017).

Through the research on the monitoring technology based on GPS and GIS, it can be seen that the research results of the monitoring technology based on GPS and GIS at home and abroad are still at a low level, and China's research work in this area is still in its infancy. The research of GPS and GIS monitoring technology needs to be expanded. In this study, the structure frame of the agricultural monitoring system based on GPS and GIS was first constructed, and the mobile database of the monitoring system was constructed, the terminal of the monitoring system was designed, and the various functional modules of the monitoring system were realized.

## MATERIALS AND METHODS

### Construction of agricultural monitoring system framework based on GPS and GIS

When constructing a monitoring system for the field position of agricultural equipment, the collection of agricultural equipment data is the key to the construction of the system. The data of agricultural equipment should be collected in real time for the operator to make decisions and analysis. This research is based on the position monitoring system of GPS and GIS technology, mainly to collect and record the information of agricultural equipment field position. In the design process, the overall design of the system is applied using UML top-level modelling, using the form of example diagrams to represent user needs, class diagrams representing object relationships, and timing diagrams representing interaction relationships. The system is composed of multiple parts. The most important part is a mobile GIS-based system that can provide data collection for the monitoring system.

The data collection process mainly includes starting maps, operations, navigation, spatial positioning, data collection, and transmission archive. In short, during the operation, turn on the GPS navigation function and path query function, move the map in the horizontal direction, keep the current position in the centre of the map, and select the appropriate display scale to facilitate monitoring operations. Next step is to collect the data: first select the type of data to be collected, the automatically generated points, lines and areas will be displayed on the map, and then the corresponding attributes will be entered for different spatial data. The above operations will be repeated until the data collection is completed. The collected data can be marked in the diagram for subsequent operations and processing, and the file can also be saved or transmitted. After all operations are completed, the monitored results should be saved in the database. The GIS server is used for communication in the saving process. The collected data is sent to the GIS and then stored in the database. The users of monitoring system data collection are mainly data collection workers. The functions that users can use include data collection, operation, deletion, editing, import, export and GPS navigation.

The monitoring system in this study can be run on mobile devices such as PDAs, with GPS as the low-level technical support. The system is an information collection system based on mobile device terminals. The main components of the system include GPRS communication, GPRS foundation, GPS, data acquisition and GIS terminal five modules. Among them, the GIS terminal can interact with GPRS and GPS modules respectively, and obtain data information from the serial port, and then transmit it to the upper layer application. The GPS module mainly provides data collection methods and can obtain positioning information. The main function of the GPRS module is to provide a wireless connection for the central server. The most critical part of the system is the embedded system, which can simplify the development of upper-layer applications and also shield the underlying hardware. The overall system architecture is shown in Figure 1.

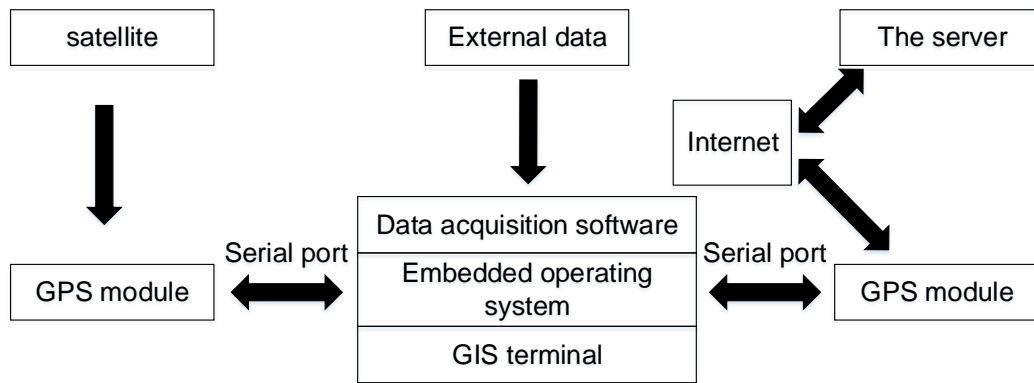


Fig. 1 - Overall architecture of the system

During the operation of the monitoring system, various types of collected data will be imported to a pre-made map to generate data objects. There are many application methods of data objects, which not only can be applied directly, but also can be used after being fused with the data in the original database. In addition, after processing the collected data, it can be added to the original base map to form a new base map. The information collection client is based on mobile smart devices, and users need to install client software on the mobile devices. This system adopts the object-oriented and modular design mode. The system mainly includes three modules: data storage, application services and user interface. The application service module mainly uses the mobile GIS component function, which can realize the basic functions of the map viewing operation, and realize the layer control and positioning sampling. The function of the data storage module is mainly to send the collected data to the central server. The GPS communication class library is mainly used for serial communication with the GPS receiver to process the received GPS data, as shown in Figure 2.

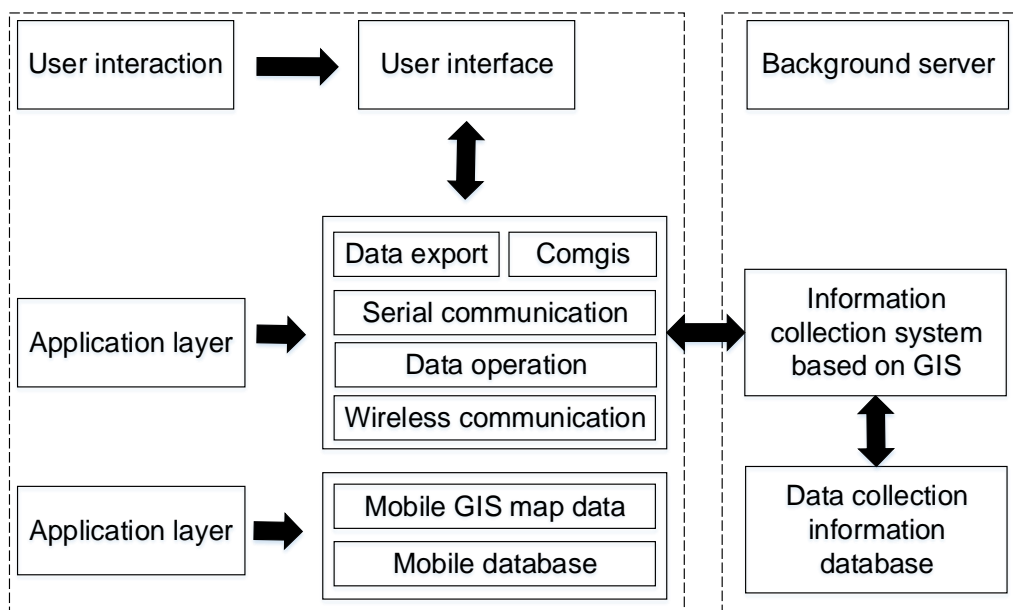


Fig. 2 - Monitoring system framework design drawing

The collection process of the monitoring system in this study can be summarized as the following processes. First process the acquired GPS, acquire the necessary data after processing, and then organize it by the mobile application layer, and transfer the organized data to the interaction layer. After acquiring the information, the user performs data-related operations and then processes it through the application layer to store the processed data in the database. The data is transmitted to the information monitoring system through the internal channel of the system, and finally the analysis-processed image is displayed on the client.

### Construction of mobile database of monitoring system

Spatial information data is mainly GPS data and attribute data collected manually. These data require a unified database for storage. According to the actual situation of this research system, most of the data is attribute data, and a relational database should be used, so this study selected Microsoft SQL Mobile 2005 as the database. The main transmission method is wireless transmission, and wired transmission can also be applied. SQL Mobile does not run independently. It belongs to a server-side agent program. It requires IIS support and provides related services as an ISAPI process. Before accepting data, SQL Server database requires SQL Mobile to transfer data. At the same time, data reception on the device side requires SQL Mobile performs data transfer.

SQL Mobile mainly includes two key technologies: remote data access (RDA) and rapid server response. RDA can perform remote access to SQL Server, perform query operations at the same time, and save query results to a local database. When operating on the local database, modifying data, etc., the update of these data information will be synchronized to the remote server database at the same time. The initiator of RDA is the client, and its data synchronization is unidirectional, and the client can only send synchronization requests to the server. The server can respond differently according to different requests; the quick response function of the server is based on the replication of the database server and merge mechanism, a response function added to the database server. This function can not only better support the data interaction between the remote server and the local mobile device, increase the automatic interaction service of the data, but also solve the conflict problem during data exchange. This function is more complex than RDA and requires more operations and configuration of the system, but its function is stronger than RDA and is more applicable in complex data application scenarios. The data design of this study included 7 tables, as shown in Table 1.

**Table 1**

Form name	Representation
Basic information of sampling	DC-CY-BASIC
Collection point summary	DCYBJOINT
Property sheet of acquisition point	DCBJOINT CY
Sampling location classification table	DC-CY-REGION
Plot information statistics	DCTBCY-LAND
Crop information record form	DC-CY-CROP
Change of soil moisture	DC-CY-SOIL

### Design of monitoring system terminal

The monitoring system in this study has a total of 6 modules, which are: map system setting, data maintenance, wireless communication, spatial analysis, collection, and operation. The collection module mainly collects data, and the collected content includes agricultural information, GPS coordinates and other data. In addition, point, line and surface data related to geographic information, agricultural equipment location, farmland area, positioning trajectory and other information data are also the information that this module needs to collect; after the original data collection is completed, the data maintenance module is required to maintain the collected data, The main function of the data maintenance module is to delete, modify and add data; the function of the operation module is to receive user instructions so that the user can directly operate the map. The main functions include area calculation, browsing and loading of the map; GPS function of the navigation module is positioning and navigation. The basic data is obtained through the serial port, matching the map and positioning information, and the navigation results and positioning information are calculated at the same time. The wireless transmission module is to import the wirelessly received data into the database.

The monitoring system is based on the HiMap platform to achieve spatial data collection, the platform provides a powerful interface for easy development of embedded GIS programs. At the same time, the hierarchical design mode is adopted, and the system design is divided into three levels. The first layer is the user interface layer, and the user can realize information interaction through the GUI interface; the second layer is the calling layer, which is composed of individual classes; the third layer is a domain class. This layer is complex to implement specific functions of the system. The overall mechanism design of data acquisition application software is shown in Figure 3.

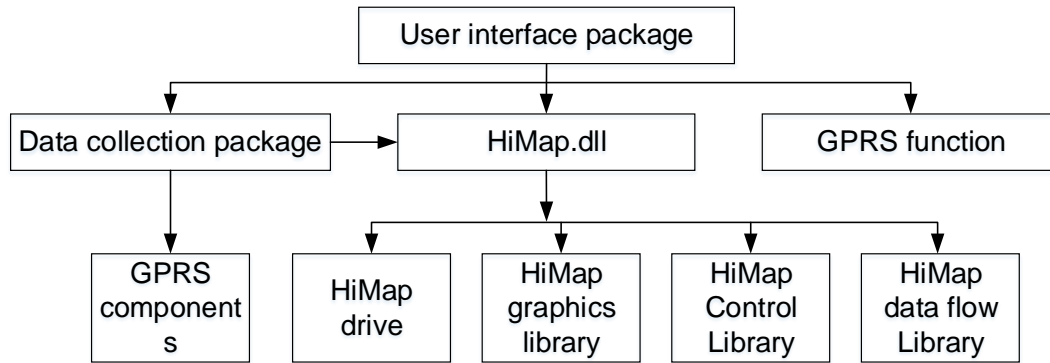


Fig. 3 - The overall mechanism design of data acquisition application software

There are many types of HiMap library, including data orientation, visualization, collection object, editing, path analysis and other types. All the functions of GIS are encapsulated in HiMap.dll component, GIS is the core of HiMap. There is a type of space mechanism in the driver, named HiMap for each object, and the location of the namespace is used for object search. The user interface package is composed of GUI components, and its function is mainly to display input and output information. The data collection package uses coordinates and communication information to modify the function library. In this process, the program interface must be referenced. The main function of the GPRS communication module is to connect the central server with the mobile intelligent terminal and is responsible for the reception and control of data signals.

**RESULTS**

**Realization of the main functions of the system**

In order to ensure the development of the monitoring system, this research requires a high level of system development environment. The design minimum requirements in terms of system hardware are as follows: computer hard disk 1024MB, CPU PXA310, memory 1024MB, operating system Windows Mobile 6, built-in Bluetooth adapter, mobile memory card 8G SD. The minimum requirements for the design of the software environment are as follows, toolkit Windows Mobile 6.0 SDK, operating system Windows XP SP3, synchronization software ActiveSync4.5, GIS toolkit HiMap net cf2.0, client database SQL Sever2005 Mobile Edition3.0, server database IIS +SQL Server2005+.Net2.0. The system design interface is shown in Figure 4.

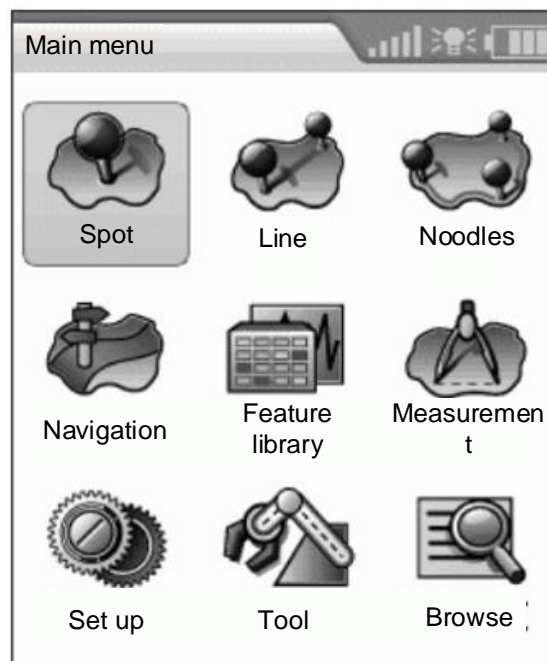
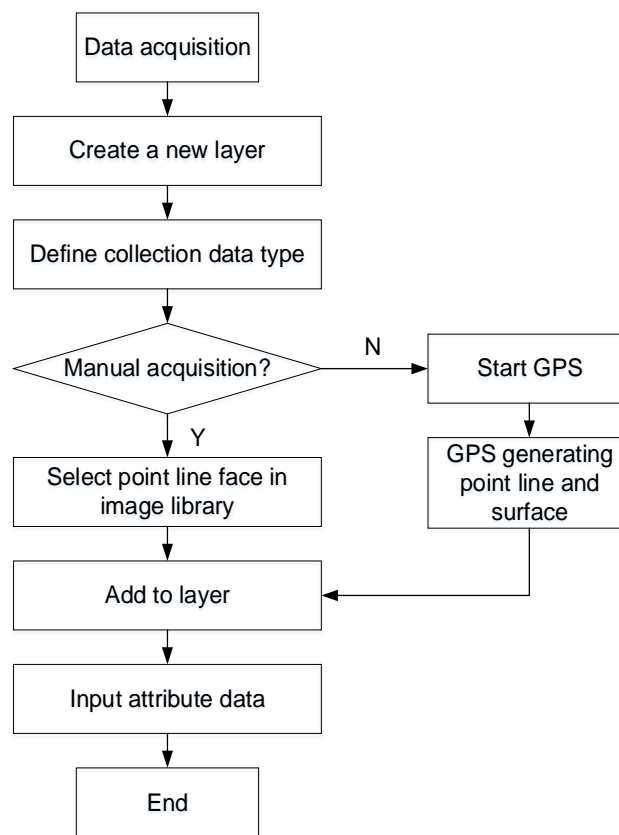


Fig. 4 - System design interface

This system design uses a variety of data storage methods and uses .Net Compact Framework to store system data, including SQL Mobile and XML. Import the collected information data into the database system, realize the wireless transmission of local data storage, and combine with the data tracked by GPS, and finally realize the data storage. The system realizes the GPS positioning data collection function connected with GPSID, through the NMEA0183 command analysis method, so that the system maintenance personnel can solve the NMEA commands. GPSID is a serial operation of the package, which mainly reflects the capability of the system, so that the data can be serially operated in the application program. Users can not only use GPSID to access GPS, but also obtain GPS information through the serial port.

There are two collection methods for users to choose from in the data collection module, namely automatic collection and manual collection. Among them, automatic collection requires the user to set the display scale, layer, data type, and collection interval in advance, and turn on the GPS data collection function, display the collected spatial data on the map, and prompt the data to be entered on the user interface Information, and then proceed to the next data collection. The corresponding implementation flowchart is shown in Figure 5 below.



**Fig. 5 - Flow chart of data acquisition module**

System data query includes attribute and graphic data query. Attribute data query must first select the appropriate layer, set the object to be queried in the layer, and query in the attribute query window.

If a point is selected, the coordinate position of the point and the ID of the point will be displayed.

If a line is selected, the length of the line, the starting and ending position coordinates and the ID of the line will be displayed.

If the surface is selected, the area of the surface will be displayed, Coordinates and ID. Attribute data query should select the target object, and use SQL query method to perform conditional query in SQL.

If the query object is a point, the corresponding attribute of the point can be obtained.

If the query object is a face, then the size of the query area needs to be set, and the attributes of all objects in the area need to be counted.

### System module test

In order to verify the realization of the system data, the system module is tested on the system. Select the basemap that needs to be analysed in the system. If you use manual acquisition, you need to select the type of object to be collected. It is one of points, lines, and areas. Select the type of data you need and add it to the corresponding position of the bottom map.

If you need to output the new basemap, you need to print the basemap, if you want to continue to query, you can store the basemap to the symbol library; if the user chooses to automatically collect, then the system will start GPS from the serial port, set the collection attributes, collect the target data through GPS, and display it on the base map. At the same time, GPS will automatically process the points, lines and planes and display them on the layer. To add attribute data on the image data object and submit data information, the test process is shown in Figure 6.

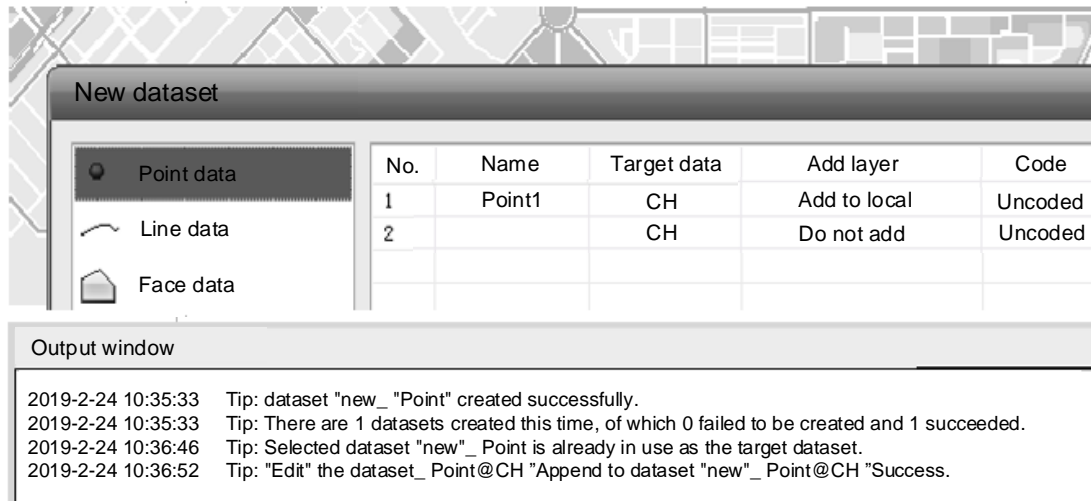


**Fig. 6 - Data collection results**

The symbol library management module can call and view the symbols in the point, line and area library, and can also add newly designed symbols in the library. As for the layer control of the data management module, it completes the layer attribute setting, realizes layer modification, deletion, addition operations, and outputs the object information of the layer. The data query function realizes the query function of attributes and graphics. When the graph query function selects a certain area or feature, it will automatically display the attribute information of a certain area or feature. The user sets the query conditions and then accesses the file; database is accessed and the query results are obtained. For the map browsing module, this module provides the zoom, move, and browse functions of the map, and all functions can be realized by clicking.



**Fig. 7 - Positioning of agricultural equipment monitoring equipment**

As shown in Figure 7, in the process of positioning data collection, for the realization of the data editing module, the database data set is actually operated, and the filling of the attribute form is used to modify the relational database to complete the attribute data editing function. For the implementation of the output module, the original or created data object is output in the set format, the image is stored in the .smw format, and the attribute data is output in the form of a table.

## CONCLUSIONS

Aiming at the technical problems of agricultural machinery field positioning monitoring, the system structure framework, system mobile database and monitoring system terminal were designed, and the system was implemented and tested on the .Net compact framework platform. The results show that this research has completed the layer attribute setting, realized the layer modification, deletion, addition operation, as well as the layer object information output. It not only realizes the query function of attribute and graph, but also realizes the output of original created data object in the set format. The image is stored in .SMW format, and the attribute data is output in the form of table, so as to provide the functions of map zooming, moving and browsing. Through the system design function, it shows the database creation, data attribute processing and graphic data input and collection functions, including map data editing, browsing and management. The data processing and output are displayed in the form of graphics or reports, which clearly shows the various functional modules of the monitoring system. Due to the limited time and ability, this study also has some deficiencies. There is little research on image data acquisition, so it is necessary to further improve the system for this kind of data acquisition. In the future research work, we will pay more attention to this aspect.

## REFERENCES

- [1] Agbalagba E O, Osimobi J C, Avwiri G O., (2016), Excess Lifetime Cancer Risk from Measured Background Ionizing Radiation Levels in Active Coal Mines Sites and Environs. *Environmental Processes*, Vol.3, Issue 4, pp.895-908, USA;
- [2] Akanwa A O, Okeke F I, Nnodu V C., (2017), Quarrying and its effect on vegetation cover for a sustainable development using high-resolution satellite image and GIS. *Environmental earth sciences*, Vol.76, Issue 14, pp.505.1-505.12, Germany;
- [3] B.A. Mert, Dag A., (2018), Development of GPS and GIS-based monitoring system for the quality of excavated coal. *Acta Montanistica Slovaca*, Vol.23, Issue 1, pp.62-71, Slovakia;
- [4] Barrile V, Meduri G M, Bilotta G., (2016), GPS- GIS and Neural Networks for Monitoring Control, Cataloguing the Prediction and Prevention in Tectonically Active Areas. *Procedia Social & Behavioural Sciences*, Vol.223, pp.909-914, England;
- [5] Brasington J., (2015), Monitoring and modelling morphological change in a braided gravel-bed river using high-resolution GPS-based survey. *Earth surface processes & landforms*, Vol.25, Issue 9, pp.973-990, England;
- [6] Cai M, Zou J, Xie J., (2015), Road traffic noise mapping in Guangzhou using GIS and GPS. *Applied Acoustics*, Vol.87, pp.94-102, England;
- [7] Choosumrong S, Raghavan V, Jeefoo P., (2016), Development of service-oriented Web-GIS platform for monitoring and evaluation using FOSS4G. *International Journal of Geoinformatics*, Vol.12, Issue 3, pp.67-77. Thailand.
- [8] Cunha D G F., (2019), Nicolás Reinaldo Finkler, Nora Gómez, et al. Agriculture influences ammonium and soluble reactive phosphorus retention in South American headwater streams. *Ecohydrology*, Vol.13, Issue 2, pp. e2184, USA;
- [9] Grzelak A, Guth M, Matuszczak A., (2019), Approaching the environmental sustainable value in agriculture: How factor endowments foster the eco-efficiency. *Journal of Cleaner Production*, Issue 241, pp.118304, England;
- [10] Holliday K M, Howard A G, Emch M., (2017), Deriving a GPS Monitoring Time Recommendation for Physical Activity Studies of Adults. *Medicine & Science in Sports & Exercise*, Vol.49, Issue 5, pp.939-947, USA;
- [11] Li Y B, Li H, Guo X N., (2020), Online Parameter Identification of Rice Transplanter Model Based on Ipso-Ekf Algorithm. *INMATEH Agricultural Engineering*, Vol.61, Issue 02, pp.25-34, Romania;
- [12] Mishra A, Das D, Saren S., (2017), GPS and GIS based soil fertility maps of Bhadrak district of Odisha, India. *Ecology Environment & Conservation*, Vol.23, Issue 1, pp.183-189, India;

- [13] Tong Y, She J, Ding B., (2016), Online minimum matching in real-time spatial data. *Proceedings of the VLDB Endowment*, Vol.9, Issue 12, pp.1053-1064, USA;
- [14] Wei W, Gong Y J., (2020), Defects Detection Method Based on K-Means With Prior Knowledge for Biomass Particles. *INMATEH Agricultural Engineering*, Vol.61, Issue 02, pp.225-232, Romania;
- [15] Xu Y W, Dong F., (2015), 3G Network Mobile Vehicle Tracking and Positioning Systems Research. *Applied Mechanics & Materials*, Vol.744-746, pp.1967-1970, Switzerland;
- [16] Yan H W, Cui Q L, Liu Z Y., (2020), Pig Face Identification Based on Improved Alexnet Model. *INMATEH Agricultural Engineering*, Vol.61, Issue 02, pp.97-104, Romania;
- [17] Zeybek M, Sanlioglu I, Ozdemir A., (2015), Monitoring landslides with geophysical and geodetic observations. *Environmental Earth Sciences*, Vol.74, Issue 7, pp.6247-6263, Germany;
- [18] Zhang S, Jiang Y, Li Z., (2016), Dynamic Monitoring and Analysis on the Changes of Soil and Water Loss of Ruxi River Based on 3S Technology. *Journal of Yangtze River Scientific Research Institute*, Vol.33, Issue 11, pp.21-27, China.

# STUDY ON TEMPERATURE FIELD OF ASYMMETRIC LARGE-SPAN ARCH SHEDS UNDER LOW-TEMPERATURE ENVIRONMENT

## 非对称大跨度拱棚低温环境下的温度场研究

Kai Zhou<sup>1)</sup>, Zhiwei Meng<sup>1)</sup>, Min Wei<sup>2)</sup>, Jialin Hou<sup>1)</sup>, Tianguo Jin<sup>3)</sup>, Tianhua Li<sup>\*1)</sup>

<sup>1)</sup> College of Mechanical and Electronic Engineering, Shandong Agricultural University, Taian 271018, China;

<sup>2)</sup> College of Horticulture Science and Engineering, Shandong Agricultural University, Taian 271018, China;

<sup>3)</sup> School of Mechatronics Engineering, Harbin Institute of Technology, Harbin 150001, China.

Tel: 18853876906; E-mail: [litianhua689@163.com](mailto:litianhua689@163.com)

DOI: <https://doi.org/10.35633/inmateh-62-25>

**Keywords:** asymmetric structure, large-span arch shed, numerical simulations, response surface methodology

### ABSTRACT

In order to improve the effective sunshine time, heat storage capacity and temperature distribution uniformity of traditional arch shed under low temperature, this paper designed a large-span arch shed which has larger sunny side span and east-west orientation. According to the numerical and measured data, it is concluded that the heat storage capacity and temperature distribution of asymmetrical arch shed are better than those of symmetrical arch shed within a certain range of the ratio between sunny and shaded side. After that, ten different asymmetric arch sheds were designed. It is concluded that the structure of 11+9 m along north-south direction has the best heat storage capacity. Besides that, the analysis of outside wind speed and opening size of top vent were carried out. It is found that the outside wind and top vent can effectively promote convection and exchange of the air, and then achieve the purpose of reducing the temperature. At the end of this paper, in order to identify the relationship of temperature with the structure of arch shed, outside wind speed, and opening size of top vent, a mathematical model was built based on response surface methodology, which would provide theoretical guidance for the design of arch sheds.

### 摘要

为提升传统拱棚低温环境下的有效日照时间、蓄热能力和温度分布均匀性，该文设计了一种东西走向的非对称大跨度拱棚。由数值计算和实测数据可以得出，向阳面和背阴面的跨度比在一定范围内时，非对称拱棚的蓄热能力和温度分布均匀性要优于对称拱棚。在此基础上，设计了 10 种不同的非对称拱棚，结果表明沿南北方向的 11+9 m 拱棚的蓄热能力最优。此外，对外界风速和顶通风口开度进行分析，研究发现外界风速和顶通风口能够有效促进棚内空气对流和交换，进而降低棚内温度。最后，为了确定温度与拱棚结构、外界风速和顶部通风口开度之间的关系，基于响应曲面法建立了数值模型，为拱棚设计提供了理论指导。

### INTRODUCTION

Arch shed is a type of greenhouse generally used in facility agriculture (Changji Zhou and Yingkuan Wang, 2001). Compared with solar greenhouse, arch shed without heat-storage wall has the advantage of high space utilization rate, simple construction, and good durability, but the performances of heat storage and thermal insulation are usually poor (Fei Qi et al., 2008; López-Martínez J. et al., 2018; Saberian A. and Sajadiye S.M., 2019). Besides that, the arch sheds usually have relatively smaller span to enhance the thermal insulation. With the in-depth studies on the performance of arch sheds, it is found that expanding the space of arch shed could not only enhance the cushioning performance against external environment, increase the space utilization rate, but also facilitate the mechanization operations. In addition, arch shed with large span could improve the heat storage capacity and illuminating uniformity significantly, and the thermal insulation at night is ensured by insulation coverage, so the large-span arch sheds have got rapid developments (Xiangli He et al., 2017; Bartzanas T. et al., 2004; Kim K. et al., 2008). Especially in recent years, the east-west asymmetric arch shed has begun to appear in production, which has a larger sunny side to increase illumination area (Mobtaker H.G. et al., 2016).

In the past, the researches on arch sheds mostly focused on the north-south symmetric arch shed. Furthermore, the researches mainly studied the influences of ventilation mode and outside environment to the flow field and temperature field in the arch shed (Majdoubi H. et al., 2009). For the east-west asymmetric arch shed, the influence of geometric structure to performance is an important research content. Similarly, the ventilation mode and the outside environment also have important impacts on performance of the arch shed.

However, there are few related studies in this area (Singh R.I. et al., 2013; Guohui Gan, 2009; Perén J.I. et al., 2015).

With the developments of CFD (computational fluid dynamics) and computer technology, CFD has been widely applied in the field of greenhouse. CFD method can obtain the detailed information of flow field and thermal environment, the cost is lower, and the repeatability is better, which has a great advantage in revealing the air flow behaviour and heat transfer in the arch shed. However, numerical simulations based on CFD generally need to combine the test method to set the boundary conditions and calculation parameters. Besides that, the reliability of numerical results should be verified by test results (Guohong Tong et al., 2018; Ghenai C. and Janajreh I., 2010; Kruggel-Emden H. et al., 2010).

The paper combined numerical method and experimental method, and analyses aiming at the east-west large-span asymmetric arch shed were conducted, which attempted to explore the mechanism of air flow behaviour and heat transfer in the arch shed, analyse the influence factors, and then enhance the performance of the arch shed. Finally, the response surface methodology was adopted to identify the relationship of temperature with structure of arch shed, outside wind speed, and opening size of top vent, which would provide theoretical guidance for the design and construction of arch sheds in different regions and for different needs.

## MATERIALS AND METHODS

### ● Geometric modelling

Based on relevant studies and industry standards, the east-west length of the arch shed is set as 50 m, the north-south span is set as 20 m, and the height of the arch shed is set as 6.5 m. The arch shed is equipped with top vent and side vent to realize ventilation. For example, the detailed structural parameters of 13+7 m arch shed are shown in Figure 1. The other structural parameters can be obtained by scaling proportionally.

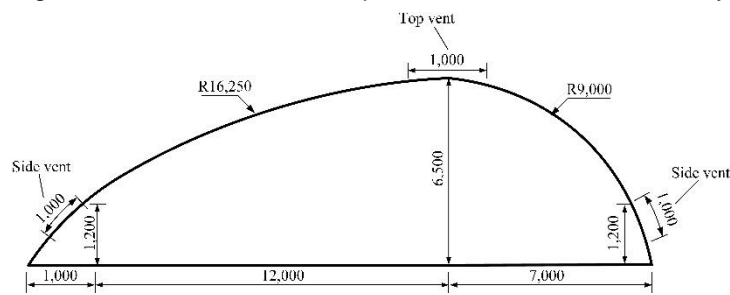


Fig. 1 - Geometric parameter of the arch shed

### ● Test arch shed and measuring method

Taking into account the construction cost, two east-west asymmetric arch sheds with a north-south sunny side span of 15 m and 13 m were constructed (North latitude 36°14', East longitude 117°32'), and a symmetric arch shed was constructed as a comparison, which is shown in Figure 2. From November 2018 to April 2019, temperature and outside wind speed were collected by sensors to exploring the differences among the three arch sheds. The test period has typical characteristics of temperate monsoon climate in the northern hemisphere, which can be described as cold, dry, and calm (Guzmán C. et al., 2019).



a)

b)

c)

Fig. 2 - Test arch sheds

a) 13+7 m arch shed; b) 15+5 m arch shed; c) 10+10 m arch shed

The temperature sensors are arranged as shown in Figure 3. The acquisition frequency is half an hour, and the data is summarized once a month. After the on-the-spot investigation, the heat preservation quilt was covered daily from 16:00 to 8:00 during the test period, and the top vents were opened daily from 12:00 to 14:00 while the side vents remained closed. The outside wind speed and direction was measured by automatic recorder, which was placed 1.5 m height in front of the arch shed. There were no crops in the arch sheds during the test period.

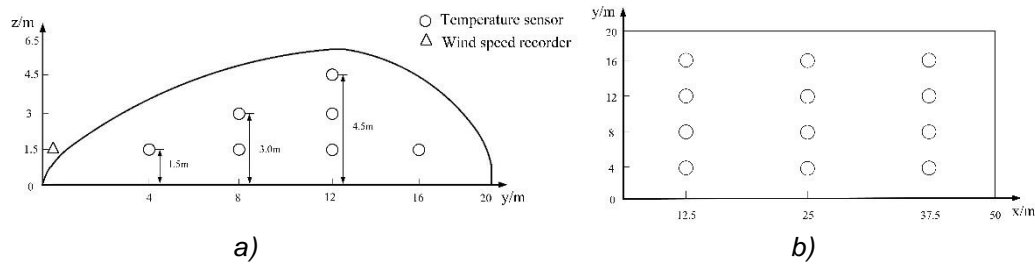


Fig. 3 - Sensors arrangement

a) Vertical distribution of sensors

b) Horizontal distribution of sensors

## ● Numerical modelling and solving

### Mesh generation

In order to ensure the accuracy of numerical simulations, the air field outside the arch shed is conducted as a part of computational domain. And the dimension of computational domain is twice as large as the arch shed, which could fully consider the convection effect between the inside and outside air field. The arch shed is placed in the centre of calculation domain, with x-axis direction as the east direction and y-axis direction as the north direction.

Tetrahedral elements are used, and the fluid domain is divided into about  $2 \times 10^6$  grid cells. Besides, refined mesh is adopted near the vents. To verify the grid independency, the simulation with smaller cell size is carried out and only 4% of the difference between the coarse grid and the fine grid is found. It can be concluded that, when the number of grid divisions is larger than  $2 \times 10^6$ , the numerical results are independent of grid divisions, and the scheme of grid division is reasonable.

### Boundary condition and solving method

The physical characteristic parameters of air, soil and shed plastic film are shown in Table 1. The east boundary of the outside fluid domain is set as velocity-inlet boundary, the west boundary is set as pressure-outlet boundary, the ground and shed film are set as wall boundary, and the other boundaries are set as symmetry boundary, which is shown in Figure 4. The temperature of ground and outside air field are set according to the measured data. The shed film is set to PE (polyethylene) material with a thickness of 0.1 mm. The radiation transmission type is set to semi-transparent material. In addition, the radiation absorptivity of shed film is set to 0.28, and the radiation transmissivity is set to 0.7. In order to fully consider the influences of radiation and air convection to the thermal environment, the DO (discrete ordinate) solar model is used. And the heat exchange is solved by coupling method between inside and outside of the plastic film. Moreover, the standard k- $\epsilon$  model is chosen as turbulence model, the second-order upwind scheme is adopted to discrete calculation, and the SIMPLE algorithm is used for steady-state solving (Piscia D. et al., 2012; Banu J.P. and Mani A., 2019; Kichah A. et al., 2012).

Thermal physical properties of materials

Table 1

Material	Density/(kg·m <sup>-3</sup> )	Specific heat/(J·kg <sup>-1</sup> ·K <sup>-1</sup> )	Thermal conductivity/(W·m·K <sup>-1</sup> )
Soil	1,200	2,500	1.5
PE	923	2,200	0.34
Air	1.18	1.003	1.003

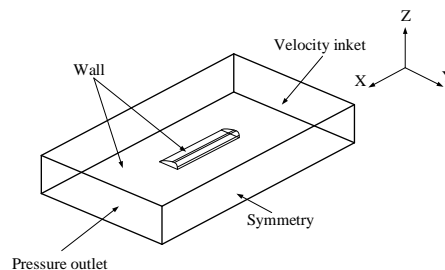


Fig. 4 - Boundary conditions

## RESULTS AND ANALYSIS

### ● Analysis of temperature field

#### Analysis of measured data

All crops have requirements for suitable temperature for growth. Take tomatoes for example, the temperature should be kept within the range of 25°C to 28°C in the daytime and 13°C to 15°C at night.

The arch shed should have the capacity of heat storage and insulation to guarantee the growth of vegetables, especially under low temperature in the winter. The measured temperatures in 13+7 m arch shed on January 6th are shown in the figure below. The weather was fine that day, and the wind speed was about 0.3 m/s. The opening size of top vent was 0.3 m from 12:00 to 14:00.

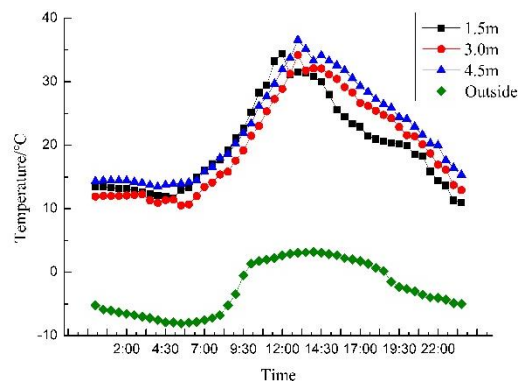


Fig. 5 - Temperature of 13+7 m arch shed over the day

It can be seen that the average temperature curves at different heights have the similar trends, and the inside temperature is obviously higher than outside temperature. According to the measured data in other north-south arch sheds, the average temperature in the daytime of east-west arch shed is significantly higher. Specifically, the temperature at the height of 1.5 m in the arch shed is 13.53°C at 0:00, and drops to 11.71°C at 5:00. This is because there is no solar radiation for a long time, and the heat is gradually transferred from inside to outside. From 7:00 to 12:00, the temperature in the shed rises fast with the decrease of solar angle of incidence. Moreover, the temperature increases in the arch shed with the increasing of the height. From 12:00 to 14:00, the temperature dropped gradually because of the opening of top vent resulting in air convection between inside and outside. After 14:00, as solar angle of incidence gradually increases, the temperature in the arch shed begins to decrease, and the heat is gradually transferred from inside to outside. Based on relevant studies, numerical simulations in the following analysis are conducted at 14:00, which can obviously reflect the heat storage capacity of the arch shed.

Table 2 shows the comparison of the average temperature at each height between the symmetrical and asymmetrical arch sheds. It can be found that the temperature in the three arch sheds gradually decreased from top to bottom, with the lowest temperature near the ground. This is because the hotter air accumulates in the upper layer to raise the temperature, and the ground with large specific heat capacity absorbs heat from the air, so the temperature near the ground is lowest. Compared with the 10+10 m arch shed, the average temperature of 13+7 m arch shed is increased by 2.97%, 3.95% and 5.62% respectively at the three heights. However, the temperature of 15+5 m arch shed is relatively lower. It is concluded that the heat storage capacity of asymmetrical arch shed is better than that of symmetrical arch shed within a certain range of the ratio between the sunny side and the shaded side.

Arch shed structure	1.5 m/°C	3 m/°C	4.5 m/°C
10+10 m	29.96	30.89	31.52
13+7 m	30.85	32.11	33.29
15+5 m	28.41	29.06	30.58

According to Figure 3, the measured data of the three arch sheds are divided into three groups of east, middle and west. The data are shown in Table 3.

Arch shed structure	Height / m	East /°C	Middle /°C	West /°C
10+10 m	1.5	29.63	30.86	29.39
	3.0	30.56	32.23	29.88
	4.5	31.35	32.74	30.47
13+7 m	1.5	30.23	32.16	30.16
	3.0	32.06	32.95	31.32
	4.5	33.08	34.13	32.66
15+5 m	1.5	28.41	28.51	28.31
	3.0	29.06	29.11	29.01
	4.5	30.57	30.62	30.55

It can be seen that the 15+5 m arch shed is the superior one in temperature distribution, but the temperature is lower. The 13+7 m arch shed has advantages in both heat storage capacity and temperature distribution compared with the 10+10 m arch shed. And the temperature distribution of 13+7 m arch shed is acceptable for the consistency of growth of crops. It is concluded that the temperature distribution of asymmetrical arch shed is better than that of symmetrical arch shed within a certain range of the ratio between the sunny side and the shaded side.

**Analysis of numerical data**

In order to further study the differences of performance between the symmetric and asymmetric arch sheds, numerical simulations are conducted taking the 13+7 m and 10+10 m arch sheds as research objects, which can also provide basic model and method for the further analysis of influence factors. The calculating parameters are set according to the measured data at 14:00 on January 6th.

The temperature and air flow fields in the arch sheds are extracted. Figure 6 shows the comparison of temperature distribution between the two arch sheds along north-south direction. It can be seen that, compared with 10+10 m arch shed, the temperature of 13+7 m arch shed is significantly higher near the crop area because of the larger sunny side span. Besides, the temperature gradient is more obvious in 13+7 m arch shed, which can result in up-down air convection. The two-dimensional velocity vectors are shown in Figure 7. It can be seen that obvious air circulations exist in 13+7 m arch shed and the intensity of the air circulations is greater compared with 10+10 m arch shed. Therefore, the asymmetric arch shed is more conducive to air convection and heat transfer, which is beneficial to growth of crops.

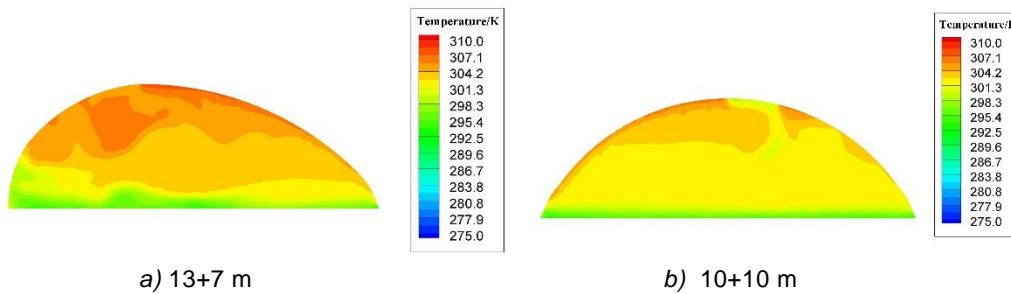


**Fig. 6 - Comparison of north-south temperature distribution**

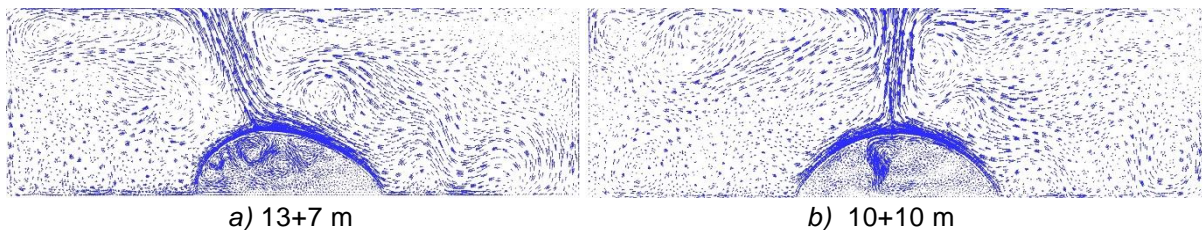


**Fig. 7 - Comparison of north-south velocity vectors**

Similarly, Figure 8 shows the comparison of temperature distribution between the two arch sheds along east-west direction.

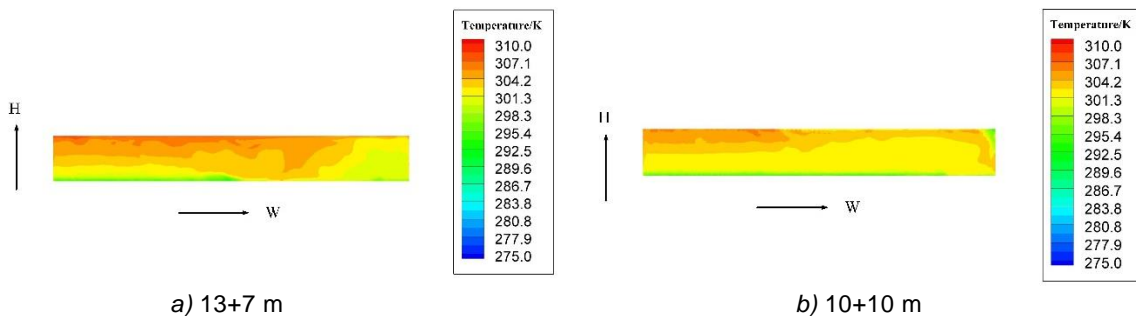


**Fig. 8 - Comparison of east-west temperature distribution**

It can be found that the two arch sheds both have a higher temperature distribution in the western part. This is because of the location of the sun and the shading effect.

However, the 13+7 m arch shed has better performance in east-west temperature distribution. The asymmetric structure enhances the solar radiation reception, and the higher-intensity air convection contributes to the heat distribution on a larger scale, which benefits to the consistency of crops' growth. And the numerical results are consistent with measured data.

#### Reliability verification of numerical results

In order to verify the reliability of the numerical analysis, numerical simulations of the 13+7 m and 15+5 m arch sheds are conducted. The test data was detected at 14:00 on January 6th, the outside wind speed was 0.3 m/s, and the temperature values at each height are averaged. The numerical results and measured data are shown in Table 4. It can be seen that the difference between the measured value and the numerical value is small, and the error is within the acceptable range, which verifies the reliability of the numerical simulation.

Table 4

Comparison of numerical results and measured data				
Arch shed structure	Height / m	Measured / °C	Simulation / °C	Error / %
13+7 m	1.5	30.85	29.34	4.89
	3.0	32.11	30.65	4.55
	4.5	33.29	4.69	4.69
15+5 m	1.5	28.41	26.99	5.00
	3.0	29.06	27.54	5.23
	4.5	30.58	28.97	5.26

#### ● Influences of structure and environmental factors

In order to further study the influences of arch structural parameters and environmental factors on the temperature field of the arch shed, considering the high cost of test method, the numerical method is adopted to analyse the influence rule and find the optimal range. The parameters of the numerical simulations are set with reference to the measured data at 14:00 on January 6th.

#### Reliability verification of numerical results

According to the analysis above, it is concluded that the heat storage capacity and temperature distribution of 13+7 m arch shed are better than those of 10+10 m arch shed. Here, in order to further analyse the influence of the span ratio between the sunny and shaded sides, ten different asymmetric arch sheds are designed, which have the sunny side span ranged from 10.5 m to 15 m with an interval of 0.5 m. Figure 9 shows the average temperature curves at the three heights. It can be found that the average temperature curves have similar trends, and the average temperature of asymmetrical arch shed is higher than that of asymmetrical arch shed within a certain range. Especially, the 11+9 m arch shed achieves the highest average temperature. However, with the span of sunny side increases, this advantage of asymmetrical arch shed is not constant and the differences of average temperature become larger at different heights. As it is known, the solar radiation reception mainly depends on solar reception area and solar angle of incidence. The relationship between the film transmittance and the solar angle of incidence is as follows.

$$\tau_t = 90 - 5 (i_t - 20) / 25.06 \quad (1)$$

Where,  $i_t$  is the solar incident angle,  $\tau_t$  is the film transmittance. With the span of sunny side increases, the solar reception area increases, but the solar angle of incidence increases correspondingly, and that is not conducive to the absorption of solar radiation. As discussed previously, the average temperature at 14:00 can represent the heat storage capacity of the arch shed, so it can be considered that the optimal span ratio between the sunny and shaded sides is about 11:9.

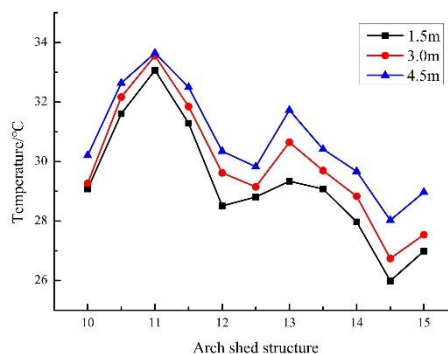


Fig. 9 - Temperature under different structures

### Influence of wind speed

In order to ensure the air exchange between inside and outside of arch shed and reduce the temperature in certain situations, the vent will be opened for ventilation. Therefore, the influence of outside wind speed on temperature field in arch shed should be considered. In this paper, the analysis mainly focuses on the low temperature situation, so the top vent is open with 0.3 m and the side vents remain closed in numerical simulations. Taking 13+7 m arch shed as an example, the average temperatures at different heights are shown in Table 5. It can be found that the average temperatures decrease significantly with the outside wind speed increases.

**Table 5**

Temperature under different outside wind speeds			
Velocity/(m/s)	1.5 m Height/°C	3 m Height/°C	4.5 m Height/°C
1.6	20.21	20.77	21.67
3.4	13.11	13.03	13.25
5.5	10.44	10.53	10.60
8.0	9.15	8.48	8.43

Figure 10 shows the comparison of two-dimensional velocity vectors under different outside wind speeds along north-south direction. When the outside wind speed equals 1.6 m/s, the air convection is relatively weak and the velocities mainly exist near the top vent. With the outside wind speed increases, the large-scale air circulations begin to appear and the velocities gradually increase. That is, the air exchange and heat transfer become fiercer. Therefore, when the outside wind speed is high, the opening time of top vent should be shortened or the opening size should be reduced to keep a suitable temperature in arch shed. In order to further verify the accuracy of the numerical results, measured data on January 1th, January 14th and January 20th are chosen to make a comparison, and the wind speed is 1.3 m/s, 2.8 m/s and 4.3 m/s respectively. The difference between measured data and numerical value is small, so the numerical results and analysis are reliable.

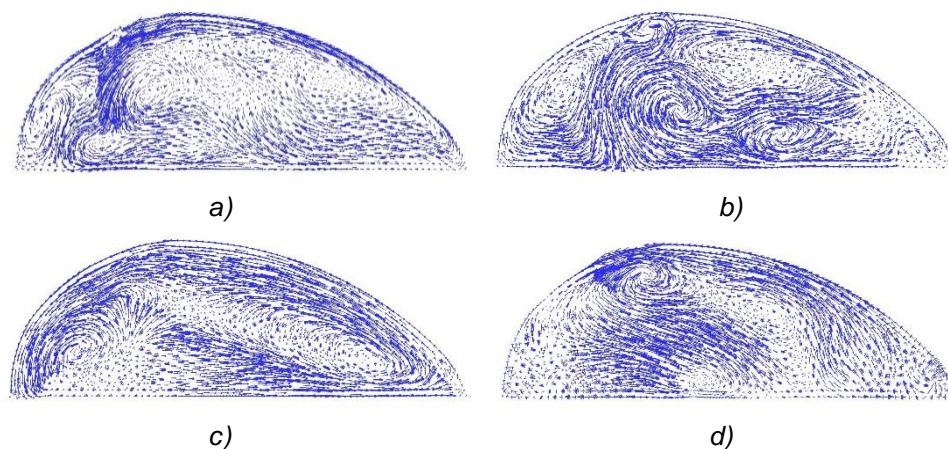


**Fig. 10 - Comparison of two-dimensional velocity vectors under different outside wind speeds**  
a)  $1.6 \text{ m}\cdot\text{s}^{-1}$  ; b)  $3.4 \text{ m}\cdot\text{s}^{-1}$  ; c)  $5.5 \text{ m}\cdot\text{s}^{-1}$  ; d)  $8.0 \text{ m}\cdot\text{s}^{-1}$

### Influence of top vent

The air exchange between inside and outside of arch shed is necessary for the growth of crops. Besides, the ventilation is an efficient measure of temperature control. Using 13+7 m arch shed as an example, the opening sizes of top vent are set to 0 m, 0.2 m, 0.3 m, 0.4 m, 0.5 m, 0.6 m, 0.7 m, 0.8 m, 0.9 m and 1.0 m to analyse the influences of top vent to temperature field, and the numerical results are shown in the Figure 11. With the increase of opening size of top vent, there appears a downward trend of average temperature in the arch shed, and the differences among different heights become smaller due to more powerful up-down air exchange and heat transfer. In agricultural production, the opening size of top vent should be determined by weather, wind speed and outside temperature. In order to further verify the accuracy of the numerical results, measured data on January 3th, January 6th and January 7th are chosen to make a comparison, and the opening size of top vent is 0.2 m, 0.3 m and 0.4 m respectively. The difference between measured data and numerical value is small, so the numerical results and analysis are reliable.

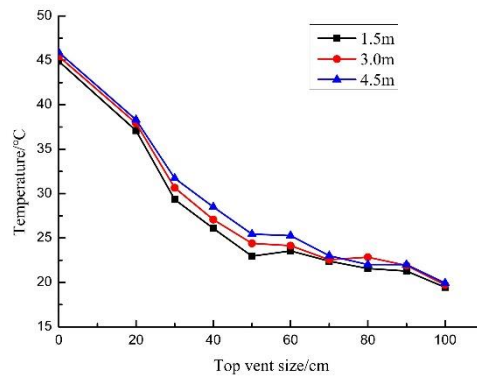


Fig. 11 - Temperature under different opening size of top vent

**Comprehensive analysis of factors**

The influences of structural parameter, outside wind speed and opening size of top vent have been discussed respectively. Here, the response surface method (RSM) is adopted to establish the mathematical relationship of temperature with structure of arch shed, outside wind speed, and opening size of top vent (Xiong Shen et al., 2012). The influence factors and division levels are shown in Table 6. The average temperature at the height of 1.5 m is taken as target parameter. Figure 12 shows the corresponding surface of any two factors.

Table 6

Division levels of influence factors			
Level	Structure of arch shed	Outside wind speed/(m·s <sup>-1</sup> )	Opening size of top vent /cm
-1.732	10.5:9.5	1.1	20
-1	11.0:9.0	1.6	30
0	11.5:8.5	2.1	40
1	12.0:8.0	2.6	50
1.732	12.5:7.5	3.1	60

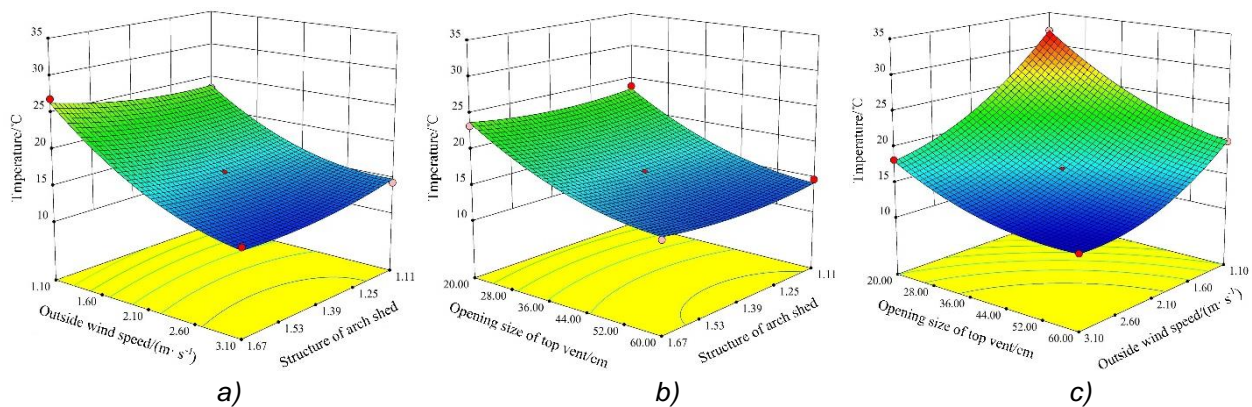


Fig. 12 - Corresponding surface of any two factors

Through the statistical analysis of Design-Expert software, it is concluded that the secondary multiple regression equation of temperature with structure, wind speed, and opening size of top vent can be described as follows.

$$Y = 70.92 - 21.91A - 13.37B - 0.77C - 3.99AB - 0.00464AC + 0.76BC + 11.18A^2 + 2.45B^2 + 0.00482C^2 \tag{2}$$

Where, A represents the level of span ratio between the sunny and shaded sides, B represents the level of outside wind speed, C represents the level of opening size of top vent, and Y represents the average temperature in arch shed. As it is shown in the formula, the structure of arch shed, outside wind speed and opening size of top vent can be adjusted for an expected temperature. The mathematical model would provide prediction and guidance for the design and construction of asymmetric arch shed.

The variance analysis of the regression model is shown in Table 7. When the P value is less than 0.0001, the influence factor is significant. It can be found that the influence factors of outside wind speed and opening size of top vent are significant, as well as their quadratic terms. The span ratio between the sunny and shaded sides is not significant. And the predicted value of the model is very close to the actual value, indicating that the mathematical relationship expression is reliable.

Table 7

Variance analysis					
Source	Sum of squares	Freedom	Mean squares	F value	P value
<b>Model</b>	483.19	9	53.69	219.18	<0.0001
<b>A</b>	0.22	1	0.22	0.91	0.3713
<b>B</b>	248.59	1	248.59	1014.88	<0.0001
<b>C</b>	171.59	1	171.59	700.52	<0.0001
<b>AB</b>	4.99	1	4.99	20.38	0.0027
<b>AC</b>	0.002704	1	0.002704	0.011	0.9193
<b>BC</b>	9.35	1	9.35	38.15	0.0005
<b>A<sup>2</sup></b>	3.23	1	3.23	13.20	0.0084
<b>B<sup>2</sup></b>	25.27	1	25.27	103.17	<0.0001
<b>C<sup>2</sup></b>	15.65	1	15.65	63.91	<0.0001
<b>Residual</b>	1.71	7	0.24		
<b>Lack of fit</b>	1.71	3	0.57		
<b>Pure error</b>	0.000	4	0.000		
<b>Cor Total</b>	484.90	16			

## CONCLUSIONS

In this paper, an east-west large-span arch shed with asymmetric structure was designed. The east-west length of the arch shed is 50 m, the north-south span is 20 m, and the height of the arch shed is 6.5 m. The sunny side has a larger span. The arch shed is equipped with top vent and side vents to realize ventilation. Based on computational fluid dynamics, numerical model of air flow behaviours and heat transfer in the arch shed was established.

According to the measured data, numerical simulations of air flow behaviour and heat transfer process in the arch shed were conducted. It is shown that the thermal environment in arch shed is affected by solar radiation and air convection. Under low outside temperature, compared with the 10+10 m arch shed, the 13+7 m arch shed has increases of temperature by 2.97%, 3.95% and 5.62% at the height of 1.5 m, 3.0 m and 4.5 m respectively. Besides that, the uniformity of east-west temperature distribution of the 13+7 m arch shed is also improved. It can be concluded that both the heat storage capacity and the temperature distribution uniformity of asymmetric arch shed are superior to those of symmetric arch shed within a certain range of the ratio between the sunny side and the shaded side.

The influences of arch shed structure, outside wind speed and opening size of top vent to the temperature in the arch shed under low outside temperature were analysed. The results show that the 11+9 m arch shed has the best heat storage performance. The outside wind and top vent can promote the air exchange between inside and outside, enhance the intensity of inside air convection, and then reduce the temperature in arch shed. Finally, the relationship of temperature with arch shed structure, outside wind speed, and opening size of top vent was built based on response surface methodology.

## ACKNOWLEDGEMENT

This work was supported by the China Postdoctoral Science Foundation (2019M662410), the National Key Research and Development Project of China (2017YFD070150) and the National Characteristic Vegetable Industry Technology System Project (CARS-24-D-01).

## REFERENCES

- [1] Banu J.P., Mani A., (2019), Numerical studies on ejector with swirl generator, *International Journal of Thermal Sciences*, Vol.137, pp.589-600;
- [2] Bartzanas T., Boulard T., Kittas, C., (2004), Effect of vent arrangement on windward ventilation of a tunnel greenhouse, *Biosystems Engineering*, Vol.88, Issue 4, pp.479-490;
- [3] Changji Zhou, Yingkuan Wang, (2001), Modern greenhouses and their performances in China, *Transactions of the Chinese Society of Agricultural Engineering*, Vol.17, Issue 1, pp.16-21;

- [4] Fei Qi, Xinqun Zhou, Yuefeng Zhang, et al., (2008), Development of world greenhouse equipment and technology and some implications to China, *Transactions of the Chinese Society of Agricultural Engineering*, Vol.24, Issue 10, pp.279-285;
- [5] Ghenai C., Janajreh I., (2010), CFD analysis of the effects of co-firing biomass with coal, *Energy Conversion and Management*, Vol.51, Issue 8, pp.1694-1701;
- [6] Guohong Tong, Christopher, D.M., Guoqiang Zhang, (2017), New insights on span selection for Chinese solar greenhouses using CFD analyses, *Computers and Electronics in Agriculture*, Vol.149, pp.3-15;
- [7] Guohui Guo, (2009), CFD modelling of transparent bubble cavity envelopes for energy efficient greenhouses, *Building and Environment*, Vol.44, Issue 12, pp.2486-2500;
- [8] Guzmán C., Carrera J., Durán H., et al., (2019), Implementation of virtual sensors for monitoring temperature in greenhouses using CFD and control, *Sensors*, Vol.19, Issue 1;
- [9] Kichah A., Bournet P.E., Migeon C., et al., (2012), Measurement and CFD simulation of microclimate characteristics and transpiration of an impatiens pot plant crop in a greenhouse, *Biosystems Engineering*, Vol.112, Issue 1, pp.22-34;
- [10] Kim K., Yoon J.Y., Kwon, H.J., et al., (2008), 3-D CFD analysis of relative humidity distribution in greenhouse with a fog cooling system and refrigerative dehumidifiers, *Biosystems Engineering*, Vol.100, Issue 2, pp.245-255;
- [11] Kruggel-Emden H., Rickelt S., Stepanek F., et al., (2010), Development and testing of an interconnected multiphase CFD-model for chemical looping combustion, *Chemical Engineering Science*, Vol.65, Issue 16, pp.4732-4745;
- [12] López-Martínez J., Blanco-Claraco J.L., Pérez-Alonso J., et al., (2018), Distributed network for measuring climatic parameters in heterogeneous environments: Application in a greenhouse, *Computers and Electronics in Agriculture*, Vol.145, pp.105-121;
- [13] Majdoubi H., Boulard T., Fatnassi H., et al., (2009), Airflow and microclimate patterns in a one-hectare canary type greenhouse: an experimental and CFD assisted study, *Agricultural and Forest Meteorology*, Vol.149, Issue (6-7), 1050-1062;
- [14] Mobtaker H.G., Ajabshirchi, Y., Ranjbar, S.F., et al., (2016), Solar energy conservation in greenhouse: thermal analysis and experimental validation, *Renewable Energy*, Vol.96, Issue 1, pp.509-519;
- [15] Perén J.I., Hooff T., Leite, B.B., et al., (2015), CFD analysis of cross-ventilation of a generic isolated building with asymmetric opening positions: Impact of roof angle and opening location, *Building and Environment*, Vol.85, pp.263-276;
- [16] Piscia D., Montero J.I., Baeza E., et al., (2012), A CFD greenhouse night-time condensation model, *Biosystems Engineering*, Vol.111, Issue 2, pp.141-154;
- [17] Saberian A., Sajadiye S.M., (2019), The effect of dynamic solar heat load on the greenhouse microclimate using CFD simulation, *Renewable Energy*, Vol.138, pp.722-737;
- [18] Singh R.I., Brink A., Hupa, M., (2013), CFD modelling to study fluidized bed combustion and gasification, *Applied Thermal Engineering*, Vol.52, Issue 2, pp.585-614;
- [19] Xiangli He, Jian Wang, Shirong Guo, et al., (2017), Ventilation optimization of solar greenhouse with removable back walls based on CFD, *Computers and Electronics in Agriculture*, Vol.149, pp.16-25;
- [20] Xiong Shen, Guoqiang Zhang, Bjerg B., (2012), Investigation of response surface methodology for modelling ventilation rate of a naturally ventilated building, *Building and Environment*, Vol.54, pp.174-185.

## INCREASING THE PERFORMANCE OF CYLINDRICAL SEPARATORS FOR CEREAL CLEANING, BY USING AN INNER HELICAL COIL

### CREȘTEREA PERFORMANȚELOR SITELOR CILINDRICE PENTRU CURĂȚIREA CEREALELOR, PRIN UTILIZAREA UNEI SPIRE INTERIOARĂ ELICOIDALĂ

Costin Mircea <sup>1)</sup>, Florin Nenciu <sup>\*1)</sup>, Valentin Vlăduț <sup>1)</sup>, Gheorghe Voicu <sup>2)</sup>,  
Iuliana Gageanu <sup>1)</sup>, Dan Cujbescu<sup>1)</sup>

<sup>1)</sup>INMA Bucharest / Romania;

<sup>2)</sup> University Politehnica of Bucharest/ Romania

E-mail: [florin\\_nenciu2000@yahoo.com](mailto:florin_nenciu2000@yahoo.com)

DOI: <https://doi.org/10.35633/inmateh-62-26>

**Keywords:** *cylindrical rotary separators, wheat grains, contaminant extraction*

#### ABSTRACT

Rotary seed sorters used for wheat processing show some functional advantages in eliminating persistent contaminants, especially due to the more aggressive treatment applied to the processed material. The objective of this paper was to design a new constructive subassembly that would increase the performance of rotary sorters used for extracting various contaminants from seeds. By testing a pilot stand that reproduces the operation of a professional equipment and developing mathematical models that fits the main operating parameters, it was possible to identify the new characteristics needed to improve cylindrical sieves and to optimize the functioning of this equipment.

#### REZUMAT

Sortatoarele rotative utilizate în procesarea grâului, prezintă unele avantaje funcționale în eliminarea contaminanților persistenți, în special datorită tratamentului mai agresiv aplicat materialului procesat. Obiectivul lucrării a fost acela de a crea un nou subsansamblu, care să crească performanțele echipamentelor rotative de extragere a contaminanților din semințe. Prin testarea unui stand pilot care reproduce fidel funcționarea unui echipament profesional și prin modelarea matematică a principalilor parametri de funcționare ai acestuia, s-au putut identifica noile caracteristici necesare pentru îmbunătățirea sitelor cilindrice, precum și optimizarea modului de funcționare a acestor echipamente.

#### INTRODUCTION

Axial and tangential rotary wheat separators, are considered to be most suited sorters when processing wheat that is fixed in different conglomerations or when the contamination with leaf and light straws is relatively high. Rotary sorters can be integrated successfully in the pre-cleaning section, before silo loading, when larger perforated sieving sheets are usually used, or at the cleaning section before milling, when smaller perforated sieving sheets are preferred.

Equipment that uses rotary motion for separation are less used than vibrating sorters due to their increased complexity, however they can bring important improvements to the separation process, especially for crops that have high contamination, high humidity, or when contaminants are stuck to the seeds.

Compared to other treatment methods, separation by rotation has the advantage of producing a more aggressive treatment of wheat, allowing easier release of the grain when caught into conglomerations. However, the process involves some disadvantages related to the fact that separation achieved by rotation is usually breaking up the straws, resulting in a reduction of the contaminating particles volume and a worse impurity retention (Casandroiu T., 1993; Bracacescu C. et al., 2016).

Păun A. et al., (2018) studied the design and installation of cylindrical sieves combined with counter-current suction and separation using a rotary seed separator for the elimination of large contaminants (e.g. straw). These large contaminants cause problems for the separation process, because they do not come out easily through the perforations of the sieves' outer wall, affecting the cleaning process. Jianbo, Y. et al., (2018), have tested rotary sieve speeds, assessing quantifiable losses associated with the increasing of rotational speeds.

Another important parameter, namely the cylindrical diameter, was researched by *Shi X. et al., (2018)*, *Yuan J. et al., (2018)*, and *Krzysiak Z. et al., (2020)*, for establishing relationships between the increase in diameter in relation to the separation efficiency and average axial grain speed.

Mathematical modelling for the evaluation of various cylindrical sieves parameters have been intensively studied in order to optimize their efficiency (*Naumenko M. et al., 2018*; *Badretdinov I. et al., 2020*; *Voicu Gh. et al., 2008*), bringing improvements to the design and construction, and obtaining superior quality of the grains.

An element which has to be taken into account when using rotary separators on an industrial scale is the high technological complexity. They must have increased efficiencies, while allowing ease of maintenance at low costs, otherwise the performance of this equipment is greatly influenced by too frequent repairs.

Our goal was to assess an experimental rotary wheat sorter functioning, identify all the working issues that may arise during operation and propose some design improvements related to the main identified shortcomings. In addition, a number of observations made by farmers using these cleaning systems has been considered.

## MATERIALS AND METHODS

A pilot experimental stand has been used to test the seed rotary sorters performances, varying a series of parameters to succeed in simulating the operating conditions of a similar industrial equipment. The analyses performed on the experimental stand have been associated with the theoretical calculation of the rotary sorters, in order to determine which design specifications could be improved to increase equipment performances.

All the important features identified in theory were varied when testing the experimental stand. This allowed identifying important characteristics to be considered when designing new equipment and legitimate certain improvements on the installation design, in order to streamline the main shortcomings.

Figure 1 shows the experimental stand that is in the custody of INMA Bucharest for evaluation and for improving its specifications. During operation, the wheat containing different types of contaminants of known dimensions and quantities, is introduced in one of the feeding inputs (5), provided with a quantity dosing flap. The rotating sieve drive motor (1) drives the sieve (2) unidirectional by means of an axis of rotation (4). The sieve is automatically cleaned by the brush (3) during the rotation preventing wheat or impurities to get trapped in the sieve holes. Impurities will be collected in the impurity collection trays (6), which will allow the analysis of the separation of the masses of impurities along the sieve, this being an important element in the evaluation processes. Total mass of clean wheat is then stored in a special tray (7), while the angle of inclination of the sieve is varied by means of the hydraulic jack (9). The equipment is equipped with a start/emergency stop button (8).

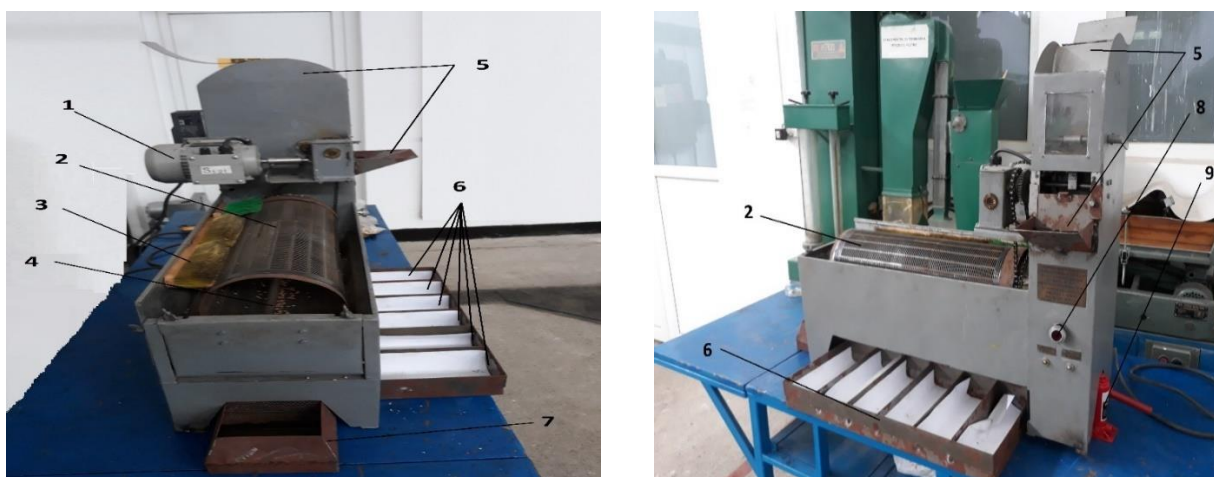


**Fig. 1 - Rotary wheat separators pilot experimental stand**

(1) drive motor, (2) sieve, (3) brushes, (4) axis of rotation, (5) feeding inputs, (6) impurity collection trays, (7) clean wheat tray, (8) start / emergency stop button, (9) hydraulic jack

The row material inserted into the rotating cylindrical sieve, was composed of mixtures of wheat and other contaminating seeds, free and in conglomerations, driven gravitationally from the feeder when lifting the hopper retainer. The impurities separated by the wheat grains fall into the collecting chambers through the sieve holes, as long as the clean material advances along the length of the sieve.

The material advancement is made either by the sieve inclination at a customizable angle, either by the rotational speed imposed to the sieve.

The mixture of seeds introduced inside the cylindrical sieve, acquires a rotational movement, along with the rotating sieve and a translational movement along the length of the sieve.

The advancement of the seeds inside the equipment takes place conditioned by the rotating sieve inclination angle. This is one of the equipment adjustable parameters which generates the speed of advancement of the processed material and might be varied depending on the level of seed contamination.

These movements allow the mixture to separate into fractions, so that the small seeds come out through the sieve holes, while the big seeds move along the sieve, towards the end of the cylinder, being collected separately.

Depending on the angular velocity of the sieve ( $\omega$ ), the following outcomes are drawn towards the movement of the seed mass, illustrated by the following three distinct cases.

- Case A when high rotation speeds are applied to the sieve ( $\Omega = \omega$ ;  $\omega \gg$ ), (where  $\Omega$  is the angular speed of the absolute movement of the seed), it is observed that seed mass adheres to the inner surface of the cylindrical sieve and rotates with it (Fig.2a). In this case the separation process does not take place, and the speed at which this phenomenon occurs is called the critical speed of the sieve (relative rest phase);
- Case B when applying angular velocities lower than the critical speed ( $\Omega = \omega$ ), the seed mass adheres to the surface of the cylindrical sieve, rotating with it up to detachment point - DP1 (where normal reaction  $N = 0$ ), after which they detach and a sliding process begins following a parabolic trajectory up to landing point – LP1, point of contact with the sieve, (Fig.2b);
- Case C when applying low angular velocities to the cylindrical sieve, the seed mass slides in the opposite direction to the movement, rotating around the cylindrical sieve rotation axis, with an angular velocity  $\Omega < \omega$ . The mass of seeds, being driven in rotational motion with an angular velocity  $\Omega < \omega$ , causes some of the seeds to pass through the sieve holes, while the rest of the seeds detach and begin to fall after a parabolic trajectory until the landing point – LP2, (Fig.2c).

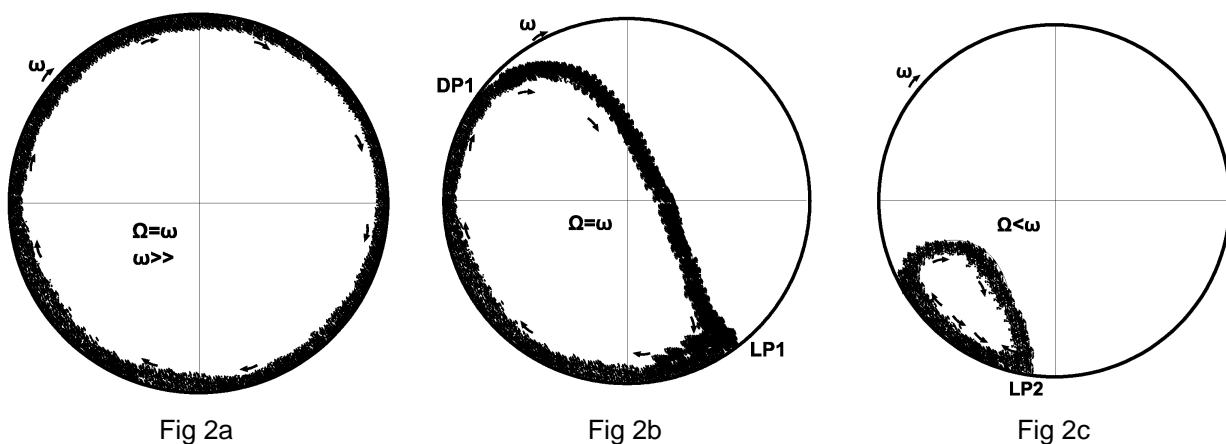


**Fig. 2 - The movement of the seed mass inside the sieve, depending on the angular velocity of the sieve**

*Case A (Fig.2a) when high rotation speeds are applied to the sieve;*  
*Case B (Fig.2b) when applying angular velocities lower than the critical speed ( $\Omega = \omega$ );*  
*Case C (Fig.2c) when applying low angular velocities to the cylindrical sieve*

However, angular velocities from the cylindrical sieve are depending on the mass of seeds entering the process, being observed that a very high intake of seeds would block or negatively affect the separation. A problem identified in practice is that as the volume of seeds introduced for processing increases, then the processing efficiency decreases significantly. Therefore, the productivity of the equipment depends on the length of the sieve, the angle of inclination, the speed of rotation and the mass of seeds introduced. The mass of seeds introduced is also dependent on the level of contamination, which is why we have introduced when testing the equipment raw material with different types and levels of contaminants.

The row material entering the cylindrical sieve, performs a complex movement relative to the sieve axis due to the rotational movement and inclination of the sieve, forming a layer that will have a certain shape and size in cross section, separation being achieved mostly in a single quadrant (Fig.3).

At the beginning of the sieve, the contamination separation will be maximum, while the mass advances along the sieve, the contamination separation decreasing. To be able to observe the percentage of contaminants that are discharged through the holes of the sieve, along its entire length, contamination seeds will be collected using six collection trays, placed along the entire length to be analysed.

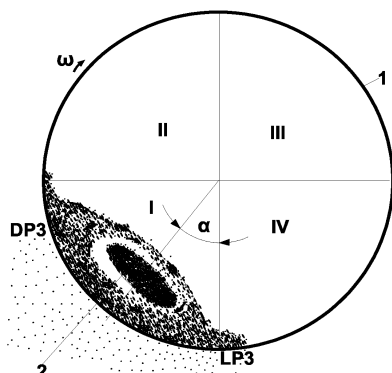


**Fig. 3 – Movement of seeds in the layer, inside the sieve**

Note: modified diagram after Jianbo, Y. et. al., (2018)

1– Cylindrical sieve; 2 - the immobile nucleus; DP3 -detachment point; LP3 - landing point

The seed layers that are in contact with the surface of the cylindrical sieve move in the same direction of rotation with the sieve and must have a lower speed than the sieve, therefore there is a relative movement between seeds and sieve – this being a mandatory condition for the separation process. In the inferior layers, the seed layers will have lower speeds, the speed of the neighbour layers gradually decreasing, cancelling in the centre, where the immobile nucleus is formed (Fig.3: pos.2-the immobile nucleus).

It is needed that the operating regime of the sieve to ensure the relative movement (sliding) of the seeds on the surface of the sieve, this being an essential condition for achieving the separation.

The seeds are driven in the same direction of movement with the sieve, up to the area where they collapse and change direction, (point DP3, Fig. 3), contrary to the first row. The seeds will then return to base in contact with the sieve at landing point LP3 and at the same time advancing along the length of the sieve to the opposite end.

In addition, a seed mixing area (MA) was identified, the area where the seeds mix between layers appears, due to the rupture caused by gravity. This aspect is extremely important because the seeds in the upper rows also come into contact with the sieve to be subjected to separation through the holes, allowing the process to take place.

The importance of the process of mixture in the efficiency of the separation process has led us to develop methods to improve the mixing of seeds in layers. One of our design proposals was to install a special designed coil inside the sieve, which would allow a better mixture of the seed layers, so that the seeds from the immobile nucleus, will get more rapidly in contact with the sieve surface, thus increasing efficiency.

Avoiding the formation of the immobile nucleus was one of our priorities because the seeds existing in this nucleus are not subjected to the separation process. The formation of the immobile nucleus is conditioned especially by the feed flow and the thickness of the seed layer. Our proposed technical improvement correlates the feed flow with the tilt angle and the newly design coil in order to have a better contact of seeds from the immobile layer to the surface of the sieve.

The analysis involved the assessing rotary sieve characteristics based on certain models, evaluating the trajectories of the grains detached from the inner surface of the sieve and the speed of movement of the sorted material inside the sieve after a helical movement given by the inclination of the sieve towards the horizontal.

We have used Panturu et. al., (1997), and Krasnicenko et. al., (1964), for the calculation of the trajectories of the grains detached from the inner surface of the sieve, and to find the movement of the material to be sorted along the cylindrical sieve during the roto-translational motion.

In order to mathematically model the seed sorting process using rotary cylindrical sieves, we have used the  $\pi$  Theorem (Buckingham's Theorem). Our purpose was to obtain a mathematical model that takes into account the specific loading rate subject to separation, using rotating sieves. From the dimensional analysis,

the following parameters that influence the selection process have been considered: specific loading flow subject to sorting  $q$  (kg/s<sup>3</sup>); the distance between the turns of the coil inside the sieve,  $De$  (m); speed of grains advancement in the helical movement  $V_M$  (m/s); the speed of the turn inside the sieve  $n_1$  (s<sup>-1</sup>); length of the sieve,  $l$  (m); the content of impurities (%); the efficiency of the selection process being evaluated by the amount of selected seed  $Q_s$  (kg).

The default function that describes the dimensional selection process, for homogeneous dimensional terms, is:

$$f(Q_s, q, V_M, n_1, De, l, c_i) = 0 \tag{1}$$

Considering as determining quantities the group  $(q, V_M, n_1)$ , and calculating according to Buckingham's Theorem the dimensionless complexes of the selection process (similarity criteria) for the physical parameters  $(Q_s, De, l)$ , we have been found the dimensionless matrix of the 6 parameters in relation to the fundamental quantities  $L$  (length),  $M$  (mass),  $T$  (time).

After setting the conditions for the dimensionless complexes, and solving the obtained systems of linear equations, the relation of the quantity of seed sorted using rotating cylindrical sieves was determined, by separating the term  $Q_s$  from the criterion equation.

$$Q_s = q n_1^3 \cdot \varphi_1 \left( \frac{De \cdot n_1}{V_M}, \frac{l \cdot n_1}{V_M}, c_i \right) = 0 \tag{2}$$

The mathematical model of the multiplication of powers was proposed, finally obtaining the equation (1), and after logarithmic linearization, the relation (2) was obtained.

$$Q_s = k \cdot q \cdot n_1^{(3+\alpha_1+\alpha_3)} \cdot De^{\alpha_1} \cdot V_M^{(-\alpha_1-\alpha_2)} \cdot l^{\alpha_2} = 0 \tag{3}$$

$$\ln Q_s = \ln k + \ln q + (3 + \alpha_1 + \alpha_2) \ln n_1 + \alpha_1 \ln De + (-\alpha_1 - \alpha_2) \ln V_M + \alpha_2 \ln l \tag{4}$$

Data processing envisaging the working process of rotating cylindrical sieves was performed by regression analysis. Constants' values from Eq. 3 are obtained by regression analysis when the exponents are calculated by linear regression based on experimental data. The feed rate of the material to be sorted ( $V_M$ ) varies within the limits of 0.075 - 0.6 m/s, while the values of coil speed ( $n_1$ ) were in the range 0.2 – 0.8 (s<sup>-1</sup>), and the distance between the elements of the coil ( $De$ ) have been first considered a fixed value of 0.0012 m. It was considered a specific load ( $q$ ) of 0.555 kg/s<sup>3</sup> and a length of the sieve  $l$  of 0.3 m. In Fig. 4 there are presented the variation curves of the sorted seed mass ( $Q_s$ ), resulting from Mathcad software.

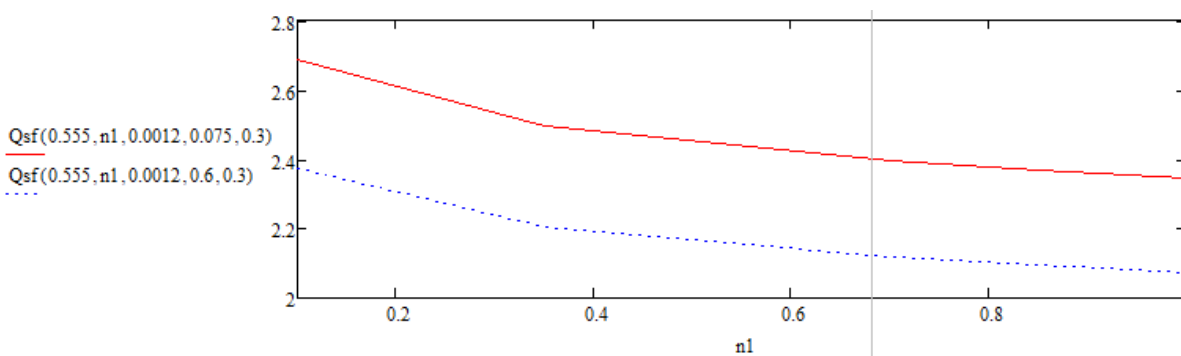


**Fig.4 – Variation of the sorted seed mass ( $Q_s$ ) depending on the speed of the coil ( $n_1$ ) and the advance speed of the grains in the helical movement ( $V_M$ )**

*Qsf* --- Variation of the sorted seed mass depending on the speed of the coil, when considering the minimum advance speed of the grains in the helical movement; *Qsf* - Variation of the sorted seed mass depending on the speed of the coil, when considering the maximum advance speed of the grains in the helical movement

From Fig 4, can be deduced that when modelling the results on the dependence of speed of the coil ( $n_1$ ) and the advance speed of the grains in the helical movement ( $V_M$ ), the sorted seed mass will have a downward curve. A short length of the sieve was imposed to the equipment, which is very common in practice. It is observed that for small sieves, the increase of the speed of the coil will produce a decrease of the efficiency

of the equipment, because the row material will not have time to separate efficiently. The higher will be the speed of the grains in the helical movement, the lower the sieve efficiency will be, therefore it is necessary to introduce some improvements to the sieve internal blades in order to be able to keep the seeds in process for a longer time, and to have a more pronounced mixture of the seeds.

The decrease also occurs due to the high weight of the wheat grains compared to the other elements in the mixture. Wheat grains will fall gravitationally on the surface of the sieve, not allowing the stalks, straw or other seeds to penetrate through the external perforations of the sieve.

The second simulation considered also Eq. 3, and calculated the variation of the sorted seed mass ( $Q_s$ ), depending on the speed of the coil ( $n_l$ ) and the distance between the elements of the coil, designed to drive the wheat grains inside the sieve ( $De$ ). It has been considered that the speed of the coil ( $n_l$ ) varies in the range 0.2-0.8 ( $s^{-1}$ ), the feed rate of the material subjected to sorting ( $V_M$ ) being 0.0075 m/s, using the distance between coil elements ( $De$ ) of 0.0012 – 0.00575 m for pre-sorting seeds by their dimension, a specific load ( $q$ ) of 0.555  $kg/s^3$ , and the length of the sieve ( $l$ ) of 0.3 m. Thus, the variation curves of the sorted seed mass  $Q_s$ , in kg are obtained, as shown in Fig. 5.

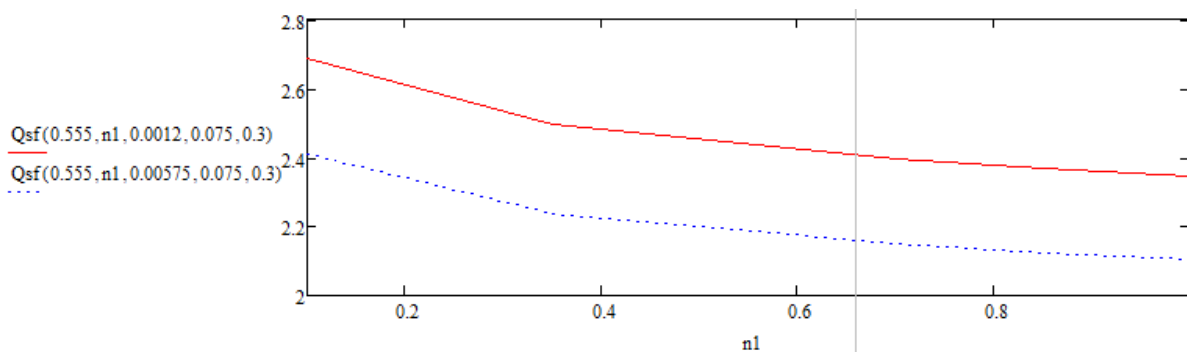


**Fig. 5 – Variation of the sorted seed mass ( $Q_s$ ) depending on the speed of the coil ( $n_l$ ) and the distance between the blades of the coil driving grain inside the sieve ( $De$ )**

*Q<sub>sf</sub> --- Variation of the sorted seed mass depending on the speed of the coil, when considering the minimum distance between the coil blades;  
Q<sub>sf</sub> - - - Variation of the sorted seed mass depending on the speed of the coil, when considering the maximum distance between the coil blades;*

In this case can be observed that the distance between the blades of the coil is inversely proportional to the efficiency. Therefore, for small sieve sizes, a small distance between the blades is needed to increase the efficiency of the equipment. A small distance between the blades will generate the installation of several more blades on the coil, so a greater mixing will occur. However, this is not enough to achieve increased efficiency for small sieves, the general tendency being to decrease the efficiency with the increase of the speed.

Following the mathematical modelling process, the sieve construction was optimized with a new inner coil design, which would increase the equipment efficiency. The new technical solution depicted in Fig 6, enhances the separation process through a more intense breaking of the seed immobile nucleus. This will cause the layers in the centre of the immobile nucleus to come into more frequent contact with the surface of the cylindrical sieve, the contaminated seeds being excluded much faster from the flow.

The subassembly has a complex construction, being made up of a perforated steel sheet on the outside (1) having perforations with the size of 2.24 x 20 mm, a rotating axis (2) which is attached to the drive gear separately from the perforated cylindrical surface, the rotating coil blades (3); while distance between the sieve and the coil (4), have been set to  $d=1$  mm. The size between the sieve and the coil have been chosen to be 1 mm so that the coil blades could lift the wheat grains that have larger sizes, while smaller contaminants will remain on the sieve surface, easily coming out through perforations. On other subassembly designs the wheat grains tend to block the sieve holes, due to their higher masses and volumes, thus making the separation more difficult. The new designed coil will overcome this problem, having a continuous action of removing the grains from the surface of the sieve and improving the separation.

In figure 7, the sieve (1) and the inner coil can be seen separately. It can be observed that the coil blades are designed so that they can be easily customized, which involves fastening the coil with screws, and not by welding. Thus, the blades are fastened through a perforated bushing on the axis of the coil (2) with 6 mm screws (3), while the wing blades are fastened with 4 mm screws (4).

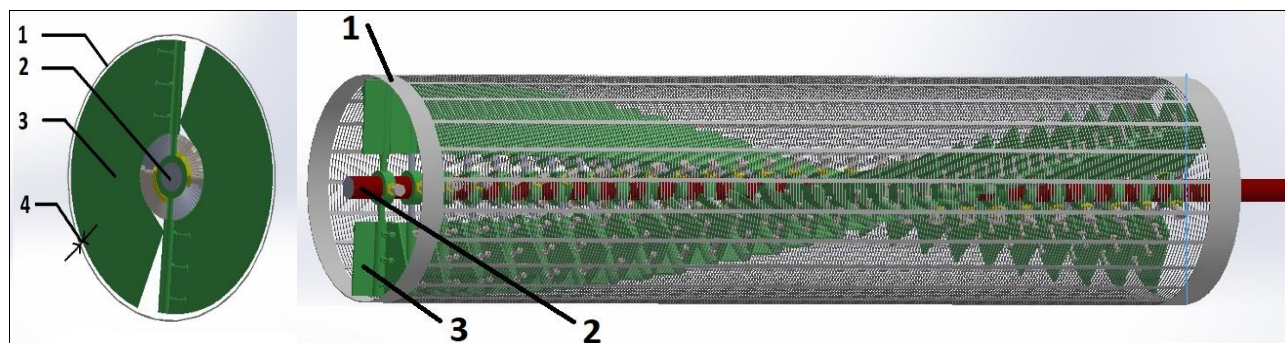


**Fig. 6 – Overview of the new proposed subassembly, made of a sieve and a helical coil with the customizable blade angle of attack set to 45 degrees**

1 – the sieve having perforations with size 2.24 x 20 mm.; 2 – the axis of the rotating coil; 3 - rotating coil blades;  
4 - distance between the sieve and the coil,  $d=1\text{ mm}$

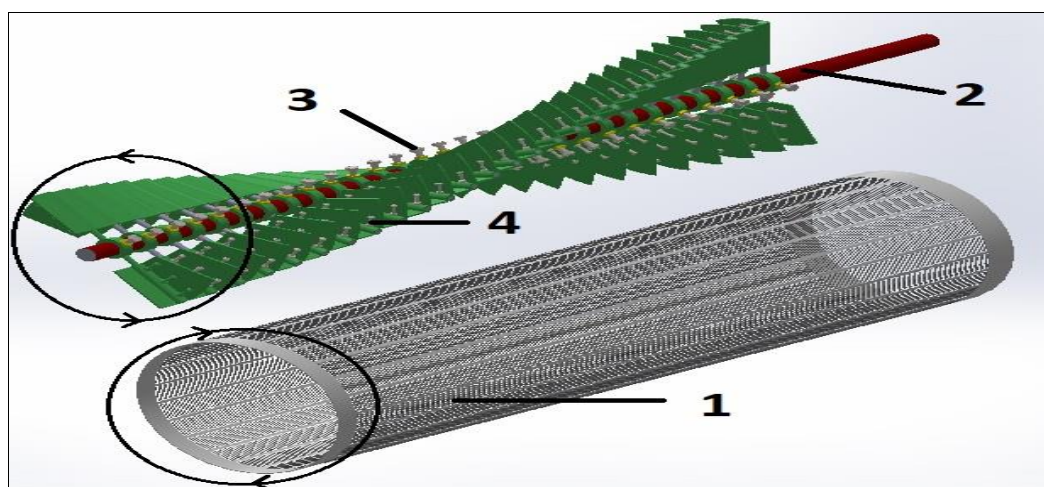


**Fig.7 – Driving assembly, designed to run in the opposite direction of the sieve and the coil increasing the agitation level of wheat grains**

1– the sieve; 2 - axis of the coil; 3– fastening the blades through a perforated bushing on the axis of the coil;  
4 – fastening the wing blade.

The detailed blades of the newly designed coil are shown in Fig 8. The coil has a high level of versatility and can adjust the rotation pitch and blade angle, to modify the equipment in case of large variations in contaminant levels, or large variations in humidity, to maintain efficiency at high levels regardless of the row material introduced.

Therefore, with the fastening screws (1) the rotation of the blades on the coil axis through a bushing (2) can be adjusted, being able to vary the winding of the coil, and with the fastening screws (3) can vary the angle of attack of the blades (4).

This technical solution further improves the breakage of any conglomerations of contaminants which adheres to wheat seeds, which are normally difficult to separate, having a more aggressive action on the row material being processed. This translates into a better separation of contaminants and a higher level of quality, because the wheat will dissociate from conglomerations reaching the separation tray.

An element of novelty is the possibility to change the pitch of the coil and the angle of the blades. The need to modify these elements comes from the different qualities of processed material, the coil pitch influencing the speed of the material crossing through the cylindrical sieve, while the positioning of the blades influences the mixing of the material in order to maximize the contact with the walls of the sieve.

Specially designed blades allow setting various inclinations facilitating the release from the sieve of heavier particles and is working in conjunction with the distance between the sieve and the coil of 1 mm, the subassembly will have a more pronounced action in taking over the large particles that would block the sieve holes. Lifting large particles allows smaller particles to come in contact with the sieve surface and pass through its holes, in the contaminant collection trays.

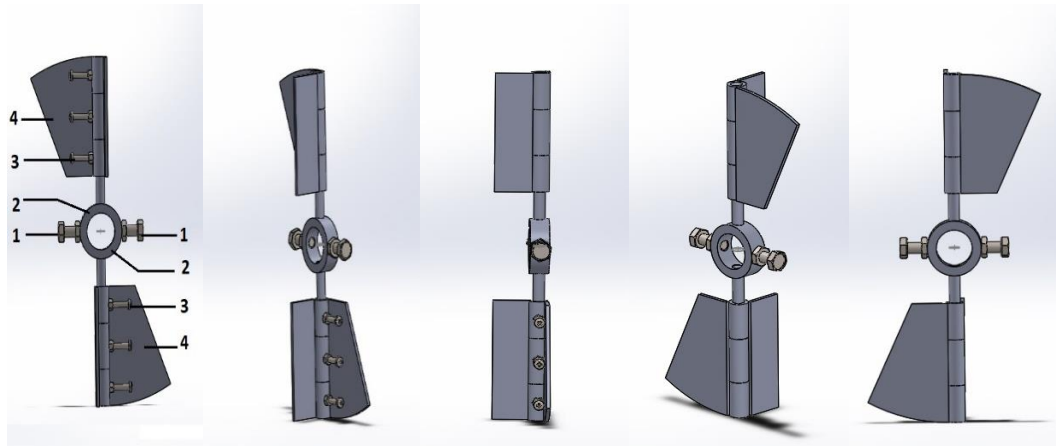
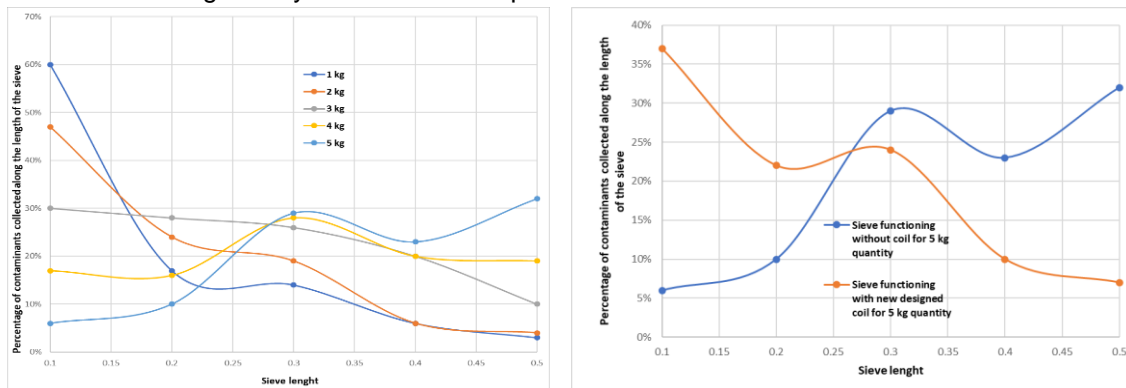


**Fig. 8 – The subassembly blades installed on the coil axis, having the role of breaking the immobile nucleus**

1– fastening screws for attaching the blade to the coil axis; 2 - bushing;  
3 - fastening screws to vary the winding of the coil; 4 – wing blade

The coil drive will be oriented in the opposite direction to the sieve direction. By rotating the coil in the opposite direction to the rotating sieve, it will also rotate in the opposite direction to the seed mass, creating agitation, vigorously mixing the seed mixture, and making the seeds from the immobile nucleus reach the sieve surface easier. The process is also positively influenced by the special construction of the coil, the customizable angle making the process more efficient and adaptable.

The distribution of seeds on the surface of the sieve is a very important indicator for evaluating separation process, because it shows how the sieve changes its performances when varying some important parameters. The experimental results are obtained on an equipment that has no technological changes inside the sieve. The paper analysed theoretically (using mathematical modelling) which would be the best constructive solutions that can be adopted to the interior of the sieve, in order to solve some of the problems identified when working with cylindrical wheat separators.



a) Distribution of contaminants collected on the sieve length, by monitoring the collection trays found under the separator sieve (0.1 m - 0.5 m), for increasing amounts of input material (1-5 kg)

b) The distribution of contaminants collected on the sieve length for a quantity of 5 kg of input material; comparison between the sieve functioning with and without the new designed coil

**Fig. 9 - Distribution of contaminants collected on the sieve length**

By varying the angle of inclination, the sieve speed and taking as constant the level of contamination, to a fix value of 10% from the total mass of material introduced for processing, and taking the volumetric mass of the seeds of  $718 \text{ kg/m}^3$ , we can measure the distribution of contaminants collected along the length of the sieve. The quantity of contaminants collected in each of the collection trays has been weighed, subsequently calculating the percentage gathered on each of the trays.

Several rotational speeds, sieve inclinations and types of contaminants were analysed for 1 kg, 2 kg, 3 kg, 4 kg and 5 kg of input material, the average results are shown in Figure 9a. It can be observed that on small input material quantities, the separation occurs in the anterior third of the sieve length (more than 90%). Once the quantity of input material increases to 5 kg, the separation is achieved in the last segments of the sieve length. The large amounts of contaminant collected on the last sieve segments indicates that the process efficiency decreases abruptly for quantities of material over 5 kg, therefore the separation is no longer carried out efficiently on the entire surface of the sieve and some of the contaminants are escaping into the selected

wheat seeds. Figure 9b shows the estimated efficiency improvement of the wheat separator when using the new designed coil installed in the rotating cylindrical sieve, according to the mathematical models, for the processing quantity of 5 kg material input. The analysis shows that the sieve functioning with new designed coil becomes more efficient, having the possibility of increasing the amount of 5 kg of material input, thus exceeding the limitations of the previous separator model.

Figure 10 shows all the new designed elements installed on a rotary equipment for separating contaminants from wheat, consisting of: (1) - sieve body which adjusts the height and stabilizes the equipment; (2) - sieve drive module in the opposite direction to the coil; (3) - inner helical coil; (4) - feeding hopper; (5) - support for collection trays; (6) - collection trays shutter; (7) - horizontal collector chamber; (8) - vertical collector chambers; (9) - motor drive group; (10) - joint; (11) - sieve angle adjustment screw; (12) - sieve cleaning brush which removes contaminants from sieve perforations.

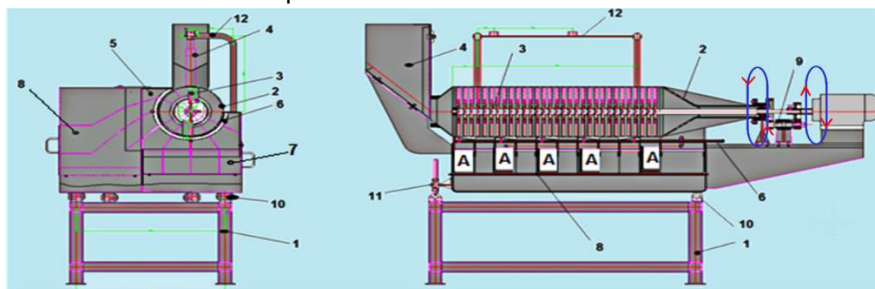


**Fig. 10 - Representation of the newly designed subassembly installation in a cylindrical rotary separator**

1- sieve body; 2- sieve drive module in the opposite direction to the coil; 3- inner helical coil; 4- feeding hopper; 5- support for collection trays; 6- collection trays shutter; 7- horizontal collecting chamber; 8- vertical collecting chambers; 9- motor drive group; 10- joint; 11- sieve angle adjustment screw; 12- sieve cleaning brush.

Vertical collecting chambers (8) are designed to determine the distribution of weights of foreign bodies along the length of the cylindrical sieve, in horizontal and angular plane. This is a very good adaptation to evaluate the capabilities of the equipment and is very useful to customize its rotating speed according to the degree of contamination. For example, if the row material is less contaminated, the operator will notice that residues will be collected only in the first chambers, while the last chambers will remain empty. Therefore, it will be possible to increase the amount of material introduced for processing or the processing speed of the equipment.

These collecting chambers can also be helpful if the equipment is used in the evaluation of the harvested material quality, by the farmer. The quality evaluation is performed by entering a weighted quantity of wheat, and operating the equipment for 10 minutes. When collecting the trays, the contaminants that are easy to extract will be found in the first chambers, while those difficult to extract in the chambers at the end of the flow.

## CONCLUSIONS

Our goal was to benefit as much as possible from the main advantage given by cylindrical separators, namely aggressive treatment of wheat, generated by the sieve rotation. From our theoretical and practical observations, it can be concluded that in the case of highly contaminated seed mixtures, the rotational movement of the sieve is not sufficient to achieve an efficient separation. If this shortcoming is solved by increasing the length of the sieve, then it would result in a too voluminous equipment, which is not desirable in industry fluxes.

In addition, we wanted to raise the amount of row material that is introduced for cleaning into the feeder, for an increased efficiency of the equipment. We could not do this just by increasing the speed of rotation because there are limitations in this respect: on the one hand because it would speed up the movement of the seed mass towards evacuation and on the other hand because exceeding the sieve speed above a calculated critical velocity, it will lead to the seed adherence to the inner surface of the cylindrical sieve and the separation process will not take place in a proper manner.

The special subassembly designed consisting from a sieve and a novel helical coil, allows increasing the speed and introducing more material into the equipment, because a much more intense mixing process takes place.

Taking into consideration the case of the equipment with a short sieve, we analysed both the main theoretical operating parameters and the practical evaluation of a pilot testing equipment which perfectly reproduces the operation of a classical industrial equipment.

The main novelty elements of the subassembly, consist in the special shape of the coil that improves the separation process, in the length of the coil blades near the surface of the sieve that facilitate the mixing. The mixing is also influenced by the angles associated with the sieve blades as well as the special designed shape. The possibility to make changes to the inner coil by varying the pitch or angle of inclination of the blades gives it a higher level of versatility depending on the degree of contamination of the inserted material.

In order to have an improved effect on breaking the conglomerations of contamination seeds/sticks/straws/leaf/dirt attached to the wheat seeds due to the intense movement, but without increasing the dimensions of the cylindrical sieve, we have introduced a direction of rotation of the coil opposite to that of the sieve. These changes to the equipment are estimated to bring a 15% improvement in operation by increasing the amount of processed material, depending on the wheat quality.

## REFERENCES

- [1] Badretdinov I., Mudarisov S., Lukmanov R., Ibragimov R., Permyakov V., Tuktaro M., (2020), Mathematical modeling and study of the grain cleaning machine sieve frame operation. *INMATEH - Agricultural Engineering*, 60(1), pp. 19-28.
- [2] Bracacescu C., Gageanu I., Popescu S., Selvi K.C., Ondokuz M., (2016), Researches concerning impurities separation process from mass of cereal seeds using vibrating sieves in air flow currents. *Conference: 15th International Scientific Conference on Engineering for Rural Development, Jelgava, Latvia*, <http://tf.llu.lv/conference/proceedings2016/Papers/N066.pdf>
- [3] Căsăndroiu T., (1993), *Equipment for primary processing and storage of agricultural products (Utilaje pentru prelucrarea primara si pastrarea produselor agricole)*. University Politehnica of Bucharest Romania;
- [4] Jianbo, Y., Chongyou, W., Hua, L., Xindan Q., Xingxing, X., Xinxin, S., (2018), Movement rules and screening characteristics of rice-threshed mixture separation through a cylinder sieve. *Computers and Electronics in Agriculture*, 154, pp. 320-329. <https://doi.org/10.1016/j.compag.2018.09.012>
- [5] Krasnicenko A.V., (1964), *Agricultural Machinery Manufacturer's Manual*, Vol.2 (translated from Russian). Technical Publishing House, Bucharest / Romania.
- [6] Krzysiak Z., Samociuk W., Zarajczyk J., Beer–Lech K., Bartnik G., Kaliniewicz Z., Dziki D., (2020), Effect of Sieve Unit Inclination Angle in a Rotary Cleaning Device for Barley Grain. *Transactions of the ASABE*. 63(3), pp. 609-618. <https://doi.org/10.13031/trans.13575>;
- [7] Naumenko M., Sokol S., Filipenko D., Guridova V., Kharytonov M.M., (2018), Numeric model of the grain mixture flow in a cylindrical sieve which revolves around the inclined axis, *INMATEH - Agricultural Engineering*, Vol.56, No.3, pp. 67-74, ref.19. <http://oaji.net/articles/2019/1672-1546466819.pdf>;
- [8] Panturu D., Birsan I.G., (1997). *Calculation and construction of equipment in the milling industry, (Calculul si constructia utilajelor din industria moraritului)*, Technical Publishing House, Bucharest / Romania.
- [9] Paun A., Stroescu G., Visan A.L., Olan M., Zaica A., Moiceanu G., (2018), Researches regarding the optimization of impurities removal technology from the cereal and industrial plant seeds for establishing ecological crops, *INMATEH - Agricultural Engineering*, 56(3), pp.83-90;
- [10] Shi X., Qi X., Wu C., Li H., Yuan J., (2018), Screening characteristics and parameter optimization of threshed rape mixture separation through a cylindrical sieve, *International Agricultural Engineering Journal*, 27(3) pp. 53-64;
- [11] Yuan J., Wu C., Li H., Qi X., Xiao X., Shi X., (2018), Movement rules and screening characteristics of rice-threshed mixture separation through a cylinder sieve, *Computers and Electronics in Agriculture*, 154 pp. 320-329;
- [12] Vasytkovskiy O., Vasytkovska K., Moroz S., Sviren M., Storozhyk L., (2019), The influence of basic parameters of separating conveyor operation on grain cleaning quality, *INMATEH - Agricultural Engineering*, 57(1), pp.63-70;
- [13] Voicu G., Casandroi T., Tarcolea C., (2008), Testing stochastic models for simulating the seeds separation process on the sieves of a cleaning system and a comparison with experimental data. *ACS - Agriculturae Conspectus Scientificus*, 73(2) pp.95-101.

# THE DESIGN OF GROUND AIR DUAL PURPOSE AGRICULTURAL INFORMATION ACQUISITION ROBOT

## 地空两用农业信息采集机器人的设计

Qinlan Li <sup>1</sup>

Tianshui Normal University, Tianshui, Gansu, 741000 / China

Tel: 13096253614; E-mail: hsmbnd@163.com

DOI: <https://doi.org/10.35633/inmateh-62-27>

**Keywords:** air ground dual use; information collection; agricultural robot; production forecast

### ABSTRACT

The key to the design of the ground air dual-purpose agricultural information acquisition robot is the application of machine vision technology to realize the collection of crop growth state information. This research mainly designs the machine vision system of the ground air dual-purpose agricultural information acquisition robot, including hardware, software and image processing algorithm. The machine vision system designed in this paper can effectively complete the collection of crop status information. In order to verify the effectiveness of machine vision system, blueberry was used as the experimental object. The control group was set up indoor and outdoor, the fruit condition and quality information were detected, and the blueberry yield was estimated according to the test results. The experimental results show that the image segmentation algorithm in the vision system can identify blueberry fruit well, and the system has strong information analysis ability, and can accurately predict the quality and yield of blueberry fruit according to the image. It can be seen that the machine vision system has a good ability of information acquisition and recognition, which has a high reference significance for the design and research of the ground air dual-purpose agricultural information acquisition robot.

### 摘要

地空两用农业信息采集机器人设计的关键是机器视觉技术的应用，实现作物生长状态信息的采集。本研究主要设计了地空两用农业信息采集机器人的机器视觉系统，包括硬件、软件和图像处理算法两部分。本文设计的机器视觉系统能有效地完成作物状态信息的采集。为了验证机器视觉系统的有效性，本研究以蓝莓为实验对象。设室内外对照组，检测果实状况和品质信息，根据检测结果估算蓝莓产量。实验结果表明，视觉系统中的图像分割算法能够很好地识别蓝莓果实，系统的信息分析能力强，能够根据图像准确预测蓝莓果实的品质和产量。可见，该机器视觉系统具有良好的信息采集和识别能力，对地空两用农业信息采集机器人的设计与研究具有较高的参考意义。

### INTRODUCTION

As a basic industry in China, the production efficiency of agriculture and forestry is very important for the development of China. At present, there are mainly two modes of agricultural production: manual and machine. Labour not only has low efficiency, but is also limited by the fatigue of labour personnel, which hinders the improvement of agricultural production efficiency (Vasconez *et al*, 2019). Machine production can not only get rid of the problem of manual operation, but also facilitate agricultural production mode and effectively improve the efficiency of agricultural operation (Bodunde *et al*, 2019). As an emerging technology, machine vision technology is widely used in the fields of crop growth information collection, crop fruit recognition and real-time monitoring of crop status due to its advantages of large data processing capacity, fast data processing speed and high data analysis accuracy (Choi *et al.*, 2015). The emergence of machine vision technology solves the high cost and low efficiency of manual work, which has a high practical significance for agricultural production automation and modernization.

---

<sup>1</sup> Qinlan L., As. PhD. Eng.

Human receiving external information is mainly realized through vision, so the robot has the function of human machine vision, which can greatly improve the machine's ability to receive external information (Blanes *et al.*, 2015). Machine vision technology refers to the ability of machine vision judgment and visual analysis through image processing algorithm and image acquisition terminal, so as to promote the machine to complete complex tasks (Zavala, 2017). Based on the machine vision technology, this paper designs the machine vision system of the ground air dual-purpose agricultural information acquisition robot, and studies the overall design scheme of the system from two aspects of its hardware and software design and image processing algorithm, in order to contribute to improving the efficiency of agricultural information collection.

This research mainly includes four parts. The second part is to explore and analyse the current application status of agricultural robot, and summarize its optimization and improvement; the third part studies the design of vision system of agricultural information acquisition robot, and points out that the design of machine vision system should be carried out from the perspectives of system software and hardware and image processing. In the fourth part, through the experimental method, the fifth part summarizes the full text and points out the significance and shortcomings of this research.

Chebroļu's team proposed a large-scale agricultural robot data set for plant classification, positioning and mapping, which is of great significance for precision agriculture research (Chebroļu *et al.*, 2017). The Adamides research group has proposed a design plan to transform the universal mobile robot platform into a semi-autonomous agricultural robot sprayer. The design scheme details the hardware and software modules that the system must install, and focuses on the user interface of remote operation. The usability of the user interface is evaluated through relevant experiments. The results show that the user interface of the system has good interactivity and can create a good experience for users (Adamides *et al.*, 2017). Raja *et al* and his colleagues have developed an autonomous agricultural mobile navigation robot, which mainly detects the field environment of crops. The function is realized by using sensor technology and GPRS technology. The sensor technology obtains the field environment data, and GPRS technology transmits the data (Raja *et al.*, 2015). An adaptive fuzzy sliding mode control model based on fuzzy logic theory to improve the control accuracy and stability of the agricultural tracked robot control system was proposed. Subsequently, by comparing with the traditional sliding mode control model, the high applicability and strong robustness of the model are proved (Jiao *et al.*, 2015). Kauser's research team has designed a compound functional agricultural robot, which can independently complete agricultural production work, such as farming, fertilizing and sowing. The robot uses solar energy as the basic energy and has high environmental protection (Kauser N., Banu S. and Yuvaraja T., 2018).

The Vijay's team has designed a robot that uses image processing and machine learning technology to detect leaf diseases. (Vijay *et al.*, 2018). Colleagues from Peña's machine introduced the development technology of a remote robot platform for urban crop monitoring and management. The platform can remotely control the robot and make the robot perform seeding, irrigation, fumigation and pruning activities on small and scalable structured crops (Peña *et al.*, 2018). Noguchi introduced a robot vehicle agricultural application technology, which is based on GPRS, combined with machine vision, image processing and sensor technology, which has great reference significance for the development of precision agriculture (Noguchi, 2018). Bogue summarizes the important research and development activities of agricultural robots in recent years, and points out that agricultural robots are mainly used in precise weed control, fertilization and crop harvest, and the main technologies used are machine vision and image processing (Jin M. *et al.*, 2020). At the same time, the market demand trend of agricultural robots in the next ten years is predicted, and it is predicted that there will be greater market demand and great development potential for agricultural robots in the future (Bogue R., 2016). Zhang C *et al.* developed a multi robot tractor system for agricultural field operation. The efficiency of the system depends on the number of robots, spatial pattern and field length. In order to determine the practicability of the system, three simulations were carried out, and the simulation results show that the system is more efficient in large field (Zhang C., Noguchi N., 2017).

Through the summary of the above, it can be found that there are many related researches on the ground operation agricultural robot, and its application field is more extensive, and it is generally used in basic agricultural field work. (Yu N. *et al.*, 2020) However, there is less research on the ground air dual-purpose agricultural robot, which is the important reason why the design and research of the ground air dual-purpose agricultural information acquisition robot is important for the technical innovation of agricultural robot.

**MATERIALS AND METHODS**

**Vision system design**

The vision system design of agricultural information collection robot can be divided into software design and hardware design. The software part mainly includes human-computer interaction interface design, image processing algorithm design and hardware driver installation; the hardware part mainly includes infrared emission module design, information processing system design and image acquisition design. The overall framework design is shown in Figure 1.

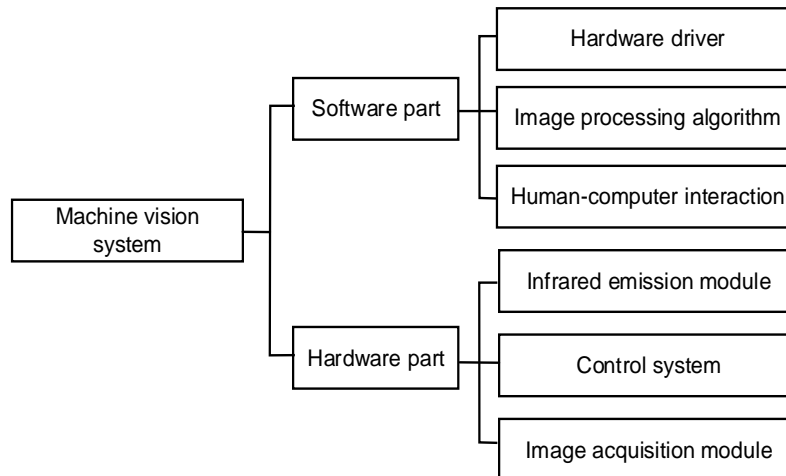


**Fig. 1 - Frame diagram of machine vision system**

The working process of agricultural information acquisition robot mainly includes two steps: firstly, the image signal of the object to be measured is collected, and the technology used in the acquisition includes infrared emission technology and image acquisition technology; secondly, the collected image signal needs to be converted into digital image, and the digital image is transmitted to the information processing system through the transmission path, and the image signal is processed in the processing system. Finally, it completes the identification of the object to be measured, information collection, yield prediction and other work, and the collected data is displayed in front of the user through the human-computer interface. The agricultural information collection robot needs to be able to collect clear and complete high-quality images. At present, the most widely used image acquisition chip is CCD chip and CMOS chip. Compared with CMOS, the application cost of CCD is lower and the quality of captured image is poor. CMOS is superior to CDD in image processing and noise reduction. Especially the latest CMOS chip, not only has ultra-high-definition camera processing technology, but the price is also low, so the comprehensive performance of CMOS is obviously better than CCD. With its high image SNR and image resolution, CMOS has gradually replaced other similar products and become the leading sensor chip for image acquisition. Therefore, the image acquisition tool in this study uses CMOS chip, and the corresponding system hardware framework is shown in Figure 2.

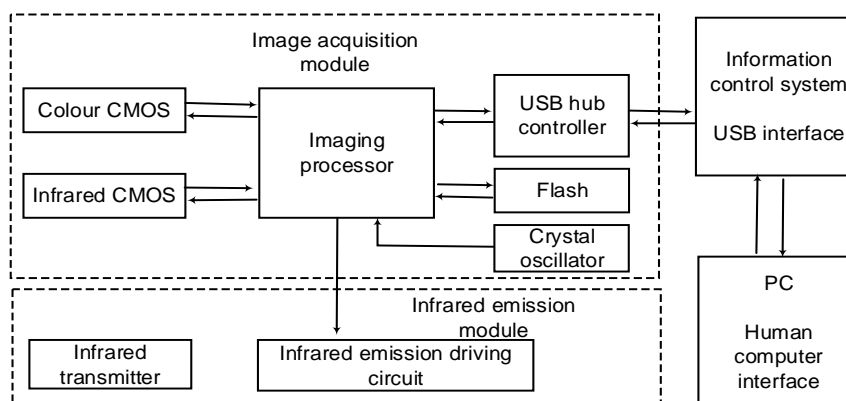


**Fig. 2 - Hardware architecture of machine vision system**

The hardware of vision system of agricultural information acquisition robot includes infrared emission module, image processing module and information control module. The signal acquisition tools of image processing module are colour CMOS and infrared CMOS. The main function of colour CMOS is to collect colour image, and the main function of infrared CMOS is to collect depth image signal. After completing the image signal acquisition, the imaging processor converts the two kinds of signals into digital images that can be recognized by the computer. The information control system needs to process the digital image, and the image processing mode of the information control system is wireless and wired. The information control system transmits the image processing results to the computer terminal, and then uses the human-computer interaction interface to output. In the process of image acquisition and processing, the specific devices supported include infrared CMOS camera, colour CMOS camera, infrared emitter and agricultural information acquisition robot. The image resolution of the colour CMOS camera is 1280 (H) x 960 (V), the shooting angle is 57°(H) x 43°(V), and the frame rate is 15fps. The depth of the camera is 320(H) x 240(V); the resolution of the camera is 0.8...4 m. Image processing requires the computer to have high speed and small volume, which is convenient for assembly on the information acquisition robot. The main function of the vision system is to identify the object to be tested and collect the relevant information. The operating environment of the software part is *LINUX* system, and the programming function is *OpenCV*, *OpenGL*. The corresponding software framework is shown in Figure 3.

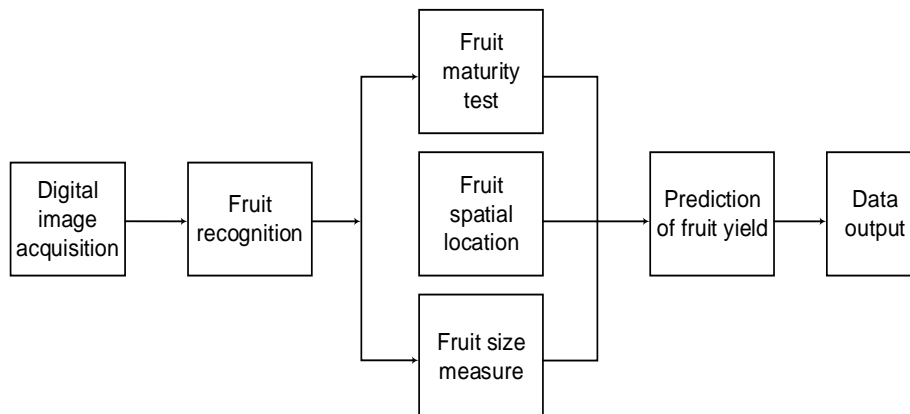


**Fig. 3 - Software architecture of machine vision system**

The data process between human-computer interaction interface and calculation mainly includes seven steps: the start-up of system and interface, the determination of data communication mode, the display of image, the conversion of C-D image, the state detection of the object to be collected, data printing and program closing. After opening the visual system and interactive interface, select the data connection mode as wired or wireless, and set the corresponding IP address; then output the corresponding image information in the computer terminal, and convert the colour image into depth image. After the image conversion is completed, we need to obtain the acquisition data of the vision system. After the acquisition is completed, the relevant data will be transmitted back to the computer to facilitate the user to view, and the data results will be printed to lay the data analysis results. After the above operations are completed, the program is closed.

### **Design of blueberry yield prediction module**

Because the working atmosphere of agricultural information collection robot is usually strong light environment, the collected data are often affected by the outside world, resulting in large error of actual results. In addition, the branches and leaves of agricultural information collection are covered by each other, which will have a great impact on the results of collection and yield estimation. In order to solve such problems, first of all, it is necessary to process the collected images, and then identify the state characteristics of the objects to be collected, such as the fruit diameter, fruit maturity rate and fruit size of crops, so as to provide convenience for subsequent crop yield prediction and evaluation. The workflow of blueberry yield estimation module is shown in Figure 4.

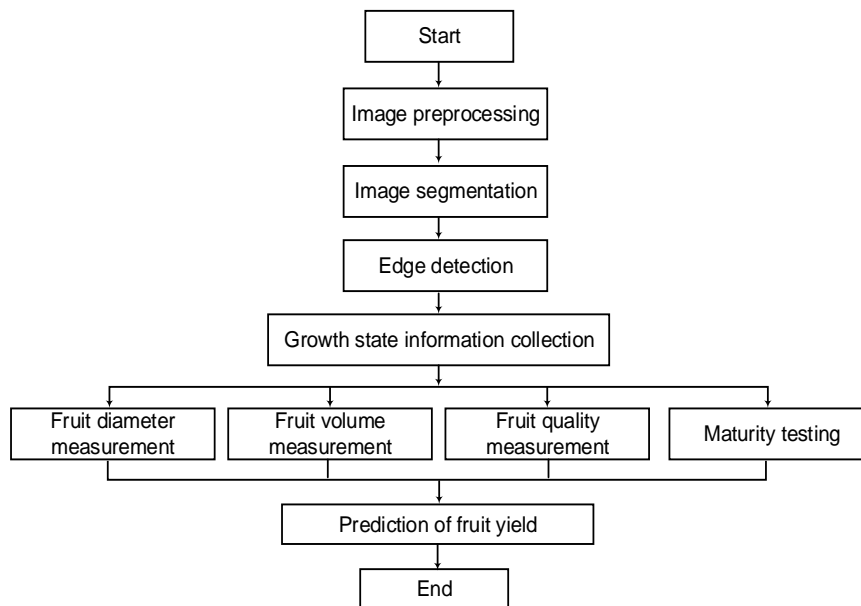


Fig. 4 - Flow chart of image processing algorithm

From the above figure, the core of blueberry yield prediction module includes image processing algorithm and blueberry production information processing. Image processing algorithm includes four steps: image preprocessing, image segmentation, image edge detection, image growth state information processing. Image preprocessing includes image denoising and image enhancement. The main function of the former is to eliminate noise interference and improve the detectability of the image, while the latter is to enhance the visibility and processability of the image and improve the efficiency of image processing. The effect of image denoising is related to the reliability of subsequent image processing, so this image preprocessing mainly introduces image denoising. At present, the most popular noise reduction algorithms are bilateral filtering, median filtering and nonlinear filtering. Experiments show that the adaptive median filter and vector median filter have good image denoising effect and can minimize the noise impact of the image. Therefore, the comprehensive median filter is mainly used to denoise the image. The comprehensive median filter includes adaptive median filter and vector median filter, and the comprehensive median filter mainly includes five processing processes.

They are vector median filtering, HSV colour space conversion, adaptive median filtering, image fusion and image conversion. In the process of vector median filtering, it is necessary to assume the relevant parameters in advance, assuming that the filter centre pixel value is  $V(x_i, y_i)$ , and the filter window length and width are  $2m-1$ ,  $2n-1$  respectively.

The correlation calculation model of window vector is shown in the following formula.

$$VMF = \{V(x_{(i-m)}, y_{(j-n)}), V(x_{(i-m+1)}, y_{(j-n)}) \dots V(x_{(i+m)}, y_{(j+n)})\} \quad (1)$$

Vector  $VMF_x \in VMF$ , vector median filter calculation formula is as follows.

$$\sum_{i=1}^N \|VMF_x - V_i\| \leq \sum_{j=1}^N \|V_j - V_i\|, j = 1, 2, 3, \dots, N \quad (2)$$

The minimum distance and vector of filtering window can be obtained by the above formula, and the output result of filtering is expressed by this value. Vector median filter has good image denoising effect, but due to the wide colour space of digital image, the denoising effect obtained by using median filter is quite different. In addition, due to the small correlation of each channel in HSV colour space, the image space conversion is realized by gray noise reduction in HSV colour space. Although the effect of adaptive median filter on noise suppression is good, the action space of the algorithm is only single channel gray image. Therefore, it is necessary to carry out h, s, V three channel median filtering processing for the above-mentioned colour space images. In the process of image fusion and image conversion, it is necessary to transform the image into RGB colour space. The evaluation indexes of filtering noise reduction effect are peak signal-to-noise ratio and minimum mean square deviation. The calculation model of peak signal-to-noise ratio is shown in the following formula.

$$PSNR = 10 \times \log_{10} \left( \frac{255^2}{MSE} \right) \quad (3)$$

There is a positive correlation between the denoising effects of PSNR images, that is, the higher the PSNR, the better the denoising effect. The formula for calculating the minimum mean square error is as follows.

$$MSE = \frac{1}{mn} \sum_{m=1}^m \sum_{n=1}^n \|I(i, j) - K(i, j)\|^2 \quad (4)$$

$m$ ,  $n$  in formula (4) respectively represents the maximum value of the horizontal and vertical coordinates of the image, and the corresponding unit is pixels; the noiseless gray value of the original image is represented by  $I(i, j)$ ; the gray value of the image after noise reduction is expressed by  $K(i, j)$ . The important basis of blueberry fruit recognition is image segmentation, and the classic image segmentation algorithm is watershed segmentation algorithm. The essence of watershed algorithm is to segment the image effectively according to the external contour of the image, and the corresponding contour can be obtained after segmentation. If the image is segmented directly by watershed algorithm, over segmentation will occur, that is, the same region is divided into more small regions, which is not conducive to the overall grasp of the image. In order to solve the above problems, the target region labelling method emerges as the times require. The essence of the target region labelling method lies in the presupposition of the seed region and eliminates the irrelevant segmentation region according to the seed region. However, there are some defects in the seed region segmentation method, which is that the seed region may damage the external contour. Therefore, Canny edge detection algorithm is used to improve the watershed segmentation algorithm, and the corresponding processing flow is shown in Fig. 5.

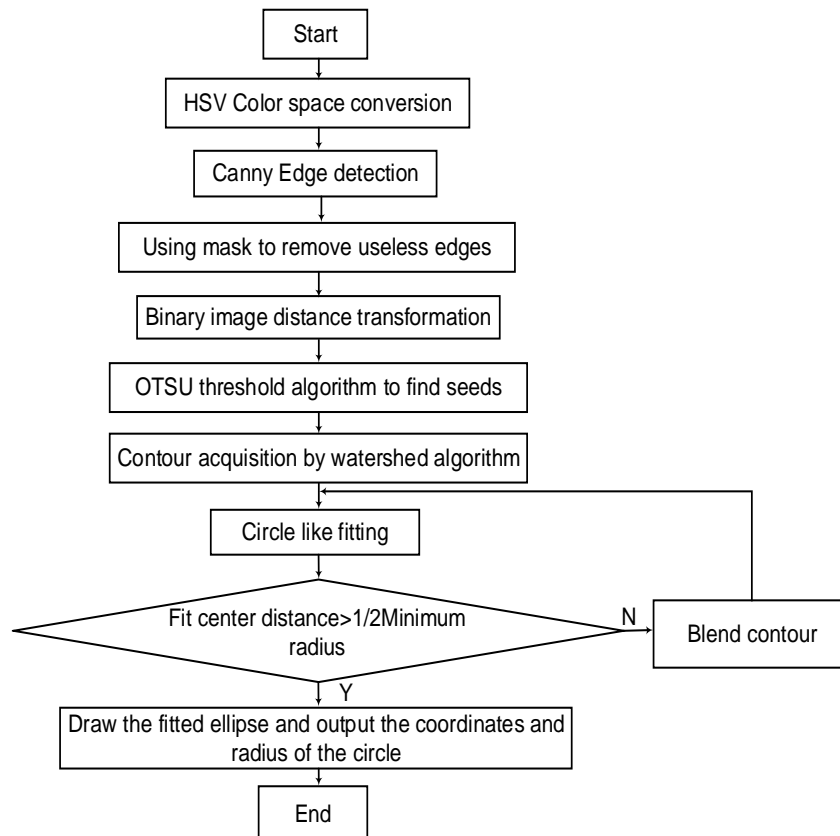


**Fig. 5 - Watershed algorithm flow based on Canny edge detection**

After image edge detection, data processing algorithm is needed to collect fruit growth information. The collected information mainly includes blueberry fruit diameter measurement, blueberry fruit volume detection, blueberry fruit density measurement, blueberry fruit quality detection, blueberry fruit maturity measurement and blueberry fruit yield prediction. The size of blueberry fruit was measured by machine vision. It was found that the size of mature blueberry fruit in the long diameter was basically the same.

Therefore, using vernier calliper to measure its short diameter size can realize the prediction of fruit volume. Electronic scale was used to measure the quality of blueberry fruit. According to the maturity, blueberry fruit can be divided into six stages: green, green with slight red, red with light green, red with blue and blue. Because the volume, hardness and colour of blueberry fruit are different under the mature state, the maturity degree of blueberry was judged by the skin colour of the fruit using machine vision technology. By calculating the mean pixel value of blueberry fruit image in channel A and channel B in lab space, the maturity of blueberry fruit can be obtained, and the ripeness greater than 0.8 is regarded as the symbol of blueberry maturity.

$$M = a \sum_{i=1}^N m_i \quad (5)$$

Formula (5) is the calculation formula of blueberry yield  $M$ .  $N$  is the number of ripe blueberry fruits under machine vision.  $m_i$  represents the individual mass of the  $i$ -th ripe blueberry;  $a$  is the weighted coefficient of blueberry yield estimation. Take an image of a blueberry in the East, West, North, South and top five directions, compare the blueberry yield shown in the image with the actual yield, and then get the specific value of  $a$ .

## RESULTS

In order to verify the performance of the vision system of agricultural information collection robot, this experiment set up indoor and outdoor blueberry information acquisition control group to test the effectiveness of the system. As the platform of this system, the ground air dual-purpose robot is responsible for image acquisition of blueberry fruit. The robot consists of four parts: ground walking device, sky flying device, machine control system and visual processing system. The vision system can walk freely through the ground air dual-purpose robot, which is convenient for collecting blueberry fruit information. The field operation effect of the ground air dual-purpose robot is shown in Fig. 6.



**Fig. 6 - Field operation of ground air dual purpose robot**

The collected fruit information is output by human-computer interaction interface, and the output data information can be visualized after relevant processing. In the experiment, 100 blueberry fruit images were selected as the sample data, and the original image was segmented and the feature pixels were processed. At the same time, the weight coefficient of the characteristic data was determined by pixel labelling method. Finally, the blueberry fruit images of the two control groups were identified by the segmentation algorithm. The effectiveness evaluation indexes of the algorithm are true positive, false positive and similarity of the segmented image. The test results shown in Table 1 are obtained after relevant operations.

According to the above Table 1, the processed image has a high true positive, which shows that the segmentation algorithm can better identify blueberry fruit, meet the needs of actual operation, and can lay the foundation for subsequent fruit contour extraction. In addition, in order to verify the accuracy of the design algorithm to obtain crop fruit information, it is necessary to measure the fruit quality and diameter through the visual system.

Table 1

\	True positive	False positive	Similarity
Blueberry fruit image 1	97.835	1.998	95.917
Blueberry fruit image2	95.756	1.262	94.563
Blueberry fruit image3	98.938	1.393	96.127
Blueberry fruit image4	96.913	2.027	95.982
Blueberry fruit image5	98.714	1.532	94.127
Blueberry fruit image6	97.194	2.919	97.028
Blueberry fruit image7	97.914	1.415	98.917
Blueberry fruit image8	95.244	1.822	95.189
Blueberry fruit image9	94.922	2.567	94.614
Blueberry fruit image10	96.892	1.817	98.032
Comprehensive	96.932	1.875	96.049

The diameter measurement tool is vernier calliper, the quality measurement tool is electronic scale, 100 measurement samples are selected, 10 groups are randomly selected for result analysis, and the measurement results are shown in Table 2. It can be seen from table 2 that the vision system has high measurement accuracy for blueberry fruit, which basically conforms to the actual measurement value of blueberry fruit.

Table 2

Blueberry fruit number	Actual diameter (mm)	Measuring diameter (mm)	Relative error (%)	Actual quality (%)	Measurement quality (%)	Relative error (%)
Blueberry 1	17.61	17.43	1.034	2.38	2.42	1.661
Blueberry 2	17.84	17.45	2.237	2.42	2.44	0.824
Blueberry 3	18.95	19.08	0.786	2.84	2.81	1.072
Blueberry 4	14.96	15.34	2.479	1.52	1.54	1.308
Blueberry 5	13.81	14.02	1.499	1.34	1.35	0.752
Blueberry 6	15.37	15.42	0.325	1.62	1.64	1.228
Blueberry 7	13.08	12.87	1.633	1.34	1.28	4.725
Blueberry 8	13.88	12.92	7.437	1.42	1.41	0.710
Blueberry 9	18.21	18.72	2.726	2.62	2.52	3.985
Blueberry 10	17.61	18.03	2.331	2.22	2.32	4.330

After the quality inspection of blueberry fruit, it is necessary to estimate the yield. Two control groups were designed for yield prediction, namely, indoor yield prediction and outdoor yield prediction. Each group of prediction samples were set as 100 groups, and 10 groups were randomly selected for result analysis. Indoor blueberry prediction needs to put the blueberry fruit on the electronic scale to get its actual value, and then use the visual system to predict the yield of blueberry fruit. The predicted results are compared with the actual results, and the comparative analysis results are shown in Table 3. It can be seen from table 3 that the predicted yield of blueberry is generally consistent with the actual situation, and the error range of yield estimation is only 0.034% - 1.078%.

Table 3

Blueberry image	Actual blueberry fruit number	Estimated number of blueberry fruit	Quality measurement of blueberry fruit	Prediction of blueberry fruit quality	Relative error of production forecast
Blueberry fruit group 1	55	55	94.39	94.34	0.054
Blueberry fruit group 2	50	50	84.03	84.83	0.944
Blueberry fruit group 3	52	52	88.93	88.96	0.034
Blueberry fruit group 4	48	48	82.41	82.55	0.17
Blueberry fruit group 5	47	47	81.19	81.14	0.062
Blueberry fruit group 6	44	43	75.38	75.22	0.213

**Table 3**  
(continuation)

Prediction results of blueberry fruit yield					
Blueberry image	Actual blueberry fruit number	Estimated number of blueberry fruit	Quality measurement of blueberry fruit	Prediction of blueberry fruit quality	Relative error of production forecast
Blueberry fruit group 7	40	39	68.68	68.56	0.176
Blueberry fruit group 8	37	36	63.27	63.96	1.079
Blueberry fruit group 9	33	33	55.74	55.93	0.340
Blueberry fruit group 10	28	28	46.52	46.91	0.832

After the prediction of blueberry fruit yield in the laboratory, it is necessary to carry out field blueberry fruit prediction experiment, and the setting and grouping of control group are the same as indoor. In the field prediction experiment, we need to collect the single cluster fruit image of wild blueberry, and then use the visual system to predict the single cluster fruit yield of wild blueberry. Finally, the electronic scale was used to measure the actual single cluster fruit yield of wild blueberry. After the completion of the two groups of tests, the yield values of the two were compared. The detailed comparative analysis results are shown in Table 4.

**Table 4**

Prediction results of blueberry fruit yield			
Blueberry image	Quality measurement of blueberry fruit(g)	Estimation of blueberry fruit quality(g)	Relative error of yield estimation (%)
Blueberry cluster 1	81.65	79.53	2.667
Blueberry cluster 2	76.79	71.94	6.743
Blueberry cluster 3	70.75	75.19	5.906
Blueberry cluster 4	67.3	75.12	10.412
Blueberry cluster 5	80.62	86.55	6.853
Blueberry cluster 6	80.66	74.59	8.139
Blueberry cluster 7	66.64	61.66	8.078
Blueberry cluster 8	99.33	90.37	9.916
Blueberry cluster 9	75.44	69.53	8.502
Blueberry cluster 10	128.64	114.41	12.439

It can be seen from table 4 that the estimated blueberry fruit yield is generally consistent with the actual blueberry fruit yield. Generally speaking, there is a small estimation error, the error range is [2.667%, 12.439], and the maximum error is less than 13%. Therefore, the vision system can accurately collect blueberry fruit information, and can predict the fruit yield according to the collected information, and the prediction error is small. It has high practicability.

## CONCLUSIONS

In the design and research of the ground air dual-purpose agricultural information collection robot, the most core is the design of machine vision system. This research designs a vision system based on the ground air dual-purpose agricultural information acquisition robot. The system design is mainly carried out from two aspects of software and hardware, image processing. The system is based on the ground air dual-purpose agricultural information acquisition robot, which can complete the crop information collection work in complex environment, so as to accurately judge the spatial position of crops and fruit maturity. In order to prove the effectiveness of the system, indoor and outdoor blueberry fruit information collection control groups were set up to verify the collection effect of the system. The fruit recognition detection results show that the fruit image processed by the vision system has high true positive, which indicates that the segmentation algorithm of the system can identify blueberry fruit better; the fruit quality detection results show that the vision system has high measurement accuracy for blueberry fruit, which basically conforms to the actual measurement value of blueberry fruit; the fruit yield prediction results show that the indoor and outdoor environment is good. The error between the predicted value and the actual value was 2.667% to 12.439%, and the maximum error was less than 13%. In conclusion, the vision system can not only effectively complete the information collection of blueberry fruit, but also has good information analysis ability.

Although this design has a certain reference significance for the research of agricultural information collection robot, there are still some problems in the experiment, such as less sample data and low experimental accuracy.

## REFERENCES

- [1] Adamides G., Katsanos C., Constantinou I., (2017), Design and development of a semi-autonomous agricultural vineyard sprayer: Human-robot interaction aspects. *Journal of Field Robotics*, Vol.34, Issue 8, pp.1407-1426, USA;
- [2] Blanes C., Ortiz C., Mellado M., (2015), Assessment of eggplant firmness with accelerometers on a pneumatic robot gripper. *Computers & Electronics in Agriculture*, Issue 113, pp.44-50, England;
- [3] Bodunde O.P., Adie U.C., Ikumapayi O.M., (2019), Architectural design and performance evaluation of a ZigBee technology based adaptive sprinkler irrigation robot. *Computers and Electronics in Agriculture*, Issue 160, pp.168-178, England;
- [4] Bogue R., (2016), Robots poised to revolutionize agriculture. *Industrial Robot an International Journal*, Vol.43, Issue 5, pp.450-456, England;
- [5] Chebrolu N., Lottes P., Schaefer A., (2017), Agricultural robot dataset for plant classification, localization and mapping on sugar beet fields. *International Journal of Robotics Research*, Vol.36, Issue 10, pp.1045-1052, England;
- [6] Choi K.H., Han S.K., Han S.H., (2015), Morphology-based guidance line extraction for an autonomous weeding robot in paddy fields. *Computers and Electronics in Agriculture*, Issue 113, pp.266-274, England;
- [7] Jiao J., Kong W., Wang Q., (2015), Self-adaptive sliding mode control based on input fuzzy for agricultural tracked robot. *Nongye Jixie Xuebao/Transactions of the Chinese Society of Agricultural Machinery*, Vol.46, Issue 6, pp.14-19 and 13, China;
- [8] Jin M., Wang C.G, Wang P.P., (2020), CFD Numerical Simulation of Temperature and Airflow Distribution in Pigsty Based on Grid Independence Verification. *INMATEH Agricultural Engineering*, Vol.61, Issue 2, pp.241-250, Romania;
- [9] Kauser N., Banu S., Yuvaraja T., (2018), IOT Based Agricultural Application Using Robot—Agrobot. *Journal of Computational and Theoretical Nanoscience*, Vol. 15, Issue 6, pp.2137-2139, China;
- [10] Noguchi N., (2018), Agricultural Vehicle Robot. *Journal of Robotics and Mechatronics*, Vol.30, Issue 2, pp.165-172, Japan;
- [11] Peña César, Riaño Cristhian, Moreno G., (2018), RobotGreen. A Teleoperated Agricultural Robot for Structured Environments. *Journal of Engineering Science & Technology Review*, Vol.11, Issue 6, pp.145-155, Greece;
- [12] Raja S.K.S., Balaji V, Vivekanandan M., (2015), Autonomous mobile navigation robot for agricultural purpose. *International Journal of Applied Engineering Research*, Vol.10, Issue 10, pp.27333-27341, Algeria;
- [13] Vasconez J.P., Kantor G A, Cheein F.A.A., (2019), Human–robot interaction in agriculture: A survey and current challenges. *Biosystems Engineering*, pp.179-35-48, USA;
- [14] Vijay K.V., Vani K.S., (2018), Agricultural Robot: Leaf Disease Detection and Monitoring the Field Condition Using Machine Learning and Image Processing. *International journal of computational intelligence research*, Vol. 14, Issue 7, pp.551-561, France;
- [15] Yu N., Wang Q., Cao S.C., (2020), Road Recognition Technology of Agricultural Navigation Robot Based on Road Edge Movement Obstacle Detection Algorithm. *INMATEH Agricultural Engineering*, Vol.61, Issue 2, pp.281-292, Romania;
- [16] Zavala Y.R., (2017), Ramírez-Mendoza, Ricardo A, García-Lara, Silverio. A 3-SPS-1S parallel robot-based laser sensing for applications in precision agriculture. *Soft Computing*, Vol.21, Issue 3, pp.641-650, USA;
- [17] Zhang C., Noguchi N., (2017), Development of a multi-robot tractor system for agriculture field work. *Computers and Electronics in Agriculture*, Issue 142, pp.79-90, England.

## EXPERIMENTAL RESEARCHES ON DETERMINING THE WEAR OF CHISEL KNIFE MADE OF THREE TYPES OF MATERIALS

/

## CERCETĂRI EXPERIMENTALE PRIVIND DETERMINAREA UZURII CUTITELOR TIP DALTA REALIZATE DIN TREI TIPURI DE MATERIALE DIFERITE

Vladutoiu L.<sup>1)</sup>, Grigore I. A.<sup>1)</sup>, Sorică E.<sup>1)</sup>, Petrea A. A.<sup>1)</sup>, Cristea O.D.<sup>1)</sup>, Dumitru I.<sup>1)</sup> <sup>1</sup>

<sup>1)</sup> National Institute for Research-Development of Machines and Installations Designed for Agriculture and Food Industry –  
INMA Bucharest / Romania

First author E-mail: [laurentiuvladutoiu82@gmail.com](mailto:laurentiuvladutoiu82@gmail.com)

DOI: <https://doi.org/10.35633/inmateh-62-28>

**Keywords:** soil, wear, active parts

### ABSTRACT

The paper presents the interaction system within soil working mechanical process, consisting of two elements, namely the soil and the tool metal, between which there is a relative movement at the level of the interface between the two elements. Research has shown that there are at least two main forces acting on the active parts: friction and impact, the action of these forces causing wear.

In order to test the soil working knives under laboratory conditions, a test stand was used to test different types of soil working knives by modifying their functional parameters, respectively the working depth, knife angle relative to the soil, lateral angle relative to the forward direction, working speed and, if necessary, granulation and moisture of the test medium respectively.

### REZUMAT

Lucrarea prezintă sistemul de interacțiune din cadrul procesului mecanic de prelucrare a solului, constituit din două mari elemente, solul și metalul sculei, între care există o mișcare relativă la nivelul interfeței dintre cele două elemente. Cercetările au arătat că există cel puțin două forțe principale care acționează asupra părților active: frecarea și impactul, acțiunea acestor forțe determinând uzura.

În vederea încercării în condiții de laborator a cutitelor de lucrat solul, s-a folosit un stand ce permite încercarea în condiții de laborator a diferitelor tipuri de cutite de lucrat solul, prin modificarea parametrilor funcționali ai acestora, respectiv a adâncimii de lucru, unghiului de așezare, unghiului lateral față de direcția de înaintare, a vitezei de lucru și respectiv, după necesități, a granulației și umidității mediului de încercare.

### INTRODUCTION

Within the main soil works, the active parts, such as: body, ploughshare, disc, chisel, etc., are quickly subjected to abrasive wear because of the contact with the soil. The active parts must be checked for wear resistance under different working conditions, so that, over an average service life, wear resistance should be determined (Mehrang *et al.*, 2019), in order to ensure the exchange of parts in a timely manner. The article presents the experimental research carried out to find out the wear resistance of chisel knives, at a certain depth, working speed and the interaction of chisel knives with a certain type of material (sand) so that between these parameters is determined a correlation, to improve the life of chisel knives (Cardei *et al.*, 2018).

Research carried out by some authors (Matache *et al.*, 2008) has shown that there are two main forces acting on the active parts: friction and impact. The action of these forces causes wear, which manifests in two distinct aspects, namely: impact wear and friction wear.

Deep soil working, without turning the furrow, is one of the works that influence the condition of crops when climatic conditions are not favourable. A special problem is the one that appears in the areas with drier climate, where the intensive soil working and the removal of vegetal residues contribute to the loss of water from the soil, accentuating the processes of drought and desertification.

<sup>1</sup> Vladutoiu L., Ph.D. Stud. Eng.; Grigore I. A., Ph.D. Stud. Eng.; Sorică E., Ph. D. Stud. Eng.;  
Petrea A. A., Ph.D. Stud. Eng.; Cristea O.D., Ph. D. Stud. Eng.; Dumitru I., Ph. D. Stud. Eng.

Chisel soil loosening equipment is designed to loosen the soil without overturning the furrow, in order to increase the thickness of the loosened layer and increase the water penetration capacity.

Chisel soil tillage is recommended prior to the establishment of straw crops (Epure, 2011, Kuht et al., 2012). Studies show that the positive effects are observed after the first year of activity and consist in increasing the porosity of the soil, as well as increasing the biological activity in the soil (Odey and Manuwa, 2018).

Changing the geometry of chisel knives, because of premature wear generated by the interaction with the soil, leads to large increases in working resistance and fuel consumption (Canarach A., 1990; Iznaga et al., 2018; Pirowski et al., 2012; Ucgul et al., 2015).

It has been shown that the hardness of the material the active parts are made of is not always the decisive factor that influences wear the most. There is an inverse relationship between the hardness of the material and its ability to withstand abrasive wear, thus carbon steels have a higher abrasion resistance than cast iron with globular graphite, but the choice of cast iron is due to low production costs (Voicu et al., 2019; Bednar et al., 2013).

As the chisel knife advances into the soil, there is a relative movement at the level of the interface between the two elements. These chisel knives are subject to variable stresses, with higher values, compared to the stress other parts of the equipment are subject to (Matache et al., 2008; Tomescu et al., 1981; Tomescu et al., 1987; Tudor et al., 2000).

Various studies have shown that the intensity of wear increases in proportion to the increase in stress and the size of the abrasive particle dimensions. Speed does not have a decisive influence on the intensity of wear. Also, the intensity of chisel knives' wear is influenced by the wear resistance of the materials they are made of.

In the present research, the phenomenon of wear that occurs as a result of the interaction between the chisel knife and the sandy material in the sample stand was analysed.

Mechanical soil working is a complex process that requires high energy and material consumption because of soil resistance to breakage and intense abrasive wear of chisel knives.

In order to optimize the process of soil mechanical working, the following parameters are taken into account:

- geometric parameters of the chisel knife;
- soil specific parameters;
- functional parameters of the process.

## MATERIALS AND METHODS

In order to test the chisel knives, a test stand (Fig. 1) made by the National Institute of Research - Development for Machines and Installations Designed for Agriculture and Food Industry - INMA Bucharest was used. With the help of this stand, different types of soil working knives can be tested under laboratory conditions, by modifying their functional parameters: working depth, angle of soil working knives, working speed (indirectly established as the tangential speed in the circular movement of the support arms), granulation and humidity of the test medium.

The stand for testing chisel knives consists of the following main subassemblies:

- Sand basin;
- Worm gear motor for driving;
- Assembly of working part support arms;

The stand allows the modification of the following functional parameters of chisel knives:

- working depth;
- lateral angle relative to the forward direction;
- working speed (by varying the speed of the drive motor).

Due to the overall dimensions and functional dimensions established, the stand allows the testing of chisel knives on a circular trajectory with a diameter of 1600 mm, at a maximum depth of 300 mm.

The main technical characteristics of the stand are:

- |                        |                               |
|------------------------|-------------------------------|
| - gear motor type:     | worm gear motor MRV 100 U02A; |
| - electric motor:      | HB2 132M B5;                  |
| - power, kW:           | 7.5;                          |
| - frequency, Hz:       | 50;                           |
| - electric tension, V: | 400;                          |

- International Protection Marking: IP55;
- speed, rpm: 1460;
- mounting position: V5;
- gear ratio: 10;
- output speed, rpm: 146;
- maximum adjustment depth: 300;
- overall dimensions, mm
  - basin outer diameter: 2000;
  - basin height: 1000.

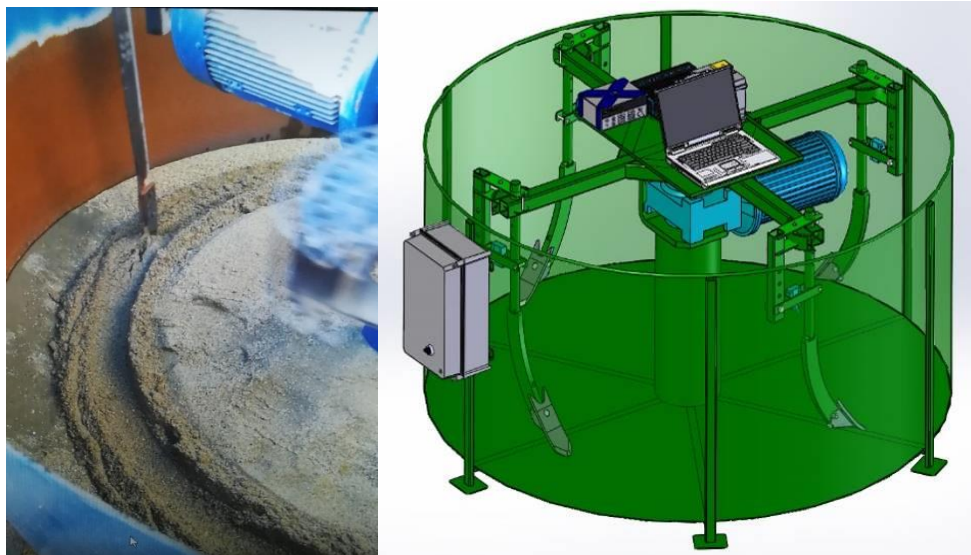


**Fig. 1 – Experimental stand for testing chisel knives**

Using the stand, the following types of chisel knives were tested under laboratory conditions:

For tests, 3 types of chisel knives (Figure 2) were made of different materials: C45 (sample 1), C45 heat-treated (sample 2), E295 (sample 3).

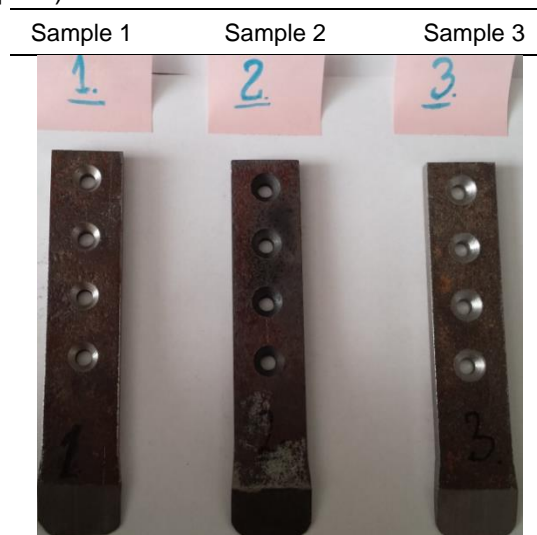


**Fig. 2 - Types of chisel knives made of different materials:**  
1 - C 45; 2 - C 45 heat-treated by hardening; 3 – E295

In order to reduce the influence of various physical parameters that characterize agricultural soil and to maximize its effect on the wear of chisel knives, it was decided to conduct experiments in a medium that favours basic observations on the chisel knife-soil interaction.

Thus, we chose as test medium fine quartz sand for dry adhesive mortars, as commercial application, obtained by washing and mechanical grading which falls within the particle size class coarse sand and fine sand (according to the Attenberg limits) with a particle diameter between 0 and 0.3 mm.

By using this test medium, it is desired to determine the data in purely fictional test mediums.

The test medium used is a fictional medium, without cohesion and without structure with maximum wear effect (wear is maximum when the percentage of abrasive particles with a size of 0.25 mm has maximum value).

A KERN EG precision balance with the following characteristics was also used:

- Division: 0.01 g;
- Maximum capacity: 4200 g;
- Minimum capacity: 500 mg;
- Minimum weight of the piece to be counted: 10 mg;
- Weighing plate size (WxD): 180x160 mm;
- Reproducibility: 0,01 g;
- Linearity: +/-0.02 g;

Penetration resistance  $F$  was calculated with the formula:

$$F = p \cdot S \quad [N] \quad (1)$$

where:  $p$  is the pressure, [MPa];

$S$  - the surface of the penetrating cone, [mm<sup>2</sup>].

The gravimetric method was used to determine the overall wear, which consisted in determining the difference between the initial mass and the mass measured after a certain period of chisel knife operating.

## RESULTS

The chisel knives were mounted one by one in the test stand (Figure 3), where they worked at an angle of attack of 27° (Figure 4) and at a depth of 22 cm in the sand of the test stand, so that their wear could be determined after a number of operating hours.



Fig. 3 - Chisel knife mounted on the experimental stand

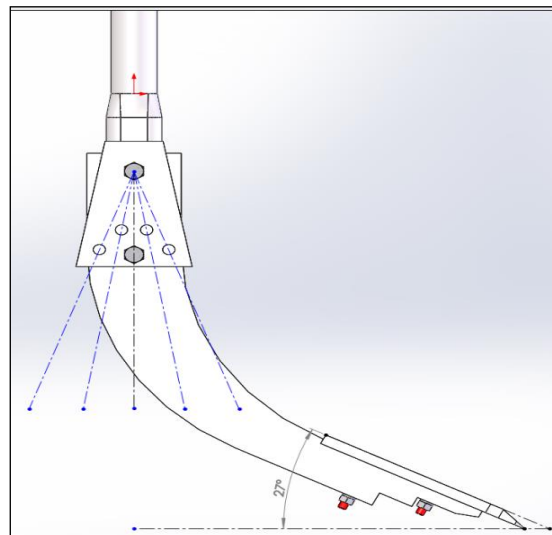


Fig. 4 - Adjusting the angle of attack on the tool holder

The chisel-type knives were weighed (Figure 5) before being mounted on the test stand and let operate for one hour, after which they were weighed and mounted back on the stand for another hour of testing, process repeated 8 times for each knife, thus tracking material losses through wear.



Fig. 5 - Chisel knives weighing

Tables 1 and 2 show the actual wear for each hour of operation. During the 8 hours of operation, the chisel knife made of E295 registered 1.07 grams wear, the one made of C45 heat treated by hardening, 1.47 grams wear and the chisel knife made of C45, 2.12 grams wear.

Table 1

Evolution of weight loss of the 3 chisel knives after 8 hours of testing

Knife type	Weight of chisel knife, after weighing, at a test time interval on the experimental stand (grams)									
	Initial	After 1 hour	After 2 hours	After 3 hours	After 4 hours	After 5 hours	After 6 hours	After 7 hours	After 8 hours	Total wear
C 45	259.51	259.15	258.96	258.82	258.57	258.14	257.85	257.59	257.39	2.12
C 45 heat treated by hardening	254.74	254.37	254.16	253.95	253.82	253.66	253.53	253.38	253.27	1.47
E295	236.75	236.63	236.55	236.38	236.24	236.05	235.91	235.8	235.68	1.07

Table 2

Mass differences (actual wear) after each test hour:

Knife type	Wear at a time interval in dry sand (grams)								
	Initial	After 1 hour	After 2 hours	After 3 hours	After 4 hours	After 5 hours	After 6 hours	After 7 hours	After 8 hours
OLC 45	0.36	0.19	0.14	0.25	0.43	0.29	0.26	0.2	2.12
OLC 45 heat-treated	0.37	0.21	0.21	0.13	0.16	0.13	0.15	0.11	1.47
OL 50	0.12	0.08	0.17	0.14	0.19	0.14	0.11	0.12	1.07

Figure 6 shows the evolution of the wear of the 3 chisel knives before and after the 8 hours of testing.

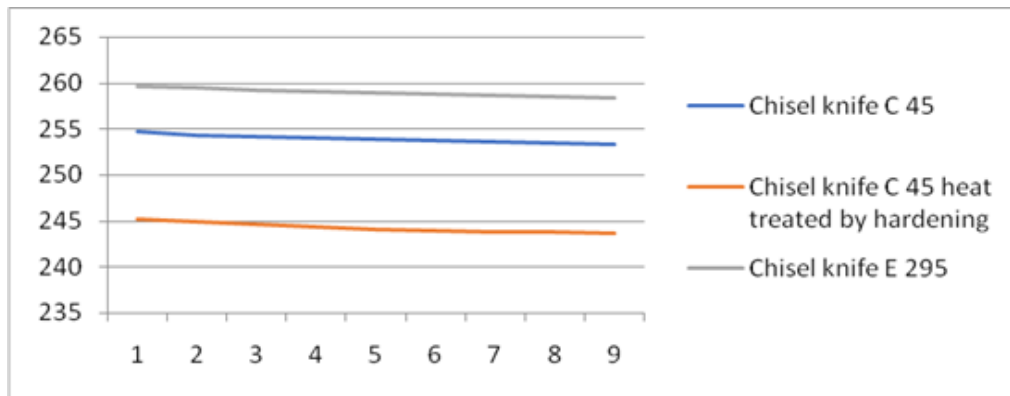


Fig. 6 - Evolution of the wear of the 3 chisel knives

Plotting the regression line of the experimental data can be seen in Figure 7, for our data choosing a polynomial distribution. It is also represented the evolution of the increase in wear degree of the 3 chisel knives, in the 8 hours of operation. Thus, it can be seen that the chisel knife made of E295 suffered less wear during the entire period of operation, followed by the chisel knife made of C 45 heat treated by hardening, while the chisel knife made of C 45 suffered the biggest wear.

It can also be seen that the chisel knives suffered the highest degree of wear in the first hours of operation, after which the degree of wear decreases.

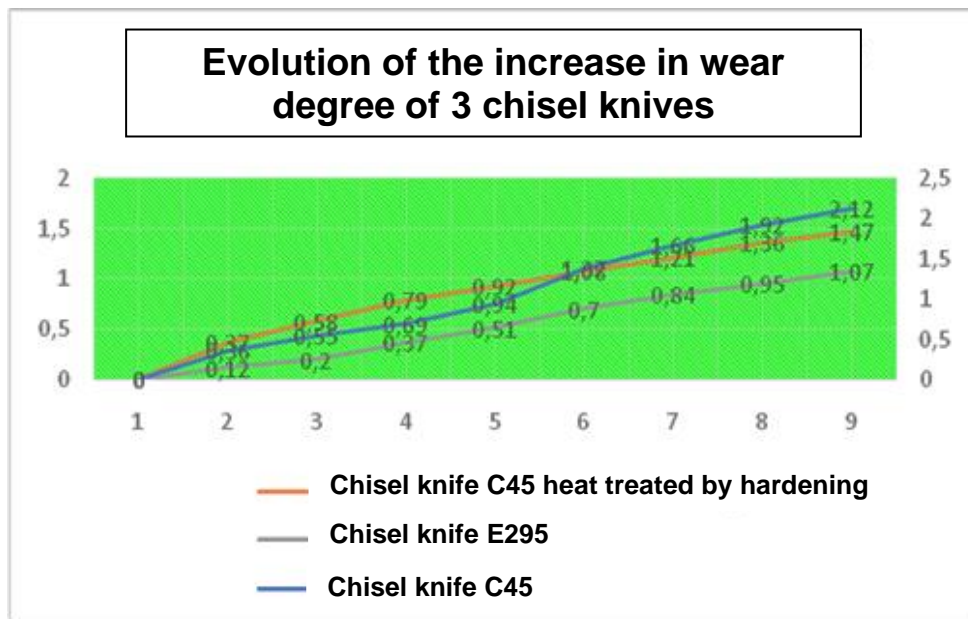


Fig. 7 - Evolution of the increase of the wear degree of the 3 chisel knives

## CONCLUSIONS

Mechanical soil working is a complex process that requires high energy and material consumption because of soil resistance to breakage and intense abrasive wear of chisel knives.

Following the tests of these chisel knives, for 8 hours each, it resulted that the E295 chisel knife suffered less wear, followed by the chisel knife made of C 45 heat treated by hardening. The chisel knife made of C 45 suffered the biggest wear.

It is important to continue the research to estimate the average operating time of the chisel knives for working the soil and to establish the appropriate maintenance intervals.

## REFERENCES

- [1] Bednar R., Votava J., Cervinka J., Fajman M., (2013), Suitability of technical materials for machinery subsoilers for soil tillage, *Acta Universitatis Agriculturae et Silviculturae Mendelianae Brunensis*, LXI (1), pp. 9-16;
- [2] Braharu D., Gângu V., Vlăduț V., Postelnicu E., Băjenaru S., (2007), Fundamental research regarding the methods of anti-wear deposit, adaptable to components for agricultural equipment, *Annals of the University of Craiova – Agriculture, Montanology, Cadastre series*, Volume XXXVII/B, pp. 36-47, Craiova / Romania;
- [3] Cujbescu D., Bungescu S., Kiss I., Vlad C., (2017), Field and laboratory wear testing of integral seedbed implement's chisel tines point, *Proceedings of the 45<sup>th</sup> International Symposium on Agricultural Engineering "Actual Tasks on Agricultural Engineering"*, Opatija – Croatia, pp. 131-140;
- [4] Canarach A., (1990), *Agricultural Soil Physics*, Ceres Publishing House, Bucharest / Romania;
- [5] Cardei P., Vladutoiu L., Chisiu G., Tudor A., Sorica C., Gheres M., Gheorghe G. and Muraru S., (2018). *Research on friction influence on the working process of agricultural machines for soil tillage*, *IOP Conference Series: Materials Science and Engineering*, Vol. 444 (2);
- [6] Epure I.C., (2011), *Theoretical and experimental modelling of the soil loosening-scarification process*, PhD thesis. TRANSILVANIA University of Brasov / Romania;
- [7] Grigore I., Marin E., Sorică E., Sorică C., Danciu A., Matache M., Vlăduț V., Gheorghe G., Ungureanu N., Mircea C. (2016), Stand for determining the wear of active bodies in accelerated regime, *Annals of the university of Craiova - Agriculture, Montanology, Cadastre*, series, vol. 46 (2), *Management, Agriculture Mechanization and Cadastre*, pp. 405-410, Romania;
- [8] Iznaga S., Lázaro A. et al., (2018), Effect of Geometry and Type of Material in Tillage Implements Wear (Efecto de la geometría y tipo de material en el desgaste de aperos de labranza). *Rev Cie Téc Agr* [online - ISSN 2071-0054], vol.27, n.1 pp. 36-45;
- [9] Kuht J., Reintam E., Edesi L., Nugis E., (2012), Influence of subsoil compaction on soil physical properties and on growing conditions of barley. *Agronomy Research*. 10(1–2), pp. 329–334;
- [10] Matache M., Ganga M., Mihai M., Postelnicu E., Bajenaru S., (2008), Researches regarding determination of mechanical and wear characteristics for friction materials, *Scientific Papers (INMATEH)*, vol. 28, pp. 120-123, Bucharest / Romania;
- [11] Mehrang S.M., Shahgholi G., Moifar A., (2019), Effect of nano coating materials on reduction of soil adhesion and external friction, *Soil and Tillage Research*, Volume 193, pp 42-49;
- [12] Odey S.O., Manuwa S.I., (2018), Subsoiler development trend in the alleviation of soil compaction for sustainable agricultural production, *International Journal of Engineering and Technology*, 7(8), pp.29-38;
- [13] Pirowski Z., Kranc M., Olszynski J., Gwizdz A., Goscianski M., (2012), Performance testing of cast agricultural tools operating in soil, *Teka Commission of motorization and energetics in agriculture*, Vol. 12, no. 2, pp. 183–188;
- [14] Popa A, Coman E., Macovei C., Căndea V., Jumate N., Matache M., Vlăduț V., Predescu C. (2010), *Iron-based composite used as a friction material and process for obtaining it*, Patent Number: RO125437-A2; RO125437-B1, OSIM Romania;
- [15] Ucgul M., Fielke J.M. and Saunders C., (2015), Defining the effect of sweep tillage tool cutting edge geometry on tillage forces using 3D discrete element modelling, *Information processing in agriculture 2*, pp. 130-141;
- [16] Tomescu D., Manciu Gh., Valentin S., (1981), *Agricultural machinery reliability*, Bucharest / Romania;
- [17] Tomescu D., Florea Șt., Benescu L., Nicolae M., (1987), *Methods, processes and technologies for reconditioning parts of agricultural machinery*, CERES Publishing House, Bucharest / Romania;
- [18] Tudor A., Tache C., Tache A., (2000), A Cutter Model for Manufacturing Winkler Brittle Material", *AIMETA International Tribology Conference, September 20-22, L'Aquila, Italy*, pp. 320-327;
- [19] Vlăduț V., Biriș S., Bungescu S., Marin E., Persu C., Grigore I., Ungureanu N., Gheorghe G., Voicea I., Ilea R., Hărmănescu M., Cujbescu D., Bolintineanu Gh., Dumitru I. (2016), Researches on determining the wear of active parts of chisel type in heavy soils, *International Symposium ISB-INMA TEH' 2016 Agricultural and Mechanical Engineering*, pp. 515-522, Bucharest / Romania;

- [20] Vlăduț V., Marin E., Grigore I., Biriș S.Șt., Ungureanu N., Gheorghe G., Matache M., Persu C., Vocea I., Cujbescu D., Bungescu S., Kiss I., Vlad C., (2017), Field and laboratory wear testing of integral seedbed implement's chisel tines point, *Proceedings of the 45<sup>th</sup> International Symposium on Agricultural engineering "Actual Tasks on Agricultural Engineering"*, pp. 131-140, Opatija / Croatia;
- [21] Vlăduț N.V., Marin E., Biriș S.S., Bungescu S., Ungureanu N., (2019), *Supplementary cutting element has wear-resistant metal element in form of arrow with geometry of lower portion in sharp-pointed form with angle extended with two parallel fins provided with concentric holes*, Patent Number: RO132740-A2k, OSIM Romania;
- [22] Vlăduț N.V., Marin E., Matache M.G., Biriș S.S., Maican E., Grigore I., Ungureanu N., (2019), *Method for determining linear intensity of wear of chisel-type active part of soil-working equipment, involves continuously measuring normal force on friction surface of chisel active portion placed on measuring stand*, Patent Number: RO132885-A2, OSIM Romania;
- [23] Voicu G., Olac B., Ilie, F., Tudor P., (2019), Aspects regarding the wear of working parts of the Agricultural scarifiers, *Research People and Actual Tasks on Multidisciplinary Sciences*, pp. 139-144, Lozenec / Bulgaria.

# THE DEVELOPMENT OF PORTABLE DETECTOR FOR APPLES SOLUBLE SOLIDS CONTENT BASED ON VISIBLE AND NEAR INFRARED SPECTRUM

/

## 基于可见光和近红外光谱的便携式苹果可溶性固形物含量检测仪的研制

Fa Peng<sup>1</sup>, ShuangXi Liu<sup>\*2</sup>, Hao Jiang<sup>2</sup>, XueMei Liu<sup>2</sup>, JunLin Mu<sup>2</sup>, JinXing Wang<sup>2</sup> <sup>1</sup>

<sup>1</sup> Beijing Agricultural Equipment Research Centre, Beijing, 100097, China;

<sup>2</sup> College of Mechanical and Engineering, Shandong Agricultural University, Taian, 271018, China;

Tel: +86 05388242336; E-mail: shuangxiliu168@163.com

DOI: <https://doi.org/10.35633/inmateh-62-29>

**Keywords:** *Apple soluble solids; Visible/near infrared spectroscopy; Portable; Adaptive Reweighted Algorithm; Successive Projections Algorithm*

### ABSTRACT

In order to detect the soluble solids content of apples quickly and accurately, a portable apple soluble solids content detector based on USB2000 + micro spectrometer was developed. The instrument can communicate with computer terminal and mobile app through network port, Bluetooth and other ways, which can realize the rapid acquisition of apple spectral information. Firstly, the visible / near-infrared spectrum data and soluble solids content information of 160 apple samples were collected; secondly, the spectral data preprocessing methods were compared, and the results showed that the prediction model of sugar content based on partial least square (PLS) method after average smoothing preprocessing was accurate. The correlation coefficient (RP) and root mean square error (RMSEP) of the prediction model were 0.902 and 0.589 ° Brix, respectively. Finally, on the basis of average smoothing preprocessing, competitive adaptive reweighted sampling (CARS) and successive projections algorithm (SPA) were used to optimize the wavelength of spectral data, and PLS model was constructed based on the selected 17 characteristic wavelengths, which can increase the accuracy of soluble solids content prediction model, increase the RP to 0.912, and reduce RMSEP to 0.511 ° Brix. The portable visible / near infrared spectrum soluble solids prediction model based on the instrument and method has high accuracy, and the detector can quickly and accurately measure the soluble solids content of apple.

### 摘要

为了快速、准确地测定苹果可溶性固形物含量，研制了基于 USB2000+ 微型光谱仪的便携式苹果可溶性固形物含量检测仪。该仪器可以通过网络端口、蓝牙等方式与计算机终端和移动应用程序进行通信，实现苹果光谱信息的快速采集。首先采集了 160 份苹果样品的可见光/近红外光谱数据和可溶性固形物含量信息；其次，对光谱数据预处理方法进行了比较，结果表明，经过平均平滑预处理后，基于偏最小二乘法（PLS）的糖含量预测模型是准确的。预测模型的相关系数（RP）和均方根误差（RMSEP）分别为 0.902 和 0.589°Brix。最后，在平均平滑预处理的基础上，采用竞争自适应重加权采样（CARS）和连续投影算法（SPA）对光谱数据的波长进行优化，并根据选取的 17 个特征波长构建了 PLS 模型，提高了可溶性固形物含量预测模型的精度，使 RP 提高到 0.912，RMSEP 降低到 0.511°Brix。基于该仪器和方法的便携式可见/近红外光谱可溶性固形物预测模型具有较高的精度，该检测仪能够快速、准确地测定苹果可溶性固形物含量。

### INTRODUCTION

Apple is one of the most popular fruits (LiYan Gong et al, 2014) in China. Its internal soluble solids (BRIX) directly affect consumers' willingness to buy (Fernando Mendoza et al, 2011; YanKun Peng et al, 2007). In recent years, with the improvement of residents' living standards, consumers have paid more and more attention to the internal quality of apples (HaiLiang Zhang et al, 2009).

The traditional soluble solids content measurement method is destructive detection (WenChuan Guo et al, 2015), which not only causes the fruit to be unable to be reused, but also time-consuming and laborious, which makes difficult to meet the actual application requirements.

<sup>1</sup> Fa Peng, SE.; ShuangXi Liu, As.Ph.D.Eng.; Hao Jiang, M.S.Stud. Eng.; XueMei Liu, M.S.Stud.Eng.; JunLin Mu, M.S. Stud. Eng.; JinXing Wang, Prof. Ph.D. Eng.

Visible / Near Infrared spectroscopy can realize nondestructive and rapid measurement of physical and chemical information of samples (Gabrieli Alves de Oliveira et al, 2014; Agus Arip Munawar et al, 2019), and is widely used in the field of fruit quality detection (HuiJun Liu et al, 2015; ZhuanWei Wang et al, 2018; BartM Nicolai et al, 2014). For the study of nondestructive testing of apple soluble solids content, YanDe Liu et al (2007) used near-infrared spectroscopy to study the influence of different sampling distances on apple spectrum measurement; XiaoBo Zou et al (2007) used Fourier near-infrared spectroscopy to model and analyse apple soluble solids, and found that using iPLS and genetic algorithm together for characteristic wavelength screening can further improve the accuracy of the prediction model; JieWen Zhao et al (2005) and the like used principal component regression (PCR) and partial least squares (PLS) method to analyse apple soluble solids content. The research results show that the PLS model is more suitable for predicting the soluble solids content of apples than the PCR model; R Beghi et al (2012) carried out the measurement of soluble solids content of different apple varieties in the orchard environment based on the near-infrared spectroscopy technology, and achieved good accuracy. However, the detection system used is complicated and inconvenient to carry. The above-mentioned apple soluble solids content detection research focuses on methodological research. Although certain research progress has been made in equipment research and development, there is a lack of a complete solution from soluble solids content detection methods to system applications, which reduces its practical application value. Although there is portable detection equipment developed by scientific research institutes (Biao Yang et al, 2019; Xinyang Yu et al, 2016; Bin Wang et al, 2017), most of the equipment adopts the traditional black-and-white calibration method, and the dark reference spectrum and white reference spectrum are only collected once. In long-term use, the spectral intensity drift caused by the aging of the light source will affect the stability of the spectrum, resulting in the decline of the prediction accuracy of the equipment without self-calibration function.

This research intends to develop a portable apple soluble solids content detector based on visible / near-infrared spectroscopy, and realize the self-calibration function of the equipment by collecting the dark reference spectrum and white reference spectrum of apple samples in real time. It can communicate with the computer and mobile APP through the network port, Bluetooth, etc., to realize the portable detection of apple soluble solids content. The detector uses the visible / near infrared spectrum data of the apple sample to build the apple soluble solids content prediction model based on PLS, and compares different spectral predictions quantitatively. The influence of processing algorithm on full-band modelling and characteristic wavelength screening can realize the accurate detection of apple soluble solids content, hoping to provide a reference for fruit soluble solids content detection.

## **MATERIALS AND METHODS**

### **DETECTOR DESIGN**

#### ***Working Principle of Detector***

The schematic diagram of the portable apple soluble solids content detector system is shown in Fig. 1.

The detector consists of an optical fibre probe, a point light source, an optical fibre loop, a microcontroller, an auxiliary circuit, a miniature spectrometer and a display interface. The light path switcher controls the opening and closing of the light path through the electromagnetic valve to realize the on and off control of the light path. The transmitting fibre 1 and the receiving fibre are both a one-to-two fibre. The receiving end of one receiving fibre directly receives the light information of the light source. The white reference spectrum is collected when the solenoid valve is opened, the dark reference spectrum is collected when the solenoid valve is closed, and the other is receiving fibre. The end receives the spectral information of the sample. When collecting the sample spectrum, the optical path switcher opens the light path between the emission fibre 1 and the emission fibre 2.

The light generated by the light source is uniformly irradiated on the surface of the apple through the ring fibre, and the light reflected by the apple surface enters the miniature spectrometer through the receiving fibre. In the soluble solids content prediction model modelling stage, the detector can receive commands from different terminals through external triggers, resistance screens, network ports, and Bluetooth modules, and perform spectral data collection and storage, and display the collected data in real time on the host computer and the resistance screen.

In the soluble solids content prediction stage, the microcontroller performs apple soluble solids content prediction based on the real-time collected spectrum data and the constructed prediction model and feeds the results back to the mobile phone APP interface and LCD screen.

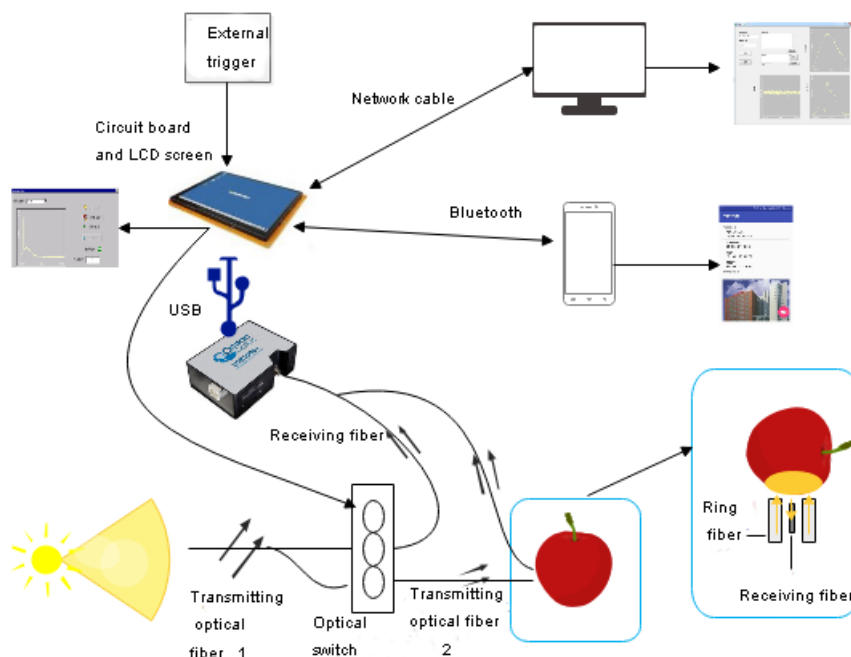


**Fig. 1 - System schematic diagram**

The physical map of the portable apple soluble solids content detector is shown in Fig. 2. The optical fibre probe has a ring optical fibre and an external trigger switch. The optical fibre loop includes a transmitting optical fibre 2 that conducts the light path of the light source and a receiving optical fibre that receives the reflected light information of the sample. The transmitting optical fibre 2 is composed of a single optical fibre and a ring optical fibre. The light source, miniature spectrometer and control circuit are located in the detector housing, and the light source adopts 3900 halogen lamps (Illumination Technologies).

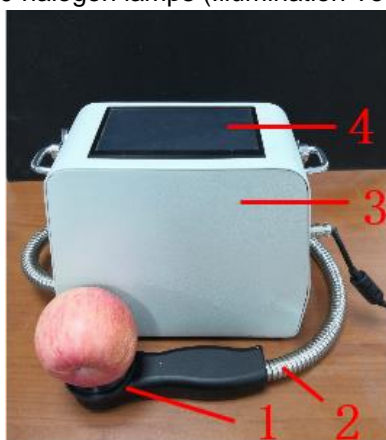


**Fig. 2 - Portable detector of soluble solids content for apples**

1) Optical fibre probe 2) Optical fibre loop 3) Detector housing 4) LCD resistive screen

**Microcontroller and Related Circuit Design**

The microcontroller of the soluble solids content detector uses a processor based on the ARM9 core, and WINCE is selected as the embedded operating system. The microcontroller directly controls the corresponding circuit through the IO port to complete the light path control, ensuring that the dark reference spectrum and the white reference spectrum for calibration can be collected at the same time when the sample spectrum data is collected. In addition, the detector also monitors the external trigger signal through IO. When the user presses a button, it can trigger a spectrum acquisition and soluble solids content measurement. The detector provides touch screen button operation for users to collect through the LCD resistive screen, which achieves the same function as the external buttons. The LCD resistive screen can display information such as spectral curves and sample soluble solids content. Because in the modelling stage of soluble solids content prediction model, the microcontroller needs to store a large amount of spectral data, therefore, an SD card is used to expand the storage space based on the FLASH storage that comes with the microcontroller.

The microcontroller can receive commands from different terminals. For example, using the TCP/IP protocol, the microcontroller can receive control commands from the host computer through the network port and send spectrum data to the host computer. In addition, the microcontroller can also be directly connected to the serial port Bluetooth module through the built-in RS232 serial port, which can ensure the small-range communication between the system and the mobile phone APP, thereby sending the predicted soluble solids content results to the mobile phone APP interface.

**Miniature Spectrometer**

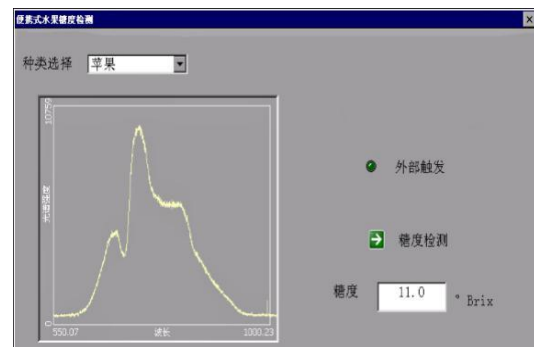
The detector uses a USB2000+ (Ocean Optics) miniature spectrometer with high signal-to-noise ratio for integrated development. The wavelength range of this spectrometer is 487-1147nm, and it has the advantages of small size, convenient installation and fixation. In addition, the miniature spectrometer has 16-bit A/D conversion resolution and 2048 wavelength points, and supports USB2.0 communication and RS232 communication. Call the USB2000+ library function in the WINCE system, and realize the parameter setting of the detector directly to the micro-spectrometer based on the USB protocol, and quickly obtain the real-time spectral data of the sample.

**Software Design**

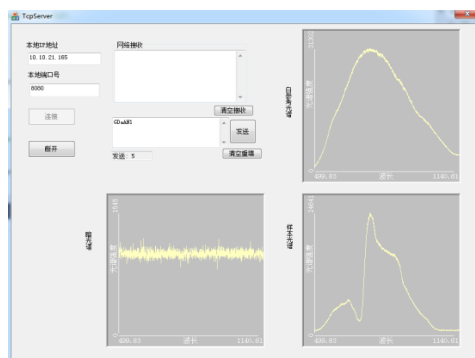
The software design of the detector includes WINCE system software, host computer software and mobile APP software design, so that the detector can be operated through different terminals to complete the collection, storage and real-time display of spectral data, as well as the construction of soluble solids content prediction model and the display of prediction results.



(A) Embedded system software interface



(B) The soluble solids content prediction interface of the embedded system



(C) Spectral data collection interface of host computer



(D) The mobile phone APP scans the Bluetooth device interface

**Fig. 3 - Display interface of system software**

The WINCE system software interface and the host computer software interface are realized by the Visual Studio platform based on C++ language programming. The WINCE system software spectrum data collection interface includes functions such as parameter setting, spectrum data collection, automatic storage, and real-time spectrum data display (Fig. 3a). Through the parameter setting function, the integration time of the spectrometer can be set; the spectral data collection can be realized through the external trigger and the soluble solids content detection button, and the spectral curve drawing and spectral data storage are automatically completed. The soluble solids content prediction interface (Fig. 3b) has user-operated touch buttons and a soluble solids content prediction result display box. The user only needs to press a button or an external trigger to complete the functions of spectral data collection, model prediction and soluble solids content display.

Because WINCE software is limited by the screen display space and flash storage space, this research further develops the host computer software (Fig. 3c). The host computer software is connected to the WINCE system software (referred to as the lower computer software) through the TCP/IP protocol. The host computer spectrum collection interface includes functions such as network port connection, spectrum collection control, spectrum curve display and automatic storage. The host computer software sends a spectrum acquisition instruction to the lower computer software, and the lower computer software automatically sends the collected dark reference spectrum, white reference spectrum and sample spectrum data to the host computer software after receiving the command. The host computer software automatically stores the collected spectrum data and displays it on the computer screen in real time. Through the displayed spectrum curve, it can be judged whether the collected signal of the spectrometer is saturated and whether the sample spectrum data is within the white reference spectrum data range.

The mobile app software (Fig. 3d) is programmed with JAVA language on the basis of Google's open source Android studio platform, which can realize the functions of device connection, soluble solids content detection and result display. The soluble solids content detection and display functions of APP software are similar to those of soluble solids content prediction interface (Fig. 3b), but not shown in Fig. 3d. The mobile app software is connected with the detector through Bluetooth, which can control the detector to collect spectral data and detect the sample soluble solids content. At the same time, the app software on the mobile phone can receive the sample soluble solids information fed back by the detector.

## APPLE SOLUBLE SOLIDS CONTENT PREDICTION MODEL DESIGN

### *Experimental Materials*

The apple samples used in the experiment were purchased from the Beijing Fruit Wholesale Market, and the variety was Yantai Fuji. A total of 160 apple samples with no obvious damage and scars were selected. In order to avoid influence of the external environment of the data, the skin cleaned apple fruit samples were placed in a laboratory environment 24 hours. Mark the equatorial position of each sample, and perform spectral data collection and soluble solids content measurement on the marked points. 120 samples were randomly selected to construct the model calibration data set, which was used to construct the apple soluble solids content prediction model, and the remaining 40 samples were used for model testing.

### *Spectrum Collection*

Use the developed portable apple soluble solids content detector to collect sample spectrum data. After preheating the light source, spectral data collection is performed on the marked position of the apple sample. Experiments have found that when the integration time of the miniature spectrometer is set to 200ms, a strong sample spectrum signal can be obtained, and the white reference spectrum will not exceed the maximum value of the acquisition signal range. Collect the spectrum data three times on the same sampling point, and take the average value as the spectrum data of the sample. At the same time, obtain the corresponding white reference spectrum and dark reference spectrum at this time. Perform calibration according to formula (1) to obtain the corresponding spectral reflectance, so as to realize the spectrum collection and dynamic correction of the fruit sample by the detector.

$$reflectance = \frac{sample - dark}{white - dark} \quad (1)$$

In the formula, sample is the sample spectrum data, dark is the dark reference spectrum, and white is the white reference spectrum.

The spectrum measurement range of the USB2000+ mini spectrometer is 487-1147nm. Since the first and last bands of the spectrometer may contain large noise, in order to improve the prediction accuracy of the model, the detector selects the spectral data in the 550-900nm band for analysis.

### **Soluble Solids Content Measurement**

Brix Apple sample measured using PAL-1 Brix detector (by ATAGO Co., LTD.'S., Tokyo, Japan) is obtained. In order to reduce the influence of storage time on the soluble solids content of the fruit, the soluble solids content of the apple sample is measured immediately after the end of the spectral data collection. For each apple sample, cut the pulp of 10mm thickness from the marked position and squeeze it to obtain the juice, drop the filtered juice onto the mirror surface of the refractometer, and record the soluble solids content displayed by the refractometer as the actual soluble solids content of the sample. Table 1 shows the statistical results of the soluble solids content of the calibration set and test set samples.

**Table 1**

Actual soluble solids content (°Brix) of apple's measured by the refractometer					
Sample set	Number of samples/pieces	Min/ °Brix	Max/ °Brix	Average/ °Brix	Standard deviation
Calibration set	120	10.1	16.6	13.15	1.21
Test set	40	10.2	16.3	13.22	1.25

## **SOLUBLE SOLIDS CONTENT PREDICTION MODEL**

### **Model Construction**

Partial least square (PLS) algorithm is widely used in spectral analysis because of its good stability and strong anti-interference ability (*Martin Andersson, 2009; Hong-Dong Li et al, 2018; Néstor F Pérez et al, 2009*). Therefore, the detector builds an apple soluble solids content prediction model based on the PLS algorithm. The optimal number of main factors of PLS algorithm is determined by the minimum root mean square error of cross validation (RMSECV). The original spectral data obtained by the spectrometer often contains random noise of the instrument. In addition, noise such as stray light will also affect the quality of the spectral data, which in turn affects the stability of the model. Therefore, this study quantitatively compared commonly used spectral data preprocessing algorithms, and determined the best preprocessing method by comparing the prediction accuracy of soluble solids content models based on different preprocessing methods. The preprocessing algorithms used in this study include: 9-point average smoothing (*XiaoLi Chu et al, 2004*), standard normal variate (SNV) (*R J Barnes et al, 1989*), maximum normalization (*RongQiang Gao et al, 2004*), 31-point first derivative method, and 51-point the second derivative method (*HaiLong Wang et al, 2015*).

### **Feature Wavelength Screening Algorithm**

Since there is a large amount of redundant and collinearity information between the spectral variables, in order to avoid the complicated model and large amount of calculation caused by redundant spectral information (*YongHuan Yun et al, 2019*), it is necessary to screen the original spectral data by characteristic wavelengths, especially for the development of portable equipment, which can increase the speed of calculation and the efficiency of detection. At present, competitive adaptive reweighted sampling (CARS) and successive projections algorithm (SPA) (*JingZhu Wu et al, 2011; YanDe Liu et al, 2013; Chu Zhang et al, 2016; ShuXiang Fan et al, 2019; YunFei Xu et al, 2019*) are widely used in many feature wavelength screening methods, and have achieved good results in spectral data analysis. Therefore, this paper attempts to use these two algorithms to screen the characteristic wavelength of apple spectral data, so as to reduce the calculation amount of the model and further improve the prediction accuracy of the model. The CARS algorithm starts with the regression coefficient of the PLS model. The larger the absolute value of the regression coefficient, the more important the wavelength is. CARS is used to retain the wavelength variables with large absolute value of regression coefficient in PLS model, and remove the variables with small weight. A series of wavelength variable subsets are obtained through multiple screening, and each wavelength subset is verified interactively. According to the minimum root mean square error of cross validation, the best wavelength variable is obtained (*HongDong Li et al, 2009*). SPA uses the projection analysis of vectors to filter the variable combinations with the least redundant information among a large number of wavelength variables, so as to minimize the collinearity between variables, reduce the number of variables used in modelling, and improve modelling efficiency (*Mário César Ugulino Araújo et al, 2001; Wei Wang et al, 2019*).

Relevant literature shows that the direct use of SPA for characteristic wavelength screening will greatly reduce the number of characteristic wavelengths, but it will often reduce the prediction accuracy of the model. Therefore, the SPA algorithm is usually combined with other algorithms (Dan Liu et al, 2014).

### Evaluation of Model Results

Correction correlation coefficient (Rc) and the predicted correlation coefficients (Rp) is a common indicator of the evaluation of the model quality. The larger the value of RC and RP, the better the prediction performance of the model. In addition, the RMSEC and RMSEP were used as the evaluation indexes of the model. The smaller RMSEC and RMSEP are and the closer they are, the better the prediction performance of the model is (ShuXiang Fan et al, 2015; ChengWen Chang et al, 2001).

## RESULTS AND ANALYSIS

### Full-Band Modelling Results Based on Different Preprocessing Algorithms

Table 2

PLS model results based on different preprocessing algorithms

Preprocessing methods	Number of main factors	RC	RMSEC / °Brix	RP	RMSEP / °Brix
None	11	0.889	0.552	0.862	0.692
Average smoothing	12	0.911	0.497	0.902	0.589
Maximum normalization	12	0.881	0.572	0.868	0.651
SNV	12	0.881	0.571	0.897	0.588
First derivative	12	0.921	0.468	0.876	0.611
Second derivative	13	0.909	0.502	0.856	0.689

The original spectrum data is preprocessed based on different preprocessing algorithms, and then the PLS algorithm is used to construct an apple soluble solids content prediction model based on the full-band spectral data. The results are shown in Table 2. Through quantitative comparative analysis, it is found that the prediction model of soluble solids content based on average smoothing pretreatment algorithm has the highest accuracy, with RC, RP, RMSEC and RMSEP of 0.911, 0.902, 0.497 ° Brix and 0.589 ° Brix, respectively. After average smoothing, the original reflectance spectral curves of 160 apple samples are shown in Fig. 4, and the prediction results of correction set and prediction set are shown in Fig. 5. Therefore, the subsequent analysis is based on the spectral data after average smoothing pretreatment.

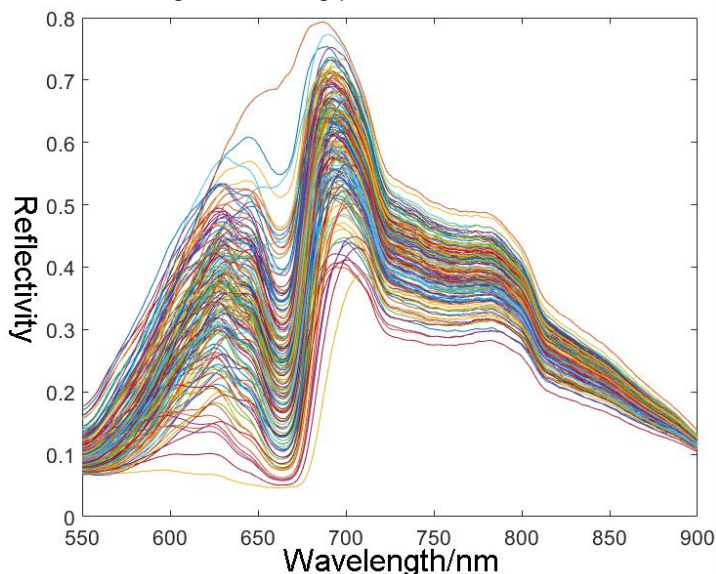


Fig. 4 - Reflectance curve of apple sample' s spectrum

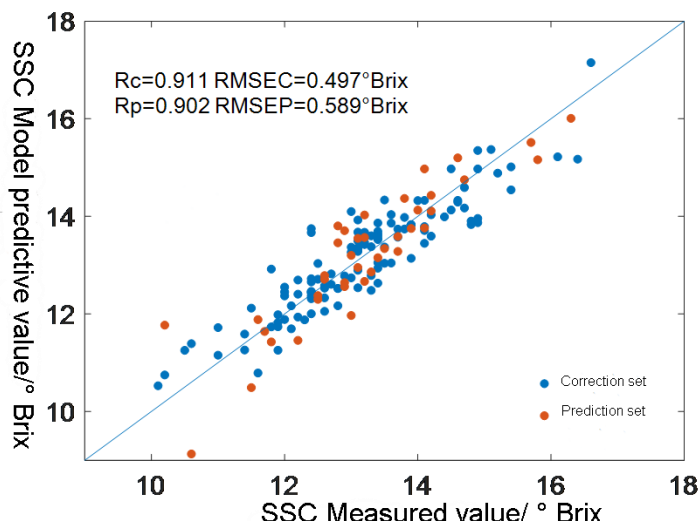


Fig. 5 - Prediction results of PLS model for apple' s SSC based on average smoothing preprocessing algorithm

**Modelling Results Based on Characteristic Wavelengths**

The CARS algorithm is used to screen the preprocessed spectral data with characteristic wavelengths, and the characteristic wavelengths with high correlation with the prediction of sample soluble solids content are selected. The results are shown in Fig. 6, as the number of sampling increases, the number of modelling variables gradually decreases, and RMSECV gradually decreases as the number of characteristic wavelengths decreases. When the sampling frequency is 47 times, the RMSECV reaches a minimum value of 0.492. In this case the model variables should be 57.

When the sampling times are further increased, the number of modelling variables continues to decrease, which leads to the elimination of characteristic wavelengths related to soluble solids content, resulting in the gradual increase of RMSECV. Therefore, the optimal number of modelling variables was determined by the minimum value of RMSECV, that is, 57 characteristic wavelengths were selected by CARS algorithm to build the prediction model of apple soluble solids content. Based on the selected 57 characteristic wavelengths, a PLS model was established to detect the soluble solids content of apple. The RC and RP were 0.937 and 0.906, RMSEC and RMSEP were 0.418 ° Brix and 0.545 ° Brix, respectively. Compared with the full band spectral analysis, the modelling wavelengths decreased from 1030 to 57, and the modelling results were slightly improved.

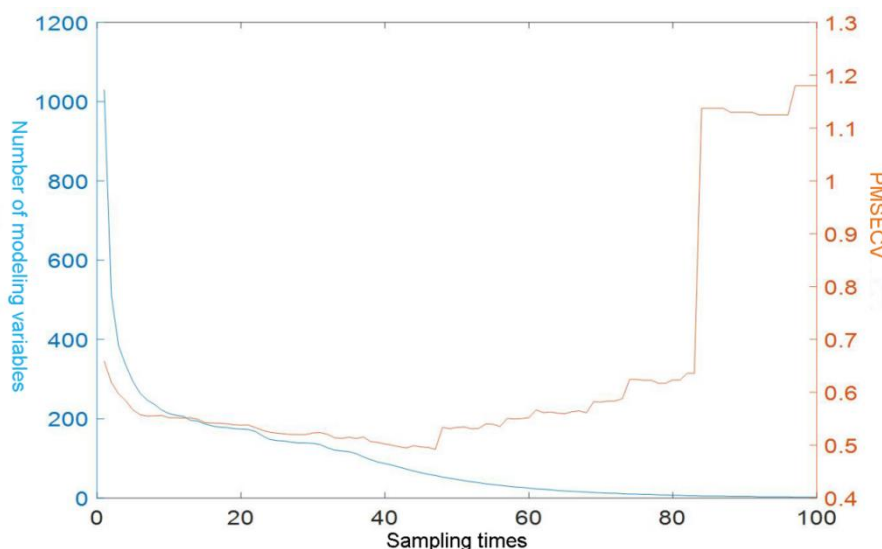
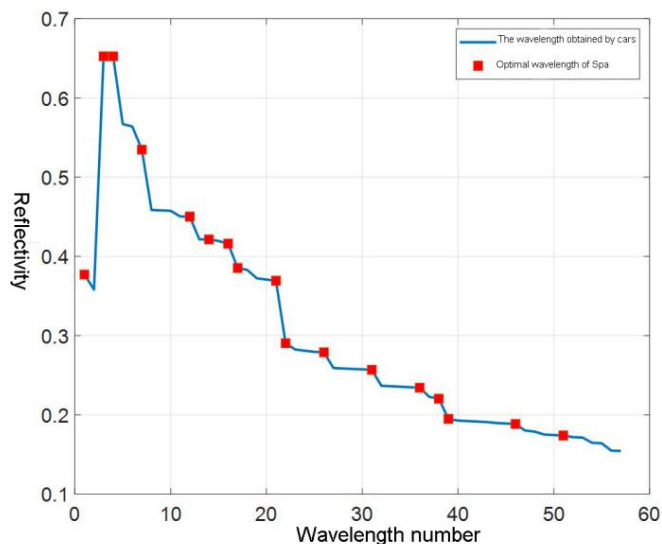


Fig. 6 - Effective wavelengths selected by CARS

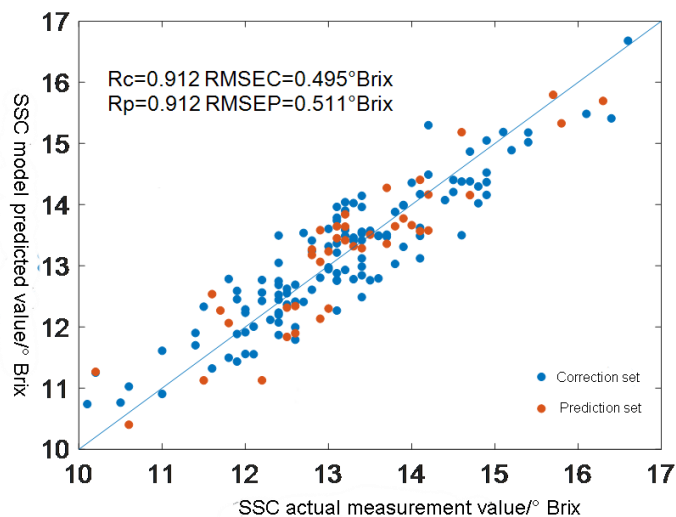
For the real-time analysis of apple soluble solids content, the shorter the characteristic wavelength, the shorter the model prediction time. In order to further improve the prediction efficiency, on the basis of the CARS algorithm, the SPA algorithm is further used to optimize the characteristic wavelength.

Fig. 7 shows 17 characteristic wavelengths selected by SPA algorithm on the basis of 57 wavelengths selected by CARS.



**Fig. 7 - Effective wavelengths selected by CARS-SPA**

The optimized prediction model of soluble solids content was constructed by using the selected 17 characteristic wavelengths. The test results are shown in Fig. 8.



**Fig. 8 - Measurement results versus prediction results of apple' s SSC using CARS-SPA simplified model**

Compared with the prediction results based on the full band, the optimized soluble solids content prediction model not only reduced the number of variables, but also improved the prediction results.

Finally, 17 characteristic wavelengths for soluble solids content analysis were determined as follows: 637.52, 691.59, 696.45, 716.11, 739, 761.67, 782.1, 795.72, 801.01, 816.16, 821.73, 834.77, 847.41, 854.5, 865.74, 868.94, 876.59 nm.

According to the above 17 characteristic wavelengths, an optimized apple soluble solids content prediction model is established, as shown in formula (2).

$$\begin{aligned}
Y = & -7.13X_{637.52} + 119.28X_{691.59} - 184.32X_{696.45} \\
& + 249.23X_{716.11} - 357.54X_{739} + 260.47X_{761.67} \\
& - 64.23X_{782.1} - 147.51X_{795.72} - 288.61X_{801.01} \\
& + 228.28X_{816.16} + 174.87X_{821.73} + 338.89X_{834.77} \\
& + 454.03X_{847.41} + 191.07X_{854.5} - 357.37X_{865.74} \\
& - 411.16X_{868.94} - 430.68X_{876.59} + 37.97
\end{aligned} \tag{2}$$

Among them, Y is the predicted soluble solids content of the apple sample, and X<sub>637.52</sub>... X<sub>876.59</sub> is the spectral reflectance corresponding to 17 wavelengths extracted by CARS-SPA algorithm. Integrate the optimized soluble solids content prediction model into the tester for fast and nondestructive testing of the soluble solids content of apples.

## CONCLUSIONS

This research intends to develop a portable apple soluble solids content detector based on near-infrared spectroscopy technology, which can realize the rapid and accurate detection of apple soluble solids content. The main research conclusions are as follows.

(1) A portable apple soluble solids content detector is designed, which is mainly composed of optical fibre probe, optical fibre loop, micro spectrometer, microcontroller and display interface. It can communicate with computer terminal and mobile app through network port, Bluetooth and other ways to realize the portable detection of apple soluble solids content. By collecting the dark reference spectrum and white reference spectrum of apple samples, the self-calibration function of the device can be realized.

(2) 160 apple samples were used to construct the prediction model of apple soluble solids content, and the prediction accuracy of models based on different preprocessing methods was quantitatively compared. The results showed that the accurate prediction of apple soluble solids content could be achieved by using average smoothing to preprocess spectral data and establishing PLS model. The RC, RP, RMSEC and RMSEP were 0.911, 0.902, 0.497 ° Brix and 0.589 ° Brix, respectively. Based on the selected 17 characteristic wavelengths, the accuracy of soluble solids content prediction model was further improved. The RC, RP, RMSEC and RMSEP were 0.912, 0.912, 0.495 ° Brix and 0.511 ° Brix, respectively.

The portable apple soluble solids content detector developed in this study realizes the rapid and nondestructive detection of apple soluble solids content, and its application scope can be further extended to the soluble solids content detection of pear, thin skin watermelon, tomato and other spherical fruits, so as to provide support for the rapid detection of fruit soluble solids content.

## ACKNOWLEDGEMENT

This work was supported in part by Youth fund of Beijing Academy of agriculture and Forestry Sciences (QNJJ201818), the National Apple Industry Technology System Project of China (CARS-27).

## REFERENCES

- [1] Andersson M., (2009), A comparison of nine PLS1 algorithms. *Journal of Chemometrics*, vol.23, issue 10, pp. 518–529;
- [2] Araújo M.C.U., Saldanha T.C.B., Galvão R.K.H., Yoneyama T., Chame H.C., Visani V., (2001), The successive projections algorithm for variable selection in spectroscopic multicomponent analysis. *Chemometrics and Intelligent Laboratory Systems*, vol.57, issue 2, pp.65-73;
- [3] Beghi R., Spinardi A., Bodria L., Mignani I., Guidetti R., (2012), Apples nutraceutical properties evaluation through a visible and near-infrared portable system. *Food and Bioprocess Technology*, vol.6, issue 9, pp.2547-2554;
- [4] Barnes R.J., Dhanoa M.S., Lister S.J., (1989), Standard Normal Variate Transformation and De-Trending of Near-Infrared Diffuse Reflectance Spectra. *Applied Spectroscopy*, vol.43, issue 5, pp.772-777;
- [5] Chu X.L., Yuan H.F., Lu W.Z., (2004), Progress and Application of Spectral Data Pretreatment and Wavelength Selection Methods in NIR Analytical Technique. *Progress in Chemistry*, vol.16, issue 4, pp.528-542;

- [6] Chang C.W., Laird D.A., Mausbach M.J., Hurburgh C. R., (2001), Near-infrared reflectance spectroscopy–principal components regression analyses of soil properties. *Soil Science Society of America Journal*, vol.65, pp. 480–490.
- [7] Fan S.X., Li J.B., Xia Y., Tian X., Guo Z.M., Huang W.Q., (2019), Long-term evaluation of soluble solids content of apples with biological variability by using near-infrared spectroscopy and calibration transfer method. *Postharvest Biology and Technology*, vol.151, pp.79-87;
- [8] Fan S.X., Huang W.Q., Guo Z.M., Zhang B.H., Zhao C.J., (2015), Prediction of soluble solids content and firmness of pears using hyperspectral reflectance imaging. *Food Analytical Methods*, vol.8, issue 8, pp.1936-1946;
- [9] Gong L.Y., Meng X.J., Liu N.q., Bi J.F., (2014), Evaluation of apple quality based on principal component and hierarchical cluster analysis. *Transactions of the Chinese Society of Agricultural Engineering (Transactions of the CSAE)*, vol.30, issue 13, pp.276-285;
- [10] Guo W.C., Fang L.J., Dong J.L., Wang Z. W., (2015), Nondestructive detection of internal qualities for pears using dielectric spectra. *Transactions of the Chinese Society for Agricultural Machinery*, vol.46, issue 9, pp.233-239;
- [11] Gao R.Q., Fan S.F., Yan Y.L., Zhao L.L., (2004), Preprocessing of Near Infrared Spectroscopic Data. *Spectroscopy and Spectral Analysis*, vol.24, issue 12, pp.1563-1565;
- [12] Liu H.J., Ying Y.B., (2015), Effect of shapes on prediction of sugar content of Huanghua pear in harvest time using visible/near infrared spectroscopy. *Transactions of the Chinese Society for Agricultural Machinery*, vol.46, issue 7, pp.233-237;
- [13] Liu Y.D., Ying Y.B., Fu X.P., Lu H.S., (2007), Experiments on predicting sugar content in apples by FT-NIR technique. *Journal of Food Engineering*, vol.80, issue 3, pp.986-989;
- [14] Li H.D., Xu Q.S., Liang Y.Z., (2018), LibPLS: An integrated library for partial least squares regression and linear discriminant analysis. *Chemometrics and Intelligent Laboratory Systems*, vol.176, pp.34-43;
- [15] Liu Y.D., Shi Y., Cai L.J., Zhou Y.R., (2013), On-line NIR detection model optimization of soluble solids content in navel orange based on CARS. *Transactions of the Chinese Society for Agricultural Machinery*, vol.44, issue 9, pp.138-144;
- [16] Li H.D., Liang W.Z., Xu Q, S., Cao D.S., (2009), Key wavelengths screening using competitive adaptive reweighted sampling method for multivariate calibration. *Analytica Chimica Acta*, vol.648, issue 1, pp.77-84;
- [17] Liu D., Sun D., Zhang X., (2014), Recent advances in wavelength selection techniques for hyperspectral image processing in the food industry. *Food and Bioprocess Technology*, vol.7, pp.307–323;
- [18] Munawar A.A., Kusumiyati, Hafidh., Hayati.R., Wahyuni D., (2019), The application of near infrared technology as a rapid and nondestructive method to determine vitamin C content of intact mango fruit. *INMATEH Agricultural Engineering*, vol.58, issue 2, pp.285-292;
- [19] Mendoza F., Lu R.F., Ariana D., Cen H.Y., Bailey B., (2011), Integrated spectral and image analysis of hyperspectral scattering data for prediction of apple fruit firmness and soluble solids content. *Postharvest Biology and Technology*, vol.62, issue 2, pp.149-160;
- [20] Nicolaï B.M., Defraeye T., De K.B., Herremans E., Hertog M.L.A.T.M., Saeys W, Torricelli A., Vandendriessche T., Verboven P., (2014), Nondestructive measurement of fruit and vegetable quality. *Annual Review of Food Science and Technology*, vol.5, issue 1, pp.285-312;
- [21] Oliverra G.A.D., Bureau s., Renard C.M.G.C., Netto A.B.P., Castilhos F.D., (2014), Comparison of NIRS approach for prediction of internal quality traits in three fruit species. *Food Chemistry*, vol.143, pp.223–230;
- [22] Peng Y.K., Lu R.F, (2007), Prediction of apple fruit firmness and soluble solids content using characteristics of multispectral scattering images. *Journal of Food Engineering*, vol.82, issue 2, pp.142-152;
- [23] Pérez N.F., Ferré J., Boqué R., (2009), Calculation of the reliability of classification in discriminant partial least-squares binary classification. *Chemometrics and Intelligent Laboratory Systems*, vol.95, issue 2, pp.122-128;
- [24] Wang Z.W., Chi Q., Guo W.C., Zhao C.J., (2018), Internal quality detection of apples during late developmental period based on near-infrared spectral technology. *Transactions of the Chinese Society for Agricultural Machinery*, vol.49, issue 5, pp.348-354;

- [25] Wang H.L., Peng J.Y., Xie C.Q., Bao Y.D., He Y., (2015), Fruit quality evaluation using spectroscopy technology: a review. *Sensors*, vol.15, issue 5, pp.11889-11927;
- [26] Wu J.Z., Xu Y., (2011), NIR quantitative model optimization of fatty acid in edible oil based on CARS-PLS. *Transactions of the Chinese Society for Agricultural Machinery*, vol.42, issue 10, pp.162-166;
- [27] Wang W., Zhao X., Chu X., Lu Y., Jia B.B., (2019), Nondestructive identification of star anise and shikimmi by visible/near infrared hyperspectral images. *Transactions of the Chinese Society for Agricultural Machinery*, vol.50, issue 11, pp.373-379;
- [28] Wang B., He J.L., Zhang S.J., Li L.L., (2017), Nondestructive testing of soluble solids content in *Cerasus humilis* using visible / near-infrared spectroscopy coupled with wavelength selection algorithm. *INMATEH Agricultural Engineering*, Vol. 61, issue 12, pp.251-262;
- [29] Xu Y.F., Zhang H.J., Zhang C., Wu P., Li J.B., Xia Y., Fan S.X., (2019), Rapid prediction and visualization of moisture content in single cucumber (*Cucumis sativus* L.) seed using hyperspectral imaging technology. *Infrared Physics & Technology*, vol.102, pp.103034;
- [30] Yang B., Guo W.C., Li W.Q., Li Q.Q., Liu D.Y., Zhu X.H., (2019), Portable, visual, and nondestructive detector integrating Vis/NIR spectrometer for sugar content of kiwifruits. *Journal of Food Process Engineering*, vol.42, issue 2, pp.e12982;
- [31] Yu X.Y., Lu Q.P., Gao H.Z., Ding H.Q., (2016), Development of a Handheld Spectrometer Based on a Linear Variable Filter and a Complementary Metal-Oxide-Semiconductor Detector for Measuring the Internal Quality of Fruit. *Journal of Near Infrared Spectroscopy*, vol.24, issue 1, pp.e12982;
- [32] Yun Y.H., Li H.D., Deng B.C., Cao D.S., (2019), An overview of variable selection methods in multivariate analysis of near-infrared spectra. *TRAC Trends in Analytical Chemistry*, vol.113, pp.102-115;
- [33] Zhang H. L., Sun X.D., Liu Y.D., Liu T., Ouyang A.G., Pan Y.Y., Gao R.J., (2009), Measurement of soluble solid content in apples using near infrared spectroscopy. *Transactions of the Chinese Society of Agricultural Engineering (Transactions of the CSAE)*, vol.25, issue 13, pp.340-344;
- [34] Zou X.B., Zhao J.W., Huang X.Y., Li Y.X., (2007), Use of FT–NIR spectrometry in non-invasive measurements of soluble solid contents (SSC) of 'Fuji' apple based on different PLS models. *Chemometrics and Intelligent Laboratory Systems*, vol.87, issue 1, pp.43-51;
- [35] Zhao J.W., Zhang H.D., Liu M.H., (2005), Nondestructive determination of sugar contents of apples using near infrared diffuse reflectance. *Transactions of the Chinese Society of Agricultural Engineering (Transactions of the CSAE)*, vol.21, issue 3, pp.162-165;
- [36] Zhang C., Jiang H., Liu F., He Y., (2016), Application of near-infrared hyperspectral imaging with variable selection methods to determine and visualize caffeine content of coffee beans. *Food and Bioprocess Technology*, vol.10, issue 1, pp.213-221.

# ANALYSIS AND OPTIMIZATION ON THE PROCESS OF ADJUSTABLE DOUBLE DRUM CASTOR SHELLING BASED ON DISCRETE ELEMENT METHOD

## 基于离散元的可调式双滚筒蓖麻脱壳过程分析及优化

Hou Junming, Zhu Hongjie, Jinpeng Li, Enchao Yao, Hu Weixue <sup>1</sup>

Shenyang Agricultural University, College of Engineering / China;

Tel: +86024-88487119 E-mail: junming\_hou@163.com

DOI: <https://doi.org/10.35633/inmateh-62-30>

**Keywords:** castor, stress analysis, size optimization, shelling machine, DEM

### ABSTRACT

The shelling stress of the castor capsule is difficult to obtain by experiments, which is vital for the design of the key components for the shelling machine. The stress analysis of the shelling process of the castor capsule is carried out. In this study, the typical variety castor Tongbi 11 is taken as the research object, and the model of castor shelling is established. The stress and rate of shelling removal of the inner drum are analysed. The effects of size optimization on the shelling results were analysed. The shelling machine was designed for the experiment. In the condition of the highest rate of shelling, the size of the outer drum is maintained, and the inner drum angle is 4.5. The length of the drum is 605mm. At this time, the shelling rate is 96.42 %, which is 0.39 % different from the fitting value. This study provides theoretical support for the design and parameter optimization of the castor shelling machine and its key components.

### 摘要

蓖麻蒴果的脱壳应力难以通过实验获得，这对脱壳机关键部件的设计非常重要。本研究对蓖麻蒴果脱壳过程进行了应力分析并对关键部件进行优化。本研究以典型品种通蓖11号为研究对象，建立了脱壳模型。分析脱壳的应力和脱壳率。得到蓖麻蒴果各阶段的最大压力、内外滚筒压力。分析尺寸优化结果对脱壳效果的影响，并设计试验台进行试验。结果表明，脱壳率最高的情况下，保持外筒尺寸不变，内筒角度为4.5°。滚筒的长度为605mm。此时脱壳率为96.42%，与拟合值相差0.39%。本研究为蓖麻脱壳关键部件的设计和参数优化提供了理论支持。

### INTRODUCTION

Castor is one of the ten oil crops in the world. Its oil is a crucial lubricating oil for aerospace, railway, and high-speed machine tools (Li Jinqin et al., 2004; Hou J.M., et al., 2020; Huang Zhihui et al., 2013; Liu Rukuan et al., 2015). Shelling is the first step of castor oil processing, which directly affects the quality of subsequent products. The existing shelling machine is low efficiency and high shelling damage rate, which reduces the quality of castor oil. (Sebastian Romuli et al., 2015; Bo Yuan Lim et al., 2014; Boyuan L. et al., 2015). The principles of the force properties among particles in the process of shelling are not clear, which leads to the unclear mechanism of shelling damage. The discrete element method can be applied to study the principles of group force in the process of shelling, which enrich the design theory of castor oil shelling equipment.

Some scholars (Wang Zhibing et al., 2015; Ali Nejat Lorestani et al., 2013; Hou Junming et al., 2015) explored the mechanical properties of agricultural material and analysed its rupture principle. Mehrdad et al., (2016), took corn as the research object, constructed two different models, explained the movement and mixing of corn in the machine, and compared with the experiment results. Coetzee et al., (2016), calibrated a gravel particle model, which established the gravel particle composed of 2, 4, and 8 particles, and compared the results with the resting angle calibration. Some scholars (Jia Honglei et al., 2018; Zhao Shuhong et al., 2016; Shi Song et al., 2015; Dun Guoqiang et al., 2016) used discrete element method to analyse the movement of particles in the seeder and compared the seeding rate, seeding leakage rate and reseeding rate were obtained by simulation analysis with the experiment.

<sup>1</sup> Hou Junming, Associate Prof., Ph.D. Eng.; Zhu Hongjie., MS. Stud. Eng.; Li jinpeng, MS. Stud. Eng.; Yao Enchao, MS. Stud. Eng.; Hu Weixue, MS. Stud. Eng.

The EDEM software was applied to study the stress on the lining board of a ball mill and analysed the interaction between pulp and coarse particles (Sun Shanshan et al., 2018; Hao Wanjun et al., 2010; Bian Xiaolei et al., 2017; Li Kunyuan et al., 2017; Cleary P W et al., 2015; and Sinnott M D et al., 2017). The key discrete element parameters of soil were calculated and the stress condition of the rotary blade under different working conditions were studied (Wang et al., 2017; Wu Tao et al., 2017; Xiong Pingyuan et al., 2017; and Xiong Pingyuan et al., 2018). That provides a reference for studies on rotary tillage, energy consumption, and blade wear. In conclusion, the research on the mechanical properties of agricultural material has made specific progress, but there are a few studies on the force analysis of the group moved in the process of shelling of particles, especially on the force between particles and shelling parts, and the force between them. We take the typical variety castor Tongbi 11 as the research object. The pressure, speed, shelling clearance, and internal drum filling amount are studied. The influence of the stress and shelling rate in the process of shelling was analysed. Experiments were applied to verify the simulation results. This study can provide theoretical support for the design of the castor shelling machine and its key components.

## MATERIALS AND METHODS

### Hertz-Mindlin bonding contact model

In this study, a castor bond model is established. In the model, the relationship between the force and displacement of particles in each contact is described by six parameters, including the stiffness and tangential stiffness, and the friction coefficient between two contact particles. The particle to particle contact, the centre of the contact area, the line between the centre point of two particles, and the centre point are established.

### Establishment of a castor capsule fragmentation model

We established the castor discrete model, and the contact model is by Hertz-Mindlin model. The whole particle is composed of three particles, which are combined by bonding to form a single castor capsule. Fig 1 is the model replacement model. Table 1 is the primary setting of parameters for the castor discrete element, and Table 2 is the setting of bonding parameters.

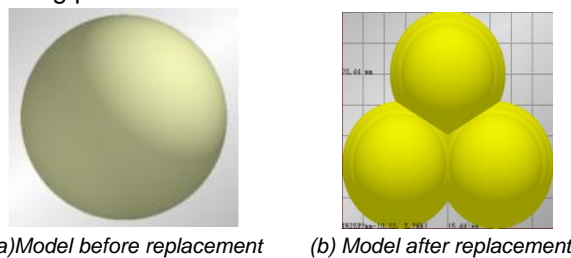


Fig. 1 - Replacement effect of castor discrete element model

Parameters setting of castor discrete element model

Table 1

Category	Value	Category	Value	Category	Value
Castor Poisson's ratio	0.3	Q235 steel Poisson's ratio	0.3	Rubber Poisson's ratio	0.45
Castor shear modulus [10 <sup>3</sup> MPa]	17	Q235 steel shear modulus [10 <sup>3</sup> MPa]	79	Rubber shear modulus [10 <sup>3</sup> MPa]	1
Castor density [kg/m <sup>3</sup> ]	1000	Steel density Q235[kg/m <sup>3</sup> ]	7800	Rubber density[kg/m <sup>3</sup> ]	9100
Castor - castor collision recovery coefficient	0.15	Collision recovery coefficient of castor-Q235 steel	0.44	Castor-rubber collision recovery coefficient	0.37
Castor - castor static friction coefficient	0.6	Static friction coefficient of castor-Q235 steel	0.4	Castor-rubber static friction coefficient	0.7
Castor oil - castor oil dynamic friction coefficient	0.05	Dynamic friction coefficient of castor-Q235 steel	0.01	Castor-rubber coefficient of kinetic friction	0.05

Table 2

Setting of bonding parameters

Bonding parameters		Value
Unit area normal stiffness	[N/m <sup>3</sup> ]	2.1×10 <sup>9</sup>
Tangential stiffness per unit area	[N/m <sup>3</sup> ]	1.4×10 <sup>9</sup>
Maximum normal force	[Pa]	2.1×10 <sup>6</sup>
Maximum tangential force	[Pa]	1.5×10 <sup>6</sup>
Bond plate radius	[mm]	1.6

### Establishment of castor capsule shelling model

It is known from the mechanical properties of the castor capsule (Fang Huimin et al., 2017) that when castor capsule is ruptured and unshelled, three-compartment separation is carried out firstly, and then single-compartment capsule is unshelled. When the three-compartment structure is destroyed, then it moves to the rubbing and pressing area for shelling. The six pressing pieces are welded at the shelling drum, which is distributed evenly on the inner drum. The pressing pieces are coated with 3.0mm thick mesh rubber. Fig.2 shows the model and the inner drum model, and Table 3 shows the parameters of the shelling machine model.

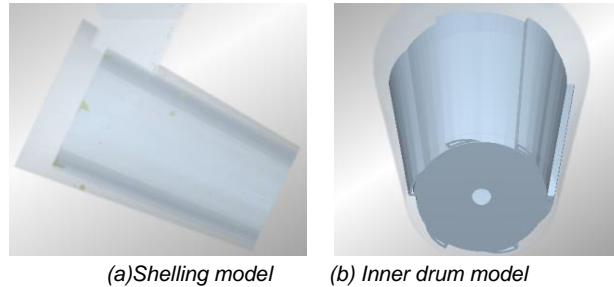


Fig. 2 - Shelling model and inner drum model

Setting of shelling machine parameters

Table 3

Name		Value	Name		Value
Minimum radius of the inner drum	[mm]	137	The roller cone angle	[°]	4
Minimum radius of the outer drum	[mm]	158	Outside of the roller cone angle	[°]	5.5
Inner drum length	[mm]	600	Inlet length	[mm]	300
Length of outer drum	[mm]	700	Inlet width	[mm]	200
Drum angle	[°]	25	Pressure height	[mm]	12
The end arc length of the pressing sheet outlet	[mm]	79	Big end arc length	[mm]	100

### Setting and results of the simulation

The response values of pressure and decanting rate of the inner drum were taken as the response values. Response surface analysis was carried out according to the results. Table 4 is the factor level for simulation.

Test factor level of Box-Behnken

Table 4

Level	A Speed	B Shelling gap	C Filling amount
	[r/min]	[mm]	[%]
-1	250	5.0	30
0	300	6.0	40
1	350	7.0	50

## RESULTS

### Analysis of inner drum stress

In the process of shelling, the stress of the inner drum is analysed. Table 5 shows the analysis of the variance of the maximum pressure of particles.

ANOVA of the model of Box-Behnken design experiment

Table 5

Error sources	Square sum	Error freedom	Mean square	F value	P value
Model	$3.74 \times 10^5$	9	41497.71	18.93	$4 \times 10^{-4}$
A	5658.36	1	5658.36	2.58	0.1522
B	$1.23 \times 10^5$	1	$1.23 \times 10^5$	56.23	$< 10^{-4}$
C	$1.40 \times 10^5$	1	$1.40 \times 10^5$	63.96	$< 10^{-4}$
AB	2126.59	1	2126.59	0.97	0.36
AC	4449.56	1	4449.56	2.03	0.20
BC	22422.07	1	22422.07	10.23	$< 10^{-2}$
A <sup>2</sup>	7124.41	1	7124.41	3.25	0.1
B <sup>2</sup>	43885.37	1	43885.37	20.02	$2.9 \times 10^{-3}$
C <sup>2</sup>	17615.84	1	17615.84	8.04	0.03

Table 5  
(continuation)

Error sources	Square sum	Error freedom	Mean square	F value	P value
Residual item	1534.86	7	2191.98		
Missing items	9782.56	3	3260.85	2.35	0.21
Pure error	5561.30	4	1390.32		
Summation	$3.89 \times 10^5$	16			

Note:  $R^2=0.9605$ ;  $R_1^2=0.9098$ ; C.V.=9.19%; Adep Precision=14.29

The coefficient of variation of C.V. is 9.19%, which shows that the test has high reliability. The Adep Precision value of 14.29 indicates that the model is of high precision, which demonstrates that the test has high reliability and accuracy. The *P* value of the missing fitting term is higher than 0.05, indicating that the quadratic polynomial equation has a high degree of fitting. Equation (1) is the quadratic polynomial equation of the shell breaking rate with all factors.

$$Y = -11455.99 + 11.24A + 1486.73B + 337.45C + 0.46AB - 0.13AC - 14.97BC - 0.02A^2 - 102.09B^2 - 2.59C^2 \quad (1)$$

Fig. 3 shows the response of the shelling clearance amount. When the shelling clearance amount is fixed, the pressure of the inner drum increases with the increase of the filling amount. When the filling amount is constant, the pressure of the inner drum decreases with the increase of the clearance. When the clearance gap is between 5.0 mm and 6.0 mm, the pressure of the inner drum decreases slowly with the growth of the filling amount. When the shelling gap is between 6.0 mm and 7.0 mm, the pressure of the inner drum decreases faster with the rise of the filling amount.

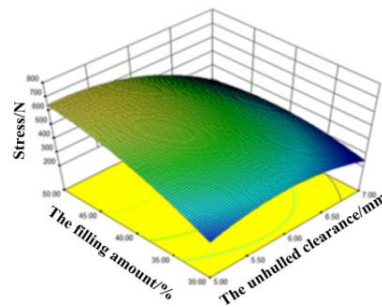


Fig. 3 - Response surface of interaction

### Shelling removal rate results

According to Table 6, the variance analysis of the shelling pellet rate was performed. It can be seen that the coefficient of variation of C.V. is 0.89%, which proves that the experiment has a high degree of credibility. The determination coefficient  $R^2$  and the adjusted determination coefficient  $R_1^2$  are both close to 1, indicating that the fitting equation is highly reliable.

Equation (2) is the quadratic polynomial equation of the shell breaking rate with all factors.

$$Y = -60.97 + 0.46A + 7.07B + 3.59C - 0.02AB - 2.9 \times 10^{-3}AC - 0.18BC - 3.25 \times 10^{-4}A^2 - 0.27B^2 - 0.02C^2 \quad (2)$$

ANOVA of the model of Box-Behnken designs experiment

Table 6

Error sources	Square sum	Freedom	Mean square	F value	P value
Model	133.39	9	14.82	22.73	$2 \times 10^{-4}$
A	11.62	1	11.62	17.82	$3.9 \times 10^{-3}$
B	67.57	1	67.57	103.63	$< 10^{-4}$
C	5.46	1	5.46	8.38	$2.32 \times 10^{-2}$
AB	4.20	1	4.20	6.45	$3.87 \times 10^{-2}$
AC	8.41	1	8.41	12.90	$8.80 \times 10^{-3}$
BC	12.57	1	12.57	19.27	$3.2 \times 10^{-3}$
$A^2$	2.77	1	2.77	4.25	$7.82 \times 10^{-2}$
$B^2$	0.31	1	0.31	0.48	0.51
$C^2$	19.90	1	19.90	30.51	$9 \times 10^{-4}$
Residual	4.56	7	0.65		
Missing items	1.94	3	0.65	0.98	0.48
Pure error	2.63	4	0.66		
Summation	137.95	16			

$R^2=0.9669$ ;  $R_1^2=0.9244$ ; C.V.=0.89%; Adep Precision=19.38

*P* value of the model is less than 0.01, so all factors of the design test have a significant impact on the rate of shelling removal. The rotational speed, shelling clearance, and filling amount have a significant impact on the shelling rate. Among them, the shelling clearance has the most significant impact, followed by the rotational speed, and the filling amount is the smallest.

The interaction between rotational speed×filling amount and shelling gap×filling amount has a significant impact on the shelling removal rate. Among them, the influence of rotational speed×filling amount is greater than the rotational speed×shelling rate.

The shelling removal rate was set as the maximum value, and the optimal parameters were obtained. When the rotational speed was 350r/min, the shelling gap was 5.0 mm, and the filling amount was 40%.

Take the shelling clearance gap as 5.0 mm and analyse the interaction between the remaining two factors. Fig.4 (a) shows the effect analysis diagram of rotational speed×filling quantity. When the rotational speed was fixed, with the increase of the filling amount, the unshelled particles first increase and then decreased. As the filling amount was 40%, the castors shell broken. If the filling amount was fixed, the shell removal rate increased with the increase of rotational speed. When the filling amount was between 30% and 40%, the shelling rate rose rapidly with the rising of rotational speed. Furthermore, if the filling amount was between 40% and 50%, the shelling rate increased slowly with the increase of rotational speed.

As the drum rotational speed was 350 r/min, the interaction between the remaining two factors was analysed. Fig. 4 (b) shows the effect analysis diagram of the shelling clearance×filling amount. When the shelling clearance was fixed, with the increase of the filling amount, the unshelled particle firstly increased and then decreased. The peak value reached when the filling amount was 40%. When the filling amount was fixed, the rate of shell removal decreased with the increase of shelling gap.

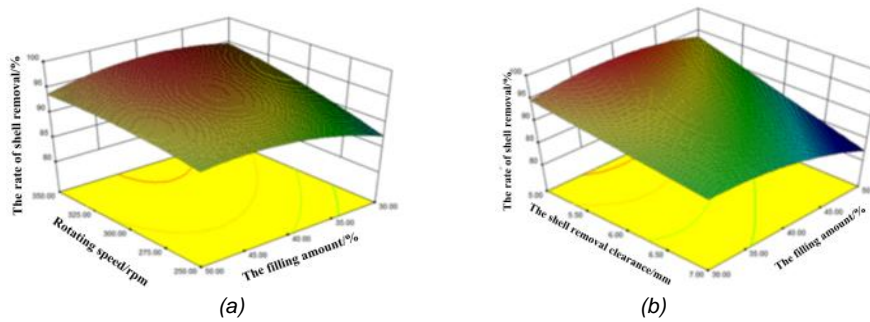


Fig. 4 - Response surface of interaction

**Single factor analysis of castor capsule shelling**

Table 7 shows the effect of rotational speed on each result. With the increase of rotational speed, the force on the inner drum first increased from 509.34N to 533.14N, and then decreased to 456.15N. The shelling rate first increased from 91.23% to 91.28% and then decreased to 88.89%.

**Influence of rotational speed on each result**

**Table 7**

Speed [r/min]	Internal drum stress [N]	Shelling rate [%]
250	509.34	91.23
300	533.14	91.28
350	456.15	88.89

Table 8 shows the influence of the shelling clearance on each result. With the increase of the shelling clearance, the force of the inner drum decreased from 576.39N to 528.14N. The shelling rate decreased from 92.50% to 83.41%.

**Influence of shelling gap on each result**

**Table 8**

Shelling gap [mm]	Internal drum stress [N]	Shelling rate [%]
5	576.39	92.50
6	560.23	89.59
7	528.14	83.41

Table 9 shows the influence of the filling amount on each result. With the increase of the filling amount, the force on the inner roller first increased from 338.58N to 603.364N. The rate of shelling decreased from 91.00% to 90.05%.

Table 9

**Influence of loading on each result**

Filling capacity	Maximum pressure	Maximum speed	Inner drum force	Shelling rate
[%]	[N]	[m/s]	[N]	[%]
30	55.86	12.99	338.58	91.00
40	68.67	12.14	543.61	90.86
50	76.93	10.86	603.36	90.05

**Size optimization of shelling parts**

When the parameters of the inner and outer drum change, the volume of the unshelled drum will change. Fig. 5 shows the dimensions of the shelling parts.

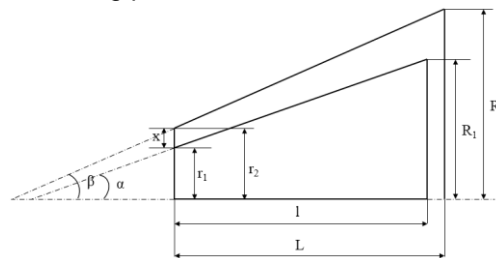


Fig. 5 - Dimensions of shelled parts

In Fig.5,  $l$  and  $L$  are the length of the inner and outer drum;  $r_1$  and  $r_2$  are the radius of the small end of the inner and outer drum respectively.  $R_1$  and  $R_2$  are respectively the large end radius of the inner and outer drum;  $x$  is the shelling clearance;  $\alpha$  and  $\beta$  are inside and outside the shelling drum cone angle respectively.

The volume change is shown in equation (3):

$$\left\{ \begin{array}{l} \Delta V = V_2 - V_1 \\ V_1 = \frac{1}{3}\pi l(r_1^2 + r_1 R_1 + R_1^2) \\ V_2 = \frac{1}{3}\pi L(r_2^2 + r_2 R_2 + R_2^2) \\ R_1 = r_1 + l \tan \alpha \\ r_2 = r_1 + x \\ R_2 = r_2 + L \tan \beta \\ \alpha < \beta \end{array} \right. \quad (3)$$

Where:  $\Delta V$  for hulling chamber volume,  $\text{mm}^3$ .

$V_1$  and  $V_2$  are respectively the volumes of the inner and outer drum,  $\text{mm}^3$ ;

$l$  and  $L$  is the length of the inner and outer drum,  $\text{mm}$ ;

$r_1$  and  $r_2$  are respectively the radius of the small end of the inner and outer drum,  $\text{mm}$ ;

$R_1$  and  $R_2$  are respectively the radius of the large end of the inner and outer drum,  $\text{mm}$ ;

$x$  is the shelling clearance,  $\text{mm}$ ;

$\alpha$  and  $\beta$ , inside and outside the drum cone angle, respectively,  $^\circ$ .

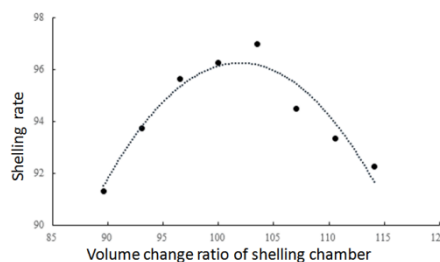


Fig. 6 - Relationship of shelling room volume changes and shelling rate

When the shelling rate was the highest, the rotational speed was 350r/min, the shelling gap was 5.0 mm, the volume of the outer drum platform was  $8.06 \times 10^{-2} \text{m}^3$ , and the volume of the shell removal chamber was  $2.40 \times 10^{-2} \text{m}^3$ . Fig. 6 shows the relationship between the volume change of the shelling chamber and the rate of shelling.

The fitting equation can be obtained as equation (4).

$$y = 0.03x^2 + 6.35x + 227.20 \tag{4}$$

As can be seen from Fig.6, with the increase of the volume of the shelling chamber, the shelling rate increased first and then decreased. From equation (3), it can be seen that the volume change of the shelling removal drum is 105.83% to that of the original shelling inner drum. That is, when the volume of the original shell removal drum is increased by 5.83%, the maximum value of the shelling clearance rate is 96.03%. As the inner drum is the main shelling part, its size parameters are optimized, while the outer drum parameters are fixed. The shelling gap is 5.0mm, so the small end radius of the inner drum is set. By changing the cone angle and length of the inner drum, the volume of the shell removal drum increases by 5.83%. By calculation, the volume of the internal drum is  $5.61 \times 10^{-2} \text{m}^3$ .

**Shelling machine design**

Based on the parameter setting of the simulation shelling model, the shelling machine was designed. We take shelling clearance and filling amount as the factors in the experiment. The experiment working conditions was compared with the simulation results. Shelling interval and filling quantity are factors, furthermore the damage rate and productivity are as an index. The experiment results were compared with the simulation results. Fig.7 is the schematic diagram of the whole machine, Fig.8 is the schematic diagram of the inner drum. Table.10 shows the adjustment parameters of the shelling machine.

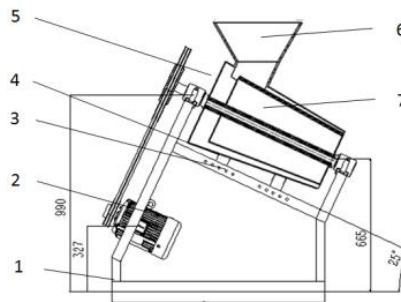


**Fig. 7 - Schematic diagram of shelling machine**

1. Motor; 2. Base frame; 3. Adjustment hole; 4. Adjustment arm; 5. Outer drum; 6. Feed hopper; 7. Inner drum

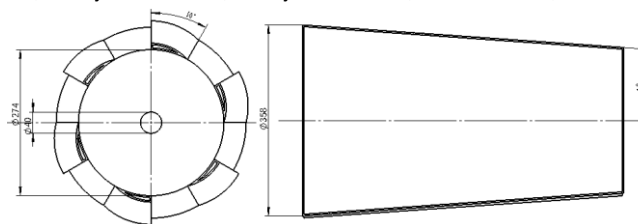


**Fig. 8 - Schematic diagram of the inner drum**

**Table 10**

**Adjustment parameters of test bench**

Adjustment parameters	Rotational speed	Shell clearance	Fill the quantity
Adjustment mode	Frequency converter control	The drum moves forward and backwards on its axis	Input material quality

**Test methods and instruments**

The rotational speed of the inner drum, the clearance clearance, and the filling amount are the test factors, while the shelling rate, damage rate, and productivity are the test indicators. The rotational speed of the inner drum is changed through the frequency converter, the position of the outer drum is adjusted to change the shelling clearance, and the amount of feed is adapted to fit the filling amount.

The camera aims at the observation window and records the status of materials in the drum. Table 11 shows the test factor level setting.

Before each group of experiments, the total amount of feed was weighed. After the experiment, the castor capsules were selected and weighed, then the rate of shelling and damage is:

$$C_1 = \frac{W_a + W_b}{W_a + W_b + W_c} \quad (5)$$

$$C_2 = \frac{W_b}{W_a + W_b} \quad (6)$$

$$C_3 = \frac{W_a + W_b + W_c}{T} \quad (7)$$

Where,  $C_1$  is the shelling rate, %;  $C_2$  is the damage rate, %;  $C_3$  is the productivity, kg/h;

$W_a$  is castor bean seed weight, kg;  $W_b$  is the seed weight of damaged castor bean, kg;

$W_c$  refers to the unpurified castor bean seed weight, kg;

$T$  is the working time, h.

Table 11

Level	A Rotational speed	B Shelling gap	C Filling amount
	[r/min]	[mm]	[%]
-1	250	5	30
0	300	6	40
1	350	7	50

The experimental material was castor Tongbi 11. When the moisture content of the material is 14.2%, the shelling experiment is carried out. Fig.9 shows the testbed for castor shelling.



Fig. 9 - Castor Shelling Test Bed

1. Host; 2. Motor; 3. Light source; 4. Adjustment hole; 5. Frequency converter; 6. Adjustment arm; 7. Shelling drum; 8. Feeding hopper; 9. Observation window; 10. Frame; 11. High speed Camera

### Analysis of test results

Table 12 shows the experiment results. It can be seen that for the shelling rate, the rotational speed is 350r/min, the shelling gap is 5.0mm, and the filling amount is 30% at the optimal level. For the damage rate, the optimal level is 250r/min, the optimal level is 7.0mm, and the optimal level is 50% of the filling amount. For productivity, the optimal speed is 350r/min, the shelling gap is 7.0mm, and the filling amount is 50%.

Test number	A	B	C	Shelling rate	Damage rate	Productivity
				[%]	[%]	[kg/h]
1	-1	-1	-1	90.56	3.06	336.73
2	-1	0	0	86.72	2.82	362.49
3	-1	1	1	85.69	2.64	386.24
4	0	-1	0	90.51	2.93	375.26
5	0	0	1	90.68	3.16	382.46
6	0	1	-1	88.21	2.71	428.72
7	1	-1	1	91.82	3.22	456.75
8	1	0	-1	94.25	3.49	395.89
9	1	1	0	87.28	2.67	483.21

Table 12



Fig. 10 - Shelling effect of the testbed

### Comparison of shelling rate

It can be seen that the influences of rotational speed and shelling clearance on the shelling rate are both higher than the filling amount. Table 13 shows the comparison of simulation and test results of the shelling removal rate. It can be seen that the differences between simulation results and the measured results are small, with the difference ratio within 9%. The significance order of each factor obtained by simulation is the shelling gap, rotational speed, and filling amount. The significance order of each factor obtained by the experiment is the shelling gap, rotational speed, and filling amount. They are in the same order. The optimal combination obtained by the simulation is 350r/min, the shelling gap is 5.0mm, and the filling amount is 40%. The optimal combination obtained by the experiment is 350r/min, shelling gap is 5.0mm, and the filling amount is 30%. Among them, the speed and the shelling gap are incredibly significant factors, and the filling amount is substantial factor.

Table 13

Comparison between simulation and experiment results on shelling rate

No.		1	2	3	4	5	6	7	8	9
Simulation results	[%]	93.29	91.36	93.17	96.24	94.23	89.47	87.96	88.32	93.17
Experiment results	[%]	90.56	86.72	85.69	90.51	90.68	88.21	91.82	94.25	87.28
Difference		3.01	5.35	8.73	6.33	3.91	1.43	4.20	6.29	6.75

### CONCLUSIONS

(1) The shelling gap and the filling amount have a significant impact on the pressure of the inner drum, while the rotational speed has no significant impact on the pressure of the inner drum. With the increase of rotational speed, the force on the inner drum first increased from 509.34N to 533.14N, and then decreased to 456.15N. With the increase of the shelling clearance, the force of the inner roller first increased from 338.58N to 603.364N and the rate of shelling increased from 91% to 90.05%.

(2) The size of the shelling drum parameters was optimized. In the conditions of highest shelling rate, the size parameter was obtained. The optimized shelling drum cone angle was 4.5 ° and the drum length was 605.0 mm. Using this group of size parameters for simulation analysis, the shelling rate was 96.42%. There was a difference of 0.39% from the fitting value.

(3) The accuracy of the simulation model is verified on the shelling machine. The shelling clearance was significantly affected by the rotational speed, shelling rate, and filling amount. The damage rate was significantly affected by the rotational speed and shelling gap. By comparing the shelling rate, it can be seen that the difference ratio between the simulation result and the test result is 8.73% at the maximum and 1.43% at the minimum. The optimal parameter combination obtained by simulation was the rotational speed of 350r/min, the shelling gap of 5.0mm, and the filling amount of 40%. The optimal parameter combination obtained by experiment was the rotational speed of 350.0r/min, the shelling gap of 5.0mm, and the filling amount of 30%.

### ACKNOWLEDGEMENT

This research was supported by the National Natural Science Foundation of China, China (51457312), the authors thank relevant scholars for their assistance in the literature.

### REFERENCES

- [1] Ali N. L., Farzad J., Rashid G., (2013), Physical and mechanical properties of castor seed. *Quality Assurance and Safety of Crops and Foods*, Vol. 4, Issue 05, pp.29-32;

- [2] Bo Y.L., Rosnah S., Robiah Y., (2014), Development and testing of a Jatropha fruit shelling process for shell-free kernel recovery in biodiesel production. *Biosystems Engineering*, Vol.121, pp.46-55;
- [3] Boyuan L., Shamsudin R., Baharudin B.T.H.T. et al., (2015), A review of processing and machinery for Jatropha curcas L. fruits and seeds in biodiesel production: harvesting, shelling, pre-treatment and storage. *Renewable & Sustainable Energy Reviews*, Vol. 52, Issue 03, pp.991-1002;
- [4] Coetsee C J., (2016), Calibration of the discrete element method and the effect of particle shape. *Powder Technology*, Vol. 297, pp.75-139;
- [5] Dun G.Q., Chen H.T., Zha S.H. (2016), Parameter optimization and validation of soybean cell wheel seeding plate type-hole based on EDEM. *Soybean Science*, Vol. 35, Issue 05, pp.204-214;
- [6] Fang H.M., Ji C.Y., Zhang Q.Y. et al., (2016), Force analysis of rotary blade based on distinct element method. *Transactions of the Chinese Society of Agricultural Engineering*, Vol. 32, Issue 21, pp.54-58;
- [7] Hao W.J., Tian Q.J., Cai Y.G., (2010), Numerical analysis on effect of media-to-material ratio on working performance of ball mill. *Mining Machinery*, Vol. 38, Issue 23, pp.72-75;
- [8] Hou J.M., Yang Y., Zhu H.J., Hu W.X., (2020), Experiment on impact damage of castor capsule and its influence factors optimization. *INMATEH-Agricultural Engineering*, Vol. 61, Issue 3, pp.87-96. <https://doi.org/10.35633/inmateh-61-10>
- [9] Huang Z.H., Cheng X.X., Li C.Z. et al., (2013), Mechanical model and major influential factors of breaking castor shell. *Journal of Shenyang Agricultural University*, Vol. 44, Issue 02, pp.185-189;
- [10] Jia H.L., Chen Y.L., Zhao J.L. et al., (2018), Design and experiment of pneumatic-mechanical combined precision metering device for soybean. *Transactions of the Chinese Society of Agricultural Machinery*, Vol. 49, Issue 04, pp.75-139;
- [11] Li J.Q., Zhu G.L., Wu G.L. et al., (2004), Correlation and path analysis between seed oil content and major quantitative characters in castor. *Chinese journal of oil crop sciences*, Vol. 26, Issue 2, pp.43-46;
- [12] Li K.Y., Tong X., Li Z.F. et al., (2017), Research on parameters of ball mill's trapezoidal liner based on DEM-FEM coupling approach. *Journal of Fujian University of Technology*, Vol.16, Issue 65, pp.23-527;
- [13] Liu R.K., Cheng X.X., Xiao Z.H. et al., (2015), Finite element simulation on mechanical property of castor capsule during husking. *Journal of the Chinese Cereals and Oils Association*, Vol.30, Issue 5, pp.62-66;
- [14] Mehrdad P., Colin H., Mojtaba G. et al., (2016), Effect of particle shape on flow in discrete element method simulation of a rotary batch seed coater [J]. *Powder Technology*, Vol. 296, pp.29-36;
- [15] Sebastian R., Shkelqim K., Joachim M., (2015), Influence of physical properties of Jatropha curcas. Seeds on shelling performance using a modified disc mill. *Industrial Crops and Products*, Vol. 77, pp.1053-1062;
- [16] Shi S., Zhang D.X., Yang L. et al., (2015), Simulation and verification of seed-filling performance of pneumatic-combined holes maize precision seed-metering device based on EDEM. *Transactions of the Chinese Society of Agricultural Engineering*, Vol. 31, Issue 03, pp.62-69;
- [17] Sinnott M.D., Cleary P.W., Morrison R.D., (2017), Combined DEM and SPH simulation of overflow ball mill discharge and trammel flow. *Minerals Engineering*, Vol.108, pp.93-108;
- [18] Sun S.S., Dong W.M., Wang Z.R. et al., (2018), The design of wave liner for SAG mill based on EDEM and ANSYS coupling method. *Mining & Metallurgy*, Vol. 17, Issue 06, pp.830-839;
- [19] Wang X.L., Hu H., Wang Q.J. et al., (2017), Calibration method of soil contact characteristic parameters based on DEM theory. *Transactions of the Chinese Society of Agricultural Machinery*, Vol. 48, Issue12, pp.78-85;
- [20] Wang Z.B., Xu W.J., Li X.W. et al., (2015), Test on the mechanical properties of kenaf capsule. *Journal of Chinese Agricultural Mechanization*, Vol. 36, Issue 06, pp.136-138;
- [21] Xiong P.Y., Yang Z., Sun Z.Q. et al., (2018), Simulation analysis and experiment for three-axis working resistances of rotary blade based on discrete element method. *Transactions of the Chinese Society of Agricultural Engineering*, Vol. 34, Issue 18, pp.113-121;
- [22] Xiong P.Y., Yang Z., Sun Z.Q., et al., (2017), Experiment on three-axis working resistances of rotary blade and working parameters optimization. *Transactions of the Chinese Society of Agricultural Engineering*, Vol. 33, Issue 19, pp.51-58;
- [23] Zhao S.H., Zhou Y., Liu H.J. et al., (2016), Design of reseed shift speed system of scoop-type metering device of corn. *Transactions of the Chinese Society of Agricultural Machinery*, Vol.47, Issue 12, pp.38-44.

# NUMERICAL SIMULATION AND EXPERIMENTAL STUDY ON PELLETING MOTION LAW OF AGROPYRON SEEDS UNDER VIBRATION FORCE FIELD

## 振动力场作用下冰草种子丸化运动规律数值模拟与试验研究

Hou Zhanfeng<sup>1)</sup>; Yi Qiu<sup>2)</sup>; Zhi Chen<sup>1\*)</sup>; Lijie Chen<sup>1)</sup>; Shao Zhiwei<sup>1)</sup>

<sup>1)</sup>Inner Mongolia Agricultural University, College of Mechanical and Electrical Engineering, Inner Mongolia, China

<sup>2)</sup>Yangzhou Polytechnic Institute, College of Transportation Engineering, Jiangsu, China

Tel: 04714309215; \*)Corresponding author E-mail address: sgchenzhi@imau.edu.cn

DOI: <https://doi.org/10.35633/inmateh-62-31>

**Keywords:** Vibration force field; Agropyron seeds; Pelleting; EDEM, Orthogonal test

### ABSTRACT

In order to improve the pelleting effect of Agropyron seeds, the pelleting experiment was conducted under different working parameters. In this paper, the discrete element simulation software EDEM was used to establish the simulation model, and the influence of the vibration frequency of coater, the tilt angle of coater, and the rotational speed of coater on the movement trajectory of the Agropyron population were analysed. The simulation results show that the rotational speed is 40r/min, the tilt angle is 35° and the vibration frequency is 20 Hz, and the amplitude is 2 mm, the optimal trajectory of Agropyron population is obtained. The orthogonal experiment of 3 factors (vibration frequency of coater, rotational speed of coater, tilt angle of coater) and 5 levels were designed. The working parameters of pelleting Agropyron seeds were optimized by investigating the 4 indexes of compressive strength, seed rate, single seed rate and pelleting qualified rate. The results show that the vibration is the main factor affecting the compressive strength and single seed rate, the rotational speed is the main factor affecting the seed rate, and the inclination angle is the main factor affecting the pelleting rate. The optimal parameters are as follows: the rotational speed is 40r/min, the tilt angle is 35° and the vibration frequency is 20Hz.

### 摘要

为了提高小粒冰草种子丸化包衣效果, 对不同工作参数下的冰草种子进行丸化处理。运用离散元仿真软件 EDEM 建立仿真模型, 分析了包衣锅振动频率、包衣锅倾角、转速对冰草种群运动轨迹的影响规律。仿真结果表明: 转速为 40r/min, 倾斜角为 35°, 振动频率为 20HZ, 振幅为 2mm 时, 冰草种群运动轨迹最佳。设计了 3 因素 (包衣锅振动频率、包衣锅转速、包衣锅倾斜角) 5 水平的正交试验, 通过考察抗压强度、有籽率、单籽率、丸化率 4 个指标, 对冰草种子丸化包衣的工作参数进行优选, 试验结果分析表明: 振动幅度是影响抗压强度、单籽率的主要因素, 转速是影响有籽率的主要因素, 倾斜角是影响丸化率的主要因素, 最优的参数水平为转速为 40r/min, 倾斜角为 35°, 振动频率为 20HZ。

### INTRODUCTION

The rapid growth of populations in pastoral areas, including Inner Mongolia, China, have caused intensive over utilization of grasslands. This represents approximately 40% of land area in China (Wu, 2013). Overgrazing and conversion of grassland to cropland has led to declines in overall agricultural productivity due to increased soil erosion, degraded soil structure and reduced soil fertility (Shen, 2016). Recently, China implemented vegetation restoration programmes to improve biodiversity in agriculture environments, soil health, and to reduce erosion and desertification (Qiu, 2017). Pelleting technology of Agropyron seeds are widely used as cover crops to reduce desertification and restore productivity on degraded grasslands.

In recent years, domestic and foreign scholars have made great progress in the research of seed pelleting technology. Qiu used biostimulant method to coat the covering crops to improve the germination rate, survival rate and seedling growth (Qiu, 2020). Pasha simulated the coating process of corn seeds in a rotary coating machine by using discrete element method (DEM), established a coating layer model to predict the coating uniformity of seeds, and studied the influence of different coating process parameters on the coating variability of batch seeds (Pasha, 2017). Amirkhani studied the formulation of broccoli seed coating agent based on plant protein hydrolysis, so as to enhance seedling and plant growth (Amirkhani, 2017).

Tamilselvi studied the physical properties of carrot seeds (particle size, shape, sphericity, 1000 grain weight), and carried out germination, hydration and crushing test on bare and pelleted carrot seeds (Tamilselvi, 2016).

Although domestic and foreign scholars have made corresponding research achievements in pelleted coating technology and equipment, there are still many problems, such as insufficient theoretical research, insufficient mechanism exploration, and inconsistent pelleting process (Hou, 2020).

## MATERIALS AND METHODS

### TEST EQUIPMENT

#### Vibration pelletizer

Vibration pelletizer was used to coat seeds in all experiments (Fig. 1). Each seed coating treatment consisted of two components (powder and liquid). For each batch, the powder and liquid were applied to the surface of the seeds in incremental amounts as they were rotating and vibrating in the pelleting machine to achieve uniform results.

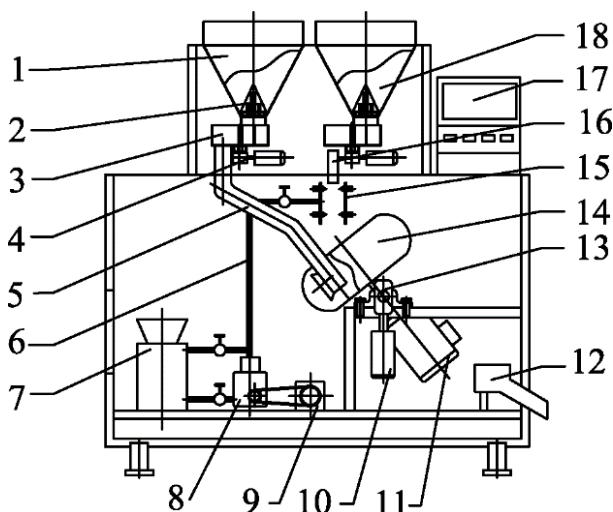


**Fig. 1 - Schematic diagram of overall structure of pelletizer for Agropyron seeds**

1. Powder feed inlet
2. Feed inlet valve
3. Weighing system
4. Step motor
5. Powder conveying pipeline
6. Liquid medicine pipe
7. Liquid medicine storage tank
8. High pressure pump
9. Motor
10. Rotary stepper motor
11. Coater motor
12. Outlet port
13. Electric vibration exciter
14. Coater
15. Nozzles
16. Seed diffuser plate
17. Controller
18. Seed feed inlet

#### Texture analyser

A texture analyser (TA-XTplusC, Texture Technologies Corp., Hamilton, MA) was used to test the compressive strength of coated seeds. The TA-XTplusC is a precision instrument used to measure the surface mechanical properties of coated seeds and the compressive strength of a single seed. The arm of the texture analyser containing a weighing sensor moves in a downward motion to compress the coated seed placed on the base of the analyser and then returns to its original position. Data are assessed as the peak load force (N). After the seed coat is completely broken, the force (N) increases until the seed inside the seed coat is crushed, and then the data is recorded.

#### Movement law of pelleting seeds

The seeds and powder move with the coater, and the movement state of the particles is different under different rotational speeds. Solid particles, like fluids, are called fluidization of particles (Sun, 2008). If the rotational speed of coater is too high, the pelleted seeds in the coater will move around the inner wall under the action of centrifugal force. At this time, there is no relative movement between the pelleting seeds and the inner wall of coater, which cannot play the role of rubbing and friction, thus losing the effect of pelleting, polishing and rounding. If the rotational speed of coater is too slow, it is difficult to drive the pelleted seeds to roll in the coater, and the pelleted seeds only slide and fall on the wall of the coater under the action of gravity. Therefore, the following assumptions are made:

1. The seeds are approximately ellipse with uniform mass distribution, and the powder is approximately spherical with uniform size and mass distribution.
2. Ignore air resistance.
3. Consider the seed as a particle.

The state of the seed in the coater is shown in Fig. 2. The distribution of seeds at different angles is shown in Fig. 3, where  $V_3$  is the speed of the coater and  $V_4$  is the speed of the seed.

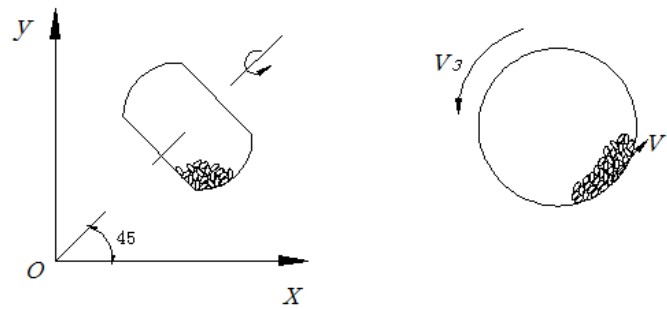


Fig. 2 - Movement diagram of Agropyron seed in coater

The tilt angle of the coater can be adjusted by the tilt angle adjusting mechanism. However, the tilt angle of the pot body shall not be less than the natural rest angle of the material, otherwise the material will stick to the surface of the pot and rotate with it and lose the function of rubbing and friction. Besides, the tilt angle affects the residence time of materials on the surface of coater. The longer the seed is placed on the coater, the denser the seed is. Therefore, on the premise of ensuring product quality and considering the improvement of production efficiency, the size of tilt angle should be reasonably selected to make the pelleted seeds mix evenly.

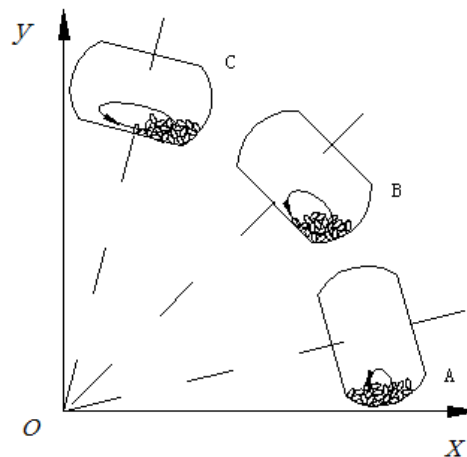


Fig. 3 - The distribution of seeds at different angles

As shown in Fig. 3, in state A, the particles fill the bottom of the coater, seeds and powder slide on the bottom of the pot, and there is no rolling phenomenon, so the coating effect is poor. In state B, the seeds rotate in the middle position, and the seeds and materials are sent to the bottom of the coater and then roll down. At this time, the materials do not move in a circle in the coater, but do similar elliptical movement, so the coating effect is better. However, in the C state, the pelleting effect became worse when the seeds rotated at the bottom of the coater.

#### Flow characteristics of powder

The solid powder in the coater presents a flow state, with the same properties as liquid, namely solid fluidized bed. Like liquid, the fluidization of solid has three flow states: laminar, turbulent and transitional flow. When the velocity is very small, the fluid flows in layers and does not mix with each other, which is called laminar flow. With the increase of flow velocity, the fluid begins to appear disordered, and some of the fluid begins to swing. This kind of flow condition is called transitional flow. When the velocity is large, the fluid oscillates violently, and in the flow field even appears vortex. The phenomenon of mixing occurs between the same layers of fluid, and each part shows irregular movement. Some move horizontally, others move vertically. This motion is called turbulence. The turbulent friction is mainly the momentum transport of fluid clusters (Qi, 2019).

Assuming that the powder particle is a sphere, the resultant force on a single powder particle can be obtained (Fig. 4).

$$\frac{1}{6} \pi \rho_s d_s^3 \frac{du_s}{dt} = \sum F \quad (1)$$

Where:  $\rho_s$ - Material density, [kg/m<sup>3</sup>];

$d_s$ - Powder radius, [mm]

$\frac{du_s}{dt}$  - Material acceleration, [m/s<sup>2</sup>];

$\sum F$  - Resultant force on materials, [N];

Due to this complex resultant movement, the kneading between powder and seed is realized, and the ideal pelleting state is achieved. Because the friction and collision between seeds and powders are caused by turbulent motion, it is necessary to analyse the flow characteristics of powder flow near the surface of seeds. It is assumed that the movement of material on the seed surface is an ideal smooth plane turbulence model. The fluid is divided into laminar and turbulent flow near the wall, in which the laminar flow derives the turbulence. From the microscopic point of view, the seed surface of Agropyron is actually uneven, and the turbulent boundary layer is divided into turbulent region, transition zone and viscous bottom zone in the direction perpendicular to the seed surface. In the process of turbulent motion, the closer to the seed surface, the smaller the velocity of solid particles and the corresponding shear stress generated by the velocity, but the velocity gradient is larger. Therefore, the viscous shear stress plays an important role. We define this region as laminar flow, that is, the turbulent region is not all turbulent layer, which is also called viscous bottom zone. Because the seed surface is affected by the thickness of viscous substrate, roughness height  $h$  and Reynolds number ( $Re$ ) (Fig. 5), it can be divided into three states.

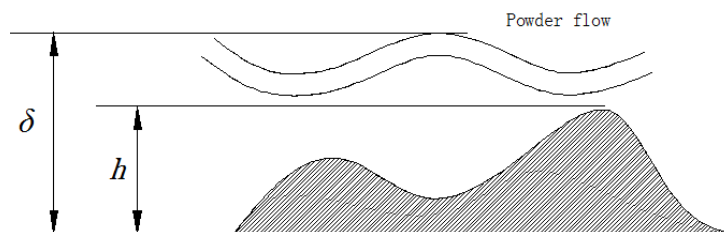


Fig. 4 - Viscous sublayer of material turbulence layer

When  $\delta > h$ , the Reynolds number ( $Re$ ) is small, and the thickness of viscous bottom layer is greater than that of rough layer. In this case, the turbulent boundary layer is called smooth region. When  $\delta < h$ , the thickness of viscous bottom layer is less than that of rough layer. At this time, the roughness height affects the movement of material flow and produces Eddy current, which increases the irregularity of material flow. The corresponding turbulent boundary layer is called turbulent rough region. When the turbulent resistance of material flow is caused by the interaction of viscosity and turbulence, the corresponding turbulent boundary layer is called turbulent transition zone.

According to the above analysis, only when the Reynolds number ( $Re$ ) is higher, the roughness height  $h$  is larger, and the thickness of viscous bottom layer is smaller, the material flow is easy to form turbulent flow. However, the turbulent friction is mainly the momentum transport of fluid micro clusters. So the viscous force between Reynolds numbers can't be dissipated by a larger inertia force. The introduction of vibration can increase the inertia force of powder and destroy the laminar flow state. The pelleting process of material flow is conducted in turbulent flow. In addition, through the irregular movement of solid materials, the surface of Agropyron seeds was repeatedly collided, and the high-quality pelleting effect was achieved.

## NUMERICAL SIMULATION

### Model parameters

Natural Agropyron seeds was selected as the research object. According to the physical characteristic parameters of Agropyron seed simulation (Table 1), the overlapping sphere model is adopted in the discrete element simulation software EDEM. It can effectively delay the occurrence of "self-locking" phenomenon, and has better fitting degree to the boundary. According to the actual measurement of the size of Agropyron seeds, its shape parameters can be defined as the long half axis  $a = 2.5$  mm and the short half axis  $b = 1.2$  mm. For such an axisymmetric ellipsoid element, multiple spheres are filled in EDEM (Fig. 5).

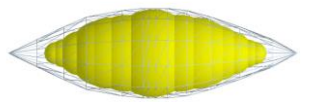


Fig. 5 - Simulation model of Agropyron seeds

Table 1

Physical characteristics and simulation parameters of Agropyron seeds

Object	Parameter	Value
Agropyron seeds	Density/(kg·m <sup>-3</sup> )	763
	shear modulus/Pa	1.08×10 <sup>7</sup>
	Poisson's ratio	0.28
Device model	Density/(kg·m <sup>-3</sup> )	7 890
	Shear modulus/Pa	1.1×10 <sup>7</sup>
	Poisson's ratio	0.269
Particle to particle interaction	Static friction factor	0.5
	Restitution coefficient	0.31
Particle to device interaction	Static friction factor	0.5
	Restitution coefficient	0.24

**RESULTS AND DISCUSSIONS**

The discrete element software EDEM was used to simulate and analyse the pelleting of seeds and nutrient soil particles under various motion modes of Agropyron seed pelleting machine under vibration. The actual trajectory of the pelleting of seeds and nutrient soil was studied intuitively, and the influence of different motion combinations on pelleting effect was analysed. There are three movements of seeds in the coater. One is that the seeds rise to a certain height with the rotation of the coater. The second is the rolling and falling of seeds on the bottom of the coater, and the third is the overturning and jumping of seeds themselves.

**Influence of vibration frequency on motion state**

The simulation experiment was conducted under the condition that the rotational speed of the coater was 40 r/min, the tilt angle of the coater was 35° and the amplitude of the coater was 2 mm. The simulation movement state of the population was shown in Fig.6.

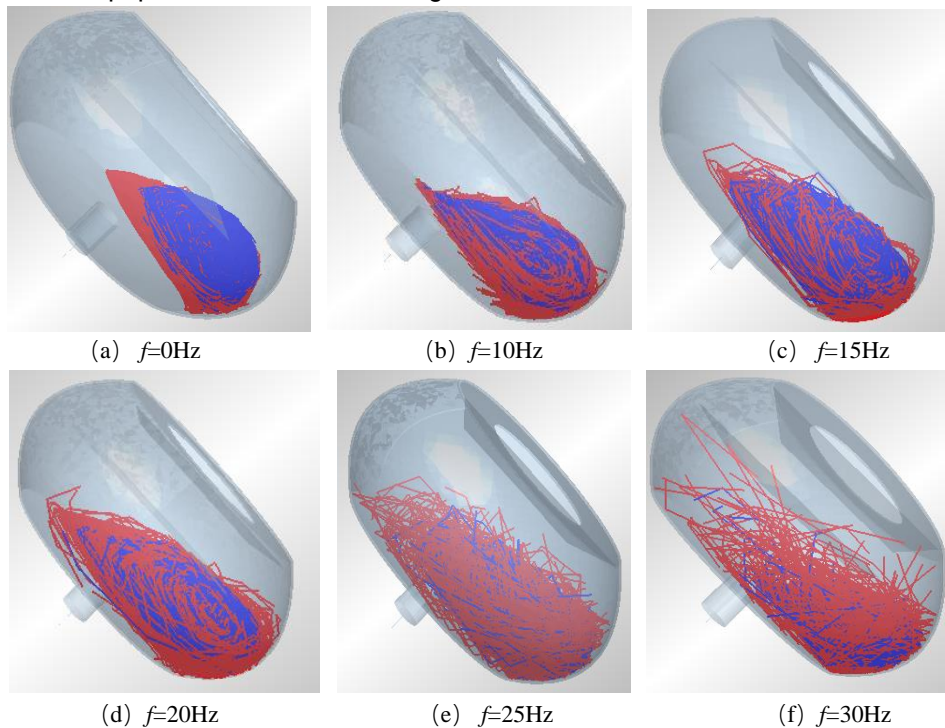


Fig. 6 - Motion trajectories at different frequencies

It can be seen from Fig. 6 that when the vibration frequency of the coater is 0 Hz (no vibration), the

Agropyron seeds and pelleting powder are at the bottom of the coater and separated from each other, resulting in poor pelleting quality. When the vibration frequency was 10 Hz and 15 Hz (with vibration), the interaction between Agropyron seed and pelleting powder began to occur, which accelerated the dispersion of seed and powder, and intensified the relative movement trend between the seed and pelleting powder, which was beneficial to the pelleting of Agropyron seeds. When the vibration frequency increased to 20 Hz and 25 Hz, the more intense the movement between the Agropyron seeds and the pelleting powder, the greater the chance of contact, collision and friction, the better the surface mechanical properties of the pelleted seeds. When the vibration frequency increases to 30 Hz, the movement trend of particle flow is obviously intensified. In the process of rapid vibration, some pelleting powder is vibrated to the top of the coater to separate from the Agropyron seeds due to its light weight, which reduces the pelleting effect. The simulation results show that when the vibration frequency is 20 Hz and 25 Hz, the mixing effect of Agropyron seeds and pelleting powder is better, and the quality of pelleting seed is better under this condition.

### Influence of rotational speed on motion state

The single factor simulation analysis method is used to determine the optimal speed range of the coater. When the vibration frequency of the coater is 20 Hz, the tilt angle of the coater is 35° and the amplitude of the coater is 2 mm, the single factor simulation experiment is conducted under the conditions of rotational speed of 30 r/min, 35 r/min, 40 r/min, 45 r/min and 50 r/min, respectively. The simulation process is shown in Fig. 7.

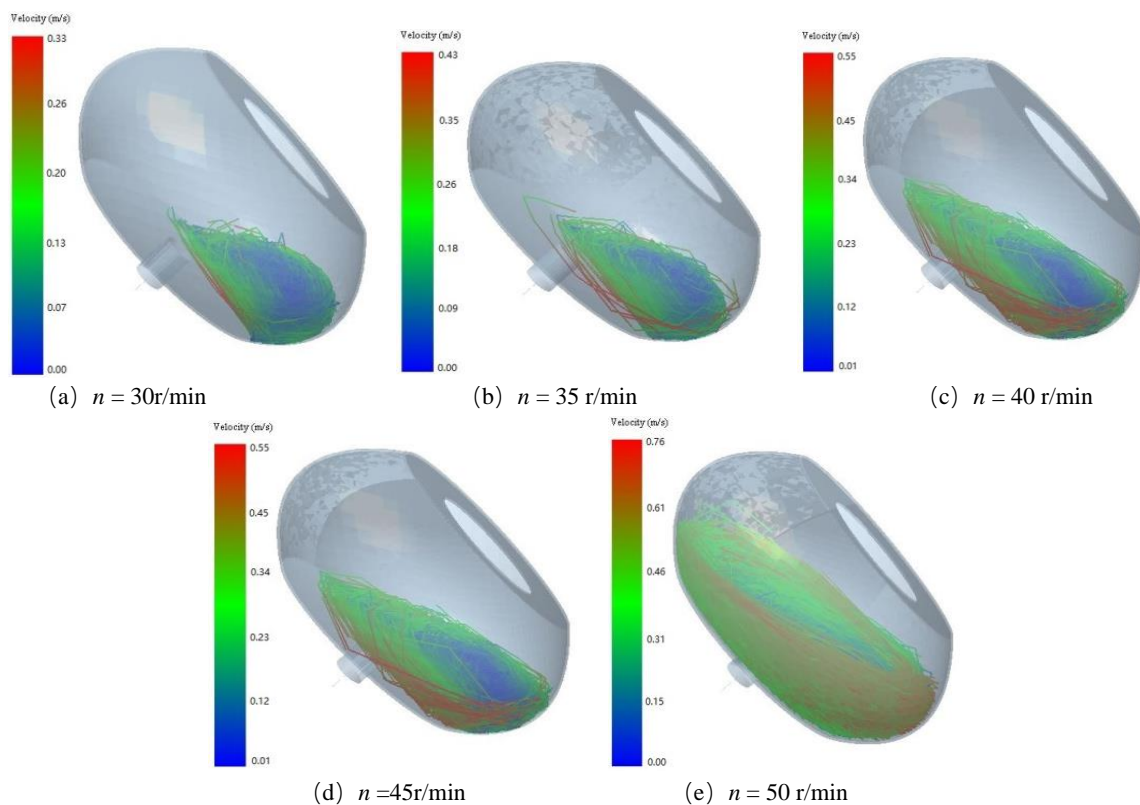


**Fig. 7 - Motion trajectories at different rotational speeds**

It can be seen from Fig. 7 that when the rotational speed of the coater is 30 r/min and 35 r/min, the seeds and powder are accumulated at the bottom of the coater, resulting in poor pelleting quality. When the speed of the coater is 40 r/min, the movement trend of the seeds and pelleting powder was intensified, which could achieve the purpose of rotating the seeds and pelleting powder with the coater. Besides, the distribution area of particles in the coater space increased, and the pelleting quality was better.

However, when the speed of the coater is 45 r/min and 50 r/min, the pelleting effect was weakened due to less chances of collision, rolling and friction between the particles. The simulation results show that when the speed of coater is 40 r/min, the mixing effect of seeds and pelleting powder is better, and the pelleting quality is higher.

### Influence of tilt angle on motion state

In order to achieve better rolling effect of Agropyron seeds and determine the influence of tilt angle of coater on the motion state, the discrete element simulation software EDEM was also used to analyse the population pelleting trajectory. The smaller the tilt angle is, the longer the retention time of Agropyron seeds on the surface of coater is, and the denser the Agropyron seeds are rolled out, but the multiple seed rate will increase. Therefore, when the speed of the coater is kept at 40 r/min, the vibration frequency is 20 Hz and the amplitude is 2 mm, the single factor simulation experiment is conducted under the conditions of tilt angle of 25°, 30°, 35°, 40° and 45° respectively. The simulation process is shown in Fig. 8.

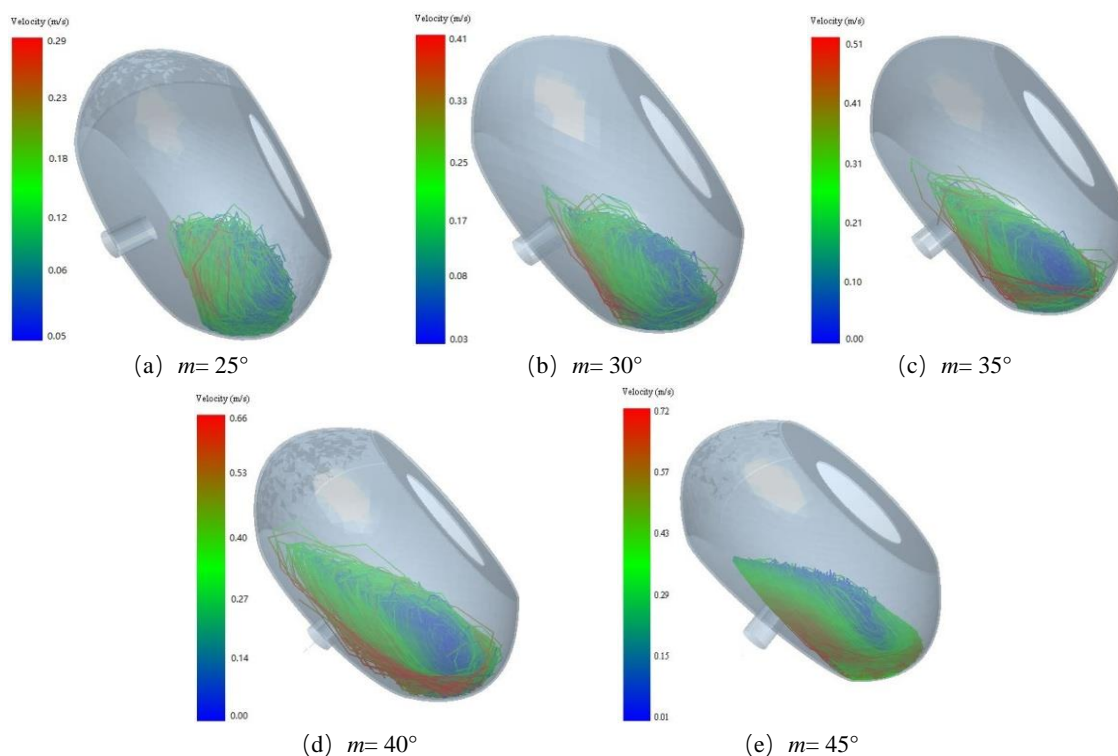


Fig. 9 - Motion trajectories at different tilt angles

It can be seen from Fig. 9 that when the coater angle is 25° and 30° respectively, the Agropyron seeds and pelleting powder are almost static relative to the coater, which easily leads to the increase of multiple seed rate and seedless rate, and the decrease of single seed rate and pelleting qualified rate. When the tilt angle of coater was 35° and 40° respectively, the movement of Agropyron seeds and pelleting powder was more intense, which was conducive to the rapid contact pelleting of seed and powder, and improved the pelleting effect and quality. However, when the coater angle was 45°, with the gradual increase of the angle, the Agropyron seeds and powder could not cover the bottom of the pot, and there was a blank area of seeds on the coater, and the seeds began to slide with the whole pot body, the pelleting effect was poor. Therefore, when the tilt angle of the coater is 35° and 40° respectively, the pelleting effect is better and the pelleting quality is higher.

### EXPERIMENT VERIFICATION

50g Agropyron seeds with 99% purity were selected for each experiment. The pelleting powder was a mixture of 500 mesh diatomite, talc powder and bentonite, and the liquid agent of pelleting was an aqueous solution of carboxymethyl cellulose and polyvinyl alcohol with mass concentration of 1.5%. The ratio of seed, powder and liquid was 1:3:1.

#### Orthogonal test

In order to determine the optimal working parameters combination of the vibration pelletizer, the compressive strength, seed rate, single seed rate and pelleting qualified rate were used as performance evaluation indexes (Li, 2017). Taking the vibration frequency, rotational speed and tilt angle of coater as experimental factors, L25 (53) orthogonal test table was selected.

The experimental factors and levels are shown in Table 2, and the orthogonal test scheme and test results are shown in Table 3.

Table 2

Factors and levels encoding table

Level	A Rotational speed of coater (r/min)	B Tilt angle of coater (°)	C Vibration frequency of coater (Hz)
1	25	40	10
2	30	35	15
3	35	30	20
4	40	25	25
5	45	20	30

Table 3

Orthogonal test scheme and test results

Test number	Test conditions			Test index			
	A Rotational speed (r/min)	B Tilt angle (°)	C Vibration frequency (Hz)	Compressive strength (N)	Seed rate (%)	Single seed rate (%)	Pelleting qualified rate (%)
1	25	40	10	46.12	88.6	78.2	66.2
2	25	35	15	64.28	90.4	85.0	82.7
3	25	30	20	100.36	91.2	84.0	70.2
4	25	25	25	67.04	90.2	85.4	58.1
5	25	20	30	116.52	87.1	76.8	74.7
6	30	40	15	62.44	91.4	93.0	82.7
7	30	35	20	102.16	88.0	85.4	72.4
8	30	30	25	115.44	92.0	80.8	71.2
9	30	25	30	103.20	91.0	74.8	68.4
10	30	20	10	38.08	89.4	80.8	69.4
11	35	40	20	88.84	92.8	92.4	84.8
12	35	35	25	118.24	92.2	80.0	75.7
13	35	30	30	147.12	94.2	83.6	73.1
14	35	25	10	64.12	90.2	83.2	72.6
15	35	20	15	92.52	87.8	81.2	59.8
16	40	40	25	147.04	90.8	78.4	75.9
17	40	35	30	91.12	94.8	85.5	79.9
18	40	30	10	48.12	91.0	86.4	80.3
19	40	25	15	95.56	95.0	82.4	72.8
20	40	20	20	97.40	94.8	87.8	60.9
21	45	40	30	93.24	88.8	75.6	60.6
22	45	35	10	97.68	93.0	87.4	68.8
23	45	30	15	78.64	90.8	83.8	71.5
24	45	25	20	110.52	90.0	82.9	85.1
25	45	20	25	65.96	91.2	82.8	79.2

### Analysis of experiment results

#### Range analysis of compressive strength

The range analysis of compressive strength, seed rate, single seed rate and pelleting qualified rate which mainly affect the coating quality was conducted. The range analysis of orthogonal test with compressive strength as index is shown in Table 4. The results of range analysis show that the order of primary and secondary factors affecting compressive strength is vibration frequency C, rotational speed A and tilt angle B. The best combination factor and level of compressive strength is A3B3C5.

Table 4

Analysis of extreme difference in compressive strength

K value	A	B	C
K1	78.86	87.54	58.82
K2	84.26	94.70	78.69
K3	102.17	97.94	99.86
K4	95.85	88.09	102.74
K5	89.21	82.10	110.24
R	23.30	15.84	51.42

### Range analysis of seed rate

The range analysis of orthogonal test with seed rate as index is shown in Table 5. The results of range analysis show that the order of primary and secondary factors affecting seed rate is rotational speed A, tilt angle B and vibration frequency C. The result shows that the combination factor and level with the highest seed rate was A4B3C3.

Table 5

K value	A	B	C
K1	89.50	90.48	90.44
K2	90.36	91.68	91.08
K3	91.44	91.84	91.36
K4	93.28	91.28	91.28
K5	90.76	90.06	91.18
R	3.78	1.78	0.92

### Range analysis of single seed rate

The range analysis of orthogonal test with single seed rate as index is shown in Table 6. The results of range analysis show that the order of primary and secondary factors affecting the single seed rate is vibration frequency of coater C, tilt angle of coater B and rotational speed of coater A. The result shows that the combination factor and level of the highest single seed rate was A3B2C3.

Table 6

K value	A	B	C
K1	81.88	83.52	83.20
K2	82.96	84.66	85.08
K3	84.08	83.72	86.50
K4	84.10	81.74	81.48
K5	82.50	81.88	79.26
R	2.22	2.92	7.24

### Range analysis of pelleting qualified rate

The range analysis of orthogonal test with pelleting qualified rate as index is shown in Table 7. The results of range analysis show that the order of primary and secondary factors affecting pelleting rate is tilt angle of coater B, rotational speed of coater A and vibration frequency of coater C. The result shows that the combination factor and level with the highest pelleting qualified rate was A4B2C3.

Table 7

K value	A	B	C
K1	70.38	74.04	71.46
K2	72.82	75.90	73.90
K3	73.20	73.26	74.68
K4	73.96	71.40	72.02
K5	73.04	68.80	71.34
R	3.58	7.1	3.34

### Determination of optimal level combination

The comprehensive balance method is obtained to select the optimal level combination. For factor A, the seed rate is the main factor, and A4 is the best. For factor B, the pelleting qualified rate is the main factor, and B2 is the best. For factor C, the compressive strength is the main factor, and C5 is the best. For the single seed rate, it is the main factor, and C3 is the best. As for the seed rate and pelleting rate, C3 is the most important factor. According to the above comprehensive balance, A4B2C3 is the best level combination for pelleting Agropyron seeds, that is, the rotational speed is 40 r/min, the tilt angle is 35° and the vibration frequency is 20Hz.

## CONCLUSIONS

1) Through the discrete element simulation (EDEM) analysis, the particle motion state under different working parameters was determined, and the pelletizing mechanism was revealed. In addition, it can be seen that the introduction of vibration force field can change the movement state of materials and improve the quality of pelleting.

2) The main factors affecting the compressive strength, seed rate, single seed rate and pelleting qualified rate were analysed by orthogonal test. The results showed that the main factor affecting the compressive strength was vibration frequency C, the main factor affecting seed rate was rotational speed A, the main factor influencing single seed rate was vibration frequency C, and the main factor influencing pelleting rate was tilt angle B. The optimum combination of pelleting was determined as A4B2C3, which was rotational speed of 40 r/min, tilt angle of 35° and vibration frequency of 20Hz.

## ACKNOWLEDGEMENTS

We acknowledge that this work was financially supported by National Natural Science Foundation Project "Research on soil wind erosion monitoring system based on wireless sensor network and its key technologies (41361058)" and "Research on seed pelleting parameters and coating mechanism under the vibration force field (2018MS05023)".

## REFERENCES

- [1] Hou Z., Qiu Y., Chen Z., Liu H., Guo F., Mi L., (2020), Optimization of process parameters of pelletizer for Agropyron seeds under vibration force field, *INMATEH-Agricultural Engineering*, Vol 60, Issue 1, pp.147-154, Inner Mongolia University / China;
- [2] Li Y., (2017), *Experimental design and data processing [M]*. Chemical Industry Press, pp. 220-232, Beijing / China;
- [3] Masoume A. Anil N. Huang W., Taylor A.G., (2016), Investigation of Soy Protein–based Biostimulant Seed Coating for Broccoli Seedling and Plant Growth Enhancement. *HortScience*, Vol. 51, Issue 9, pp.1121-1126, Cornell University / USA;
- [4] Mu S., Zhou S., Chen Y., Li J., Ju W., Odeh, (2013), Assessing the impact of restoration-induced land conversion and management alternatives on net primary productivity in Inner Mongolian grassland, *China. Glob. Planet.* Vol 108, Issue 4, pp. 29–41, Inner Mongolia University / China;
- [5] Pasha M., Colin H., Mojtaba G., Alfeno G., Patrick M.P., (2017), Inter-particle coating variability in a rotary batch seed coater. *Chemical Engineering Research and Design*, Vol 120, Issue 4, pp. 92-101, University of Leeds / UK;
- [6] Qi H., Wang J., Gu X., Feng L., (2019), Research progress on agglomeration mechanism and fluidization characteristics of viscous particles. *Journal of process engineering*, Vol 19, Issue 1, pp. 55-63, Zhejiang University / China;
- [7] Qiu Y., Amirkhani M, Mayton H., Chen Z., Taylor A.G., (2020), Biostimulant Seed Coating Treatments to Improve Cover Crop Germination and Seedling Growth, *Agronomy*, Vol 10, Issue 2, pp. 154, Cornell University / USA;
- [8] Qiu Y., Chen Z., Hou Z.F., Song T., Mi L.K., Shao Z.W., (2017), Numerical simulation and experiment on improving pelleted coating of forage grass seeds by vibration force field. *Transactions of the CSAE*, Vol 33, Issue 19, pp. 86–93, Inner Mongolia University / China;
- [9] Shao Z., Chen Z., Hou Z., Mi L., Qiu Y. (2018). Analysis of pelleting movement characteristics of BYW-400 type vibrating seed coating machine for wheatgrass. *Transactions of the CSAE*, Vol 34, Issue 3, pp. 57-64, Inner Mongolia University / China;
- [10] Shen H., Zhu Y., Zhao X., Geng X., Gao S., Fang J., (2016), Analysis of current grassland resources in China (in Chinese). *Chin Sci Bull*, Vol 61, Issue 2, pp.139–154, Inner Mongolia/China;
- [11] Sun Q., Wang G., (2008). Reviews of granular flow mechanics and its discrete models. *Advance in Mechanics*, Vol 38 Issue 1, pp. 87-100, Tsinghua University / China;
- [12] Tamilselvi P., Manohar J., (2016), A Study on Physical Properties of Pelleted Carrot (*Daucus carota*. L) Seeds. *Advances in Life Sciences*, Vol 5, Issue 4, pp. 1220-1224, Tamil Nadu Agricultural University / India.

## ASSESSMENT OF APPLE DAMAGE CAUSED BY A FLEXIBLE END-EFFECTOR

## 柔性末端执行器抓握过程苹果损伤评估

LingXin Bu<sup>1)</sup>, ChengKun Chen<sup>1,2)</sup>, GuangRui Hu<sup>1)</sup>, JianGuo Zhou<sup>1)</sup>, Adilet Sugirbay<sup>1,3)</sup>, Jun Chen<sup>\*1)</sup> <sup>1</sup>

1) College of Mechanical and Electronic Engineering, Northwest A&amp;F University, Yangling 712100, China;

2) Guizhou University of Traditional Chinese Medicine, Guiyang, 550025, China;

3) Technical faculty, S. Seifullin Kazakh Agro Technical University, Astana 010000, Kazakhstan

Tel: +86 135721917773; E-mail: chenjun\_jdxy@nwsuaf.edu.cn

DOI: <https://doi.org/10.35633/inmateh-62-32>**Keywords:** apple cortex, end-effector, damage factor, finite element method**ABSTRACT**

In recent years, apple harvesters have become a research hotspot. Interaction control between the robot end-effector and the fruit is crucial to reduce mechanical damage to the fruit and achieve high picking performance. In this article, the damage degree was also quantified using a damage factor based on the damage plasticity model. A flexible three-finger end-effector was designed based on the Fin-Ray effect, and finite element models were established in ABAQUS to simulate the cortex damage during grasping. The results showed that the maximum von Mises stress was 0.159 MPa for the apple skin, 0.082 MPa for the cortex, and 4.178 N for the contact force, respectively. The result of the verification test showed that the maximum contact force was 4.572 N, and the relative error between the simulation and experimental results was 8.62%. Simulation and verification tests showed that the flexible three-finger end-effector achieved non-destructive grasping of apples.

**摘要**

近年来, 苹果收获机器人成为研究热点, 收获过程中末端执行器与果实的交互作用控制对减少果实损伤起到至关重要的作用。本文基于果肉的损伤塑性模型, 测算了果肉在拉伸和压缩过程中的损伤因子, 量化了损伤程度; 基于鳍条效应设计了柔性三指末端执行器, 并建立了末端执行器和苹果的有限元模型。仿真结果表明, 果皮 Mises 最大应力为 0.159 MPa, 果肉最大应力为 0.082 MPa, 接触压力最大为 4.178 N。验证试验中, 最大接触力为 4.572 N。最大接触力仿真值与实际最大接触力的误差为 8.62%。仿真与验证试验均表明该柔性三指末端执行器可以实现苹果的无损抓取。

**INTRODUCTION**

The China Agriculture Yearbook of 2019 indicates that the apple planting area in China was 1.94 million hectares, accounting for 16.3% of the national planting area, making China the world's largest apple producer. Furthermore, apple production reached 39.233 million metric tons, accounting for 22.3% of the total fruit production. Apple harvesting is both time- and labour-intensive, and the workers require experience and skill. Since the 20th century, a reduction in agricultural employment has posed a serious challenge in many countries. Mechanization could be a solution to tackle this problem in the fruit industry. In recent years, apple harvesters have become a research hotspot. Interaction control between the robot end-effector and the fruit is crucial to reduce the mechanical damage to the fruit and achieve high picking performance.

Owing to the integration of finite element software and enhanced visualization, finite element analysis has become an effective method. A drop test simulation was used to optimize the material, height, and direction of the fruit collection units (Lewis, Yoxall, Canty et al., 2007; Celik, Rennie, Akinci, 2011). Compression and impact were used to simulate dynamic and static load states during fruit transport (Lewis, Yoxall, Marshall et al., 2008; Dintwa, Van Zeebroeck, Ramon, 2008). In particular, Dintwa, Van Zeebroeck, Ramon et al., (2008) pointed out that the viscoelastic properties obtained from stress relaxation experiments were not applicable to describe the transient behaviour of fruits, and a highly accurate theoretical evaluation was required. Ji W., Qian Z., Xu B. et al., (2019), analysed the viscoelastic response of different parts of the fruit at different velocities of the grasp and estimated the equivalent stress when plastic damage occurred.

<sup>1</sup> LingXin Bu, Ph.D. Stud. Eng., ChengKun Chen, M.S. Stud. Eng., GuangRui Hu, M.S. Stud. Eng., JianGuo Zhou, M.S. Stud. Eng., Adilet Sugirbay, Ph.D. Stud. Eng., Jun Chen, Prof. Ph.D. Eng.

Ahmadi, Barikloo and Kashfi M. (2016) considered a nonlinear time-dependent contact in the modelling of fruit-plane collision and fruit-fruit collision and analysed the influence of the mechanical properties, shape, size, and relative velocity of the object on the kinetic energy loss of the fruit collision.

In contrast, a simpler and more effective method to eliminate the effects of 'hard contact' is the use of a flexible gripper. In this study, a flexible three-finger end-effector was designed based on the Fin-Ray effect, and the parameters of the Ogden third-order model were obtained through the stress-strain response of the thermoplastic polyurethane (TPU) material. Based on the damage plasticity model, the stress-strain response behaviour of the apple cortex during stretching and compression was tested. Furthermore, finite element models of the apple and end-effector were established using ABAQUS software and the material parameters to simulate cortex damage during grasping and evaluate the feasibility of the proposed end-effector.

## MATERIALS AND METHODS

### End-effector design

The design principles of the end-effector include a simplified structure, improved grasping reliability, and prevention of damage to the fruit. The end-effector consists of a stepping motor, a moving plate, links, finger mounts, soft fingers, and a base frame, as shown in Fig. 1(a). The moving plate, links, and the frame consist of aluminium alloy, and the finger mounts are made of plastic. Flexible fingers are designed based on the fin effect with a V-shaped skeleton structure embedded in a series of supports. The soft fingers made of TPU material (Shall hardness 90 HA) were 3d printed by WeiLaiGongChang Co., Shenzhen, Guangdong, as shown in Fig. 1(b). The characteristic of this structure is that when one side is subjected to a force, the free end will bend in the opposite direction of the force applied so that the side surface of the skeleton is closely attached to the grasped object, forming an effective grip (Crooks, Vukasin, O'Sullivan et al., 2016; Crooks, Rozen-Lev, Trimmer et al., 2017; Elgeneidy et al., 2019; Shan and Birglen L., 2020). In the no-load condition, the stepping motor drives the moving plate to translate, making the finger mount rotate 0.5 rad within 0.5 s.

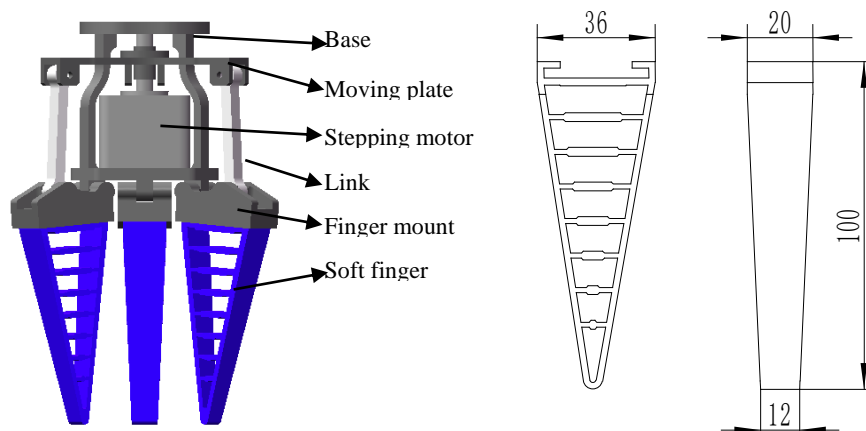


Fig. 1 - Schematic drawing of end-effector structure (a) and the soft finger (b)

### TPU mechanical properties

The tensile tests were conducted on an electronic universal testing machine (type: DDL10, range: 0-10 kN; manufactured by Sino test Equipment Co., Ltd., China). The samples of the tensile tests were prepared according to the ISO 37-2011 standard. A loading rate of 500 mm/min was applied in the tensile tests. The stress-strain response results of the tensile test were used to fit the mathematical model. As a widely used mathematical model, the Ogden model (Ogden R.W., 1972) provides a good fit to the test data within a strain of 700% (Kim B., Lee S.B., Lee J. et al. 2012). Therefore, the Ogden 3N model was used to fit the experimental results. The strain energy density function is defined as follows (SIMULIA 2018):

$$W = \sum_{i=1}^N \frac{\mu_i}{\alpha_i} (\lambda_1^{\alpha_i} + \lambda_2^{\alpha_i} + \lambda_3^{\alpha_i} - 3) \quad (1)$$

where  $\lambda_j$  ( $j=1,2,3$ ) are the principal stretch ratio;  $N$  is a material parameter;  $\mu_i$  and  $\alpha_i$  are empirically determined material constants.

The experimental data fitting of the mathematical model was performed using ABAQUS 2018 software (version 2018, Dassault Systemes Simulia Corp., USA).

**Apple cortex mechanical properties**

The mechanical properties of the apple cortex were measured by tensile and compression tests to estimate the degree of damage during stretching and compression, respectively of the apple cortex. The tensile tests and compression tests followed the standard (ASAE S368.4 DEC2000, 2017) and were conducted on an electronic universal testing machine with a loading speed of 3 mm/min (0.05 mm/s). The test samples were Pink Lady apples picked in November 2019. The samples for the compression test were cylinders, and the samples for the tensile test were cylinders cut into type I. The test samples and their shape parameters are shown in Fig. 2 and Table 1. Each group of experiments was repeated ten times.

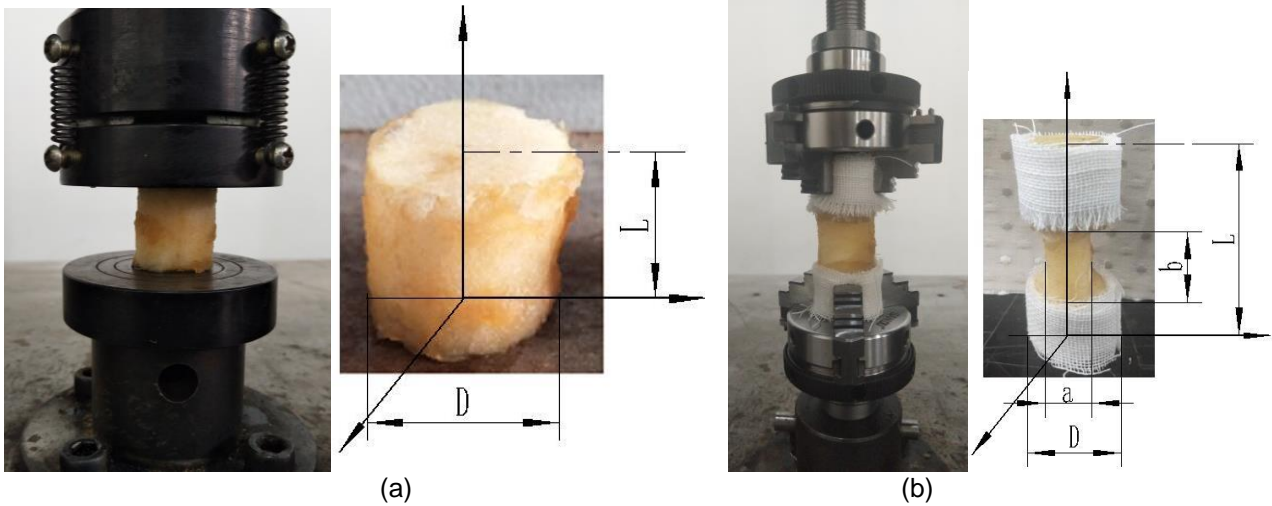


Fig. 2 - Cortex samples for compression test (a) and tensile test (b)

Table 1

**Shape parameters of cortex samples**

	L [mm]	D [mm]	a [mm]	b [mm]
<b>Cortex samples for compression test</b>	21.457±0.343	21.050±0.074	-	-
<b>Cortex samples for tensile test</b>	60.434±0.535	21.079±0.103	9.977±0.501	26.832±1.013

The damage plasticity model was used to describe the response behaviour of the cortex during stretching and compression and quantify the degree of apple cortex damage, as shown in Fig. 3. Based on the energy equivalence principle (Sidoroff F., 1982), the damage factor  $d$  was calculated (Eqs. (2)-(5)) and represented the damage degree of the apple cortex.

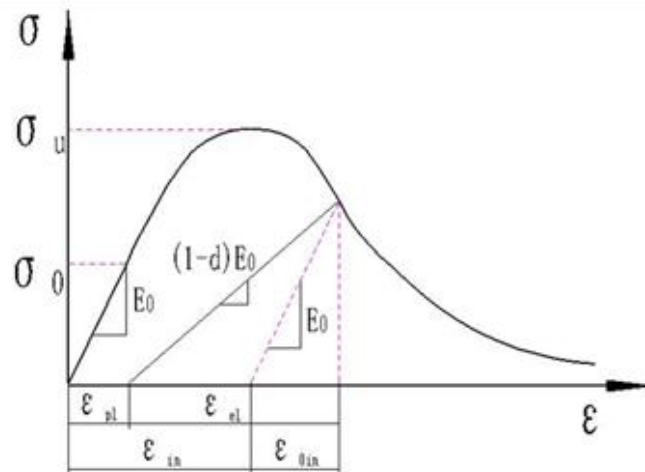


Fig. 3 - Schematic diagram of damaged-plasticity model

$$\varepsilon^{in} = \varepsilon - \varepsilon_0^{el} \quad (2)$$

$$\varepsilon_0^{el} = \frac{\sigma}{E_0} \quad (3)$$

$$\varepsilon^{pl} = \varepsilon^{in} - \frac{d}{1-d} \varepsilon_0^{el} \quad (4)$$

$$d = 1 - \sqrt{\frac{\sigma}{E_0 \varepsilon}} \quad (5)$$

Where:

$\varepsilon^{in}$  is the inelastic strain,  $\varepsilon_0^{el}$  is the elastic strain for the initial stiffness  $E_0$ ,  $\varepsilon^{pl}$  is plastic strain, and  $d$  is the damage factor.

### **Simulation and verification test of dynamic grasping process of the end-effector**

A 3D apple model consisting of the skin, cortex, and core was established using SolidWorks (version 2018, Dassault Systemes Simulia Corp., USA). The physical measurements of the apples were obtained applied from a previous work (Bu L., Hu G., Chen C. et al., 2020). The reconstructed model was imported into Abaqus Software (version 2018, Dassault Systemes Simulia Corp., USA), and the material properties were defined. The material parameters are listed in Table 2. The end-effector was simplified as three fingers and their mounts. The soft fingers were meshed into 6933, 6953, and 6884 elements, respectively. Meanwhile, the mounts were meshed into 13964, 14778, and 14819 elements. The number of elements of the skin, cortex, and core were 12409, 37150, and 7313, respectively. All the elements were C3D4 (4-node linear tetrahedron) cells. The rotation speed of the soft finger was set at 1 rad/s for 0.5 s. The normal behaviour of the finger-skin contact was set to hard contact, and the tangential friction coefficient was 0.3. The Von Mises stress, contact stress, and contact force were the outputs of the simulation.

The test device is shown in Figure 4a. In addition to the end-effector (1), a thin-film pressure sensor (4) was attached to the soft finger. An STM32 Microcontroller (3) converted the signal from the voltage output module (2) to the pressure signal. The relationship between voltage and pressure is shown in Figure 4(b).

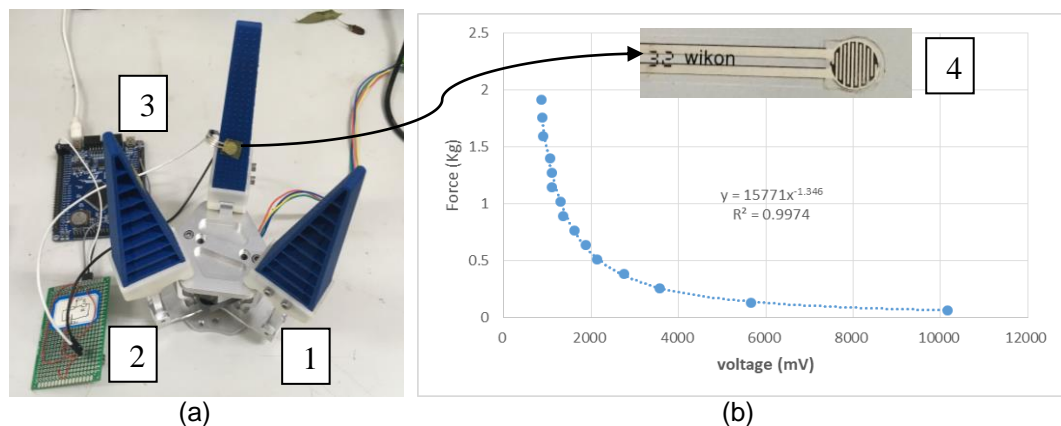


**Fig. 4 - Schematic diagram of the test device (a) and voltage and pressure diagram after calibration (b)**  
1 - end-effector; 2 - voltage output module; 3 - STM32 Microcontroller; 4 - thin-film pressure sensor

## **RESULTS AND DISCUSSION**

### **Stress-strain characteristics of TPU**

The comparison of the tensile test results and the Ogden 3N model fitting is shown in Fig. 5. The tensile test result shows that the stress increases nonlinearly with the strain; the strain of the sample exceeds 460% with stress of over 25 MPa when the fracture occurs. Compared with the experimental results, the fitting results of the Ogden 3N model show relatively good accuracy within strain values of 300%.

The parameters of the Ogden 3N model are shown in Table 2.

So far, the material characteristics of apple cortex and TPU have been mentioned, and the parameters of relevant materials used for simulation are listed in Table 2.

Mechanics parameters of the materials

Table 2

	Density [kg/m <sup>3</sup> ]	$\mu_i$	$\alpha_i$
TPU	120	-8.00934697	3.11633812
		4.79631477	3.34227895
		10.0632388	-5.22676310
	Density [kg/m <sup>3</sup> ]	Elasticity modulus E [MPa]	Poisson's ratio $\nu$
Aluminium alloy <sup>a</sup>	2750	69000	0.35
plastic <sup>b</sup>	120	2388	0.37
cortex	840	3	0.35
skin <sup>c</sup>	840	12	0.35
core <sup>c</sup>	950	7	0.35

a: data from (Liu, Y., Liu, H., Chen, Z., et al. 2019)

b: data from (Pastor-Artigues, M.-M., Roure-Fernández, F., Ayneto-Gubert, X., et al. 2020)

c: data from (Ahmadi, E., Barikloo, H., and Kashfi, M., 2016)

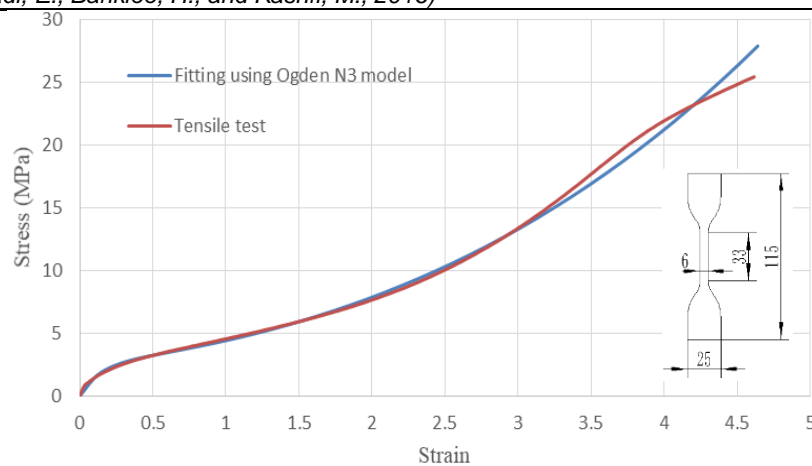


Fig. 5 - Strain-stress curve of the tensile tests and fitting using the Ogden N3 model of the TPU specimen

**Stress-strain characteristics of apple cortex**

The responses of the apple cortex to stretching and compression are different, as shown in Figure 6.

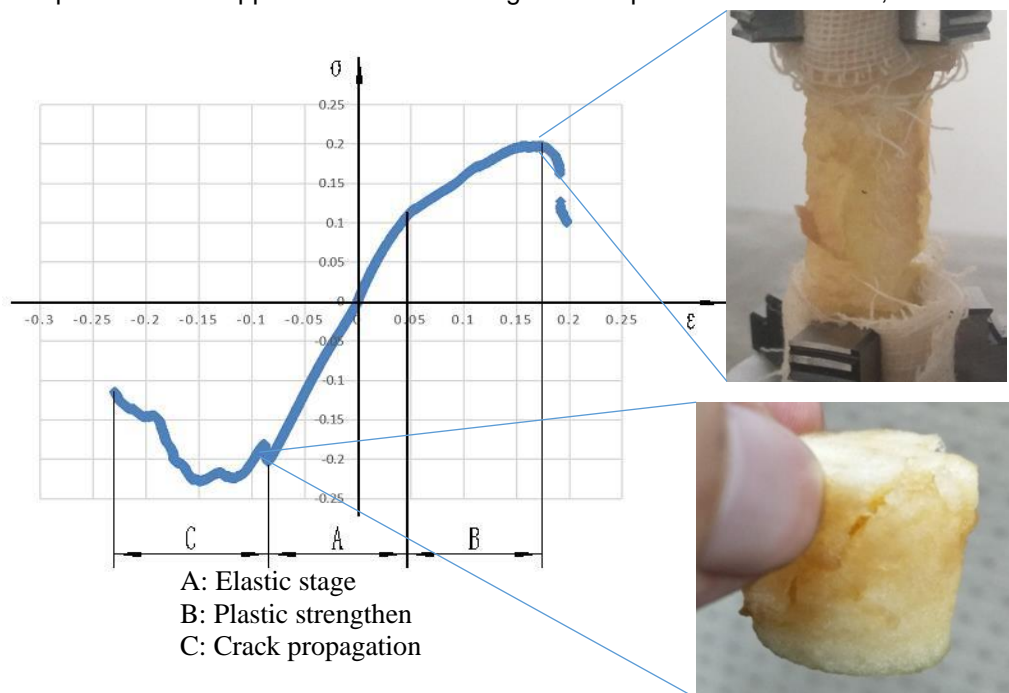


Fig. 6 - The stress-strain curve of the apple cortex during the tensile test and compression test

The elastic modulus  $E_0$  of the elastic stage is  $2.33 \pm 0.46$  MPa, which is smaller than that reported by Ji W., Li J., Yang J. et al., (2015), Ji W., Qian Z., Xu B. et al., (2017), Ahmadi E., Barikloo H., Kashfi M. et al., (2016). Possible reasons include the apple variety and texture differences. During the tensile test, the cortex shows the characteristics of bilinear strengthening; the yield stress is about 0.1 MPa, and the strength limit is about 0.2 MPa. In the compression process, the sample cracked at an inclination angle of  $45^\circ$  due to shear failure when the stress was 0.2 MPa and then continued to collapse until complete failure occurred. This result is consistent with those of Khan A.A. and Vincent, (1993), Holt J, and Schoorl D., (1982).

Figure 7 presents the correlation between the damage factor and the inelastic strain. In the tensile test, fracture failure occurred after significant yielding had occurred. The reason was intercellular damage in addition to the expansion of the pores during the stretching process; thus, the pulp damage factor was less than 0.6 when the fracture occurred. Meanwhile, during compression, after the occurrence of fault cracks along the  $45^\circ$  inclined plane, the stiffness began to decrease significantly because the cells were gradually crushed and failed, and the damage factor continued to rise.

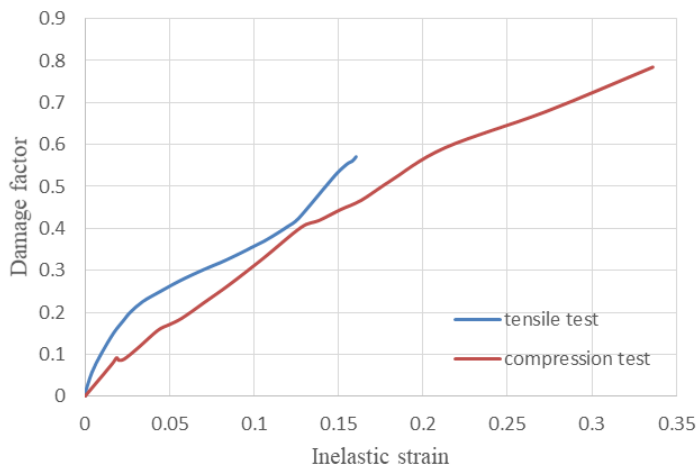


Fig. 7 - Correlation between the damage factor and the inelastic strain during the tensile test and compression test

**Simulation results and experimental verification**

Figure 8(a), (b), and (c) show the von Mises stress results of the grasping process of the end-effector obtained from the finite element analysis.

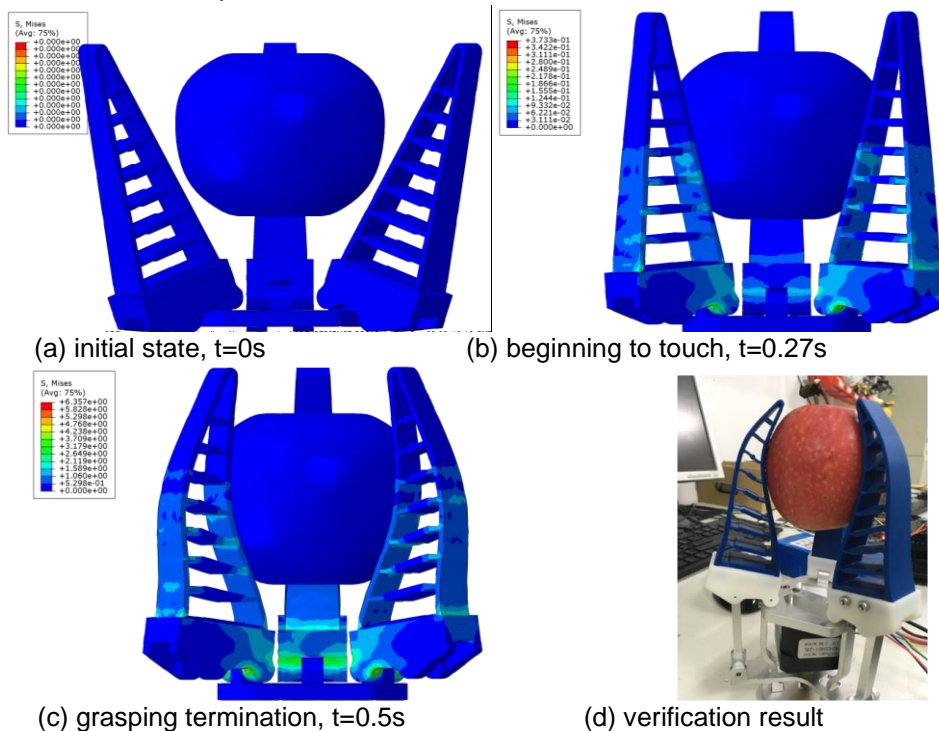


Fig. 8 - Stress cloud diagram of the grasping process of the end-effector in the simulation and verification test

As shown in Fig. 9, in the simulation experiment, the soft finger contacts the apple at about 0.27 s, and the contact stress and contact force gradually increase. At about 0.325 s, the contact stress and contact force of the pericarp suddenly drop due to tangential slippage. Then the contact stress and contact force gradually rise until the simulation ends and reach the maximum value; the maximum values of the contact stress and contact force are 0.159 MPa and 4.178 N, respectively. In addition, the maximum von Mises stress of the apple cortex is 0.082 MPa, which is considerably less than 0.2 MPa, which may cause damage. A comparison of the contact force in the simulation and the verification test shows the same trend, which also reflects the process of tangential slippage. The maximum contact force in the verification test is 4.572 N, with a relative error of 8.62% compared with the simulated value. The error could be due to the irregular shape of the apple and the placement of the pressure sensor.

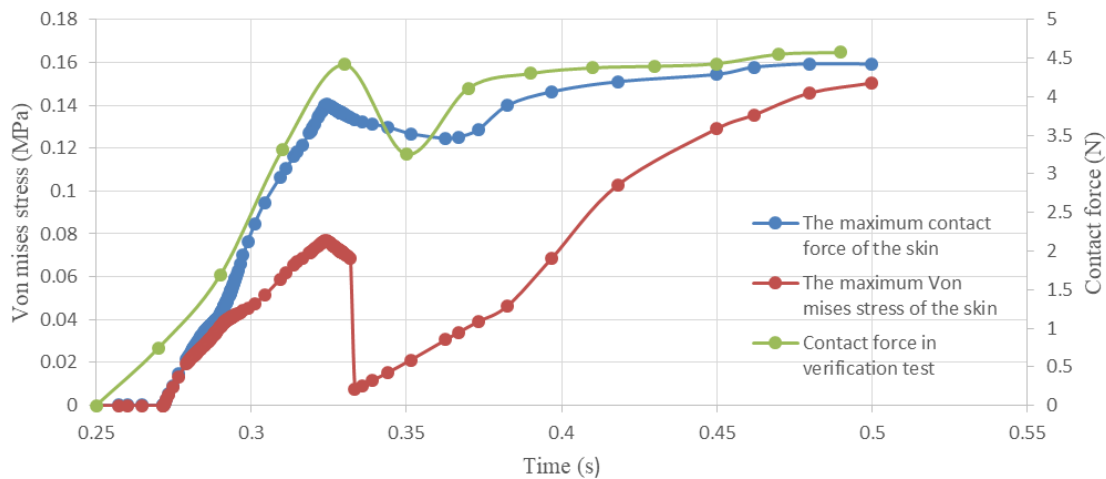


Fig. 9 – Simulation results of the maximum Von Mises stress and maximum contact force of the apple skin

## CONCLUSIONS

In this study, the damage factor of the apple cortex during stretching and compression was calculated based on the damage plasticity model, and the damage degree was quantified. A flexible three-finger end-effector was designed based on the Fin-Ray effect, and the parameters of the Ogden third-order model were obtained from the stress-strain response of the TPU material. Based on the material properties, a finite element model of the apple and end-effector was established using ABAQUS software to simulate the cortex damage during grasping. The results showed that the maximum von Mises stress was 0.159 MPa for the apple skin, 0.082 MPa for the cortex, and 4.178 N for the contact force. In the verification test, the thin-film pressure sensor was mounted at the position of the maximum contact force in the simulation test, and the maximum contact force was 4.572 N. The error between the simulated value and the experimental value of the maximum contact force was 8.62%. Simulation and verification tests showed that the flexible three-finger end-effector achieved non-destructive grasping of the apple.

## ACKNOWLEDGEMENT

The work in this paper was supported by the National Key Research and Development Program (No. 2018YFD0701102) and the Key Research and Development Program of Shaanxi Province (2018NY160).

## REFERENCES

- [1] Ahmadi, E., Barikloo, H., & Kashfi, M. (2016). Viscoelastic finite element analysis of the dynamic behaviour of apple under impact loading with regard to its different layers. *Computers and Electronics in Agriculture*, 121, 1-11. <https://doi.org/10.1016/j.compag.2015.11.017>
- [2] Bu, L., Hu, G., Chen, C., Sugirbay, A., & Chen, J. (2020). Experimental and simulation analysis of optimum picking patterns for robotic apple harvesting. *Scientia Horticulturae*, 261, 108937.
- [3] Celik, H. K., Rennie, A. E. W., & Akinci, I. (2011). Deformation behaviour simulation of an apple under drop case by finite element method. *Journal Of Food Engineering*, 104(2), 293-298.
- [4] Crooks, W., Rozen-Levy, S., Trimmer, B., Rogers, C., & Messner, W. (2017). Passive gripper inspired by *Manduca sexta* and the Fin Ray® Effect. *International Journal of Advanced Robotic Systems*, 14(4), 1729881417721155. <https://doi.org/10.1177/1729881417721155>

- [5] Crooks, W., Vukasin, G., O'Sullivan, M., Messner, W., & Rogers, C. (2016). Fin ray® effect inspired soft robotic gripper: From the roboSoft grand challenge toward optimization. *Frontiers in Robotics and AI*, 3, 70. <https://doi.org/10.3389/frobt.2016.00070>
- [6] Dintwa, E., Van Zeebroeck, M., Ramon, H., & Tijskens, E. (2008). Finite element analysis of the dynamic collision of apple fruit. *Postharvest Biology and Technology*, 49(2), 260-276.
- [7] Elgeneidy, K., Lightbody, P., Pearson, S., & Neumann, G. (2019). *Characterising 3D-printed Soft Fin Ray Robotic Fingers with Layer Jamming Capability for Delicate Grasping*. Paper presented at the 2019 2nd IEEE International Conference on Soft Robotics (RoboSoft).
- [8] Holt, J., & Schoorl, D. (1982). Mechanics of failure in fruits and vegetables. *Journal Of Texture Studies*, 13(1), 83-96. <https://doi.org/10.1111/j.1745-4603.1982.tb00879.x>
- [9] Ji, W., Ding, Y., Xu, B., Chen, G., & Zhao, D. (2020). Adaptive Variable Parameter Impedance Control for Apple Harvesting Robot Compliant Picking. *Complexity*, 2020, 4812657.
- [10] Ji, W., Li, J., Yang, J., Ding, S., & Zhao, D. (2015). Analysis and validation for mechanical damage of apple by gripper in harvesting robot based on finite element method (机器人采摘苹果抓取损伤机理有限元分析及验证). *Transactions of the Chinese Society of Agricultural Engineering*, 31(5), 17-22.
- [11] Ji, W., Qian, Z., Xu, B., Chen, G., & Zhao, D. (2019). Apple viscoelastic complex model for bruise damage analysis in constant velocity grasping by gripper. *Computers and Electronics in Agriculture*, 162, 907-920. <https://doi.org/10.1016/j.compag.2019.05.022>
- [12] Ji, W., Qian, Z., Xu, B., Tang, W., Li, J., & Zhao, D. (2017). Grasping damage analysis of apple by end-effector in harvesting robot. *Journal Of Food Process Engineering*, 40(6), e12589.
- [13] Khan, A. A., & Vincent, J. F. (1993). Compressive stiffness and fracture properties of apple and potato parenchyma. *Journal Of Texture Studies*, 24(4), 423-435.
- [14] Kim, B., Lee, S. B., Lee, J., Cho, S., Park, H., Yeom, S., & Park, S. H. (2012). A comparison among Neo-Hookean model, Mooney-Rivlin model, and Ogden model for chloroprene rubber. *International Journal of Precision Engineering and Manufacturing*, 13(5), 759-764. <https://doi.org/10.1007/s12541-012-0099-y>
- [15] Lewis, R., Yoxall, A., Canty, L. A., & Romo, E. R. (2007). Development of engineering design tools to help reduce apple bruising. *Journal Of Food Engineering*, 83(3), 356-365. <https://doi.org/10.1016/j.jfoodeng.2007.03.005>
- [16] Lewis, R., Yoxall, A., Marshall, M. B., & Canty, L. A. (2008). Characterising pressure and bruising in apple fruit. *Wear*, 264(1-2), 37-46. <https://doi.org/10.1016/j.wear.2007.01.038>
- [17] Liu, Y., Liu, H., & Chen, Z. (2019). Post-fire mechanical properties of aluminum alloy 6082-T6. *Construction and Building Materials*, 196, 256-266. <https://doi.org/10.1016/j.conbuildmat.2018.10.237>
- [18] Ogden, R. W. (1972). Large deformation isotropic elasticity—on the correlation of theory and experiment for incompressible rubberlike solids. *Proceedings of the Royal Society of London. A. Mathematical and Physical Sciences*, 326(1567), 565-584. <https://doi.org/10.1098/rspa.1972.0026>
- [19] Pastor-Artigues, M.-M., Roure-Fernández, F., Ayneto-Gubert, X., Bonada-Bo, J., Pérez-Guindal, E., & Buj-Corral, I. (2020). Elastic asymmetry of PLA material in FDM-printed parts: considerations concerning experimental characterisation for use in numerical simulations. *Materials*, 13(1), 15. <https://doi.org/10.3390/ma13010015>
- [20] Shan, X., & Birglen, L. (2020). Modeling and analysis of soft robotic fingers using the fin ray effect. *The International Journal of Robotics Research*, 0278364920913926.
- [21] Sidoroff, F. (1982). Incremental constitutive equation for large strain elasto plasticity. *International Journal Of Engineering Science*, 20(1), 19-26. [https://doi.org/10.1016/0020-7225\(82\)90068-4](https://doi.org/10.1016/0020-7225(82)90068-4)
- [22] SIMULIA. (2018). *Abaqus 2018 documentation*. Waltham, MA: Dassault Systemes.
- [23] Zhao, D. A., Lv, J., Ji, W., Zhang, Y., & Chen, Y. (2011). Design and control of an apple harvesting robot. *Biosystems Engineering*, 110(2), 112-122. <https://doi.org/10.1016/j.biosystemseng.2011.07.005>
- [24] Zulkifli, N., Hashim, N., Harith, H. H., & Mohamad Shukery, M. F. (2020). Finite element modelling for fruit stress analysis - A review. *Trends In Food Science & Technology*, 97, 29-37. <https://doi.org/10.1016/j.tifs.2019.12.029>
- [25] \*\*\* ASAE S368.4 DEC2000, (2017). *Compression Test of Food Materials of Convex Shape*. American Society of Agricultural Engineers (ASAE) Standards. <https://elibrary.asabe.org/pdfviewer.aspx?GUID=B8900210-E17F-4BB4-B484-2F832BDA6BAE>

# INFLUENCE OF THE SWEEP ANGLE OF THE CROSS KNIFE OPENER ON SOIL DISTURBANCE

## 十字槽开沟器横刀后掠角对土壤扰动的影响

Chengcheng Guo<sup>1)</sup>, Guohua Li<sup>1)</sup>, Junchang Zhang<sup>\*1)</sup>, Xiunan Jin<sup>1)</sup>, Jingfeng Xue<sup>1)</sup>, Chenxi He<sup>1)</sup>, Liquan Lu<sup>1)</sup>

<sup>1)</sup> College of Mechanical and Electronic Engineering, Northwest A&F University, Yang ling 712100, China;

Tel: +86 15662046180; E-mail: ccguo@nwafu.edu.cn

DOI: <https://doi.org/10.35633/inmateh-62-33>

**Keywords:** EDEM, Tracer Method, Soil disturbance, Work resistance

### ABSTRACT

The cross-slot opener is a new type of seeding opener. The sweep angle, which is a key structural parameter of the cross knife, has an important influence on soil disturbance. In this paper, discrete element method and tracer method are used to study the conditions of working speed of 0.83m/s and ditching depth of 130mm, the sweep angles of the transverse knife are 0°, 10°, 20°, 30°, 40°, respectively. The influence of time opener on soil disturbance and working resistance. The simulation analysis of the operation process of the cross groove opener shows that the trenching process under different sweep angles of the transverse knife is basically the same, and the standing knife is the main cause of soil disturbance; both the tracer method and the simulation results show the surface and shallow soil particle disturbance. The proportional and horizontal working resistance first decrease and then increase with the increase of the sweep angle of the cross-slot opener. When the sweep angle of the cross-slot opener is 20°, the micro-disturbance of soil particles and the horizontal work resistance are the least; The relative error of the soil disturbance ratio obtained by the tracer method and the discrete element method are both within 15%, and the relative error of the horizontal working resistance is 6.5%. The established discrete element simulation model can more accurately simulate the soil disturbance process of the cross-slot opener.

### 摘要

十字槽开沟器是一种新型播种开沟器，作为横刀关键参数的后掠角对土壤扰动具有重要影响。本文应用离散元法和示踪法，研究了横刀后掠角分别为 0°、10°、20°、30°、40° 时开沟器对土壤扰动和工作阻力的影响。示踪法与仿真结果皆显示表层和浅层土壤颗粒扰动比例和水平工作阻力随着横刀后掠角的增加先减小后增大，当十字槽开沟器横刀后掠角为 20° 时，对土壤颗粒微观扰动和水平工作阻力均最小；通过示踪法与离散元法获取的土壤扰动比例相对误差均在 15% 以内，水平工作阻力的相对误差为 6.5%，建立的仿真模型能够准确模拟十字槽开沟器的工作过程。

### INTRODUCTION

At present, most of the research on soil contact parts focuses on improving the design through experimental methods (He J et al., 2018). In order to study the performance of soil-contacting parts, we must first explore the law of soil movement and the force exerted on the soil during its work (Jia H L et al., 2017). The discrete element method (DEM) can be used to simulate the microscopic and macroscopic deformations of granular materials and study materials, allowing the formation and destruction of contact between granular materials, and is also suitable for simulating the interaction between soil and rigid bodies. Scholars have conducted extensive studies on the interaction process between soil and farming tools based on DEM. These studies have confirmed that discrete element simulation can simulate the farming process (Hang C.G. et al. 2018; Tanaka H. et al., 2000). In the discrete element, the movement of soil particles can be tracked, and the forces and disturbances of the soil particles during the cultivation process can be analysed (Fang H.M. et al. 2016b). The tracing method can also measure the change of soil displacement, which can reflect the mixing condition of the upper and lower dry and wet soil layers after the opener is operated. The tracer method is mainly to arrange the tracer in the soil to replace the fixed-point soil particles before operation. By observing the position change and movement process of the tracer before and after the operation, infer the position change of the soil particle and the movement law of the soil particle at the replacement point of the tracer. Aliakbar Solhjoui et al. studied the influence of openers with different structural parameters on the amount of soil side throw, and used the tracker tracing method to record the position changes of the tracer (Barr J et al.

2016; Solhjoui A et al. 2013; Solhjoui A et al. 2012; Solhjoui A et al. 2014). When Cao X.D. improved the design of the traditional core-shaft opener, he used the discrete element method and the tracker tracing method to study the soil microscopic movement changes after the trenching operation and determined the optimal structural parameters. James Barr et al. combined the two methods to analyse the influence of the structural parameters of the open-leg opener on soil disturbance (Barr J B et al. 2020). These two methods can accurately analyse the soil disturbance quantity. In a comprehensive analysis, domestic scholars mainly use discrete element method in their research on the optimization of soil touching parts, but few use tracer method to study the soil touching parts, and even fewer study the combination of the two aspects of discrete element method and tracer method to optimize the structural parameters of soil touching parts.

The cross-slot opener is a new type of opener developed by our research team. One-time ditching can realize the double-sided application of corn seeds and seed fertilizer and the layered application of seed fertilizer and base fertilizer, reducing the operation of the opener (Zhang J C et al., 2019). The sweep angle of the cross knife is a key structural parameter of the cross-slot opener, which has a great influence on soil disturbance and horizontal working resistance during the working process. However, the influence of the sweep angle of the cross-slot opener on soil disturbance and working resistance is still unclear. Therefore, this research takes the cross-slot opener as the object and uses the discrete element method and the tracer method to study the influence of the sweep angle of the transverse knife on the soil disturbance and horizontal working resistance during the trenching process, so as to provide a reference for the determination of the sweep angles of the transverse knife.

## MATERIALS AND METHODS

### Tracer test

- Experiment material

The cross-slot opener is mainly composed of a vertical knife and a horizontal knife on both sides, as shown in Fig.1. In the process of corn sowing and fertilization, the opener uses a vertical knife to open the base fertilizer ditch to realize the deep application of base fertilizer. A horizontal knife is installed on both sides of the vertical knife, and a seed ditch and a seed fertilizer ditch are opened on both sides of the upper part of the base fertilizer ditch in the lower layer of the soil. The falling soil above affects seeding and fertilization, realizing the two-sided application of seed and seed fertilizer.

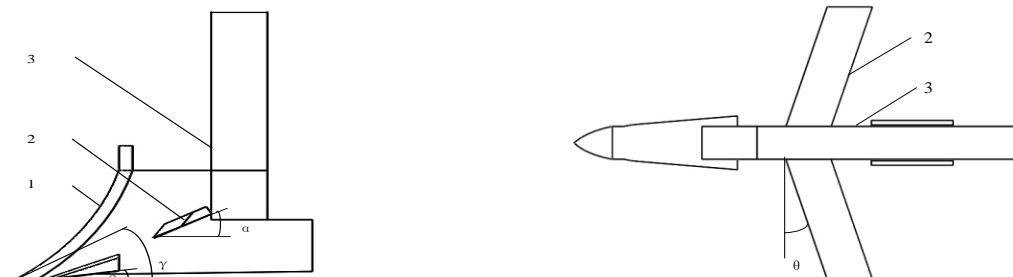


**Fig. 1 - Cross-slot opener**

1. Vertical knife; 2. Horizontal knife; 3. Column

Li G.H., (2018), Zhang J.C. et al., (2019), studied to determine the structural dimensions of the cross-slot opener, the horizontal knife entry angle  $\alpha$  is  $30^\circ$ , the vertical knife entry angle  $\gamma$  is  $31^\circ$ , and the vertical knife entry clearance angle  $\beta$  is  $8^\circ$ . In order to loosen the seed bed and facilitate ditching and fertilization, the projected length of the unilateral transverse knife in the direction of the seed furrow section is 80mm. From a theoretical analysis, when the sweep angle  $\theta$  increases, the soil changes from cutting to sliding, and the resultant horizontal force decreases; when the sweep angle  $\theta$  is too large, the projected length of the transverse knife on the seed trench section remains unchanged. The total length of the horizontal knife will increase, and the area of soil disturbance will increase. In order to reduce working resistance and soil disturbance, combined with the spacing of corn seed fertilizer and the installation position of the cross knife of the cross-slot opener, the maximum sweep angle of the cross knife is determined to be  $40^\circ$ .

Li G.H. (2018) and Zhang J.C. (2019) only theoretically and partially analysed the influence of the sweep angle of the transverse knife on the working resistance, but the influence of the sweep angle of the transverse knife on the soil disturbance is still unclear. Therefore, this study determines that the sweep angle  $\theta$  of the transverse knife is  $0^\circ$ ,  $10^\circ$ ,  $20^\circ$ ,  $30^\circ$ , and  $40^\circ$ .

- **Experimental procedure**

The tracer test was carried out in the digital soil tank of the Agricultural Machinery Laboratory of Northwest A&F University. The soil is loess with granular structure. The parent material is secondary loess and loamy clay. It belongs to the agricultural soil developed on the loess parent material (*Ding S.P. et al., 2018*). In the tracer test, according to the soil parameters in the field when the corn was sowed, the soil in the soil trough was prepared by a layered preparation method to ensure that the soil trough test was basically consistent with the soil parameters of the field environment (*Zhang J C et al., 2016*). After preparation, the average moisture content of the soil in the soil tank was 16.2%, and the soil hardness was 1447 kPa. Rotary tillage and soil compaction are shown in Fig.2.

With the opener working centre as the X-axis direction as the reference, tracers are arranged within 150mm on the left and right. The tracer uses a PVC cube with a material density of 1.2g/cm<sup>3</sup> and a side length of 10mm. Use a soil drill to drill a 150mm deep circular hole vertically downward at each location. First put the light blue tracer in the round hole, then put the soil taken out by the soil extractor, and after compacting it to the same layer of soil hardness, keep the upper and lower layer tracers 30mm apart. The depths are 120mm, 90mm, 60mm, 30mm, 0mm, respectively, fill in pink, yellow, green, blue and red tracers, put in an appropriate amount of soil and compact to close to the hardness of the same layer of soil, after tilling, use three-dimensional positioning. The measuring instrument measures the position of the tracer in the X, Y, and Z directions, and studies the position changes of the tracers in each layer, as shown in Fig.3.

The experiment was carried out under the conditions of a tillage depth of 130mm and a speed of 0.83m/s, using an electric variable frequency four-wheel drive soil tank test vehicle (*Hang C G et al., 2018*). In order to ensure the consistency of the test process and the reliability of the data, the first 3m of the soil-bin is the acceleration stage, the last 3m is the deceleration stage, and the middle area is the test area and the data collection area.



**Fig. 2 - The soil preparation process of the soil trough**



**Fig. 3 - Tracer layout and position measurement**

### Discrete element simulation analysis of cross-slot opener

The interaction between the cross-slot opener and the cultivated soil is a complex movement process. Discrete element simulation can study the interaction between the cross-slot opener and the soil from a macro and micro perspective.

- **Simulation modelling**

In order to ensure the reliability of the simulation results, the Solidworks2018 software is used to establish a 3D model of the cross-slot opener with 5 different horizontal knife sweep angles in the test at a 1:1 ratio, and save it in the .IGS format and import it into EDEM2018. The decrease of soil particle size in EDEM simulation will cause the simulation time to increase geometrically. Therefore, the particle size in the simulation is limited by calculation time and computer performance, and is always larger than the real soil particle size (*Ucgul M. et al., 2014; Fang H.M et al., 2016a*). In this paper, the soil particle model has a spherical particle with a radius of 3mm, and the Hertz-Mindlin with bonding model is selected (*Chen Y. et al. 2013*). The model is to bond two particles together through a bond, which can withstand a certain tangential force and normal

force. When the tangential force and normal force both reach the maximum value, the bond between the two particles is damage. After that, the separated particles are treated as rigid spheres, and contact solutions are performed.

- **Soil model parameters**

In EDEM simulation software, model parameters mainly include material parameters and contact parameters. The material parameters mainly include the density, Poisson's ratio and shear modulus of soil and cross-slot opener (65Mn). The contact parameters mainly include the coefficient of restitution, dynamic friction factor and static friction factor between materials. The basic parameter references of the discrete element simulation model are shown in the table (Ding S.P. et al. 2018; Wang X.Z. et al. 2018).

Basic parameters of the discrete element model

Table 1

PARAMETER	VALUE
Density of 65Mn steel /(kg·m <sup>-3</sup> )	7830
Poisson's ratio of 65Mn steel	0.35
Shear modulus of 65Mn steel	$7.27 \times 10^{10}$
Soil particle density /(kg·m <sup>-3</sup> )	1404
Poisson's ratio of the soil particles	0.40
Shear modulus of the soil particles /Pa	$6 \times 10^7$
Coefficient of restitution between soil and soil	0.6
Coefficient of rolling friction between soil and soil	0.4
Coefficient of static friction between soil and soil	0.58
Coefficient of restitution between soil and 65Mn steel	0.6
Coefficient of rolling friction between soil and 65Mn steel	0.5
Coefficient of static friction between soil and 65Mn steel	0.34
Normal Stiffness per unit area (N m <sup>-1</sup> )	2400000
Shear Stiffness per unit area (N m <sup>-1</sup> )	1700000
Critical Normal Stress (Pa)	235000
Critical Shear Stress (Pa)	186000
Bonded Disk Radius (mm)	3.5

- **Simulation test method**

After the soil parameter setting is completed, a virtual soil trough with a length × width × height of 1000mm×800mm×150mm will be generated by the pellet factory dynamically generating and accumulating pellets. In order to meet the requirements of corn planting and fertilization operations and the working depth of the cross-slot opener, the virtual soil slot model is divided into surface soil (above-10mm), shallow soil (-10mm~-40mm), middle and lower soil (-40mm~-70mm) and bottom soil (-70mm~-150mm) four parts, as shown in Fig.4. Based on the coordinate system in the simulation, the three-dimensional movement direction of the particles is explained as follows: horizontal movement occurs in the X direction; lateral movement occurs in the Y direction; vertical movement occurs in the Z direction. The forward direction of the cross-slot opener is -X direction, the forward speed is 0.83m/s, the total simulation time is 8.5s, and the depth of the opener is 130mm.

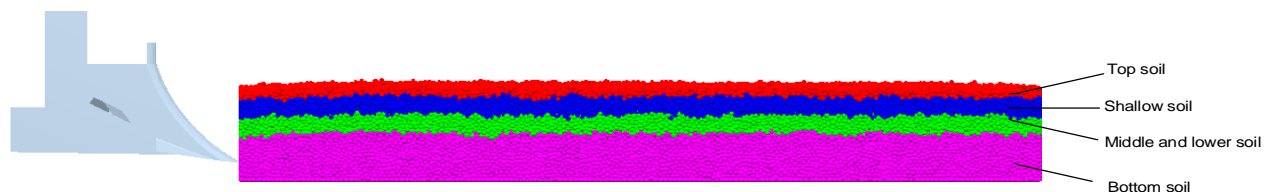


Fig. 4 - Discrete element farming model

## RESULTS

### Comparative analysis of soil disturbance state

It was difficult for the traditional test methods to determine the soil disturbance process during the operation of the cross-slot opener, in order to determine the changes of soil disturbance state at different depths with the different horizontal knife sweep angles (Hang C G et al. 2018). Using the discrete element method, a lateral cross-sectional view of the soil model at 7.6s (the cross-slot opener is in the middle of the tillage stroke) was carried out, and the cross-slot opener's lateral centre was at 0mm of the cross-sectional

view, according to the projection length of the cross knife 80mm and the lateral disturbance of the opener to the soil, the section spacing in the vertical tillage direction was selected to be 40mm, and the tillage direction section under different horizontal knife sweep angles was shown in Fig.5.

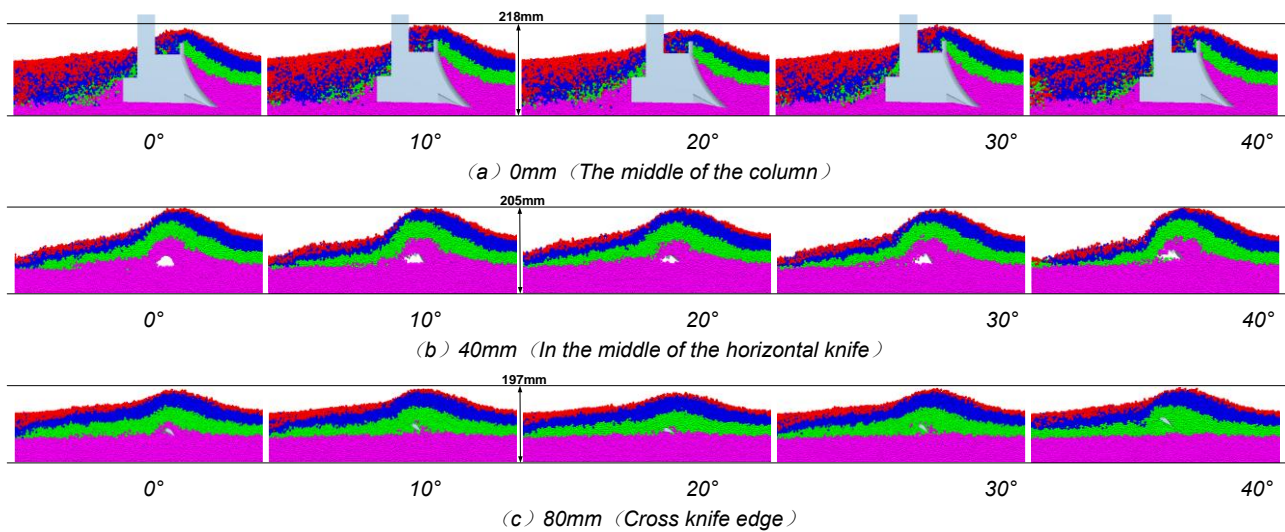


**Fig. 5 - Effect of the back-inclining angle on portrait disturbance quality of soil in different layers**

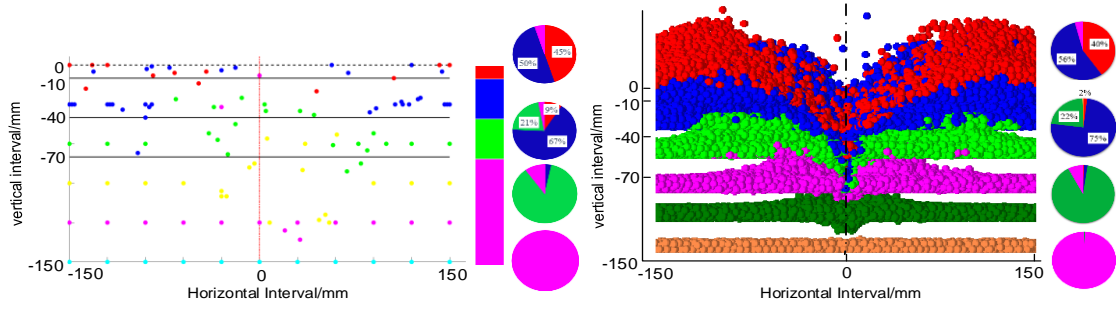
It could be seen from Fig.5 that in the middle of the vertical knife, the vertical uplift of the soil by the cross-slot opener and the mixing degree of the upper and lower soil layers were the largest. The soil disturbance area was mainly concentrated near the vertical knife, and the horizontal knife disturbance was small. With the increase of the lateral distance from the middle of the vertical knife, the vertical lifting height of the opener to the soil and the mixing degree of the upper and lower soil layers gradually decreased, and the vertical lifting height of the soil in the middle of the vertical knife was larger than the edge of the horizontal knife 21mm. With the increase of the sweep angle of the cross-slot opener, the disturbance range of the opener to the shallow and middle and lower soil layers gradually increased. As the sweep angle of the horizontal knife increased, the height of the soil lifted by the opener decreased and then increased in the middle of the vertical knife and the edge of the horizontal knife. When the sweep angle of the horizontal knife was 20°, the height of the soil lifted by the opener was the smallest (Fig.5a, c). In the middle of the horizontal knife, the influence trend of the horizontal knife sweep angle on the soil uplift height remained basically unchanged, but the slope of the ridge formed after the soil uplift gradually increased (Fig.5b).

### Comparative analysis of the effect of sweep angle on soil microscopic movement

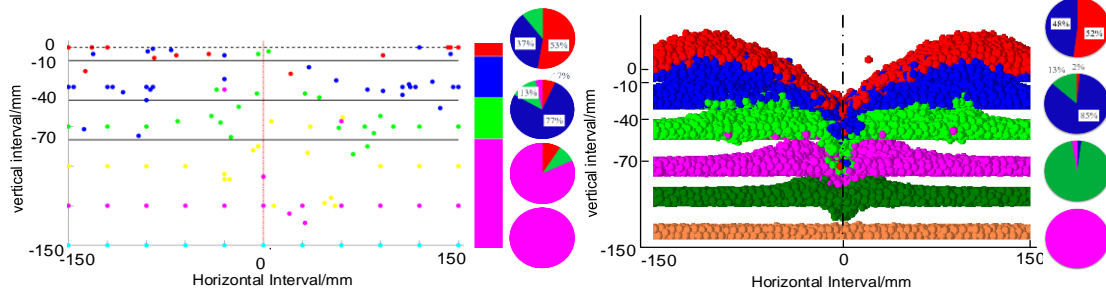
It could be seen from Fig.6 that the soil particles moved upward as a whole when the cross-slot opener was working. After work, the surface soil was mainly composed of surface and shallow soil particles. The shallow soil was mainly composed of surface, shallow and middle and lower soil particles. The middle and lower soil was mainly composed of shallow, middle and lower soil particles.

The bottom soil was mainly composed of bottom soil particles, there was almost no disturbance. Surface and shallow soil were used as maize sowing areas, which had higher requirements for soil moisture, especially in arid and semi-arid areas for maize germination and growth. The middle, lower and bottom soils were mainly composed of soil particles in the wet soil layer, which had little effect on the growth of corn. Therefore, the analysis of the particle composition in the surface and shallow soils was mainly carried out. It could be seen from the test results of the tracer method in Fig. 6(a) that with the increase of the sweep angle of the horizontal knife, the proportion of the shallow and middle-lower soil particles in the surface soil first decreased and then increased, and the proportion of the surface soil particles in the shallow soil decreased first and then increased.

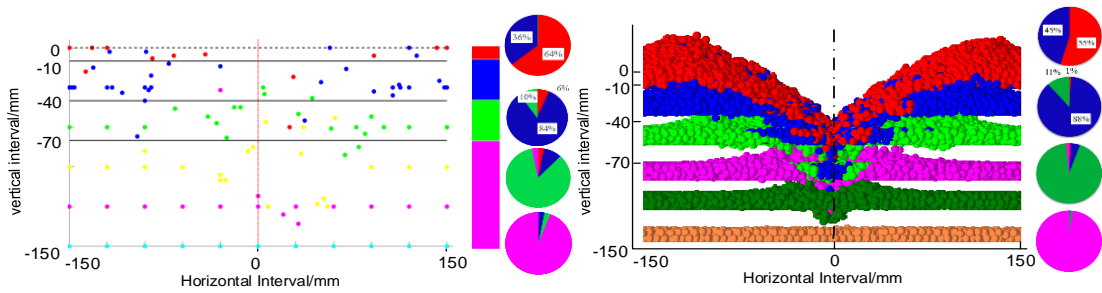
When the sweep angle of the transverse knife was 40°, the proportion of surface soil particles was 18%, and the proportion of surface soil particles in the other transverse knife sweep angles was not much different, all below 10%. When the sweep angle of the horizontal knife was 20°, the proportion of the shallow and middle-lower soil particles in the topsoil was at least 36%, which was 24%. From the simulation results in Fig. 6(b), it could be seen that with the increase of the sweep angle of the transverse knife, the proportion of the shallow and middle-lower soil particles in the surface soil first decreases and then increases.



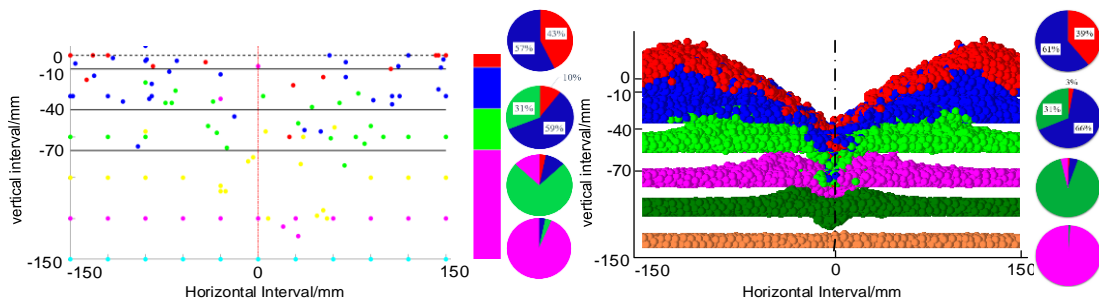
(a) Sweep angle 0°



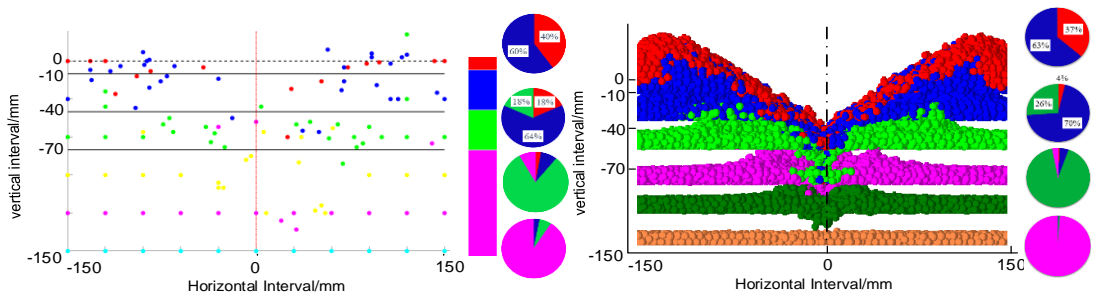
(b) Sweep angle 10°



(c) Sweep angle 20°



(d) Sweep angle 30°



(e) Sweep angle 40°

Tracer

EDEM Predicted

Fig. 6 - Soil microscopic movement of cross-slot opener

When the sweep angle of the transverse knife was 40°, the shallow and the proportion of middle and lower soil particles was as high as 63%, and the proportion of surface soil particles in the shallow soil first decreased and then increased, but the overall difference was not significant, all below 4%. When the sweep angle of the horizontal knife was 20°, the shallow and middle-lower soil particles in the surface soil were the least, accounting for 45%, which was 18% lower than when the sweep angle was 40°, and accounting for only 1% of the shallow soil.

### Influence of the sweep angle of the horizontal knife on tillage resistance

It could be seen from Fig.7 that the horizontal working resistance varied between 275-593N under different sweep angles of the transverse knife. The horizontal working resistance of the cross-slot opener under different sweep angles of the horizontal knife was quite different. When the sweep angle of the cross knife was 0° and 10°, the horizontal working resistance of the cross-slot opener did not change significantly. When the horizontal knife sweep angle increased from 10° to 20°, the horizontal working resistance decreased sharply. When the sweep angle increased from 20° to 40°, the horizontal working resistance increased sharply, mainly because the sweep angle increased, the length of the cross knife increased, which lead to a larger disturbance area, thereby increasing the horizontal working resistance. The average error between the simulated value and the experimental value of the horizontal working resistance of the cross-slot opener with 5 different horizontal knife sweep angles was 6.5%.

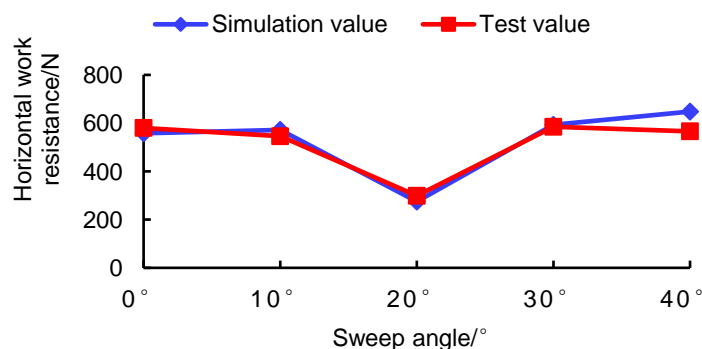


Fig. 7 - The influence of the sweep angle of the horizontal knife on the horizontal working resistance

### CONCLUSIONS

(1) The relative error between the tracing method tested results and the discrete element simulation results was less than 15%, indicating that the established discrete element simulation model could more accurately reflect the soil disturbance during the operation of the cross-slot opener.

(2) With the increase of the sweep angle, the action form of the cross knife on the soil changes from cutting to sliding cutting. With the further increase of the sweep angle of the transverse knife, the increase in the total length of the transverse knife gradually increases the range of soil disturbance. With the further increase of the sweep angle, the increase in the length of the cross blade would gradually increase the range of soil disturbance, which would inevitably lead to an increase in working resistance.

(3) There was a certain error between the experimental results of the tracer method and the discrete element simulation results, especially the proportion of other soil particles in the surface soil. The following two reasons could be explained: due to the small layout of the tracer blocks, some tracer blocks would be lost or moved out of the statistical area after the cross-slot opener works; the radius of the soil particles and the tracer blocks in the simulation had a certain difference in size.

### ACKNOWLEDGEMENT

The authors thank the editing team of Editor Bar for improving the English language fluency of our paper. The work in this paper was supported by the Key Research and Development Program of Shaanxi Province (No.2017NY-127) and the Key Research and Development Program of Shaanxi Province (No. 2020NY-119).

### REFERENCES

- [1] Barr, J., Desbiolles, J., Ucgul, M., & Fielke, J. M. (2020). Bentleg furrow opener performance analysis using the discrete element method. *Biosystems Engineering*, 189, 99-115. <https://doi.org/10.1016/j.biosystemseng.2019.11.008>;

- [2] Barr, J. B., Desbiolles, J. M. A., & Fielke, J. M. (2016). Minimising soil disturbance and reaction forces for high speed sowing using bentleg furrow openers. *Biosystems Engineering*, 151, 53-64. <https://doi.org/10.1016/j.biosystemseng.2016.08.025>;
- [3] Chen Y., Munkholm, L. J., & Nyord, T. (2013). A discrete element model for soil–sweep interaction in three different soils. *Soil and Tillage Research*, 126, 34-41. <https://doi.org/10.1016/j.still.2012.08.008>;
- [4] Ding S.P., Bai L., Yao Y.X., Yue B., Fu Z.L., Zheng Z.Q., & Huang, Y.X., (2018). Discrete element modelling (DEM) of fertilizer dual-banding with adjustable rates. *Computers and Electronics in Agriculture*, 152, 32-39. <https://doi.org/10.1016/j.compag.2018.06.044>
- [5] Fang H.M., Ji C.Y., Chandio F., Guo J., Zhang Q.Y., & Arslan C., (2016a). Analysis of soil dynamic behaviour during rotary tillage based on distinct element method, *Transactions of the Chinese Society for Agricultural Machinery*, Vol.47, pp.22-28;
- [6] Fang H.M., Ji C.Y., Tagar, A., Zhang Q.Y., & Guo J., (2016b). Simulation Analysis of Straw Movement in Straw-Soil-Rotary Blade System, *Transactions of the Chinese Society for Agricultural Machinery*, Vol.47, pp.60-67;
- [7] Hang C.G., Gao X.J., Yuan M.C., Huang Y.X., & Zhu R.X., (2018). Discrete element simulations and experiments of soil disturbance as affected by the tine spacing of subsoiler. *Biosystems Engineering*, 168:73-82. <https://doi.org/10.1016/j.biosystemseng.2017.03.008>;
- [8] He J.W., Li H.W., Chen H.T., Lu C.Y., & Wang Q.J., (2018). Research Progress of Conservation Tillage Technology and Machine, *Transactions of the Chinese Society for Agricultural Machinery*, Vol.49, pp.1-19;
- [9] Jia H.L., Zheng J.X., Yuan H.F., Guo M.Z., Wang W.J., & Jiang X.M., (2017). Design and experiment of profiling sliding-knife opener, *Transactions of the Chinese Society of Agricultural Engineering*, Vol.33, pp.16-24;
- [10] Li G.H., (2018). Structural design and experimental study of cross-slot opener, Northwest A&F University/China;
- [11] Solhjoui, A., Desbiolles, J. M. A., & Fielke, J. M. (2013). Soil translocation by narrow openers with various blade face geometries. *Biosystems Engineering*, 114(3), 259-266. <https://doi.org/10.1016/j.biosystemseng.2012.12.018>;
- [12] Solhjoui, A., Fielke, J. M., & Desbiolles, J. M. A. (2012). Soil translocation by narrow openers with various rake angles. *Biosystems Engineering*, 112(1), 65-73. <https://doi.org/10.1016/j.biosystemseng.2012.02.006>;
- [13] Solhjoui, A., Fielke, J. M., Desbiolles, J. M. A., & Saunders, C. (2014). Soil translocation by narrow openers with various bent leg geometries. *Biosystems Engineering*, 127, 41-49. <https://doi.org/10.1016/j.biosystemseng.2014.08.008>;
- [14] Tanaka, H., Momozu, M., Oida, A., & Yamazaki, M. (2000). Simulation of soil deformation and resistance at bar penetration by the Distinct Element Method. *Journal of Terramechanics*, 37(1), 41-56. [https://doi.org/10.1016/S0022-4898\(99\)00013-0](https://doi.org/10.1016/S0022-4898(99)00013-0);
- [15] Ucgul, M., Fielke, J. M., & Saunders, C. (2014). 3D DEM tillage simulation: Validation of a hysteretic spring (plastic) contact model for a sweep tool operating in a cohesionless soil. *Soil and Tillage Research*, 144, 220-227. <https://doi.org/10.1016/j.still.2013.10.003>;
- [16] Zhang J.C., Yan X.L., Li G.H., Cao X.D., Liu N., Sun L.W., & Tong M., (2019). Cross – groove fertilizer application and layered fertilizer opener design, *Journal of Agricultural Mechanization Research*, Vol.41, pp.86-90;
- [17] Zhang J.C., Yan X.L., Lin Z.K., & Zhu R.X., (2016). Design and experiment of self-exciting vibration deep-loosening and sub-soiling machine, *Transactions of the Chinese Society for Agricultural Machinery*, Vol.47, pp.44-49.

**NUMERICAL 3D ANALYSIS OF A MINI WIND TURBINE WITH HORIZONTAL AXIS,  
FOR IMPLEMENTATION IN AGRICULTURAL FARMS****ANALIZA NUMERICA 3D A UNEI TURBINE EOLIENE DE PUTERE MICA CU AX  
ORIZONTAL IN VEDEREA IMPLEMENTARII IN FERMELE AGRICOLE**

**George Ipate<sup>1)</sup>, Gabriel Alexandru Constantin<sup>1)</sup>, Sorin Ștefan Biris<sup>1)</sup>,  
Gheorghe Voicu<sup>1)</sup>, Carmen Otilia Rusanescu<sup>1)</sup>, Vasilica Ștefan<sup>2)</sup>**

<sup>1)</sup> Universities Polytechnic Bucharest, Faculty of Biotechnical Systems Engineering / Romania

<sup>2)</sup> National Institute for Research-Development of Machines and Installations Designed for Agriculture  
and Food Industry - INMA Bucharest / Romania

Tel: 0766445321; E-mail: [puiu.ipate@gmail.com](mailto:puiu.ipate@gmail.com)

DOI: <https://doi.org/10.35633/inmateh-62-34>

**Keywords:** power, wind, turbine, numerical simulation, CFD

**ABSTRACT**

*The purpose of this paper is the numerical study of the effects of the fluid interaction with the blades of the working bodies of the renewable energy conversion systems. The paper presents the results of numerical research regarding the influence of the blade shape (straight), the number of blades (2, 3, 4) or the wind speed in the area on the output power of the small capacity wind turbines. The validation of the simulation data was performed by comparison with the experimental data obtained on a Windtrainer Junior laboratory wind energy system. Computed power coefficients are in good agreement with the experimental results. Increasing the efficiency of energy conversion for small wind turbines for their implementation in green farms represents a significant step in the concept of sustainable rural development.*

**REZUMAT**

*Scopul acestei lucrări este studiul numeric al efectelor interacțiunii fluidului cu lamele corpurilor de lucru ale sistemelor de conversie a energiei regenerabile. Lucrarea prezintă rezultatele cercetărilor numerice cu privire la influența formei lamei (drepte), numărul de pale (2, 3, 4) sau viteza vântului în zona pe puterea de ieșire a turbinelor eoliene de mică capacitate. Validarea datelor simulate a fost efectuată prin comparație cu datele experimentale obținute pe un sistem de energie eoliană de laborator Windtrainer Junior. Coeficienții de putere calculați sunt în acord cu rezultatele experimentale. Creșterea eficienței conversiei energiei pentru turbinele eoliene mici pentru implementarea lor în ferme ecologice reprezintă un pas semnificativ în conceptul de dezvoltare rurală durabilă.*

**INTRODUCTION**

The need to reach a higher standard of living and increase the world's population have produced a dramatic increase in energy consumption globally. All energy sources affect the environment to a greater or lesser extent. There is no completely "clean" power source. Most of our energy comes from 85% fossil fuels - coal, oil and natural gas, and the burning of these fuels causes pollution of the environment in which we live. To reduce the long-term impact of the energy industry on the environment, strategies are developed and implemented to increase the efficiency of energy use, to capitalize on alternative sources and on sustainable development.

Wind energy is one of the renewable energy sources that can be harnessed due to its quite good potential. Generating small scale electricity is closer to the final user, significantly reducing transport losses. This leads to lower energy costs for consumers and ensures greater efficiency. In isolated areas, where electricity grids are missing or are isolated and have low transport capacity, individual turbines or small groups of turbines of different sizes are located. Small-scale electricity generation can be considered to be more reliable, cheaper, more efficient and more environmentally friendly than centralized production.

The ability of modern computing systems to operate quickly with a large volume of data offers the unique opportunity for researchers to investigate problems whose practical approach would be too costly, long-lasting or even impossible. Thus, the researcher can obtain optimal technical solutions that approach the experimental reality in a reasonable time.

*Mara et al., (2014)*, study a model for aerodynamics simulation of Magnus wind rotor blades using Ansys CFX. They evaluated various strategies for obtaining the grid and models of turbulence to accurately validate the model in relation to the experimental data published by *Bychkov et al. (2007)*. *Rogowski et al., (2017)*, performed a numerical analysis of a small-size vertical-axis wind turbine performance. They developed a two-dimensional model of vertical-axis wind turbine based on the experimental Darrieus wind turbine, and show that velocity profile becomes more asymmetric in relation to upper tip speed ratios if the rotor is operating at lower tip speed ratios.

*Nigam et al., (2017)*, perform a CFD analysis of a Vestas V82-1.65 MW horizontal axis wind turbine blade and NACA 634 -221 airfoil profile of wind turbine using k-SST turbulence model in Ansys Fluent. The results obtained for the traction coefficient and the moment of depositing at different angles of attack or lift coefficient are compared with the experimental results and show a good correlation. They also concluded that the air velocity is higher on the upper surface of the wing, while the air pressure on the lower surface of the wing is also increased.

*Wenehenubun et al., (2015)*, studied the performance of Savonius wind turbines related with the number of blades. For this work the ANSYS 13.0 software simulations were used to show the pressure distribution of wind turbine. *WuBow et al., (2007)*, studied the airflow around a wind turbine (WT) of the type Enercon E66 with emphasis on the turbulent wake by using CFD simulations. It was found that the local values of turbulence intensity and the amplitude of the velocity inside the trace fits quite well with the measurements. *Bose et al., (2014)*, studied numerically, using a commercial CFD code, the effect of pitch angle on the performance of a three bladed straight H-Darrieus vertical axis wind turbine. They showed that the presence of vortices close to the trailing edge deteriorates the performance of the turbine.

The main purpose of the present paper is the theoretical and experimental argumentation of the aerodynamic characteristics of a wind turbine in the aspect of increasing the energy conversion efficiency for low power wind turbines. In order to achieve the formulated purpose, CFD simulations were performed for different wind speeds to determine the performance factor of the developed rotor and the aerodynamic forces acting on the blade, or to model the fluid's interaction with the blade structure to verify the resistance of the blade in stationary regime.

## MATERIALS AND METHODS

The wind turbine works due to the difference of forces exert on each blade according to *Wenehenubun, (2007)*. The maximum power of wind turbine  $P_t$  is determined as:

$$P_t = T \cdot \omega \text{ [Watt]} \quad (1)$$

where:

$T$  is the torque (Nm) and  $\omega$  is the angular velocity of rotor ( $s^{-1}$ ).

The performance of wind turbine can be expressed in the form of torque coefficient ( $C_t$ ) and the coefficient of power ( $C_p$ ). The tip speed ratio or  $TSR$  ( $\lambda$ ) is a parameter related with rated wind speed and rotor diameter. As the ratio between the speed of tip blade and wind speed through the blade,  $TSR$  can be determined with relation (2) according to *Hameed and Afaq, (2013)*:

$$\lambda = TSR = \frac{V_{rotor}}{V} = \omega \cdot d/V \quad (2)$$

where:

$V_{rotor}$  is the tip speed or the peripheral velocity of rotor (m/s),  $V$  is the wind speed (m/s) and  $d$  is the diameter of the rotor (m). The coefficient of torque or  $C_t$  is defined as the ratio between the actual torque develop by the rotor ( $T$ ) and the theoretical torque available in the wind ( $T_w$ ) as,

$$C_t = \frac{T}{T_w} = \frac{4T}{\rho_{air} \cdot d \cdot A_s \cdot V^2} \quad (3)$$

where:

$\rho_{air}$  is the density of air ( $kg/m^3$ ) and  $A_s$  is the swept area of blades ( $m^2$ ). The power coefficient of a wind turbine ( $C_p$ ) can be determined from the ratio between the maximum power obtained from the wind or the mechanical ( $P_t$ ) and the total power available from the wind ( $P_w$ ),

$$C_p = \frac{P_t}{P_w} = \frac{P_t}{0.5 \cdot \rho_{air} \cdot A \cdot V^3} \quad (4)$$

The relationship between the power coefficient  $C_p$  and the tip speed ratio  $\lambda$  is an effect of solidity of the wind turbine performance. The electric power produced by wind turbine is computed from the relation:

$$P_e = \eta_b \cdot \eta_m \cdot \eta_e \cdot P_w \quad (5)$$

where:  $\eta_b$  is blade aerodynamic efficiency,  $\eta_m$  is mechanical efficiency and  $\eta_e$  electrical efficiency.

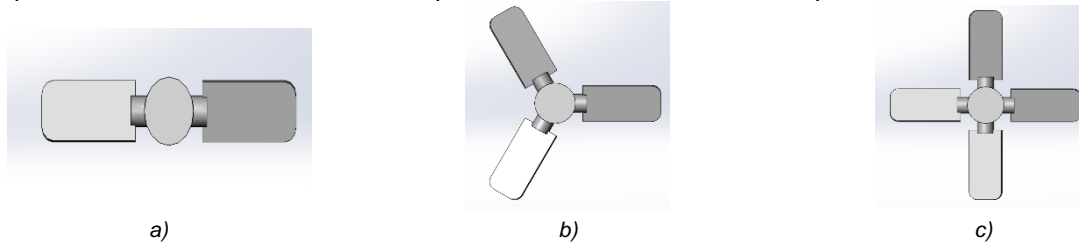


**Fig. 1 – Blade profile and rotor geometry**

a) 2PaIDREP; b) 3PaIDREP; c) 4PaIDREP

The experiment used a wind turbine model with two, three and four straight blades (with acronym 2PaIDREP, 3PaIDREP and 4PaIDREP), as shown in Fig. 1. The dimensions of the blades of the wind turbine model are length = 40mm, width = 20mm, thickness = 2mm, angle of attack of the profile  $\alpha = 15$  degrees, rotor diameter = 110mm. The model of wind turbine was performed in an open circuit wind turbine as shown in Fig. 2. The controllable wind machine (low voltage) was started to produce wind and an anemometer measured the velocity of wind. When the wind produced by the centrifugal fan pushed the blades of the model, the rotor of wind turbine will rotate. Each experiment with two, three and four blades respectively used the speed of wind from 4.5 to 12.5 m/s. The power of the generator depending on the wind force was measured using the 2 multimeters (U-volt / I-ampere) with 2 mm connectors.

ANSYS Workbench platform was used for numerical modelling. For the dynamic calculation of fluid flow, the Ansys - CFX5 module was used. The three-dimensional geometry was realized in the computer-aided design program SolidWorks 2016 and subsequently exported to the DesignModeler program in the Workbench environment.



**Fig. 2 – The experimental laboratory system Windtrainer Junior**

In the pre-processing phase, the calculation domain was created as follows: a stationary domain consisting of a rectangular parallelepiped of length  $L=0.45$ m, height  $H=0.14$ m and width  $B=0.13$ m over which a semicylinder whose radius is superposed is  $R=0.065$ m; a rotational domain having a cylindrical shape with a height of  $H_c=0.01$ m or the radius of the turbine and a radius of the base  $R_b=0.08$ m. The fixed domain is obtained by the operation of removing the cylinder and the assembly: turbine support block (a rectangular parallelepiped with dimensions  $L_b=0.12$ m,  $H_b=0.04$ m,  $B_b=0.08$ m) tower turbine (a cylinder with dimensions  $D_t=0.02$ m,  $H_t=0.08$ ) and turbine platform (a cylinder with dimensions  $D_n=0.04$ m,  $H_n=0.06$ m) from the stationary domain. The two domains are connected topologically by the surface of the cylinder having a double grid on its surface (non-conforming interface), one coming from the fixed domain and another coming from the rotating domain. To avoid unwanted interpolation errors when moving from one computing domain to another, the size of the elements at the interface is approximately the same on both sides of the cylinder.

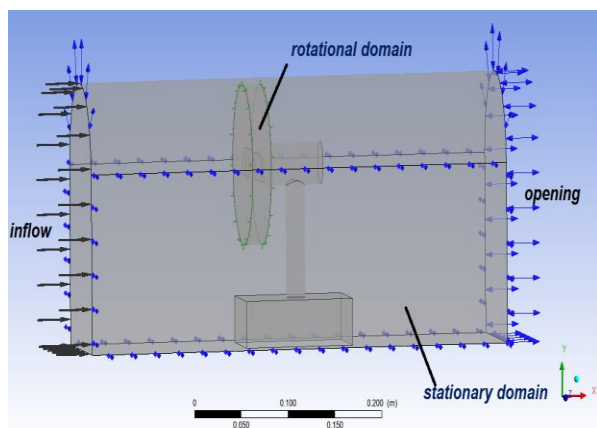


Fig. 3 - Detail domain and boundary conditions

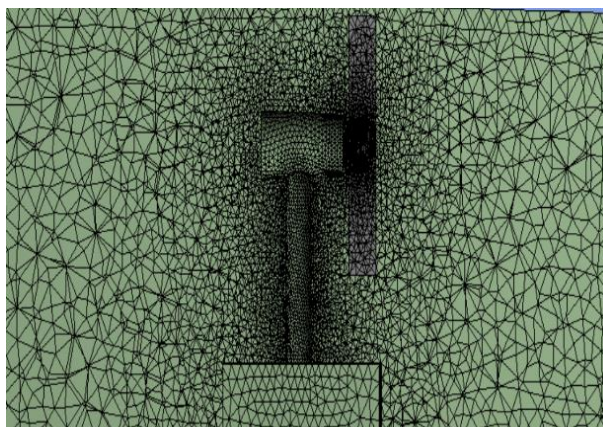


Fig. 4 – Model discretization

Figure 4 shows the discretized domain and the level of refinement of the network in the rotor region. The calculation grid was created in the Ansys Mesh program that allows the creation of grids with refined tetrahedral elements by halving the sides of the elements. For all the calculation scenarios, the same computing network (grid) was used, consisting of 417969 elements and 77217 nodes, distributed as follows: 261544 elements and 47647 nodes in the grid associated with the fixed domain and 156425 elements and 29570 nodes for the grid in the rotating domain. The boundary conditions applied to the simulation are shown in figure 3.

The assumptions made in setting the calculation case can be summarized as follows:

- the flow is completely turbulent on the blade and the nacelle;
- the infinite upstream current is uniform and has a speed of 4.5 - 12.5 m/s;
- at infinite upstream the turbulence fluctuations have an intensity of 5% compared to the average speed;
- at infinite upstream the pressure is constant and equal to 1 atm, idem temperature is 288.15K.
- the flow is a stationary one, although we have rotation, the formed slope has a periodic character, and the aerodynamic coefficients do not vary after a certain period.

Current cases required approximately 10.5GB RAM, and the simulation time for convergence (decreasing residuals by 5 orders of magnitude and stabilizing aerodynamic coefficients) on a dual-core processor at 2.6 GHz took more than 15.2 hours.

## RESULTS

In this paper, the results obtained from the flow simulations carried out for the turbine with two, three and four straight blades are presented below. The simulations were performed for a speed ratio at the tip of the blade ( $TSR$ ) of 0.026, at the air inlet speed of 6.9 m/s, and a power coefficient  $C_p = 0.00342$  for the 2-blade model,  $C_p = 0.02843$  for the model with 3 blades, respectively,  $C_p = 0.06764$  for the 4 blade model. The very low coefficient of power made us investigate the possibility of using the protective cap as an element of limiting the effect of the "infinite extent" that leads to the decrease of the load and the appearance of the induced resistance, factors that decrease the aerodynamic momentum.

The power coefficient curve obtained from the CFD results is compared with the experimental data obtained, the numerical results for the power coefficient curve showing a fairly good agreement with the experimental data. The simulation results include velocity distribution, pressure distribution along the flow direction, turbulent kinetic energy distribution behind the wind turbine and turbine power.

Because the ratio of the speed to the blade type is dependent on the angular velocity and the wind speed, the angular velocities are unchanged in each run, because the design is simulated at the constant wind speed. In order to obtain the aerodynamic properties of the model, the lifting and traction forces, the calculation function from the results processing file from Ansys CFX was used. Thus, the normal force along the X axis, which is equivalent to the lifting force, and the normal force along the Z axis, which is equivalent to the tensile force, were obtained. Similar results were reached by *Mara et al., (2014)*.

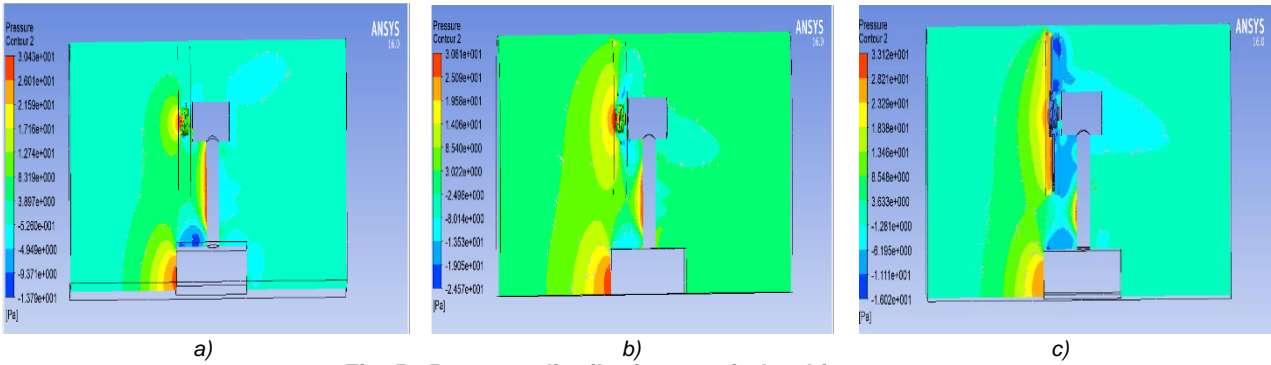


**Fig. 5 - Pressure distribution on wind turbine rotor**  
 a) two blades; b) three blades; c) four blades

Fig. 5 shows pressure distribution for wind turbine rotor with two blades (a), three blades (b) and four blades (c). Pressure on four blades is higher than pressure on two and three blades with result that the deviation of drag forces will rotate the rotor. As shown in Fig. 5 (a) and (b), pressure in front of the blades is higher than that at the back and wind turbine rotor will rotate. The pressure differences between the front area and the back of the wind turbine blades are clearly outlined in Fig. 5 (c). This makes the four-blade wind rotor have the highest torque compared to the other types of wind turbine rotors.

Figure 6 gives a snapshot of the unsteady turbulent wake and show contour plots of velocity magnitude ranging from 0 to 7.6 m/s. Blue areas denote areas of very low wind speed in the vicinity of the walls and close downstream of the tower, as *WuBow (2007)* found it too. Distribution of pressure on both sides, top and bottom, contributes to the lift. Pressure drag is the part of drag force connected to the pressure distribution around the airfoil, as *Nigam et al., (2017)* and *Bose et al., (2014)* described too. In accordance with those found by *Jang et al. (2019)*, as the pressure of the fluid increases, the flow velocity decreases, resulting in the lowest value inside the rotor and the maximum value on the outer surface.

Figure 7 shows the evolution of the turbulence kinetic energy for the three types of rotors since the beginning of the wind action on the blade, for values of the wind speed considered of 6.9 m/s. It is noted: the lower the stabilized flow velocity of the fluid, the turbulence intensity initially has higher bursts, but they occur later than those produced at higher speeds, and the stabilization of the turbulence intensity occurs at higher values and with more pronounced oscillations.

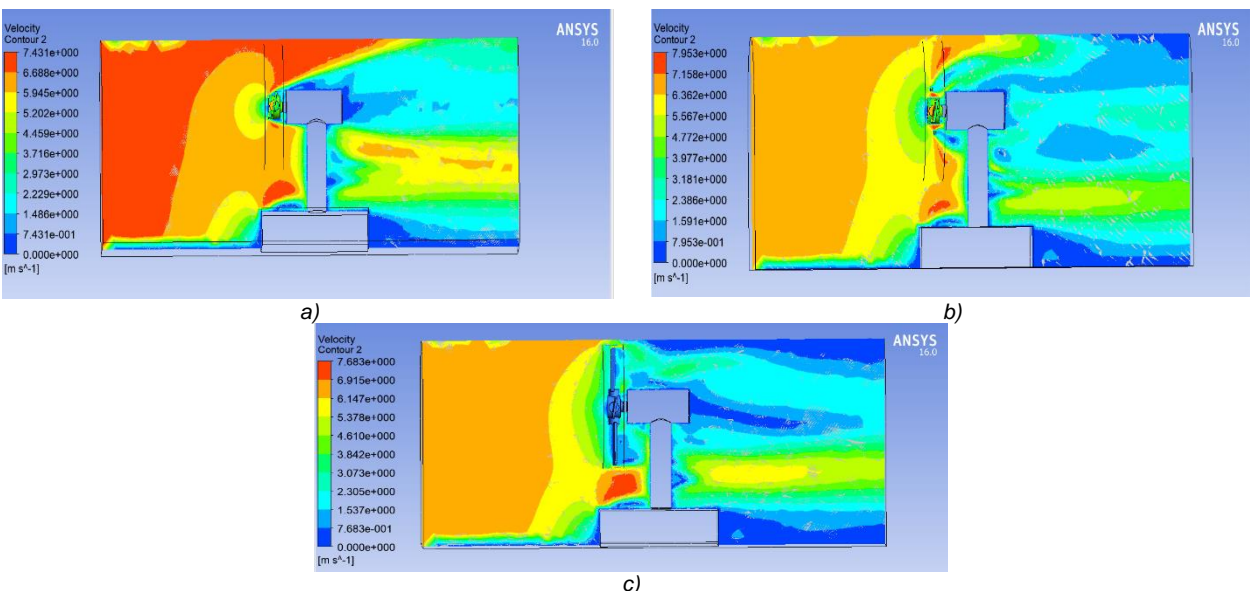


**Fig. 6 - Contours of air velocity magnitude in plane section at an input speed of 6.9 m/s**  
 a) two blades; b) three blades; c) four blades

The intensity of the turbulence, for the values of the fluid current acting on the blade, is in the range  $(0 \div 1.87) \text{ m}^2/\text{s}^2$ , which is considered to be low values, so a rather small value of the intensity of the turbulence (*Tudor, 2015*). With this help you can see the areas with the highest potential for hydrodynamic losses, in

which the energy of the fluid is consumed unnecessarily. In the detail of figure 7 b) and c) an area of maximum kinetic energy is highlighted, which appeared at the interface between the stationary and the rotational zone, due to the existence of a very small intersection.

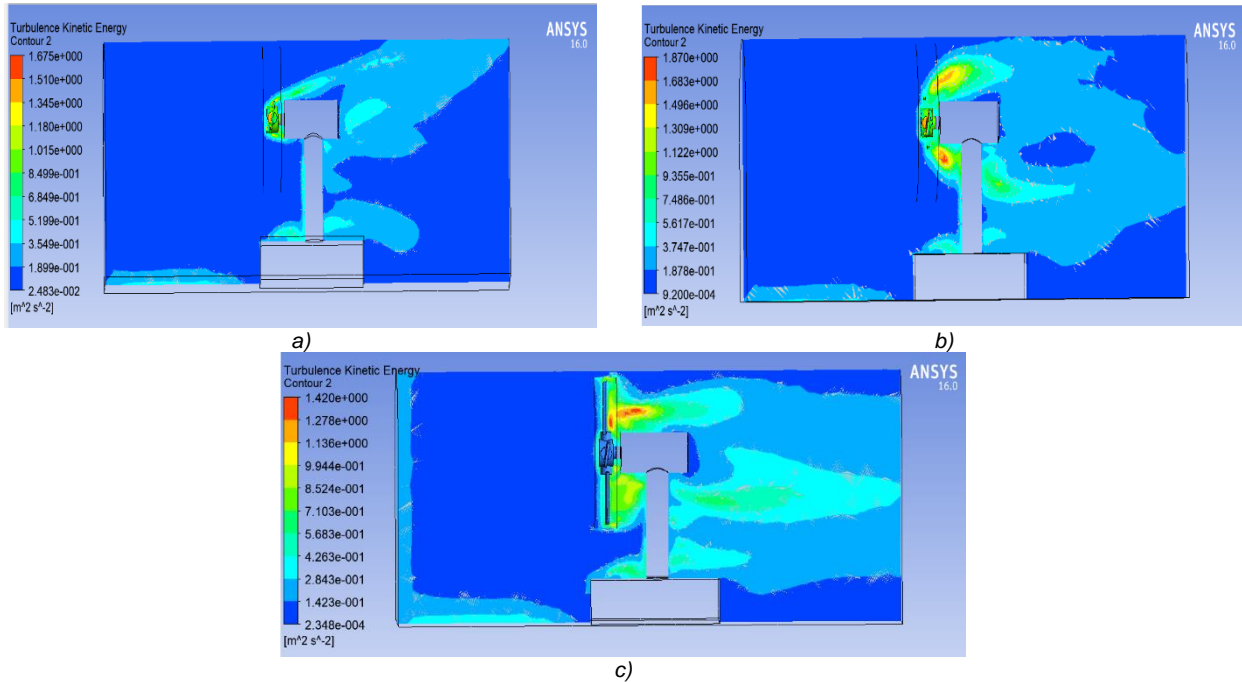


**Fig. 7 – Turbulence kinetic energy distribution**  
 a) two blades; b) three blades; c) four blades

The representations of the temporal evolutions of the analysed parameters (static pressure, air velocity after the impact with the turbine blade, turbulence intensity, for wind speeds between 4.5 - 12.5 m/s) show that the disturbances introduced by them behind the turbine rotor are manifested more pregnant to a distance of 0.23 m.

During operation the wind turbine rotor is required at variable wind speeds that cause centrifugal forces and shear strength forces that bend the blade tip. The maximum aerodynamic forces for the wind speed of 6.9 m/s were determined using the CFX module to check the blade resistance. Then, these forces were transferred to the Structural analysis module with which the structural analysis of the blade was performed. The hub blade was fixed to the base by means of a rotational joint and required with aerodynamic forces distributed over its entire surface. The axial component of the aerodynamic forces was obtained by approximately 0.116823 N. Regarding the values of lift and traction coefficient, they were very small for all the tip speed ratios, which can lead to a significant average error. Figure 8 illustrates the pressure distributed over the entire surface of the blade in the form of vectors.

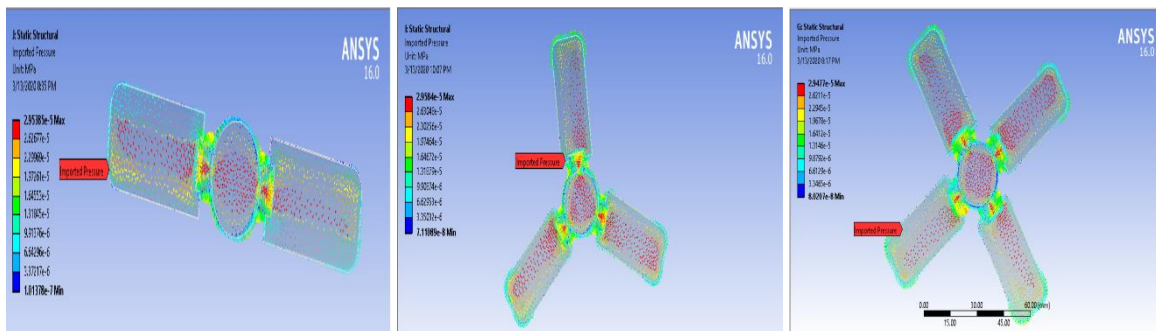


**Fig. 8 – Distribution of pressure on rotor blades**

The purpose of the structural analysis is to check the rigidity of the blade, to determine the stresses that appear in the blade as well as the moment of rotation, as *Paulesn et al (2013)* analyse too.

The 2-blade rotor has been discretized into 5999 nodes and 27330 elements, the 3-blade rotor into 8309 nodes and 37572 elements, respectively, the 4-blade rotor into 10152 nodes and 45585 finite elements, and the results of the static blade analysis are shown in Fig. 9. It can be easily observed that the maximum Von Mises equivalent stress appear when the blades are embedded in the rotor hub and have values in the range 2.1845e-002 MPa - 2.8533e-002 MPa.

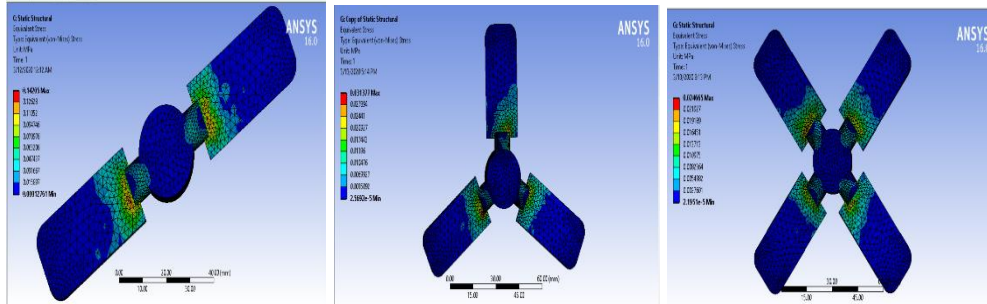


Fig. 9 - Distribution of Von Mises equivalent stress on rotor blades

For the validation of model and solution methodology the numerical predictions of coefficient of power  $C_p$  have been compared with the experimental results. The simulations have been done using the methodology described in the previous section, and  $C_p$  is plotted against wind speed  $V$  [m/s] as shown in Fig. 10. At very lower values of  $TSR$  ( $\lambda > 0.026$ ) the numerical predictions over predict the experimental values. This is in contradiction with those observed in the numerical predictions of *Bose et al., (2014)*. In contrast, although all numerical results show similar trends, they vary significantly. The largest deviations are observed in figure 10 between  $C_p$  curves (*computed* - black line and *experimental* - green dot line) obtained for the 4-blades model and can be attributed to the 3D effects and the strong interaction of the blades with the vortices as well as to the considered turbulence model.

The aerodynamic power, also known as the power coefficient, in figure 10 was calculated using Equation (4). In case of experimental power coefficient, we need to consider external environmental condition, such as electrical losses and overspeed protection, which alter the torque-speed schedule of the generator and finally the turbine power performance.

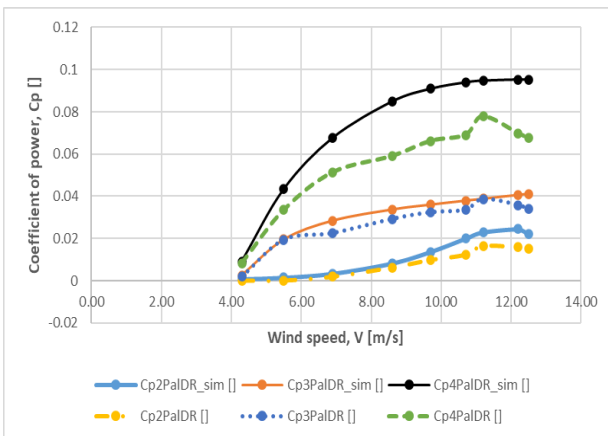


Fig. 10 – Coefficient of power vs. wind speed

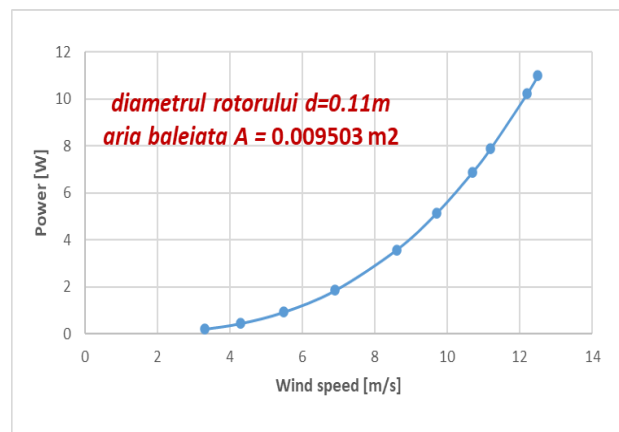


Fig. 11 – The power curve of the turbine depending on the wind speed

In order to make a comparative analysis of the conversion capacity of the turbine with the existing rotor, the power curve was calculated (Fig. 11), without considering the mechanical losses.

**CONCLUSIONS**

Based on the CFD numerical simulations of the turbine rotor:

- the dimensions of the computational domain of the fluid were chosen so as to ensure the free flow without influencing the domain boundaries;

- the torque moments developed at the rotor shaft and the wind pressure distribution on the surface of the blade were determined for different wind speeds (4.5 - 12.5 m/s);
- the power curve was calculated, without considering the mechanical losses, and compared with the results of the experimental researches performed for this turbine;
- the resistance structure of the blade was checked in for the wind speed limit of 6.9 m/s - based on the simulation results of the fluid interaction with the blade structure;
- an area of maximum turbulent kinetic energy was highlighted, which appeared when the fluid interacted with the rotor blades and where the areas with the highest potential can be observed of aerodynamic losses, in which the energy of the fluid is consumed.

It was found that, as expected, the rotor of the four-blade wind turbines has a higher torque compared to the rotor of the two or three blades

## REFERENCES

- [1] Bose, S.R., Chandramouli, S., Premasai, T.P., Prithviraj, P., Vivek, M., Kishore, V.R. (2014). Numerical analysis of effect of pitch angle on a small-scale vertical axis wind turbine. *International Journal of Renewable Energy Research*, 4(4), 929-935.
- [2] Guțu, M. (2017). *Optimizing the resistance structure of aerodynamic blades for wind turbines*. Doctoral thesis, Chisinau, Moldova.
- [3] Bychkov, N.M., Dovgal, A.V., Kozlov, V.V. (2007). Magnus wind turbines as an alternative to the blade ones, *J. Phys.: Conf. Ser.* 75 012004
- [4] Hameed, M.S., Afaq, S.K. (2013). Design and analysis of a straight bladed vertical axis wind turbine blade using analytical and numerical techniques, *Ocean Engineering*, 57, 248–255.
- [5] Jang, H., Paek, I., Kim, S., Jeong, D. (2019). Performance prediction and validation of a small-capacity twisted Savonius wind turbine, *Energies*, 12,17-21.
- [6] Mara, B.K., Mercado, B.C., Mercado, L.A., Pascual, J.M., Lopez, N.S. (2014). Development and validation of a CFD model using ANSYS CFX for aerodynamics simulation of Magnus wind rotor blades, *Proceedings of 7th International Conference Humanoid, Nanotechnology, Information Technology Communication and Control, Environment and Management (HNICEM), Palawan, Philippines*.
- [7] Nigam, P.K., Tenguria, N., Pradhan, M.K. (2017). Analysis of horizontal axis wind turbine blade using CFD, *International Journal of Engineering, Science and Technology*, 9 (2), 46-60.
- [8] Paulsen, U.S., Madsen, H.A., Hattel, J.H., Baran, I., Nielsen, P.H. (2013). Design optimization of a 5 MW floating offshore vertical-axis wind turbine, *Energy Procedia*, 35, 22-32.
- [9] Rogowski, K., Maronski, R., Piechna, J. (2015). Numerical analysis of a small-size vertical-axis wind turbine performance and averaged flow parameters around the rotor, *Archive of mechanical engineering, LXIV (2)*, 205-218.
- [10] Tudor, C.I. (2015). *Research regarding the implementation, adaptation and functioning of the wind turbines for small consumers*, Doctoral thesis, Brasov, Romania.
- [11] Wenehenubun, F., Saputra, A., Sutanto, H. (2015). An experimental study on the performance of Savonius wind turbines related with the number of blades, *Energy Procedia*, 68, 297–304;
- [12] Wußow, S., Sitzki, L., Hahm, T. (2007). 3D-simulation of the turbulent wake behind a wind turbine, *Journal of Physics Conference Series*, 75 (1), 012033.

# OPTIMAL ANALYSIS OF FARM AGRICULTURAL MACHINERY EQUIPMENT BASED ON MATHEMATICAL MODELLING

## 基于数学模型的农业机械设备优化分析

As. PhD. Eng. Zefeng Zhang

School of Mathematics and Computer Science, Xinyang Vocational and Technical College, Xinyang, 464000 / China

\*Tel: 13550255635; E-mail: xomnpx@163.com

DOI: <https://doi.org/10.35633/inmateh-62-35>

**Keywords:** *mathematical modelling, linear programming, agricultural machinery, optimization, equipment*

### ABSTRACT

*With the development of science and technology, the degree of agricultural mechanization is getting higher and higher. Agricultural machinery is an important support for the development of agricultural modernization. Optimizing the allocation of agricultural machinery is conducive to improving agricultural production efficiency and economic benefits. In this paper, mathematical modelling method is mainly used in the analysis and optimization of agricultural machinery configuration. By determining the objective function and constraint equation, combined with the actual situation of Xinjiang Production and Construction Corps, the linear programming model and workload model of agricultural machinery and equipment optimization are established. Finally, the actual number of agricultural machinery and equipment and the number of optimal allocations of Xinjiang Production and Construction Corps farm were compared. The effectiveness of the optimization model is verified by comparing the optimized agricultural machinery equipment with the actual equipment. The results show that the optimized equipment model has good optimization effect. On the basis of reducing the number of agricultural machinery and equipment, the matching rate of agricultural machinery is improved, and the operation cost of agricultural machinery is effectively reduced. It is hoped that this study can provide certain reference and reference for the optimization analysis of agricultural machinery and equipment based on mathematical modelling.*

### 摘要

随着科学技术的发展，农业机械化程度越来越高，是农业现代化发展的重要支撑。优化农机配置，有利于提高农业生产效率和经济效益。本文在分析和优化农机具配置时，主要采用数学建模方法。通过确定目标函数和约束方程，结合新疆生产建设兵团的实际情况，建立了农机设备优化的线性规划模型和工作量模型，最后对新疆某生产建设兵团农场的实际农机设备数量与优化配置数量进行了比较。并将优化后的农机设备与实际设备的对比结果，验证了农机设备优化模型的有效性。研究表明，优化后的设备模型具有良好的优化效果，在减少农机设备数量的基础上提高了农机具的匹配率，有效降低了农机作业成本。希望本研究能为基于数学建模的农机设备优化分析提供一定的参考和参考。

### INTRODUCTION

Agriculture is the basis for human survival, an important guarantee for human food and clothing, and it plays an important role in economic prosperity and social stability. With the development of science and technology, the degree of agricultural mechanization is getting higher and higher, which is an important support for the development of agricultural modernization. Agricultural mechanization is conducive to ensuring long-lasting, efficient and high-quality agricultural operations. It can also resist natural disasters to a certain extent, liberate rural farm labour productivity, and further increase farmers' income (Rangkuti A.R., Saleh A., 2011). The reasons for the unreasonable farm machinery and equipment deployment include two aspects. On the one hand, there is a lack of a scientific plan for farm machinery and equipment. On the other hand, it is the pursuit of the quantity and performance of agricultural machinery, regardless of whether the equipment is reasonable (Li Y.B., Li H. and Guo X., 2020). In this case, the existing agricultural machinery and equipment supporting production in Xinjiang Production and Construction Corps are more complex, and the types of machinery and equipment are also more complex, resulting in the waste of agricultural funds and labour (Wang B., He J., Zhang S. and Li L.L., 2020). In a certain way, the problem is transformed into a model, and the relationship between the problems is found. Therefore, this study uses mathematical

modelling to analyse the optimal allocation of farm machinery and tools in order to achieve the purpose of rationally optimizing the allocation of agricultural machinery and tools.

*Gorucu et al* analysed the proficiency of farm youths in using tractors, trucks and cars through questionnaires when they studied the farm youth's mastery of the technology used in agricultural equipment. This research provided a certain degree for young people working on the farm (*Gorucu S. and Murphy D., 2018*). When studying the situation of safety accidents on the farm, *Gorucu S. and others* mainly investigated the incidents or character characteristics of collisions with agricultural equipment, carriages, etc. recorded by the transportation department. The results show that the root cause of the farm accidents is the improper operation of equipment by farm personnel (*Gorucu S., Kassab D.M.C., 2016*). *Ceylan H. et al* conducted a series of tests when studying the impact of heavy farm implements on rigid pavement structures, including the response of rigid pavement to agricultural vehicles, and compared the response with the response of a standard semi-trailer (*Ceylan H., Wang S. and Kim S., 2015*). When studying agricultural activities in Nagaran, *Paneque R.P.* and others analysed the agricultural mechanization strategy of improved tools. This strategy mainly maximizes the economic benefits of agriculture through the improvement of agricultural equipment, indicating that agricultural mechanization is very beneficial to agricultural production (*Paneque R.P., Morejon M.Y. and Fernandes H.C., 2019*). *Mehlhorn S.A. and others* analysed the impact of a special plan on road drivers' understanding of agricultural tools when studying the problems of agricultural equipment on public roads. The program made the drivers realize the necessity of sharing public roads with farm equipment drivers through special presentations (*Mehlhorn S.A., Darroch B. and Jackson S.W., 2017*).

When studying the influence of infrared convection on potato thin layers, *Teshome F.B. et al* used mathematical modelling methods to dry potatoes at thicknesses of 3mm, 5mm, and 7mm, and infrared convection of 500W, 700W, and 900W, respectively. The results show that with the increase of infrared power and potato thickness, the sample water content and drying time are reduced (*Teshome F.B., Degu Y.M., 2019*). *Mohd T.A.T. and others* established a simulation model of an all-electric vehicle on the MATLAB simulation platform, used mathematical modelling equations to draw and discuss the corresponding simulation results, and used the torque and speed of the electric vehicle involved in the modelling process to determine its energy flow and performance (*Mohd T.A.T., Hassan M.K. and Aziz W.A., 2015*). When studying the influence of air temperature and speed on potato drying, *Naderinezhad S.* established a corresponding mathematical model of drying, and conducted drying experiments under certain conditions of temperature and wind speed. The results show that drying temperature is an important parameter that affects the drying rate of potatoes (*Naderinezhad S., Etesami N. and Poormalek Najafabady A., 2016*). When studying the activity of dehydrogenase, *Matyja K. et al* established a mathematical model based on the Lagergren's pseudo-first-order equation to describe the short-term change of dehydrogenase activity, and verified the effectiveness of the model through corresponding examples (*Matyja K., Ma A.J.A. and Mazur A.K., 2016*). When studying the evolution of brain heterogeneous modules, *Yamaguti Y. and others* used genetic algorithms to construct a mathematical model. The model included two randomly coupled functional areas. The optimization of the functional area parameters verified the effectiveness of the mathematical model (*Yamaguti Y. and Tsuda I., 2015*). *Bouزيد L. et al* established a mathematical model of AISI420 stainless steel based on the surface response method. During the model building process, a statistical simulation of the relationship between cutting parameters, cutting force components and the absolute roughness of the workpiece surface was carried out. The results show that the cutting depth affects the stainless steel, the main factor of surface roughness (*Bouزيد L., Yallese M. A and Chaoui K. 2015*).

It can be seen that the research at home and abroad mainly involves the relevant situation of farm agricultural machinery and the application of mathematical models in various aspects. Among them, farm operations mainly include agricultural mechanization, farm tool design, etc.; mathematical models are mainly used in various aspects of industry, biomedicine, production and life (*Yan H., Cui Q. and Liu Z., 2020*). The related researches are less concerned with the application of mathematical models in the analysis of the optimization of agricultural machinery and equipment. Therefore, this study analyses the optimization of the farm agricultural machinery and equipment based on the mathematical model.

## **MATERIALS AND METHODS**

### **Linear programming analysis and optimization of farm machinery**

In the management of agricultural mechanization, the most important and fundamental task is to rationally configure farm machinery and implements to achieve the highest economic benefits at the least cost. The deployment of farm machinery and equipment needs to be based on the actual situation of local

agronomy, taking full account of economic and technological development, and following certain principles. The main principles include the principle of existing models, economic principles, reasonable equipment, agronomy and agricultural machinery. Combining the principles and the principle of one machine with multiple purposes, this study mainly used mathematical modelling to conduct research and analysis when studying the problems of farm machinery and equipment deployment, and combined linear programming and workload methods to the farms of the Xinjiang Production and Construction Corps. Among them, the linear programming model mainly includes the objective function and the constraint equation. The constraint equation is mainly composed of agricultural capacity constraints, operating capacity constraints, tractor reserve constraints and variable non-negative constraints. The steps of establishing a linear programming model mainly include the following aspects: first, the objective function is determined. The objective function of the linear programming in this study is the cost of agricultural operations, and that must be minimized. The objective function is constructed as shown in the formula (1).

$$S_{\min} = C_f + C_v \quad (1)$$

In the formula (1),  $S_{\min}$  is the minimum value of the function  $S$  of the cost of the farm operations;  $C_f$  is the fixed cost of farm machinery operations throughout the year;  $C_v$  is the variable cost of farm machinery operations throughout the year. The fixed fee can be expressed as follows:

$$C_f = \sum (a_i X_i + b_j X_j) \quad (2)$$

where  $i$  represents the serial number of the tractor in the farm;  $j$  represents the serial number of the farm tool; the tractors and farm tools in the farm are numbered to facilitate the later research work;  $a_i$  represents the fixed cost of the  $i$  type tractor operation for the whole year, Yuan/unit;  $b_j$  is the  $i$  type agricultural tool operation the fixed cost required for the whole year;  $X_i$  is the number of tractors equipped throughout the year. The variable costs of farm machinery operations throughout the year can be expressed as equation (3).

$$C_v = \sum C_{mn} W_{mn} X_{mn} \quad (3)$$

where  $m$  represents the serial number of agricultural machinery operations;  $n$  represents the number of units that complete the first operation of the farm,  $C_{mn}$  represents the variable cost of the  $n$  type farm operation tools when carrying out the farm operation  $m$ , Yuan/mu (1 mu = 666.66 square meters, 1 RMB = 0.1530 USD);  $W_{mn}$  represents the productivity of the  $n$  type farm operation tool when performing the  $m$  item farm operation, mu/unit shift;  $X_{mn}$  represents the  $n$  type farm operation tool when performing the  $m$  item farm operation number of machine shifts. Then, after the objective function is determined, the constraint equation is determined, and the workload constraint can be expressed as follows:

$$\sum W_{mn} X_{mn} \geq A_m \quad (4)$$

where:  $A_m$  represents the area of operation required to complete the  $m$  operation in farm operations, acres.

The constraint conditions of the equipped amount of the tractor can be expressed as follows.

$$\sum X_{im} \leq T_m M_{im} X_i \quad (5)$$

where:  $X_{im}$  represents the number of  $i$  class tractor shifts required to complete the  $m$  operation,  $T_m$  represents the probability of the tractor's available ground time in the  $m$  farm operation stage;  $M_{im}$  represents the  $m$  operation completed.  $X_i$  is the number of the  $i$  type tractor equipped. The constraint amount of farm implements can be expressed as follows:

$$\sum X_{jm} \leq T_m M_{jm} X_j \quad (6)$$

where  $T_m$  represents the probability of the agricultural machinery being able to land on the  $m$  farm operation stage;  $X_{jm}$  is the number of the  $j$  farm implement shifts required to complete the  $m$  farm operation, and  $X_j$  represents the number of farm agricultural equipment equipped,  $M_{jm}$  is the largest farm operation shift to complete the  $m$  operation.

The corresponding workload model can be established as follows.

$$n_{rm} = \frac{U_{rm}}{D_m \alpha_m W_{rm}} \quad (7)$$

where the agricultural machinery serial number is indicated by  $r$ ;  $n_{rm}$  is the number of  $r$  type agricultural machinery required to complete the  $m$  farm operation;  $U_{rm}$  is the area of the  $r$  farm operation required to complete the  $m$  agricultural machinery, and  $D_m$  is the phase  $m$  farm operation;  $\alpha_m$  is the operable shift per day when the  $m$  operation is performed, and  $W_{rm}$  is the productivity of each shift of the  $r$ -type agricultural machinery when the  $m$  farm operation is completed.

### Optimal equipment of farm machinery in Xinjiang Production and Construction Corps farm

Aiming at the problem of optimal allocation of agricultural machinery and equipment, the optimization of agricultural machinery and equipment of Xinjiang production and Construction Corps was studied as an example. Xinjiang production and Construction Corps has some differences in climate conditions, natural environment, crop planting conditions, agricultural machinery and equipment conditions. In this study, the status of agricultural planting and agricultural machinery and equipment of Xinjiang production and Construction Corps is taken as the research object. The main food crops of Xinjiang production and Construction Corps are corn, wheat, cotton, tomato and pepper. At the same time, it has a high degree of agricultural mechanization and agricultural machinery equipment. The deployment of Xinjiang production and Construction Corps is also at the forefront.

According to the existing tractor types of Xinjiang production and Construction Corps, combined with the safety, efficiency, reliability and agronomic adaptability of agricultural machinery operation, two models were selected, namely High-power Tractor Dongfanhong lx2204 and medium horsepower tractor John Deere Jd5-750, taking cotton, corn and tomato as the main research objects, established the corresponding optimization model of agricultural machinery and equipment. The planting process of Xinjiang production and construction corps farm is shown in Table 1. It can be seen from the table that the business items include whole tomato field, cotton field and corn field, tomato planting, cotton planting, corn planting and weeding. The operation area of tomato field is 10000 mu, cotton field is 64340 mu, and corn field is 20000 mu.

**Table 1**

**Xinjiang production and construction corps farm annual agricultural machinery operation process**

Farm project	Operating area (mu)	Production unit shift productivity (mu/shift)	
		LX2204	JD5-750
Turn the tomato field	10000	400	400
Turn the cotton field	64340	210	260
Turn the cornfield	20000	130	130
Tomato sowing	10000	400	400
Cotton sowing	64340	210	260
Corn sowing	20000	130	130
Tomato field weeding	10000	400	400
Cotton field weeding	64340	210	260
Cornfield weeding	20000	130	130

The amount of farm machinery equipment includes the following variables,  $X_1$  is the number of LX2204 tractors;  $X_2$  is the number of JD5-750 tractors;  $X_3$  is the number of sprayers;  $X_4$  is the number of combined soil preparation machines;  $X_5$  is the number of cotton seeders;  $X_6$  is the number of tomato planters;  $X_7$  is the number of tillage and fertilization machines;  $X_8$  is the number of ploughs;  $X_9$  is the cotton stalk returning machine. The number of shifts of the John Deere JD5-750 tractor group includes the following variables:  $X_{10}$  is the number of shifts for removing weeds in tomato fields;  $X_{11}$  is the number of shifts for removing weeds in cotton fields;  $X_{12}$  is the number of shifts for removing weeds in corn fields;  $X_{13}$  is the number of shifts for sowing tomatoes;  $X_{14}$  is the amount of cotton planted;  $X_{15}$  is the number of machine shifts for planting corn;  $X_{16}$  is the number of machine shifts for whole tomato fields;  $X_{17}$  is the number of machine shifts for whole cotton field;  $X_{18}$  is the number of machine shifts for whole corn field. The number of shifts of Dongfanhong LLX2204 tractor group includes the following variables:  $X_{19}$  is the number of tractors in the whole tomato field;

$X_{20}$  is the number of tractors in the whole cotton field;  $X_{21}$  is the number of tractors in the whole corn field;  $X_{22}$  is the number of tractors in the tomato field;  $X_{23}$  is the shift number of cotton field tractors;  $X_{24}$  is the number of tractor tool benches in the corn field;  $X_{25}$  is the number of tractors in the weeding field;  $X_{26}$  is the number of tractor tool benches in the weeding field;  $X_{27}$  is the number of tractor shifts in the corn field. After the determination of the variables is completed, the constraint equation containing the variables is established. The constraint equation for the whole tomato field is shown in the following formula:

$$400X_{16} + 400X_{19} \geq 10000 \quad (8)$$

The constraint equation of the whole cotton field is expressed as follows.

$$260X_{17} + 210X_{20} \geq 64340 \quad (9)$$

The constraint equation of the whole corn field is expressed as follows.

$$130X_{18} + 130X_{21} \geq 20000 \quad (10)$$

The constraint equation for tomato planting fields is expressed as follows.

$$400X_{13} + 400X_{22} \geq 10000 \quad (11)$$

The constraint equation of cotton planting field is expressed as follows.

$$260X_{23} + 210X_{14} \geq 64340 \quad (12)$$

The constraint equation for sowing corn field is expressed as follows.

$$130X_{15} + 130X_{24} \geq 20000 \quad (13)$$

The constraint equation for weed removal in tomato field is expressed as follows.

$$400X_{10} + 400X_{25} \geq 10000 \quad (14)$$

The constraint equation for weed removal in cotton field is expressed as follows.

$$260X_{26} + 210X_{11} \geq 64340 \quad (15)$$

The constraint equation for weed removal in corn field is expressed as follows.

$$130X_{12} + 130X_{27} \geq 20000 \quad (16)$$

The constraint equations of this model include dynamic constraint equation, implement constraint equation and workload constraint equation. When carrying out the dynamic constraint, it is necessary to consider the different operation items of the same tractor in a certain period of time, that is, the sum of the teams using a certain tractor in a certain stage should not exceed the maximum number of teams provided by the function. The general agricultural tools are not universal and cannot provide multiple operations in the same operation period. Therefore, when the agricultural tools are constrained, the sum of the use teams of agricultural tools should not exceed the total team of agricultural tools. Workload constraint, that is, each team completes the required amount of work within the specified time.

Then, establish the objective equation of the farm equipment of the Corps. The operating cost of agricultural machinery mainly includes fixed costs and variable costs, which can be obtained from the expression of the above farm operating costs.

$$S_{\min} = \sum (a_i X_i + b_j X_j + C_{mn} W_{mn} X_{mn}) \quad (17)$$

The annual fixed cost of farm operations includes the annual fixed cost of power machinery and the annual fixed cost of agricultural tools. Among them, the fixed cost of agricultural machinery and tools consists of depreciation expenses, management fees of agricultural machinery and tools, and fixed capital occupancy interest. The calculation expression is as follows:

$$\text{Annual fixed fee} = \text{Agricultural machinery purchase price} \times \left( \begin{array}{l} \text{Annual depreciation rate} + \\ \text{Annual management expenses} \\ + \text{Annual capital occupancy rate} \end{array} \right) \quad (18)$$

$$\text{Annual fixed expenses after apportionment} = \text{Original fixed fee} \times \frac{\text{Annual farmland operations}}{\text{Annual total workload}}$$

In addition, the calculation expression of annual fixed cost is shown in the following formula.

$$\text{Annual fixed cost of agricultural tools} = \frac{\text{Farm tool price} - \text{Residual value}}{\text{Service life}} \quad (19)$$

According to the relevant survey of the Xinjiang Production and Construction Corps, the annual fixed occupancy rate of the Xinjiang Production and Construction Corps is 3.9%, the residual value of agricultural machinery is 10% of the purchase value, and the management fee rate of agricultural machinery is 2.4%. The useful life of most agricultural machinery is about 8 years. The fixed cost of farm machinery of the Xinjiang Production and Construction Corps can be obtained from formula (19) and formula (20) as shown in Table 2. It can be seen from the table that it mainly includes the prices and annual fixed costs of two tractors, sprayers, combined field preparation machines, cotton film planters, tomato planters, and cultivating fertilizer machines. In addition, the variable costs of farm operation units mainly include wages, fuel costs and maintenance costs.

Table 2

Name of agricultural machinery	Price/yuan	Annual fixed fee/yuan
Dongfanghong LX2204	517000	84382
John Deere JD5-750	126000	20649
Sprayer	42000	4836
Combined soil preparation machine	38000	4386
Cotton film planter	28000	3260
Tomato planter	27000	3048
Cultivator fertilizer applicator	15000	564

## RESULTS

According to the established optimization model of agricultural machinery and equipment in Xinjiang Production and Construction Corps, the corresponding optimization results of agricultural machinery and equipment are obtained. In the study of Xinjiang Production and Construction Corps equipment configuration, the main planting plants are tomato, cotton and corn, which account for 76.82% of the farm planting area of Xinjiang production and Construction Corps. Therefore, the number of general agricultural machinery and equipment needs to be divided by 0.7682 to get the number of agricultural machinery and equipment needed by Xinjiang Production and Construction Corps to grow all crops. The actual situation and optimization of agricultural machinery and equipment of Xinjiang Production and Construction Corps are shown in Table 3 and table 4.

Table 3

Name of agricultural machinery	Large tractor	Medium tractor	Sprayer	Combined soil preparation machine	Cotton planter	Tomato planter	Cultivator fertilizer applicator
Actual equipped quantity/set	186	528	120	102	148	36	123
Optimize the amount of equipment / Machine	35	51	34	35	37	16	44
Overweight/set	151	477	86	67	111	20	79
Overmatch rate/%	81.18	90.34	72	65.69	75	55.56	64.23

The comparison results of actual agricultural machinery and equipment and optimized equipment in Xinjiang production and construction corps farm are shown in Table 3. It can be seen from the table that the actual number of farm implements in Xinjiang Production and construction corps farm exceeds the number of optimized equipment. Among them, 186 large tractors are actually equipped and 35 are optimized. The actual equipment capacity exceeded the optimized equipment by 151 units, and the overstaffing rate was 81.18%. The actual capacity of medium tractors is 528, and the optimized equipment is 51. The actual equipment capacity exceeded the optimized equipment by 477, and the overstaffing rate was 90.34%. The actual number of sprayer sets is 120, the optimized equipment 34, the actual equipment 86, overshoot rate 71.67%. 65% of the actual number, and the actual number has been optimized. The actual configuration of 148 cotton machines, optimized configuration of 37 cotton machines, the actual configuration of more than 111 cotton machines, overrun rate of 75.0%. There are 36 tomato planters, 16 optimized pieces of equipment and more than 20 optimized pieces of equipment. The overstaffing rate was 55.56%. The actual configuration of the cultivator and fertilizer applicator is 123, the optimized equipment is 44, and the overweight/set is 79.

The over provision rate was 64.23%. From the optimization of the number of agricultural machinery and equipment, compared with the actual agricultural machinery and equipment, the number of optimized agricultural machinery and equipment is greatly reduced, which can effectively reduce the number of farm equipped with agricultural machinery, and then improve the matching rate of agricultural machinery and reduce the operating cost of agricultural machinery.

Table 4

Comparison of actual equipment and optimized equipment

Index	Actual equipment	Optimization Results	Growth rate/%
Power Machinery Equipped	714 units	83 units	-87.68
Agricultural machinery power	43700kW	10390kW	-76.22
Amount of farm tools	1143 units	237 units	-62.74
Annual total cost of mechanical operations	152.595 million	110.1016 million	-27.9
Operating cost per unit area	124.26 yuan/mu	89.59 yuan/mu	-27.9
Matching ratio of agricultural machinery	1:1.6	1:2.7	68.75

The comparison between the optimized agricultural machinery and the actual equipment of Xinjiang Production and Construction Corps is shown in Table 4. It can be seen from the table that the indicators include the number of power machinery, agricultural machinery power, the number of agricultural machinery equipment, the total cost of machinery operation in the whole year, the operating cost per unit area, the matching rate of agricultural machinery, etc. from the number of power machinery, the actual number of equipment is 714, and the optimized number of equipment is 83. The number of optimized equipment is 87.68% less than that of actual equipment, which indicates that the power machinery of Xinjiang Production and Construction Corps, including large and medium tractors, has a serious surplus of equipment, resulting in a serious waste of power. From the actual power of agricultural equipment, 103700kw is optimized. The optimized equipment is 76.22% less than the actual equipment. In terms of the number of agricultural equipment, the actual configuration is 1143, and the optimized configuration is 237. The number of optimized equipment is 62.74% less than that of actual equipment. From the total operating cost of mechanical equipment in the whole year, the actual operating cost is 15.2595 million yuan, and the optimized operating cost is 11.016 million yuan. The optimized equipment cost is 27.99% lower than the actual equipment cost. From the operating cost per unit area, the actual cost of the equipment is 124.26 yuan/mu, and the optimized equipment cost is 89.59 yuan/mu. The operating cost per unit area of the optimized equipment is 27.9% lower than the actual operating cost per unit area. The optimized agricultural machinery equipment increased by 68.75%. On the whole, the optimized proportion of agricultural machinery in the farm is better, and the operation cost of agricultural machinery is reduced on the basis of reducing the number of agricultural machines.

## CONCLUSIONS

The most important thing to develop agricultural mechanization is to optimize agricultural machinery and equipment. In this study, the linear programming model and workload model are used to analyse the optimal allocation of agricultural machinery in Xinjiang Production and Construction Corps. By comparing the construction workload and equipment quantity of Xinjiang production and Construction Corps in actual production, the construction workload and equipment quantity of Xinjiang Production and Construction Corps are determined, and the optimized agricultural machinery and equipment are compared with the actual agricultural machinery and equipment. The results show that the model optimizes the power machinery, agricultural machinery equipment and machinery operation cost. Xinjiang Production and Construction Corps has a serious surplus of power machinery and equipment. The overrun rate of large tractors was 81.18%, and that of medium tractors was 90.34%. The allocation of agricultural machinery is unreasonable. After optimization, the matching rate of agricultural machinery increased from 1:1.6 to 1:2.7, and the total operation cost of the equipment yard was 27.9% lower than that of the actual equipment. The optimized equipment model has good optimization effect, improves the matching rate of agricultural machinery on the basis of reducing the number of agricultural machinery equipment, and effectively reduces the cost of agricultural machinery operation. This study verified the effectiveness of the optimized equipment model for the rational allocation of agricultural machinery model, but its wide applicability needs further study.

## REFERENCES

- [1] Bouzid L., Yallese M.A, Chaoui K., (2015), Mathematical modelling for turning on AISI 420 stainless steel using surface response methodology. *Proceedings of the Institution of Mechanical Engineers Part B Journal of Engineering Manufacture*, Vol. 229, Issue 1, pp.45-61, England;
- [2] Ceylan H., Wang S., Kim S., (2015), Impact of Farm Equipment Loading on Low-Volume Concrete Road Structural Response and Performance. *The Baltic Journal of Road and Bridge Engineering*, Vol.10, Issue 4, pp.325-332, Latvia;
- [3] Gorucu S., Kassab D.M.C., (2016), Injury Risks for On-Road Farm Equipment and Horse and Buggy Crashes in PA: 2010–2013. *Traffic Injury Prevention*, Vol.18, Issue 3, pp.286-292, USA;
- [4] Gorucu S., Murphy D., (2018), Technology Use Among Youth While Operating Farm Equipment. *Journal of Agromedicine*, Vol.23, Issue 4, pp. 305-314, USA;
- [5] Li Y.B., Li H., Guo X., (2020). Online Parameter Identification of Rice Transplanter Model Based on Ipso-Ekf Algorithm. *INMATEH Agricultural Engineering*, Vol.61, Issue 2, pp.25-34, Romania;
- [6] Matyja K., Ma A.J.A., Mazur A.K., (2016), Assessment of toxicity using dehydrogenases activity and mathematical modelling. *Ecotoxicology*, Vol.25, Issue 5, pp.924-939, USA;
- [7] Mehlhorn S.A., Darroch B., Jackson S.W., (2017), Raising Awareness of Farm Equipment on Public Roadways in Tennessee. *Journal of Agricultural Safety & Health*, Vol.23, Issue 4, pp.241-246, USA;
- [8] Mohd T.A.T., Hassan M.K., Aziz W.A., (2015), Mathematical Modelling and Simulation of an Electric Vehicle. *International Journal of Mechanical Sciences*, Issue 8, pp.1312-1321, England;
- [9] Naderinezhad S., Etesami N., Poormalek Najafabady A., (2016), Mathematical modelling of drying of potato slices in a forced convective dryer based on important parameters. *Food Science & Nutrition*, Vol.4, Issue 1, pp.110-118, USA;
- [10] Paneque R.P., Morejon M.Y., Fernandes H.C., (2019), Current Situation of Agricultural Mechanization and Conservation Agriculture in Latin America. *Agricultural mechanization in Asia, Africa and Latin America*, Vol.50, Issue 2, pp.13-19, Japan;
- [11] Rangkuti P.A., Saleh A., (2011), Path Analysis Communication Model of Cooperation Organization in the Development Agricultural Mechanization (Village Unit Cooperative/Vuc Rice Milling Utilization Case in Karawang and Cianjur District West Java Province). *Business and Entrepreneurial Review*, Vol.10, No.2, pp.97-120;
- [12] Teshome F.B., Degu Y.M., (2019), Design of Combined Press Tool for the Manufacturing of Rice Thresher Blade (Case Study at Amhara Agricultural Mechanization and Food Science Research Centre-Ethiopia). *International Journal of Engineering Science*, Vol.3, Issue 4, pp.90-107, England;
- [13] Wang B., He J., Zhang S., Li L.L., (2020). Nondestructive Testing of Soluble Solids Content in *Cerasus Humilis* Using Visible / Near-Infrared Spectroscopy Coupled with Wavelength Selection Algorithm. *INMATEH Agricultural Engineering*, Vol.61, Issue 2, pp.251-262; Romania;
- [14] Yamaguti Y., Tsuda I., (2015), Mathematical modelling for evolution of heterogeneous modules in the brain. *Neural Networks*, Issue 62, pp.3-10, England;
- [15] Yan H., Cui Q., Liu Z., (2020). Pig Face Identification Based on Improved AlexNet Model. *INMATEH Agricultural Engineering*, Vol.61, Issue 2, pp.97-104, Romania.

## PARAMETER OPTIMIZATION AND EXPERIMENTAL RESEARCH ON THE HAMMER MILL

### / 锤片式粉碎机参数优化与试验研究

Di Wang, Changbin He, Haiqing Tian\*, Fei Liu, Tao Zhang, Hongqi Zhang<sup>1</sup>

Inner Mongolia Agricultural University, College of Mechanical and Electrical Engineering, Hohhot/China;

Tel: +86-0471-4309215; E-mail: [hqtian@126.com](mailto:hqtian@126.com)

DOI: <https://doi.org/10.35633/inmateh-62-36>

**Keywords:** Hammer mill, Feed, Corn grain, Grinding, Parameter optimization

#### ABSTRACT

Low productivity and high electricity consumption are considered problems of the hammer mill, which is widely used in current feed production. In this paper, the mechanical properties of corn grain ground by a hammer mill were analysed, and the key factors affecting the performance of the hammer mill were determined. The single-factor experiment and three-factor, three-level quadratic regression orthogonal experiment were carried out with the spindle speed, corn grain moisture content and number of hammers as experimental factors and the productivity and electricity consumption per ton as evaluation indexes. The results showed that the order of influence on the productivity was spindle speed > corn grain moisture content > number of hammers and that the order of influence on the electricity consumption per ton was corn grain moisture content > spindle speed > number of hammers. The parameters were optimized based on the response surface method with the following results: the spindle speed was 4306 r/min, the corn grain moisture content was 10%, and the number of hammers was 24. The validation experiment was carried out with the optimal parameters' combination. The productivity and electricity consumption per ton were 988.12 kg/h and 5.37 kWh/t, respectively, which were consistent with the predicted results of the model.

#### 摘要

针对目前生产中普遍使用的锤片式粉碎机存在生产率低、能耗高的问题。对锤片式粉碎机粉碎玉米颗粒力学特性进行分析，确定了影响锤片式粉碎机性能的关键因素。为确定锤片式粉碎机最佳工作参数组合，以主轴转速、玉米颗粒含水率、锤片数量为试验因素，以生产率和吨料电耗为评价指标，开展了单因素试验和三因素三水平二次回归正交试验。结果表明，影响生产率的主次因素为：主轴转速>玉米颗粒含水率>锤片数量；影响吨料电耗的主次因素为：玉米颗粒含水率>主轴转速>锤片数量。基于响应面法进行参数优化，优化结果为：主轴转速为 4306 r/min，玉米颗粒含水率为 10%，锤片数量为 24。以优化后参数组合进行试验验证，结果为：生产率和吨料电耗分别为 988.12 kg/h，5.37 kWh/t，与模型预测结果一致。

#### INTRODUCTION

Feed grinding can increase the surface area of feed and improve its palatability and digestibility for livestock. Therefore, a large amount of feed needs to be ground every year (Mugabi et al., 2017; Xie., 2016; Barnwal et al., 2015). The hammer mill is a widely used piece of equipment in feed processing, and it has the advantages of low price, simple structure and easy operation (Chen et al., 2017; Wang. et al, 2013; Liu et al., 2011). However, there are still some problems, such as low productivity and high energy consumption with the hammer mill (Li et al., 2019; Cao et al., 2016).

In recent years, research on the hammer mill by scholars at home and abroad has mainly focused on the structural improvement and application experiments of the main parts, including the hammer, the shape of grinding chamber, the structure of rotor, etc. Xu Wei et al., (2021), took the minimum deformation of the hammer as the optimization objective and used the response surface method and genetic algorithm to optimize the structure parameters of the hammer. Bochat et al., (2015), designed a new hammer and performed comparative experiments. The results showed that the new hammer was more efficient than the traditional hammer. Moiceanu et al., (2019), used the finite element method to analyse the rotor of the

<sup>1</sup> Di Wang, Ph.D. Stud. Eng.; Changbin He, Lec. Ph.D. Eng.; Haiqing Tian, Prof. Ph.D. Eng.; Fei Liu, As. Prof. Ph.D. Eng.; Tao Zhang, Lec. Ph.D. Eng.; Hongqi Zhang, Prof. Ph.D. Eng.

hammer mill and obtained some mechanical data on the hammer mill. Zhang Yongjie et al., (2019), used ANSYS Workbench software to carry out static calculation and modal analysis of hammer frame plate and carried out topology optimization design for the hammer frame plate according to the analysis results.

In this paper, considering the existing problems with the hammer mill, the mechanical properties of corn grain grinding were analysed, and the key factors affecting the performance of the hammer mill were determined. The orthogonal experiment and response surface method were used to optimize the working parameters of the hammer mill, and the optimal parameters combination was determined. The research results can provide a reference for the optimal design of the hammer mill.

## MATERIALS AND METHODS

### • Experiment materials and equipment

Corn grain was selected as the experiment material, and the variety of corn used was XIANYU-355. The experimental equipment included a frequency converter, a tachometer, a grain moisture meter, an electronic scale (accuracy of 0.01 kg), an electric energy meter and a stopwatch.

### • Overall structure and working principle

The hammer mill used in this study is mainly composed of an outlet, a frame, a motor (3 kW), a feeding hopper, a sieve (sieve hole diameter is 3 mm), and a hammer. The structure diagram of the hammer mill is shown in Fig. 1. When the hammer mill is working, the feed enters the grinding chamber through the feeding hopper. It is first ground by the hammer and then further ground by the impact between the feed and sieve. When the feed grain size is smaller than the sieve hole diameter, the feed is discharged from the outlet.

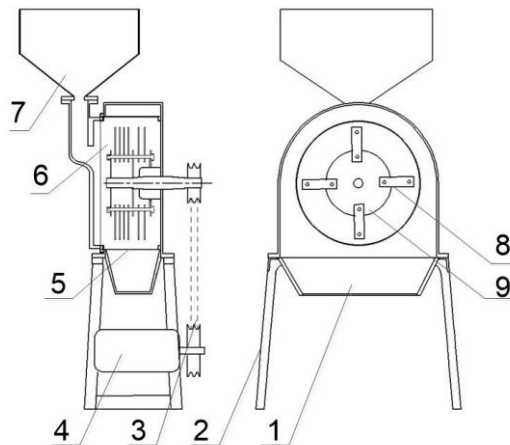


Fig. 1 – Structure diagram of the hammer mill

1 – Outlet; 2 – Frame; 3 – V-belt; 4 – Motor; 5 – Sieve; 6 – Grinding chamber; 7 – Feeding hopper; 8 – Hammer; 9 – Hammer plate

### • Mechanical properties analysis of corn grain

After entering the grinding chamber, the corn grain was hit by the hammer, as shown in Fig. 2. According to impulse theorem and momentum theorem (Zhang, 2009), the following formula can be obtained:

$$m_1 v_1 + m_2 v_2 = (m_1 + m_2) v_3 \quad (1)$$

$$I = m_2 v_3 = F \Delta t \quad (2)$$

$$v_1 = \frac{\pi n R}{30} \quad (3)$$

$$v_3 = \frac{\pi m_1 R}{30(m_1 + m_2)} \quad (4)$$

According to formula 1-4, the hitting force of corn grain was obtained as shown in formula 5 (Because  $v_2$  is very small relative to the velocity of hammer, in this paper,  $v_2=0$ ).

$$F = \frac{\pi m_1 m_2 R}{30(m_1 + m_2) \Delta t} \quad (5)$$

Where:

- $v_1$  is the linear velocity of the hammer, [m/s];
- $v_2$  - the velocity of corn grain before being hit, [m/s];
- $v_3$  - the velocity of corn grain after being hit, [m/s];
- $m_1$  - the mass of the hammer, [kg];
- $m_2$  - the mass of the corn grain, [kg];
- $n$  - spindle speed, [r/min];
- $R$  - the rotor radius, [m];
- $I$  - the impulse of hammer and corn grain, [N·s];
- $\Delta t$  - the hitting time of corn grain, [s];
- $F$  - the hitting force of corn grain, [N].

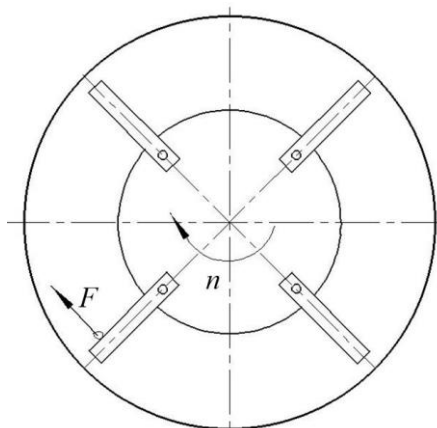


Fig. 2 – Schematic diagram of hitting force of corn grain by the hammer

An analysis of formula (5) shows that as the spindle speed increases, the hitting force on the corn grain increases. When the hitting time of corn grain is shorter, the hitting force is greater. The hitting time of the hammers on the corn grain is related to the hardness of the corn grain. The hitting time is shorter when the hardness of corn grain is greater. The hardness of the corn grain is related to the moisture content; the hardness of the corn grain is greater when the corn grain moisture content is lower (Feng *et al.*, 2003). In addition, the number of hammers has a greater influence on the performance of the hammer mill. The larger the number of hammers is, the greater the hitting force, and the higher the probability of corn grain being hit. However, the larger the number of hammers, the higher the power consumption (Zhang *et al.*, 2013). Therefore, the key to improving the performance of the hammer mill is to determine the optimal spindle speed, corn grain moisture content and number of hammers.

#### • Experimental design

According to the above analysis results, the spindle speed, corn grain moisture content and number of hammers were selected as the experimental factors. According to the agricultural machinery design manual (China Agricultural Science and Technology Press, 2007), the range for each factor was determined as follows: the spindle speed was 3800-4600 r/min, the corn grain moisture content was 10-18 %, and the number of hammers was 20-28. Each group of experiments is repeated three times, and the average value is taken.

#### • Performance evaluation of the hammer mill

According to the Chinese national standard (GB/T 6971-2007), the productivity and electricity consumption per ton were taken as the performance evaluation indexes. The calculation formulas are given by formulas (6) and (7) (China National Standardization Committee, 2007).

$$E_c = \frac{Q_c}{T_c} \quad (6)$$

$$G = \frac{G_n}{Q_c / 1000} \quad (7)$$

Where:

$E_c$  is the productivity of the hammer mill, kg/h;

$Q_c$  - the mass of the fragmented experiment sample, kg;

$T_c$  - the duration of grinding of a single experiment sample, h;

$G$  - the electricity consumption per ton of the hammer mill, kWh/t;

$G_n$  - the electricity consumption during grinding of a single experiment sample, kWh.

**RESULTS**

• **Single-factor experiment results and analysis**

*Effect of spindle speed on the performance of the hammer mill*

The corn grain moisture content was set at 14%; the number of hammers was 24; and the spindle speed was adjusted to 3800, 4000, 4200, 4400 and 4600 r/min. The relationship between the spindle speed and productivity and electricity consumption per ton is shown in Fig. 3.

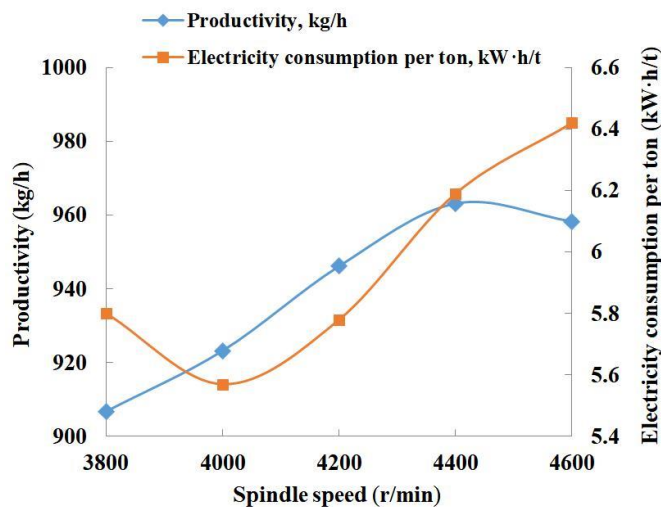


Fig. 3 – Effect of spindle speed on the machine performance

It can be seen from Fig. 3 that when the spindle speed was 3800-4600 r/min, the productivity increased first and then decreased with the increase in spindle speed, and the electricity consumption per ton decreased first and then increased with the increase in spindle speed. When the spindle speed was 4000-4400 r/min, the productivity was high, and the electricity consumption per ton was low, which was the best spindle speed range for the hammer mill.

*Effect of corn grain moisture content on the performance of the hammer mill*

The spindle speed was set at 4200 r/min; the number of hammers was 24; and the corn grain moisture content was adjusted to 10, 12, 14, 16 and 18 %. The relationship between the corn grain moisture content and productivity and electricity consumption per ton was obtained, as shown in Fig. 4.

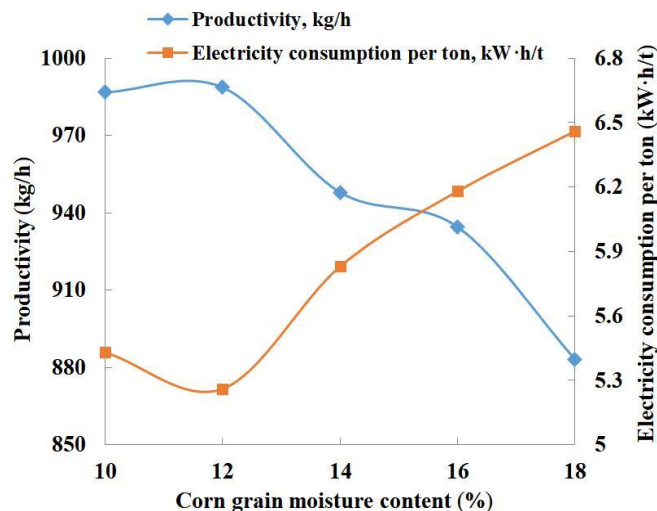


Fig. 4 – Effect of corn grain moisture content on the machine performance

As shown in Fig. 4, when the corn grain moisture content was 10-12 %, the productivity increased slowly with the increase in the corn grain moisture content, and the electricity consumption per ton decreased with the increase in the corn grain moisture content. When the corn grain moisture content was 12-18%, the productivity decreased with the increase in the corn grain moisture content, and the electricity consumption per ton increased with the increase in the corn grain moisture content.

It can be concluded that when the corn grain moisture content was 10-14%, the comprehensive performance of the hammer mill was the best.

#### Effect of number of hammers on the performance of the hammer mill

The spindle speed was set at 4200 r/min; the corn grain moisture content was 14%; and the number of hammers was adjusted to 20, 22, 24, 26 and 28. The relationship between number of hammers and productivity and electricity consumption per ton was obtained, as shown in Fig. 5.

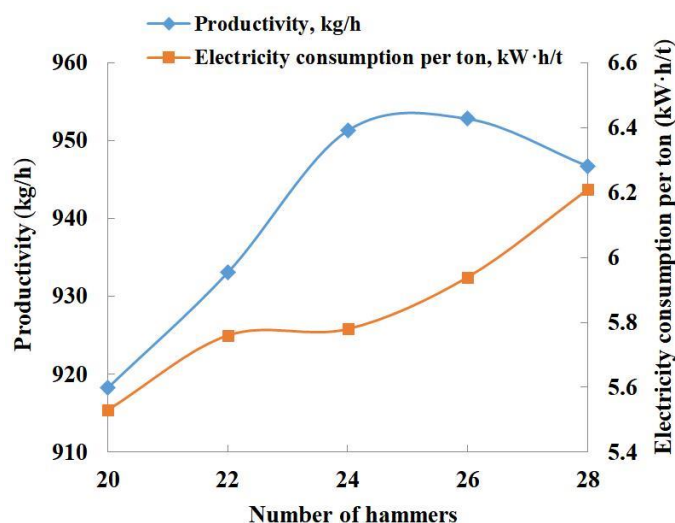


Fig. 5 – Effect of number of hammers on the machine performance

As shown in Fig. 5, the productivity increased first and then decreased slowly with the increase in the number of hammers, and the electricity consumption per ton increased gradually with the increase in the number of hammers. It can be concluded that when the number of hammers was 22-26, the comprehensive performance of the hammer mill was the best.

#### • Orthogonal experiment results and analysis

In order to obtain the optimal working parameters combination of the hammer mill, three-factor, three-level quadratic regression orthogonal experiment were carried out based on the Box-Behnken experimental method (Du et al., 2019).

According to the single-factor experiment results, the level of each factor was determined as shown in Table 1.

Table 1

Experimental factors and levels			
Levels	Spindle speed	Corn grain moisture content	Number of hammers
	A	B	C
	[r/min]	[%]	[-]
-1	4000	10	22
0	4200	12	24
1	4400	14	26

The experiment results are shown in Table 2.

Table 2

The experiment results					
Test number	Spindle speed A	Corn grain moisture content B	Number of hammers C	Productivity	Electricity consumption per ton
	[r/min]	[%]	[-]	[kg/h]	[kWh/t]
1	-1	0	-1	932.63	5.6
2	0	1	-1	928.66	5.86
3	0	0	0	974.49	5.36
4	1	0	-1	977.86	5.8
5	0	0	0	987.97	5.25
6	1	-1	0	1018.18	5.52
7	-1	0	1	953.74	5.76
8	-1	-1	0	949.26	5.25
9	1	0	1	997.42	6.26
10	1	1	0	956.58	6.21
11	0	0	0	977.75	5.34
12	0	0	0	981.17	5.29
13	0	-1	1	976.3	5.76
14	0	0	0	982.31	5.22
15	-1	1	0	923.4	5.69
16	0	1	1	936.52	5.97
17	0	-1	-1	972.44	5.2

#### • Analysis of productivity

##### Variance analysis of productivity

Variance analysis of productivity was performed with Design-Expert 10 software, and the results are shown in Table 3. It can be concluded that the regression model was extremely significant, and the lack of fit was not significant. The regression model of productivity was established as shown in formula 8, and the fit coefficient ( $R^2$ ) was 0.9788. The order of influence on the productivity was spindle speed  $A >$  corn grain moisture content  $B >$  number of hammers  $C$ .

$$E_c = 980.74 + 23.88A - 21.38B + 6.55C - 8.93AB - 0.39AC + 1.00BC - 3.48A^2 - 15.41B^2 - 11.85C^2 \quad (8)$$

where:  $A$  is the spindle speed, r/min;  $B$  is the corn grain moisture content, %; and  $C$  is the number of hammers.

Variance analysis results of productivity

Table 3

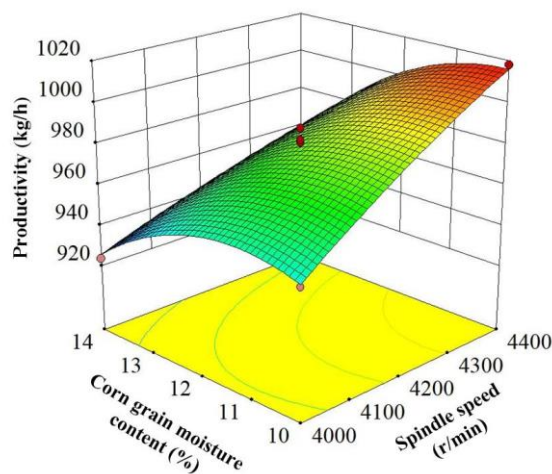
Source	Squares	DF	MS	F Value	P Value
Model	10665.47	9	1185.05	35.86	< 0.0001**
A	4560.60	1	4560.60	138.00	< 0.0001**
B	3655.98	1	3655.98	110.63	< 0.0001**
C	343.09	1	343.09	10.38	0.0146*
AB	319.34	1	319.34	9.66	0.0171*
AC	0.60	1	0.60	0.02	0.8966
BC	4.00	1	4.00	0.12	0.7381
A <sup>2</sup>	50.85	1	50.85	1.54	0.2548
B <sup>2</sup>	999.57	1	999.57	30.25	0.009**
C <sup>2</sup>	591.28	1	591.28	17.89	0.0039**
Lack of Fit	128.41	3	42.80	1.66	0.3104
Pure Error	102.93	4	25.73		
Cor Total	10896.81				

Note:  $P < 0.01$  (extremely significant, \*\*),  $P < 0.05$  (significant, \*).

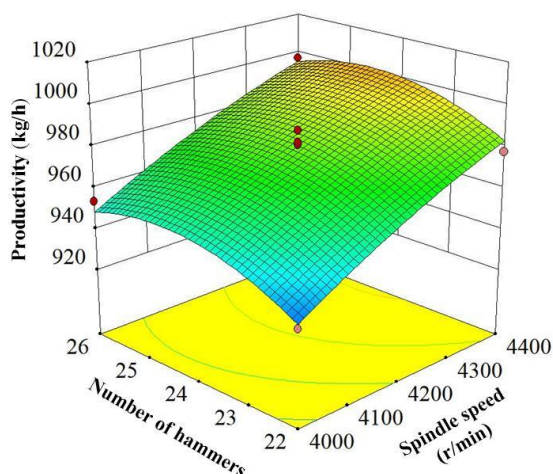
### Response surface analysis of productivity

The response surface of spindle speed, corn grain moisture content and number of hammers to productivity is shown in Fig. 6. When the number of hammers was 24, the productivity increased with the increase in the spindle speed and decreased with the increase in the corn grain moisture content. When the corn grain moisture content was 12%, the productivity increased with the increase in the number of hammers and spindle speed. When the spindle speed was 4200 r/min, the productivity decreased with the increase in the corn grain moisture content and increased with the increase in the number of hammers.

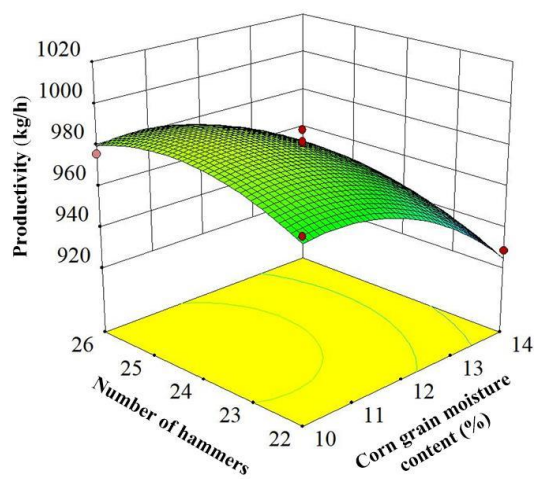
The overall influence trend of the experimental factors on productivity was as follows: the spindle speed was high, the number of hammers was large, and the corn grain moisture content was low, thereby increasing the productivity. The main reasons are as follows: when the spindle speed was high, the hitting force of the hammers on the corn grain was great, and the grinding efficiency increased. When the corn grain moisture content was low, the brittleness of the corn grain was greater, the hitting time of the corn grain was shorter and the corn grain was easily ground. When the number of hammers was large, the hitting force was great, and the probability of the corn grain being hit was high, thereby increasing the productivity.



a.  $E_c(A, B, 24)$



b.  $E_c(A, 14, C)$



c.  $E_c(4200, B, C)$

Fig. 6 – Response surface of various factors on productivity

### • Analysis of electricity consumption per ton

#### Variance analysis of electricity consumption per ton

The results of the variance analysis of electricity consumption per ton are shown in Table 4. The regression model of electricity consumption per ton was established as shown in formula 9, and the fit coefficient ( $R^2$ ) was 0.9875. From Table 4, we can see that the regression model was extremely significant, and the lack of fit was not significant. The order of influence on the electricity consumption per ton was corn grain moisture content  $B >$  spindle speed  $A >$  number of hammers  $C$ .

$$G = 5.29 + 0.19A + 0.25B + 0.16C + 0.063AB + 0.075AC - 0.11BC + 0.27A^2 + 0.11B^2 + 0.30C^2 \quad (9)$$

where:  $A$  is the spindle speed, r/min;  $B$  - the corn grain moisture content, %; and  $C$  - the number of hammers.

Variance analysis results of electricity consumption per ton

Table 4

Source	Squares	DF	MS	F Value	P Value
Model	1.86	9	0.21	61.28	< 0.0001**
A	0.28	1	0.28	82.12	< 0.0001**
B	0.50	1	0.50	147.96	< 0.0001**
C	0.21	1	0.21	61.56	0.0001**
AB	0.016	1	0.016	4.62	0.0686
AC	0.022	1	0.022	6.66	0.0365*
BC	0.051	1	0.051	14.98	0.0061**
A <sup>2</sup>	0.30	1	0.30	88.49	< 0.0001**
B <sup>2</sup>	0.050	1	0.050	14.80	0.0063**
C <sup>2</sup>	0.37	1	0.37	109.54	< 0.0001**
Lack of Fit	0.0098	3	0.0033	0.94	0.5006
Pure Error	0.014	4	0.0035		
Cor Total	1.89	16			

Note: P < 0.01 (extremely significant, \*\*), P < 0.05 (significant, \*).

Response surface analysis of electricity consumption per ton

The response surface of spindle speed, corn grain moisture content and number of hammers to electricity consumption per ton is shown in Fig. 7.

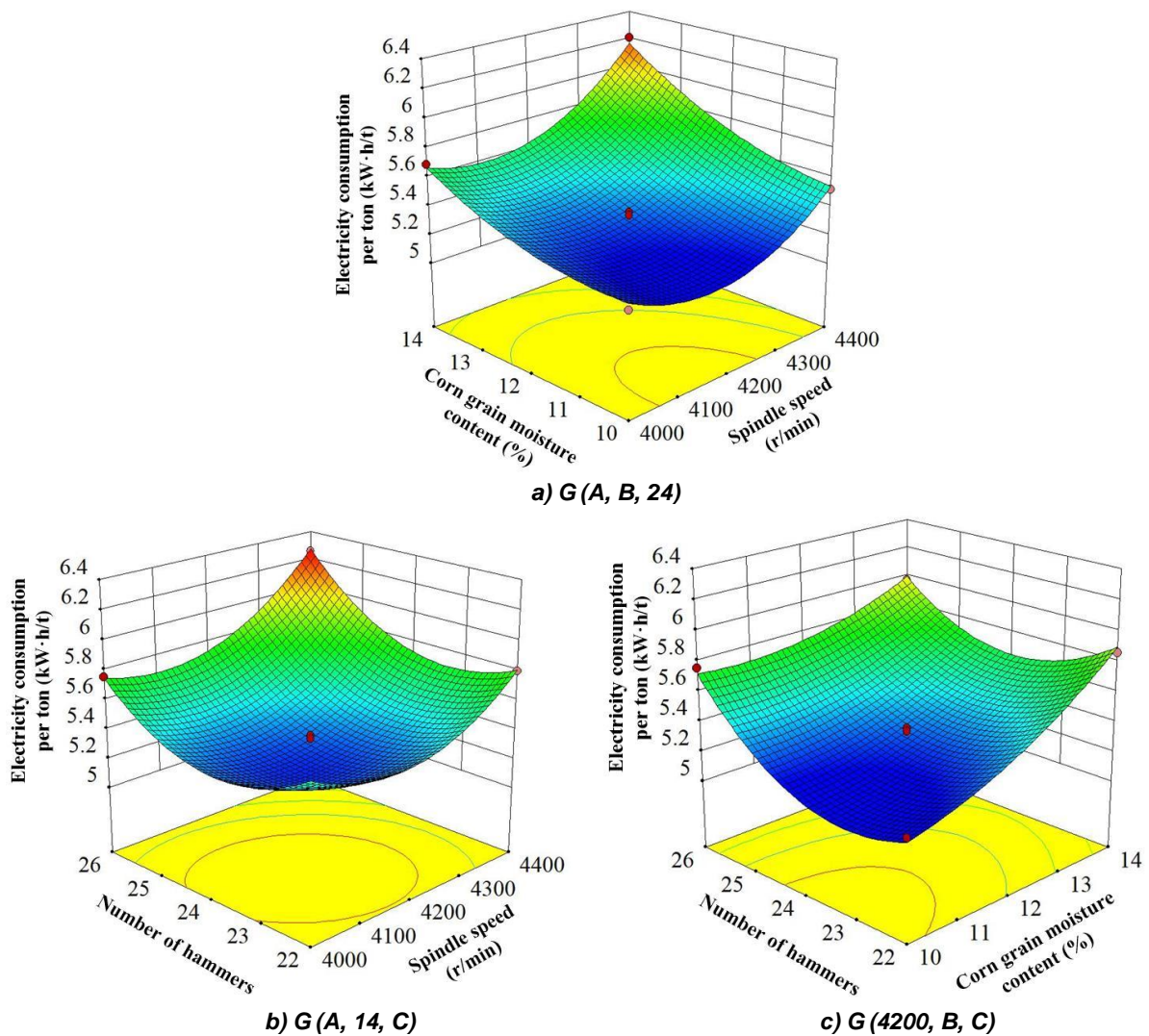


Fig. 7 – Response surface of various factors on electricity consumption per ton

When the number of hammers was 24, the electricity consumption per ton decreased first and then increased with the increase in the spindle speed and increased gradually with the increase in the corn grain moisture content. When the corn grain moisture content was 12%, the electricity consumption per ton decreased slowly first and then increased with the increase in the spindle speed and number of hammers. When the spindle speed was 4200 r/min, the electricity consumption per ton increased with the increase in the corn grain moisture content, and the electricity consumption per ton decreased first and then increased with the increase in the number of hammers.

The overall influence trend was that the electricity consumption per ton was low when the spindle speed and number of hammers were moderate and the corn grain moisture content was low. The main reasons are as follows: when the corn grain moisture content was high, the cohesion of the corn grain was large, and it was not easily ground, so it consumed more electricity. When the spindle speed was low, the hitting force was small, and the grinding efficiency decreased. When the spindle speed was high, the motor load increased, resulting in increased electricity consumption. When the number of hammers was small, the hitting force was small. When the number of hammers was large, the mass of the rotor increased, and the moment of inertia increased, thus increasing the electricity consumption per ton.

#### • Parameter optimization and validation

To obtain the best working parameters of the hammer mill, the maximum productivity and the minimum electricity consumption per ton were taken as the optimization objectives, and the optimization module in Design-Expert software was used to solve the optimal parameters. The objective function and constraint conditions are shown in formula 10:

$$\begin{cases} \text{Max}E_c \\ \text{Min}G \\ A \in [4000 - 4400\text{r} / \text{min}] \\ B \in [10 - 14\%] \\ C \in [22 - 26] \end{cases} \quad (10)$$

After optimization calculation, the optimal working parameters were obtained as follows: the spindle speed was 4306 r/min, the corn grain moisture content was 10% and the number of hammers was 24.

The predicted value of the productivity and electricity consumption per ton were 1000.94 kg/h and 5.23 kWh/t, respectively.

The validation experiment was carried out with the above optimization parameters. The results were as follows: the productivity was 988.12 kg/h, and the electricity consumption per ton was 5.37 kWh/t, which were consistent with the prediction results of the model, and the prediction errors were less than 3%.

## CONCLUSIONS

1. Based on the mechanical properties' analysis of corn grain grinding, the hitting force formula of corn grain was obtained, and the key factors affecting the performance of the hammer mill were determined as follows: spindle speed, corn grain moisture content and number of hammers.

2. The variance analysis showed that the order of influence on the productivity was spindle speed > corn grain moisture content > number of hammers, and that the order of the influence on the electricity consumption per ton was corn grain moisture content > spindle speed > number of hammers.

3. Taking maximum productivity and minimum electricity consumption per ton as optimization objectives, the optimal working parameters were obtained as follows: the spindle speed was 4306 r/min, the corn grain moisture content was 10% and the number of hammers was 24. The predicted value of productivity was 1000.94 kg/h, and the electricity consumption per ton was 5.23 kWh/t. The validation experiment results showed that the productivity was 988.12 kg/h and the electricity consumption per ton was 5.37 kWh/t, which were consistent with the prediction results of the model.

## ACKNOWLEDGEMENTS

This research was funded by the National Natural Science Foundation of China (51765055), the Inner Mongolia Special Project for Transformation of Scientific and Technological Achievement (2019CG034), and the Inner Mongolia Natural Science Foundation (2017MS0537).

## REFERENCES

- [1] Barnwal, P., Singh, K. K., Sharma, A. et al. (2015). Influence of pin and hammer mill on grinding characteristics, thermal and antioxidant properties of coriander powder. *Journal of Food Science and Technology*, 52(12), 7783-7794. <https://doi.org/10.1007/s13197-015-1975-0>
- [2] Bochat, A., Wesolowski, L., Zastempowski, M. (2015). A comparative study of new and traditional designs of a hammer mill. *Transactions of the ASABE*, 58(3), 585-596. <https://doi.org/10.13031/trans.58.10691>
- [3] Cao Liying, Zhang Yuepeng, Zhang Yubao, et al. (2016). Influence of screen parameters optimization on screening efficiency of feed hammer mill. *Transactions of the Chinese Society of Agricultural Engineering*, 32(22), 284-288. <https://doi.org/10.11975/j.issn.1002-6819.2016.22.039>
- [4] Chen Junyu, Liu Bao, Li Pengfei. (2017). Study on motion state of mill hammer based on clearance joint. *Modern Machinery*, (4), 55-59. <https://doi.org/CNKI:CDMD:2.1018.960617>
- [5] Du Xiaobin, He Junlin, He Yongqiang, et al. (2019). Parameter optimisation and experiment on the combing of *Cerasus humilis*. *INMATEH-Agricultural Engineering*, 57(1), 103-114. [https://doi.org/10.35633/inmateh\\_57\\_11](https://doi.org/10.35633/inmateh_57_11)
- [6] Feng Heping, Mao Zhihui. (2003). Experimental study on the effect of moisture content, drying temperature and stress crack on the mechanical properties of corn. *Cereals and Oils Processing*, 33(4), 48-50.  
<http://kns.cnki.net/kcms/detail/detail.aspx?FileName=NJSP200304015&DbName=CJFQ2003>
- [7] Li Zhen, Wei Anning, Cao Liying, et al. (2019). Experimental research and optimal design of new feed hammer grinder's smashing performance. *Feed Industry*, 40(5), 6-10. <http://kns.cnki.net/kcms/detail/detail.aspx?FileName=FEED201905002&DbName=CJFQ2019>
- [8] Mugabi, R., Eskridge, K. M., Weller, C. L. (2017). Comparison of experimental designs used to study variables during hammer milling of corn bran. *Transactions of the ASABE*, 60(2), 537-544. <https://doi.org/10.13031/trans.11656>
- [9] Moiceanu, G., Paraschiv, G., Maican, E. et al. (2019). Aspects regarding FEM simulation of stress in hammer mill working tool. *E3S Web of Conferences, 8th International Conference on Thermal Equipment, Renewable Energy and Rural Development (TE-RE-RD 2019)*. Vol. 112. <https://doi.org/10.1051/e3sconf/201911203018>
- [10] Wang Jianxin, Zhang Guangyi, Cao Liying, et al. (2013). Research of materials motion law in separation flow of new type hammer feed grinder. *Transactions of the Chinese Society of Agricultural Engineering*, 29(9), 18-23. <https://doi.org/10.3969/j.issn.1002-6819.2013.09.003>
- [11] Xie Yixiao. (2013). Research progress in feed grinding technology. *Journal of Grassland and Forage Science*, (1), 10-13. <https://doi.org/10.3969/j.issn.1673-8403.2016.01.003>
- [12] Xu Wei, Cao Chunping, Sun Yu. (2021). Optimization design of hammer structure parameters of hammer mill. *Journal of Agricultural Mechanization Research*, 43(1), 27-33. <http://kns.cnki.net/kcms/detail/detail.aspx?FileName=NJYJ202101007&DbName=CJFQTEMP>
- [13] Liu Bao, Zong Li, Zhang Dongxing. (2011). Force and motion states of hammer mill at unloaded running. *Transactions of the Chinese Society of Agricultural Engineering*, 27(7), 123-128. <https://doi.org/10.3969/j.issn.1002-6819.2011.07.021>
- [14] Zhang Yongjie, Xu Hongmei, Liu Shuang, et al. (2019). Finite element analysis and topology optimization of hammer feed grinder frame plate. *Journal of Huazhong Agricultural University*, 38(4), 1-5. <http://kns.cnki.net/kcms/detail/detail.aspx?FileName=HZNY201905022&DbName=CJFQ2019>
- [15] Zhang Lei, Ruan Jinglan. (2013). The analysis of influence factor and research status of hammer mill. *Packaging and Food Machinery*, 31(6), 1-5. <https://doi.org/10.3969/j.issn.1005-1295.2013.06.014>
- [16] Zhang Sanqiang. (2009). The experimental study on the performance of 9R-40 tearing chopper [MSc dissertation, Inner Mongolia Agricultural University]. Hohhot/China. <https://doi.org/10.7666/d.y1474055>
- [17] \*\*\* China Academy of Agricultural Mechanization Sciences. (2007). *Agricultural Machinery Design Manual*. China Agricultural Science and Technology Press.
- [18] \*\*\* China Agricultural Machinery Standardization Technical Committee. (2007). *Test method for feed mill*. (GB/T 6971-2007). Standards Press of China.  
<http://c.gb688.cn/bzgk/gb/showGb?type=online&hcno=79C30463354F4A66F774B13FC17C1EB2>

# DESIGN AND APPLICATION OF MULTIFUNCTIONAL PERFORMANCE TEST PLATFORM FOR SOIL-ENGAGING TILLAGE COMPONENTS

## 多功能触土耕作部件性能检测平台设计与应用

Zhiquan Sun<sup>1)</sup>, Zhou Yang<sup>2, 3)</sup>, Jieli Duan<sup>2)</sup>, Jun Li<sup>2)</sup>

<sup>1)</sup> Experimental Basis and Practical Training Centre, South China Agricultural University, Guangzhou / China;

<sup>2)</sup> College of Engineering, South China Agricultural University, Guangzhou / China;

<sup>3)</sup> Guangdong Provincial Key Laboratory of Conservation and Precision Utilization of Characteristic Agricultural Resources in Mountainous Areas, Meizhou / China

Tel: +86 02085280783; E-mail: duanjieli@scau.edu.cn

DOI: <https://doi.org/10.356.33/inmateh-62-37>

**Keywords:** tillage components, multifunctional, test platform, soil-engaging

### ABSTRACT

Parts that come into contact with the soil are ones of the important energy consuming parts in tillage operations. In order to improve the research and development efficiency of tillage components, it is necessary to develop a performance test platform for tillage components with high interchangeability, convenience and comprehensive data collection. Therefore, a performance test platform for combined powered and passive tillage components was designed. Strength analysis and structural design optimization of key components was based on ANSYS. A real-time measurement and control software was developed based on LabVIEW platform. The related tests results show that the test platform can be used to simulate the actual condition and meet the test requirements.

### 摘要

在耕作作业中，触土部件是耕作机械重要耗能部件之一。为提高耕作部件的研发效率，需研制具有较高互换性、便捷性和数据采集全面的耕作部件性能检测平台，本文研发了同时适用于主动和被动耕作部件的小型性能测试平台，基于 ANSYS 对关键部件进行强度分析和结构设计优化，开发了基于 LabVIEW 平台的实时测控软件。利用所研发的测试平台，对双翼铲和微耕刀工作性能进行试验分析。研究表明：1) 检测平台可实时调整耕作部件工作参数并在线采集、显示与存储试验数据；2) 检测平台可测试被动耕作部件耕深范围为 0 ~ 400mm；对于主动开沟部件，可检测的耕深范围为 0 ~ 350 mm、转速在 100 ~ 700 r/min 之间；3) 双翼铲开沟器前进阻力、竖直方向阻力及侧向阻力与行进速度成正比，且侧向阻力远大于其它两方向阻力，旋转圆盘开沟器工作扭矩与前进速度成正比，所设计检测平台能够模拟实际工况，满足试验要求。

### INTRODUCTION

The energy consumption of tillage machinery accounts for more than 50% of the energy consumption of field operations, and the soil contact resistance of tillage part is one of the important factors in the energy consumption (Zhijun Guo et al., 2011). Therefore, the interaction characteristics between tillage part and soil during the tillage operations is of great significance for optimizing the design of tillage machinery, improving tillage efficiency, saving energy, and reducing emissions, thus promoting the process of agricultural mechanization in China (Honglei Jia et al., 2017). At present, the researches on tillage components mainly focus on the simulation of the soil-touching process and the work effect in the field of the tillage machinery. However, there are obvious differences between the actual situation and the ideal simulated test conditions, so simulation studies need to be tested and verified (Shoutai Li et al., 2011; Huimin Fang et al., 2016). The field detection is usually applied to test the performance of the complete machine, which is limited by environment and electric power, so the detection accuracy is low and the data collection is difficult. Test platform with the characteristics of controllable soil factors, make easy recovery of soil state, easy debugging of test equipment and repetitive test results. The indoor test platform is not affected by seasons or weather (Yonglei Li et al., 2012), so the indoor test platform is the developing direction in future.

The United Kingdom, Germany, France, the United States, Canada, Israel and other countries have started indoor test platform research earlier, and have reached a fairly high level of automation (Ani et al., 2018;

Hemmat et al., 2014). China's indoor test platform is mainly large-scale type, which is mainly used to test the performance and work effect of rotary tillers, micro-farming machine and other complete machines (Weixing Wang et al., 1997; Hua Yan et al., 2010; Xincheng Sun et al 2015; Yan Yu et al., 2011). Currently existing small test platforms are mostly used to test the performance of passive tillage component, the test object and mode are single (Yanjie Li et al., 2010; Jianneng Chen et al., 2015). Furthermore, low universality and interchangeability of the small test platform also limit the testing and development of tillage components. Therefore, it is very important to develop a test platform which is suitable for a variety of tillage components.

In this paper, a multifunctional test platform was designed and can be used for the testing of passive tillage equipment such as plough and powered tillage equipment such as rotary tiller blades, chain ditcher or vertical spiral ditcher. The small sized and interchangeable test platform has advantages such as having wide in application range, being accurate in data acquisition and efficient in testing.

**MATERIALS AND METHODS**

**Overall structure of test platform**

The overall structure diagram of the test platform is shown in Fig. 1. The test platform consists of four parts: traction drive system, soil box, tillage equipment drive system and test platform measurement and control system. The traction system drives the wire ropes to move the trolley on the straight track. The tillage equipment drive system is mounted on the trolley, and the trolley guide wheel device is designed to ensure the trolley to run straight and avoid friction with the track. The motor drives the rotary tillage equipment to work. A LabVIEW-based measurement and control system is developed to adjust the working performance of the tillage equipment and collect test data in real time online.

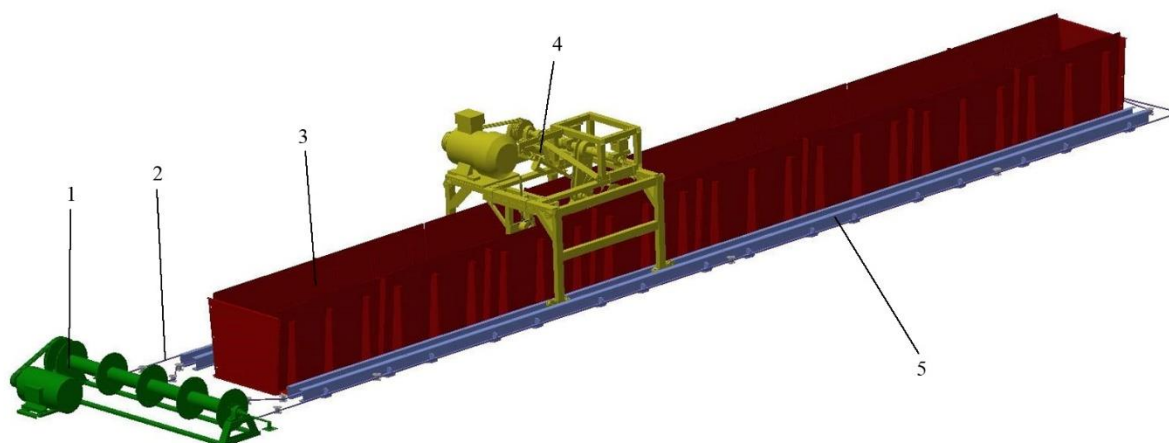


**Fig. 1 - General model of test platform**

1 – Traction drive system; 2 – Steel wire rope; 3 – Soil box; 4 – Tillage equipment drive system; 5 – Track

**Table 1**

**Performance parameters of the trolley**

Tillage components	Maximum drive power	Deceleration ratio	Speed range	Depth range of ploughing
	[kW]		[rpm]	[mm]
Powered	15	1.57	200~700	0~350
		3	100~460	
Passive	4			0~400

**Tillage trolley**

The parameters of the trolley are listed in Table 1 (Yanshan Yang et al., 2016; Zhou Yang et al., 2013; Wenfeng Ji, 2010). In order to improve the universality of the test platform and meet the test requirements of different tillage modes and tillage equipment, a multifunctional test trolley is designed (in Fig. 2) (Jianguo Zhao et al., 2019; Kan Zheng et al., 2017).

The tillage drive system is the main working part of the test platform, which can be used to detect the powered tillage equipment, the passive tillage equipment and the powered-passive combination tillage equipment (Chinese Academy of Agricultural Mechanization Sciences, 2007). The main body of the tillage drive system is mounted on the trolley.

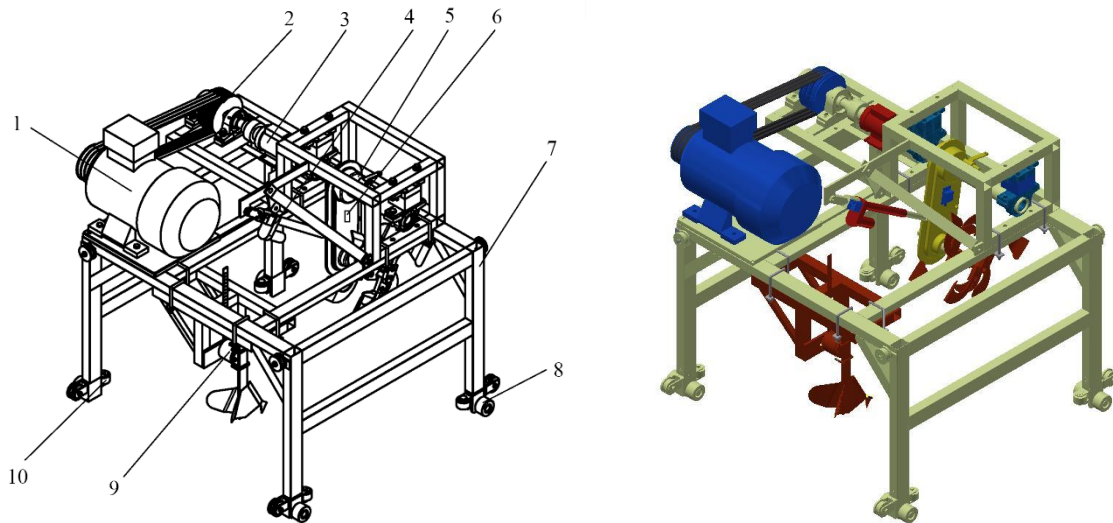


Fig. 2 - Integral design of tillage trolley

1 – Motor; 2 – Pulley; 3 – testing device for powered tillage components; 4 – Frame; 5 – Road wheel; 6 – Testing device for passive tillage components 7 – sheave

**Key component design**

Soil factors have a great influence on the performance of tillage machines and tools (Bashar M et al., 2015). In order to ensure that the soil box has enough strength, the ANSYS software is used to analyse the stress on the soil box and optimize the structural design. When compacting the soil, the stress on the sidewall of the soil box is greatest. From the foundation soil stress theory of generalized Hooke’s law, soil physical property measurement and calculation method (Caihong Jia, 2013), lateral stress of soil on the inner wall soil, bulk density and soil gravity are calculated by the following equations.

$$p = k_0(\gamma z + \sigma_c) \text{ [kPa]} \tag{1}$$

$$rs = \frac{m_0}{V(1+0.01w_0)} \text{ [g/cm}^3\text{]} \tag{2}$$

$$\gamma = \frac{rs \cdot g}{1000} \text{ [kN/m}^3\text{]} \tag{3}$$

where:

$p$  is the lateral static soil stress;  $\gamma$  is the fill weight;  $z$  is the calculated point depth;  $k_0$  is the lateral pressure coefficient;  $\sigma_c$  is the additional stress;  $rs$  is the soil bulk density;  $m_0$  is the quality of the model wet soil;  $V$  is the volume of the ring cutter;  $w_0$  is the moisture content of the soil sample;  $g$  is the acceleration of gravity.

In addition, the Boussinesq’s formula (Caihong Jia, 2013) establishes a three-dimensional coordinate system with the base point of the rectangular load as the origin, and the additional stress at any depth  $z$  under the base corner point:

$$\sigma_z = \frac{3p_0}{2\pi} \int_0^l \int_0^b \frac{z^3 dx dy}{(x^2+y^2+z^2)^{5/2}} \text{ [MPa]} \tag{4}$$

where:

- $p_0$  is the load strength;  $\sigma_z$  is the additional stress at depth  $z$ ;
- $l$  is the load length;
- $b$  is the load width.

The integral result of equation (4) is:

$$\sigma_z = \alpha_c p_0 \text{ [MPa]} \tag{5}$$

The soil gravity parameter in equation (1) is consistent with the soil bulk density parameter (Jia Caihong, 2013), and  $\sigma_c$  is substituted into equations (2), (3), and (5) with  $\sigma_z$  to obtain equation (6).

$$p = k_0 \left( \frac{m_0 g}{V(1000+10w_0)} z + \alpha_c p_0 \right) \text{ [MPa]} \tag{6}$$

When the compaction wheel compacts the soil, the stress distribution is roughly elliptical. The maximum vertical stress is distributed on the axle vertical line. The vertical stress decreasing from top to bottom and decreasing from the axle vertical line to both sides along the advancing direction (Zhenjia Zhao et al., 2012; Ruxin Li et al., 2001). Due to the complex stress variation during compaction of the soil, it is difficult to detect accurately. The elliptical surface is divided into three internal stress zones according to the stress distribution trend. Each area is divided into three parts: left, centre and right. Vertical stress distribution is shown in Fig. 3.

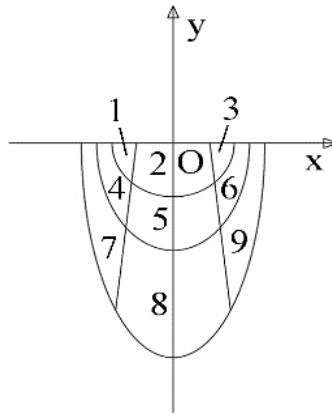


Fig. 3 - Soil vertical stress distribution

In order to improve the feasibility of the simulation and make it as possible as close to the actual conditions, the central stress of each block is taken as the plane stress of this block. The soil bulk density was measured using a standard soil wreath knife with a volume of 60 cm<sup>3</sup> and soil hardness was measured by a serpentine sampling method (Nanjing Hydraulic Research Institute, 2003).

The measurement site is the citrus orchard of the Institute of Fruit Research, Guangdong Academy of Agricultural Sciences. The measured soil wet weight  $m_0=100.6$  g, soil moisture content  $w_0=13.3\%$ , and soil firmness are listed in Table 2.

Table 2

Soil parameter of the citrus orchard of the Institute of Fruit Research, Guangdong Academy of Agricultural Sciences

Depth [cm]	Soil firmness [kPa]													Average value [kPa]
	60	241	245	231	262	380	352	293	145	153	146	250	203	418
120	272	331	335	362	401	370	303	195	159	137	361	333	399	304.46
180	29	346	458	424	469	446	376	172	121	243	401	384	474	354.38
240	273	415	469	387	464	502	449	289	326	357	441	430	487	406.85
300	411	461	482	452	443	541	483	299	319	460	428	462	438	436.85
360	431	456	467	452	582	514	514	281	426	448	428	475	405	452.23

According to the measured soil parameters, take  $k_0=0.5$ ,  $g=9.81$  N/kg,  $p_0=350$  kPa. According to surface length  $l=400$  mm, width  $b=200$ mm, look up the table to get the value of  $\sigma_c$ . Substituting the values into the equation (6), the results are listed in Table 3 (Chunlin Li, 2009). Consider the symmetry relationship of stress distribution, the results of only one side stress are listed in Table 3. The material used is Q235 steel plate, the allowable stress is 156.67 MPa (safety factor is 1.5).

In order to facilitate loading the stress, the load plate covering the inner side wall of the soil box is designed according to the stress region division aforementioned. The material selection unit is type SOLID187, Poisson's ratio is 0.3, elastic modulus is  $2.06 \times 10^5$  MPa, density is 7800 kg/m<sup>3</sup>. The model adopts automatic mesh division in the process of simulation. Stress load is applied on the load plate and stress intensity analysis based on the third strength theory is performed. It is necessary to optimize the design of the soil box to ensure the safety and reliability of test platform.

Generally, increasing the thickness of the steel plate or increasing the sidewall ribs can reinforce the soil box. So the simulation calculation method is used to determine the thickness of the steel plate that meets the strength requirements. Two designs are simulated with a gradient of 0.5 mm of steel plate. The results are listed in Table 5.

The soil box without ribs needs 8.5 mm thick steel plate, 9mm thick steel plate is used in the actual condition. The 2mm thick steel plate with grooved ribs can meet the requirements. Due to the harsh working environment of the tillage equipment, the soil box with grooved ribs is finally designed to use 3mm plates. Under the premise of meeting the safety and reliability of the test platform, the ribbed soil box will save 52.19% of material compared to the non-ribbed soil box. The stress cloud diagram of soil box is shown in Fig. 4, the maximum stress of the soil box with grooved ribs is 124.06MPa, and the maximum displacement is 0.18mm.

Table 3

Stress values at different locations

Load point	x	y	Stress coefficient	Horizontal stress [MPa]
1	-85	-30	0.235	0.076
2	0	-50	0.239	0.084
4	-100	-70	0.226	0.040
5	0	-150	0.166	0.058
7	-110	-160	0.226	0.040
8	0	-300	0.093	0.033

Table 4

Simulation calculation result of two designs

Type of soil box	Thickness of steel plate	Maximum stress	Maximum displacement	Meet the conditions
	[mm]	[MPa]	[mm]	
non-ribbed	8	204.07	4.75	NO
	8.5	138.99	4.01	YES
	9	120.48	3.41	YES
grooved ribs	1.5	170.87	0.44	NO
	2	142.12	0.30	YES

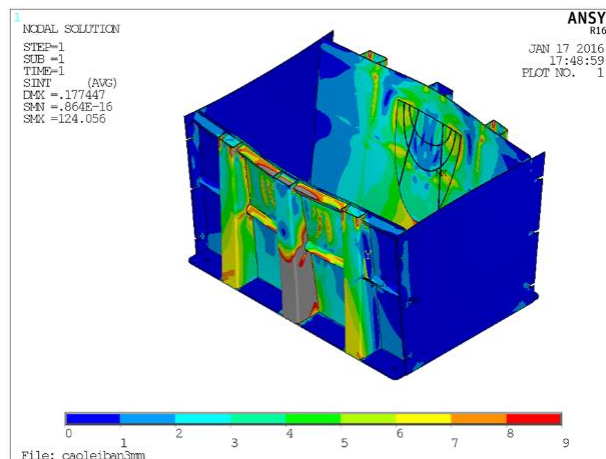


Fig. 4 - ANSYS stress cloud diagram of 3 mm thick steel plate soil box with grooved ribs

**Measurement and control system design**

**Measurement and control system hardware design**

The measurement and control system consists of the host computer, the lower computer and the actuator. The parameters of the torque, rotation speed, tillage depth and three-dimensional resistance of passive tillage equipment and forward speed of the trolley can be detected and displayed in real time. The sensor is used to convert the physical phenomena to a standard voltage signal.

The signal is collected by the data acquisition card and then processed and displayed by the test platform. The data is collected by two data acquisition cards (PCI-1706U and USB-4711A), which were produced by Advantech. The lower computer 1 and 2 adopts Shanghai Hongqitai RF300A15kW and Siemens M4407.5kW inverter, as the controller of traction drive system and tillage drive system, respectively, controls the inverter through the analogue and digital output ports of the acquisition card; adopts STC89C52RC MCU as the lower computer 3, based on the VISA driver of LabVIEW, the RS232 serial communication is used to establish the master-slave relationship between the PC and the MCU. The MCU controls the electric push rod to adjust tillage depth (Shun Xu et al., 2017; Bin Xie et al., 2013). The structure of measurement and control system hardware is shown in Fig. 5.

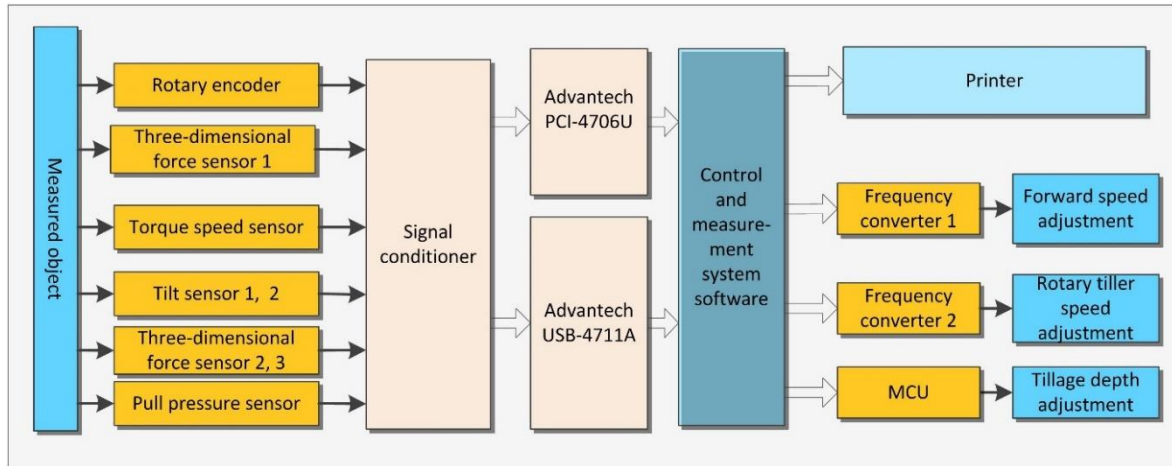


Fig. 5 - Overall structure of the measurement and control system

**Measurement and control system software design**

Based on the LabVIEW platform, the measurement and control software for the test platform is developed (Chunlin Xu et al., 2013). The software can fulfil the requirements of test parameter adjustment, real-time data display and storage, with a friendly operation interface and strong human-computer interaction. The software includes four tabs: system calibration, test platform control, passive tillage equipment test, and powered tillage equipment test. The calibration program is used to select the COM port that communicates the host computer with the MCU, and mark  $\theta_0$ . When no load occurs torque magnitude is marked. The system realizes the functions of adjusting the direction and speed of the trolley, controlling the steering and rotating speed of the powered tillage equipment and saving the data. The human-computer dialogue of the software is shown in Fig. 6.



Fig. 6 - LabVIEW-based measurement and control system software

**RESULTS**

The tillage equipment is mounted on the corresponding detection device as shown in Fig. 7. Double shovel plough width  $B=70$  mm, penetration angle  $\alpha < 90^\circ$ . Micro rotary tiller blades bending radius is  $R=30$  mm, bending angle  $\varphi=120^\circ$ , width  $B_1=42$  mm, slip angle  $\gamma=30^\circ$ , as shown in Fig. 8. A single factor test was designed with the tillage depth being 100 mm, the blades rotation speed 320 r/min, the forward speed of 0.1, 0.2, and 0.3 m/s.



**Fig. 7 - The test platform**

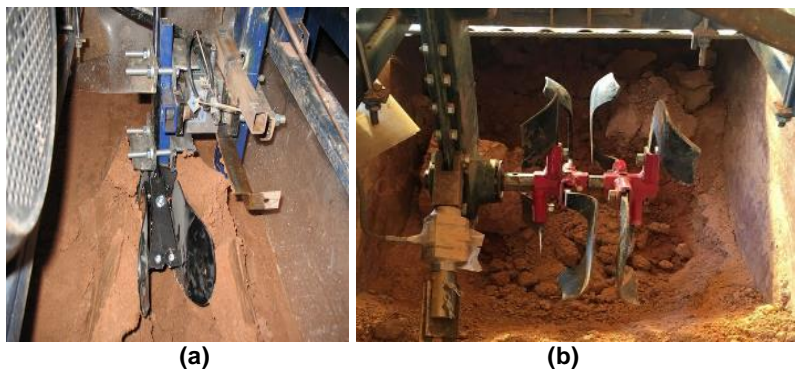


**Fig. 8 - Double shovel plough and micro rotary tiller blades assembly**

As shown in Fig. 9 and Fig. 10, when the forward speed increases from 0.1 m/s to 0.2 m/s under the condition of 100 mm tillage depth, the average forward resistance ( $F_x$ ) of the double shovel plough opener increases from 70.43N to 143.01N, an increase of 50.75%. The average resistance in the vertical direction ( $F_y$ ) increased from 121.09N to 256.98N, an increase of 52.88%, the lateral average resistance ( $F_z$ ) increased from 853.70N to 1166.81N, an increase of 26.83%; the forward speed increased from 0.2m/s to 0.3m/s,  $F_x$  increased from 143.01N to 211.64N, an increase of 32.43%,  $F_y$  from 256.98N to 362.46N, an increase of 29.10%,  $F_z$  from 1166.81N to 1389.15N, an increase of 16.01%. The three-dimensional resistance of the double shovel plough is proportional to the forward speed, but the three-dimensional resistance increases slowly as the speed increases.

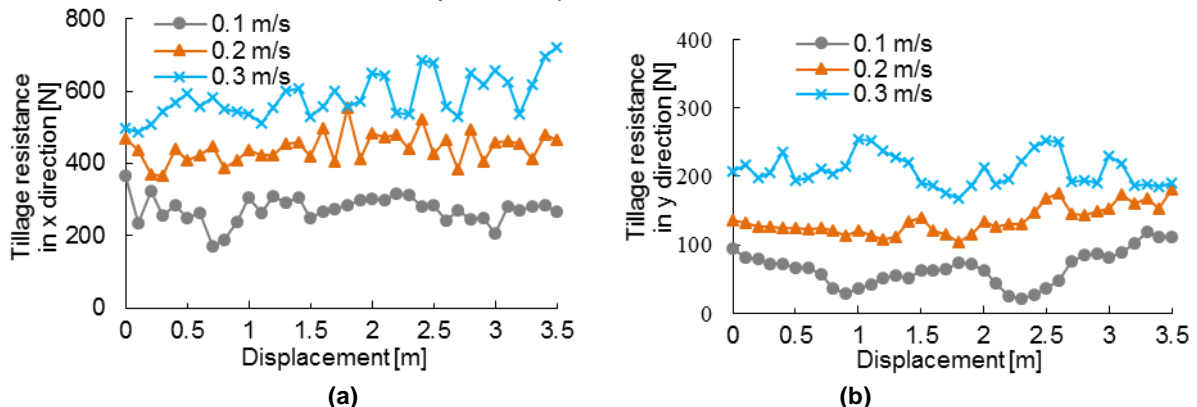


**Fig. 9 – Tillage resistances of double shovel plough in X and Y directions**

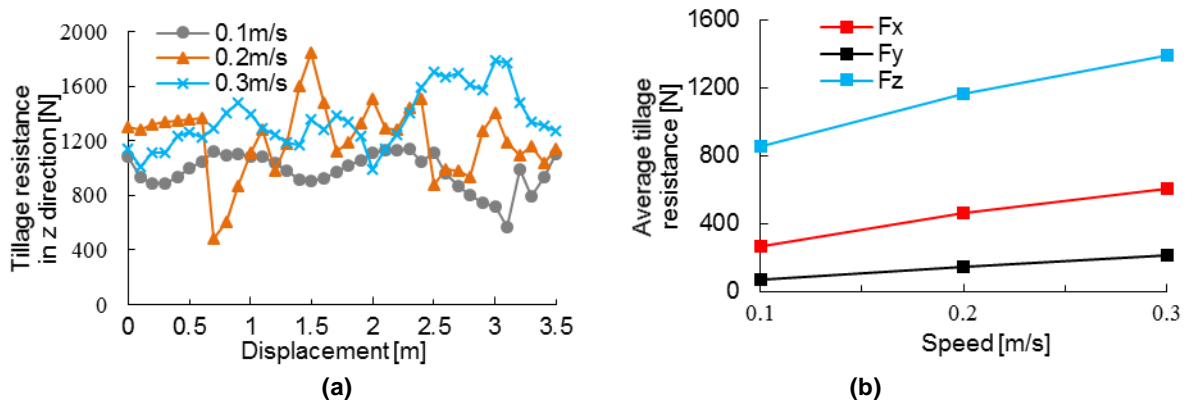


Fig. 10 – Tillage resistance of double shovel plough in z direction and average resistance in x, y and z directions

It can be seen from Fig. 10(b) that the lateral resistance  $F_z$  is much larger than the other two directions. This is because the central symmetry plane of the double shovel plough has a certain angle with the advancing direction during installation or the two sides of the shovel are not symmetrical during the manufacturing process. Therefore, the passive equipment devices such as the double shovel plough have high accuracy on manufacturing and assembly, otherwise there will be greater additional resistance and will lead to affect machine life. Fig. 11 shows the test result of micro rotary tiller blades. When the forward speed increases from 0.1 m/s to 0.2 m/s, the average working torque ( $T$ ) of the cutter head increases from 12.90 nm to 22.10 nm, an increase of 41.64%. When the forward speed increases from 0.2 m/s to 0.3 m/s, it increases from 22.10 nm to 27.97 nm, an increase of 20.99%, and the working torque of the micro rotary tiller blades is proportional to the forward speed under the conditions of 100 mm of tillage depth and 320 rpm of rotation speed, but the working torque increases slowly with the forward speed increasing. The test platform can effectively simulate the field soil and the working conditions of the tillage equipment in different modes. The test platform is highly interchangeable, and the performance parameters of different types of tillage equipment can be effectively collected.

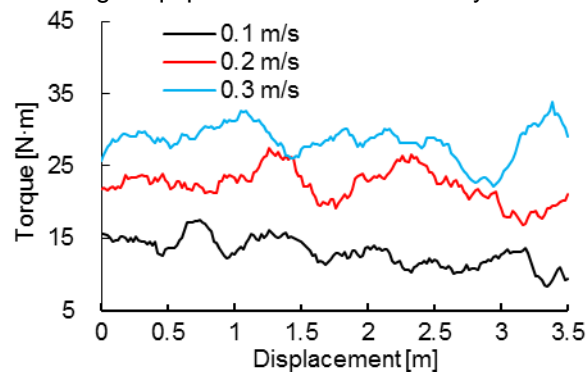


Fig. 11 - Working torque of micro rotary tiller blades

## CONCLUSIONS

1) The multi-mode tillage equipment test platform can test the passive tillage components at a depth of 0–400 mm, and test the powered tillage equipment with a depth of 0–350 mm at speed of 100–700 rpm. The test platform has the characteristics of small floor area, movable, strong comprehensiveness and high interchangeability. It can be used for a variety of tillage equipment and multiple tillage modes, thereby reducing the research and development cost of tillage equipment and improving the development efficiency.

2) The measurement and control system software is developed based on the LabVIEW platform, which can adjust the forward speed of the tillage equipment, the tillage depth, the blades rotation speed in real time. The test data such as the forward speed, the working torque and the rotation speed of the blades, and the three-dimensional tillage resistance of the passive tillage equipment are displayed in real time online and stored by the software. The software improves the automation of the test platform, and is convenient to use and easy to operate.

3) Based on the soil mechanics theory and ANSYS simulation, the design and optimization of the soil box is carried out. The simulation results show that the grooved rib soil box saves 52.19% of material compared with the non-ribbed soil box under the condition of meeting the strength requirement. The design method and simulation result can provide a reference for the design of soil box.

4) The test results of the double shovel plough and the micro tiller blades indicate that the forward resistance, the vertical resistance and the lateral resistance of the double shovel plough are all proportional to the advancing speed, and the three-dimensional resistance increases slower when the speed increases. The working torque of the micro tiller blades is proportional to advancing speed, and the torque increases slower when the speed increases. The designed test platform can simulate the actual condition and meet the actual work needs.

## ACKNOWLEDGEMENT

This work was supported by Key-Area Research and Development Program of Guangdong Province (2019B020223002), Natural Science Foundation of Guangdong Province (2020A1515010793), and National Banana Industry Technology System Construction Project of China (CARS-31-10).

## REFERENCES

- [1] Ani O.A., Uzoejinwa B.B., Ezeama A.O., Onwualu A.P., Ugwu S.N., Ohagwu C.J. (2018). Overview of soil-machine interaction studies in soil bins. *Soil and Tillage Research, USA*, 175, 13-27. <https://doi.org/10.1016/j.still.2017.08.002>
- [2] Chen J. N., Ye J., Xia X. D., Zhao Y. (2015). Design and application of rotary round soil-bin test bed driven by tyre friction. *Transactions of the Chinese Society of Agricultural Machinery*, 46(7), 66-71. [http://www.cnki.com.cn/Article\\_en/CJFDTotal-NYJX201507010.htm](http://www.cnki.com.cn/Article_en/CJFDTotal-NYJX201507010.htm)
- [3] China Academy of Agricultural Mechanization Science, (2007). Design manual of agricultural machinery. Issue I, *China Agricultural Science and Technology Press, China*, 75-259.
- [4] Fang H. M., Ji C. Y., Zhang Q. Y., Guo J. (2016). Force analysis of rotary blade based on distinct element method. *Transactions of the CSAE*, 32(21), 54-59. [http://www.cnki.com.cn/Article\\_en/CJFDTOTAL-NYGU201621007.htm](http://www.cnki.com.cn/Article_en/CJFDTOTAL-NYGU201621007.htm)
- [5] Guo Z. J., Du G., Zhou Z. L., Zhang P., Li Y. X. (2011). Actuality analysis of resistance-reducing properties on soil cultivating components with different macroscopic soil-engaging surfaces. *Transactions of the Chinese Society of Agricultural Machinery*, 42(6), 47-52. <https://www.researchgate.net/publication/288996856>
- [6] Hemmat A., Rahnema T., Vahabi Z. (2014). A horizontal multiple-tip penetrometer for on-the-go soil mechanical resistance and acoustic failure mode detection. *Soil and Tillage Research, USA*, 138, 17-25. <https://doi.org/10.1016/j.still.2013.12.003>
- [7] Ji W. F., Jia H. L., Tong J., Tan H. J., Liu Z.C., Ma C. L. (2010). Analysis of influencing factors on power consumption and field test of universal blade. *Transactions of the Chinese Society of Agricultural Machinery, China*, 41(2), 35-41. <https://www.researchgate.net/publication/289204345>
- [8] Jia C. H. (2013). Soil mechanics. *Peking University Press*, 53-67.
- [9] Jia H. L., Wang W. P., Chen Z., Zhang T. Z., Zhang P., Zhuang J. (2017). Research status and prospect of soil-engaging components optimization for agricultural machinery. *Transactions of the Chinese Society of Agricultural Machinery*, 48(7), 1-13. [http://en.cnki.com.cn/Article\\_en/CJFDTOTAL-NYJX201707001.htm](http://en.cnki.com.cn/Article_en/CJFDTOTAL-NYJX201707001.htm)
- [10] Li C. L. (2009). Stress behaviour in agricultural soil compacting process and the development and application of its monitoring system. *Nanjing Agricultural University*, 7-9. DOI:10.7666/d.Y1762838
- [11] Li S. T., Chen X. B., Chen W., Zhu S.P., Li Y. W., Yang L., Xie S. Y. (2018). Soil-cutting simulation and parameter optimization of handheld tiller's rotary blade by smoothed particle hydrodynamics modelling and Taguchi method. *Journal of Cleaner Production, USA*, (179), 55-62. <https://www.sciencedirect.com/science/article/pii/S0959652617332183>
- [12] Li Y. J., Xu Y., Zhao D. (2010). Development and manufacture of a mini-soil-bin device for soil dynamics experiments. *Journal of Mechanical Engineering*, 46(15), 65-70. [https://en.cnki.com.cn/Article\\_en/CJFDTOTAL-JXXB201015028.htm](https://en.cnki.com.cn/Article_en/CJFDTOTAL-JXXB201015028.htm)
- [13] Li Y. L., Song J. N., Dong X. Q., Zhang J. K., & Wang J. C. (2012). Design of test device for rotary tiller components based on soil bin. *Transactions of the CSAE*, 28(17), 38-43

- [http://en.cnki.com.cn/Article\\_en/CJFDTOTAL-NYGU201217008.htm](http://en.cnki.com.cn/Article_en/CJFDTOTAL-NYGU201217008.htm)
- [14] Li R. X., Song H. B., & Gao H. W. (2001). Prediction of soil compaction by small tractor using finite element method. *Transactions of the CSAE*, 17(4), 66-69.  
[http://www.cnki.com.cn/Article\\_en/CJFDTOTAL-NYGU200104016.htm](http://www.cnki.com.cn/Article_en/CJFDTOTAL-NYGU200104016.htm)
- [15] Nanjing Hydraulic Research Institute. (2003). Technical manual of geotechnical test. *Communication Press, China*, 34-35.
- [16] Sun X. C., Ye J., Yan J. J., Chen J. N. (2015). Running stability control method and test verification of soil groove test rig for rotary agricultural machine. *Transactions of the CSAE*, 31(13), 46-52.  
<https://www.researchgate.net/publication/282903191>
- [17] Taghavifar, H., Mardani, A. (2014), Analyses of energy dissipation of run-off-road wheeled vehicles utilizing controlled soil bin facility environment. *England*, 66, 973-980.  
<https://doi.org/10.1016/j.energy.2014.01.076>
- [18] Wang W. X., Luo X. W., Ou Y. G., & Luo X. W. (1997). Research on computerized simulation loading system for soil trough tests. *Transactions of the CSAE*, 13(4), 27-30.  
[http://www.tcsae.org/nygxcb/ch/reader/view\\_abstract.aspx?file\\_no=19970406](http://www.tcsae.org/nygxcb/ch/reader/view_abstract.aspx?file_no=19970406)
- [19] Xie B., Li H., & Zhu Z. X. (2013). Measuring tillage depth for tractor implement automatic using inclinometer. *Transactions of the CSAE*, 29(4), 16-21.  
<https://www.researchgate.net/publication/289213268>
- [20] Xu C. L., Li L. H., Zhao D. Y., Li X. Q., Li M. J., & Zhang W. (2013). Field real time testing system for measuring work dynamic parameters of suspension agricultural implement. *Transactions of the Chinese Society of Agricultural Machinery, CHINA*, 44(4), 82-88.  
<https://www.researchgate.net/publication/289319964>
- [21] Xu S., Tong J., & Li M. (2017). Performance testing of vegetable chopping machine based on LabVIEW and operation parameter optimization. *Transactions of the CSAE, CHINA*, 33(3), 250-256.  
<https://www.researchgate.net/publication/316254466>
- [22] Yan H., Wu J. M., & Lin J. T. (2010). Design of micro-cultivator or testing platform with annular soil bin. *Transactions of the Chinese Society of Agricultural Machinery*, S1(41), 68-72.  
[http://en.cnki.com.cn/Article\\_en/CJFDTOTAL-NYJX2010S1016.htm](http://en.cnki.com.cn/Article_en/CJFDTOTAL-NYJX2010S1016.htm)
- [23] Yang Y. S., Ding Q. S., Ding W. M., Xue J. L., Qiu W., & He R. Y. (2016). Design and application of multi-purpose in-situ tillage tool testing platform. *Transactions of the Chinese Society of Agricultural Machinery*, 47(1), 68-74. <https://www.researchgate.net/publication/298714193>
- [24] Yang Z., Chen C. H., Duan J. L., Yan G. Q., Pan X. W., Yan L. L., & Liu J. L. (2013). Performance test of hand-held electric hole-digger for fertilization in orchard. *Transactions of the CSAE*, 29(12), 25-31. <https://www.researchgate.net/publication/289176183>
- [25] Yu Y., Gong L. N., & Shang S. Q. (2011). Development of soil bin test dynamic parameters measurement system. *Transactions of the CSAE*, 27(S1), 323-328.  
<https://www.researchgate.net/publication/291289304>
- [26] Zhao J. G., Wang A., Ma Y. J., Li J. C., Hao J. J., Nie Q. L., Long S. F., & Yang Q. F. (2019). Design and test of soil preparation machine combined subsoiling, rotary tillage and soil breaking. *Transactions of the CSAE*, 35(8), 46-54. [https://en.cnki.com.cn/Article\\_en/CJFDTOTAL-NYGU201908006.htm](https://en.cnki.com.cn/Article_en/CJFDTOTAL-NYGU201908006.htm)
- [27] Zhao Z. J., Zou M., Xue L., Wei, C. G., & Li J. Q. (2012). Simulation analysis of effect of compaction on soil stress distribution. *Transactions of the Chinese Society of Agricultural Machinery*, 43(S1), 311-313. <https://www.researchgate.net/publication/289056143>
- [28] Zheng K., He J., Li H. W., Zhao H. B., Hu H. N., & Liu W. Z. (2017). Design and experiment of combined tillage implement of reverse-rotary and subsoiling. *Transactions of the Chinese Society of Agricultural Machinery*, 48(8), 61-71. <https://www.researchgate.net/publication/320430124>

## OPTIMIZATION ON EFFICIENT COMBUSTION PROCESS OF SMALL-SIZED FUEL ROLLS MADE OF OLEAGINOUS FLAX RESIDUES

/

## ОПТИМІЗАЦІЯ ЕФЕКТИВНОГО ПРОЦЕСУ ГОРІННЯ МАЛОГАБАРИТНИХ ПАЛИВНИХ РУЛОНІВ ІЗ ЗАЛИШКІВ ПІСЛЯ ЗБИРАННЯ ЛЬОНУ ОЛІЙНОГО

Svitlana Yaheliuk<sup>1)</sup>, Volodymyr Didukh<sup>2)</sup>, Vitaliy Busnyuk<sup>2)</sup>, Galina Boyko<sup>3)</sup> Oleksandr Shubalyi<sup>4)</sup>

<sup>1)</sup> Lutsk National Technical University, Department of Commodity Research and Expertise Customs, Lutsk, Ukraine;

<sup>2)</sup> Lutsk National Technical University, Department of agricultural engineering, Lutsk, Ukraine;

<sup>3)</sup> Kherson National Technical University, Department of Commodity Studies, Standardization and Certification / Kherson, Ukraine;

<sup>4)</sup> Lutsk National Technical University, Department of Economics, Lutsk, Ukraine

Tel: +380955371898; E-mail: s.yagelyuk@Intu.edu.ua

DOI: <https://doi.org/10.35633/inmateh-62-38>

**Keywords:** *solid biofuels, environmental safety, carbon monoxide, efficient combustion, Box-Behnken design*

### ABSTRACT

Currently, the use of secondary agricultural raw material is a topical issue. There are various applications of agricultural crop residues possible, but they are finance- and energy-consuming. Burning crop residues is very harmful for the environment. One of the ways to solve the problem is the production of solid biofuel that can be used to heat buildings. The authors suggest producing solid biofuel in the form of small-sized fuel rolls / pellets (SFR), which are made of oleaginous flax residues. As a result of the conducted experimental investigations, the authors have proved the efficiency and the environmental safety of SFR consumption. The new fuel can be recommended if the requirement of efficient and ecologically safe combustion is met. Thus, the influence of small-sized fuel rolls' properties on the process of their combustion as well as quantitative and qualitative analysis of the combustion gases from burning solid fuel made of oleaginous flax residues have been investigated. The paper presents the results proving that SFR combustion is the most efficient on condition of providing reduced moisture (10-12%) and reasonable density (80 kg/m<sup>3</sup>) in the process of pellet production. In addition, it has been determined that there is a significant reduction of harmful CO emissions and normalization of CO<sub>2</sub> concentration. The application of the suggested solid biofuel can make it possible to solve the problem of using oleaginous flax residues and provide cheap fuel for household purposes.

### РЕЗЮМЕ

На сьогодні актуальне використання вторинної сільськогосподарської сировини. Є різні можливості застосування рослинних сільськогосподарських відходів, проте вони фінансово- та енерговитратні. Спалювання залишків сільськогосподарських культур шкодить навколишньому середовищу. Шляхом вирішення проблеми є виготовлення твердого біопалива для опалення будівель. Автори пропонують використовувати у якості твердого біопалива малогабаритні паливні рулони (МПР), які виготовляють із відходів, що залишаються після збирання олійного льону. В результаті проведених експериментальних досліджень, автори встановили ефективність та високу екологічну безпечність спалювання МПР. Нове паливо може бути рекомендованим, якщо воно задовольняє умову ефективного та екологічного горіння. Тому дослідження впливу властивостей малогабаритних паливних рулонів на час їх ефективного горіння та кількісний й якісний аналіз димових газів від згорання твердого палива з відходів збирання олійного льону є актуальним. В статті наведені результати які доводять, що найбільшій ефективності горіння (МПР) можна досягти зниженням вологості та дотриманням раціональної щільності під час виробництва. Також виявлено, що спалювання характеризується суттєвим зниження шкідливих викидів СО, зниженням концентрації СО<sub>2</sub>, приведеної до нормальних умов. Використання запропонованого нового твердого біопалива дозволить вирішити задачу використання залишків рослинної сільськогосподарської сировини олійного льону та забезпечить населення дешевим видом палива.

### INTRODUCTION

A large amount of plant residues remain in the field after crops harvesting. By now, the farmers have not found many ways to utilize these residues. Burning them is the fastest and easiest way to dispose of plant

agricultural waste. This is a standard practice for different countries around the world. As a result of agricultural residues burning, there can be two problems: air pollution and damage to fertile soils. At the same time, there is a steady increase in the cost and reduction of existing energy resources. Therefore, more and more attention is paid to modern, "green" technologies.

The burning of plant agricultural waste is also an urgent problem for Ukraine. During the harvesting done by the oleaginous flax harvester, windrows of the stem fibre mass, that are of a considerable size, remain on the field. That is why conversion of oleaginous flax stem fibre mass to solid biofuel is a good opportunity to overcome the energy crisis in Ukraine. Production of such fuel from oleaginous flax residues will improve environmental safety and does not require large financial costs. As a result of research this type of fuel was produced (Yaheliuk S. *et al.*, 2019). Solid biofuel obtained from oleaginous flax residues is in the form of dense small-sized fuel rolls of a small diameter, which can be used for heating buildings during the cold season. They are suitable for all boilers that are designed to use solid fuel.

Most boilers normally produce carbon monoxide as a part of their operation. Such emissions must comply with the European Commission's ambient air quality requirements (Air Quality Standards, 2019) and international requirements for boilers (Technical Safety BC, 2018).

In order to use a new type of solid biofuel effectively, it is necessary to experimentally study the performance characteristics, namely the effective combustion time, as well as the environmental safety of smoke gas emissions produced by the combustion of this biofuel. This type of studies have not been conducted before and this article is dedicated to them.

Conservation of energy and the environment, the search for new environmental types of fuel are the important challenges of our time. At the same time, the production of plant raw materials is a significant factor in environmental pollution. After all, combustion remains the main mean of plant residues disposal. Nowadays a lot of attention is paid to air pollution throughout the world. The World Health Organization has highlighted the damage that air pollution causes to humankind (WHO, 2018). The Fact Sheet of the Commission for Environmental Cooperation stated that combustion emission of agricultural raw materials contained an unacceptable amount of dioxins. Prospects for reduction of flue gas from agricultural waste are to be analysed (CEC, 2014).

A majority of EU Member States have implemented the ban of open air burning of agricultural plant waste according to Amann M., (2017). Especially hazardous is air pollution with carbon monoxide, carbon dioxide and other chemicals emitted by the combustion processes (Gaba A., Iordache S.F., 2011). The effects of agricultural waste incineration related to soil, air, water and health were examined by Kumar P., (2015). There are many studies on the potential uses of plant agricultural waste. The manufacture of fuel briquettes from various plant wastes was proposed except for oleaginous flax (Gregory M., 2016). Oleaginous flax is an important industrial culture. It has a worldwide distribution and it is rapidly developing in Ukraine (Yaheliuk S. *et al.*, 2018). However, there is a problem of processing stem fibre mass (SFM) after collecting seeds. The definition of problems and directions of use can be found in Berglund D.R. (2002).

The use of flax waste as a component of composite materials was suggested by Baley C., *et al.* (2019). There are also attempts to use the oleaginous flax waste collection to manufacture fibre. The results of a study of the possibility of fibre extraction from oleaginous flax were obtained by Ouagne P. *et al.*, (2017). The studies of oleaginous flax fibres were conducted thorough out by Tuluchenko N.*et al.*, (2016). An innovative technology to obtain such fibre was proposed by Chursina L., (2019). There have been attempts to use oleaginous flax for the production of biodiesel (Dixit S. *et al.*, 2012). However, all scientists note the high-energy consumption of such production and the need for significant financial costs.

The production of solid biofuel from oleaginous flax does not require significant financial costs and can provide the solutions to many problems. Until now, this kind of production was not possible, since modern means of forming rolls from agricultural materials were solely able to produce the rolls of a huge diameter up to 3.5 m (Gummert M. *et al.*, (2020). This makes them impossible to be used as a fuel for modern boilers, since the dimensions of boilers fuel holes are limited in diameter (up to 0.9 m).

The authors proposed a technology and equipment for manufacturing small-sized fuel rolls (SFR) as a solid fuel from oleaginous flax waste (Didukh V. *et al.*, 2019).

However, the dependency of the effective time of the small-sized fuel rolls combustion on their technological parameters has not been determined. There is also no assessment on such fuel combustion environmental safety. Smoke gases in the solid fuel boilers chimneys during the combustion of oleaginous flax waste SFR have not been analysed. The authors consider the raised questions in this article.

## MATERIALS AND METHODS

The research was conducted to justify the feasibility of producing a new type of biofuel - SFR based on the study of its effective combustion time and the quantitative and qualitative composition of smoke gases from combustion in solid fuel boilers.

The factors that influence the efficient combustion of solid biofuel are the geometric dimensions (diameter  $X_1$ ), the humidity ( $X_2$ ), and the density of the material ( $X_3$ ). Therefore, the small-sized fuel rolls made of oleaginous flax residues, with a diameter of 300, 400, 500 (mm) were produced for the research; the roll density was 80, 95, 110 ( $\text{kg/m}^3$ ); the SFR humidity was changed by 10, 15, 20 (%). The experimental combustion was performed in the KALVIS 400 boiler (Lithuania).

The experimental study of the effective time of combustion was conducted by the method of experiment mathematical planning. We used a symmetric non-positional Box-Behnken Experimental Design (Aslan N., Cebeci Y., 2007). In order to implement a three-factor experiment up to this plan, it is necessary to conduct 15 experiments.

For the purpose of compiling the factors and levels of variation table (Table 1) we took into account the previous studies' results and information available from written sources. The Box-Behnken plan is designed to use three levels for each factor: upper (+1), main (0), and lower (-1).

**Table 1**

**Variables and their levels in Box-Behnken design**

Levels of variation	$X_1$ - Roll diameter D, mm	$X_2$ - Material humidity W, %	$X_3$ - Roll density $\rho$ , $\text{kg/m}^3$
Upper (+1)	500	20	110
Main (0)	400	15	95
Lower (-1)	300	10	80
Range of variation	100	5	15

The experiment planning matrix is presented in Table 2 in a coded form. The order of experiments was established using a table of random numbers. The response function (effective burning time) in the area of factor, space is presented as a nonlinear regression equation (1):

$$Y_i = b_0 + b_1 X_1 + b_2 X_2 + b_3 X_3 + b_{12} X_1 X_2 + b_{13} X_1 X_3 + b_{23} X_2 X_3 + b_{11} X_1^2 + b_{22} X_2^2 + b_{33} X_3^2 \quad (1)$$

The obtained data were processed using the developed program in the Mathcad environment.

During the experiments, both the qualitative and quantitative composition of smoke gas emission produced by the combustion of each variant of oleaginous flax waste SFR were controlled.

A portable gas analyser Testo 350 was used for the analysis of smoke gases from the combustion of oleaginous flax waste SFR ([www.testo350.com](http://www.testo350.com)). It has everything required to study the parameters of the combustion process of oleaginous flax waste SFR.

The device can be used in the adverse environmental conditions. The Testo 350 gas analyser consists of three separate parts: a control unit, an analyser unit and measuring probes. The main parameters of Testo 350 include the oxygen  $\text{O}_2$ , carbon monoxide CO and nitrogen oxides  $\text{NO}_x$  volume fractions measurements. The qualitative and quantitative composition of the oleaginous flax SFR combustion products' residues were measured using a portable Testo 350 gas analyser (Fig. 1).

**Table 2**

**Design of experiment**

Experiment number	Roll diameter D, mm	Material humidity W, %	Roll density $\rho$ , $\text{kg/m}^3$
1	500	20	95
2	300	20	95
3	500	10	95
4	300	10	95
5	500	15	110
6	300	15	110
7	400	15	80
8	400	15	80
9	400	20	110

Experiment number	Roll diameter D, mm	Material humidity W, %	Roll density $\rho$ , kg/m <sup>3</sup>
10	400	10	110
11	400	20	80
12	400	10	80
13	400	15	95
14	400	15	95
15	400	15	95

The oxygen O<sub>2</sub>, carbon monoxide CO and nitrogen oxides NO<sub>x</sub> volume fractions in smoke gases were measured. These parameters of the gas-air environment make it possible to determine rational modes of fuel combustion with a maximum coefficient of performance (COP) and with minimal emission of harmful gases into the atmosphere. Smoke gases from the combustion of oleaginous flax SFR samples were studied. An ordinary firewood was burned and smoke gases were studied as well. A KALVIS-400 boiler was used for the purpose of research. It is an industrial solid fuel boiler with manual fuel loading.

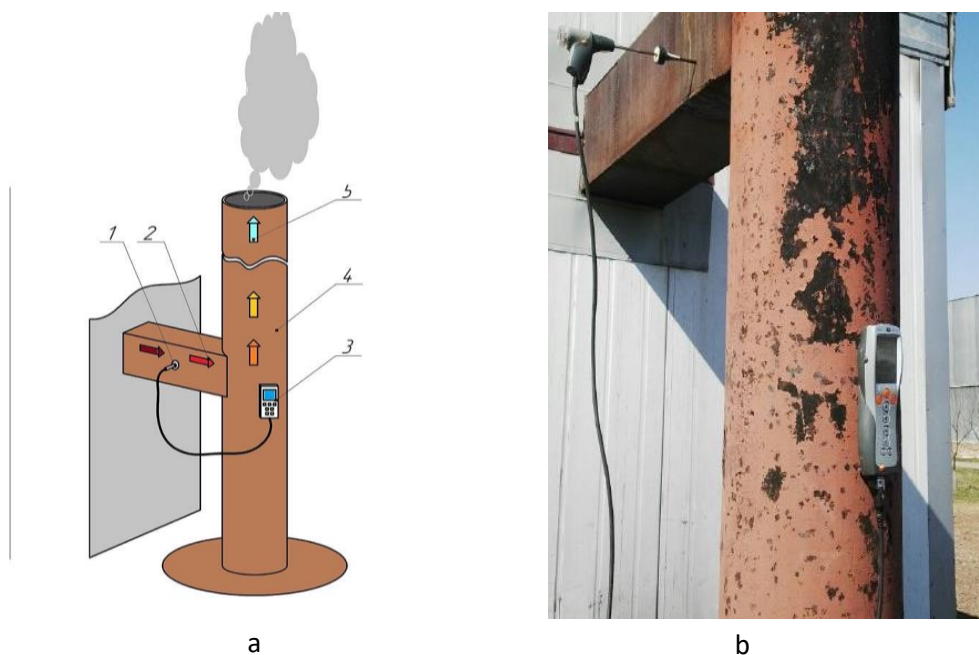


**Fig. 1 - A study of the qualitative and quantitative composition of the smoke gases obtained from the combustion of oleaginous flax SFR waste**

a) The scheme of analysis of smoke gases produced by conventional wood combustion:

1. Sensor probe of gas analyser Testo 350, 2. The chimney of the boiler, 3. Gas analyser Testo 350, 4. Tube, 5. The motion of smoke gases; b) picture of the study process

The investigation was carried out in the following order. Firstly, the sensors were put into thermal mode, and the presence of an indication of the volume fraction of oxygen O<sub>2</sub> and carbon monoxide CO was checked. Secondly, the installation of zero value for the carbon monoxide CO sensor was controlled. In order to make it, the hose to supply the mixture from the gas duct was disconnected from the CO sensor. Lastly, the gas analyser was ready to take measurements after monitoring the condition of the oxygen O<sub>2</sub> and carbon monoxide CO channels.

## RESULTS AND DISCUSSION

The experiment conducted according to the Box-Behnken design allows to obtain a mathematical model in the form of a regression equation that allows us to set the effective combustion time of SFR based on its technological characteristics: diameter, humidity and density. An analysis of the regression equation makes it possible to evaluate the performance characteristics of the new type of solid biofuel.

Processing data from the results of a three-factor experiment using a three-level second-order plan and using a program created in Mathcad - 2015 allowed us to obtain the regression equation for the effective

combustion time of SFR from flex stem fibre mass at different values of its technological characteristics (2).

The adequacy of the received regression equation was checked using the F - Fischer criterion according to (Aslan N., Cebeci Y., 2007). The calculated value of the Fisher criterion is  $F_{count}=6.642$  with the variance of inadequacy  $S^2=3.417$  and the variance of reproducibility  $S_y^2=0.514$ . The tabular value of the Fisher criterion at the accepted 5% significance level and degrees of freedom  $f_1=2, f_2=9$  was  $F_{table} = 19.4$ . Since  $F_{count} = 6.642, F_{table} = 19.4$  the resulting model is adequate.

Finally, the regression equation for the effective combustion time of flex stem fibre mass SFR due to different values of its technological characteristics with natural factors was (2):

$$Y(D, W, \rho) = 76.90 + 0.10 \rho + 1.98 W + 0.24 D + 0.001 \rho^2 + 0.07 W^2 + 0.0003 D^2 \quad (2)$$

where:  $D$  – roll diameter, mm;  $W$  – material humidity, %;  $\rho$  – roll density,  $\text{kg/m}^3$

The response surfaces (Fig. 2) and their contour plots (Fig. 3) are constructed using the regression equation (2).

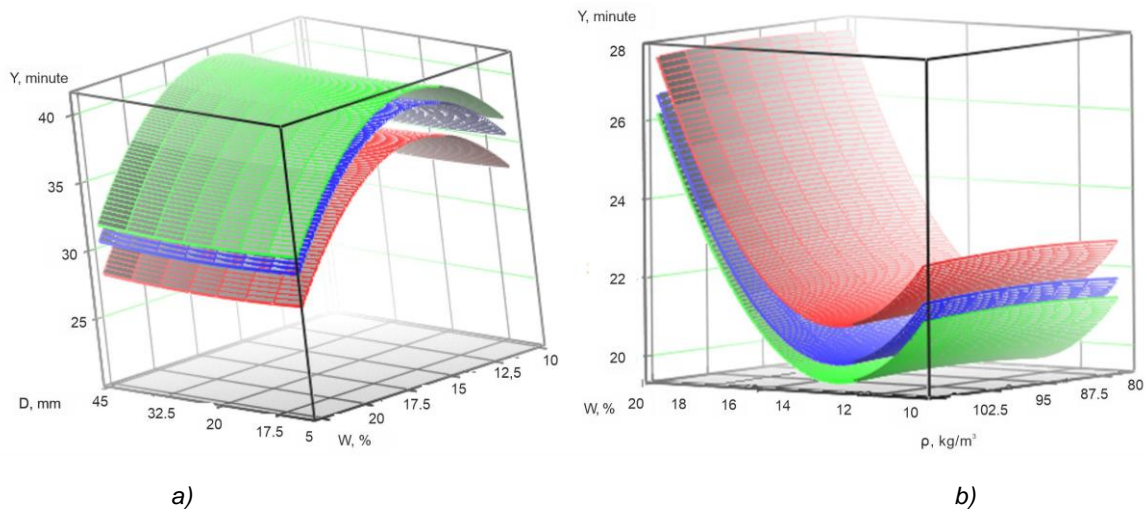


**Fig. 2 - The surface response characterizing the effective combustion of SFR, taking into account:**  
 a) the diameter of the SFR and humidity of the SFM from oleaginous flax waste; b) the density of SFR and humidity of the SFM

As can be seen from the graphs, the optimal effective combustion time of the rolls (25-35 minutes) will be provided if the humidity of the flax stem fibre mass (SFM) from oleaginous flax is within 10-12%. In Fig. 2, it is shown that the SFR diameter does not significantly affect the effective combustion time. However, it is limited by the technological characteristics of the heating boiler. In turn, according to Fig. 3, the rational value of the SFR density is within 80  $\text{kg/m}^3$ . Ensuring rational SFR parameters depends on the quality of the manufacturing process and the quality of the oleaginous flax harvesting.

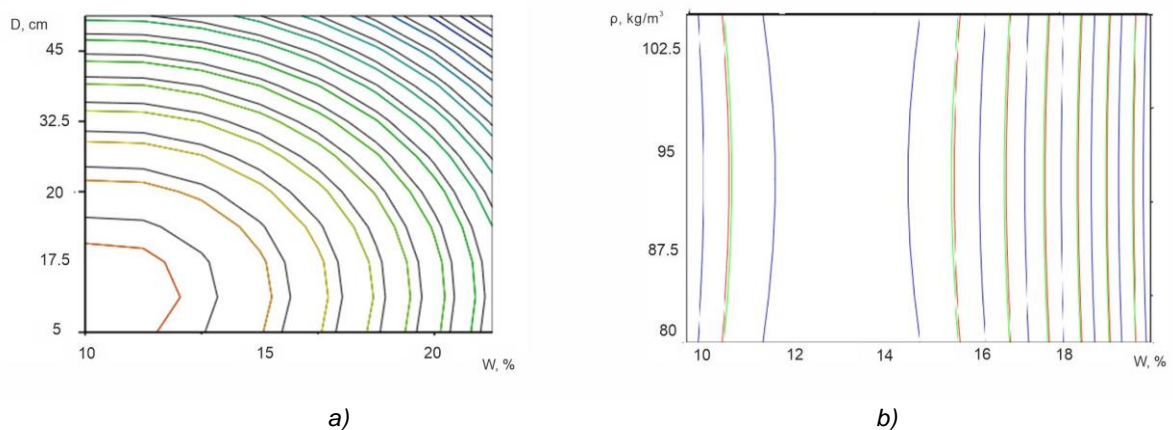


**Fig. 3 - The contour plot of the response surfaces**  
 a) diameter of SFR and humidity of flax stem fibre mass (SFM) from oleaginous flax;  
 b) density of SFR and humidity of flax stem fibre mass (SFM) from oleaginous flax

An analysis of the surfaces in Fig. 2a shows that the diameter of the SFR does not affect the effective burning time. Therefore, according to *Yaheliuk S et al, (2019)*, the SFR diameter of 40-45 cm can be recommended. One of the important indicators for evaluating the quality of SFR from oleaginous flax waste is the quantitative and qualitative analysis of flue gases from combustion. The research was carried out in the boiler room of the sports complex of the Lutsk National Technical University. The boiler room is equipped with a typical KALVIS-400 hot water boiler. It is adapted for the combustion of firewood, wood waste, briquettes, coal, etc. For comparison, the combustion was carried out and the flue gases of the combustion of conventional firewood were studied. The results of the study of flue gases from the combustion of SFR from oleaginous flax waste and conventional firewood are presented in Table 3.

Table 3

Parameters of flue gases from the combustion of SFR from oleaginous flax waste and firewood

Parameter Description	Unit	Regular Firewood	SFR from oleaginous flax waste
Boiler heat output	Gcal/h	0.341	0.447
Flue gas temperature in the stack mouth	°C	111.1	112.6
Concentration in the flue gas:			
CO <sub>2</sub>	%	4.27	6.6
O <sub>2</sub>	%	16.6	14.2
CO	ppm	3822	92
NO <sub>x</sub>	ppm	25	38
Excess air ratio		4.75	3.07
Heat loss:			
– with flue gases	%	16.01	11.00
– with chemical undersupply	%	5.003	0.085
– to the environment	%	0.55	0.48
Boiler COP	%	78.44	88.44
Fuel consumption	kg/h	120	120
Specific fuel consumption per 1 Gcal of heat produced:	kg/Gcal	182.12	161.52
Saving specific fuel equivalent	kg/Gcal		20.60
Number of boiler hours	h.	4380	4380
Annual equivalent fuel savings	tons/year.		40.31
NO <sub>x</sub> concentration reduced to normal conditions and O <sub>2</sub> =3%	mg/m <sup>3</sup>	209.46	205.84
CO concentration reduced to normal conditions and O <sub>2</sub> =3%	mg/m <sup>3</sup>	19590.91	304.89
Annual fuel economy	m <sup>3</sup> /year		34.367

According to the data obtained, it was found that SFR from oleaginous flax waste during combustion in solid fuel boilers of the KALVIS-400 type give a heating capacity (boiler capacity) higher 0.1 Gcal/hour than in the case of firewood. The experiments showed that the SFR from oleaginous flax waste is characterized by a significant decrease in the content of carbon monoxide CO (up to 92 ppm). The CO content for firewood is 3822 ppm. A significant decrease in the concentration of CO<sub>2</sub> was established, reduced to normal conditions and O<sub>2</sub> = 3%. This means that less soot will form on the walls of the boiler, which in turn increases the efficiency and reduces labour costs for cleaning the boiler. It is also a reduction in heat loss from 21.69% for firewood to 11.56 %for SFR from oleaginous flax waste. However, there is a slight increase in nitrogen oxides NO<sub>x</sub> in the SFR from oleaginous flax waste. The results of the study showed that the flue gases from the combustion of SFR from oleaginous flax waste comply with the environmental standards.

## CONCLUSIONS

Studies have shown the prospects of using small-sized fuel rolls. After all, their production and use as a new type of solid biofuel makes it possible to solve several important tasks at once: processing stem fibre mass that remains in the field after harvesting oleaginous flax, providing the population with fuel to heat buildings, and obtaining new innovative products from ecological plant raw materials.

A regression equation (mathematical model) can assist to determine the effective combustion time of SFR. The model takes into account the technological parameters of small fuel rolls: diameter, density, humidity.

The analysis of the response surfaces and their contour plots shows that SFR humidity is the parameter that affects the most the combustion time.

Considering the conditions for manufacturing and storage of this type of fuel, it is recommended to keep the humidity within 10-12% to achieve maximum efficiency.

The rational density of the roll is considered to be 80 kg/m<sup>3</sup>. The reduction of harmful emission of carbon monoxide CO and the concentration of carbon dioxide CO<sub>2</sub> has been established. It has been proved that SFR obtained from oleaginous flax waste is characterized by an increase in heating capacity of the boiler by 0.1 Gcal/h and a reduction of harmful CO emission of up to 92 ppm compared to firewood (3822 ppm).

The paper proves the sufficiency and environmental safety of using SFR made of oleaginous flax waste. In the future, the authors would recommend to develop technical regulations for small fuel rolls. This would allow producers to efficiently produce and consumers to use this type of solid biofuel.

## REFERENCES

- [1] Amann M., (2017), Measures to address air pollution from agricultural sources. Access mode: [https://ec.europa.eu/environment/air/pdf/clean\\_air\\_outlook\\_agriculture\\_report.pdf](https://ec.europa.eu/environment/air/pdf/clean_air_outlook_agriculture_report.pdf);
- [2] Aslan N., Cebeci Y., (2007), Application of Box–Behnken design and response surface methodology for modeling of some Turkish coals. *Fuel*. Vol.86, Issues 1–2, 90-97. <https://doi.org/10.1016/j.fuel.2006.06.010>.
- [3] Baley C., Gomina M., Breard J., Bourmaud A., Drapier S., Ferreira M., Le Duigou A., Liotier P.J., Ouagne P., Soulat D., Davies P., (2019), Specific features of flax fibres used to manufacture composite materials. *International Journal of Material Forming*. Volume 12, Issue 6, pp 1023–1052;
- [4] Berglund D.R., (2002), Flax: New uses and demands. p. 358–360. In: J. Janick and A. Whipkey (eds.), *Trends in new crops and new uses*. ASHS Press, Alexandria;
- [5] Chursina L., Tikhosova H., Holovenko T., Shovkomud O., Kniaziev O., Yanyuk T., (2019), Innovative technologies of oilseed flax straw mechanical processing and quality of obtained fibres. *INMATEH - Agricultural Engineering*. Vol. 57, No. 1 pp. 207 – 214, Bucharest / Romania;
- [6] Didukh V., Busniuk V., Boychuk B., Yaheliuk S., (2019), *Fuel Roll Forming Machine*. Patent for useful model 135725 Ukraine, MPC 2006.01 A01D43/04 / № u201901620; Declared 18.02.2019; Published by 10.07.2019, Byul. No.13, 4 p;
- [7] Dixit S., Kanakraj S., Rehman A., (2012), Linseed oil as a potential resource for bio-diesel. *Renewable and Sustainable Energy Reviews*. Volume 16, Issue 7, pp 4415–442. <https://doi.org/10.1016/j.rser.2012.04.042>;
- [8] Gaba A., Iordache S.F., (2011), Reduction of Air Pollution by Combustion Processes, *The Impact of Air Pollution on Health, Economy, Environment and Agricultural Sources*, Edited by Mohamed K. Khallaf, IntechOpen, DOI: 10.5772/16959. <https://www.intechopen.com/books/the-impact-of-air-pollution-on-health-economy-environment-and-agricultural-sources/reduction-of-air-pollution-by-combustion-processes>
- [9] Gummert M., Van Hung N., Chivenge P., Douthwaite B. (2020), Sustainable Rice Straw Management Mechanized Collection and Densification of Rice Straw. Springer International Publishing, Switzerland, Chapter 2, 192p. ISBN: 978-3-030-32373-8;
- [10] Marian, Gr., (2016), *Solid biofuels: producer and property (Biocombustibilii solizi: producere și proprietăți)*, Tipogr. “Bons Offices”, 172 p, ISBN 978-9975-87-166-2 / Chișinău / Moldova;
- [11] Kumar P., Kumar S., Joshi L., (2015), Socioeconomic and Environmental Implications of Agricultural Residue Burning, A Case Study of Punjab, India. *Springer Briefs in Environmental Science*, Springer, ISBN 978-81-322-2146-3, 157 p., doi 10.1007/978-81-322-2014-5\_7;
- [12] Ouagne P., Barthod - Malat B., Evon P., Labonne L., Placet V., (2017), Fibre extraction from oleaginous flax for technical textile applications: influence of pre-processing parameters on fibre extraction yield, size distribution and mechanical properties. *Procedia Engineering*. Vol. 200, pp. 213-220;
- [13] Tuluchenko N., Chursina L., Kruglii D., (2016), Homogeneity investigation of oil flax processing products by quality indexes. *Eastern-European Journal of Enterprise Technologies* Vol 6, No 3 (84), pp. 46-53. [doi.org/10.15587/1729-4061.2016.83593](https://doi.org/10.15587/1729-4061.2016.83593);
- [14] Yaheliuk S., Tkachuk V., Rechun O., (2018), Formation of agricultural crops market in Ukraine. (Формування ринку сільськогосподарських культур в Україні). *Technical sciences and technologies: Scientific journal Chernigov NTU* No 1 (11), pp. 195-206.

- [15] Yaheliuk S., Didukh V., Tom'yk V., (2019), Justification of the new Technology of Processing Residues of Flax Stem Mass in Western Polissya. *Teka Commission of Motorization and Energetic in Agriculture*. Vol. 19, No.1, pp. 5-12;
- [16] \*\*\**Air Quality Standards* (2019). <https://ec.europa.eu/environment/air/quality/standards.htm>;
- [17] \*\*\*CEC, (2014), *Burning Agricultural Waste: A Source of Dioxins*. Montreal, Canada: Commission for Environmental Cooperation. 6 p.;
- [18] \*\*\*Technical Safety BC, (2018), *Guidelines for the Gas Service Industry: Carbon Monoxide Access mode*: <https://www.technicalsaftybc.ca/guidelines-gas-service-industry-carbon-monoxide>;
- [19] \*\*\*WHO, (2018), 9 out of 10 people worldwide breathe polluted air, but more countries are taking action. Access mode: <https://www.who.int/news-room/detail/02-05-2018-9-out-of-10-people-worldwide-breathe-polluted-air-but-more-countries-are-taking-action>.

## DEVELOPMENT OF THE AERODYNAMIC DRYING METHOD FOR THE CHOPPED VEGETAL MASS

### /

### ELABORAREA METODEI DE USCARE AERODINAMICĂ A MASEI VEGETALĂ TOCATĂ

**Hăbășescu I.<sup>1)</sup>, Cerempei V.<sup>2)</sup>, Molotcov Iu.<sup>1)</sup>, Popa L.<sup>3)</sup>**

<sup>1)</sup> "Mecagro" Institute of Agricultural Technology, Republic of Moldova-Chișinău / Moldova;

<sup>2)</sup> State Agrarian University of Moldova - UASM Chisinau / Republic of Moldova

<sup>3)</sup> National Institute for Research-Development of Machines and Installations Designed  
for Agriculture and Food Industry - INMA Bucharest / Romania

Tel: + (373) 796 77728; E-mail: cerempeivalerian@gmail.com

DOI: <https://doi.org/10.35633/inmateh-62-39>

**Keywords:** *vegetal mass, thermal agent, flow, vortex dryer, conical pipe*

#### ABSTRACT

*The article presents the theoretical study and elaborates the calculation methodology of the technological and constructive parameters of the aerodynamic dryers: the saltation speed of the vegetal mass particles, the speed of the thermal agent flow, the length of the dryer pipes and the duration of the moist particles contact with the thermal agent. The comparative analysis of the aerodynamic dryers was performed: with direct and vortex flow. The advantages of vortex dryers, recommended for implementation in production, are theoretically argued. In the research of the developed conical shape dryer, it has been identified a phenomenon of vortex flow parameters self-regulation to the material to be dried inside the dryer, under the condition of varying the amount of material feeding the dryer, allowing automatic creation of optimal drying conditions, when the supply of raw material and/or its humidity were changed within the studied limits. It has been demonstrated the possibility to increase up to 12-15 times the duration of contact of the raw material particles with the thermal agent and, respectively, to reduce the overall dimensions of the developed vortex dryer, compared to the known ones, which have direct air flow.*

#### REZUMAT

*În acest articol este prezentat studiul teoretic și elaborată metodică de calcul a parametrilor tehnologici și constructivi ai uscătoarelor aerodinamice: viteza de flotație a particulelor masei vegetale, viteza fluxului agentului termic, lungimea conductelor uscătoarelor, durata contactului particulelor umede cu agentul termic. A fost efectuată analiza comparativă a uscătoarelor aerodinamice: cu curentul direct și turbionar. Sunt argumentate teoretic avantajele uscătoarelor turbionare, recomandate pentru implementare în producție. În procesul cercetărilor uscătorului de forma conică elaborat, a fost identificat un fenomen de autoreglare a parametrilor fluxului turbionar cu materialul supus uscării în spațiul interior al uscătorului, în condițiile varierii cantității de materie primă care alimentează uscătorul, ceea ce a permis crearea automată a condițiilor optime de uscare, atunci când a avut loc schimbarea dozei de alimentare a materiei prime și/sau a umidității acesteia în limitele studiate. S-a demonstrat posibilitatea majorării de până la 12-15 ori a duratei contactului particulelor de materia primă cu agentul termic și respectiv, micșorării dimensiunilor de gabarit ale uscătorului turbionar elaborat, în raport cu cele cunoscute, care au curentul de aer direct.*

#### INTRODUCTION

Specialists in the world economy pay increased attention to biomass drying technologies, with the aim of conditioning the raw material, which in most cases consists in reducing humidity by up to 8-12% (in this case and further on considered relative humidity). It should be noted that the humidity of the raw material in the initial phase can far exceed the required level. For example, tree branches after cutting have a humidity of up to 50%. For economic reasons, reducing the high humidity of the vegetal mass is most rational to be achieved under natural conditions, using solar energy, removing most or all of the excess moisture (*Ericsson and Werner, 2014; Iftekhar et al., 2017*).

The final value of the moisture of the dried vegetal mass under natural conditions depends a lot on the humidity of the surrounding air. The porous material of the vegetal mass has the property of removing or absorbing water vapour from the surrounding air, obtaining the so-called equilibrium humidity. The dependence of the equilibrium humidity values of the wood material (fig.1) (*Ivanov, 1956*) demonstrates that, for example,

at the ambient air temperature  $t_a = 25^\circ\text{C}$  and its humidity  $\varphi_a = 85\%$  (real values for the climate of Moldova) wood can be dried under natural conditions up to a minimum humidity of 18% (point A in fig.1). Therefore, in order to obtain the raw material in accordance with the technological requirements, it must be further dried under artificial conditions.

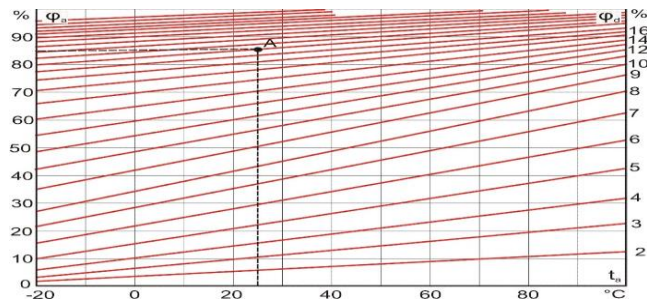


Fig. 1 - Humidity of wood particles  $\varphi_d$  as a function of temperature  $t_a$  and humidity  $\varphi_a$  of the atmospheric air (Ivanov V., 1956)

Of all the variety of artificial drying methods and installations (Gavrilenkov *et al.*, 2014) the most promising, in our view, is convective aerodynamic drying, in which the thermal agent (air or an air mixture with flue gas), in addition to performing the base function, it also performs the transportation of raw material particles, simplifying the construction of the dryer. At the same time, the use of flue gas as a thermal agent increases the efficiency of the dryer.

In the typical technological process (fig.2) the aerodynamic drying of the chopped vegetable raw material is performed with the use of flue gas, produced by the thermal generator 1, in which different fuels can be used for combustion. To decrease the flue gas temperature from  $500\text{--}700^\circ\text{C}$  to  $150\text{--}300^\circ\text{C}$ , they are diluted with fresh air using the temperature regulator 2 (Gavrilenkov *et al.*, 2014; Hăbășescu *et al.*, 2015; Hăbășescu *et al.*, 2016b). Moist raw material is further introduced into the mixture of fresh air and flue gas using the mixer 3, which moves in the direction of the aerodynamic dryer 4. From the moment of contact with the thermal agent, water vapour is extracted from the raw material due to heat convection. The dried particles of the raw material ( $\varphi_d = 8\text{--}12\%$ ) are conveyed by the thermal agent into the cyclone 5, where they separate from the thermal agent with high humidity and are transported for further processing. The thermal agent used is discharged into the atmosphere by means of the suction fan 6, which at the same time ensures the required amount of fresh air in the burner (heat generator) 1.

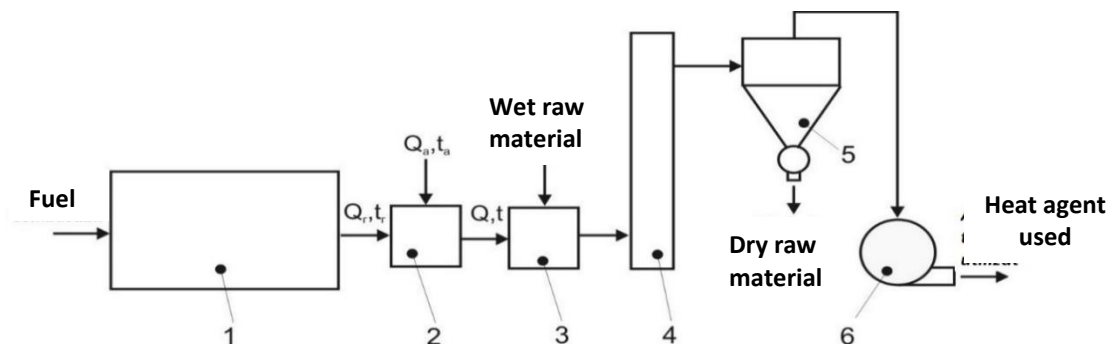


Fig. 2 - Scheme of the technological process of the chopped vegetable mass aerodynamic drying using flue gas

1- thermal generator; 2- device for regulating the temperature of the flue gases; 3- mixer; 4- vertical aerodynamic drying pipe (dryer); 5- cyclone; 6- fan

In some versions of placing the components of the drying equipment, the fan 6 is installed between the dryer 4 and cyclone 5. In this case, two phenomena occur simultaneously: the positive one (increased pressure in the cyclone, which improves the operating conditions of the shutter) and the negative one (intense abrasive wear of the fan blades).

The incontestable advantages of the aerodynamic dryers contribute to their widening spread in various branches of industry and agriculture (Konovalov *et al.*, 2002; <http://www.ecomihis.ro/>), but, in our view, some useful properties of the vortex flows in the aforementioned dryers, are not given deserved importance. This refers, first of all, to the Ranque-Hilsch vortex effect, which consists in the separation of fluids into two phases during their vortex motion in a cylindrical pipe (Guțol, 1997; Koleadin & Vinogradov, 2004). As a result, the

helical flow with a higher temperature is formed at the periphery, and in the centre, the helical flow with a lower temperature (fig. 3). It should be noted that the rotation of the central flow takes place in the opposite direction to that of the periphery. Unfortunately, with the vortex flows speed that are used in the drying processes, the thermal phenomena of the Ranque-Hilsch effect practically do not occur, but the flow configuration is maintained even at relatively low speeds, which is important for our subsequent observations.

The configuration of the vortex flows of the fluids in pipes with different shapes, which can be assimilated with the vertical aerodynamic dryers, is presented in fig. 3.

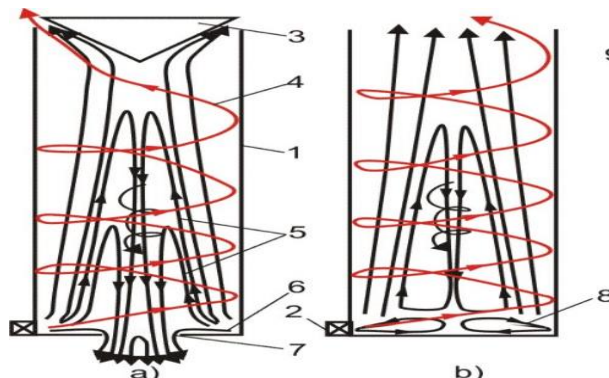


**Fig. 3 - Configuration of gas flows in pipes with different shapes (Guřol, 1997)**

a) cylindrical pipe with rolling valve and bottom diaphragm;  
b) cylindrical pipe with free flow discharge and compact bottom

The first configuration (fig. 3a) illustrates the classical distribution of flows with currents in opposite directions in Ranque pipe. The peripheral vortex flow is formed by a vortex device 2, which has a tangential or snail shape and is located at the bottom of the pipe together with the bottom diaphragm 7. At the top of the pipe there is a metering valve 3, which together with the cylindrical housing 1 forms an annular outlet. As a consequence of the movement of the peripheral vortex flow from the vortex device to the upper annular outlet is the formation of a vortex flow in the opposite direction which is discharged through the bottom diaphragm (Fig. 3a). An explanation of the cause of the flow in the opposite direction is given by *Guřol A., (1997)*: "with the movement of the flow that rotates intensely along the pipe, its circular (tangential) speed decreases because of the braking in contact with the chamber walls, the radial pressure difference decreases, respectively. If the speed of the translational movement of the gas along the pipe, which simultaneously rotates, is relatively low, i.e. the gradient of the longitudinal pressure drop at the periphery of the pipe is insignificant, then the rapid decrease of the radial pressure difference along the pipe leads to a negative pressure gradient along the axis of the pipe which is also the cause of the gas flow in the opposite direction". Although currently there is a large number of explanations and mathematical equations which describe vortex flows, a viable theory that fully describes the dynamics of such flows is still missing. However, existing knowledge allows the practical application of vortex flows.

If the bottom diaphragm and the metering valve are missing in the vortex pipe, then the configuration of the vortex flows is different: a new vortex area appears with the frontal flow 8, which is formed by the interaction of the ascending peripheral flow and the descending central flow. In both cases (fig. 3a, 3b) the downward flow takes the form of a cone, which is caused, in our opinion, by the displacement of the peripheral vortex flow from the inlet to the outlet and the decrease of its tangential velocity due to friction with the inner walls of the pipe. As a result, the diameter of the vortex path increases and more and more "pushes" on the central region, compressing the newly formed downward vortex flow.

Technologies and installations for drying vegetal plant mass for energy needs, as well as feed and food needs, have been researched for several years. The result of this research is the development and assimilation in production of aerodynamic dryers, but there remain a number of problems that need to be solved: increasing energy efficiency and reducing the specific cost of dry raw material. Therefore, the purpose of our work is to conduct research on technological and constructive parameters of aerodynamic dryers and to develop the improved method and installation for drying vegetal mass.

## MATERIALS AND METHODS

Carrying out the research requires development and exploitation of activities of aerodynamic dryers which have improved functional parameters to dry the vegetal mass. The first stage of this research is the theoretical study of the mentioned dryers.

In order to achieve the established goal, the following objectives were met:

- developing a concept of research and a study protocol;
- carrying out the analysis of the bibliographical references regarding the patterns of the aerodynamic dryers' construction and also the mathematical dependencies of the vegetal particles saltation speed and the working speed of the flow of the thermal agent as a function of the particles' as well as thermal agent's properties;
- determining, on this basis, of the theoretical postulates;
- developing the methodology for calculation of constructive and technological parameters;
- developing the method and improved construction of the aerodynamic dryer;
- physical modelling and studying of the working process inside the aerodynamic dryers.

In order to be able to transport the moist particles, it is necessary that the speed of the thermal agent exceeds the saltation speed of the particles at the given temperature. For the vertical pipe, which is also the case of the aerodynamic dryer, the particles' saltation speed can be calculated according to the equation given by *Boico V., (2008)*.

$$V_f = Re \frac{\nu}{d}, \text{ [m/s]} \quad (1)$$

where:

$Re$ - is the Reynolds criterion number;

$\nu$  - kinematic viscosity of the air at the maximum temperature of the working process, [m<sup>2</sup>/s];

$d$  - equivalent diameter of the particles, [m].

The equivalent diameter  $d$  of the particle is the diameter of the sphere, calculated based on the formula:

$$d = 1,24 \sqrt[3]{\frac{M}{\rho_t}}, \quad (2)$$

where:

$M$  - is the mass of a particle, [kg];

$\rho_t$  - density of the transported particulate material, [kg/m<sup>3</sup>]

In this case (Equation 1) the Reynolds criterion does not indicate the character of the movement of the whole flow in relation to the dryer pipe, but characterizes the movement of the vegetal particles in relation to the heating agent:

$$Re = \frac{Ar(1 - \beta)^{4,75}}{18 + 0,61\sqrt{Ar(1 - \beta)^{4,75}}} \quad (3)$$

where  $\beta$  is the volume ratio of the solid phase in the air flow ( $0 < \beta < 1$ ):

$$\beta = \frac{1}{1 + \frac{\rho_t}{\mu \rho_a}} \quad (4)$$

Where:

$\rho_a$  is the air density at the maximum temperature of the process [kg/m<sup>3</sup>];

$\mu$  – ratio of particles in the heat flow:  $\mu = \frac{m_t}{m_a}$  (when  $m_t \rightarrow 0$ , then  $\mu \rightarrow 0$  and  $\beta \rightarrow 0$ );

$m_t$  - mass of transported particles, [kg];

$m_a$  - mass of air used for transport, [kg];

$Ar$  - Archimedes' criterion (number).

$$Ar = \frac{d^3 g (\rho_t - \rho_a)}{\rho_a \nu^2} \quad (5)$$

Archimedes number  $Ar$  presents a similarity criterion that characterizes the ratio between Archimedes' force (caused by the difference in densities at various locations in the studied system) and the viscosity forces in the base flow. The mentioned number is used in the calculations in which the movement of bodies in the fluid environment is studied, caused by the inhomogeneous density in the "body - external environment" system (*Chemist's Guide, 1968; Önsan Zeynep Ilsen and Avci Ahmet Kerim, 2016*).

According to the research conducted by *Boico, (2008)*, the reliable transport of the particles will occur when the actual speed of the air will exceed the value calculated by equation (1).

In vertical pipes, the real value of the air speed is calculated based on the equation:

$$V = 2 V_f, \text{ [m/s]} \quad (6)$$

For horizontal pipes this value will be:

$$V_o = 2 V = 4 V_f \text{ [m/s]} \quad (7)$$

It is easy to show that, subject to the conditions from equations (6) and (7), the diameter of the vertical drying column can be greater than at least 1.4 times that of the horizontal pipe. The above condition is used in practice (fig.2) to maximize the time of maintaining the material subjected to the drying process in the flow of the thermal agent.

Using Sveatcov's empirical equation (Zakirov and Zakirova, 2016; Teterin, 1972), the saltation speed,  $V_f$ , can be calculated with the necessary precision, for particles with an equivalent diameter  $d > 0.4$  mm:

$$V_f = 0.14 \sqrt{\frac{\rho_t}{(0,02 + \frac{\varepsilon}{d}) \rho_a}} \text{ [m/s]} \quad (8)$$

where  $\varepsilon$  is the coefficient taking into account the shape of the particles.

For particles with a square or semi-round cross section,  $\varepsilon = 1.1$ ;

For particles with a rectangular section or of a similar shape,  $\varepsilon = 0.9$ .

If  $d < 0.4$  mm, it is recommended using the empirical equation from Arhangheliskii V. (Zakirov and Zakirov, 2016):

$$V_f = 0.135 \rho_t^{0,5} \cdot d^{0,25}, \text{ [m/s]} \quad (9)$$

According to the authors Orehova and Uvarov, (2013), Romancov and Raşcovscaia, (1968), the velocity of the transported particles  $V_t$  is lower than that of the air flow  $V$ , the difference is equal to the saltation velocity  $V_f$ :

$$V_t = V - V_f \text{ [m/s]} \quad (10)$$

Where:

$V$  is the velocity of the thermal agent in a particular sector of the aerodynamic dryer [m/s].

To achieve the purpose, at the initial stage, the Institute for Agricultural Technology MECAGRO - Chisinau, Republic of Moldova (Hăbăşescu et al., 2016a), using the ANSYS software, developed computer simulations of the vortex flow in the dryer column. Subsequently, the experimental research was performed on the same model of the dryer, installed in the technological line as shown in fig.2.

As raw material there have been used tree branches and straw, which have been chopped, with the following fractional distribution (% mas.): particle size  $> 5$  mm - 3%; 3...5mm - 33%; 2...3 mm - 30.2%; 1...2 mm - 19.3%;  $< 1$ mm - 14.5%.

Raw material moisture is within 25 and 30%, which represents the maximum level for practical cases. The mass of the samples was determined by weighing with the electronic scale Alex Kern with a  $\pm 1\%$  margin of error, and the duration was recorded with the SOP timer pr-2a-2-010. The temperature was measured with a thermocouple and an electronic device (Vento Company), the pressure and the speed of the workflow, respectively, were measured, using an anemometer equipped with a Pitot TA 400 tube (Trotec Company).

## RESULTS

The results of the experimental research performed by the authors show that the required saltation speed of the particles in the drying process depends on the density of the air, especially at high temperature, ( $\rho_a = f(t)$ ), so we have modified equation (9) as follows:

$$V_f = 0.135 \cdot \left(\frac{\rho_t}{\rho_a}\right)^{0,5} d^{0,25} \text{ [m/s]} \quad (11)$$

The correction carried out allows, at high drying temperature ( $t > 150^\circ\text{C}$ ), when in some cases problems arise in transporting the particles, obtaining higher values of the speed  $V_f$  than that from the original equation (9), and therefore, it will increase the reliability of transporting chopped particles by means of heated air.

The values calculated based on equations (8, 9, 11) of the saltation velocities  $V_f$  of the wood particles ( $\rho_t = 600 \text{ kg/m}^3$ ) are shown in fig. 4.

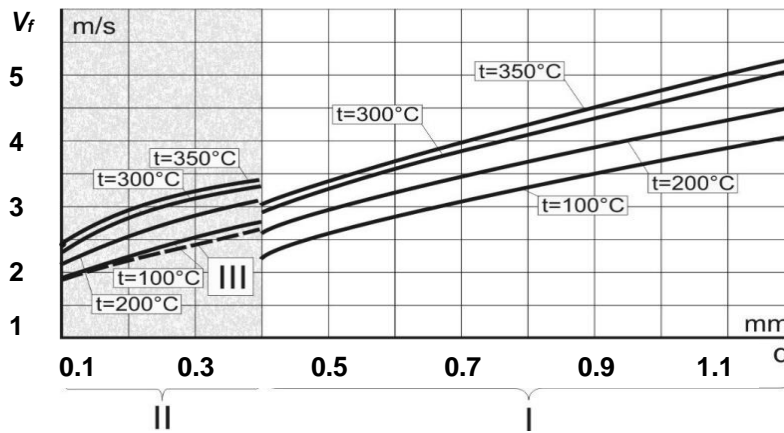


**Fig. 4 - Calculated values of the saltation velocity  $V_f$  of wood particles depending on the temperature of the thermal agent  $t$  and the equivalent diameter  $d$  of the particles**  
 (Note: values are obtained based on empirical formulas)

Thus, knowing the working size of the drying machine, it is possible to evaluate the duration of the contact  $\tau$  with heating agent of the particles subjected to drying, i.e. the duration of the drying process:

$$\tau = \sum_{i=1}^n \frac{L_i}{V_{ti}}, [s] \tag{12}$$

where:

- $L_i$  is the length of the segment  $i$  of the drying installation, [m];
- $V_{ti}$  - the particle velocity in the segment  $i$ , [m/s]. (See equation (10)).

Using equation (12) the particles' drying time was calculated for the dryer ST-300 (China) (horizontal pipe diameter - 200 mm) (fig.3):  $\tau \sim 2-3$  s.

Even at the initial temperature of the thermal agent of 300-350°C, the calculated value of the duration  $\tau$  may be insufficient to obtain the raw material with the required humidity. At the same time, it is necessary to take into account that the speed of the heating agent, in any segment of the dryer, may be less than that calculated by the equations (6), (7), which is based on the actual situation  $V = (2-4)V_f$ , and thus essentially limiting the measures to increase the duration of the drying process.

To increase the duration  $\tau$ , in many cases consecutive coupling of several drying columns (fig.2) or other procedures are used, which lengthen the trajectory of the drying flow.

Such measures have the consequence of increasing metal consumption for manufacturing the added columns and/or the energy at the intake fan, and therefore a reduced economic efficiency of the process.

In the world practice there are used aerodynamic dryers equipped with drying columns (pipes), in which the flow moves on paths parallel to the longitudinal axis of the column (fig.5a,c) or a helical path along the column (fig.3; fig.5b,d).

The computer modelling of the flow in the dryer performed by the authors showed that, in the case of its tangential entry in the inner space of the column with certain ratios of geometric parameters (fig.5b), a vortex flow is formed (fig.5d), which increases the trajectory length of the particles subjected to drying and respectively the duration of the contact between the moist material and the thermal agent.

Calculations based on the developed models (gauge geometric parameters in both dryers are identical, fig. 5a, b) have shown that the movement of the vortex flow in the column (fig. 5d) exhibit a 3-4 fold increase in trajectory length of the particles, (i.e.  $\tau \sim 5...12$  s) compared to the direct current dryer ( $\tau \sim 2...3$ s, fig.5c).

But, although a complex movement inside the vortex flow is quite convincingly demonstrated by the authors *Ahmetov et al., (2014)*, because of a lack of convincing theoretical base to be used in the calculation algorithm, the rotation of the external layers of the flow were no taken into consideration.

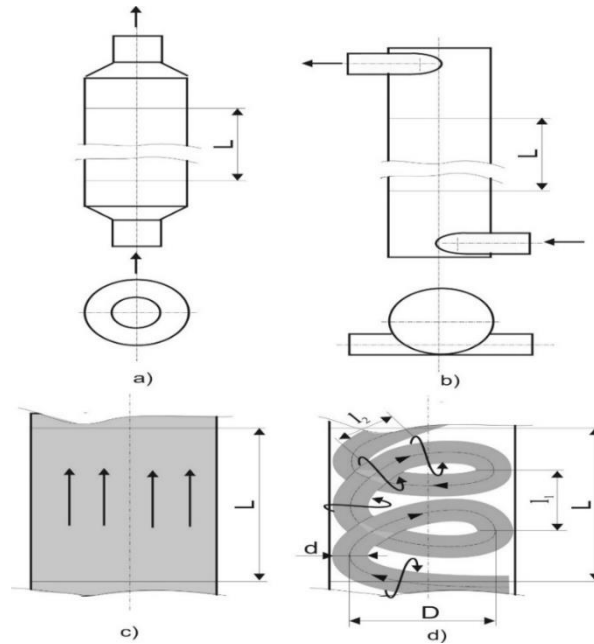


**Fig. 5 - Configuration of the flow of thermal agent mixture + ground raw material in dryers: with direct current (a, c) and vortex (b, d)**

$l_1$  – the step of the helical trajectory of the complete flow;  $l_2$  – the step of the helical trajectory of the outer layers of the flow;  $d$  – the diameter of the flow cord;  $D$  – vortex flow diameter

Taking into account the existence of two trajectories of particles' motion in the vortex flow (fig.5d), their total path  $L_t$  in the segment of length  $L$  of the vortex dryer will be equal to:

$$L_t = n_1 \sqrt{(\pi D)^2 + l_1^2} + n_2 \sqrt{(\pi d)^2 + l_2^2} \quad [m] \quad (13)$$

where :

$D$  – is the diameter of the peripheral vortex flow, [m];

$l_1$  – step of the helical trajectory of the complete flow, [m];

$n_1$  – the number of turns of the vortex flow in the sector of the column with length  $L$ ;

$d$  – diameter of the flow cord, [m];

$l_2$  – the step of the helical trajectory of the outer layers of the flow, [m];

$n_2$  – the number of turns in the helical path around the axis of the outer layers of the cord in the length  $L$ .

Based on the formulas (12), (13) and on the aerodynamic model created (fig. 5d) the value of the contact duration of the moist particles with the heating agent was specified:  $\tau \sim 13...24$  s. The last value includes all the movements of the particles inside the vortex column, including the rotation of the outer layers of the flow in relation to its axis (fig. 5d). The known aerodynamic models (fig. 3) and the ones we elaborated (fig. 5) for vortex flows, made it possible to make a hypothesis.

Because the particles of the raw material subjected to drying are not at homogeneous moisture levels inside the vortex column, they are classified as follows: particles with relatively low humidity move only in the ascending peripheral flow, and particles with higher humidity in the peripheral flow reach the central descending flow, and after their humidity is reduced return to the peripheral flow, being discharged from the column. This phenomenon allows the homogenization of the particulate moisture at the exit of the dryer and the optimal use of thermal energy and reduced consumption. Simultaneously, this hypothesis demonstrates the importance of the trajectories' form, both peripheral as well as the central ones.

To achieve the hypothesis described above, it was proposed the construction of the conical-shaped vortex dryer (Hăbășescu et al., 2016a). The computer simulations of the proposed dryer operation (fig. 6a) showed that, the tangential speed of the peripheral flow can be equalized (stabilized) vertically to a certain limit, which decreases the diameter of the peripheral flow  $D$  (i.e., the cross section of the internal space), proportional to the energy loss caused by friction with the inside walls of the dryer and obtaining its conical shape. The stability of the flow may be further increased, by using a tangential outlet nozzle (Hăbășescu et al., 2016a).

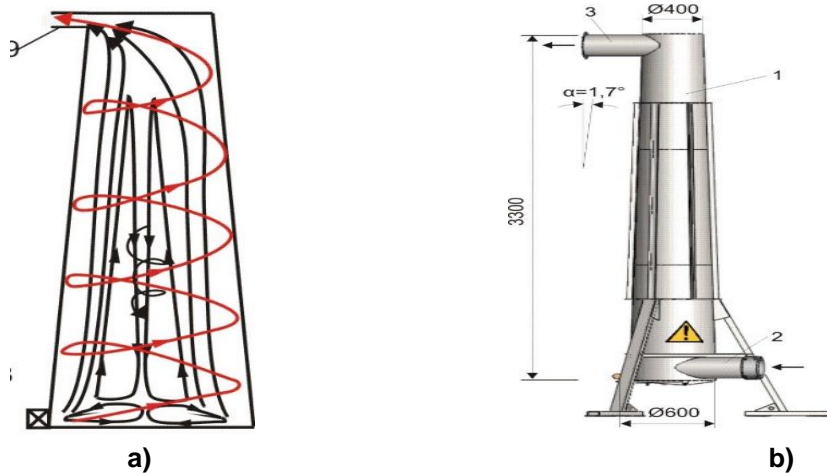


**Fig. 6 a) The configuration of the gas flows in the conical pipe with the compact bottom and the tangential outlet channel ; b) General view of the vortex dryer (Hăbășescu et al ., 2016a)**  
 1– conical housing; 2–power supply connection; 3–exhaust connection

In the conical vortex pipe (fig.6a) the conical trajectory of the descending flow becomes more extended vertically compared to the previous shapes of the pipes (fig.3). From the analysis, it is expected that the conical dryer (fig.6) would, first of all, provide better conditions for the drying of the ground vegetal mass, and simultaneously reduce the power consumption as well as the manufacturing materials for the column.

Research performed on an experimental model of the conical vortex dryer (fig.6b) with a height of 3.3m (diameter of horizontal pipes - 200 mm, suction fan flow - approx. 1500 m<sup>3</sup>/h) has demonstrated that the duration of the movement of the raw material particles from the place of loading (mixer 3, fig.2) to the place of unloading (cyclone 5, fig.2) was  $\tau = 30-35s$ . This duration is 10-15 times longer than that obtained in the direct current aerodynamic dryer (ST-300).

In the research process, an interesting phenomenon was identified, namely: self-regulation of vortex flow parameters with the material subjected to drying in the interior of the dryer when varying the amount of raw material added to the dryer. The phenomenon discovered allowed automatic creation of optimal conditions for drying, when the supply of raw materials and/or the humidity has changed within the studied limits.

The identified phenomenon was presented as follows. When the working space of the dryer was empty and the fan was running, a stable vortex flow was formed inside the dryer (fig.7a). The temperature of the thermal agent at the entrance to the dryer had a value of 300°C, and the flow rate was maximum. It should be mentioned that the vortex flow of air resulted in increased air resistance, therefore the fan flow decreased to 3500 m<sup>3</sup>/h (exhibited before mounting on the machine) to 2300- 2500 m<sup>3</sup>/h.

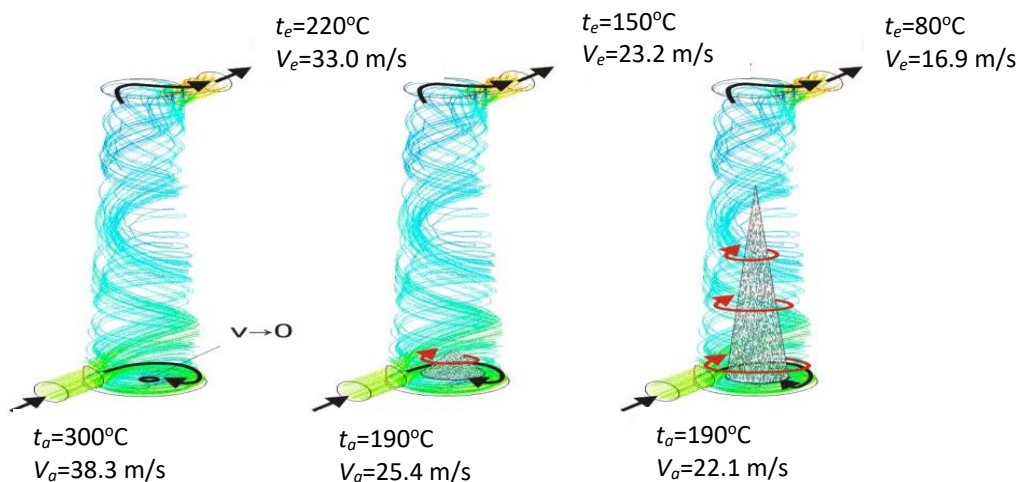


**Fig. 7 - Steps for forming the cone of the material subjected to drying inside the aerodynamic dryer**  
 $t_a$ = heating agent temperature at the inlet;  $t_a$ = heating agent temperature at the outlet;  
 $V_a$ =heating agent speed at the inlet;  $V_e$ = heating agent speed at the outlet;

Continuously adding the raw material to the flow of the thermal agent, at a humidity of 18-20% and an hourly rate of 350- 400 kg/h, the temperature at the dryer inlet fell from 300°C to 190°C and the flow rate from 38.3 m/s to 25.4 m/s (fig.7 a, b). The intensity of the vortex flow inside the dryer also decreased, simultaneously increasing the diameter of the helical path. The flow rate on the axis of this path was high, and at the peripheral layers it decreased, reducing the transport capability of moist particles.

This phenomenon, along with the speed close to 0 m/s along the longitudinal axis of the dryer, leads to the formation on the bottom of the dryer of a conically shaped pile of the moister particles, which rotated the same direction as the base flow, but at a lower angular velocity. Adding raw materials, the cone in the centre of the dryer increased in height until the space between the inner walls of the dryer and the surface of the cone became optimal for the concrete values of the aerodynamic properties of the flow of the mixture heat-raw material on one hand, and of the real temperature of the thermal agent (fig.7c), on the other hand.

In this case, the stabilization of the flow velocity in the supply pipe also took place ( $V_a = 22.1$  m/s), the flow rate having a value of 1500 m<sup>3</sup>/h. As they dried, particles from the outer layers of the cone were discharged from the flow, and their place was taken up by new particles. In the case of an increase of the initial humidity of the raw material, the diameter of the base of the cone also increased and vice versa. In the first case, the flow rate increased, and in the second, it decreased. This is how the self-regulation of the drying process took place. Due to the conical shape of the dryer, it was also possible to compensate for the loss of flow velocity, caused by its friction with the walls of the dryer and thus stabilize the value of the diameter of the flow path formed in the space between the dryer walls and the inner cone. At the top of the dryer, the diameter of the outlet was almost equal to twice the diameter of the helical flow path. As a result, swirling turns began to touch each other, forming complex turbulences which limited the increase in cone height. After this, the mixed flow of thermal agent-dry material is discharged into the cyclone (fig.2). After stopping the supply of raw material, the intensity of the vortex flow increased, completing the evacuation of the dry particles in 5-10 minutes (depending on the initial humidity of the raw material).

The increase of the duration of the vegetal mass particles contact with the heating agent obtained in the experimental investigations ( $\tau = 30-35$  s) compared to the calculated value of the duration ( $\tau \sim 13..24$  s) can be justified by the fact that, under real conditions, the tangential velocity of the outer vortex flow decreases. At the same time, the phenomenon of separation of dry and moist particles of the vegetal mass inside the vortex dryer also serves to increase the duration of contact  $\tau$  of the particles subjected to drying with the thermal agent. It is expected that the increase of the duration  $\tau$  will have positive effects, namely: a) increasing the homogeneity of humidity in the dry raw material; b) the extension of the options for managing possibilities of the technological process of drying the raw material.

## CONCLUSIONS

1) The bibliographic study demonstrates that for drying the chopped vegetal mass, which is intended for producing densified solid biofuels, a promising method is the convective aerodynamic dryer in which the thermal agent executes the base function i.e. drying, and the auxiliary one i.e. the transportation of the biomass particles, which essentially simplifies the construction of the drying machine, and the use as a thermal agent of the flue gases increases the efficiency of the process. In the category of aerodynamic dryers the vortex type dryers are also included, which show higher performances: the calculated value of the contact time of the particles with the thermal agent is 6-8 times higher than in the case of aerodynamic dryers with direct contact. For both dryers, the geometric and technological parameters were identical.

2) The theoretical and empirical equations that allow the calculation of the aerodynamic and technological parameters of the drying process were determined: the saltation speed of the biomass particles, the working speed of the vortex flow and the duration of contact of the particles with the thermal agent. The vortex effect was analysed: we analysed the Ranque-Hilsch vortex effect under working drying conditions, and we developed configurations of the gas flow for dryers of various shapes, which demonstrated the advantages of the improved conical form dryer.

3) The research carried out on an experimental model of an improved aerodynamic dryer, with a conical shape of the pipe, confirmed the results of theoretical research, the actual real value of the duration of the particle contact with the thermal agent was increased by 12-15 fold compared with the dryer with direct contact. During the research, while varying the quantity of material fed to the dryer, we identified a self-regulation phenomenon of the parameters of the vortex flow of material to be dried in the interior of the dryer.

This allowed for automatic generation of the optimum drying conditions when there was a change in the quantity of supplied material and/or in its humidity within the studied limits.

## REFERENCES

- [1] Ahmetov Iu. M., Zanghirov E.I., Svistunov A. V., (2014), The mechanism of the possible flow of the swirl flow (*Возможный механизм течения вихревых закрученных потоков*). *MFTI Annals*, vol. 6, № 2, Aerohydromechanics, pp. 99-105, Ufa -Moscow / Russia;
- [2] Voico V. I., (2008), *Calculation of pneumatic conveying installations (Расчёт установок пневмотранспорта)*. Tomsk Polytechnic University, 145p., Tomsk / Russia;
- [3] Ericsson K., Werner S., (2014), The introduction and expansion of biomass use in Swedish district heating systems, *Biomass Bioenergy*, vol. 94, pp. 57-65;
- [4] Gavrilencov A.M. et al., (2014), Methods of substantiation of the choice of drying method and type of drying units for agro-industrial complex (CAI) (Методика обоснования выбора способа сушки и типа сушильных установок для АПК). *Technologies in the food industry and the processing CAI - healthy eating products*, №2, 2014, pp. 35-43; Russia;
- [5] Gutol A. F., (1997), Ranque Effect. Methodical notes (Эффект Ранка. Методические заметки), *Achievements of the physical sciences (Успехи физических наук)*, vol.167, №6, pp. 664 - 667, Russia;
- [6] Hăbășescu I., Cerempei V., Molotcov Iu., Balaban N., (2015), *Device for obtaining hot air for dryers. Patent, No. 906, Republic of Moldova*;
- [7] Hăbășescu I., Cerempei V., Molotcov Iu., Balaban N., Ruschih D., (2016a), *Dryer and drying process of friable materials. Patent, No.1054, Republic of Moldova*;
- [8] Hăbășescu I., Cerempei V., Molotcov Iu., (2016 b), *Device for obtaining hot air for dryers, Patent, No.1097, Republic of Moldova*;
- [9] Iftekhhar C.M., Norton H.B., Duffy A., (2017), Technological assessment of different solar-biomass systems for hybrid power generation in Europe, *Renewable and Sustainable Energy Reviews*, vol.68, pp. 1115–1129;
- [10] Ivanov V.F., (1956), *Wooden constructions (Деревянные конструкции)*. Literature for constructions and architecture, 254 p.; Leningrad-Moscow / Russia;
- [11] Koleadin E. A., Vinogradov S. V., (2004), *Effect of thermal classification of gases (Ranque effect). (Эффект температурного разделения газов (эффект Ранка))*. Newsletter. Ed. Astrakhan State Technical University, № 1, 2004, pp.45-52, Russia;
- [12] Konovalov V. I., Orlov A. Iu., Gatapova N.Т., (2002), Drying and other processes in the Ranque-Hilsch vortex tube: opportunities and experimental technique (*Сушка и другие технологические процессы с вихревой трубой Ранка–Хилша: Возможности и экспериментальная техника*). Newsletter. Ed. TGTU, Vol.16, №4, 2002, pp.803-825;
- [13] Orehova T.N., Uvarov V.A., (2013), Determination of material particle velocity in the pneumatic mixer of dry construction mixtures (*Определение скорости частиц материала пневмосмесителя сухих строительных смесей*), *Fundamental Research (Фундаментальные исследования)*, 2013 № 4 (Part.3), pp. 592-596; Russia;
- [14] Önsan Z.I., Avci A.K., (2016), *Multiphase Catalytic Reactors-Theory, Design, Manufacturing, and Applications*. John Wiley & Sons, p.83, ISBN: 978-1-118-11576-3;
- [15] Romancov P.G., Rașcovscaia N.B., (1968), *Suspended drying: theory, construction, calculation (Сушка во взвешенном состоянии: Теория, конструкция, расчет)*. Chemistry, 353 p. Moscow / Russia;
- [16] Teterin L.A., (1972), Heat exchange in the process of drying shredded wood in a suspended state (*Теплообмен при сушке измельченной древесины во взвешенном состоянии*). *Bulletin of higher education institutions, Forest Journal*, №3,1972, pp.89-93, Russia;
- [17] Zakirov D.I., Zakirov A.V., (2016), *Combined-type aerodynamic dryer (ASKT) (Аэродинамическая сушилка комбинированного типа АСКТ)*. Patent, No. 2577 670, Russia;
- [18] \*\*\* (1968), The Chemist's Guide. Chapter III. Hydrodynamics of granular materials (Справочник химика. Раздел III. Гидродинамика зернистых материалов), vol. 5, *Chemistry*, pp.426-467, Moscow Leningrad / Russia;
- [19] \*\*\*(2020), Aerodynamic dryer UA 280 <http://www.ecomihis.ro/uscatior-aerodinamic/>

## DYNAMICS OF PROPORTIONAL SPEED CONTROL VERSUS SERVO SPEED CONTROL OF A HOSE / CABLE SPOOLING DEVICE FOR DRUM

### DINAMICA REGLĂRII PROPORȚIONALE A VITEZEI VERSUS SERVOREGLAREA VITEZEI DEPĂNĂTORULUI DE FURTUN / CABLU AL TAMBURULUI

Alexandru-Polifron Chiriță<sup>\*1)</sup>, Marian Blejan<sup>1)</sup>, Teodor-Costinel Popescu<sup>1)</sup>, Ana-Maria Popescu<sup>1)</sup>

<sup>1)</sup> INOE 2000 - Subsidiary Hydraulics and Pneumatics Research Institute / Romania

E-mail: [chirita.ihp@fluidas.ro](mailto:chirita.ihp@fluidas.ro)

DOI: <https://doi.org/10.35633/inmateh-62-40>

**Keywords:** speed control, hose / cable spooling device, irrigation

#### ABSTRACT

*This article presents and analyses in two cases the dynamic performance of regulation and control of the linear speed of an electro-hydraulically driven mechatronic axis. In the first case, the flow control is performed with a proportional hydraulic directional control valve, while in the second case the control is performed with a servo-valve. The linear mechatronic axis is part of a complex subsystem used in both agriculture and industry that allows the precise winding of a hose / cable on a drum with the help of a spooling device, which conditions the positioning of the hose. The speed control of the hydraulic cylinder with bilateral rod on whose liner the spooling device is fixed is performed in a closed loop with the help of transducers and a programmable controller (PLC).*

#### REZUMAT

*Articolul de față prezintă și analizează în două situații performanțele dinamice de reglaj și control al vitezei liniare a unei axe mecatronice acționate electro-hidraulic. În prima situație reglarea debitului este realizată cu un distribuitor hidraulic proporțional, iar în cea de a doua situație reglarea se realizează cu o servovalvă. Axa mecatronică liniară face parte dintr-un subsistem complex folosit atât în agricultură cât și în industrie ce permite înfășurarea precisă a unui furtun /cablu pe un tambur cu ajutorul unui depănător care condiționează poziționarea furtunului. Controlul vitezei cilindrului hidraulic cu tijă bilaterală pe a cărui cămașă este fixat depănătorul este realizat în buclă închisă cu ajutorul traductorilor și a unui controler programabil (PLC).*

#### INTRODUCTION

In plant life, depending on the vegetation phases and development stages, there are periods during which the water scarcity affects the level and quality of production. These periods are known as "critical phases for humidity". Meteorological factors (air humidity, heat, light, precipitation) in turn have a direct influence on the need for irrigation. Precipitation is the most important source of moisture for the soil and an important parameter for assessing the need for irrigation; it is characterized by the multiannual average, with high variability for different climatic zones. By irrigating crops is meant bringing and distributing water on cultivated soils, for the following purposes: (*Biolan et al, 2010; www.scrigroup.com, 2020*)

- to increase the soil moisture to the limit required by each cultivated plant, so that the growth takes place normally;
- to protect crops from heat and drought;
- to remove or dilute harmful salts from saline soils;
- to ensure the performance of agricultural works in optimal conditions. (*www.sere-transilvania.ro, 2020*)

The methods of arranging the agricultural crops for irrigation and the technical elements of irrigation (watering norm, minimum requirements, intensity of application and degree of water spraying) depend fundamentally on the type and properties of the soils. In the correct management of the completion of the water necessary for the plants by irrigations, knowing the water consumption of the plants in the given soil and climate conditions plays an essential role. Sprinkler watering, which is one of the most efficient methods of distributing water to plants, is applied by means of irrigation equipment with positional watering or watering while the equipment moves. The sprinkler system with watering while the equipment moves, with drum and hose, model type IATF, RAINSTAR and GH + MTP, has been developed in several constructive variants regarding the driving group: group with hydraulic bellows motor with single / double effect, driving group with turbine or thermal engine, Figure 1.

The drive group ensures the recovery and controlled rolling (one coil next to another) of the hose on the drum for feeding the sprinkler trolley. Irrigated surfaces are strips with a length of 300-600 m and a width of 36, 40, 44 and 54 m, for working pressure values of 3.0; 3.5; 4; 4.5 bar.



**Fig. 1 - Drum and hose irrigation system**

([www.bauer-at.com](http://www.bauer-at.com), 2020; [www.ferbo.net](http://www.ferbo.net), 2020; Roiss et al, 2020)

Use of the irrigation system: the system is transported to the irrigation site; it is connected to utilities and by means of the tractor, the hose is unrolled. At its end there is the trolley that ensures irrigation with sprinklers; simultaneously with the irrigation process recovery of the hose, whose linear speed is constant to ensure the prescribed watering norm, also begins. The dependence between the watering norm and the hose recovery speed is presented in Figure 2.

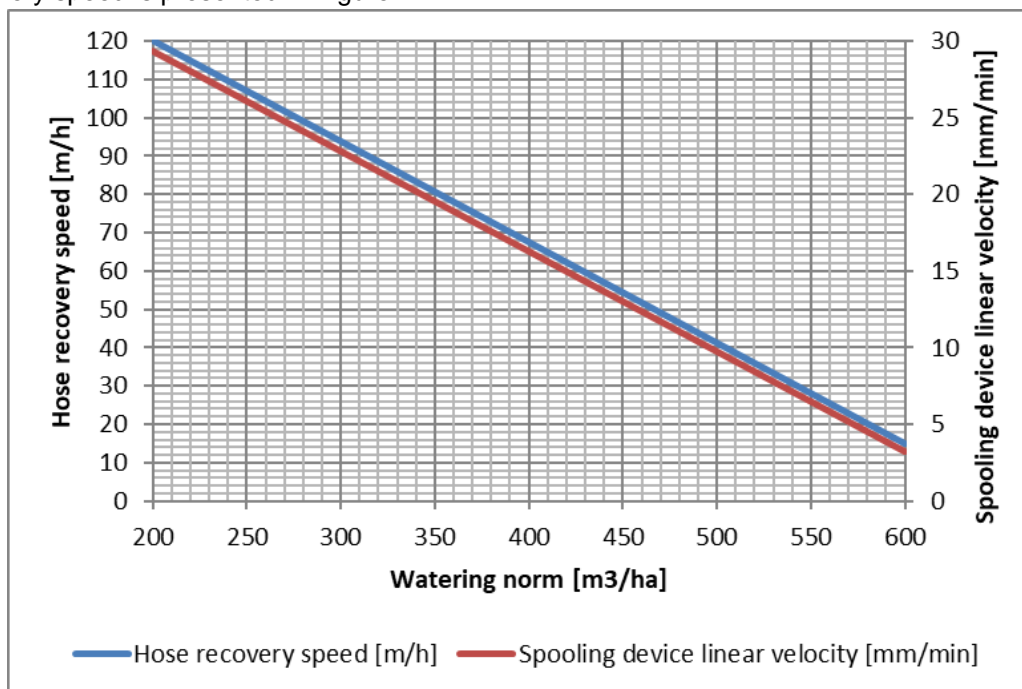


**Fig.2 - Variation of hose recovery speed and linear velocity of hose spooling device depending on watering norm**

At the end of the winding cycle of the few layers of the hose, the equipment is rotated 180 degrees or is moved to irrigate a new plot of land, and the cycle repeats until irrigation of the crop is completed.

The graph in Figure 2 presents the variation of the parameters hose recovery speed (m/h) and spooling device speed (mm/min), for values of the watering norm in the range 200-600 m<sup>3</sup>/ha. The minimum watering norm (200 m<sup>3</sup>/ha) is ensured for a recovery speed of the hose of 120 m/h, and a recovery speed of the spooling device of 29.25 mm/min, whereas the maximum watering norm (600 m<sup>3</sup>/ha) - for a recovery speed of the hose of 13 m/h, and a recovery speed of the spooling device of 3.25 mm/min. For watering norms between the minimum and maximum values, assessments can be made regarding the technical and functional parameters of the driving group, the recovery speed of the hose and also the linear velocity of the spooling device. For example, for the watering norm of 400 m<sup>3</sup>/ha the hose recovery speed will be 64.5 m/h and the spooling device speed - 15 mm/min.

The spooling device is shown in Figure 3 with a black outline; it consists of a hydraulic cylinder and four rollers that have the role of guiding the hose. The hydraulic cylinder has bilateral rods that are fixed and through which the two chambers of the cylinder are fed with hydraulic oil. (Pott et al, 2013)

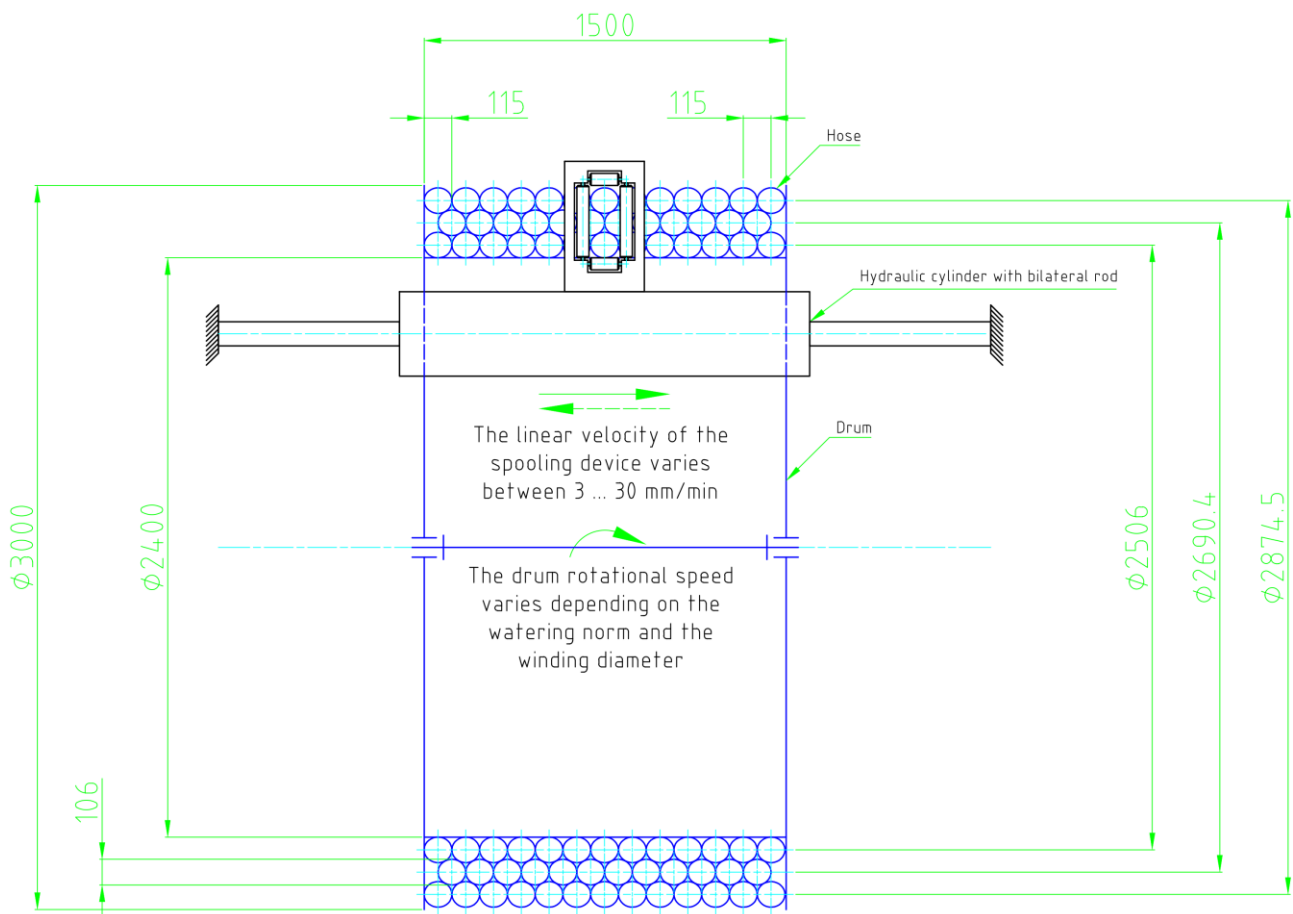


Fig. 3 - Schematic diagram of the process

Table 1 presents the results of several calculations from which the numerical simulation was started.

Table 1

The results of the calculations for the chosen irrigation system variant

	Layer 1	Layer 2	Layer 3	Total
Drum winding diameters	2506 mm	2690.4 mm	2874.5 mm	-
Hose circumference by diameter	7.873 m	8.452 m	9.031 m	-
Number of turns per layer	13	13	13	39
Hose length per layer	102.347 m	109.878 m	117.397 m	329.62 m
Hose recovery speed	107 m/hr (for 250 m <sup>3</sup> /ha watering norm)			-
Hose recovery time on the layer	3443.4 s	3696.8 s	3949.8 s	11090 s
Linear travel velocity (process value)	26.137 mm/min	24.345 mm/min	22.786 mm/min	-

**MATERIALS AND METHODS**

The numerical simulation showing the dynamic speed control performances in the two distinct control cases has been performed by using Simcenter AMESim 2020.1. The automatic electrohydraulic system for adjusting the linear velocity of the spooling device and also the simulation parameters are shown in the Figure 4 below. (Xu et al, 2020; Zhang et al, 2020)

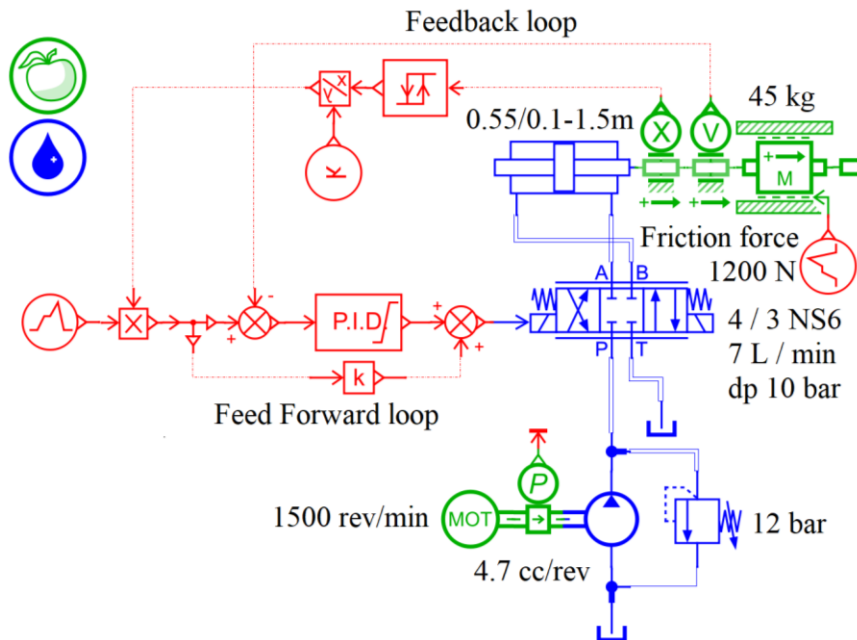


Fig. 4 - Schematic diagram of the process

The proposed solution involves driving the spooling device with a hydraulic cylinder whose velocity is regulated by a PID controller with feedback and feed-forward, which improves the adjustment precision and controls an electrohydraulic device for regulating the flow of the proportional control valve.

The simulation settings are shown in Figure 5, in which one can notice that the simulation time is about 3 hours, the sampling frequency is 166 Hz, and print interval is 0.006 s. (Ali et al, 2020; Wang, 2020)

**Simulation settings**

Parameter	Value	Unit
Start time	0	s
Final time	11000	s
Print interval	0.006	s

Continuation run  
 Use old final values

**Simulation type**

Single run  
 Batch Design matrix

**Parallel processing**  
Preferences

**Result file(s)**  
Number of saved variables: 128  
Estimated size: 1.82 GB

**Integrator type**

Standard integrator  
 Fixed step integrator

**Information**

*i* Print interval: 0.006 s  
Number of points: 1833335  
Sampling frequency: 166.666666666667 Hz  
Easily observable frequency: 16.6667 Hz

**Miscellaneous**

Monitor time  
 Statistics  
 Generate CSV

**Integrator settings**

Parameter	Value	Unit
Tolerance	1e-04	
Maximum time step	0.006	s

**Simulation mode**

Dynamic  
 Stabilizing  
 Stabilizing + Dynamic

**Solver type**

Regular  
 Cautious

**Error type**

Mixed  
 Relative  
 Absolute

Fig. 5 – Simulation settings

The Ziegler – Nichols tuning method with some overshoot was used to calibrate the PID controller. The response to the step signal before calibrating the two systems is shown in Figure 6. (Afram et al, 2020)

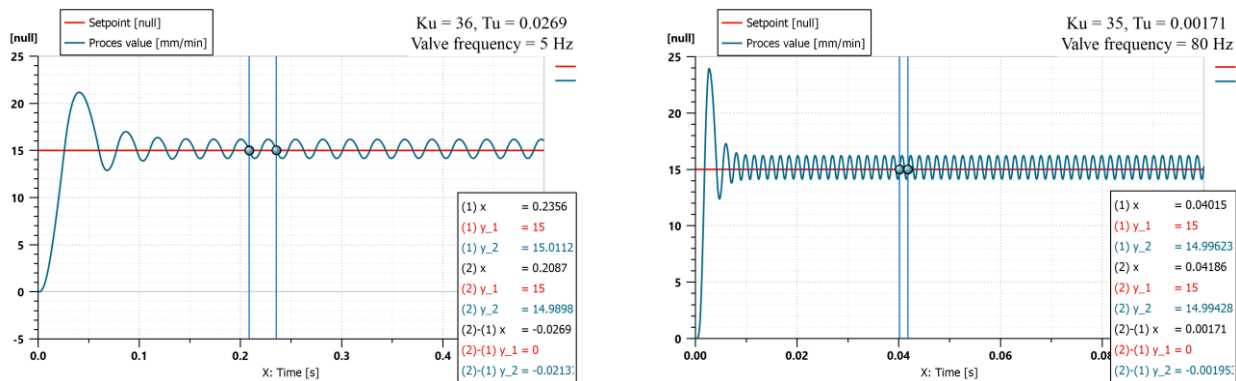


Fig.6 - The response of the two systems (proportional control valve - on the left side and servo valve – on the right side) to the step signal before calibration

Figure 7 shows the adjustment performance of the two compared systems and the parameters chosen for the PID controllers; one can notice that the system with proportional control valve (left side) is 4 times slower and has a stabilization time of about 0.2 seconds. (Fliess and Join, 2009; Samyгина et al, 2018)

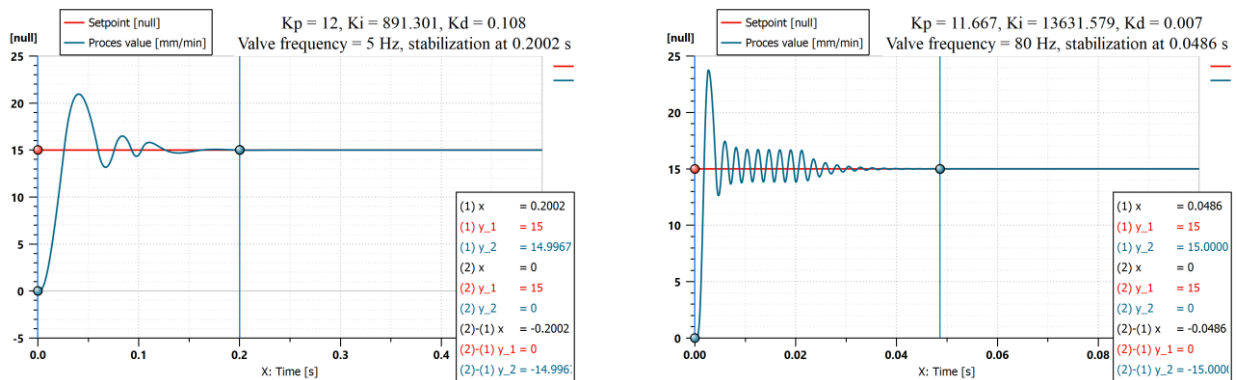


Fig.7 - The response of the two systems (proportional control valve - on the left side and servo valve – on the right side) to the step signal after calibration

## RESULTS

The group of graphs in Figure 8 below shows the variations over time of the mechanical and hydraulic parameters of the system.

The graph in the upper left corner shows the input parameters of the hydraulic pump, for example the pump is driven by a thermal engine with a constant speed of 1500 rev/min, evolution is shown in red on the graph, the torque required for the pump is shown in blue and its numerical value is 0.9 N/m. If the speed and torque are constant, the power consumed by the system can also be only constant - presented in orange and with a value of 140 W.

The graph in the upper right corner shows in red the constant flow rate of hydraulic oil circulated by the pump in the system; it has a value of about 7 l/min; the orange curve shows the system pressure which has a constant value of 12 bar because the excess flow of the system (shown on the graph with the blue curve) is discharged through the pressure valve at the pressure at which it is adjusted in order to achieve resistive flow regulation.

The graph in the lower left corner shows in red the evolution over time of the spooling device position. One can notice that it makes 3 strokes corresponding to the 3 diameters of the hose winding on the drum; the blue curve shows the variation of the linear speed of the spooling device over time, and its acceleration is presented in orange.

The graph in the lower right corner shows in red the evolution in time of the position of the directional control valve spool, and in blue the velocity of the spool valve.

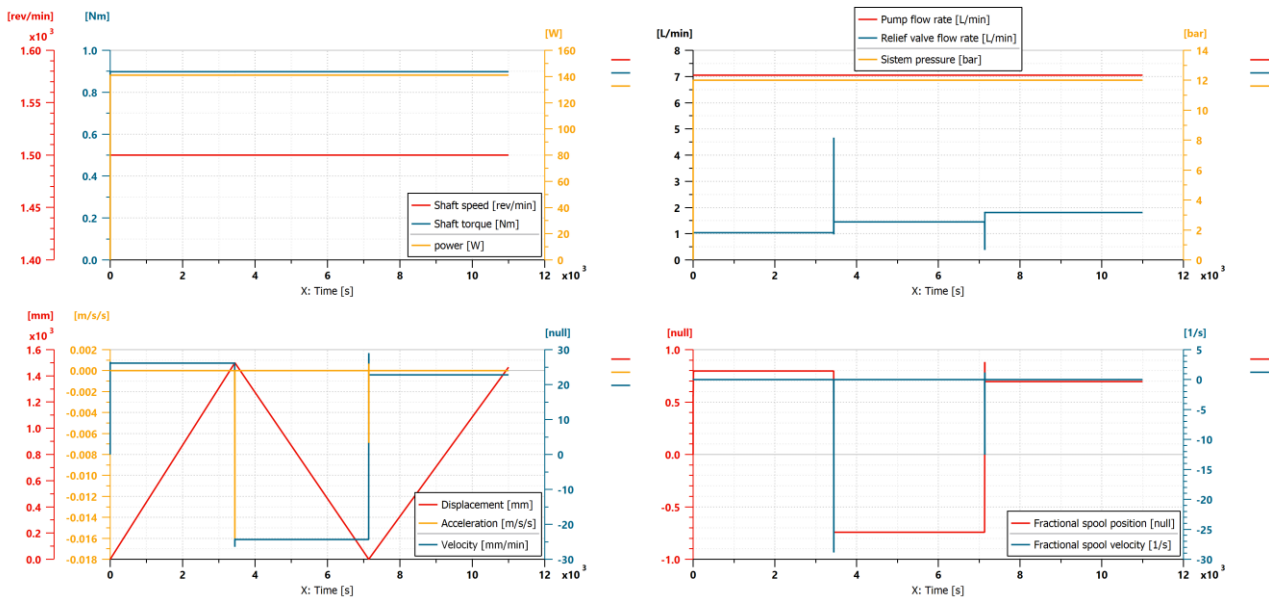


Fig. 8 - Variations over time of the mechanical and hydraulic parameters of the system

The group of graphs presented in Figure 9 shows the evolution in time of the internal (the bottom of the chart) and external (the top of the chart) parameters of the PID controller. (Gao and Ye, 2020)

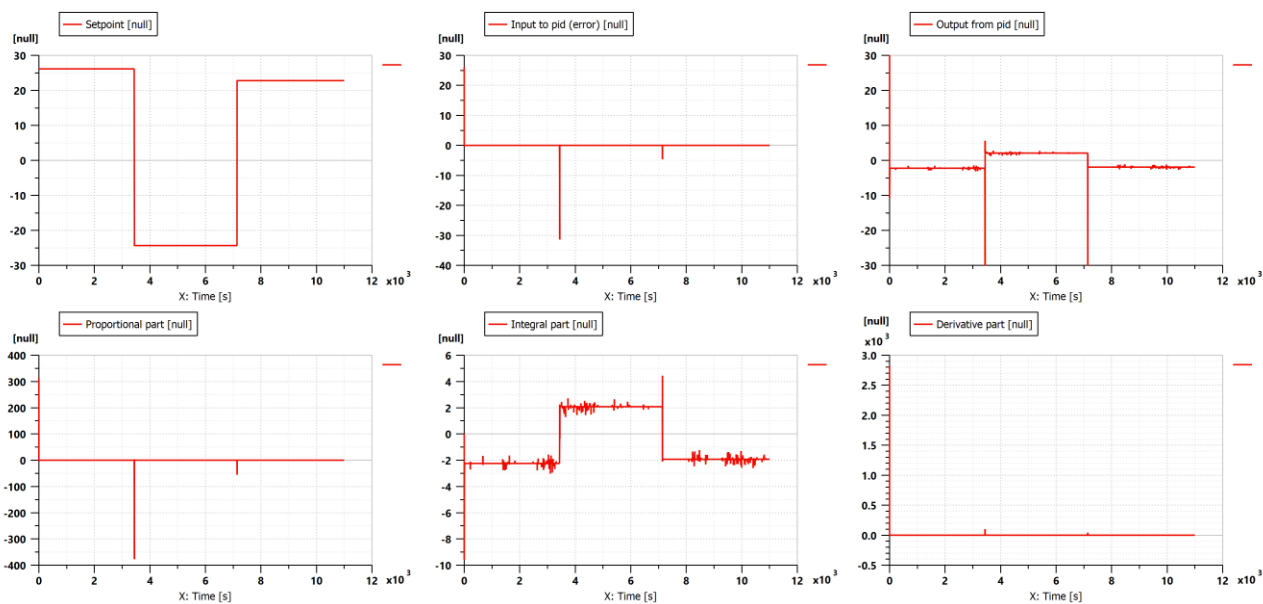


Fig. 9 - Evolution in time of the internal and external parameters of the PID controller

The group of graphs in Figure 10 shows: • the evolution in time of the setpoint parameter that represents the system control and the desired evolution in time of the process; • the process value which represents the variation in time of the system response to the setpoint parameter and • the error of the adjustment process. On the same graph one can also see the evolution over time of the adjustment error (in red), which has high values when changing the direction of travel or at start-up.

The graphs in figures 11 and 12 show in detail the variation over time of the same parameters presented in Figure 10. Figure 11 shows the stabilization time at start, which has a value of 0.3 s, and the value of the speed error - 26 mm/min. Figure 12 shows the stabilization time when changing the direction of travel; in this case, unlike the previously discussed case, the stabilization time is large, almost double – it has a value of 0.5 seconds; this delay is due to the fact that the proportional control valve must switch from the parallel position of the spool valve to the crossed position (or vice versa) passing through the centre position, the closed one. This problem can be prevented by using a 4/2 proportional directional control valve. In the same figure, one can notice that the error is 32 mm/min.

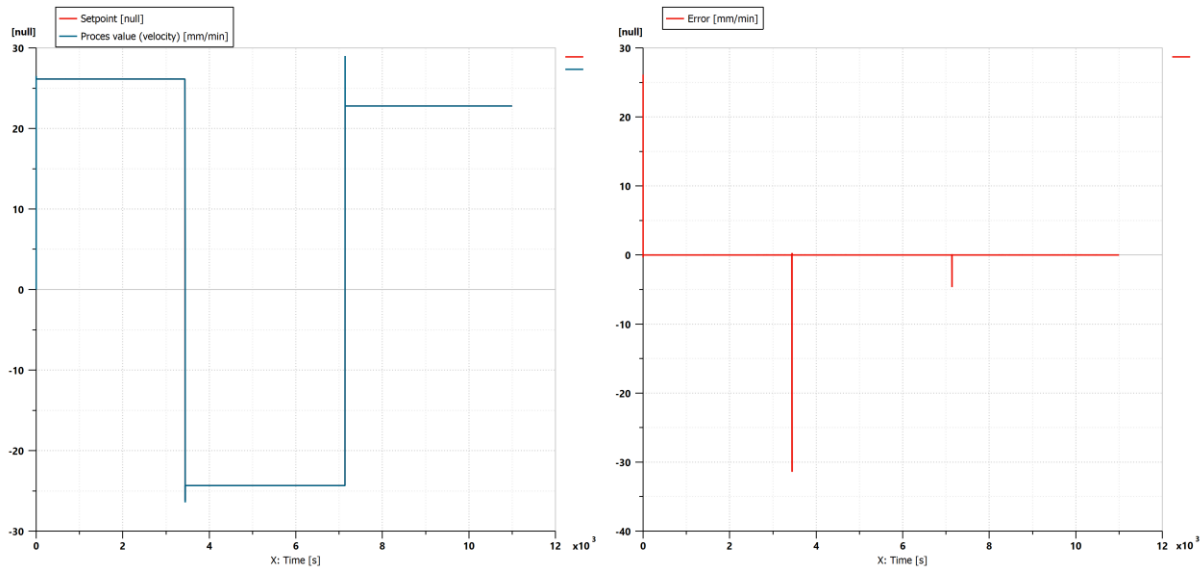


Fig. 10 - Evolution in time of the setpoint, process value and its error

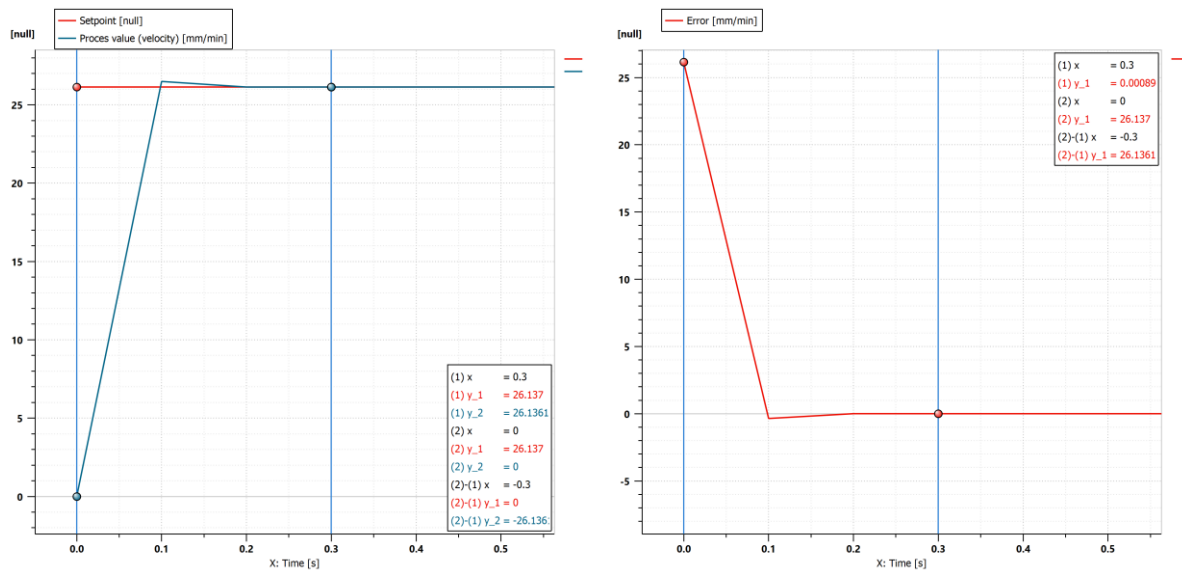


Fig. 11 - System stabilization time and error at start-up

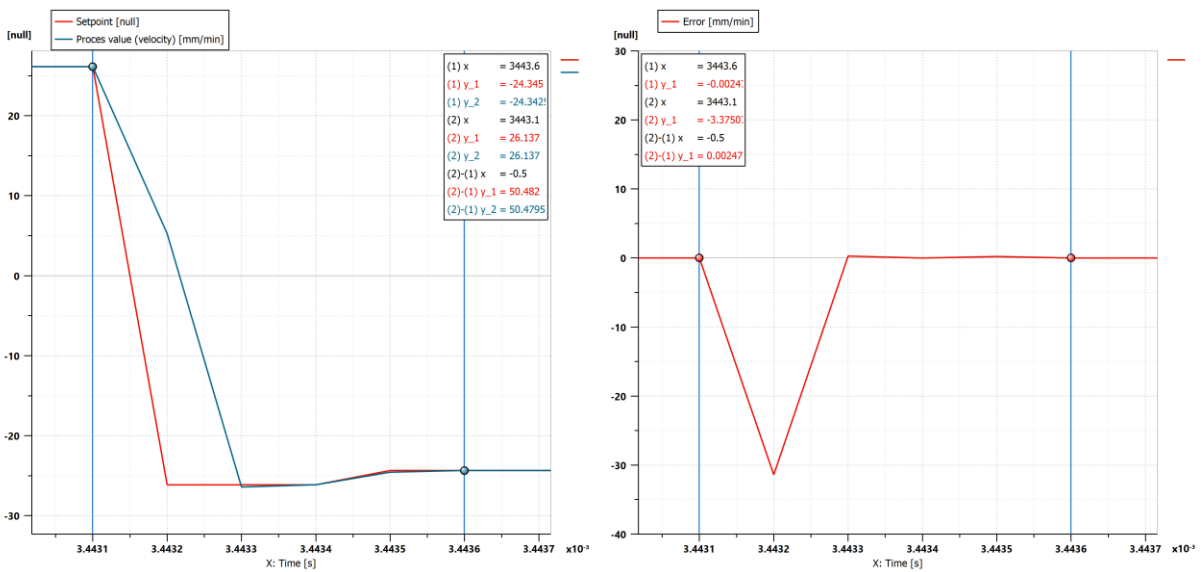


Fig. 12 - System stabilization time and error when changing the direction of travel

Figure 13 shows a detail of the error of adjusting the linear velocity of the spooling device with proportional control valve.

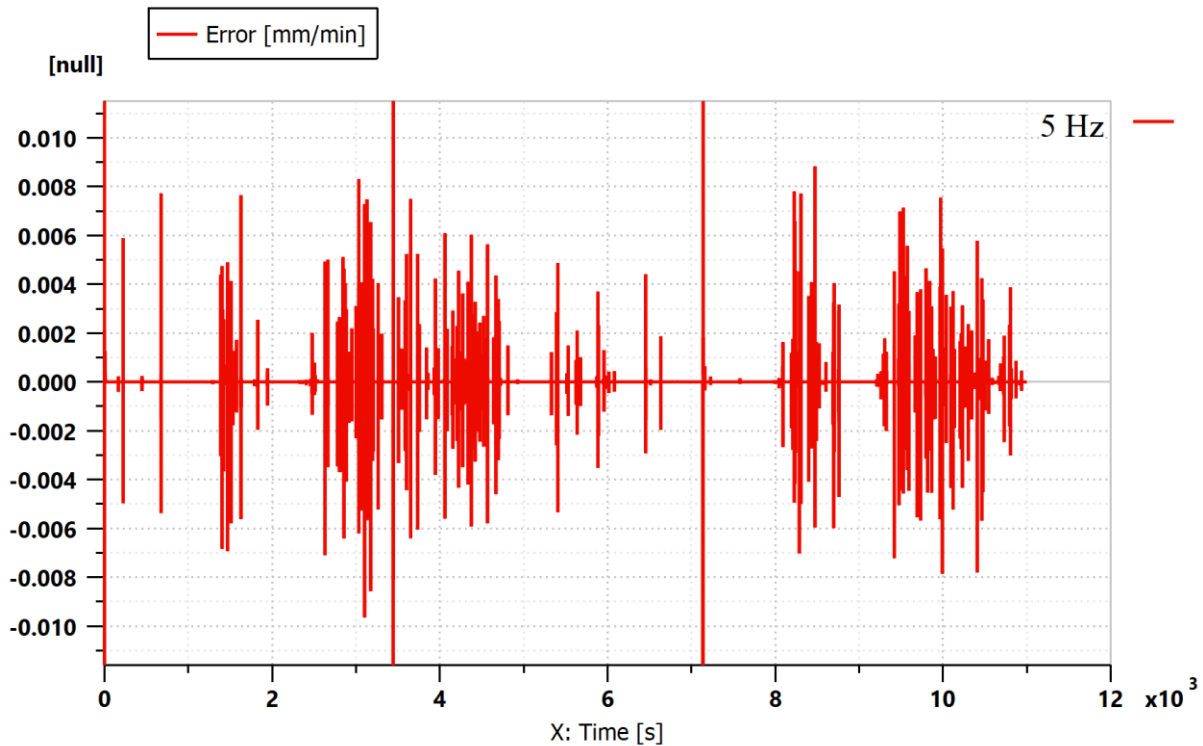


Fig. 13 - Detail - the error of adjusting the linear velocity of the spooling device with proportional control valve

Figure 14 shows a detail of the error of adjusting the linear velocity of the spooling device with servo valve.

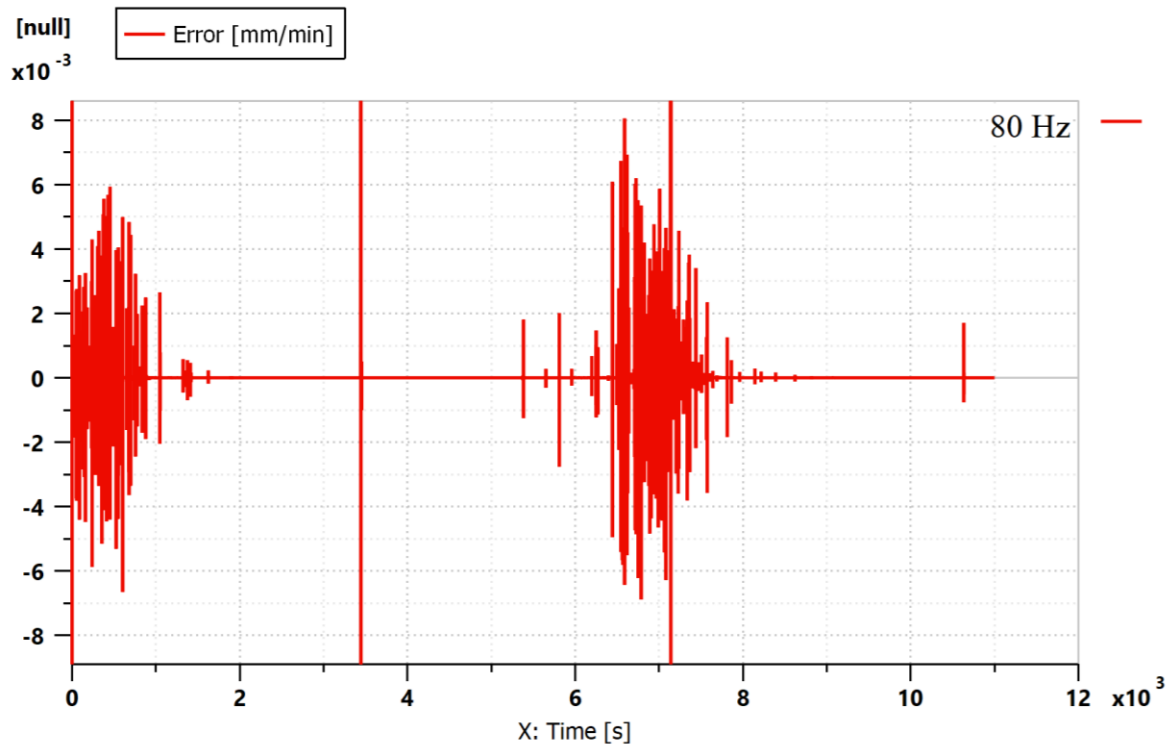


Fig. 14 - Detail - the error of adjusting the linear velocity of the spooling device with servo valve

Only the comparative graphs of the two speed control systems which showed significant differences were presented; among these, there are figures 6 and 7, as well as figures 13 and 14.

## CONCLUSIONS

Comparing the two speed control systems analysed in this article, the following conclusions can be drawn:

The control system with proportional directional valve is suitable for this system because the technological process is slow.

Both systems perform a sufficiently precise adjustment of the process, but the servo system is at least 4 times more expensive than a system consisting of a proportional directional valve and a PLC.

The servo valve control system has better accuracy and superior stability, which is suitable for faster technological processes, but it also has disadvantages, such as: high cost; it requires fine oil filtration; vibrations during the technological process can negatively influence the performance of process adjustment.

An important advantage of the control system with proportional control valve is that the pressure drops on it at maximum flow is only 10 bar, while at servo regulation the drop is 70 bar. Given that the pressure drop required to adjust the linear velocity is small and some of irrigation systems have as primary source of energy the pressure and flow from the irrigation pipe that drive a turbine which in turn drives the drum, the same turbine could also drive the hydraulic pump by means of a speed multiplier, and in this case a heat engine would no longer be necessary.

## ACKNOWLEDGEMENT

This paper has been developed in INOE 2000-IHP and funded by a grant of the Romanian Ministry of Research and Innovation under the National Research Programme NUCLEU, Financial agreement no. 18N/08.02.2019, Additional Act no. 9/2020, Project acronym: OPTRONICA VI, Research theme PN 19-18.01.02, titled: "Advanced research on developing synergic border architectures used in solving global challenges and improving knowledge-based competitiveness", Phase no. 6, titled: 'Methods, procedures and equipment for experimental validation of mathematical models and numerical simulations, used for modernizing hydraulic equipment in order to reduce energy losses'.

## REFERENCES

- [1] Afram, R. M., Hussien, A. A., Marie, M. J. (2020). Design and Implementation of Optimal PID Controller Using PLC for Al-Tahady ESP. *International Journal of Image, Graphics and Signal Processing (IJIGSP)*, 12(5), 1-12. <https://doi.org/10.5815/ijigsp.2020.05.01>
- [2] Ali, H.H., Mustafa, A.W., Al-Bakri, F.F. (2020). A new control design and robustness analysis of a variable speed hydrostatic transmission used to control the velocity of a hydraulic cylinder. *International Journal of Dynamics and Control*. <https://doi.org/10.1007/s40435-020-00716-w>
- [3] Biolan, I., Serbu, I., Sovaiala, Gh., Mardare, F. (2010). *Techniques and technologies for fertigation of agricultural crops (Tehnici si tehnologii de fertirigare a culturilor agricole)*. A.G.I.R. Publishing House, ISBN: 978-973-720-344-1
- [4] Fliess, M., Join, C. (2009). Model-Free control and intelligent PID controllers: towards a possible trivialization of nonlinear control?, *Proceedings of 15th IFAC Symposium on system identification, France*, 1531-1550. <https://hal.inria.fr/inria-00372325/file/IFAC09.pdf>
- [5] Gao, B., Ye, Y. (2020). Research on Position / Velocity Synergistic Control of Electro Hydraulic Servo System. *Recent Patents on Mechanical Engineering*, 13(4), 366-377. <https://doi.org/10.2174/2212797613999200420082115>
- [6] Pott, A., Mütterich, H., Kraus, W., Schmidt, V., Miermeister, P., Verl, A. (2013). *IPAnema: A family of Cable-Driven Parallel Robots for Industrial Applications*. In: Bruckmann, T., Pott, A. (eds). *Cable-Driven Parallel Robots. Mechanisms and Machine Science*, 12. Springer. [https://doi.org/10.1007/978-3-642-31988-4\\_8](https://doi.org/10.1007/978-3-642-31988-4_8)
- [7] Roiss, O., Melikhov, V. V., Medvedeva, L. N. (2020). Logical architecture for green technology applications in Roehren-und Pumpenwerk BAUER GmbH (Austria). *IOP Conference Series: Earth and Environmental Science*, 577, *Mathematical modelling of technical and economic systems in agriculture II*, Russian Federation, 012016. <https://doi.org/10.1088/1755-1315/577/1/012016>
- [8] Samygina, E. K., Rassudovand, L. N., Balkovoi, A. P. (2018). Comparison of linear position and velocity control strategies for a direct servodrive. *2018 25th International Workshop on Electric Drives:*

- Optimization in Control of Electric Drives (IWED)*, Russian Federation, 1-5, <https://doi.org/10.1109/IWED.2018.8321382>
- [9] Wang, L. (2020). *PID Control System Design and Automatic Tuning using MATLAB/Simulink*. Wiley-IEEE Press. <https://doi.org/10.1002/9781119469414.ch4>
- [10] Xu, W., Junejo, A. K., Liu, Y., Hussien, M. G., Zhu, J. (2020). An Efficient Anti-Disturbance Sliding-Mode Speed Control Method for PMSM Drive Systems. *IEEE Transactions on Power Electronics*. <https://doi.org/10.1109/TPEL.2020.3039474>
- [11] Zhang, S., Li, S., Minav, T. (2020). Control and Performance Analysis of Variable Speed Pump-Controlled Asymmetric Cylinder Systems under Four-Quadrant Operation. *Actuators*, 9(4), 123. <https://doi.org/10.3390/act9040123>
- [12] [www.bauer-at.com/en/products/irrigation/rainstar/pdf](http://www.bauer-at.com/en/products/irrigation/rainstar/pdf)
- [13] [www.ferbo.net/en/product/serie-ghemtp/](http://www.ferbo.net/en/product/serie-ghemtp/)
- [14] \*\*\* Irrigation of fruit plantations and soil protection issues (Irigarea plantatiilor pomicole si problematica protectiei solului). [www.scrigroup.com/casa-masina/pomicultura/IRIGAREA-PLANTATIILOR-POMICOLE73188.php](http://www.scrigroup.com/casa-masina/pomicultura/IRIGAREA-PLANTATIILOR-POMICOLE73188.php)
- [15] \*\*\* The need for water in vegetable crops in greenhouses and solariums (Necesarul de apă în culturile legumicole din sere și solarii). [www.seretransilvania.ro/ro/blog/post/necesarul-de-apa-in-culturile-legumicole-din-sere-si-solarii/](http://www.seretransilvania.ro/ro/blog/post/necesarul-de-apa-in-culturile-legumicole-din-sere-si-solarii/)

## WRITING INSTRUCTIONS

### Article Types

Three types of manuscripts may be submitted:

1. **Regular articles:** These should describe new and carefully confirmed findings, and experimental procedures should be given in sufficient detail for others to verify the work. The length of a full paper should be the minimum required to describe and interpret the work clearly (max.10 pages, even number);
2. **Reviews:** Submissions of reviews and perspectives covering topics of current interest are welcome and encouraged (max.10 pages, even number).

Manuscripts should be written in English (American or British usage is accepted, but not a mixture of these) and submitted **electronically** at the following e-mail addresses: ***inmatehjournal@gmail.com***

Please be sure to include your full affiliation and e-mail address (see Sample manuscript)

The authors are responsible for the accuracy of the whole paper and references.

There are allowed 2 papers by each first author.

The text layout should be in single-column format. To avoid unnecessary errors, it is strongly advised to use the "spell-check" and "grammar check" functions of your word processor.

### Review Process

All manuscripts are reviewed by 2 members of the Scientifically Review Office. Decisions will be made as rapidly as possible and the journal strives to return reviewers' comments to authors in approx.3 weeks.

The editorial board will re-review manuscripts that are accepted pending revision.

### NOTE:

Submission of a manuscript implies: that the work described has not been published before (excepting as an abstract or as part of a published lecture or thesis) that it is not under consideration for publication elsewhere.

### 1. REGULAR ARTICLES

- Manuscripts should be concise, in ***1.15 line spacing***, and should have 2 cm all over margins. The font should be ***Arial 10 pt.*** Ensure that each new paragraph is clearly indicated, using ***TAB at 1 cm.***
- Title will be ***Arial 12 pt.*** and explicit figures will be ***Arial 9 pt.***
- Text will be written in English.
- Chapters' titles are written by ***Arial 10 pt, Bold, Uppercase*** (e.g. **INTRODUCTION, MATERIALS AND METHODS**), between chapters is left a space for 10 pt. At the beginning of each paragraph, TAB of 1 cm.
- The paper body will be written in ***Arial 10 pt., Justify alignment.***

**TITLE** ***Arial 12 pt., Uppercase, Bold, Center*** (in English language) and ***Bold Italic*** (in native language).

Should be a brief phrase describing the contents of the paper. Avoid long titles; a running title of no more than 100 characters is encouraged (without spaces).

**AUTHORS** ***ARIAL 9, Bold, Centre alignment***

Under the paper's title, after a space (enter) 9 pt., write ***authors' names*** and ***affiliations (Arial 8 pt.-Regular)***

When the paper has more than one author, their name will be followed by a mark (Arabic numeral) as superscript if their affiliation is different. ***Less than 6 authors.***

***Corresponding author's name*** (next row), ***(Arial 8 pt.)***. Should be added also: phone, fax and e-mail information, for the paper corresponding author ***(font: 8 pt., Italic)***.

**KEYWORDS** ***(In English)*** about 4 to 7 words that will provide indexing references should be listed (**title:** ***Arial 10pt, bold italic,*** **text** ***Arial 10 pt., Italic***).

A list of non-standard **Abbreviations** should be added. In general, non-standard abbreviations should be used only when the full term is very long and used often. Each abbreviation should be spelled out and introduced in parentheses the first time it is used in the text. Standard abbreviations (such as ATP and DNA) need not to be defined.

**ABSTRACT** ***(in English and Native language, Arial 10 pt.)***, the title ***bold***; the text of abstract: ***Italic*** should be informative and completely self-explanatory, briefly present the topic, state the scope of the experiments, indicate significant data, and point out major findings and conclusions. The Abstract should be max.250 words. Complete sentences, active verbs, and the third person should be used, and the abstract should be written in the past tense. Standard nomenclature should be used and abbreviations should be avoided. No literature should be cited.

**INTRODUCTION** (*Arial 10 pt.*) should provide a clear statement of the problem, the relevant literature on the subject, and the proposed approach or solution. It should be understandable to colleagues from a broad range of scientific subjects. We should refer to the current stage of researches performed in the field of the paper to be published, by quoting up-to-date specialty studies, preferably published after 2006, excepting certain referential specialty books/studies, especially papers issued in magazines/journals/conferences/ISI quoted symposia or in other international data bases, which are well known and available.

**MATERIALS AND METHODS** (*Arial 10 pt.*) should be complete enough to allow experiments to be reproduced. However, only truly new procedures should be described in detail; previously published procedures should be cited, and important modifications of published procedures should be mentioned briefly. Methods in general use need not be described in detail.

**RESULTS** (*Arial 10 pt.*) should be clearly presented. The results should be written in the past tense when describing findings in the authors' experiments. Results should be explained, but largely, without referring to the literature. Discussion, speculation and detailed interpretation of data should not be included in the Results, but should be put into the Conclusions section.

**CONCLUSIONS** (*Arial 10 pt.*) The main conclusions drawn from results should be presented in a short Conclusions section. Do not include citations in this section.

**Formulae, symbols and abbreviations:** Formulae will be typeset in Italics (preferable using an Equation Editor) and should be written or marked as such in the manuscript, unless they require a different styling. They should be referred to in the text as Equation (4) or e.g. (4). The formulae should be numbered on the right side, between brackets (*Arial 10 pt.*):

$$P = F \cdot v \quad (1)$$

Terms of the equation and the unit measure should be explained, e.g.

*P* is the power, [W];

*F* – force, [N];

*v* – speed, [m/s]

SI units must be used throughout.

**Tables** should be self-explanatory without reference to the text. The details of the methods used in the experiments should preferably be described in the legend instead of in the text. The same data should not be presented both in table and graph form or repeated in the text.

Table's title will be typed *Arial 9 pt, Bold, Centered*

In the table, each row will be written Arial 9 pt, single-spaced throughout, including headings and footnotes.

The table should be numbered on the right side, *Arial 10 pt. (E.g.: Table 1)*

**Figures** (*Arial 9 pt., Bold, Center*) should be typed in numerical order (Arabic numerals). Graphics should be high resolution (e.g. JPEG). Figure number is followed by what represent the figure or graph e.g.:

**Fig.1 – Test stand**

**Legend:** *Arial 8 pt, Italic, Center, e.g.:*

*1 - plansifter compartments; 2- break rolls; 3 – semolina machines; 4 – reduction rolls; 5 – flour*

**ACKNOWLEDGMENTS** (*Arial 10 pt.*) of people, grants, funds etc should be brief (*if necessarily*).

**REFERENCES** (*Arial 10 pt.*)

*(In alphabetical order, in English and in the original publication language).*

*Minimum 10 references, last 10 years, minimum 3 references from the last 2 years*

It can be used “**References**” tool from the **Word Editor. APA Style (American Psychological Association)**  
<https://apastyle.apa.org/style-grammar-guidelines/references/examples>

**Authors are fully responsible for the accuracy of the references.**

References should be **alphabetically**, with complete details, as follows:

Examples:

**Books:** <https://apastyle.apa.org/style-grammar-guidelines/references/examples/book-references>

Jackson, L. M. (2019). *The psychology of prejudice: From attitudes to social action* (2nd ed.). American Psychological Association. <https://doi.org/10.1037/0000168-000>

Kesharwani, P. (2020). *Nanotechnology based approaches for tuberculosis treatment*. Academic Press.

Sapolsky, R. M. (2017). *Behave: The biology of humans at our best and worst*. Penguin Books.

Torino, G. C., Rivera, D. P., Capodilupo, C. M., Nadal, K. L., & Sue, D. W. (2019). *Microaggression theory: Influence and implications*. John Wiley & Sons. <https://doi.org/10.1002/9781119466642>

**In text:**

- **Paranthesisal citations:** (Jackson, 2019; Sapolsky, 2017)
- **Narrative citations:** Jackson (2019) and Sapolsky (2017)

**Journal Article:**

<https://apastyle.apa.org/style-grammar-guidelines/references/examples/journal-article-references>

Grady, J. S., Her, M., Moreno, G., Perez, C., & Yelinek, J. (2019). Emotions in storybooks: A comparison of storybooks that represent ethnic and racial groups in the United States. *Psychology of Popular Media Culture*, 8(3), 207–217. <https://doi.org/10.1037/ppm0000185>

**In text:**

- **Paranthesisal citation:** (Grady et al., 2019)
- **Narrative citation:** Grady et al. (2019)

**Conference or Symposium:**

<https://apastyle.apa.org/style-grammar-guidelines/references/examples/conference-proceeding-references>

Duckworth, A. L., Quirk, A., Gallop, R., Hoyle, R. H., Kelly, D. R., & Matthews, M. D. (2019). Cognitive and noncognitive predictors of success. *Proceedings of the National Academy of Sciences, USA*, 116(47), 23499–23504. <https://doi.org/10.1073/pnas.1910510116>

**In text:**

- **Paranthesisal citation:** (Duckworth et al., 2019)
- **Narrative citation:** Duckworth et al. (2019)

**Dissertation / Thesis:**

<https://apastyle.apa.org/style-grammar-guidelines/references/examples/published-dissertation-references>

Zambrano-Vazquez, L. (2016). *The interaction of state and trait worry on response monitoring in those with worry and obsessive-compulsive symptoms* [Doctoral dissertation, University of Arizona]. UA Campus Repository. <https://repository.arizona.edu/handle/10150/620615>

**In text:**

- **Paranthesisal citations:** (Kabir, 2016; Miranda, 2019; Zambrano-Vazquez, 2016)
- **Narrative citations:** Kabir (2016), Miranda (2019), and Zambrano-Vazquez (2016)

<https://apastyle.apa.org/style-grammar-guidelines/references/examples/unpublished-dissertation-references>

Harris, L. (2014). *Instructional leadership perceptions and practices of elementary school leaders* [Unpublished doctoral dissertation]. University of Virginia.

**In text:**

- **Paranthesisal citation:** (Harris, 2014)
- **Narrative citation:** Harris (2014)

**Patents:** Names and initials of authors, year (between brackets), patent title (Italic), patent number, country:

Grant, P. (1989). *Device for Elementary Analyses*. Patent. No.123456. USA.

**Legal regulations and laws, organizations:**

<https://apastyle.apa.org/style-grammar-guidelines/references/examples/iso-standard-references>

International Organization for Standardization. (2018). *Occupational health and safety management systems—Requirements with guidance for use* (ISO Standard No. 45001:2018). <https://www.iso.org/standard/63787.html>

Occupational Safety and Health Administration. (1970). *Occupational safety and health standards: Occupational health and environmental control: Occupational noise exposure* (OSHA Standard No. 1910.95). United States Department of Labor.

<https://www.osha.gov/laws-regs/regulations/standardnumber/1910/1910.95>

In text:

- **Parenthetical citations:** (International Organization for Standardization, 2018; Occupational Safety and Health Administration, 1970)
- **Narrative citations:** International Organization for Standardization (2018) and Occupational Safety and Health Administration (1970)

**Web references:** The full URL should be given in text as a citation, if no other data are known. If the authors, year, and title of the documents are known and the reference is taken from a website, the URL address has to be mentioned after these data.

**Citation in text**

Please ensure that every reference cited in the text is also present in the reference list (and vice versa).

**Do not cite references in the Abstract and Conclusions !**

Unpublished results, personal communications as well as URL addresses are not recommended in the references list. Making personal quotations (one, at most) should not be allowed, unless the paper proposed to be published is a sequel of the cited paper. Articles in preparation or articles submitted for publication, unpublished, personal communications etc. should not be included in the references list.

**Citations style**

**Text:** All citations in the text may be made directly (or parenthetically) as bellow.

- **single author:** the author's name (without initials, unless there is ambiguity) and the year of publication:  
"as previously demonstrated (Brown, 2010)".
- **two authors:** both authors' names and the year of publication: (Adam and Brown, 2008; Smith and Hansel, 2006; Stern and Lars, 2009)
- **three or more authors:** first author's name followed by "et al." and the year of publication: "As has recently been shown (Werner et al., 2005; Kramer et al., 2000) have recently shown ...."

**Citations of groups of references should be listed first alphabetically, then chronologically.**

**Units, Abbreviations, Acronyms**

- Units should be metric, generally SI, and expressed in standard abbreviated form.
- Acronyms may be acceptable, but must be defined at first usage.

**2. REVIEWS**

Summaries, reviews and perspectives covering topics of current interest in the field, are encouraged and accepted for publication. Reviews do not have the requirements for regular articles. However, should include: (\*) an introductory chapter, (\*\*) a careful and critical presentation of the relevant aspects of the topic approached and (\*\*\*) emphasis of the aspects that aren't known and require further research to progress. Reviews should be concise (max. 12 pages).



**Edited by: INMA Bucharest**

6, Ion Ionescu de la Brad Blvd., sect. 1, Bucharest, ROMANIA

Tel: +4021.269.32.60; Fax: +4021.269.32.73

[https:// inmateh.eu/](https://inmateh.eu/)

e-mail: [inmatehjournal@gmail.com](mailto:inmatehjournal@gmail.com)